frontiers | Research Topics

Optimal design and efficiency improvement of fluid machinery and systems, volume II

Edited by
Leilei Ji, Ramesh K. Agarwal, Kan Kan, Yongfei Yang, Ran Tao, Yang Yang and Alexandre Presas

Published in
Frontiers in Energy Research

ISSN 1664-8714
ISBN 978-2-8325-6701-2
DOI 10.3389/978-2-8325-6701-2

Generative AI statement
Any alternative text (Alt text) provided alongside figures in the articles in this ebook has been generated by Frontiers with the support of artificial intelligence and reasonable efforts have been made to ensure accuracy, including review by the authors wherever possible. If you identify any issues, please contact us.

About Frontiers

Frontiers is more than just an open access publisher of scholarly articles: it is a pioneering approach to the world of academia, radically improving the way scholarly research is managed. The grand vision of Frontiers is a world where all people have an equal opportunity to seek, share and generate knowledge. Frontiers provides immediate and permanent online open access to all its publications, but this alone is not enough to realize our grand goals.

Frontiers journal series

The Frontiers journal series is a multi-tier and interdisciplinary set of open-access, online journals, promising a paradigm shift from the current review, selection and dissemination processes in academic publishing. All Frontiers journals are driven by researchers for researchers; therefore, they constitute a service to the scholarly community. At the same time, the *Frontiers journal series* operates on a revolutionary invention, the tiered publishing system, initially addressing specific communities of scholars, and gradually climbing up to broader public understanding, thus serving the interests of the lay society, too.

Dedication to quality

Each Frontiers article is a landmark of the highest quality, thanks to genuinely collaborative interactions between authors and review editors, who include some of the world's best academicians. Research must be certified by peers before entering a stream of knowledge that may eventually reach the public - and shape society; therefore, Frontiers only applies the most rigorous and unbiased reviews. Frontiers revolutionizes research publishing by freely delivering the most outstanding research, evaluated with no bias from both the academic and social point of view. By applying the most advanced information technologies, Frontiers is catapulting scholarly publishing into a new generation.

What are Frontiers Research Topics?

Frontiers Research Topics are very popular trademarks of the *Frontiers journals series*: they are collections of at least ten articles, all centered on a particular subject. With their unique mix of varied contributions from Original Research to Review Articles, Frontiers Research Topics unify the most influential researchers, the latest key findings and historical advances in a hot research area.

Find out more on how to host your own Frontiers Research Topic or contribute to one as an author by contacting the Frontiers editorial office: frontiersin.org/about/contact

Optimal design and efficiency improvement of fluid machinery and systems, volume II

Topic editors

Leilei Ji — Jiangsu University, China
Ramesh K. Agarwal — Washington University in St. Louis, United States
Kan Kan — College of Energy and Electrical Engineering, China
Yongfei Yang — Nantong University, China
Ran Tao — China Agricultural University, China
Yang Yang — Yangzhou University, China
Alexandre Presas — Universitat Politecnica de Catalunya, Spain

Citation

Ji, L., Agarwal, R. K., Kan, K., Yang, Y., Tao, R., Yang, Y., Presas, A., eds. (2025). *Optimal design and efficiency improvement of fluid machinery and systems, volume II*. Lausanne: Frontiers Media SA. doi: 10.3389/978-2-8325-6701-2

Table of contents

frontiers | Frontiers in Energy Research

TYPE Editorial
PUBLISHED 30 July 2025
DOI 10.3389/fenrg.2025.1636660

OPEN ACCESS

EDITED AND REVIEWED BY
Francois M. A. Marechal,
Swiss Federal Institute of Technology
Lausanne, Switzerland

*CORRESPONDENCE
Leilei Ji,
leileiji@ujs.edu.cn

RECEIVED 28 May 2025
ACCEPTED 23 July 2025
PUBLISHED 30 July 2025

CITATION
Yang Y, Ji L, Agarwal RK, Kan K, Tao R and Presas A (2025) Editorial: Optimal design and efficiency improvement of fluid machinery and systems: volume II.
Front. Energy Res. 13:1636660.
doi: 10.3389/fenrg.2025.1636660

Editorial: Optimal design and efficiency improvement of fluid machinery and systems: volume II

Yang Yang[1,2], Leilei Ji[3]*, Ramesh K. Agarwal[4], Kan Kan[5], Ran Tao[6] and Alexandre Presas[7]

[1]College of Hydraulic Science and Engineering, Yangzhou University, Yangzhou, China, [2]Key Laboratory of Fluid and Power Machinery, Ministry of Education, Chengdu, Sichuan, China, [3]National Research Center of Pumps, Jiangsu University, Zhenjiang, China, [4]Department of Mechanical Engineering and Materials Science, Washington University in St. Louis, St. Louis, MO, United States, [5]College of Energy and Electrical Engineering, Hohai University, Nanjing, China, [6]College of Water Resources and Civil Engineering, China Agricultural University, Beijing, China, [7]Centre of Industrial Diagnostics and Fluid Dynamics (CDIF), Universitat Politècnica Catalunya (UPC), Barcelona, Spain

KEYWORDS

fluid machinery, optimization, energy dissipation, hydraulic performance, computational fluid dynamics

Editorial on the Research Topic
Optimal design and efficiency improvement of fluid machinery and systems: volume II

Introduction

Fluid machinery is integral to a wide range of industries, from energy generation to transportation, and from industrial processing to environmental protection. The challenge of improving the performance, reliability, and efficiency of these systems has led to significant advancements in their design and operation. *Optimal Design and Efficiency Improvement of Fluid Machinery and Systems: Volume II* compiles 13 insightful research papers that tackle a variety of issues in fluid machinery, including optimization techniques, performance enhancement, and energy efficiency. These contributions offer both theoretical insights and practical applications, helping to address complex challenges in modern fluid systems.

This volume covers a wide spectrum of fluid machinery, including pumps, turbines, compressors, and hydrodynamic couplings, and uses cutting-edge methodologies such as numerical simulations, experimental validation, and optimization algorithms. The papers have been categorized into three major themes: Optimization and Performance Enhancement, Cavitation and Flow Instabilities, and Fluid-Structure Interaction and Hydraulic Losses. Each category reflects the critical areas of research in the field of fluid machinery.

Optimization and performance enhancement

This category addresses the ongoing efforts to optimize the design and improve the performance of various fluid machinery systems. Zhai et al. present a study on hydrogen circulation pumps (HCPs) that introduces a multifactor and multi-objective optimization method for improving hydrogen utilization efficiency. The optimization of key parameters, such as the rotor blade number and the helix angle, has led to significant performance improvements, as demonstrated by experimental validation. Similarly, Yang et al. explore the design of electric coolant pumps (ECPs) for electric vehicles, with a focus on how suction pipe structures affect hydraulic performance and efficiency. Their findings highlight the importance of optimizing the flow patterns within the pump to improve energy efficiency.

The research conducted by Wang et al. on marine gas turbines explores how inlet distortion impacts the turbine's aerodynamic stability, providing a novel simulation device to predict and analyze pressure distortion. Their work offers a critical tool for ensuring stable turbine performance under varying conditions. Additionally, Ma et al. investigate the performance of self-priming jet pumps in irrigation systems, emphasizing the challenges of achieving optimal performance while maintaining compact designs. This research has important implications for developing more efficient and stable irrigation systems.

Cavitation and flow instabilities

Cavitation and flow instability are two of the most critical challenges in fluid machinery design and operation, affecting performance and reliability. The study by Xiao et al. provides a deep analysis of pressure pulsation in pump turbines, a major contributor to operational instability. Using the Hilbert Huang transform, they uncover complex frequency characteristics that inform the design of more stable turbines. Similarly, Lang et al. explore cavitation monitoring in non-clogging pumps, utilizing an optimized neural network for cavitation detection. Their findings provide a robust methodology for real-time diagnosis, which could significantly improve the operational reliability of pumps.

Cui et al. focus on the cavitation behavior in hydrodynamic couplings, a common component in heavy-duty mining equipment. Their work emphasizes the instability caused by cavitation in low-speed ratios, providing a model that predicts cavitation development and its detrimental effects on performance. In the same vein, Zhang et al., Zhang et al. delve into cavitating and non-cavitating wake flows around circular cylinders. By employing large eddy simulation (LES) and the Schnerr-Sauer cavitation model, they provide valuable insights into how cavitation alters energy dissipation and vortex dynamics in fluid systems.

Fluid-structure interaction and hydraulic losses

Understanding the complex interactions between fluid flows and structural components is essential for improving the efficiency of fluid machinery. Zhu et al. study the impact of the number of blades on energy dissipation and flow patterns in mixed-flow pumps, highlighting the role of fluid-structure interaction in optimizing pump performance. The increase in blade number improves flow characteristics but can also induce rotating stall under certain conditions. Huo and Zha investigate how blade inlet geometry impacts the efficiency and hydraulic losses in mixed-flow pumps. Their findings underscore the importance of blade design in minimizing flow losses and enhancing overall pump performance.

Chang et al. take a different approach by studying the wear characteristics of U-shaped elbows using a CFD-DEM coupling model. Their research investigates how particle flow dynamics, including collision frequency and wear rate, are influenced by factors such as bend spacing and particle concentration. The insights gained here are crucial for optimizing the design and operation of piping systems in industrial applications.

Lastly, Yan et al. introduce a novel fluidic oscillator design, employing movable feedback channels and resonators to regulate jet frequency. This design offers a more stable and efficient solution for flow control applications, particularly in compressor systems, where frequency adaptation is critical under varying operational conditions.

Summary

In conclusion, the studies presented in Volume II of Optimal Design and Efficiency Improvement of Fluid Machinery and Systems provide valuable advancements in the field of fluid machinery optimization. The research addresses critical challenges such as cavitation, flow instability, energy dissipation, and fluid-structure interaction, offering innovative solutions to improve the design and performance of fluid systems across a variety of industrial applications.

Gratitude is extended to all the authors for their dedicated contributions and to the reviewers whose insightful feedback has significantly enhanced the quality of this Research Topic. Appreciation is also due to the editorial board and publication team for their continuous support and effort in ensuring the successful compilation and publication of this volume.

Finally, thanks are given to the readers for their engagement with this Research Topic. It is hoped that the findings and insights shared in this volume will inspire further research and innovation in the optimization of fluid machinery, leading to the development of more efficient and sustainable systems in the future.

Author contributions

YY: Writing – original draft. LJ: Writing – review and editing. RA: Writing – review and editing, Supervision. KK: Writing – review and editing. RT: Writing – review and editing, Supervision. AP: Supervision, Writing – review and editing.

Funding

The author(s) declare that financial support was received for the research and/or publication of this article. This editorial

was supported by the National Natural Science Foundation of China (Grant Nos 52409122; 52309112), Natural Science Foundation of Jiangsu Province (Grant No. BK20220587), Open Research Subject of Key Laboratory of Fluid Machinery and Engineering (Xihua University), Sichuan Province (Grant No. LTDL-2024005), China Postdoctoral Science Foundation (Grant No. 2022TQ0127).

Conflict of interest

The authors declare that the research was conducted in the absence of any commercial or financial relationships that could be construed as a potential conflict of interest.

Generative AI statement

The author(s) declare that no Generative AI was used in the creation of this manuscript.

Publisher's note

All claims expressed in this article are solely those of the authors and do not necessarily represent those of their affiliated organizations, or those of the publisher, the editors and the reviewers. Any product that may be evaluated in this article, or claim that may be made by its manufacturer, is not guaranteed or endorsed by the publisher.

frontiers | Frontiers in Energy Research

TYPE Original Research
PUBLISHED 20 July 2023
DOI 10.3389/fenrg.2023.1236087

OPEN ACCESS

EDITED BY
Ran Tao,
China Agricultural University, China

REVIEWED BY
Di Zhu,
China Agricultural University, China
Faye Jin,
Tsinghua University, China

*CORRESPONDENCE
Weiyu Lu,
weiyu_lu@njtech.edu.cn

RECEIVED 07 June 2023
ACCEPTED 30 June 2023
PUBLISHED 20 July 2023

CITATION
Yan Z, Lu Y, Yang X, Deng Q and Lu W (2023), Characteristics of a novel fluidic oscillator with movable feedback channels and resonators.
Front. Energy Res. 11:1236087.
doi: 10.3389/fenrg.2023.1236087

Characteristics of a novel fluidic oscillator with movable feedback channels and resonators

Zhoujun Yan, Yongtong Lu, Xiangfen Yang, Qiulin Deng and Weiyu Lu*

School of Physical and Mathematical Sciences, Nanjing Tech University, Nanjing, China

In this study, a novel fluidic oscillator suitable for use as a key component of a flow control device is proposed and investigated through numerical simulations. The new layout adds resonators to a typical fluidic oscillator with dual feedback channels, and the length of the feedback loop is designed to be adjustable. This fluidic oscillator with movable feedback channels and resonators can generate a jet with an adjustable frequency, and it has smaller total pressure loss than the baseline model. Numerical results show that the movement of the feedback channels regulates the degree of coupling between the feedback channels and resonators to generate different orders of jet frequencies. This self-excited fluidic oscillator with adjustable jet frequency is more adaptive than typical designs when dealing with complex flow separation conditions, and it will be more stable because the frequency adjustment requires neither high-frequency movable mechanisms nor external energy input. Moreover, the frequency switching phenomenon is observed in special cases, which may help improve the efficiency of the compressor blades with a drastically changed dominant frequency under off-design conditions or with multiple dominant frequencies, such as tip leakage flow and shock–boundary layer interaction.

KEYWORDS

fluidic oscillator, feedback channel, resonator, unsteady flow control, numerical simulation

1 Introduction

The efficiency and stability of compressors at high loads directly affect the performance of aeroengines. When blade loads are increased to levels far above the current aerodynamic design level, flow separation usually occurs due to high inverse pressure gradients or shock–boundary layer interaction, causing a dramatic decrease in fluid mechanical efficiency and even engine surge. Through flow control techniques, flow separation can be reduced or even eliminated, thereby improving the pressure ratio, efficiency, and stability margin of compressors considerably (Liu et al., 2019; Qin et al., 2020; Lu et al., 2022).

Flow control mainly includes steady and unsteady flow control. In recent decades, researchers have shown great interest in unsteady flow control techniques that utilize flow instabilities. The main difference between steady and unsteady flow control techniques lies in whether or not the flow control excitation is time-dependent. The advantage of unsteady flow control over steady flow control is that it can achieve the same control effect with an energy saving of one to two orders of magnitude (Greenblatt and Wygnanski, 2000). Therefore, unsteady flow control has elicited attention from researchers and has become a focus of flow control research.

Unsteady flow control mainly includes acoustic excitation (Lepicovsky et al., 1986; Nishioka et al., 1987; Açıkel and Genç, 2016), synthetic jets (Glezer and Amitay, 2002) (Cao et al., 2020), unsteady blowing and suction (Kim et al., 2017), wall oscillation (Choi et al., 2002), and traveling wave wall control (Wu et al., 2003) (Lu et al., 2019). Belonging to unsteady blowing, fluidic oscillators are devices that can create a sweeping jet with a fixed frequency through a stable mass flow input. Oscillation in fluidic oscillators is produced by the Coanda effect, which attaches the fluid stream alternatively to one of the adjacent walls in the mixing chamber. The produced oscillation is self-induced and self-sustained (Tomac and Sundström, 2019). If the inlet and outlet of a fluidic oscillator are connected to a high-pressure and a low-pressure air source, respectively, the fluidic oscillator can utilize the flow instability to enable the outlet to generate a periodic sweeping jet, which can be used as the unsteady excitation required for unsteady flow control. As an unsteady flow control method, self-excited fluidic oscillators have a simple, reliable, low-maintenance geometry and can generate a self-sustaining and oscillating periodic jet without the use of movable parts. Thus, they have good application prospects. Their potential has been explored in many areas, such as fluid mechanics and aeronautics. Therefore, the demand for fluidic oscillators in engineering applications has increased considerably.

Fluidic oscillators have the potential to function as flow control devices by producing oscillating velocity fields. However, their utilization as unsteady flow control devices has received wide attention from researchers since 2010s. Many typical fluidic oscillators are very efficient in generating oscillating velocity fields and their effects and mechanism have been thoroughly studied in recent years due to their robustness and potential to meet most of the application requirements. Cerretelli and Kirtley (Cerretelli and Kirtley, 2009) experimentally investigated the control effect of a fluidic oscillator on flow separation in a diffuser and found that the fluidic oscillator can save 60% jet momentum compared with steady flow control when the flow field is fully reattached. Koklu (Koklu, 2018) compared the jet generated by a fluidic oscillator with those generated by several common flow control methods, such as steady jet, vortex-generating jet, and vortex generator through experiments and reported that the control performance of the fluidic oscillator is better than that of the steady jet and vortex-generating jet in the separation flow of the ramp structure. Wang et al. (Wang et al., 2019) proposed the concepts of high-pressure compressed wave and low-pressure expansion wave and used pressure wave reflection theory to explain oscillation behavior. Ostermann et al. (Ostermann et al., 2017) (Ostermann et al., 2019) addressed the flow control mechanism of fluidic oscillators and found that because the sweeping jet is on a plane perpendicular to the external crossflow, the effect of the jet is similar to that of the streamwise vortical structures generated by a vortex generator. Tomac and de Luzan (Tomac and de Luzan, 2020) experimentally and numerically investigated and characterized a synchronized fluidic oscillator, which is especially helpful for solving flow control problems exhibiting two separation points, such as flow-over cylinders or surfaces exposed to differential pressure (i.e., wingtips). Some researchers have also focused on self-excited fluidic oscillators for engineering applications and have conducted full-scale experiments and numerical simulations. Cerretelli et al. (Cerretelli et al., 2010) used a built-in fluidic oscillator to control a DU96 airfoil representing a typical wind turbine blade and discovered that appropriate control parameters can increase the airfoil lift by up to 60%. Shmilovich et al. (Shmilovich et al., 2018) placed an array of multiple fluidic oscillators on the vertical tail of an aircraft and verified the effectiveness of this flow control approach through numerical simulations and experiments at the whole-aircraft level of the B757 demonstrator.

Unsteady flow control devices require a broad range of excitation frequencies for effective operation in some cases. For example, in a compressor at an off-design point, the dominant frequency of the separated flow differs from that at the design point. This condition means that the optimum flow control frequency also changes, so the frequency of unsteady flow control devices, such as fluidic oscillators, needs to be adjusted under different operating conditions. Flows with tip leakage, corner separation, or shock–boundary layer interactions also have two different dominant frequencies. Under different operating conditions, modes with different dominant frequencies need to be controlled. Thus, researchers have attempted to establish methods to change the frequency of flow control devices. As unsteady fluid control devices, fluidic oscillators typically adjust the sweeping frequency of the output jet through its mass flow rate. However, other existing methods can be used to adjust the jet frequency. For example, Tomac and Sundström (Tomac and Sundström, 2019) added two control jets in the fluidic oscillator mixing chamber. This approach can change the jet frequency of the oscillator through the K-H instability between the two control jets and the mainstream to generate ultra-high frequency jets. Culley (Culley, 2006) added a solenoid pressure valve to the inlet of the oscillator to regulate the pressure in the control channel and thus control the frequency of the jets generated by the devices. The highest frequency measured from this experimental device is 312 Hz due to the limitations in the switching speed of the solenoid valve. This frequency may still be relevant for some applications, but this device cannot handle flow control situations that require frequencies higher than 312 Hz. In addition, the constant external excitation and high-frequency motion of the components increase the energy consumption and reduce mechanical reliability. Moreover, Gregory et al. (Gregory et al., 2009) used a piezoelectric bender to control the frequency of a fluidic oscillator. Their design is similar to these with solenoid valves. Given that a bending tube is added, the frequency is affected by the characteristics of the moving parts when this method is adopted. In the frequency range of 0–250 Hz, oscillation frequency is independent of supply pressure. However, the efficiency of this approach decreases at frequencies exceeding the piezoelectric bender's resonance frequency (121 Hz). Analysis of the existing techniques for changing the frequency of fluidic oscillators indicates that changing the frequency by adding movable parts, electric devices, or additional accessories may raise new issues, such as reduced engineering reliability, increased maintenance costs, shortened service life, and reduced energy utilization efficiency.

Aside from fluidic oscillators that can adjust jet frequency, we consider a new configuration that avoids using external excitation, high-frequency movable parts, or electromagnetic actuators. At

present, there are two typical types of wall-attachment fluidic oscillator designs: with feedback channels and with resonators (Gregory and Tomac, 2013). For the fluidic oscillator with feedback channels, the frequency of the jet generated by the device is proportional to the flow rate through the oscillator (Ostermann et al., 2019). Thus, jet frequency can be adjusted via the flow rate. However, generating ultra-high-frequency jets is difficult. For the fluidic oscillator consisting of a conjugate acoustic resonator (Tesař et al., 2013), jet frequency is constant and independent of the flow rate through the fluidic oscillator. Ultra-high-frequency jets can be generated, but the jet frequency is difficult to adjust because it is determined by the geometry of resonators. Thus, we consider a new fluidic oscillator with movable feedback channels and resonators and attempt to combine the advantages of both, namely, the ability to adjust the frequency by flow rates while generating high frequencies and the ability to modulate the Strouhal number of the oscillator by moving the feedback channels, thus changing the oscillator characteristics.

In this study, the characteristics of the fluidic oscillator with feedback channels and resonators are studied numerically. In Section 2, the concept of the fluidic oscillator is introduced in terms of structural design ideas and principles. In Section 3, the numerical method used in this study is presented together with the structural parameters, mesh generation, and solver settings. Simulation reliability is also verified through a comparison with existing experimental results. In Section 4, we present the theoretical basis for the sweeping frequency in fluidic oscillators with only feedback channels and those with only resonators. In Section 5, we analyze the numerical results to express our understanding of the unique characteristics of the new fluidic oscillator. With this study, we hope to improve the understanding and application of fluidic oscillators with adjustable frequencies.

2 Concept of a fluidic oscillator with movable feedback channels and resonators

We propose a new fluidic oscillator with adjustable jet frequencies and sweeping amplitudes. For easy distinction, we refer to the baseline model used for reference as the "prototype model" and to the new proposed oscillator as the "modified model". In terms of geometry, on the basis of the prototype fluidic oscillator shown in Figure 1A (adopted from Ref. (Cerretelli et al., 2010)), we add resonators at the beginning and end of each of the two feedback channels so that the fluidic oscillator has both feedback channels and resonators. We expect this design to combine the advantages of the two typical types of oscillators mentioned in the Introduction. The feedback channel is designed to move laterally within the stroke, thus allowing the adjustment of the oscillation characteristics to produce sweeping jets with different characteristics.

The specific structure of the fluidic oscillator with feedback channels and resonators is shown in Figure 1B. It includes an inlet, a mixing chamber, and an outlet, which are sequentially located on the central axis of the device and constitute the main flow path. A feedback loop consisting of a feedback channel and a resonator is provided both on the left and right, respectively, of the central axis of the device. If the resonator is not considered, the main flow path in the mixing chamber will adhere to the left or right wall surface of the mixing chamber due to the Coanda effect. For example, if the main flow path is attached to the right wall of the mixing chamber, the jet will be attached to the left wall of the outlet and form a right feedback loop, and the flow along the right feedback loop will push the main flow path at the entrance of the mixing chamber to attach it to the left wall of the mixing chamber. Next, the jet will flow along the right wall of the outlet and form a left feedback loop. These two processes

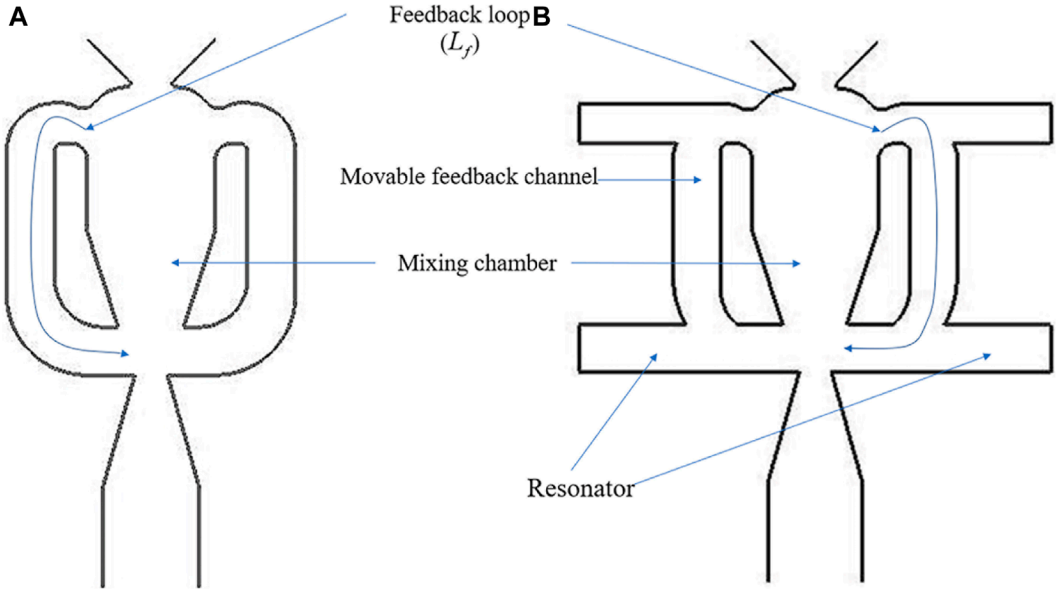

FIGURE 1
Comparison between **(A)** the prototype fluidic oscillator (Cerretelli et al., 2010) and **(B)** the fluidic oscillator with both feedback channels and resonators.

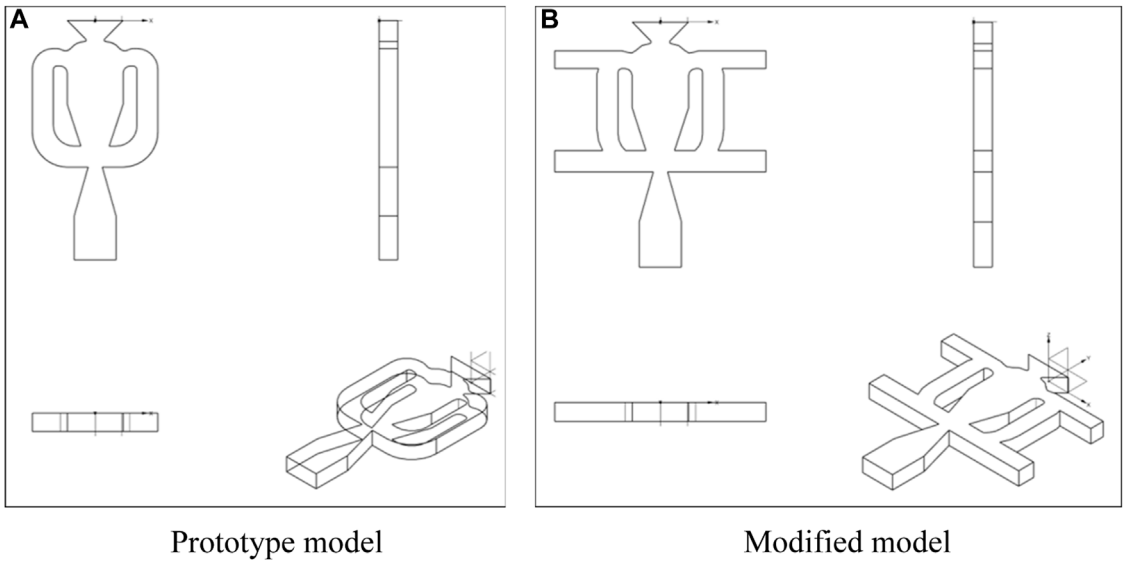

FIGURE 2
Geometric configurations of **(A)** Prototype model and **(B)** Modified model in 3D perspective.

occur alternately, thus forming a certain frequency of the sweeping jet at the outlet. Moreover, if the feedback channel is not considered, a standing wave with a fixed frequency will be generated at the entrance of the mixing chamber due to the presence of resonators on both sides of the entrance of the mixing chamber, making the jet frequency consistent with this standing wave frequency (Field and Fricke, 1998).

Given that resonators and feedback channels exist simultaneously, the characteristics of the oscillator in this study are formed by the joint action and mutual coupling of resonators and feedback channels. By changing the feedback loop length through the movement of the feedback channel, the jet characteristics are likely to be changed. And the jet sweeping angle and frequency can be adjusted through the different degrees of coupling between the feedback channels and resonators. This approach can effectively control the flow for different separation vortex frequencies and improve the adaptability of the device to the working conditions.

3 Numerical methods

In this study, the sweeping jet is generated by a fluidic oscillator with both feedback channels and resonators (Figure 2). This oscillator is a modification of a prototype oscillator, which has been examined and characterized in various studies (e.g., Ostermann et al., 2018). The spatial oscillations of the jet are induced only by internal dynamics and geometry, so the generated jet is self-induced and self-sustained. With reference to the modified fluidic oscillator, the width d of the outlet (i.e., throat) is 25 mm, the length of the resonator (denoted as L_R) is 128 mm, and the outlet semi-spread angle is 50° (Table 1). The compressibility effect can be ignored in this study because the highest Mach number at the throat is estimated to be 0.28 under the maximum mass flow rate supply.

TABLE 1 Main parameters of the fluidic oscillator.

Part	Parameter	Value
Prototype Fluidic Oscillator	Throat width	25 mm
	Outlet semi-spread angle	50°
	Feedback channel length	218.6 mm
Modified Fluidic Oscillator	Throat width	25 mm
	Outlet semi-spread angle	50°
	Maximum feedback channel length	321.8 mm
	Minimum feedback channel length	207.8 mm
	Length of resonators	128 mm
	Mixing chamber length	174.4 mm

A computational fluid dynamics (CFD) approach is used to evaluate the characteristics of the fluidic oscillator in different modes, including the effect of the length of the feedback channels on the sweeping frequency of the fluidic oscillator and the total pressure loss of the oscillator. The simulations are implemented on a workstation that uses an octa-core Intel Core i7 9700 CPU. An unsteady flow case needs about 20 h to finish computation. The validity and feasibility of the numerical method are verified based on the prototype. The modified model includes the design of the feedback channel as a movable mechanism so that the total length of the feedback loop can be adjusted within a certain range, which may also result in a variation in the Strouhal number.

To simulate the sweeping jet generated by the fluidic oscillator with moveable feedback channels and resonators, a structured mesh is constructed using ANSYS ICEM. The mesh topology is shown

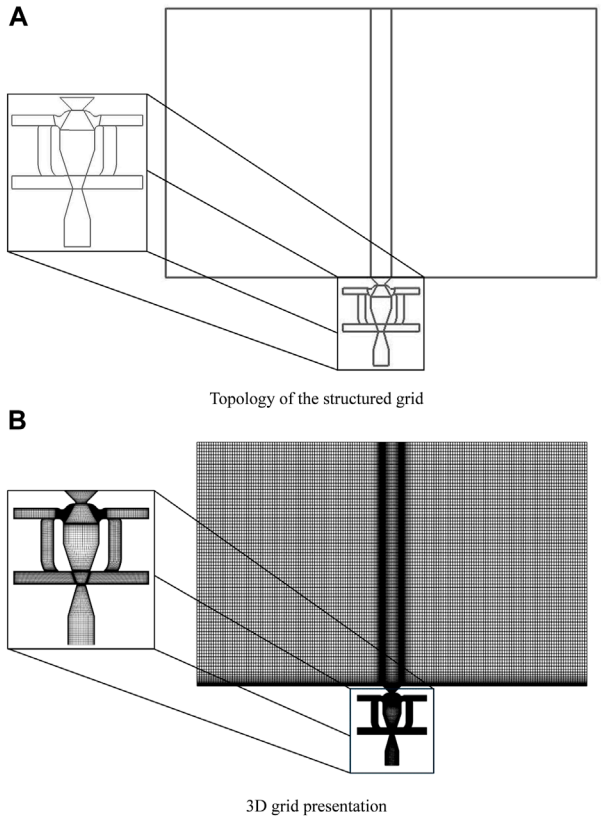

FIGURE 3
(A) Grid topology and **(B)** 3D Grid of the fluidic oscillator with both feedback channels and resonators.

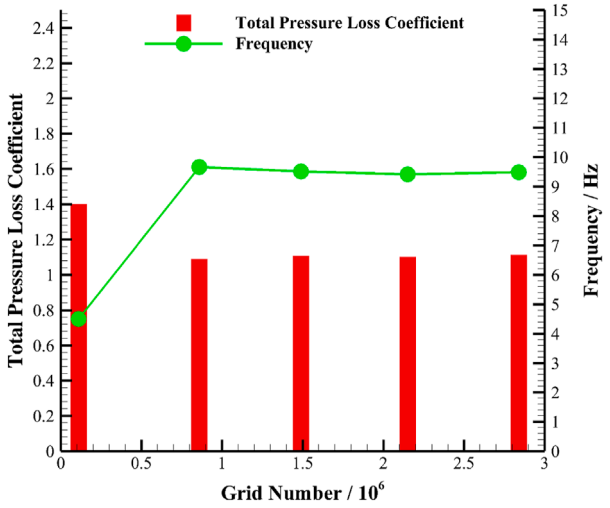

FIGURE 4
Grid dependence results.

in Figure 3, and 16 3D blocks are used. A grid-independence test is performed based on the prototype, and Figure 4 shows that the jet frequency and total pressure loss coefficient generated by the prototype are nearly invariant for grid numbers larger than 860,000. Therefore, using the grid number of about 1,000,000 can save computational resources while obtaining a sufficiently high computational accuracy. The grid of the feedback channel part is divided independently, and the moving mesh is used to generate meshes at different positions. Before the mesh is moved to the designed position, the translational speed is maintained at a low level to avoid unsteady effects.

The ideal air model is selected as the fluid model. The k-omega shear stress transport (k-ω SST) turbulence model is used in ANSYS Fluent to calculate the steady flow as the initial field, and unsteady numerical simulations are performed using large eddy simulation (LES). In LES, the wall-adapting local eddy–viscosity (WALE) sub-grid model is selected. Given that the mesh of the feedback channels and the main body of the oscillator structure are divided separately, interfaces are set between the moving mesh (feedback channel mesh) and the stationary mesh (the rest of the mesh) so that each part of the mesh is connected. The boundary condition at the inlet of the fluidic oscillator is constrained by a given mass flow rate, and a constant static pressure of standard atmosphere is provided at the outlets. Moreover, a periodic boundary is set in the staggered direction, thus reducing the cost of the 3D LES calculation. In this calculation, dual time stepping is employed, and the physical time step is set to 1×10^{-3} s. The flow losses of the device are evaluated by the total pressure loss coefficient, which is defined as follows:

$$\omega = \frac{P_0^* - P_1^*}{0.5\rho V^2}, \tag{1}$$

where P_0^* is the time-average total pressure at the inlet, P_1^* is the time-average total pressure at the outlet, ρ is the density of the fluid, and V is the velocity magnitude of the sweeping jet.

The numerical simulation (CFD) results of the prototype fluidic oscillators are compared with the experimental results (Ostermann et al., 2018), as illustrated in Figures 5A, B. Figure 5A shows the transient sweeping jet angle of the prototype fluidic oscillator obtained by the simulation (operating at a jet velocity of 19 m/s) and experiment (the experimental data obtained from Ref. (Ostermann et al., 2018)). Figure 5B presents the jet frequency as a function of velocity obtained from the numerical simulations and experiments. In CFD, the jet angle is obtained by monitoring the normal and tangential flow velocity components at the throat of the outlet, whereas in the experiments, the sweeping angle is monitored on a section at a certain distance from the outlet. Thus, the two results show some differences. According to Figures 5A, B, the CFD results generally agree with the experimental results. The sweeping angle of the jet obtained by CFD demonstrates a cyclic trend that approximates a sinusoidal function, which is consistent with the experimentally obtained results. In addition, the experimental dominant frequency of the jet is 9.31 Hz, which is very close to the value of 9.66 Hz obtained by CFD. Figures 5A, B illustrate that the numerical method can predict the transient characteristics of the unsteady flow field of the oscillator. Therefore, this numerical method can be applied to the numerical computation of the modified fluidic oscillator in the subsequent sections.

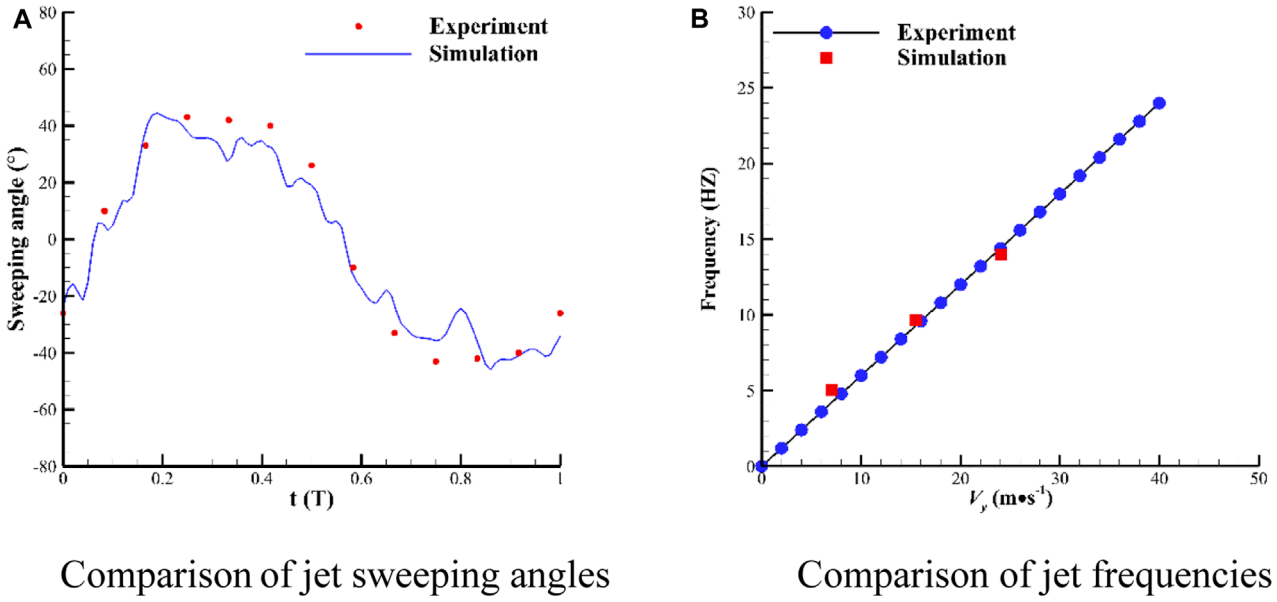

FIGURE 5
Comparison of **(A)** jet sweeping angles (T denotes a time period) and **(B)** jet frequencies between numerical and experimental results.

4 Theory of sweeping frequency in two types of fluidic oscillators

In the prototype, jet frequency is proportional to velocity at low jet velocities, but the jet frequency of the fluidic oscillator with resonators is related only to the structural parameters (e.g., length of the resonator). The modified fluidic oscillator combines the structural features of the two oscillators. So, the following sections analyzes the frequency characteristics of the prototype and modified fluidic oscillator theoretically.

4.1 Fluidic oscillators with feedback channels only

In this section, we analyze the theoretical formulation of jet frequency in the prototype oscillator and apply numerical data to it.

For fluidic oscillators with feedback channels only, jet sweeping frequency is related to the geometry and mass flow rate of the oscillator. Ostermann et al. (Ostermann et al., 2019) and Simões et al. (Simões et al., 2005) proposed the equation for the sweeping jet frequency of a fluidic oscillator with feedback channels as follows:

$$f = \frac{1}{T} \approx \frac{1}{2} \frac{1}{\left(\frac{L_f}{c} + \frac{\xi L}{V_y}\right)}, \tag{2}$$

where L_f is the length of the feedback channel, c is the speed of sound, V_y is normal (y-axis direction as illustrated in Figure 2) jet velocity, L is the length of the mixing chamber, and ξ is the empirical constant for correction. When $V_y \ll c$, $\frac{L_f}{c}$ is considered to be a negligible quantity, and Eq. 2 can be simplified as follows:

$$f \approx \frac{1}{2} \frac{V_y}{\xi L}. \tag{3}$$

Thus, f is proportional to V_y (referred to as linear relation, and this situation is illustrated in Figure 5). When $O\left(V_y/c\right) = 1$, that is, when the compressibility of the fluid needs to be considered, f and V_y are nonlinearly related (referred as nonlinear relation).

We use the relations in Eqs 2, 3 to fit the numerical simulation results of the prototype, as shown in Figure 6. In Figure 6, when the jet velocity is below 30 m/s, the Mach number is much lower than 0.3, and the compressibility effect is negligible. Under this circumstance, the frequency of the jet generated by the oscillator is approximately proportional to the jet velocity, and the Strouhal number obtained from the numerical simulation is calculated from this slope as 0.0157, which basically coincides with the experimental value of 0.015 in Ref. (Ostermann et al., 2018). When the jet velocity is higher than 30 m/s, the increment in jet frequency decreases with the increase in the Mach number, indicating a nonlinear relationship.

In Eq. 2, ξ is an empirical constant. According to Ref. (Simões et al., 2005), the value of ξ for an oscillator varies with velocity and oscillation frequency. From the numerical simulation results, we find that in this case, the empirical constant ξ obtained is approximately proportional to the inlet flow rate or normal jet velocity V_y (Figure 7), and the fitting relation is

$$\xi = 0.0515 V_y + 3.6877. \tag{4}$$

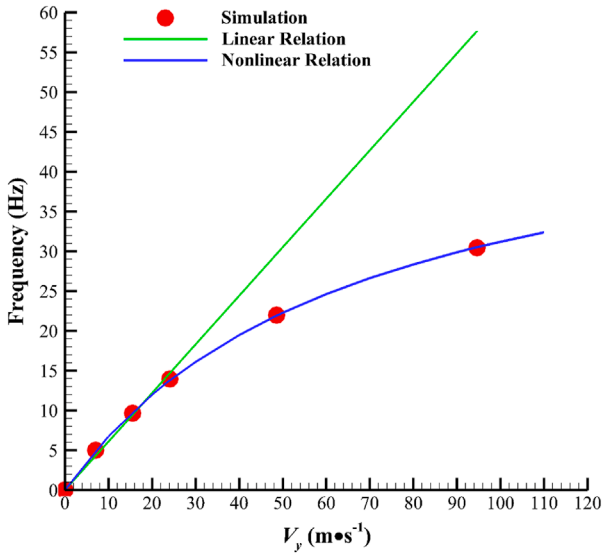

FIGURE 6
Relationship between jet frequency and velocity in the prototype.

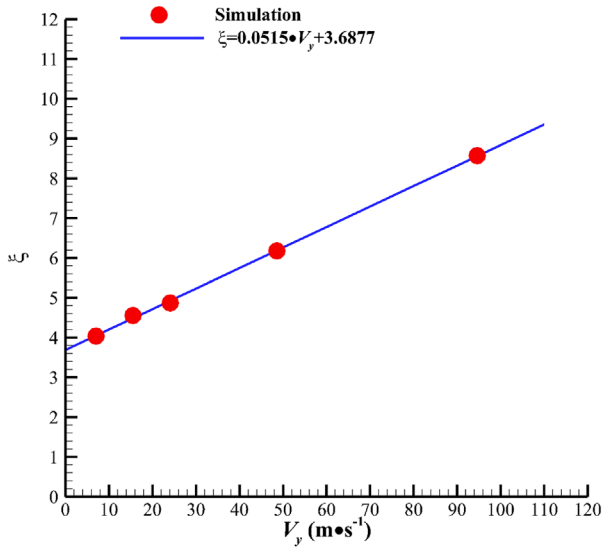

FIGURE 7
Relationship between empirical constant ξ and jet normal velocity V_y in the prototype.

By substituting ξ in Eq. 4 into Eq. 2, we obtain the nonlinear relation between the oscillation frequency and jet velocity of the prototype. As illustrated by the nonlinear relation in Figure 7, the nonlinear Eq. 2 obtained by considering the relation of ξ and V_y is in good agreement with the numerical simulation results. Considering that the fluidic oscillator analyzed in this study is proposed by modifying the prototype, we use this relation as the basis for evaluating the effect of geometric parameters when we investigate the characteristics of the modified model in the following sections.

4.2 Fluidic oscillator with dual quarter-wave resonators

In this section, we derive the jet frequency law of the fluidic oscillator with dual quarter-wave resonators. The relationship between jet frequency and resonator length in a fluidic oscillator with a single quarter-wave resonator has been proposed in Ref. (Field and Fricke, 1998). The relationship between jet frequency and resonator length needs to be derived for oscillators with dual resonators because modified fluidic oscillators have two symmetrical resonators. The derived equations for an oscillator with two symmetrical resonators are similar to those with a single quarter-wave resonator.

In a bounded medium, such as resonator structures in an oscillator, a quarter-wave resonator has two boundaries where reflection can occur: the open end and the closed end. Unlike a progressive wave in an unbounded medium, a wave set in a linear system, such as a fluidic oscillator with a resonator, is reflected off the two boundaries. Therefore, it propagates continuously between the two boundaries. Each time a vibratory source acts on the open end of the resonator, the vibratory source transfers energy to the air in the resonator cavity. This process forms standing waves in the cavity, creating a resonant state.

Next, the frequency equation of the modified fluidic oscillator (with two resonators) is derived. The wave generated in one direction is

$$\varphi_1 = a\sin[2\pi(kx - ft) + \alpha], \tag{5}$$

where a is the wave amplitude, k is the wave number, f is the frequency, and α is the wave initial phase.

The wave generated in the other direction is

$$\varphi_2 = a\sin[2\pi(kx + ft) + \beta], \tag{6}$$

where β is another wave initial phase. The two expressions are known solutions of the wave equation. The superposition principle can be used because the wave equation is a second-order linear differential equation. As a result of the superposition of the incident and reflected waves, the formation of a standing wave can be expressed as

$$\varphi = \varphi_1 + \varphi_2 = 2a\sin\left(2\pi kx + \frac{\alpha+\beta}{2}\right)\cos\left(2\pi ft + \frac{\alpha-\beta}{2}\right). \tag{7}$$

We know that $x = 0$ and $x = 2L_R$ are rigid ends of the resonator, and $x = L_R$ is in the open, where LR is the length of a quarter-wave resonator. Thus, the boundary conditions at the two rigid ends are

$$\begin{cases} x = 0, \varphi = 0 \\ x = 2L_R, \varphi = 0 \end{cases}. \tag{8}$$

In accordance with the first boundary condition, the following expression is obtained:

$$2a\sin\left(\frac{\alpha+\beta}{2}\right)\cos\left(2\pi ft + \frac{\alpha-\beta}{2}\right) = 0. \tag{9}$$

Therefore, $\frac{\alpha+\beta}{2} = 0$, i.e., $\beta = -\alpha$. From Eq. 7, we derive

$$\varphi = 2a\sin(2\pi kx)\cos(2\pi ft + \alpha). \tag{10}$$

From the second boundary condition, the following expression is obtained:

$$2a\sin(4\pi kL_R)\cos(2\pi ft+\alpha)=0. \tag{11}$$

Thus, $\sin(4\pi kL_R)=0$ or $4kL_R=n$ (n is a positive integer). According to the relations between wave number k and frequency f,

$$k=\frac{1}{\lambda}=\frac{f}{c}. \tag{12}$$

Hence, we can deduce that

$$f=\frac{nc}{4L_R},(n=1,2,3...). \tag{13}$$

The minimum value of n is 1, so the minimum or characteristic frequency calculated by Eq. 13 describing the dual symmetrical resonator fluidic oscillator is:

$$f=\frac{c}{4L_R}. \tag{14}$$

When the modified model has resonators only, the two near-inlet resonators play the main role in determining the jet frequency. The frequency of the jet may be fractional or integral multiples of the characteristic frequency of the resonators (i.e., subharmonic or harmonic frequency) because of the nonlinear effect in the flow field and the coupling between the resonator and feedback channel.

For the prototype fluidic oscillator (Ostermann et al., 2019), when the shape of the fluidic oscillator is fixed, the value of the Strouhal number is nearly invariant. Strouhal number St is related to jet frequency f_j, width of the throat d, and jet velocity V_y, as shown by the following equation:

$$St=\frac{f_j d}{V_y}. \tag{15}$$

However, the present study changes the structure of the feedback loops through the movement of the movable feedback channels, thus causing St to change accordingly.

Given that the jet frequency generated by the fluidic oscillator with resonators is fixed, according to Eq. 16, St is inversely proportional to V_y, that is, as the flow rate through the jet changes, the Strouhal number also changes (Field and Fricke, 1998). The modified fluidic oscillator discussed in this work has the structural features of fluidic oscillators with feedback channels and those with resonators, which may adjust both the Strouhal number and the frequencies by the movable feedback channel and flow rate. The characteristics, such as flow losses, oscillation amplitude, and unsteady characteristics, are unknown and will be discussed below by simulation.

5 Numerical results and analysis—characteristics of the fluidic oscillator with both feedback channels and resonators

In this study, the feedback channel is designed as a movable component on the basis of the prototype model. To reflect the relative length of the feedback channel, the ratio of feedback channel length to resonator length is defined as

$$R=\frac{L_f}{L_R}. \tag{16}$$

Thus, three typical states represented by R = 1.62, 2.07, and 2.51 are investigated, and each state is given three different inlet mass flow rates (corresponding to inlet velocities of 10, 20, and 40 m/s) in the unsteady calculations.

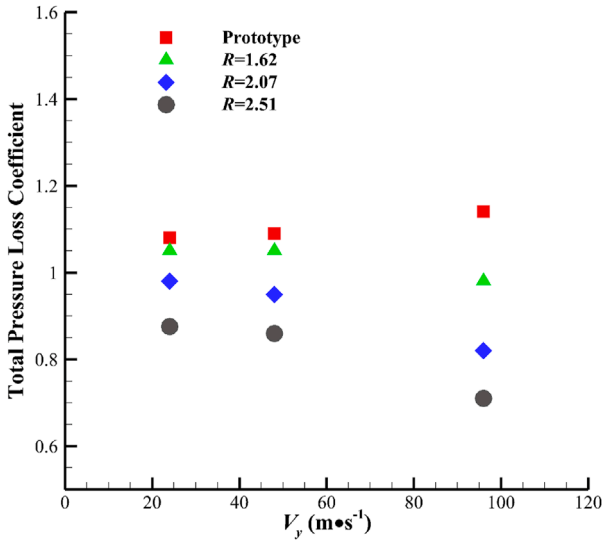

FIGURE 8
Comparison of the total pressure loss coefficients of the prototype and modified model under different R values (R = 1.62, R = 2.07, and R = 2.51).

5.1 Flow loss characteristics

The fluidic oscillator, as a flow control method, is designed to suppress external flow separation losses, and it requires a low level of flow losses within itself. In the numerical simulation, the total pressure loss coefficient (Eq. 1) is used to evaluate the flow loss characteristics of the device, and Figure 8 shows the comparison of total loss coefficients between the prototype and the modified model (R = 1.62, 2.07, and 2.51) at different inlet mass flow rates.

Numerical calculations of the prototype and the modified fluidic oscillator with different R values are performed at three given mass flow rates. The total pressure loss coefficient of the prototype increases slightly with the increasing normal jet velocity V_y (reflecting the mass flow rate), as shown in Figure 8. Also, compared with the total pressure loss coefficient of the prototype, that of the modified model at R = 1.62, R = 2.07, and R = 2.51 is 14%, 28.1%, and 37.7% lower, respectively, at the jet velocity of 96 m/s.

The modified oscillator in the R = 1.62 condition only differs from the prototype in terms of the resonator (the lengths of the feedback channels are approximately equal). In comparison with the prototype model, in the modified model of R = 1.62, the total pressure loss coefficient is 2.8% lower at a jet velocity of 24 m/s, 3.7%

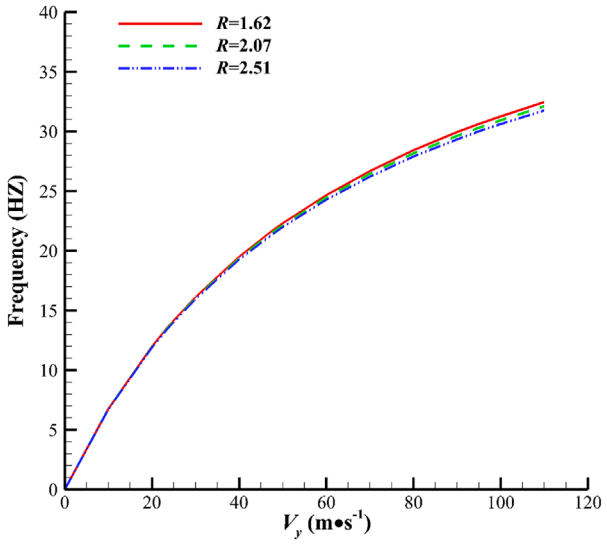

FIGURE 9
Theoretically calculated jet sweeping frequency versus V_y curve describing fluidic oscillators with feedback channels and resonators (different R values).

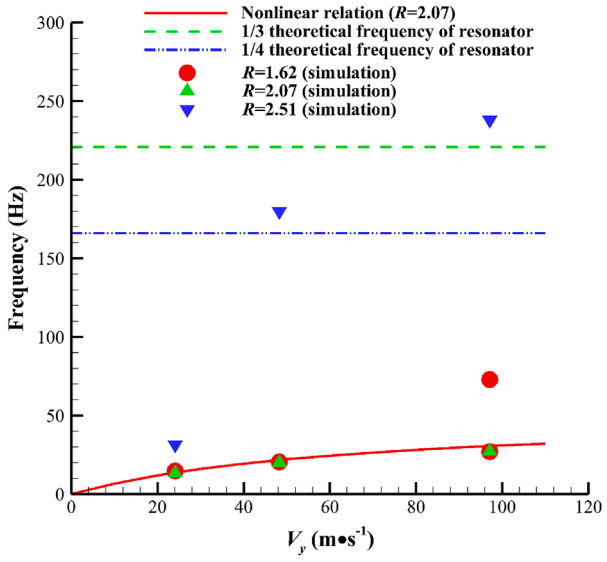

FIGURE 10
Simulated (for different R values) and theoretical frequency versus jet velocity.

lower at 48 m/s, and 14.0% lower at 96 m/s due to the existence of feedback channels. A decrease in the total pressure loss coefficient occurs in the modified model as V_y increases. Moreover, the cases with other different R values (R = 2.07 and 2.51) show that the modified model has smaller internal flow loss than the prototype model over a wide range of jet velocities.

Furthermore, with the increase in R, the decrement degree of the total pressure loss coefficient expands when V_y is increased. As R increases, the farther the movable feedback channel is from the main flow path, the more considerable the influence of the resonators becomes. Therefore, we believe that the resonators are the dominant factor in the loss reduction.

5.2 Frequency characteristics

The sweeping frequencies for different R values at different jet velocities are calculated with Eq. 2, as shown in Figure 9. According to the theoretical model, difference in jet sweeping frequency at different R values is not significant, indicating that theoretically, for the fluidic oscillator with both mixing chamber and feedback channels, regulating the jet sweeping frequency substantially by simply adjusting the length of the feedback channels is difficult.

In Figure 10, the theoretical jet frequency of the fluidic oscillator is calculated with Eq. 2, and the theoretical characteristic frequency of the fluidic oscillator with symmetrical resonators is calculated with Eq. 4. The one-third and one-quarter theoretical frequencies of the resonator are also plotted. Analysis is conducted by comparing the theoretical relations and simulated results. Observation of the corresponding frequencies at three velocities in the condition R = 1.62 suggests that the relationship between frequency and velocity in this condition is roughly in accordance with the nonlinear relation of the prototype model with only feedback channels. Therefore, when the feedback channel is short (R = 1.62), the feedback channel is close to the main flow path, and the jet frequency characteristics are dominated by the feedback channels. The self-excitation mechanism of this modified model (R = 1.62) is similar to that of the prototype model.

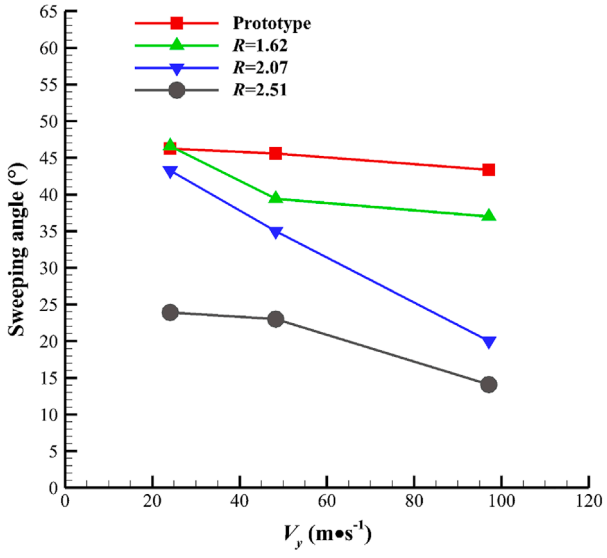

FIGURE 11
Relationship between jet sweeping angle and V_y for different R values and the prototype.

Notably, we obtain a new finding, as shown in Figure 10. The red dot (R = 1.62) in Figure 10 at the jet velocity of 96 m/s indicates frequency bifurcation, which means the sweeping frequency alternately switches between 27 Hz and 73 Hz, where 27 Hz is in accordance with the theoretical relation and 73 Hz is unexpected. The sweeping angle also presents the switching

10.3389/fenrg.2023.1236087

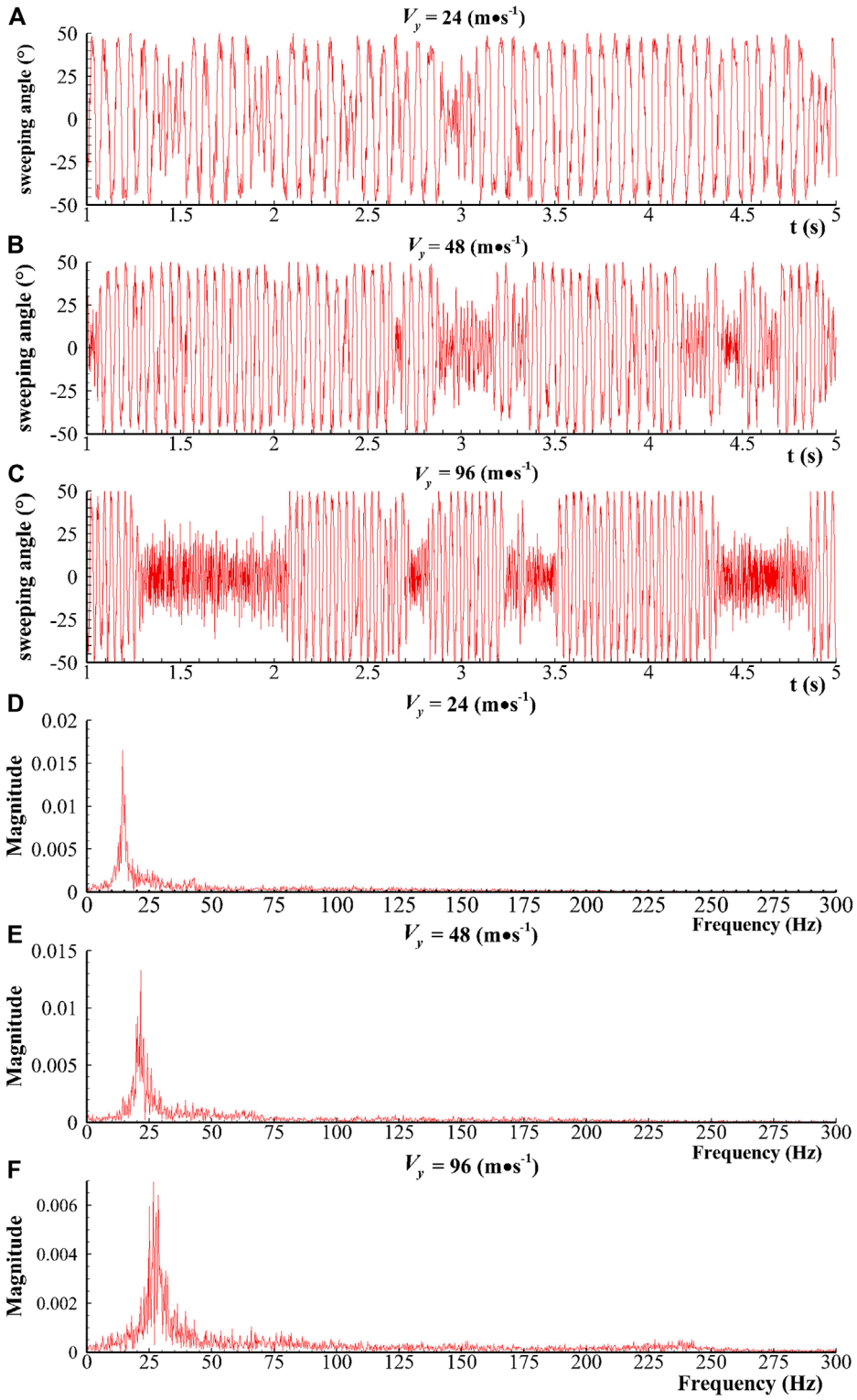

FIGURE 12
(A–C) Sweeping angle in time domain and **(D–F)** frequency magnitude in frequency domain (R = 1.62).

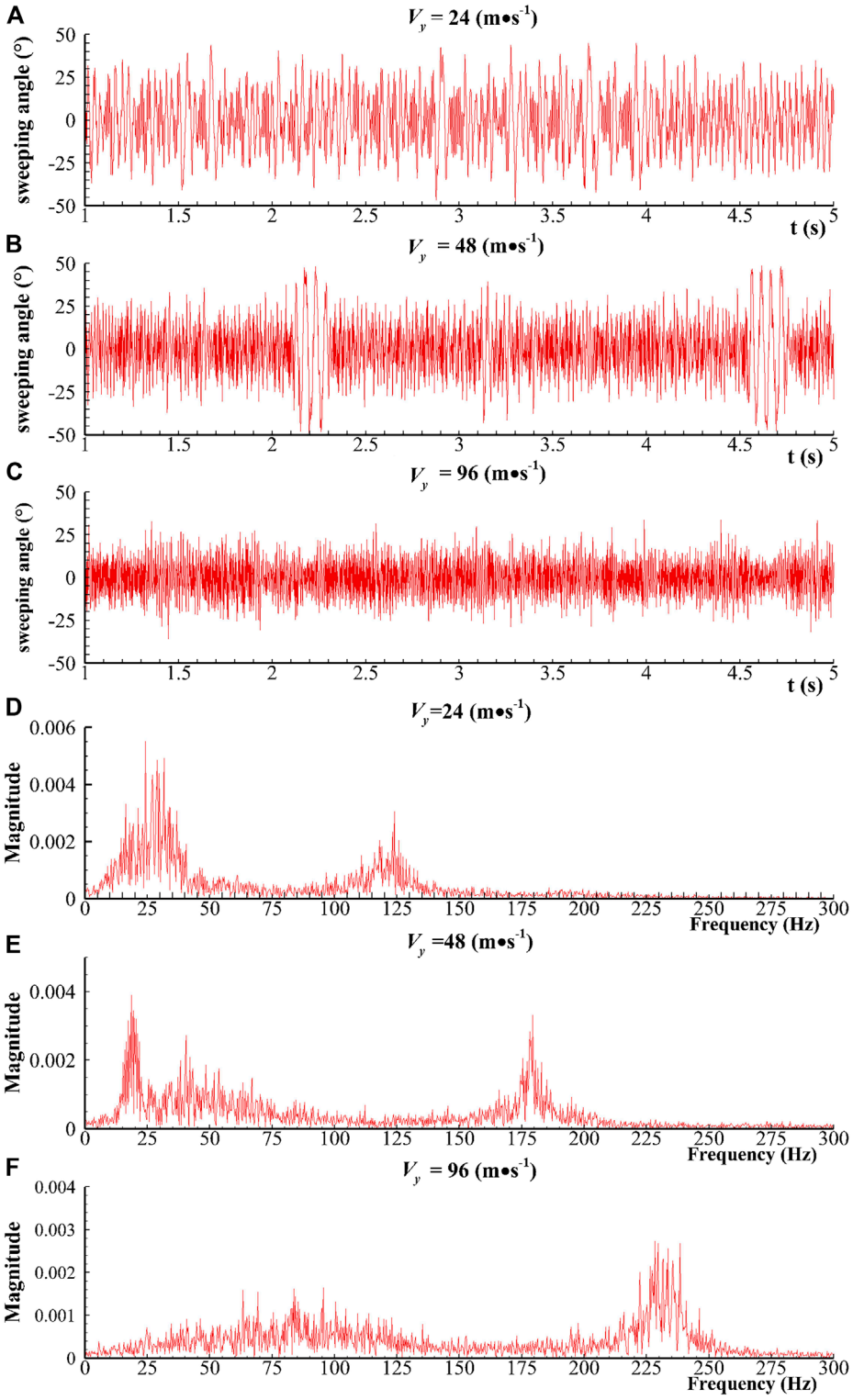

FIGURE 13
(A–C) Sweeping angle in time domain and **(D–F)** frequency magnitude in frequency domain (R = 2.51).

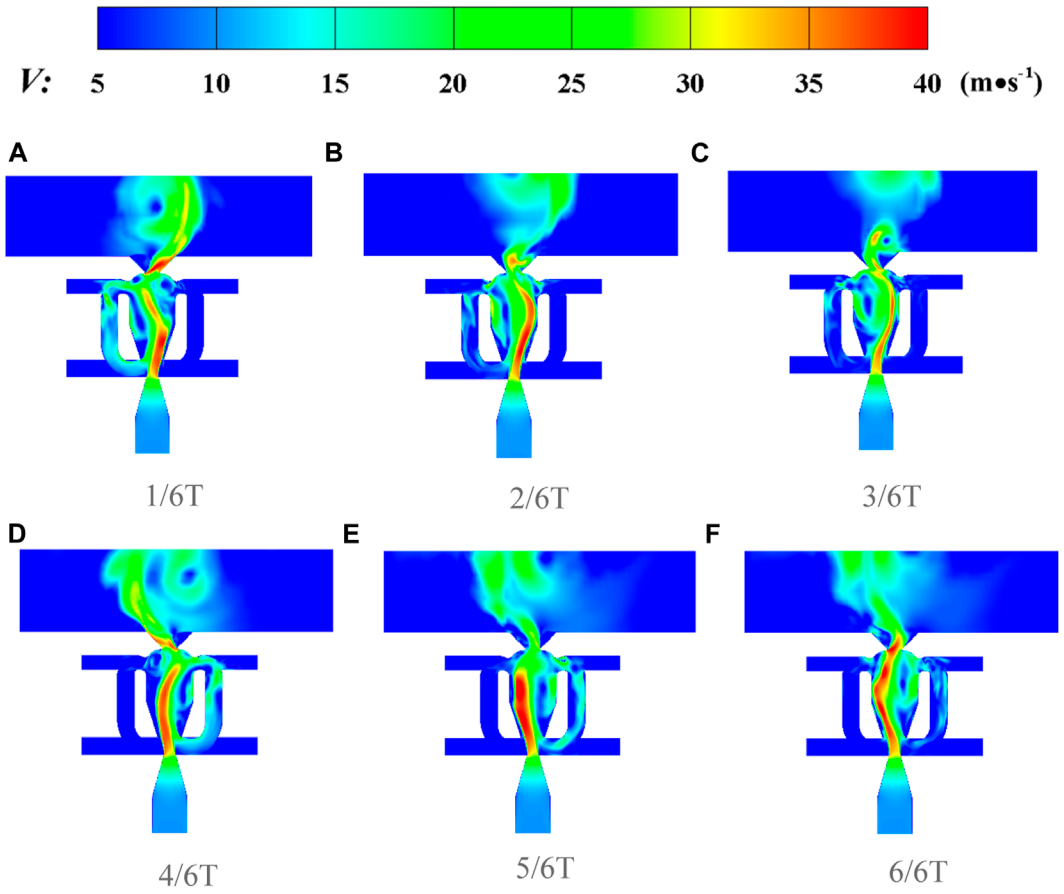

FIGURE 14
Transient velocity contour of the flow field at **(A)** 1/6*T*, **(B)** 2/6*T*, **(C)** 3/6*T*, **(D)** 4/6*T*. **(E)** 5/6*T*, and **(F)** 6/6*T* modes (*T* is a sweeping period and R = 1.62 and V_y = 24 m/s).

phenomenon, which will be discussed further in Section 5.3. This phenomenon is the state of switching from a low frequency and a high amplitude to a high frequency and a low amplitude over time (Figure 12C, which illustrates the time-domain curve ofthe sweeping angle). Given that this phenomenon is only observed in cases with high jet velocity, the phenomenon occurs beyond a certain Reynolds number threshold. As shown in Figure 10, the low frequency is determined by the feedback channel, and the high frequency is related to the resonator. The authors suggest that the phenomenon is relevant to the competition of the feedback channel and the resonator for dominating the main stream alternately, but a certain randomness exists in the domination at a certain moment (Figure 12C), which will be described in detail in Section 5.4.

Figure 10 also depicts the simulated corresponding frequencies at three different velocities in the R = 2.07 condition, and the relationship between the frequencies and velocities in this condition is consistent with the theoretical calculation of the modified model at R = 2.07. Therefore, the dominant mechanism factor of model action in the R = 2.07 condition is similar to that of the prototype with a feedback channel. Compared with R = 1.62 and R = 2.07 conditions, the R = 2.51 condition shows a substantial change in jet frequency, particularly when the jet velocity is high. For the modified model in the R = 2.51 condition, the frequency at low jet velocities is more than twice the frequency of the modified model at R = 2.07. At high velocities, the frequencies are roughly equal to the subharmonic frequencies of the characteristic frequency of the fluidic oscillators with resonators only. A possible reason for the high frequency in the R = 2.51 condition is that the feedback channel and the mixing chamber are far apart, so the feedback channel cannot effectively affect the frequency of the jet, and the jet frequency is dominated by resonance and determined mainly by the length of the resonant cavity. Thus, a high-frequency jet is generated.

The role of this oscillator is to adjust the frequency. The movement of the feedback channel changes the length of the feedback loop (denoted by different R values) and the characteristics of the oscillator. Then, through the feedback channel and resonators with different degrees of coupling, the sweeping angle and frequency of the jet are adjusted. At a constant mass flow rate, a considerable change in frequency occurs when the feedback channel length is adjusted. At a low jet velocity (V_y = 24 m/s), the frequency changes by about a factor of two from the shortest feedback channel (R = 1.62) to the longest (R = 2.51). At a high jet velocity (V_y = 48 and 96 m/s), the sweeping frequency increases up to 8.8 times, which

10.3389/fenrg.2023.1236087

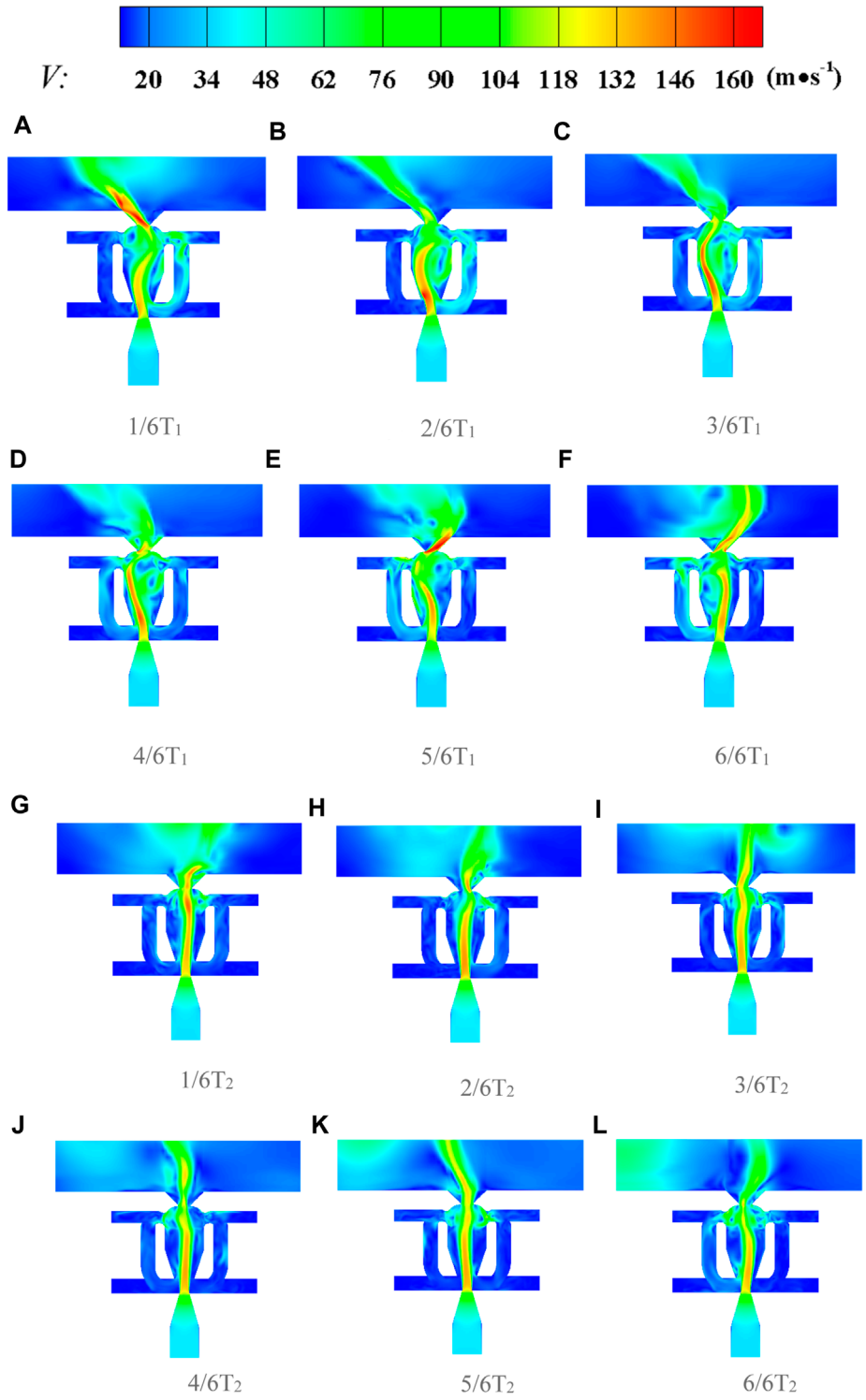

FIGURE 15
Transient velocity contour of the flow field at **(A)** $1/6T_1$, **(B)** $2/6T_1$, **(C)** $3/6T_1$, **(D)** $4/6T_1$, **(E)** $5/6T_1$, **(F)** $6/6T_1$, **(G)** $1/6T_2$, **(H)** $2/6T_2$, **(I)** $3/6T_2$, **(J)** $4/6T_2$, **(K)** $5/6T_2$, and **(L)** $6/6T_2$ modes (T_1 is one oscillation period at a lower frequency, and T_2 is one oscillation period at a higher frequency. The figure presents a process of frequency switching from period T_1 to T_2. The time required for this process varies and the figure shows a typical transition. (R = 1.62 and V_y = 96 m/s in this figure).

is impossible for a typical oscillator with a mixing chamber and feedback channel (a change in the length of the feedback channel has little effect on frequency, as shown in Figure 9). This is an important advantage of the proposed solution in this study.

5.3 Sweeping magnitude characteristics

This section analyzes the sweeping angle magnitude of the jet. A data processing method is needed to obtain the effective sweeping angle amplitude because the jet angle curve is only approximately sinusoidal. We treat the jet angle as an oscillation described as $u = U_m \cdot \sin(\omega t + \phi)$, where U_m is the amplitude, ω is the circular frequency, and ϕ is the initial phase. We know that the electrical voltage described as $u = U_m \cdot \sin(\omega t + \phi)$ has the following relation,

$$U_m = \sqrt{2} \cdot U, \tag{17}$$

where U is the effective or root mean square voltage, which can be calculated using the following discretized relation:

$$U = \sqrt{\frac{\sum_{i=1}^{n} (u_i - \overline{u})^2}{n-1}}. \tag{18}$$

where $\overline{u}$ is the averaged u_i. Through this method, the effective value (U) of voltage is obtained (the amplitude is difficult to be determined directly, so it is processed indirectly) and then multiplied by the square root of 2 to derive the voltage amplitude (U_m).

By imitating the calculation of voltage magnitude and using Eqs. (17) and (18), we can obtain the magnitude of the sweeping angle produced by the fluidic oscillator. Figure 11 shows a comparison of the amplitude values of the prototype and the modified model with different R values at different jet velocities. The maximum sweeping angle of the jet is close to 45° for both the prototype and R = 1.62. Given different R values at the same jet velocity, the figure indicates that the long feedback channel model (R = 2.51) has lower amplitudes compared with the prototype and the modified model with shorter (R = 1.62 and 2.07) feedback channels. At this point, the sweeping jet with high frequency and low amplitude is mainly produced by the dominant action of the resonators. Under a varying jet velocity at the same R value, the amplitude decreases as the jet velocity increases because as the velocity increases (i.e., an increase in the Reynolds number), the fluid inertia effect increases, and the viscous effect decreases. Meanwhile, the Coanda effect is related to viscosity, thus making the jet less likely to produce oscillation at this time. In addition, the amplitude of the sweeping angle switches between 17° and 49° when R = 1.62, V_y = 96 m/s, as illustrated in Figure 12C. This unusual unsteady characteristic will be discussed in detail in Section 5.4.

5.4 Unsteady characteristics

This section analyzes some special unsteady characteristics due to different parameters of jet velocity V_y and different values of R. In consideration of these characteristics, two typical states with minimum (R = 1.62) and maximum R (R = 2.51) are used to analyze and demonstrate the transient sweeping angle and flow field. A comparison of sweeping angle versus time for different jet velocities at V_y = 24, 48, and 96 m/s in the R = 1.62 condition is presented in Figures 12A–C. In Figure 12C, the frequency switching phenomenon can be seen clearly. The dominant frequencies obtained from the frequency-domain plots (Figures 12D–F) are 14 Hz, 20 Hz and 27 Hz (with a subdominant frequency around 70 Hz) when V_y = 24, 48 and 96 m/s, respectively. However, the frequency switching phenomenon is not significantly reflected in the frequency domain plots. We attribute this to the small amplitude of the oscillations around 70 Hz, which is therefore not significant in the frequency domain diagram. Moreover, the sweeping angle in R = 2.51 condition (Figures 13A–C) shows that the amplitude of the sweeping angle decreases as the inlet mass flow rate gradually increases. As illustrated in Figures 13D–F, frequency-domain plots show that the frequency switching phenomenon is presented obviously (See Figure 13E). Therefore, the frequency switching phenomenon appears to be related to the R value and jet velocity.

To clearly illustrate the frequency switching phenomenon, two typical unsteady flow fields at R = 1.62 are selected for demonstration. By comparing the unsteady flow field between R = 1.62, V_y = 24 m/s (Figure 14) and R = 1.62 and V_y = 96 m/s (Figure 15), we find that when V_y = 24 m/s, the flow fields are similar to those of the prototype. When V_y = 96 m/s, initially, the jet characteristics are similar to those when V_y = 24 m/s. However, after some time, they change to a higher frequency and smaller sweeping angle (because of the low flow rate and weak mobility of the flow in the feedback channels, the effect of the feedback channel can be ignored), and a clear frequency and amplitude switching phenomenon can be observed. The authors suggest that this frequency switching phenomenon may be applied in some flow control scenarios having two dominant modes with different frequencies and weights, such as shock–boundary layer interaction and blade tip leakage flow.

6 Conclusion

In this study, we propose a fluidic oscillator with feedback channels and resonators and investigate its characteristics in terms of internal flow losses, jet frequencies, sweeping angles, and unsteady flow field characteristics through numerical simulation. The main conclusions are as follows.

1. The total pressure loss of the prototype fluidic oscillator will increase by 5.6% when the normal velocity of the sweeping jet V_y ranges from 24 m/s to 94 m/s. By comparison, the total pressure loss of the modified fluidic oscillator with movable feedback channels and resonators decreases by 6.7% (R = 1.62), 16.3% (R = 2.07) and 18.9% (R = 2.51) when V_y increases from 26 m/s to 112 m/s. In addition, the decrement degree of the total pressure loss expands with the increase in V_y. The above phenomenon indicates that the new fluidic oscillator has better economic benefits when utilized as a flow control device.
2. The analysis of jet frequency indicates that theoretically, a change in the feedback channel length (denoted by a nondimensional parameter R in this study) has little effect on frequency. However, in the simulation, the frequency changes up to 8.8 times when the R value is gradually enlarged. Specifically, when

the R value changes from 1.62 to 2.51, the frequency ranges from 27Hz to 238 Hz. The reason for its change is that the change in the feedback channel length results in a weakened role of the feedback channel, which is in a state where the resonators dominate the role and produce high frequency. The fluidic oscillator can produce jets with different frequencies and sweeping angles under the combination of flow velocity and feedback channel length changes.

3. Frequency switching, a phenomenon where the jet randomly switches from 27Hz frequency and 49° amplitude to 73Hz and 17°, is observed in the R = 1.62, V_y = 96 m/s mode. The authors suggest that this phenomenon arises as the feedback channels and resonators compete for control and alternately dominate the mainstream, but randomness still exists with regard to which one dominates at a given moment. This finding may provide a potential solution to the problem of controlling flow with more than one dominant frequency in highly loaded compressors that require varying jet frequencies at off-design point conditions., such as tip leakage flow and shock–boundary layer interaction, which can produce two different dominant frequencies.

Data availability statement

The raw data supporting the conclusion of this article will be made available by the authors, without undue reservation.

Author contributions

ZY: date Curation, Writing—Original Draft. YL: date Curation, Writing—Original Draft. XY: Writing—Original Draft. QD: Date Curation. WL: conceptualization, Methodology, Writing—Review and Editing. All authors contributed to the article and approved the submitted version.

Funding

This research was funded by the National Natural Science Foundation of China (grant number 52106046), the Natural Science Foundation of Jiangsu Province (grant number BK20200680) and the National Students' platform for innovation and entrepreneurship training program (grant number 202310291089Z).

Acknowledgments

The authors wish to express their gratitude to Department of Engineering Mechanics (affiliated with School of Physical and Mathematical Sciences, Nanjing Tech University) for technical support.

Conflict of interest

The authors declare that the research was conducted in the absence of any commercial or financial relationships that could be construed as a potential conflict of interest.

Publisher's note

References

Açıkel, H. H., and Genç, M. S. (2016). Flow control with perpendicular acoustic forcing on NACA 2415 aerofoil at low Reynolds numbers. *Proc. IMechE, Part G - J. Aerosp. Eng.* 230, 2447–2462. doi:10.1177/0954410015625672

Cao, S., Dang, N., Ren, Z., Zhang, J., and Deguchi, Y. (2020). Lagrangian analysis on routes to lift enhancement of airfoil by synthetic jet and their relationships with jet parameters. *Aerosp. Sci. Technol.* 104, 105947. doi:10.1016/j.ast.2020.105947

Cerretelli, C., and Kirtley, K. (2009). Boundary layer separation control with fluidic oscillators. *J. Turbomach.* 131 (4), 29–38. doi:10.1115/1.3066242

Cerretelli, C., Wuerz, W., and Gharaibah, E. (2010). Unsteady separation control on wind turbine blades using fluidic oscillators. *AIAA J.* 48 (7), 1302–1311. doi:10.2514/1.42836

Choi, J., Xu, C. X., and Sung, H. J. (2002). Drag reduction by spanwise wall oscillation in wall-bounded turbulent flows. *AIAA J.* 40, 842–850. doi:10.2514/3.15133

Culley, D. (2006). "Variable frequency diverter actuation for flow control," in 3rd AIAA Flow Control Conference, AIAA Paper, San Francisco, California, 05 June 2006 - 08 June 2006. 2006-3034.

Field, C. D., and Fricke, F. R. (1998). Theory and applications of quarter-wave resonators: A prelude to their use for attenuating noise entering buildings through ventilation openings. *Appl. Acoust.* 53 (3), 117–132. doi:10.1016/s0003-682x(97)00035-2

Glezer, A., and Amitay, M. (2002). Synthetic jets. *Annu. Rev. Fluid Mech.* 34, 503–529. doi:10.1146/annurev.fluid.34.090501.094913

Greenblatt, D., and Wygnanski, I. J. (2000). The control of flow separation by periodic excitation. *Prog. Aerosp. Sci.* 36, 487–545. doi:10.1016/s0376-0421(00)00008-7

Gregory, J., and Tomac, M. N. (2013). "A Review of fluidic oscillator development and application for flow control," in 43rd Fluid Dynamics Conference, San Diego, CA, 24 Jun 2013-27 Jun 2013.

Gregory, J. W., Gnanamanickam, E. P., Sullivan, J. P., and Raghu, S. (2009). Variable-frequency fluidic oscillator driven by a piezoelectric bender. *AIAA J.* 47 (11), 2717–2725. doi:10.2514/1.44078

Kim, J., Moin, P., and Seifert, A. (2017). Large-eddy simulation-based characterization of suction and oscillatory blowing fluidic actuator. *AIAA J.* 55 (8), 2566–2579. doi:10.2514/1.j055445

Koklu, M. (2018). Effects of sweeping jet actuator parameters on flow separation control. *AIAA J.* 56 (1), 100–110. doi:10.2514/1.j055796

Lepicovsky, J., Ahuja, K., Brown, W. H., and Morris, P. J. (1986). Acoustic control of free jet mixing. *J. Propuls. Power* 2, 323–330. doi:10.2514/3.22890

Liu, H., Qin, Y., Wang, R., Zhang, D., and Lu, B. (2019). The performance of the self-supplying vortex generator jets on a high-speed compressor cascade. *Int. J. Turbo Jet-Engines* 36 (1), 113–125. doi:10.1515/tjj-2016-0056

Lu, W., Huang, G., Wang, J., and Yang, Y. (2019). Flow separation control in a curved diffuser with rigid traveling wave wall and its mechanism. *Energies* 12, 192. doi:10.3390/en12010192

Lu, W., Jiao, Y., and Fu, X. (2022). Concept of self-excited unsteady flow control on a compressor blade and its preliminary proof by numerical simulation. *Aerosp. Sci. Technol.* 123, 107498. doi:10.1016/j.ast.2022.107498

Nishioka, M., Asai, M., and Yoshida, S. (1987). Control of flow separation by acoustic excitation. *AIAA J.* 28, 1909–1915. doi:10.2514/3.10498

Ostermann, F., Woszidlo, R., Nayeri, C. N., and Paschereit, C. O. (2018). Properties of a sweeping jet emitted from a fluidic oscillator. *J. Fluid Mech.* 857, 216–238. doi:10.1017/jfm.2018.739

Ostermann, F., Woszidlo, R., Nayeri, C. N., and Paschereit, C. O. (2019). The interaction between a spatially oscillating jet emitted by a fluidic oscillator and a cross-flow. *J. Fluid Mech* 863, 215–241. doi:10.1017/jfm.2018.981

Ostermann, P., Godbersen, F., Woszidlo, R., Nayeri, C. N., and Paschereit, C. O. (2017). Sweeping jet from a fluidic oscillator in crossflow. *Phys. Rev. Fluids* 2 (9), 090512. doi:10.1103/physrevfluids.2.090512

Qin, Y., Song, Y., Wang, R., and Liu, H. (2020). Numerical investigation of three-dimensional separation control on a high-speed compressor stator vane with tailored synthetic jet. *Int. J. Turbo Jet-Engines* 37 (4), 383–397. doi:10.1515/tjj-2017-0036

Shmilovich, A., Yadlin, Y., and Whalen, E. A. (2018). Active flow control computations: From a single actuator to a complete airplane. *AIAA J.* 56 (12), 4730–4740. doi:10.2514/1.j056307

Simões, E. W., Furlan, R., Leminski, R. E. B., Gongora-Rubio, M. R., Pereira, M. T., Morimoto, N. I., et al. (2005). Microfluidic oscillator for gas flow control and measurement. *Flow Meas. Instrum.* 16 (1), 7–12. doi:10.1016/j.flowmeasinst.2004.11.001

Tesař, V., Zhong, S., and Rasheed, F. (2013). New fluidic-oscillator concept for flow-separation control. *AIAA J.* 51 (2), 397–405. doi:10.2514/1.j051791

Tomac, M. N., and de Luzan, C. F. (2020). Synchronization of a pair of opposed facing oscillators in a side-by-side configuration. *Int. J. Heat Fluid Flow* 84, 108605. doi:10.1016/j.ijheatfluidflow.2020.108605

Tomac, M. N., and Sundström, E. (2019). Adjustable frequency fluidic oscillator with supermode frequency. *AIAA J.* 57 (8), 3349–3359. doi:10.2514/1.j058301

Wang, S., Batikh, A., Baldas, L., Kourta, A., Mazellier, N., Colin, S., et al. (2019). On the modelling of the switching mechanisms of a Coanda fluidic oscillator. *Sensors Actuators a Phys.* 299, 111618. doi:10.1016/j.sna.2019.111618

Wu, C., Xie, Y., and Wu, J. (2003). "Fluid roller bearing" effect and flow control. *Acta Mech. Sin.* 19 (5). doi:10.1007/BF02484582

frontiers | Frontiers in Energy Research

TYPE Original Research
PUBLISHED 29 August 2023
DOI 10.3389/fenrg.2023.1235277

OPEN ACCESS

EDITED BY
Kan Kan,
College of Energy and Electrical Engineering, China

REVIEWED BY
Boshen Liu,
University of Science and Technology Beijing, China
Gangfeng Tan,
Wuhan University of Technology, China

*CORRESPONDENCE
Hongwei Cui,
cuihongwei@tyut.edu.cn

RECEIVED 06 June 2023
ACCEPTED 31 July 2023
PUBLISHED 29 August 2023

CITATION
Cui H, Zhang J, Li L and Wang G (2023), Numerical simulation of transient cavitation characteristics of valve-controlled liquid-filled hydrodynamic coupling.
Front. Energy Res. 11:1235277.
doi: 10.3389/fenrg.2023.1235277

Numerical simulation of transient cavitation characteristics of valve-controlled liquid-filled hydrodynamic coupling

Hongwei Cui[1,2]*, Jiahua Zhang[3], Li Li[1] and Guoqiang Wang[1]

[1]College of Mechanical and Vehicle Engineering, Taiyuan University of Technology, Taiyuan, China, [2]Shanxi Key Laboratory of Fully Mechanized Coal Mining Equipment, Taiyuan University of Technology, Taiyuan, China, [3]School of Mechanical Engineering, Beijing Institute of Technology, Beijing, China

In high-power impeller industries, valve-controlled liquid-filled hydrodynamic couplings are widely used in the soft startup of heavy-duty scraper conveyors for mining. However, the water circulation speed in internal flow fields is higher at lower speed ratios, making the hydrodynamic couplings prone to severe cavitation, which further results in severe performance degradation, noise, vibration, or even erosion failure. Meanwhile, because a hydrodynamic coupling is a piece of closed-loop multicomponent turbomachinery, internal transient cavitation flow behavior cannot be easily controlled. To reasonably predict the characteristics of cavitation and its influence on the working performance of the hydrodynamic coupling, a high-quality structured mesh model of the internal flow field for an impeller was established. Considering the periodic structural characteristics of the impeller, a scale-resolving simulation turbulence model was combined with a Rayleigh–Plesset cavitation model to establish a single-cycle hydrodynamic coupling calculation model. The cavitation distribution characteristics and torque transmission of the flow field under different working conditions were obtained, and the effect of cavitation on the soft startup performance was analyzed. The results demonstrated that cavitation in the hydrodynamic coupling mainly occurred under low speed ratios. The degree of cavitation decreased as speed ratio increased. The worst-case scenario for cavitation occurred when the speed ratio was zero. Most of the cavitation bubbles were generated at the tip of the blades, resulting in unstable variation in torque characteristics and deterioration of the working performance of the hydrodynamic coupling. The analysis reveals that the cavitation process in the impeller is highly unstable and periodic, and the cavitation development near the tip of the blades occurs in four stages: birth, growth, separation, and disintegration. The generated steam accumulates in the inner ring of the impeller. Therefore, a method for accurately predicting the cavitation characteristics of hydrodynamic couplings based on high-precision technology is proposed, and a theoretical basis for coupling design and cavitation suppression technology is provided.

KEYWORDS

valve-controlled liquid-filled hydrodynamic coupling, cavitation, scale-resolving simulation, CFX, torque characteristic

1 Introduction

Efficient and safe mining equipment plays a vital role in coal mining and utilization. Scraper conveyors often encounter harsh working conditions, such as excessively hard coal walls, sudden changes in coal production, stagnation of scraper chains, and unbalanced loads. These conditions can cause unexpected shutdowns, affect production efficiency, and affect the reliability and service life of the motor and scraper conveyor. Commonly used transmission devices in mines include valve-controlled liquid-filled hydrodynamic couplings, controlled start transmission, and frequency conversion drive devices. Compared with other transmission methods, valve-controlled liquid-filled hydrodynamic couplings use water as the working medium. The amount of liquid in the hydrodynamic coupling is varied via a hydraulic valve; speed regulation and soft starting of the load are then realized. As a commonly used soft start device on conveyors, this hydrodynamic coupling exhibits the advantages of a large starting torque coefficient, flexible transmission, simple structure, reliable performance, low equipment investment, and low maintenance cost (Zhang et al., 2020).

With the rapid development of computing power and various commercial finite-element software packages, the application of computational fluid dynamics (CFD) technology has become crucial to solve the problem of fluid calculation. To study hydraulic transmission, several researchers have conducted numerical computations for various hydraulic components based on CFD technology.

At present, most scholars focus on the cavitation characteristics of torque converter flow field in various operating conditions. Liu Cheng et al. revealed the fluid field mechanism of the influence of charging oil conditions on torque converter cavitation behavior, providing practical guidelines for suppressing cavitation in torque converter (Liu et al., 2022). Ran Zilin et al. developed a cavitation suppression technique by slotting one side of the stator suction side, which was proven to be able to significantly shorten the cavitation duration (Ran et al., 2022). Guo Meng et al. developed a full flow passage geometry and a computational fluid dynamics (CFD) model with cavitation to analyze the flow behavior in the torque converter (Guo et al., 2022a). Xiong Pan et al. optimized the Joukowsky airfoil used in the design of stator blades, which greatly reduced the probability of cavitation and improved the performance and service life of the torque converter (Pan et al., 2021).

Cavitation is a transient phase change phenomenon. Vapor bubbles occur, grow, and collapse in liquids with variations in the local pressure. This is a common issue in fluid machinery. To face complex coal conditions underground, mining equipment with high power that can sustain high loads are being developed. This has increased the demand for the soft start and stable transmission capabilities of the hydrodynamic coupling. A higher power density results in a higher circulation velocity and lower local pressure in the internal flow field. Simultaneously, because the working medium of the high-power hydrodynamic coupling for mining is water, a large amount of dissolved gas and undissolved microbubbles are present in the medium. Therefore, cavitation can easily occur, particularly on the blade surface, leading to unstable transmission and reduced power, thus reducing the life of the impeller.

At present, research on the cavitation phenomenon of the hydraulic transmission device primarily entails the torque converter. Anderson et al. (Anderson et al., 2003) investigated cavitation signatures under the stall condition in an automotive torque converter using a microwave telemetry technique. Liu et al. (Liu et al., 2018a; Liu et al., 2019) studied the influence of the stator blade shape on the cavitation process of a hydraulic torque converter and found that cavitation is directly related to the internal mass flow rate. Robinette et al. (Robinette, 2007; Robinette et al., 2008a; Robinette et al., 2008b) investigated the effects of torque converter design and operating conditions on the onset of cavitation during vehicle launch using a nearfield acoustical technique. From their numerical results, Dong et al. (Yu et al., 2002) determined that the cavitation on the stator leading edge grew in size with increasing pump speed, resulting in severe performance degradation in the torque converter. Zhao (Zhao et al., 2016) used the full channel transient CFD calculation model to simulate the mechanism of bubble breakup in a hydraulic torque converter by implanting bubbles in it, and they calculated the high incidence area of bubble breakdown. Watanabe et al. (Watanabe et al., 1996; Watanabe et al., 1997; Watanabe et al., 2007) established a cavitation observation model based on a transparent plastic torque converter. A high-speed camera was used to observe the cavitation in the torque converter, which was combined with dynamic torque testing to confirm that the cavitation process produced high-frequency torsional vibration. Kang (Kang et al., 2017) and Dong (Dong et al., 2017) studied the flow structure and cavitation phenomena in a hydraulic retarder. In addition, several important results have been obtained from research on hydrofoil cavitation (Sun et al., 2019; Bai et al., 2018; Cheng et al., 2020). Chai et al. (Chai et al., 2022) revealed the three-dimensional morphological characteristics of cavitation flow under extreme working conditions through high-precision numerical simulation and analysis of the cavitation flow field of a flat torque converter. Guo et al. (Guo et al., 2021; Guo et al., 2022b) proposed full-flow CFD models with and without cavitation for torque converters, and studied the effects of different pump impeller speeds, pump turbine speed differences and cavitation parameters on the internal flow field of the torque converter. Xiong et al. (Xiong et al., 2021) modified the torque converter stator blades through Joukowsky airfoil transformation, which greatly reduced the probability of cavitation.

Because hydraulic transmission machinery is a closed multi-impeller rotating machine, the internal two-phase flow phenomenon cannot be easily observed (Timoshevski et al., 2016). The current research results are mainly on the torque characteristics and two-phase flow field under part filling conditions (Da Silva et al., 2008; Hur et al., 2016; Hur et al., 2017). However, there is still no reasonable explanation for the formation of two-phase flow in the coupling. Xuesong Li (Li et al., 2020) studied the formation of two-phase flow state and flow mechanism of the flow field in the hydraulic retarder from the point of view of cavitation phenomenon, and the object of the study is highly similar to the structure of the hydrodynamic coupling, so similar theories can be used to analyze the two-phase flow. In addition, theoretical speculations suggest that, owing to the particularity of the working medium and working conditions of the mining high-power valve-controlled liquid-filled hydrodynamic coupling, the cavitation phenomenon has a greater

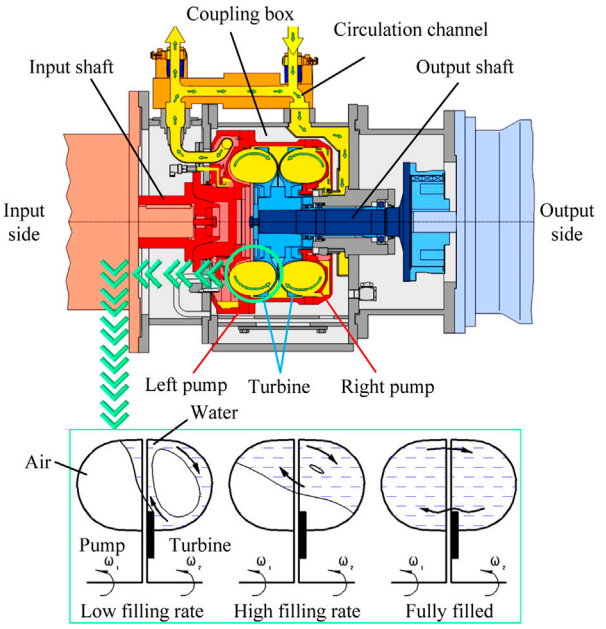

FIGURE 1
Structure and working principle of hydrodynamic coupling.

impact on the working characteristics of the coupling under the condition of an impeller high-speed difference. Therefore, this study aims to analyze the occurrence and development of cavitation in the flow field of high-power hydrodynamic couplings as well as to examine their external characteristics. This is of great significance for improving the accuracy of the prediction of hydrodynamic coupling characteristics and for improving performance and durability.

The research object in this study was a high-power mine-adjustable double-chamber hydrodynamic coupling with a circulation circle outer diameter of 575 mm. A single-channel calculation model of the impeller flow field on the output side was established. A SBES(Stress-Blended Eddy Simulation) calculation model was used to study the effect of cavitation on the performance of the fluid coupling. The development of the torque characteristics and cavitation distribution of the fluid coupling under closed working conditions was analyzed. The results provide a high-precision research method for the cavitation characteristics of fluid couplings; they also provide a reliable theoretical basis for the optimization of the structure of fluid couplings.

2 Numerical simulation

2.1 Geometric and mesh model

The structure and working principle of the valve-controlled liquid-filled hydrodynamic coupling are shown in Figure 1.

The speed-adjusting double-chamber hydrodynamic coupling with the outer diameter D = 575 mm was considered as the analysis model. The numbers of pump wheels and turbine blades were 46 and 45, respectively. Because the two pairs of impellers of this coupling had symmetrical structures, the flow field of the output impeller was used as the calculation model. The speed ratio of the hydrodynamic coupling was defined as $i = n_T/n_P$, n_T was the turbine rotation speed and n_P was the pump rotation speed. To describe the spatial position of the impeller blades accurately, the surfaces of the different side blades of the pump and turbine were defined according to the impeller rotation direction. The parameters of the coupling impeller are listed in Table 1, and the process of establishing the flow field model is shown in Figure 2A.

TABLE 1 Structure parameters of the coupling impeller.

Parameters	Value
Circular circle outer diameter, D (mm)	575
Circular circle inner diameter, d (mm)	276
Baffle diameter, d_B (mm)	320
Baffle thickness, h_B (mm)	5
Impeller material	ZL101 A
Rotation speed of pump, n_P (r/min)	1475
Number of pump blades, BN_P	46
Number of turbine blades, BN_T	45
Minimum blade thickness, h (mm)	3

To improve the computation efficiency and obtain a high flow field mesh density, a single flow channel calculation model of 1/x (where x is the number of impeller blades) was obtained by utilizing the cyclically symmetric structural characteristics of the inner flow field. The structured hexahedral grid in ICEM CFD was used to discretize the flow field model of a single channel of a fluid coupling. Moreover, o-division and mesh refinement were performed at the circle of curvature and the blade wall surface to improve the computational efficiency and mesh quality. This was because the three-dimensional circulation of the flow field in the coupling was complicated, and the cavitation was distributed under extremely unsteady conditions. Therefore, a high-quality mesh was required to calculate the actual flow state and capture the transient cavitation flow behavior. The process of establishing the single-channel mesh model is shown in Figure 2B.

Taking the internal flow field of the pump wheel as an example, the boundary condition setting method is shown in Figure 3, which mainly includes the no-slip wall at the wall surface of the pump wheel blades and the wall surface of the flow channel, the periodic surface of the pump wheel field according to its own geometric cycle symmetry structure, and the coupling surface of the flow solving area between the pump wheel internal flow field and the turbine internal flow field. Interface). Based on the viscous qualities of the fluid, the flow field near the wall of the existence of a thin layer of flow velocity and the wall of the same speed of the fluid, the thin layer of fluid and the wall of the wall of the relative slip does not exist, so the wall of the wall of the wall of the speed of the fluid unit of the velocity of the surface layer to take the value.

The accuracy and efficiency of the solution are directly affected by the quality and quantity of the mesh. In theory, a higher number of grids produce better calculation accuracy, but more grids require

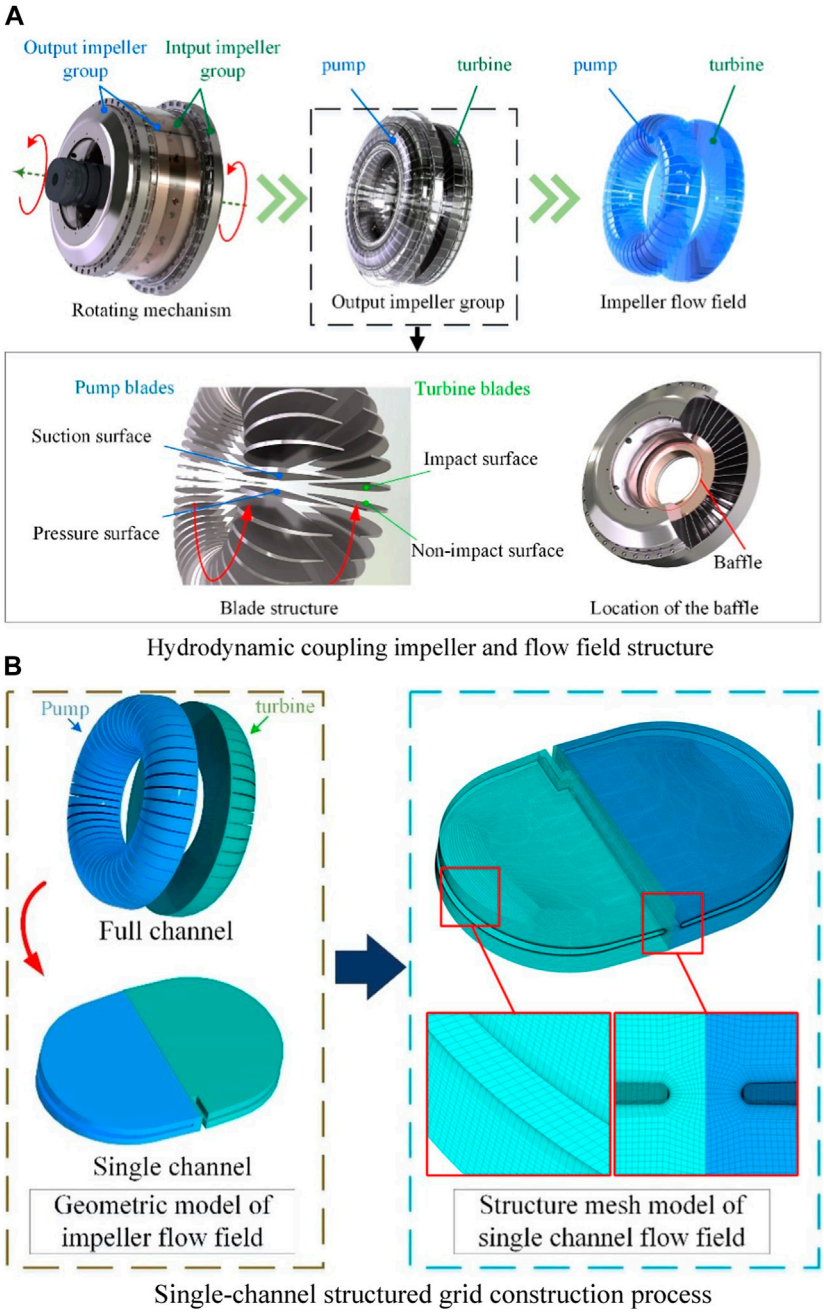

FIGURE 2
Geometric model and mesh model.

greater computing resources. Therefore, an appropriate mesh density should be determined to achieve an appropriate balance between accuracy and computational cost. The calculated torque change rate $f(\mathrm{n})$ of the mesh with different grid densities is

$$f(\mathrm{n}) = \frac{T(\mathrm{n}-1) - T(\mathrm{n})}{T(\mathrm{n})} \tag{1}$$

where $T(\mathrm{n})$ is the computation result under the current density mesh, and $T(\mathrm{n}-1)$ is the computation result under the previous mesh with lower density. When the change rate of the calculation result between the two meshes with different densities is less than 2%, the influence of the current mesh density on the calculation result is acceptable—that is, the calculation result is independent of the grid. Mesh independence tests were performed on seven models with different grid resolutions. The results are listed in Table 2 and shown in Figure 4.

When the global size of the mesh is less than 1.7 mm, the torque change generated by further increasing the number of grids is less than 2% and the model is considered to be mesh-independent. Considering the calculation efficiency and precision comprehensively, the global grid size is selected to be 1.7 mm. The grids number of the turbine flow field is 948,230, and the grids number of the turbine flow field is 1,157,138.

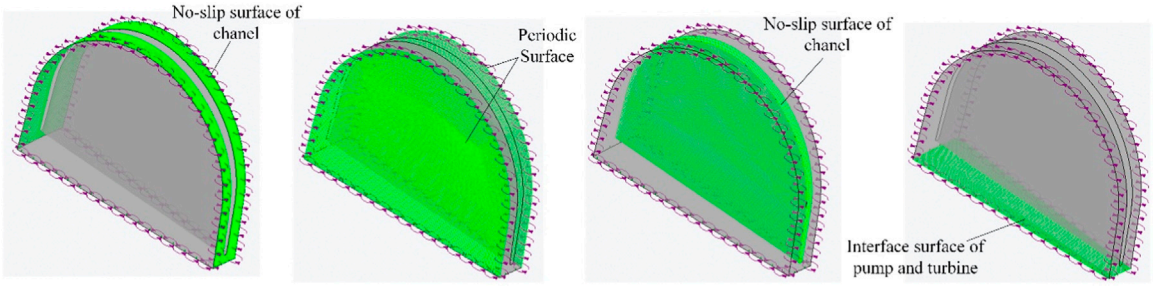

FIGURE 3
Fluid boundary.

TABLE 2 Structural mesh independence analysis results.

Number of grids in pump flow field	Global size setting (mm)	Time consumption (min)	Pump wheel torque (N·m)	$f(n)_{pump}$ (%)
83,036	3.5	6	286.377	
121,512	3	10	277.062	3.24
163,254	2.5	16	269.734	2.96
248,045	2	30	261.862	2.66
364,704	1.7	50	258.997	1.59
679,386	1.3	89	257.700	0.89
1,406,380	1	140	256.837	0.34

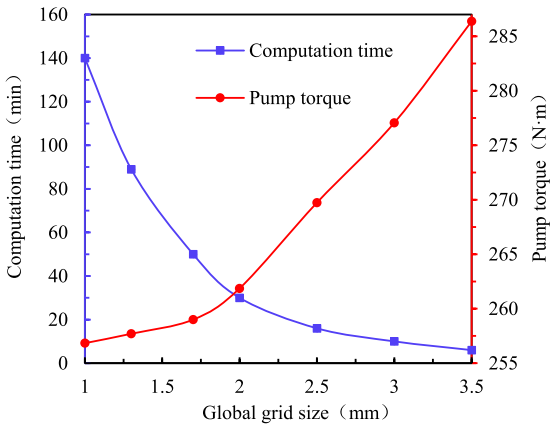

FIGURE 4
Analysis results of grid independence test.

To ensure the accuracy of the boundary layer flow field computation, the minimum boundary layer size was set to 0.01 mm, which ensured that the minimum y + value around the blade was less than 10. The grid thickness growth rate was set to 1.15.

2.2 Multiphase model

In this study, the multiphase flow field caused by cavitation in the completely filled liquid flow field was obtained. In addition to the general set of mass conservation equations, the mass exchange between liquid and non-condensable vapor is governed by the following transport equation (Zhou et al., 2017):

$$\frac{\delta}{\delta t}\left(f_l \rho_l\right) + \frac{\delta}{\delta x_j}\left(f_l \rho_l v_j\right) = \dot{m} \tag{2}$$

The key to solving the cavitation problem is the determination of the interphase mass transfer rate, i.e., cavitation rate, which is driven by the difference between local pressure and vapor pressure (Wang et al., 2013). Assuming that no interphase slip or heat transfer exists between the liquid and vapor, the radius of a spherical vapor bubble can be described by the Rayleigh–Plesset equation in its first-order approximation form as follows:

$$\frac{\mathrm{d}R_B}{\mathrm{d}t} = \sqrt{\frac{2}{3}\frac{p_v - p}{\rho_l}} \tag{3}$$

Then, the cavitation rate during vaporization can be given as

$$\dot{m} = \frac{3 f_v \rho_v}{R_B}\sqrt{\frac{2}{3}\frac{p_v - p}{\rho_l}} \tag{4}$$

TABLE 3 CFD model settings.

Analysis step	I	II	III	IV
Analysis type	Steady state	Steady state	Steady state	Transient
Interface model	Stage	Stage	Stage	Transient rotor–stator
Cavitation model	None	None	Rayleigh–Plesset	Rayleigh–Plesset
Turbulence model	SST	SST	SST	SBES
Advection scheme	Upwind	High resolution	High resolution	High resolution
Time step	1e-3s	Auto timescale	Auto timescale	Auto timescale
Convergence target	RMS 1e-4	RMS 1e-5	RMS 1e-5	RMS 1e-5
Fluid properties	ρ_{water} = 970 kgm^{-3}, μ_{water} = 8.9e-4 Pas			
Vapor properties	ρ_{vapor} = 2.3e-2 kgm^{-3}, μ_{vapor} = 9.8e-6 Pas			
Pump status	Fixed at 1475 rpm			
Turbine status	Varied from 0 to 1465.2 rpm			
Boundary details	No slip and smooth wall			
Heat transfer model	50 °C isothermal			
Saturation pressure	12333.43 Pa			

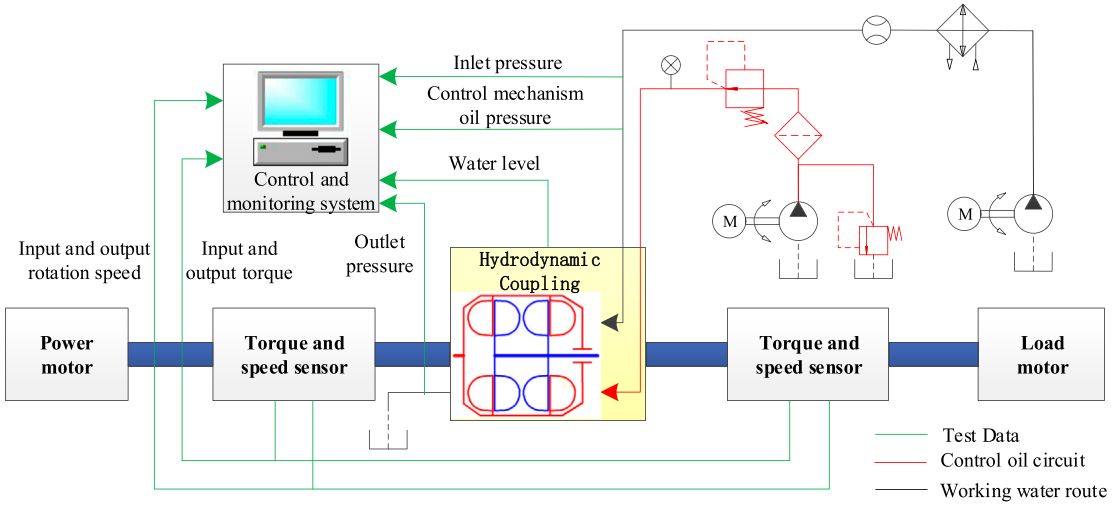

FIGURE 5
Macro characteristics test plan.

Because the nucleation site density decreases when the vapor volume fraction increases, the vapor volume fraction f_v is replaced by $f_{nuc}(1 - f_v)$ to yield the following (Jin et al., 2018):

$$\dot{m}^- = -F_{vap}\frac{3f_{nuc}(1-f_v)\rho_v}{R_B}\sqrt{\frac{2}{3}\frac{p_v - p}{\rho_l}} \quad (5)$$

When the partial pressure exceeds the vapor condensation pressure, the mass transfer rate becomes

$$\dot{m}^+ = F_{cond}\frac{3f_v\rho_v}{R_B}\sqrt{\frac{2}{3}\frac{p - p_v}{\rho_l}} \quad (6)$$

Because the condensation process is generally much slower than vaporization, different empirical factors are assumed as follows: F_{vap} = 50, F_{cond} = 0.01, f_{nuc} = 5e-4, and R_B = 1e-6 m.

A homogeneous multiphase condition is also assumed to simplify the model; thus, the liquid and vapor share the same velocity and turbulence profiles. The mixture of fluid and vapor is treated as a pseudofluid whose density ρ_m and dynamic viscosity μ_m are defined as follows:

$$\rho_m = (1 - f_v)\rho_l + f_v\rho_v \quad (7)$$

$$\mu_m = (1 - f_v)\mu_l + f_v\mu_v \quad (8)$$

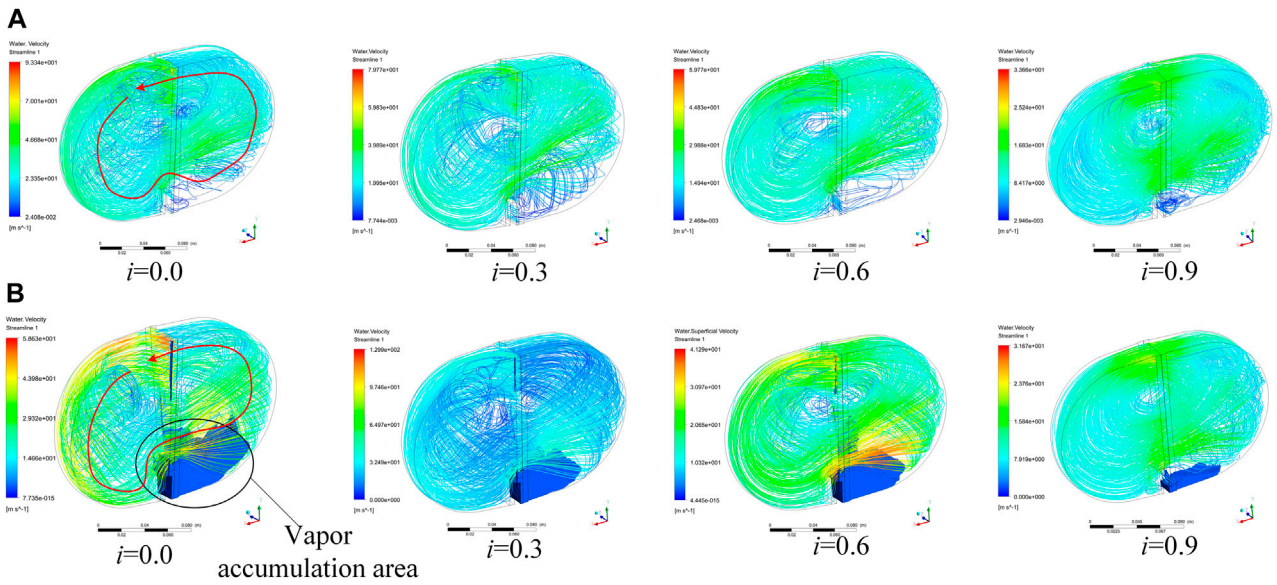

FIGURE 6
Velocity streamline distribution.A,B

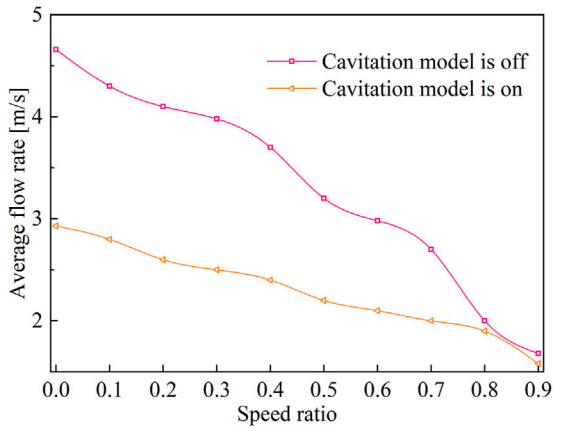

FIGURE 7
Change in mean flow velocity in the flow field.

2.3 Simulation settings

First, the upwind steady-state model was used to determine the flow field characteristics of the fluid coupling without cavitation. The high-resolution convection scheme was then used to perform steady-state computations to provide accurate flow field conditions. Based on the results of the noncavitation model, a high-resolution scheme was used to simulate the steady-state cavitation behavior. Finally, with the steady-state cavitation output as the initial condition, a transient CFD cavitation model was established to simulate the dynamic cavitation process in the internal flow field.

For the interface between the flow field and impeller wall surface and blade wall surface, the nonslip wall surface treatment was adopted, while the wall surface roughness was neglected. In the steady-state computation stage, the stage interface model was used to exchange data between the pump–turbine flow field interface. In the transient computation stage, the transient rotor–stator interface model was used to capture more transient flow characteristics. The corresponding CFD multistep solution model settings are listed in Table 3.

To obtain accurate cavitation characteristics and corresponding flow field characteristics, the SST SBES DSL model in the scale-resolving simulation is used in transient computations. Compared with the DES, this model features a considerably improved shielding function to protect RANS boundary layers from the impact of the grid-dependent term; further, this model can automatically switch between existing RANS and LES models (Liu et al., 2018b).

The shielding function developed can be used in the following manner for achieving a blending on the stress level between RANS and LES formulations (Li, 2018):

$$\tau_{ij}^{SBES} = f_{SBES}\tau_{ij}^{RANS} + (1 - f_{SBES})\tau_{ij}^{LES} \tag{9}$$

where τ_{ij}^{RANS} is the RANS portion and τ_{ij}^{LES} is the LES portion of the modeled stress tensor. In cases where both models are based on eddy viscosity concepts, the formulation can be simplified as follows:

$$\nu_t^{SBES} = f_{SBES}\nu_t^{RANS} + (1 - f_{SBES})\nu_t^{LES} \tag{10}$$

3 Experimental research

A macro characteristic test was conducted, wherein a motor was used to provide power at the input end and load at the output end, to

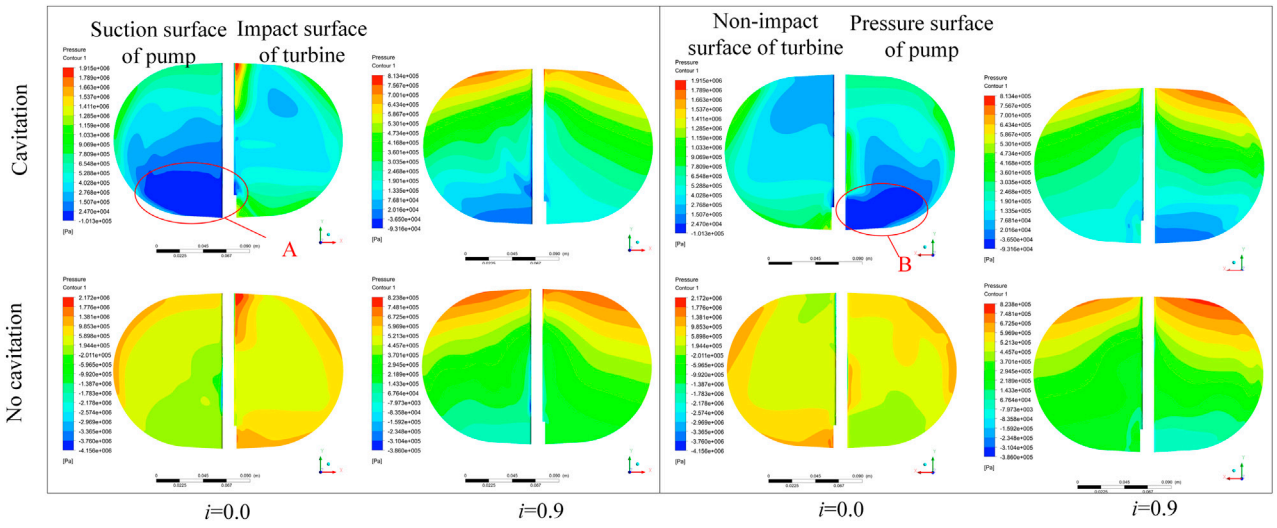

FIGURE 8
Comparison of blade pressure distribution.

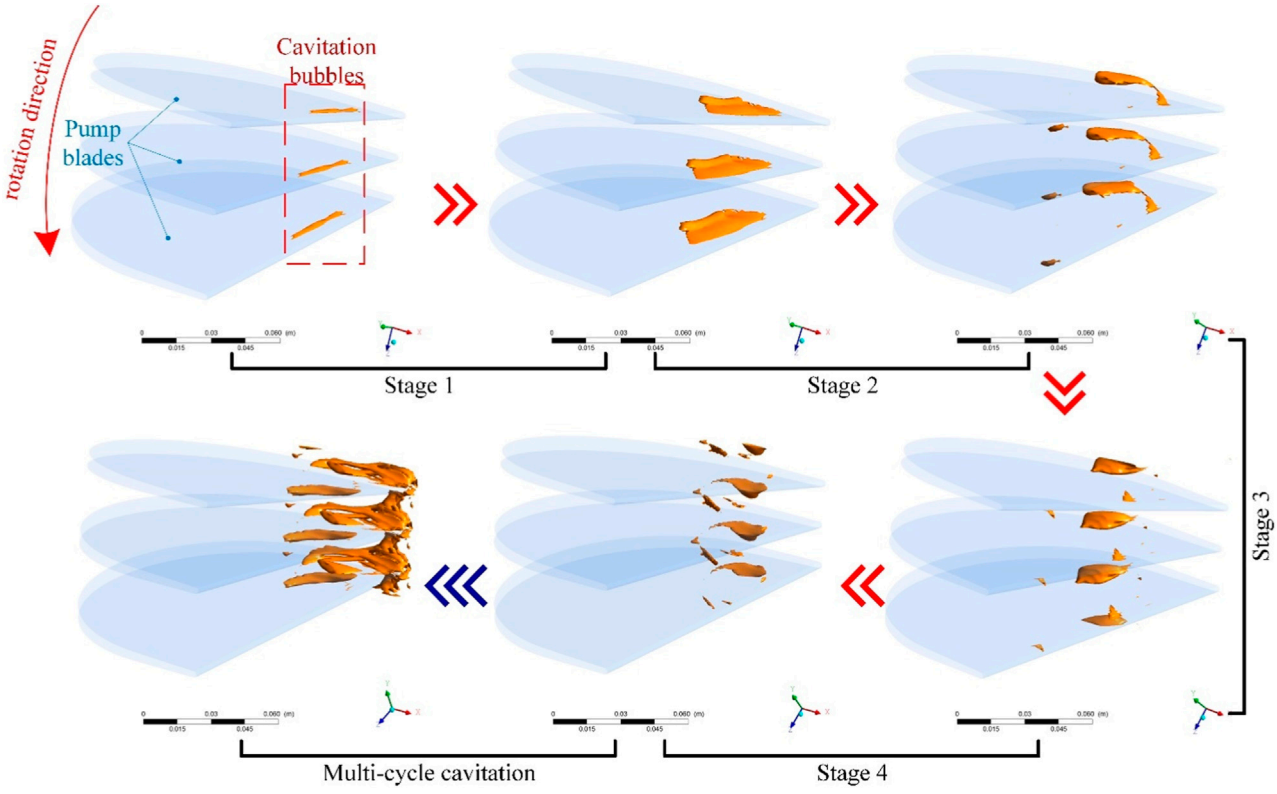

FIGURE 9
Evolution of cavitation bubbles.

simulate the working conditions of the downhole fluid coupling. A pump station was used to control the inlet and outlet pressures of the valve control oil and working water, complete the startup of the coupling, and test the macroscopic characteristics of the hydrodynamic coupling at different speed ratios. The rotation speed and torque sensors were used to obtain the dynamic hydraulic performance of the coupling. According to the comprehensive analysis results of the torque transmission characteristic computation data and test data, the prediction accuracy of the torque characteristic was verified. The macro

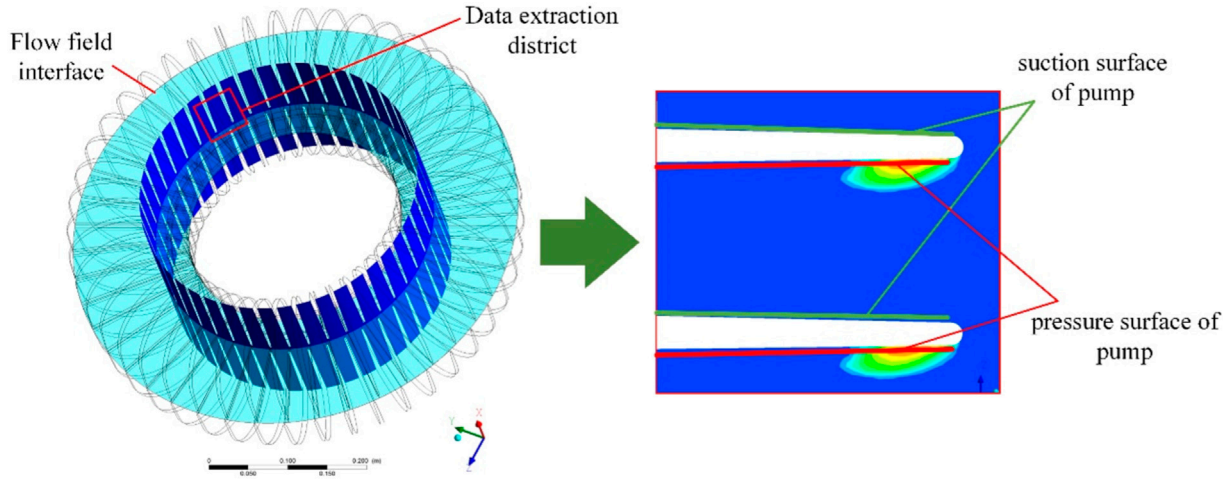

FIGURE 10
Schematic of cross-sectional position.

characteristic test plan and parameter settings of the hydrodynamic coupling are shown in Figure 5. Test device parameters mainly include that the power of power motor was set to 2500kW, rated input rotation speed of test bench and hydrodynamic coupling was set to 1475rpm, the water supply flow was greater than 240L/min, and rated power of hydrodynamic coupling was 1200 kW.

Data collection system: The test system data were collected by an efficiency meter industrial control computer. The main collection parameters were as follows: input torque, input speed, output torque, output speed, coupling liquid level pressure, coupling working chamber temperature, filling and discharging liquid valve action signal, and other data.

According to the test plan, a macro characteristic testbed was built. Carry out several repeated tests from starting and running to complete filling, draining, circulating and changing fluids. The working performance and reliability of the equipment were examined.

Test procedure: The drag motor was started at no load, drag motor was maintained at 1475 rpm, and coupling was filled with liquid. The coupling was then loaded until it reached the rated power and remained at the rated working conditions. After 8 h of operation, the coupling ran smoothly without abnormal noise. The input and output speed and torque data were collected and analyzed during the loading process.

4 Results and discussion

4.1 Cavitation distribution characteristics of steady flow field

According to the numerical analysis results of steady-state cavitation two-phase flow under fully filled working conditions, following the multicycle cavitation and steam accumulation processes in the flow field of the hydrodynamic coupling, a stable inner ring steam accumulation area was formed. The field resulted in a more stable circulation characteristic. The distribution characteristics of cavitation were analyzed at different speed ratios, combined with the liquid velocity and blade pressure distribution trends obtained before and after the cavitation computation model was opened at different speed ratios, which was required to realize complete filling. This analysis was then used to analyze the influence of cavitation on the flow field distribution characteristics.

Figure 6 and Figure 7 show the distribution characteristics of the flow field velocity streamlines when the cavitation computation model is turned off (Figure 6A) and turned on (Figure 6B), respectively. Comparative analysis shows that the water–liquid circulationSR velocity gradually decreased as the speed ratio increased. Because the steam generated in the cavitation process accumulated in the inner ring of the impeller, the water–liquid circulation state changed, and the circulation velocity was lower than that without the cavitation model. With an increase in the speed ratio, the volume of the vapor accumulation zone decreased because of the decrease in the degree of water cavitation, and its influence on the state of water circulation and flow velocity also decreased.

A comparative analysis of the effects of steam accumulation on the blade pressure field distribution under different steady-state cavitation simulation conditions is shown in Figure 8. The overall pressure distribution trends at the blade wall before and after opening the cavitation computation model were the same. Owing to the change in the circulation characteristics, the overall pressure distribution of the blade after cavitation was reduced. Simultaneously, because of the existence of the vapor accumulation area, the corresponding area generates low-pressure areas A and B, and the pressure gradient of the blade was evident.

4.2 Characteristics of transient cavitation

According to the distribution law of cavitation bubbles, the bubbles are mainly generated in the pump flow field. To analyze the distribution pattern and evolution law of the cavitation field in the pump flow field, a speed ratio of 0.6 was considered as an example to

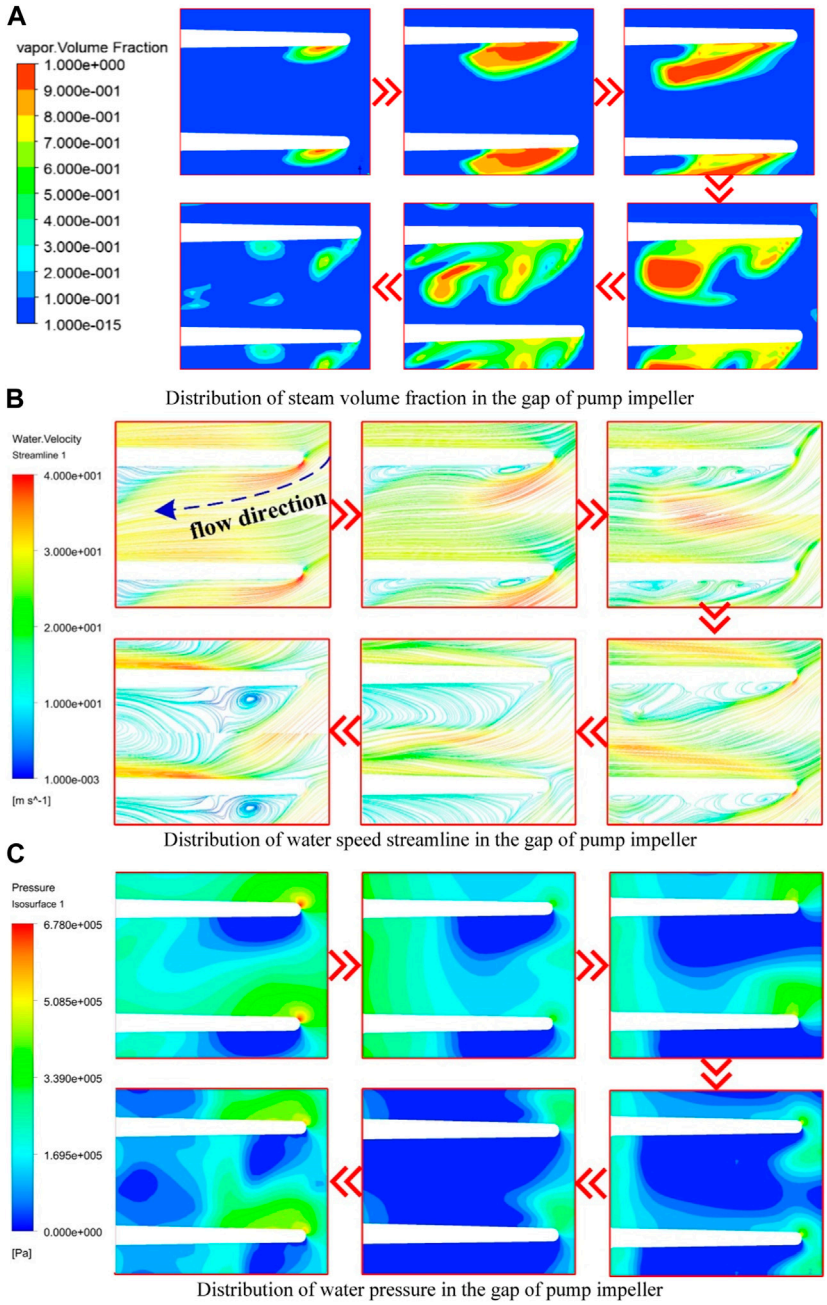

FIGURE 11
Simulated cloud image.

analyze the volume rate distribution of cavitation in different development stages.

Because the flow field in the fluid coupling is complex and three-dimensional, the cavitation bubble movement in the flow field is also complex and three-dimensional. Figure 9 shows the development of the cavitation bubble characterized by the 90% steam volume rate isosurface. The figure shows that the evolution of cavitation bubbles can be divided into four stages. In Stage 1, the banded bubble is born around the tip on the suction surface side of the pump blade; this bubble follows the steam in the cavitation bubble. Cloudy bubbles form in the accumulation of phases. In Stage 2, cavitation bubbles always adhere to the surface of the blades. As the bubbles leave the blades, some bubbles enter the flow channel and gradually form ellipsoidal bubbles. In Stage 4, when the volume of ellipsoidal bubbles increases and reaches a certain level, they break away from the surface of the blade. They then enter the flow channel and burst after covering a certain distance. Some steam condenses, and the remaining gas continues to move in the flow field, forming broken bubbles with irregular shapes and sizes and moving toward the inner ring of the pump wheel. Eventually, as cavitation continues to accumulate, a vapor concentration area is formed.

To obtain the volume rate, pressure, and speed distribution data of the cavitation observed near the blade tip of the pump wheel, located near the inner ring, at a speed ratio of 0.6, a circular data

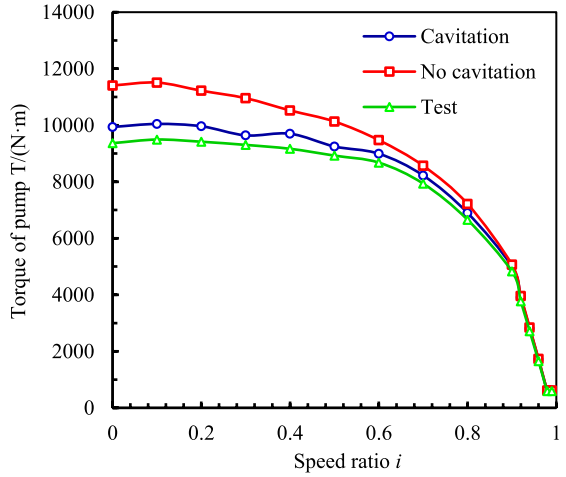

FIGURE 12
Transmission torque of flow field in impeller.

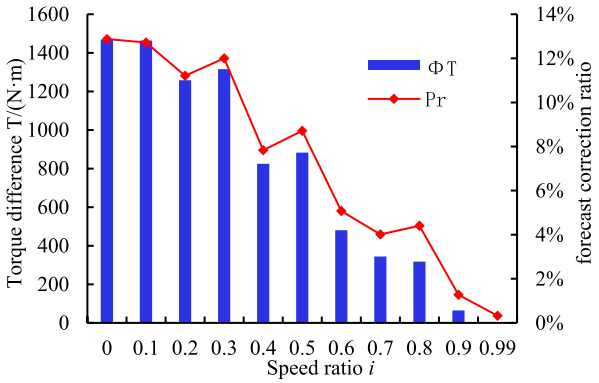

FIGURE 13
Torque correction distribution of cavitation model.

analysis cross section with a diameter of da = 180 mm was established, as shown in Figure 10.

Figure 11A shows the distribution of the steam volume fraction at the cross section. Figure 11B shows the distribution of water speed streamline. The evolution of cavitation from birth, growth, separation, and disintegration is evident. According to the transient changes in cross-sectional pressure and velocity, combined with the volume fraction distribution characteristics, part of the high-speed water from the turbine inner ring outlet enters the pump wheel and hits the blade tip; the flow rate then decreases rapidly and a local high pressure forms at the blade tip area. After passing through the tip area, the flow is affected by the local high pressure. Simultaneously, this flow is driven by other incoming flows to form a high-speed jet close to the blade surface as well as an angle with the surface. Therefore, on the pressure surface side of the impeller blades, a low-pressure region, wherein the pressure is below the vapor pressure, is formed near the tip of the blade; a severe cavitation phenomenon occurs in this region. As the cavitation bubble grows, the flow into the pump wheel is hindered by the bubble, and the jet angle increases. When the growth of cavitation is large, reverse flow can be found near the blade wall, and strong vortices are observed in the corresponding areas. This causes the internal pressure to decrease and promotes the formation of bubbles. As the cavitation bubble moves toward the inner circle of the circulation circle and breaks up, the jet angle decreases and promotes the birth of new cavitation bubbles.

The pressure distribution in Figure 11C shows that, owing to the increase in the jet angle and the appearance of strong vortices near the blade, the range of the low-pressure area near the tip area of the blade pressure surface becomes large, which promotes the growth of cavitation.

As the cavitation bubble grows further, under the influence of the bubble surface tension and the surrounding high-pressure water flow, the shape of the cavitation bubble gradually becomes irregular. As the bubble volume increases, the surface tension is insufficient to maintain the growth of the bubble, the bubble ruptures under the surrounding high pressure, and a small range of low-pressure fragmented bubble areas and new cavitation bubble birth areas form in the flow channel.

4.3 Torque characteristics

Figure 12 shows a characteristic diagram of torque transmission in a fluid coupling considering cavitation and noncavitation. Without cavitation computation, the overall output torque tends to decrease. As the speed ratio increases, the rate of decline continues to increase. The overall trend remains unchanged when the cavitation model is considered. Further, the transmission torque under cavitation is lower than that under noncavitation.

At low speed ratios, owing to the large rotational speed difference between the pump and turbine, the water–liquid circulation speed was rapid, and the cavitation phenomenon was severe. At this time, the torque transmission characteristic also severely deteriorated, and the output torque dropped significantly. As the speed ratio increased, the degree of cavitation in the flow field continued to decrease. At a speed ratio of approximately 0.9, cavitation had little effect on the flow state. Therefore, the occurrence of the cavitation phenomenon considerably affected the overload starting and working ability of the coupling. This phenomenon had relatively little influence on the torque transmission ability under rated working conditions.

To analyze the degree of influence of cavitation on the torque transmission characteristics accurately, P_T was defined as the torque forecast correction ratio, T_{N-C} as the torque computational result without considering the cavitation, T_C as the torque computational result considering the cavitation, and Φ_T as the characteristic difference.

The characteristic difference is

$$\Phi_T = T_{N-C} - T_C \tag{11}$$

The torque characteristic prediction correction is

$$P_T = \Phi_T / T_C \tag{12}$$

A comparative analysis of the correction of the torque transfer value of the flow field at different speed ratios is shown in Figure 13. The P_T is affected by the amount of cavitation vapor accumulation and the degree of cavitation occurrence, and the overall trend is a

downward trend as SR increases. At i = 0, P_T and Φ_T reach the maximum. At this time, the characteristic difference is 1468.35 N·m, and the correction ratio is 12.85%. At a speed ratio of 0.99, because the degree of cavitation is the lowest at this time, the correction factor is 0.32%.

5 Conclusion

In this study, CFD technology and experiments were used to investigate the unsteady flow field affected by the cavitation characteristics of fluid coupling. Based on the numerical simulation data, the cavitation distribution, evolution characteristics, and their effects on the torque transmission characteristics were analyzed. The study clarified the following:

1) The flow field results demonstrate that the severity of cavitation in the internal flow field of the coupling decreases with increasing SR, and the generated steam mainly accumulates at the inner ring of the pump wheel. The formation of a stable steam accumulation area reduces the circulation velocity and flow state of the flow field. Compared with the pressure distribution gradient obtained in the region not affected by cavitation, that on the blade surface affected by cavitation is larger, forming a low-pressure region near the inner ring.
2) Transient cavitation simulation demonstrates that cavitation bubbles are generated near the tip of the blade pressure surface of the internal flow field. Affected by the flow characteristics of water, the evolution process has four stages: birth, growth, separation, and disintegration. This is a periodic cyclic process. The generated steam is finally concentrated inside the circulation circle of the pump wheel. The flow velocity and pressure at the blade surface are both reduced.
3) An analysis of the torque transmission characteristics revealed that the torque drop is considerably affected by severe cavitation at a low speed ratio. The computation results demonstrate that the introduction of the cavitation calculation model can improve the accuracy of torque prediction by approximately 13% under a low speed ratio. The effect of cavitation is smaller at high speeds.

Data availability statement

The raw data supporting the conclusion of this article will be made available by the authors, without undue reservation.

Author contributions

The author contributions are as follows: HC was in charge of the whole trial; JZ wrote the manuscript; LL and GW assisted with sampling and laboratory analyses. All authors contributed to the article and approved the submitted version.

Funding

Supported by the Fund for Shanxi "1331 Project". Supported by Key Project of Key Research Programs of Shanxi Province (Grant No. 03012015002).

Acknowledgments

The authors would like to acknowledge their appreciation for the continuous assistance with the experiment from Prof. Teng Wang at China Coal Science and Technology Group.

Conflict of interest

The authors declare that the research was conducted in the absence of any commercial or financial relationships that could be construed as a potential conflict of interest.

Publisher's note

All claims expressed in this article are solely those of the authors and do not necessarily represent those of their affiliated organizations, or those of the publisher, the editors and the reviewers. Any product that may be evaluated in this article, or claim that may be made by its manufacturer, is not guaranteed or endorsed by the publisher.

References

Anderson, C. L., Zeng, L., Sweger, P. O., Narain, A., and Blough, J. R. (2003). Experimental investigation of cavitation signatures in an automotive torque converter using a microwave telemetry technique. *Int. J. Rotating Mach.* 9, 403–410. doi:10.1155/s1023621x03000381

Bai, X. R., Cheng, H. Y., Ji, B., and Long, X. p. (2018). Large eddy simulation of tip leakage cavitating flow focusing on cavitation-vortex interaction with Cartesian cut-cell mesh method. *J. Hydrodynamics* 30 (4), 750–753. doi:10.1007/s42241-018-0068-8

Chai, B. S., Wang, G. Y., and Yan, D., (2022). Numerical simulation of cavitation in torque converter and analysis of its influence on performance. *J. Jilin Univ. Eng. Technol. Ed.*, 1–9.

Cheng, H. Y., Bai, X. R., Long, X. P., Ji, B., Peng, X., and Farhat, M. (2020). Large Eddy Simulation of the Tip-leakage Cavitating flow with an insight on how cavitation influences vorticity and turbulence. *Appl. Math. Model.* 77, 788–809. doi:10.1016/j.apm.2019.08.005

Da Silva, M. J., Lu, Y., Sühnel, T., Schleicher, E., Thiele, S., Kernchen, R., et al. (2008). Autonomous planar conductivity array sensor for fast liquid distribution imaging in a fluid coupling. *Sensors Actuators A Phys.* 147 (2), 508–515. doi:10.1016/j.sna.2008.06.019

Dong, L., Xiao, J. W., and Ming, J. Y., (2017). Numerical simulation and experimental study on cavitation behavior of hydraulic retarder model. *J. Drainage Irrigation Mach. Eng.* 35 (1), 1–5. doi:10.3969/j.issn.1674-8530.15.0287

Guo, M., Liu, C., Yan, Q. D., Ke, Z., Wei, W., and Li, J. (2021). Evaluation and validation of viscous oil cavitation model used in torque converter. *Appl. Sci.* 11 (8), 3643. doi:10.3390/app11083643

Guo, M., Liu, C., Yan, Q. D., Wei, W., and Khoo, B. C. (2022b). The effect of rotating speeds on the cavitation characteristics in hydraulic torque converter. *Machines* 10 (2), 80. doi:10.3390/machines10020080

Guo, M., Liu, C., Yan, Q., Wei, W., and Khoo, B. C. (2022a). The effect of rotating speeds on the cavitation characteristics in hydraulic torque converter. *Machines* 10 (2), 80. doi:10.3390/machines10020080

Hur, N., Kwak, M., Moshfeghi, M., Chang, C. S., and Kang, N. W. (2017). Numerical flow analyses of a two-phase hydraulic coupling. *J. Mech. Sci. Technol.* 31 (5), 2307–2317. doi:10.1007/s12206-017-0427-3

Hur, N., Moshfeghi, M., and Lee, W. (2016). Flow and performance analyses of a partially-charged water retarder. *Comput. Fluids* 164, 18–26. doi:10.1016/j.compfluid.2016.10.033

Jin, W., Xu, X., Tang, Y., Zhou, H., Zhou, H., and Ren, X. (2018). Coefficient adaptation method for the Zwart model. *J. Appl. Fluid Mech.(JAFM)* 11, 1665–1678. doi:10.29252/jafm.11.06.28784

Kang, C., Mao, N., and Zhang, G. F. (2017). Highly confined floes and cavitation phenomenon in a hydraulic retarder. *J. Eng. Thermophys.* 38 (10), 2151–2158.

Li, X., Wu, Q., Miao, L., Yak, Y., and Liu, C. (2020). Scale-resolving simulations and investigations of the flow in a hydraulic retarder considering cavitation. *J. Zhejiang University-Science A* 21 (10), 817–833. doi:10.1631/jzus.a1900466

Li, Y. (2018). *Scale-resolving simulation and experimental verification of different working media flow based on stator/rotor*. Changchun, China: Jilin University.

Liu, C. B., Li, J., Bu, W. Y., Xu, Z. x., Xu, D., and Ma, W. x. (2018b). Application of scale-resolving simulation to a hydraulic coupling, a hydraulic retarder, and a hydraulic torque converter. *J. Zhejiang Univ. Sci.* 19 (12), 904–925. doi:10.1631/jzus.a1700508

Liu, C., Guo, M., and Yan, Q. D., "Numerical investigation on the transient cavitating flow inside a torque converter," in Proceedings of the 2019 IEEE 8th International Conference on Fluid Power and Mechatronics (FPM), Wuhan, China, April 2019, 208–216. doi:10.1109/FPM45753.2019.9035838

Liu, C., Guo, M., Yan, Q., and Wei, W. (2022). Influence of charging oil condition on torque converter cavitation characteristics. *Chin. J. Mech. Eng.* 35 (1), 49. doi:10.1186/s10033-022-00727-y

Liu, C., Wei, W., Yan, Q. D., Weaver, B. K., and Wood, H. G. (2018a). Influence of stator blade geometry on torque converter cavitation. *ASME J. Fluids Eng.* 4 (4), 0411021–04110210. doi:10.1115/1.4038115

Pan, X., Xinyuan, C., Hongjun, S., Jiping, Z., Lin, W., and Huichao, G. (2021). Effect of the blade shaped by Joukowsky airfoil transformation on the characteristics of the torque converter. *Proc. Institution Mech. Eng. Part D J. Automob. Eng.* 235 (14), 3314–3321. doi:10.1177/09544070211014291

Ran, Z., Ma, W., and Liu, C. (2022). Design approach and mechanism analysis for cavitation-tolerant torque converter blades. *Appl. Sci.* 12 (7), 3405. doi:10.3390/app12073405

Robinette, D. L. (2007). *Detecting and predicting the onset of cavitation in automotive torque converters*. Michigan, United States: Michigan Technological University.

Robinette, D. L., Schweitzer, J. M., Maddock, D. G., Anderson, C. L., Blough, J. R., and Johnson, M. A. (2008a). Predicting the onset of cavitation in automotive torque converters—Part I: Designs with geometric similitude. *Int. J. Rotating Mach.* 2008, 1–8. doi:10.1155/2008/803940

Robinette, D. L., Schweitzer, J. M., Maddock, D. G., Anderson, C. L., Blough, J. R., and Johnson, M. A. (2008b). Predicting the onset of cavitation in automotive torque converters—Part II: A generalized model. *Int. J. Rotating Mach.* 2008, 1–8. doi:10.1155/2008/312753

Sun, T. Z., Wei, Y. J., Zou, L., Jiang, Y., Xu, C., and Zong, Z. (2019). Numerical investigation on the unsteady cavitation shedding dynamics over a hydrofoil in thermo-sensitive fluid. *Int. J. Multiph. Flow* 111, 82–100. doi:10.1016/j.ijmultiphaseflow.2018.11.014

Timoshevski, M. V., Zapryagaev, L. L., and Peryunin, K. S., (2016). Cavitation control on a 2D hydrofoil through a continuous tangential injection of liquid: Experimental study. *AIP Conf. Proc.* 1770 (1), 030026. doi:10.1063/1.4963968

Wang, C., Guo, H. P., and Zhang, L. X., (2013). Influence of leading-edge suction on hydrodynamic and cavitation performance of hydrofoil. *J. Ship Mech.* 17 (12), 1361–1370. doi:10.3969/j.issn.1007-7294.2013.12.001

Watanabe, H., Yoshida, K., and Yamada, M., (1996). Flow visualization and measurement in the stator of a torque converter. *JSAE Rev.* 17 (1), 25–30. doi:10.1016/0389-4304(95)00058-5

Watanabe, H., Yoshida, K., and Yamada, M., (1997).*Flow visualization and measurement of torque converter stator blades using a laser sheet lighting method and a laser Doppler velocimeter* Warrendale, Pennsylvania, United States: SAE Transaction, 1196–1206.

Watanabe, M., Sasaki, K., and Miyamoto, K., (2007). *Toyota's new six-speed automatic transmission AB60E for RWD vehicles*. Warrendale, Pennsylvania, United States: SAE Technical Paper.

Xiong, P., Chen, X. Y., Sun, H. J., Jiping, Z., Lin, W., and Huichao, G. (2021). Effect of the blade shaped by Joukowsky airfoil transformation on the characteristics of the torque converter. *Proc. Institution Mech. Eng. Part D J. Automob. Eng.* 235 (14), 3314–3321. doi:10.1177/09544070211014291

Yu, D., Vamshi, K., and Pradeep, A., (2002). *Torque converter CFD engineering part 2: Performance improvement through core leakage flow and cavitation control*. Warrendale, Pennsylvania, United States: SAE Transaction, 1272–1285.

Zhang, J. H., Cui, H. W., and Wang, T.,(2020). Two-phase circulation characteristics prediction of variable speed hydrodynamic coupling. *Chin. Hydraulics Pneumatics* (4), 73–81.

Zhao, L. L., Dong, Z. Q., and Lian, J. Y.,(2016). Fast steerable principal component analysis. *Hydraulics Pneumatics Seals* 9, 1–12. doi:10.1109/TCI.2016.2514700

Zhou, H. C., Xiang, M., and Wu, Z. P., "Analysis and optimization of the effect of cavitation model parameters on calculation of cavitation flow field," in Proceedings of the 14th National Congress on Hydrodynamics and the 28th National Hydrodynamics Symposium, Pasadena, California, USA, September, 2017, 337–335.

Nomenclature

BN_P	Number of pump blades
BN_T	Number of turbine blades
D	Circular circle outer diameter [mm]
d	Circular circle inner diameter [mm]
da	A circular data analysis cross section diameter [mm]
d_B	Baffle diameter [mm]
F_{vap}	Cavitation vaporization coefficient
F_{cond}	Cavitation condensation coefficient
f(n)	Torque change rate
f_l	Liquid volume fraction
f_v	Vapor volume fraction
f_{nuc}	The nucleation site volume fraction
f_{SBES}	The fraction of RANS in the SBES model
h	Minimum blade thickness
h_B	Baffle thickness [mm]
i	i = n_T/n_P, The speed ratio
$\dot{m}$	The interphase mass transfer rate
$\dot{m}^+$	Mass condensation rate
$\dot{m}^-$	Mass vaporization rate
n_T	The turbine rotation speed [r/min]
n_P	The pump rotation speed [r/min]
P_v	Pressure in the bubble [Pa]
P_T	The torque forecast correction ratio
P	Liquid pressure [Pa]
R_B	Mean radius the cavitation [m]
T(n)	The computation result under the current density mesh [N·m]
T (n-1)	The computation result under the previous mesh with lower density [N·m]
T_C	The torque computational result considering the cavitation [N·m]
T_{N-C}	The torque computational result without considering the cavitation [N·m]
v_j	Liquid phase velocity [m/s]
v_t^{SBES}	Model viscosity [m2/s]
v_t^{RANS}	v_t^{RANS}:RANS portion of the mdeled viscosity [m2/s]
v_t^{LES}	v_t^{LES}:LES portion of the mdeled viscosity [m2/s]
ρ_l	ρ_l:Liquid density [kg/m3]
ρ_v	ρ_v:Vapor density [kg/m3]
ρ_m	ρ_m:Mixed fluid density [kg/m3]
μ_m	μ_m:Mixed fluid dynamic viscosity [Pa·s]
μ_l	μ_l:Liquid dynamic viscosity [Pa·s]
μ_v	μ_v:Vapor dynamic viscosity [Pa·s]
τ_{ij}^{SBES}	τ_{ij}^{SBES}:Model stress [Pa]
τ_{ij}^{RANS}	τ_{ij}^{RANS}:RANS portion of the modeled stress tensor [Pa]
τ_{ij}^{LES}	τ_{ij}^{LES}:LES portion of the modeled stress tensor [Pa]
Φ_T	Φ_T:The characteristic difference of the torque [N·m]

frontiers | Frontiers in Energy Research

TYPE Original Research
PUBLISHED 26 October 2023
DOI 10.3389/fenrg.2023.1292387

OPEN ACCESS

EDITED BY
Leilei Ji,
Jiangsu University, China

REVIEWED BY
Qixiang Hu,
Changzhou Institute of Technology, China
Hao Chang,
Jiangsu University, China

*CORRESPONDENCE
Zhenggang Huo,
zganghuo@126.com

RECEIVED 11 September 2023
ACCEPTED 11 October 2023
PUBLISHED 26 October 2023

CITATION
Huo Z and Zha X (2023), Influence of blade leading-edge form on the performance and internal flow pattern of a mixed-flow pump.
Front. Energy Res. 11:1292387.
doi: 10.3389/fenrg.2023.1292387

Influence of blade leading-edge form on the performance and internal flow pattern of a mixed-flow pump

Zhenggang Huo[1]* and Xiaoting Zha[2]

[1]College of Civil Science and Engineering, Yangzhou University, Yangzhou, China, [2]Jiangsu Hydraulic Engineering Construction Co, Ltd., Yangzhou, China

In this article, a typical mixed-flow pump was adopted as the research object to investigate the influence of the inlet structure within the impeller on the performance and internal flow patterns of the mixed-flow pump. First, three different blade inlet structure cases, which are forward bending, straight, and backward bending, were proposed and modeled separately. Second, the performance of mixed-flow pumps featuring different cases was carefully compared and analyzed. The results show that the inlet structure of the blades has a small impact on the head of the mixed-flow pump. However, it has a significant impact on the efficiency and shaft power of the pump at the rated flow condition. Among them, the performance of the straight and backward bending cases is significantly better than that of the front bending case. At the same time, the accuracy of the numerical results was verified by the experimental results. Finally, the internal flow and hydraulic loss laws with different inlet structures were deeply studied. It is found that the case of forward bending will cause the media to strike the middle of the inlet edge of the blade first and then generate a secondary flow along the inlet edge. The secondary flow will induce stronger media crowding at the inlet side near the shroud and hub. Due to the large curvature of the shroud and hub at the position of intersection with the inlet side of the blade, media crowding induces flow interference of the media on each span of the impeller channel. This ultimately leads to increased flow losses within the impeller and diffuser, reducing the hydraulic performance of the mixed-flow pump. This finding clarifies the influence mechanism of the inlet side geometry of the inlet blade on the performance and internal flow of the mixed-flow pump, which can provide a theoretical basis for improving the performance of the mixed-flow pump.

KEYWORDS

mixed-flow pump, unsteady flow, leading edge, secondary flow, turbulence

1 Introduction

The specific speed of the mixed-flow pump is larger, which makes it easier to obtain higher hydraulic efficiency. This is why they are applied in many fields, such as the chemical industry, water conservancy, and agriculture (Li et al., 2020; Yang et al., 2021; Kan et al., 2022). At the same time, many use environments also put forward higher requirements for their performance and operation stability (Yang et al., 2022a; Yang et al., 2023). Therefore, researchers have carried out several studies to improve its performance and operational

stability (Li et al., 2021; Yang et al., 2022b; Ji et al., 2023). A large number of studies have shown that the geometric structure of the impeller blades of a mixed-flow pump has a very significant impact on pump performance (Tan et al., 2017; Ji et al., 2021). Wu et al. (2015) made the flow structure in the impeller channel more uniform by geometrically correcting the outlet side of the impeller blades of the mixed-flow pump, which significantly widened the flow range of the mixed-flow pump and improved its hydraulic efficiency under high-flow conditions. Based on numerical simulation and experiments, Bing and Cao (2014) explored in detail the influence of position parameters at the inlet and outlet of the blade on the hydraulic loss and performance of the mixed-flow pump. It is found that reducing the blade angle on the blade trailing edge is conducive to reducing the absolute velocity in the outlet area, which, in turn, reduces the hydraulic loss in the region and improves the hydraulic efficiency of the mixed-flow pump. Bing and Cao (2013) also took multiple geometric parameters of the impeller blade as independent variables at the same time, carried out a large number of numerical simulations, and conducted performance tests on the case with better performance. It is found that the hydraulic performance of the mixed-flow pump can be effectively improved by combining different geometric parameters of the blades to carry out a large number of numerical simulations, but this work requires a lot of computational resources and time. Tan et al. (2018) investigated the influence of tip position and shape of mixed-flow pump blades on tip leakage and performance of the mixed-flow pump, and proposed the structure of a T-shaped tip. This structure can not only improve the hydraulic efficiency of the pump but also significantly reduce the pressure fluctuation intensity at the blade tip clearance.

Among the parameters of the mixed-flow pump blade, the parameters of the leading edge were found to have a significant impact on the pump performance and operation stability. Zhu et al. (2019) optimized the symmetric leading-edge shape of the mixed-flow pump based on a genetic algorithm and numerical simulation. The results show that the fine-tuning of the blade inlet side section can significantly improve the cavitation performance without affecting the efficiency and head of the pump. Kim et al. (2022) investigated the effect of the transition surface shape from the working surface to the back surface at the inlet side of the blade on the flow structure within the impeller of a mixed-flow pump in the non-cavitation state *versus* the cavitation state. It was shown that the transition surface shape of the square shape induces significant flow separation and vortex generation in the non-cavitation state. In the cavitation state, the greater the ellipticity of the transition connection between the working surface and the back surface, the stronger its anti-cavitation performance. Brennen (2011) studied the influence of the sharp degree of the blade inlet edge shape on the performance of the mixed-flow pump under non-cavitation and cavitation conditions. It is found that the sharper the shape of the blade inlet edge, the better the performance of the mixed-flow pump. However, when the inlet edge is too sharp, there is a risk of being left out of focus because of the shutter. Tao et al. (2018) similarly carried out research on the influence of inlet side structures with different shapes on the cavitation performance of the pump at rated flow. It is found that the shape of the leading edge of the blade will strongly affect the flow separation, pressure drop, and cavitation of the medium, and the prediction of the low-pressure region at the position of the leading edge can be used as a critical assessment index for the pump cavitation performance. Ardizzon et al. (1995) studied the influence of the blade leading-edge attack angle on medium flow. The influence of the incident angle of the medium on the cavitation performance of the pump was discussed. It was found that the flow mode and local pressure peak of the medium were the most closely related parameters to the cavitation performance.

Scholars have already recognized that the geometric structure of the blade inlet edge has a significant impact on the pump performance and operation stability. However, the existing research mainly focuses on the influence of the blade leading-edge shape on pump cavitation performance, while the influence of the inlet edge shape on pump performance has not been found. Based on the research method of combining numerical calculations and experimental verification, this paper studies the influence of the inlet edge shape on the performance and internal flow structure of the mixed-flow pump in order to provide some help for improving the performance and operation stability of mixed-flow pumps.

2 Geometry and parameters

The research object of this paper is a small mixed-flow pump used for water cooling of a large mechanical system. The structure of the mechanical system limits the outer diameter of the pump body to no more than 100 mm. So, the maximum radial size of the model meridian is limited to 90 mm. The design flow of the mixed-flow pump model is Q_r = 30 m^3/h. In order to meet the requirements of the piping arrangement of the mechanical system, the head of pump H_r under the design flow shall not be less than 10 m. The rated operating speed of the water pump is n_r = 6000 r/min. On this basis, we can determine the specific speed of the hydraulic model under the rated flow as follows:

$$n_s = \frac{3.65 n_r \sqrt{Q_r}}{H^{3/4}} = 355.5. \quad (1)$$

Due to the high head and efficiency requirements of this hydraulic model under the rated flow condition, the impeller is of the meridian closed type, and the pressure chamber adopts the space diffuser to meet the design requirements. Figure 1 shows the meridian of the main overflow components of the mixed-flow pump. Figure 2 shows the hydraulic model of the impeller blade inlet side of the three geometric structures of the program. The main dimensions marked in the figure have been listed in Table 1.

3 Numerical modeling

3.1 Mathematical model

NX software is adopted for three-dimensional modeling of the mixed-flow pump hydraulic system in this paper. As the most central hydrodynamic components, the blade modeling accuracy of the impeller and diffuser has a great impact on the accuracy of the numerical results. Therefore, the method of determining surfaces from point sets is used for blade modeling of impellers and diffusers. The large amount of point data in the point set not only ensures the accuracy of blade modeling but also ensures that the shape of the blade in the numerical simulation model has a high degree of consistency with that of the rapid prototyping blade used for testing. For this mixed-flow pump, its inlet and outlet pipelines in the cooling system are straight pipes, and

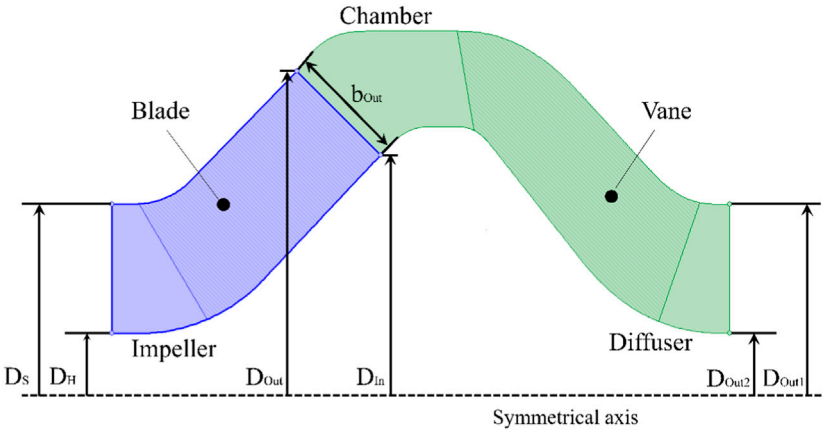

FIGURE 1
Meridian of the main overflow components of mixed-flow pumps.

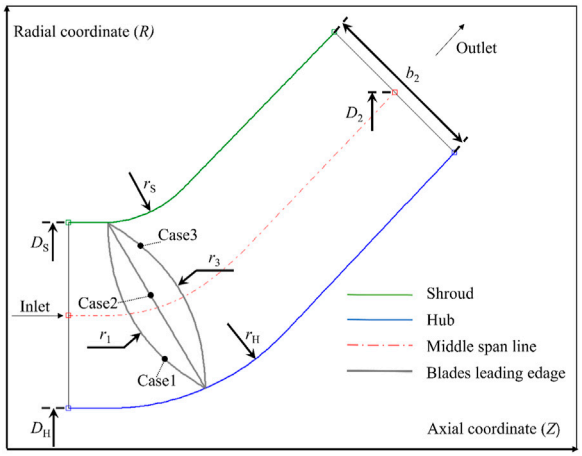

FIGURE 2
Three geometric structure cases for the inlet side of impeller blades.

the inlet and outlet pipe lengths are long. Therefore, the inlet and outlet pipes in the three-dimensional modeling process are also in the form of straight pipes, and the length is 10 times the impeller inlet diameter to ensure the accuracy of the numerical simulation.

3.2 Grids

The use of a structured hexahedron grid in numerical calculation not only improves the speed of data transmission and thus reduces the time of numerical simulation but also improves the quality of data transmission and the convergence of numerical calculation. The grids used in different numerical calculation cases in this paper are all hexahedral structured grids which are generated in Ansys TurboGrid software. At the same time, 15 layers of the boundary layer are arranged near the solid wall within the calculation domain, and the growth rate of the boundary layer is set as 1.05. However, at the inlet side of the impeller blade, the number of layers of the boundary layer is set to 20 in order to capture the fine flow structure of the medium. The grid assembly of the main computational domain and the details of each case are shown in Figure 3.

In order to further reduce the influence of the grid on the numerical results, the grid independence analysis was also carried out in this paper. On the basis of ensuring that the included angles of the edges are greater than 18°, the performance analysis of the mixed-flow pump in case 2 was carried out for the change of the single side length of the hexahedral grid (the maximum control size of the grid). It can be seen from Table 2 that when the control size of the grid does not exceed 1.8, the fluctuation of the numerical prediction results of the head and efficiency of the mixed-flow pump does not exceed 1%. At this time, the influence of the grid on the results of numerical calculations is small, so 1.8 is chosen as the control size of the subsequent grid used for numerical calculations.

3.3 Boundary conditions

In order to further improve the accuracy of numerical calculations, the pre-settings of the numerical cases should take into account the convergence of the case and the real situation of the mixed-flow pump. As shown in Figure 4, in order to enhance the convergence of the numerical case, the boundary conditions in this paper adopt the inlet total pressure and the outlet mass flow rate. Because the impeller of the mixed-flow pump is made of precision-cast stainless steel, its roughness is low, so the solid wall in the calculation domain is set to no-slip wall, and the roughness is set to 10 um. In addition to the impeller calculation domain being set to rotate, the other calculation domains are set to stationary. The impeller and the front and back calculation domains are connected by the frozen rotor to ensure the accuracy of data transfer. The convergence accuracy of the numerical calculation is set to 10^{-4} to ensure the accuracy of the calculation results.

The k-ω SST turbulence model has obvious advantages in high-precision boundary layer simulation, and it has high accuracy in predicting the flow structure near the wall of the impeller blade. The resolution of the boundary layer needs to be more than 10 points to

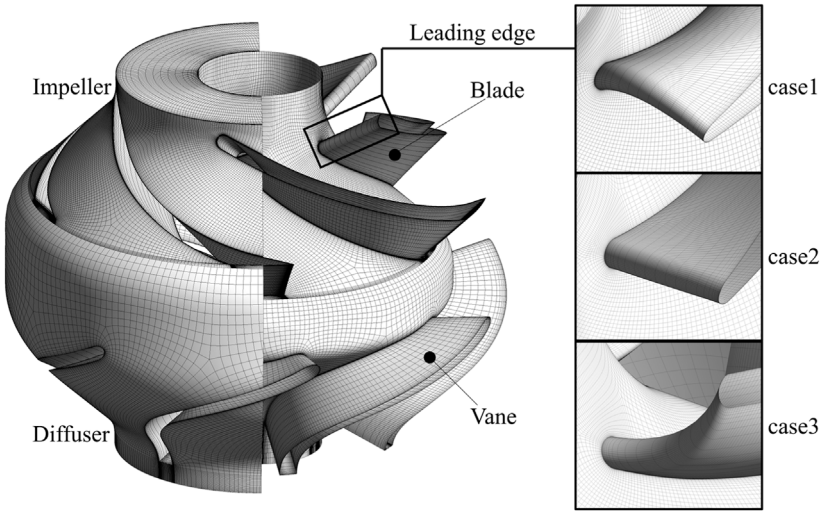

FIGURE 3
Grid details of main hydraulic components.

TABLE 1 Geometric specifications of the impeller and the diffuser.

Impeller		Bridge radius of hub r_H (mm)	18.63
Number of blade Z_1	5	Leading-edge radius of case 1 r_1 (mm)	15.5
Diameter of the shroud D_S (mm)	50	Leading-edge radius of case 3 r_3 (mm)	15.5
Diameter of the hub D_H (mm)	21.6	Diffuser	
Diameter of the outlet D_{Out} (mm)	79.19	Number of vane Z_2	7
Width of the outlet b_{Out} (mm)	13	Diameter of outlet outer D_{Out1} (mm)	21.6
Impeller diameter D_2 (mm)	70	Diameter of outlet inner D_{Out2} (mm)	50
Bridge radius of the shroud r_S (mm)	8.75		

TABLE 2 Grid independence analysis.

Maximum grid size (mm)	2.4	2.2	2	1.8	1.6
Number of grids (*10^6)	2.9	4.8	5.7	7.0	9.1
Predicting head (m)	19.68	18.97	18.57	18.46	18.42
Predicting efficiency (%)	77.21	76.88	76.02	75.98	75.96

ensure the conditions for the use of the model (Menter, 1994). The grid used in this paper fully meets the requirements, so the numerical calculation model used in this paper is the *k*-*ω* SST turbulence model. The following two equations are the transport equations for the turbulent kinetic energy, *k*, and the turbulence frequency, *ω*.

The *k*-equation is represented as follows:

$$\frac{\partial(\rho k)}{\partial t} + \nabla\cdot(\rho \boldsymbol{U} k) = \nabla\cdot\left[\left(\mu + \frac{\mu_t}{\sigma_k}\right)\nabla k\right] + P_k + P_{kb} - \beta'\rho k\omega. \quad (2)$$

The *ω*-equation is expressed as follows:

$$\frac{\partial(\rho\omega)}{\partial t} + \nabla\cdot(\rho \boldsymbol{U}\omega) = \nabla\cdot\left[\left(\mu + \frac{\mu_t}{\sigma_\omega}\right)\nabla\omega\right] + \alpha\frac{\omega}{k}P_k + P_{\omega b} - \beta\rho\omega^2. \quad (3)$$

Here, μ_t is the turbulence viscosity. P_{kb} and $P_{\omega b}$ represent the influence of the buoyancy forces. P_k is the production rate of turbulence.

4 Results and discussion

4.1 Pump performance validation

In order to further ensure the accuracy of numerical calculation results, performance test verification was carried out in this paper. In the three cases, the impeller blade inlet side structure in case 2 is a straight line from the shroud to the hub, which is the most convenient for the machining accuracy verification of the test model. Therefore, case 2 is selected to carry out the verification performance test. The test was carried out on a closed test bench.

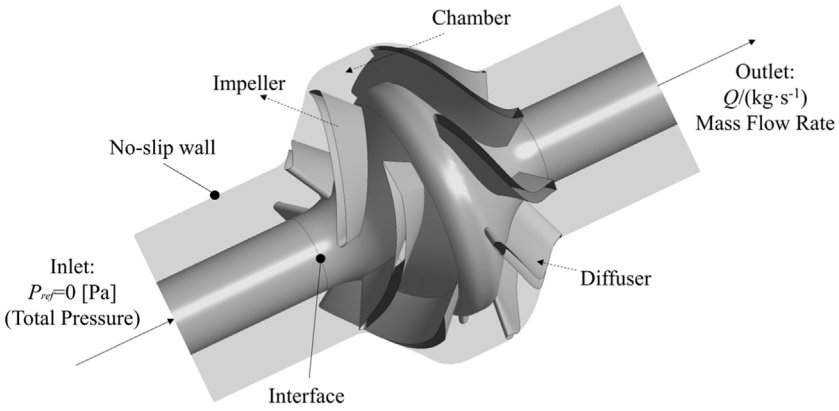

FIGURE 4
Computational domain model and boundary conditions.

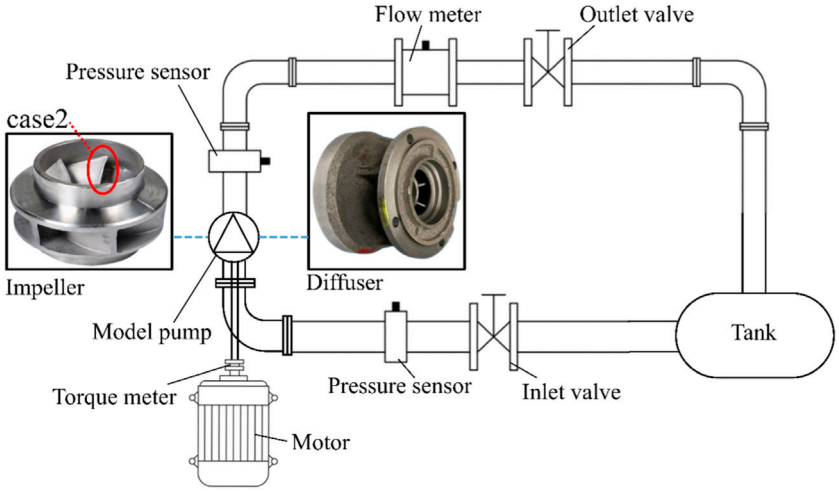

FIGURE 5
Test bench system.

The pressure at the inlet and outlet of the mixed-flow pump was collected using the pressure sensor at the inlet and outlet, and transmitted to the computer in real time to calculate the pump head. The real-time flow of the pump is obtained using the electromagnetic flowmeter, and the shaft power and pump speed are obtained using the torque meter. Figure 5 shows a sketch of the experimental system and for the case 2 impeller and diffuser in kind. The impeller is made of stainless steel by precision casting, and the diffuser is made of the original physical model of the pump manufacturer. The production process is the disappearing mold casting.

Figure 6 shows the comparison between the numerical prediction results of the model of case 2 and the experimental results. Under the rated flow condition, the numerically predicted head is 1.08% higher than the experimental head, and the numerically predicted efficiency is 1.15% higher than the experimental efficiency, so the numerically predicted results have high accuracy. The reason that the numerical prediction results are slightly higher than the experimental results under the rated flow condition is that there is a small amount of volumetric and mechanical losses during the experimental process. Under the small flow condition, the error between the numerically predicted head and the experimental head remains small. However, the error between the numerically predicted and experimental efficiencies increases slightly and reaches a maximum value of 4.24% at 0.6 times the rated flow condition. At high flow conditions, the predictions of head and efficiency increase with the increase in the flow rate. At 1.4 times the rated flow condition, the numerical prediction error of the head reaches a maximum of 1.61 m, and the numerical prediction error of efficiency reaches a maximum of 3.99%. The main reason for the increased deviation of the numerical prediction results for the non-rated flow condition compared to the rated flow condition is the elevated intensity of the unsteady flow in the flow field. The true head and efficiency of the pump show periodic

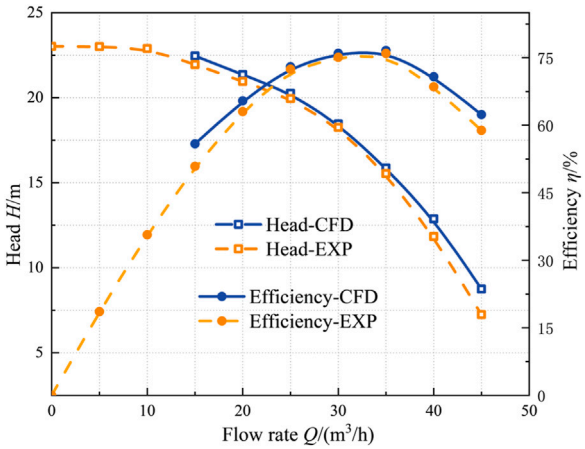

FIGURE 6
Comparison of numerical predictions of pump performance with test results.

fluctuations, which cannot be reproduced by steady-state numerical simulation. In conclusion, the numerical method in this paper has a small error in predicting the pump performance near the rated flow condition, and the error in predicting the performance under the deviation from the rated flow condition is slightly improved, but the prediction error in the full flow range does not exceed 4.5%. Moreover, the numerical prediction of head and efficiency in the trend of change with the test results also maintains a high degree of consistency, and the prediction of the pump's highest efficiency point is very accurate. In summary, the numerical method used in this paper has high accuracy.

4.2 Comparison of performance under different inlet side cases

Figure 7 shows the performance comparison of the mixed-flow pump under three different impeller blade inlet side cases. It can be seen from Figure 7A that the pump head of case 1 is higher than that of the other two cases under small flow and large flow conditions.

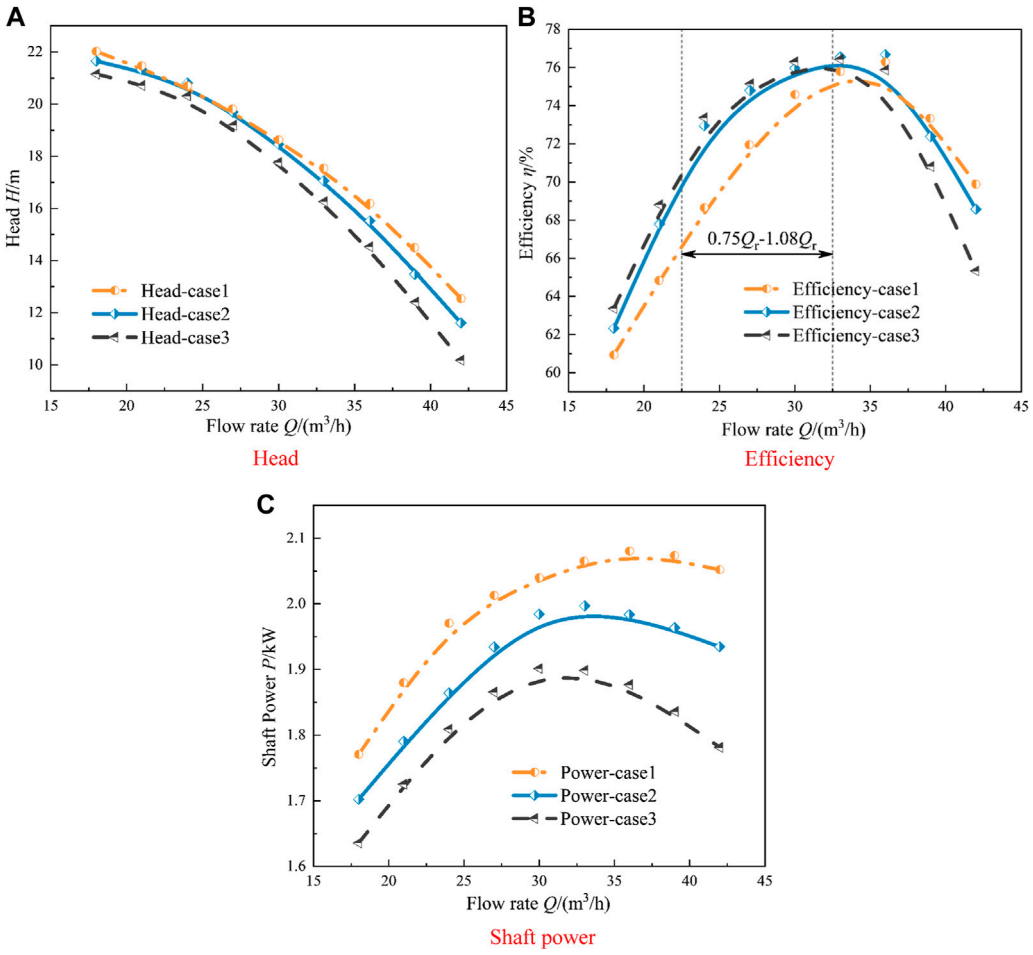

FIGURE 7
Performance under different inlet side cases.

However, within the range of 0.8 Q_r~1.0 Q_r, the difference between the pump heads of case 1 and case 2 is small. The head of case 3 is smaller than that of the other two cases under full flow conditions. Combined with the axial projection of each case in Figure 1, it can be seen that the axial projection area of case 3 is the smallest, so the contact area between the impeller blade and the medium is the smallest, which is the reason for its low head. For case 3, the minimum projected area of its axial plane causes its head to be low, but Figure 7C shows that its axial power is significantly lower than that of the other two cases under full flow conditions. Moreover, compared with the other two cases, the maximum shaft power point shifts to the rated flow point, so it has better non-overload performance. Comparing the efficiency of the three cases, it can be seen that the efficiency performance of case 1 is the worst in the range of 0.6 Q_r~1.0 Q_r, the efficiency performance of case 3 is the worst under the condition of large flow (1.4 Q_r), and the efficiency range of case 2 is the largest. Since this mixed-flow pump often operates in the range of 0.75 Q_r ~1.08 Q_r, the energy-saving effect of case 2 and case 3 is significantly better than that of case 1.

4.3 Flow field pattern with a mixed-flow pump

Figure 8 shows the circumferential flow angle of the medium on the mid-span of the impeller channel of different cases. Under the condition of a small flow rate, the media flow angle of each case has an obvious uneven distribution in the circumferential direction, and the difference between each case is small. The specific performance is that the media flow angle of the medium near the back of the blade is significantly smaller than that near the working surface of the blade. Meanwhile, the uniformity of the medium flow angle in the circumferential direction of each scheme is significantly improved at rated flow conditions. However, the distribution difference among the cases is significantly elevated. Near the back of the impeller blade, the high media flow angle area of case 1 extends to the impeller outlet. This indicates that the media at this position has a secondary flow perpendicular to the mainstream direction. However, near the working surface of the blade, the media flow angle distribution of the media and other areas of the channel have obvious stratification. This may be caused by the impact of the media at the blade inlet on the blade inlet edge. At the same time, the secondary flow in the channel caused by the uneven distribution of the media flow angle in the channel will also induce the uneven distribution of the impeller outlet flow in the circumferential direction. It can be seen that the media flow angle in region 2 is significantly smaller than that in the regions on both sides, which will lead to stronger "wake-jets" in the medium at the impeller outlet and, thus, induce a stronger rotor–stator interaction. Compared with case 1, case 2 and case 3 have a significantly more uniform circumferential distribution of the media flow angle under rated flow

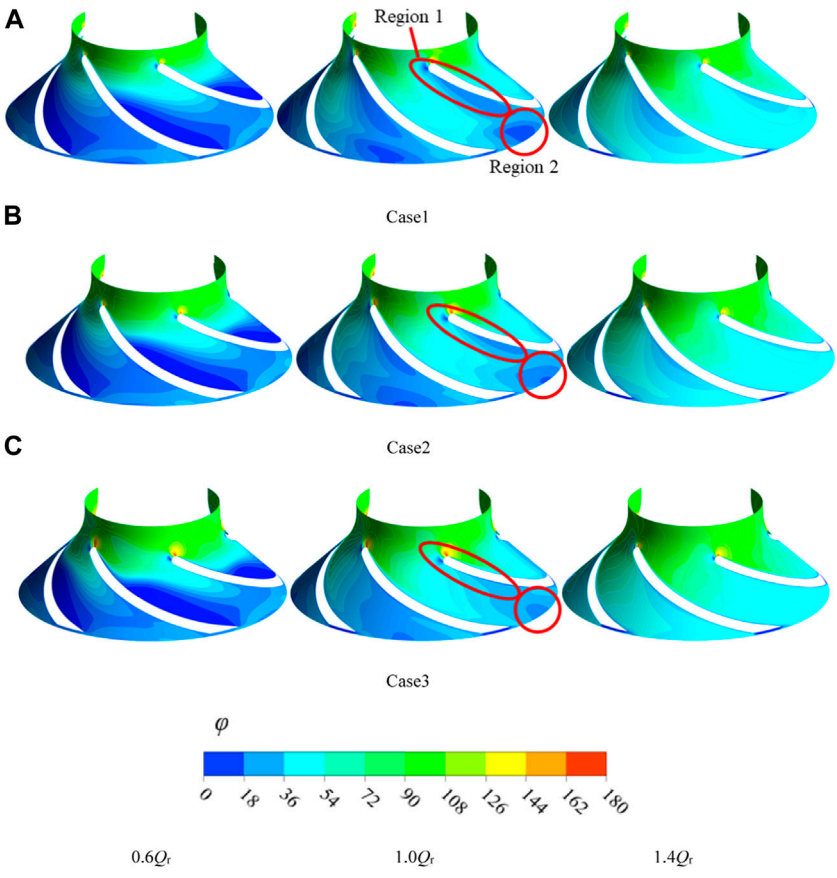

FIGURE 8
Circumferential media flow angle on the mid-span of the impeller channel for different cases.

conditions, which is more conducive to reducing its hydraulic loss and improving its operation stability.

The velocity gradient distribution in the span direction at the mid-span position of the impeller channel for different cases is shown in Figure 9. Under small flow conditions, the overflow area of the impeller channel is larger than the area required for uniform media overflow. As a result, there is an obvious interference of the medium on each span, which is manifested in the presence of a clear region of high values of the velocity gradient in the first half of the impeller channel. Among them, the region of high values of the velocity gradient in case 1 is from the position of the blade inlet and occupies the entire flow path from the back of the blade to the working surface. It indicates that in these regions, there is flow interference of the medium in the span direction. Compared to case 1, the influence range of this high-velocity gradient region in case 2 is slightly reduced, but the flow interference of the medium on each span is still more obvious. Case 3 is in the region of the smallest range of influence, and its location is not near the impeller blade inlet edge but in the middle of the impeller channel near the back of the blade. This suggests that the shape of the blade inlet edge of case 3 is effective in reducing the media flow interference on each span. It also indicates that the high-velocity gradient region in cases 1 and 2 may be caused by the flow separation between the inlet edge and the middle position of the flow path. Under the rated flow condition, the effect of the blade inlet edge structure on the media flow interference on each span still exists. First, the overall velocity gradient in the flow

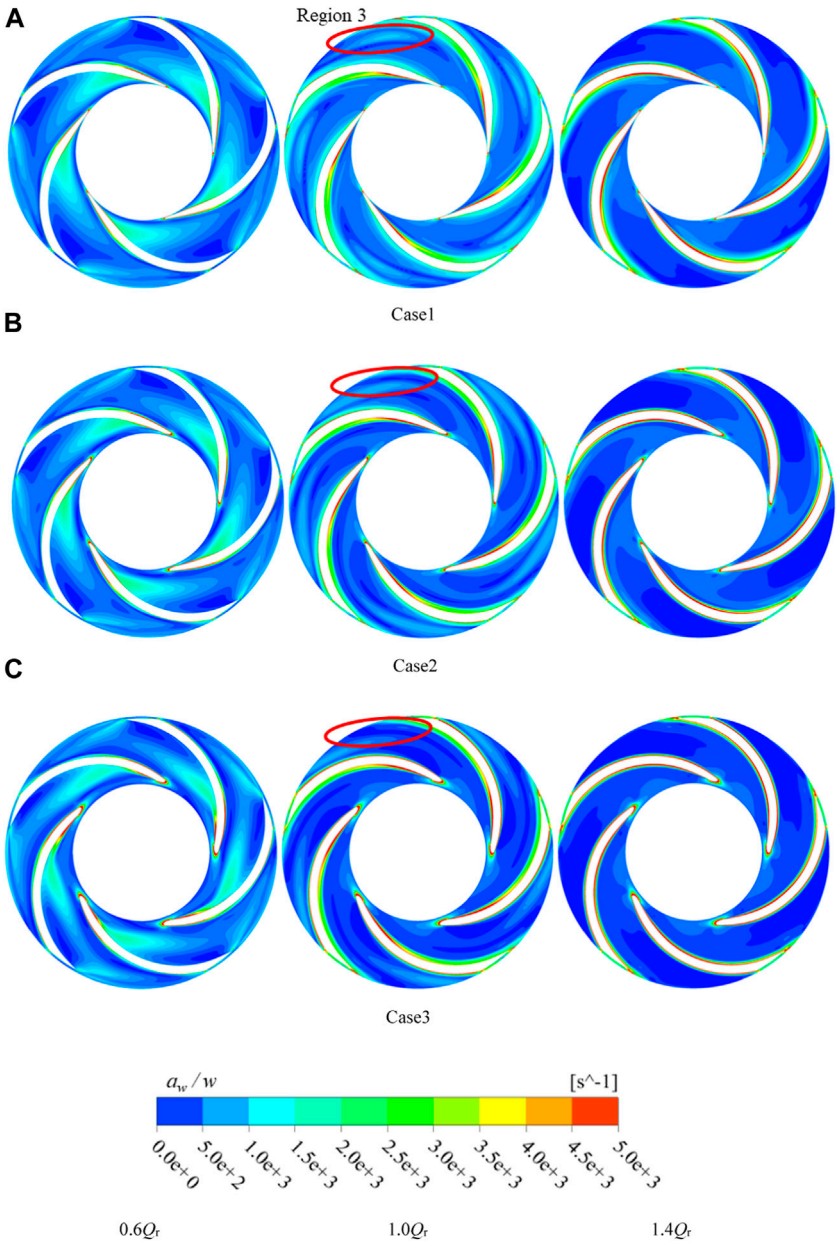

FIGURE 9
Flowfield pattern at the mid-span surface of cavities under different flow conditions.

channel of case 1 is significantly higher than that of the other two cases, and case 3 has the smallest overall velocity gradient. At the same time, there is an obvious flow interference in region 3 between the spans at the impeller outlet position in case 1. This also shows that the change in the geometric structure of the inlet side of the blade not only affects the flow in the impeller channel but also directly changes the flow pattern of the medium at the outlet of the impeller, which, in turn, affects the flow structure of the medium in the diffuser.

In order to further analyze the flow difference of the medium in the direction from the shroud to the hub, Figure 10 shows the medium flow rate on the 0.8-span cross section near the shroud and the 0.2-span cross section near the hub under the rated flow condition. Combined with the flow interference analysis of each span in Figure 10, the axial projection diagram of the influence of the impeller blade inlet structure on the medium flow is drawn. At the position of the 0.2-span cross section, the influence of the blade inlet structure on the distribution of medium velocity is very obvious. The forward curved inlet edge structure in case 1 will cause the medium to hit the middle of the inlet edge the first time. Because the inlet edge has a certain thickness, its crowding out of the medium will cause the medium to generate a secondary flow along the path of the dotted line in the schematic diagram. This will inevitably lead to an increase in the flow on the 0.2 span and 0.8 span cross sections near the shroud and hub and, thus, strengthen the medium crowding at the blade inlet near the cover plate. From the velocity distribution diagram, it can be seen that the 0.8-span cross section of case 1 has an obvious low-velocity region near the inlet side of the blade, which is caused by the medium hitting the inlet of the blade. The low-velocity region is bound to cause more hydraulic losses. In addition, in case 2, the low-speed area of the scope of the obvious reduction, this is because the program does not have the above secondary flow. However, comparing the velocity distributions at the 0.2 span and 0.8 span inlet locations in cases 1 and 2, it can be found that the inlet crowding phenomenon on the 0.8-span cross section is significantly stronger than that on the 0.2-span cross section. This is because the excessive arc curvature of the shroud is smaller, and the change of the flow direction of the medium is more obvious when it passes near this position, and flow interference between the spans is more likely to occur, which leads to hydraulic loss. On the other hand, on

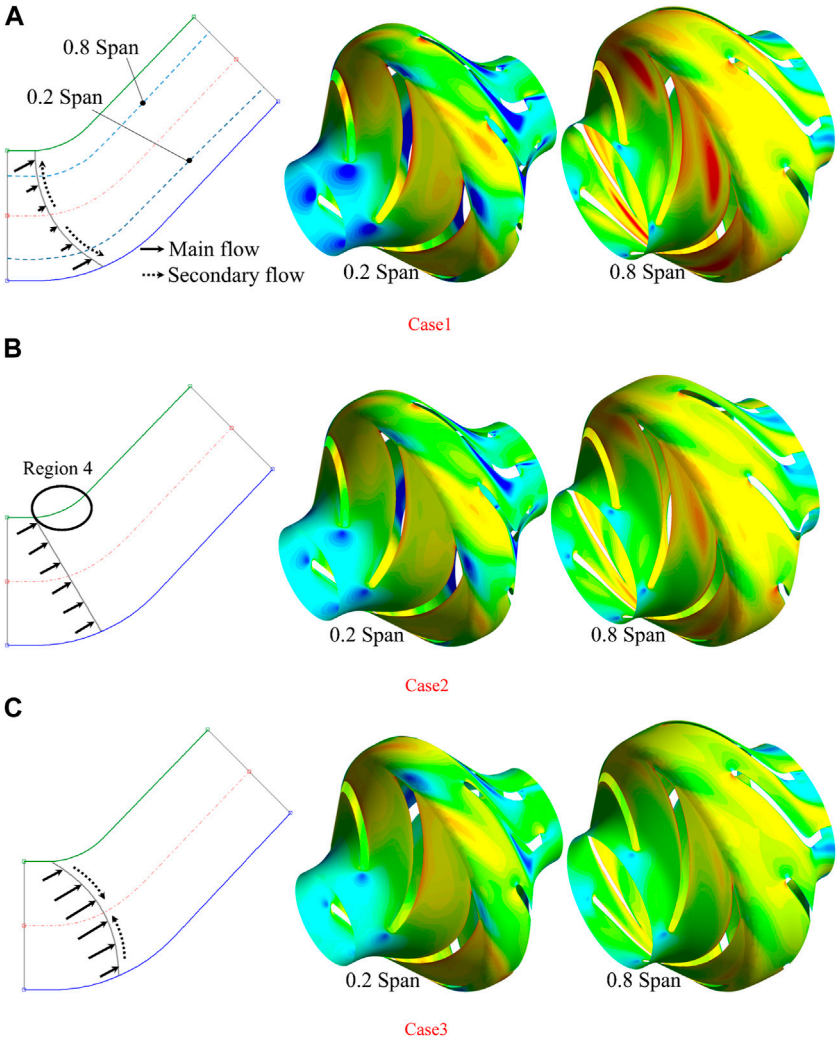

FIGURE 10
Media flow rate in the 0.8-span cross section and 0.2-span cross section at the rated flow condition and media flow near the inlet.

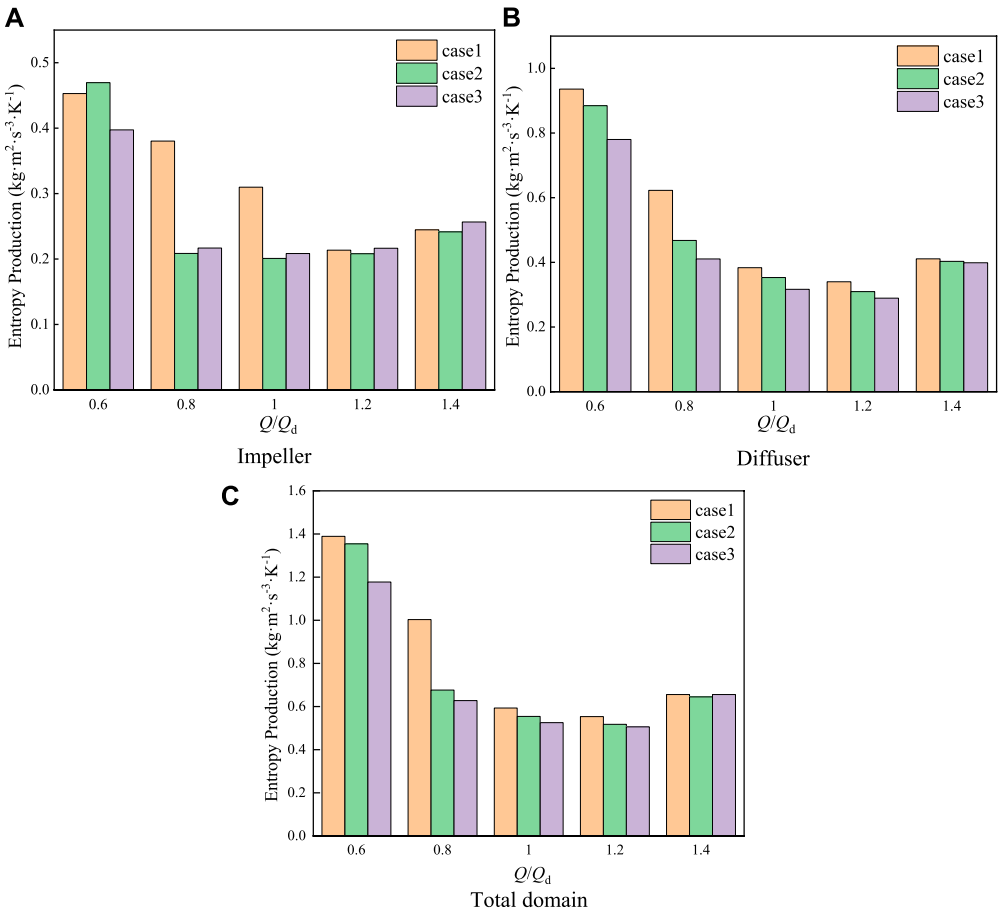

FIGURE 11
Pressure distribution on the mis-span midline within the chamber.

0.2 span, the large curvature transition section of the rear cover plate is helpful in preventing inter-span flow interference. In case 3, the medium first hits the inlet side of the blade near the shroud and hub, which causes the secondary flow in the opposite direction of case 1. This avoids the superposition of the high-intensity region of the flow interference between the spans and the region near the shroud with a smaller curvature. The media crowding at the inlet side of the blade near shroud is significantly reduced. At the same time, the case 2 and case 3 impeller outlet position of the media flow distribution is also significantly more uniform, which is conducive to reducing the rotor–stator interaction of the hydraulic system.

The entropy production statistics in the impeller, diffuser, and overall calculation domains of different cases are shown in Figure 11. For the impeller calculation domain, the entropy production of case 1 under 0.8 Q_r and 1.0 Q_r flow conditions is significantly larger than that of the other two cases, which is in good agreement with the previous analysis. In addition, from Figure 10B, it can be seen that there is also a significant difference in the hydraulic losses within the diffuser under different inlet side structures. The previous analysis found that the uneven flow phenomenon of the medium near the impeller outlet in case 1 is more obvious, which directly leads to the entropy production within the diffuser in the working condition range of 0.6 Q_r~1.2 Q_r that is significantly higher than in the other two cases. The entropy production statistics of the overall calculation are shown in Figure 10C, and the difference in entropy production under the 0.8 Q_r working condition of each case is the largest, which coincides with the results of the efficiency analysis in Figure 8.

5 Conclusion

The influence of the blade leading-edge structure on the performance and internal flow pattern of a mixed-flow pump is studied in this work. Different impeller blade leading-edge cases which are forward curved, straight, and backward curved are designed. Numerical calculations are carried out for different cases. The performance difference of each case is carefully compared and analyzed with respect to the internal flow characteristics. As it is shown, the main conclusions can be extracted as follows:

1) Based on the performance test, the numerical prediction error at the rated flow condition is less than 1.2%. Meanwhile, the numerical prediction error is less than 4.5% under off-rated flow rates. More importantly, the prediction of the performance

change law is quite accurate. Therefore, the numerical method adopted in this paper ensures a high degree of accuracy.

2) The forward curvature of the inlet side of the blade induces a secondary flow of the medium across the span near this location, which, in turn, leads to a stronger medium crowding that occurs close to the location of the shroud. This region will overlap with the region of a greater curvature of the shroud, resulting in greater hydraulic losses.
3) The unsteady flow described in the second conclusion will also result in the presence of a significantly uneven flow in the impeller outlet medium. This will not only increase the flow losses within the diffusers but will also increase the intensity of the rotor–stator interaction in the hydraulic system.

Data availability statement

The original contributions presented in the study are included in the article/Supplementary material; further inquiries can be directed to the corresponding author.

Author contributions

ZH: writing–original draft. XZ: writing–review and editing.

Funding

The author(s) declare financial support was received for the research, authorship, and/or publication of this article. The authors thank Scientific Research and Innovation Plans for Postgraduate of Jiangsu Province (No. KYCX22_3437).

Conflict of interest

Author XZ was employed by Jiangsu Hydraulic Engineering Construction Co, Ltd.

The remaining author declares that the research was conducted in the absence of any commercial or financial relationships that could be construed as a potential conflict of interest.

Publisher's note

References

Ardizzon, G., and Pavesi, G. (1995). Theoretical evaluation of the effects of the impeller entrance geometry and of the incident angle on cavitation inception in centrifugal pumps. *Proc. Institution Mech. Eng. Part C J. Mech. Eng. Sci.* 209 (1), 29–38. doi:10.1243/PIME_PROC_1995_209_119_02

Bing, H., and Cao, S. (2013). Multi-parameter optimization design, numerical simulation and performance test of mixed-flow pump impeller. *Sci. China Technol. Sci.* 56, 2194–2206. doi:10.1007/s11431-013-5308-0

Bing, H., and Cao, S. (2014). Parametrization of blade leading and trailing edge positions and its influence on mixed-flow pump performance. *Proc. Institution Mech. Eng. Part C J. Mech. Eng. Sci.* 228 (4), 703–714. doi:10.1177/0954406213490104

Brennen, C. E. (2011). *Hydrodynamics of pumps*. Cambridge: Cambridge University Press.

Ji, L., Li, S., Li, W., Huang, Y., Shi, W., Yang, Y., et al. (2023). Study on passive suppression method of rotating stall in mixed-flow pump: using different impeller rim structures. *Proc. Institution Mech. Eng. Part A J. Power Energy* 237, 965–984. doi:10.1177/09576509231153304

Ji, L., Li, W., Shi, W., Tian, F., and Agarwal, R. (2021). Effect of blade thickness on rotating stall of mixed-flow pump using entropy generation analysis. *Energy* 236, 121381. doi:10.1016/j.energy.2021.121381

Kan, K., Binama, M., Chen, H., Zheng, Y., Zhou, D., Su, W., et al. (2022). Pump as turbine cavitation performance for both conventional and reverse operating modes: a review. *Renew. Sustain. Energy Rev.* 168, 112786. doi:10.1016/j.rser.2022.112786

Kim, Y. I., Yang, H. M., Lee, K. Y., and Choi, Y. S. (2022). Numerical investigation on blockage-related cavitation surge and pressure gain of a mixed-flow pump with influence of blade leading edge shape on suction performance. *J. Fluids Eng.* 144 (9), 091205. doi:10.1115/1.4053956

Li, W., Ji, L., Li, E., Shi, W., Agarwal, R., and Zhou, L. (2021). Numerical investigation of energy loss mechanism of mixed-flow pump under stall condition. *Renew. Energy* 167, 740–760. doi:10.1016/j.renene.2020.11.146

Li, W., Li, E., Ji, L., Zhou, L., Shi, W., and Zhu, Y. (2020). Mechanism and propagation characteristics of rotating stall in a mixed-flow pump. *Renew. Energy* 153, 74–92. doi:10.1016/j.renene.2020.02.003

Menter, F. R. (1994). Two-equation eddy-viscosity turbulence models for engineering applications. *AIAA J.* 32 (8), 1598–1605. doi:10.2514/3.12149

Tan, L., Xie, Z., Liu, Y., Hao, Y., and Xu, Y. (2018). Influence of T-shape tip clearance on performance of a mixed-flow pump. *Proc. Institution Mech. Eng. Part A J. power energy* 232 (4), 386–396. doi:10.1177/0957650917733129

Tan, L., Yu, Z., Xun, Y., Liu, Y., and Cao, S. (2017). Role of blade rotational angle on energy performance and pressure fluctuation of a mixed-flow pump. *Proc. Institution Mech. Eng. Part A J. power energy* 231 (3), 227–238. doi:10.1177/0957650917689948

Tao, R., Xiao, R., and Wang, Z. (2018). Influence of blade leading-edge shape on cavitation in a centrifugal pump impeller. *Energies* 11 (10), 2588. doi:10.3390/en11102588

Wu, D., Yan, P., Chen, X., Wu, P., and Yang, S. (2015). Effect of trailing-edge modification of a mixed-flow pump. *J. Fluids Eng.* 137 (10), 101205. doi:10.1115/1.4030488

Yang, F., Li, Z., Hu, W., Liu, C., Jiang, D., Liu, D., et al. (2022b). Analysis of flow loss characteristics of slanted axial-flow pump device based on entropy production theory. *R. Soc. Open Sci.* 9 (1), 211208. doi:10.1098/rsos.211208

Yang, F., Li, Z., Yuan, Y., Lin, Z., Zhou, G., and Ji, Q. (2022a). Study on vortex flow and pressure fluctuation in dustpan-shaped conduit of a low head axial-flow pump as turbine. *Renew. Energy* 196, 856–869. doi:10.1016/j.renene.2022.07.024

Yang, Y., Zhou, L., Shi, W., He, Z., Han, Y., and Xiao, Y. (2021). Interstage difference of pressure pulsation in a three-stage electrical submersible pump. *J. Petroleum Sci. Eng.* 196, 107653. doi:10.1016/j.petrol.2020.107653

Yang, Y., Chen, X., Bai, L., Yao, Y., Wang, H., Ji, L., et al. (2023). Quantification and investigation of pressure fluctuation intensity in a multistage electric submersible pump. *Phys. Fluids* 35 (3). doi:10.1063/5.0136664

Zhu, D., Tao, R., and Xiao, R. (2019). Anti-cavitation design of the symmetric leading-edge shape of mixed-flow pump impeller blades. *Symmetry* 11 (1), 46. doi:10.3390/sym11010046

frontiers | Frontiers in Energy Research

TYPE Original Research
PUBLISHED 26 October 2023
DOI 10.3389/fenrg.2023.1282739

OPEN ACCESS

EDITED BY
Ran Tao,
China Agricultural University, China

REVIEWED BY
Ye Changliang,
Hohai University, China
Faye Jin,
Tsinghua University, China
SHI Guangtai,
Xihua University, China
Yongyao Luo,
Tsinghua University, China

*CORRESPONDENCE
Hao Chang,
changhao@ujs.edu.cn
Guangjie Peng,
pgj@ujs.edu.cn

RECEIVED 24 August 2023
ACCEPTED 10 October 2023
PUBLISHED 26 October 2023

CITATION
Chang H, Ji G, Yu D, Peng G, Hong S and Du J (2023), Research on wear characteristics of U-shaped elbows based on CFD-DEM coupling. *Front. Energy Res.* 11:1282739. doi: 10.3389/fenrg.2023.1282739

Research on wear characteristics of U-shaped elbows based on CFD-DEM coupling

Hao Chang[1,2,3]*, Guangchao Ji[1], Dehui Yu[4], Guangjie Peng[1,3]*, Shiming Hong[1] and Jialin Du[1]

[1]Research Center of Fluid Machinery Engineering and Technology, Jiangsu University, Zhenjiang, China, [2]International Shipping Research Institute, Gong Qing Institute of Science and Technology, Jiujiang, China, [3]Fluid Machinery of Wenling Research Institute, Jiangsu University, Wenling, China, [4]Chongqing Pump Industry Co Ltd, Chongqing, China

The C++ programming language is employed to improve the Computational Fluid Dynamics (CFD)- Discrete Element Method (DEM) coupling interface in this paper, the accuracy of solid-liquid two-phase flow numerical model are validated through experiments. Subsequently, the wear characteristics of the U-shaped elbows under different elbows spacing, bending diameter ratio, particle volume concentration, and particle size are investigated. The research results indicate that as the spacing between bends is increased, the phenomenon of particle sedimentation is intensified, and the maximum collision angle in elbow 2 is increased. The location of the maximum collision angle is closer to the outlet of elbow 2. However, both the collision frequency and wear rate are reduced due to the decrease in the number of particles. Smoother particle flow and a reduction in the collision angle and wear rate of particles on both bends are achieved by increasing the bend ratio. During the variation of the particle volume fraction from 0.5% to 7%, the increase in collision frequency and wear rate of both bends is slowed down. A greater decrease is observed in elbow 2, but the "shielding effect" is not observed. Furthermore, at low volume fractions, kinetic energy is lost by particles as they flow through elbow 1, resulting in a lower average wear rate in elbow 2 compared to elbow 1. Conversely, at high volume fractions, the opposite effect occurs. Finally, when keeping the particle volume fraction constant, an increase in the particle size leads to a smaller wear area in both bends. The wear rate in elbow 1 increases at a slower rate, while the wear rate in elbow 2 exhibits an initial increase followed by a decrease trend.

KEYWORDS

wear characteristics, two-phase flow, CFD-DEM, U-shaped elbows, elbow erosion

1 Introduction

Pipeline transportation has the advantages of large transportation volume, continuous, stable, low investment, and less land occupation. It is widely used in long-distance transportation of oil, natural gas, ore, *etc.* Transportation types usually involve slurry transportation and gas transportation. In slurry transportation, the conveying medium commonly incorporates particles like sand and ore. The interaction of these particles with the pipe wall through friction and impact can result in erosion and wear of the conveying pipeline, leading to thinning or even complete deterioration of the pipe wall. Consequently, the anticipated service life of the pipeline is significantly reduced. Moreover, with pipe wear, eddy currents may arise

within the transported fluid, causing an uneven distribution of the slurry across the pipe cross-section and consequently impacting the efficiency of the transportation process (Wang et al., 2021; Sun et al., 2022a; Wang et al., 2022; Wang et al., 2023). Therefore, research on the mechanism of pipeline wear has important theoretical value and engineering significance for reducing pipeline system failure.

In the pipeline transportation system, the elbow is usually utilized as a turning component and is prone to wear. Consequently, the wear mechanism of elbows in pipeline systems has been the focus of domestic and foreign scholars. The wear removal mechanism of brittle and ductile materials was first discussed by Finnie (Finnie, 1960; Finnie, 1979), and the theory of micro cutting corrosion wear was proposed. Bitter (Bitter, 1963a; Bitter, 1963b) believed that the removal of wall materials is primarily due to the repeated deformation of particles and cutting action of particles during the collision with the wall, and a related wear model was established. The wear models were established by Archard (Archard, 1953), Ahlert (Ahlert, 1994; Oka et al., 2005; Oka and Yoshida, 2005) based on specific experimental conditions. Such models can predict pipeline wear in industrial applications in some specific engineering environments. The effect of particle flow velocity on the wear of a 90° elbow under low concentration mass load for two-phase gas-solid flow was measured by (Vieira et al., 2016) through experiments. They established a related wear model and verified the accuracy of the wear model using CFD simulation.

The influence of particle mass load on elbow wear under different S_t numbers was studied by (Pouraria et al., 2020) through gas-solid two-phase flow experiments. The results indicated that there exists a critical particle mass load beyond which the wear rate of the elbow gradually declines. Moreover, the study found that the critical particle mass load of low S_t number flow is larger. (Bilal et al., 2021). used the paint removal method to investigate the wear of elbows with bending angles of 45° and 90° under curvature radii of 1.5*D*, 2.5*D*, and 5*D* based on multiphase flow. The results revealed that the wear rate declines with increasing bend radius. (Zhao et al., 2023).studied the influence of the sealing structure of the front chamber of the slurry pump on its sealing surface wear characteristics, and the research results provide a certain reference for the anti wear design of pipelines. (Li et al., 2023).research provides a certain reference for further optimizing hydraulic and structural design, and improving wear conditions. (Zeng et al., 2014). used array electrode technology to measure the wear rate at different positions of the X65 pipe elbow. This experiment provides a reference for the accuracy verification of the wear model in this paper. (Jia et al., 2021). studied the influence of gas velocity and fluid PH on the wear of a 90° elbow during the transport of gas-liquid-solid three-phase flow. The most serious wear areas were found to be the axial angle of the elbow between 20° and 50°, while the opposite phenomenon was observed at the corresponding position between 50° and 70°.

Although the most realistic wear of the elbow can be reflected by experiments, the details of the interaction between particles-particles and particle-walls cannot be directly observed. With the continuous development of Computational Fluid Dynamics (CFD), the application of Discrete Phase Models (DPM) and Computational Fluid Dynamics coupled with Discrete Element Method (CFD-DEM) for predicting wear caused by solid particles in fluids is gradually increasing (Hu et al., 2019; Xu et al., 2020; Zhong et al., 2021). The effects of parameters such as pipe diameter, particle size, inlet velocity, particle mass flow rate, and bending diameter ratio on the wear of elbows were studied by (Peng and Cao, 2016) based on DPM. However, as DPM itself ignores the interaction between particles, the wear rate continued to increase as the mass flow rate increased, which contradicts the simulation results of (Zheng et al., 2008), and the lift force on the particles was not considered in the simulation process. (Duarte et al., 2017). studied the effect of wall roughness, friction coefficient, and particle mass load on the wear of elbow pipe in gas-solid two-phase flow using CFD-DEM. The results showed that the wear depth decreases with the increase of wall roughness and the particle mass load, and rises with the improvement of friction coefficient.

The influence of particles with different sphericity on gas-solid two-phase flow wear in the elbow was studied by (Zeng et al., 2018) based on CFD-DEM and E/CRC wear model. The results indicated the impact velocity and angle have a significant influence on the elbow wear, whereas when the sphericity is greater than 0.77, the elbow wear is mainly caused by the impact concentration. (Laín and Sommerfeld, 2019). used the Euler-Lagrangian method to study the influence of spherical particles under different mass loads on the wear of the elbow during pneumatic conveying. The results suggested that with the increase of the particle mass load, the collision frequency between particles and particle walls increases; however, the wear rate of the elbow declines due to the decrease of the particle collision velocity and angle.

(Farokhipour et al., 2020) employed the CFD-DEM coupling model and E/CRC wear model, the wear rate, collision speed, and frequency are selected as evaluation parameters to study the influence of mass loads on elbow wear during pneumatic conveying. The results presented that as the mass load increases, the wear of the pneumatic conveying system reaches saturation due to the low velocity and frequency of particles collision with the end region, which forms a "shield effect". The wear characteristics of square pipes and round pipes during pneumatic conveying were investigated by (Zolfagharnasab et al., 2021) based on CFD-DPM coupling model, and it was discovered that the wear rate of square pipes is lower than that of circular pipes, especially under higher conveying speeds or larger particle size conditions. (Zhao et al., 2022). studied the effect of particle volume fraction on the wear of the elbow using the CFD-DEM and the E/CRC wear model. The study revealed that the wear rate of the outermost side of the elbow nonlinearly increases with the improvement of the particle volume fraction. However, when the particle volume fraction reaches a specific value, the wear rate no longer increases.

In summary, in gas-solid two-phase flow and solid-liquid two-phase flow, domestic and foreign scholars have conducted a large number of experiments and simulation studies on the influence of particle mass load, particle size, pipe diameter, and other factors on the wear of an individual elbow. At the same time, (Zhang et al., 2023). Compared the effects of three two-fluid turbulence models on the calculation results of solid phase concentration and velocity in circular tubes under different solid phase conditions and different inlet liquid phase velocities,

which provided a calculation model reference for this article. (Sun et al., 2022b). Used the SSTk-ω turbulence model and Tabakoff abrasion model to study the abrasion laws of Francis turbines with high sand content. The research results provide a certain reference for the prevention of abrasion. (Bai et al., 2022). Chose the drag model in dense gas-solid two-phase flow to improve the accuracy of numerical simulation results. Based on the CFD-DEM two-way coupling method, they numerically simulated the gas-solid fluidized bed, which provided a certain direction for the research of this article. (Zhao et al., 2022). showed that compared with the Saffman and Magnus lift developed by gas-solid two-phase flow, the Loth lift is more suitable for particle motion in solid-liquid two-phase flow, and the pressure gradient force and virtual mass force are also particularly important for particle motion in solid-liquid two-phase flow. Therefore, the C++ programming language was utilized to improve the CFD-DEM coupling interface in this paper, the Loth lift, virtual mass force, and pressure gradient force were introduced for simulating solid-liquid two-phase flows. Meanwhile, the transient fluctuations of flow velocity were employed on the particle motion by using the DRW model. The accuracy of numerical simulation was verified through experiments of the previous research. Subsequently, the improved numerical model of solid-liquid two-phase flow is employed to investigate the wear characteristics of U-shaped elbow under different parameters such as elbow spacing, bending diameter ratio, particle volume concentration, and particle size, which can provide the theoretical value and engineering significance for reducing pipeline system failure.

2 CFD-DEM mathematical theory model

2.1 Fluid governing equations

In this paper, the incompressible fluid is employed, and the solution is based on the Reynolds time-averaged Navier-Stokes equations. Moreover, considering the high local particle volume fraction generated during the simulation, the continuity and momentum equations of the fluid can be formulated:

$$\frac{\partial}{\partial t}\left(\alpha_f \rho_f\right) + \nabla\left(\alpha_f \rho_f \boldsymbol{v}_f\right) = \boldsymbol{0} \tag{1}$$

$$\frac{\partial}{\partial t}\left(\alpha_f \rho_f \boldsymbol{v}_f\right) + \nabla\left(\alpha_f \rho_f \boldsymbol{v}_f \boldsymbol{v}_f\right) = -\alpha_f \nabla \boldsymbol{p} + \nabla\left[\alpha_f\left(\mu_f + \mu_t\right)\left(\nabla \boldsymbol{v}_f + \nabla \boldsymbol{v}_f^T\right)\right] + \alpha_f \rho_f \boldsymbol{g} - \frac{1}{V}\sum_{i=1}^{m} \boldsymbol{f} \tag{2}$$

Where ρ_f represents the fluid density, v_f represents fluid mean velocity, p stands for pressure, μ_f denotes fluid dynamic viscosity, μ_t signifies turbulent viscosity, f denotes the resultant force on particle i within a computational unit, m represents the number of particles in a computational unit, and V represents the volume of the computational unit. Additionally, α_f represents the volume fraction occupied by the fluid and can be expressed as follows:

$$\alpha_f = 1 - \frac{\sum_{k=1}^{m} V_k}{V} \tag{3}$$

In the formula, V_k is the volume of particle k in the calculation unit. In this paper, the *RNG k-ε* turbulence model is adopted, and its turbulent kinetic energy and turbulent dissipation rate governing equations can be expressed as:

$$\frac{\partial}{\partial t}\left(\alpha_f \rho_f k\right) + \frac{\partial}{\partial x_i}\left(\alpha_f \rho_f k u_i\right) = \frac{\partial}{\partial x_j}\left[\alpha_f \alpha_k \mu_{eff}\frac{\partial k}{\partial x_j}\right] + \alpha_f G_k + \alpha_f G_b - \alpha_f \rho_f \varepsilon + S_k \tag{4}$$

$$\frac{\partial}{\partial t}\left(\alpha_f \rho_f \varepsilon\right) + \frac{\partial}{\partial x_i}\left(\alpha_f \rho_f \varepsilon u_i\right) = \frac{\partial}{\partial x_j}\left[\alpha_f \alpha_\varepsilon \mu_{eff}\frac{\partial \varepsilon}{\partial x_j}\right] + \alpha_f C_{\varepsilon 1}\frac{\varepsilon}{k}\left(G_k + C_{\varepsilon 3} G_b\right) - \alpha_f C_{\varepsilon 2}\rho_f \frac{\varepsilon^2}{k} + S_\varepsilon \tag{5}$$

In the formula, k and ε are the turbulent kinetic energy and turbulent dissipation rate, G_k is the turbulent kinetic energy caused by the average velocity gradient, G_b is the turbulent kinetic energy caused by buoyancy, α_k and α_ε are the effective Prandtl reciprocals of k and ε, respectively. $\alpha_k = 1.00$, $\alpha_\varepsilon = 1.20$, $C_{\varepsilon 1} = 1.44$, $C_{\varepsilon 2} = 1.92$, $C_{\varepsilon 3} = C_{\varepsilon 2} C_{\varepsilon p} Re_s^{1.416}$, $C_{\varepsilon p} = 0.058$, S_k and S_ε are the source terms of turbulent kinetic energy and turbulent dissipation rate.

2.2 Particle governing equations

The equation of motion for a single particle is described by the following first-order ordinary differential equation:

$$m_s \frac{d\boldsymbol{v}_s}{dt} = \boldsymbol{F}_{\mathrm{drag}} + \boldsymbol{F}_{\mathrm{bg}} + \boldsymbol{F}_{\mathrm{loth}} + \boldsymbol{F}_{\mathrm{pg}} + \boldsymbol{F}_{\mathrm{vm}} + \boldsymbol{F}_c \tag{6}$$

$$I_s \frac{d\boldsymbol{\omega}_s}{dt} = \sum \boldsymbol{T}_c + \boldsymbol{T}_f \tag{7}$$

$$I_s = 0.1 m_s d_s^2 \tag{8}$$

In this formula, $\boldsymbol{F}_{\mathrm{drag}}$ represents the drag force on the particle, $\boldsymbol{F}_{\mathrm{bg}}$ is the resultant force of gravity and buoyancy on the particle, $\boldsymbol{F}_{\mathrm{loth}}$ is the Loth lift force acting on the particle, $\boldsymbol{F}_{\mathrm{pg}}$ stands for the pressure gradient force on the particle, $\boldsymbol{F}_{\mathrm{vm}}$ denotes the additional mass force on the particle, and $\boldsymbol{F}_c$ denotes the force of contact between particles as well as between particles and the wall surface. Additionally, ω_s is the particle angular velocity, I_s the moment of inertia of the particle, $\boldsymbol{T}_c$ and $\boldsymbol{T}_f$ represent the particle contact torque and the torque generated by fluid phase, $d\boldsymbol{v}_s/dt$ denotes particle translational acceleration, m_s represents particle mass, and d_s signifies particle size.

2.2.1 Di Felice drag force

The Di Felice drag force model is employed in the calculation (Di Felice, 1994), which considers the influence of fluid volume fraction and porosity on the drag force. The expression for this model is as follows:

$$\boldsymbol{F}_{\mathrm{drag}} = \frac{1}{8}\pi d_s^2 \rho_f C_D \left|\boldsymbol{v}_f + \boldsymbol{v}_f' - \boldsymbol{v}_s\right|\left(\boldsymbol{v}_f + \boldsymbol{v}_f' - \boldsymbol{v}_s\right)\alpha_f^{(1-\alpha)} \tag{9}$$

$$\alpha = 3.7 - 0.65\,exp\left[-\frac{(1.5 - log_{10}Re_{s,\alpha})^2}{2}\right] \tag{10}$$

Where $Re_{s,\alpha}$ represents the particle Reynolds number considering the fluid volume fraction, which can be expressed as follow:

$$Re_{s,\alpha} = \frac{\rho_f d_s \alpha_f \left|v_f + v_f^{'} - v_s\right|}{\mu_f} \tag{11}$$

The drag coefficient C_D for spherical particles can be expressed by the following formula:

$$\begin{cases} C_D = \dfrac{24}{Re_{s,\alpha}} & Re_{s,\alpha} \le 1 \\ C_D = \left[0.63 + \dfrac{4.8}{Re_{s,\alpha}^{0.5}}\right]^2 & Re_{s,\alpha} > 1 \end{cases} \tag{12}$$

The calculation formula for drag coefficient C_D of non-spherical particles adopts the research results of Haider and Levensoiel (Haider and Levenspiel, 1989):

$$C_D = \frac{24}{Re_{s,\alpha}}\left(1 + b_1 Re_{s,\alpha}^{b_2}\right) + \frac{b_3 Re_{s,\alpha}}{b_4 + Re_{s,\alpha}} \tag{13}$$

In this formula, the calculation formulas for b_1, b_2, b_3 and b_4 are provided as follows:

$$b_1 = exp\left(2.3288 - 6.4581\psi + 2.4486\psi^2\right) \tag{14}$$

$$b_2 = 0.0964 + 0.5565\psi \tag{15}$$

$$b_3 = exp\left(4.905 - 13.8944\psi + 18.4222\psi^2 - 10.2599\psi^3\right) \tag{16}$$

$$b_4 = exp\left(1.4681 + 12.2584\psi - 20.7322\psi^2 + 15.8855\psi^3\right) \tag{17}$$

2.2.2 The resultant force of gravity and buoyancy

The following formula can be used to express the resultant force of gravitational buoyancy:

$$F_{bg} = m_s\left(\frac{\rho_s - \rho_f}{\rho_s}\right)g \tag{18}$$

In this formula, the particle density ρ_s and gravitational acceleration g are utilized.

2.2.3 Loth lift force

The Loth lift force is employed in this paper, the lift coefficient in the Loth lift (Zhao et al., 2021) is composed of shear and rotation lift coefficients. The expression for lift force is as follows:

$$F_{loth} = \frac{\pi}{8}\rho_f C_L d_s^2 \left|v_f + v_f^{'} - v_s\right|\left[\left(v_f + v_f^{'} - v_s\right) \times \frac{\omega_f}{|\omega_f|}\right] \tag{19}$$

The formula involves the fluid vorticity ω_f and the lift coefficient C_L, which can be expressed by the following formula:

$$C_L = J^{\star}\frac{12.92}{\pi}\sqrt{\frac{\omega_f^{\star}}{Re_s}} + \omega_{s,eq}^{\star} C_{L,\omega}^{\star} \tag{20}$$

$$J^{\star} \cong 0.3\left\{1 + tanh\left[\frac{5}{2}\left(log_{10}\sqrt{\frac{\omega_f^{\star}}{Re_s}} + 0.191\right)\right]\right\} \times \left\{\frac{2}{3} + tanh\left[6\sqrt{\frac{\omega_f^{\star}}{Re_s}} - 1.92\right]\right\} \tag{21}$$

$$C_{L,\omega}^{\star} = 1 - \left\{0.675 + 0.15\left(1 + tanh\left[0.28\left(\omega_s^{\star} - 2\right)\right]\right)\right\} tanh\left[0.18 Re_s^{1/2}\right] \tag{22}$$

$$\omega_{s,eq}^{\star} = \frac{\omega_f^{\star}}{2}\left(1 - 0.0075 R_{s,\omega}\right)\left(1 - 0.062 Re_s^{1/2} - 0.001 Re_s\right) \tag{23}$$

$$\omega_f^{\star} = \frac{|\omega_f| d_s}{\left|v_f + v_f^{'} - v_s\right|} \tag{24}$$

$$\omega_s^{\star} = \frac{|\omega_s| d_s}{\left|v_f + v_f^{'} - v_s\right|} \tag{25}$$

$$Re_{s,\omega} = \frac{\rho_f d_s^2 |\omega_f|}{\mu_f} \tag{26}$$

In this formula, the relative vorticity $\omega_f^{\star}$ of the fluid, the relative angular velocity $\omega_s^{\star}$ of the particle, and the Reynolds number $R_{s,\omega}$ of the particle rotation are all included.

2.2.4 Pressure gradient force and virtual mass force

The pressure gradient force is induced by the movement of particles in a flow field with a pressure gradient, while the surface of the particle is subjected to the pressure difference generated when the fluid accelerates:

$$F_{pg} = -V_s \nabla p \tag{27}$$

When the velocity of the particle is greater than the velocity of the surrounding fluid, the additional mass force is generated which can push the surrounding fluid to do accelerated motion:

$$F_{vm} = \frac{\rho_f}{2\rho_s}\left[v_s \nabla\left(v_f + v_f^{'}\right) - \frac{dv_s}{dt}\right] \tag{28}$$

2.2.5 Particle contact force

In EDEM, the Hertz-Mindlin (no slip) model is utilized for the contact force model between particles and walls. This model is bifurcated into normal contact force and tangential contact force *via* the soft-sphere model (Tarodiya and Gandhi, 2019). The corresponding $\zeta_{n,AB}$ and $\zeta_{t,AB}$ denote the normal displacement and tangential displacement of particles, respectively. Furthermore, $F_{cn,AB}$ and $F_{ct,AB}$ represent the normal contact force and tangential contact force:

$$F_{c,AB} = F_{cn,AB} + F_{ct,AB} \tag{29}$$

$$F_{cn,AB} = -k_{n,AB}\zeta_{n,AB} - \gamma_{n,AB} v_{n,AB} \tag{30}$$

$$F_{ct,AB} = -k_{t,AB}\zeta_{t,AB} - \gamma_{t,AB} v_{t,AB} \tag{31}$$

In this formula, $k_{n,AB}$ and $k_{t,AB}$ denote the normal elastic stiffness and tangential elastic stiffness of the spring, respectively. Moreover, $\gamma_{n,AB}$ and $\gamma_{t,AB}$ represent the normal and tangential damping coefficients, while $v_{n,AB}$ and $v_{t,AB}$ indicate the normal and tangential relative velocity vector of particles A and B during contact.

When the sliding friction is generated, the tangential contact force $F_{ct,AB}$ can be expressed as Coulomb friction:

$$F_{ct,AB} = -f_s\left|F_{cn,AB}\right|\frac{\zeta_{t,AB}}{\left|\zeta_{t,AB}\right|} \tag{32}$$

Where f_s is the sliding friction coefficient and $\zeta_{t,AB}/|\zeta_{t,AB}|$ is the tangential unit vector.

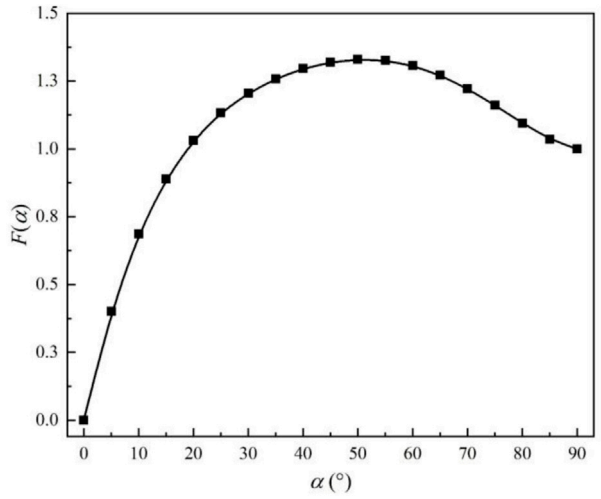

FIGURE 1
The relationship between $F(\alpha)$ and α.

2.2.6 Discrete random walk model

The application of the instantaneous fluctuation of flow velocity to drive particle movement is implemented in the DRW model utilized throughout this paper. It should be noted that in eddy currents, the instantaneous fluid velocity is comprised of both an average velocity and a fluctuation velocity:

$$V_f = v_f + v_f' \tag{33}$$

By assuming that a Gaussian probability distribution governs turbulent fluctuation velocity, the following formula can be utilized for its expression:

$$\begin{cases} u' = \xi_i \sqrt{\overline{u'^2}} \\ v' = \xi_j \sqrt{\overline{v'^2}} \\ w' = \xi_k \sqrt{\overline{w'^2}} \end{cases} \tag{34}$$

In this formula, the random numbers ξ_i, ξ_j and ξ_k are governed by the Gaussian distribution. If the turbulent flow is isotropic, the root mean square (RMS) of fluctuating velocity can be calculated by:

$$\sqrt{\overline{u'^2}} = \sqrt{\overline{v'^2}} = \sqrt{\overline{w'^2}} = \sqrt{2\frac{k}{3}} \tag{35}$$

Where k is the turbulent kinetic energy parameter, which can be calculated by the *RNG* k-ε turbulence equation.

2.2.7 E/CRC wear model

In the present paper, the E/CRC model is applied, which is developed by Zhang (Zhang et al., 2007) for predicting erosion in elbows, tees, and several other pipe fittings. The mathematical expression is provided as follows:

$$ER = C(BH)^{-0.59} F_s v_s^n F(\alpha) \tag{36}$$

$$F(\alpha) = 5.3983\alpha - 10.1068\alpha^2 + 10.9327\alpha^3 - 6.3283\alpha^4 + 1.4234\alpha^5 \tag{37}$$

TABLE 1 EDEM simulation parameters.

	Parameter name	Unit	Numerical calibration
Particle properties	Density	kg/m^3	2450
	Particle size	mm	2.32
	Volume concentration	%	2.33
	Flow rate	m/s	1.888
	Poisson's ratio	—	0.3
	Young's modulus	pa	1×10^7
Wall properties	density	kg/m^3	2150
	Poisson's ratio	—	0.3
	Young's modulus	pa	2.6×10^8

Where ER is the wear rate expressed by the wear amount of material under unit load per unit time (unit: kg/kg), BH is the Brinell hardness of the wall material, F_s is the shape factor of particles. Notably, the sharp particles are designated as $F_s = 1$, semicircular particles as $F_s = 0.53$, and round particles as $F_s = 0.2$. Furthermore, the empirical constants $C = 2.17 \times 10^{-7}$ and $n = 2.41$ are also utilized, α is the particle impact angle (unit: radian).

According to Formula 36, the value of $F(\alpha)$ plays a dominant role in influencing the wear rate of the outer wall with the specific materials and working conditions. The relationship between $F(\alpha)$ and α is illustrated in Figure 1, it can be seen that $F(\alpha)$ exhibits a trend of sharp increase followed by gradual decrease with the improvement of α. Notably, when α reaches approximately 50°, the corresponding value of $F(\alpha)$ attains its maximum point, indicating that the wear rate is also maximum at this point.

3 Verification of solid-liquid two-phase flow model and wear model

3.1 Validation of solid-liquid two-phase flow model

Particle transport experiments in the vertical pipe are conducted by (Alajbegović et al., 1994), and the ratio of the radius of the concentric circle (r) to the radius of the vertical pipe (R) is defined as r/R. The particle velocity, fluid velocity, and particle volume fraction are measured in the vertical pipe. Notably, the diameter of vertical pipe D is 30.6mm, while the length of pipe L is 3060 mm. The Standard k-ε model is adopted in the turbulence model, with a turbulence intensity set at 3.5%. The grid height of the first wall layer is configured at 0.5mm, while the calculated y + range is kept within 30-40. Meanwhile, the particle is generated at the entrance in EDEM, with the particle entry time is 0.01s. The calculation time step is set at 2×10^{-5}s in EDEM, and the velocity inlet (1.888 m/s) and the pressure outlet (1atm) are applied. The calculation time step is set at 2×10^{-4}s in Fluent, the total simulation time is 4s, the detailed calibration parameters of relevant EDEM simulations are included

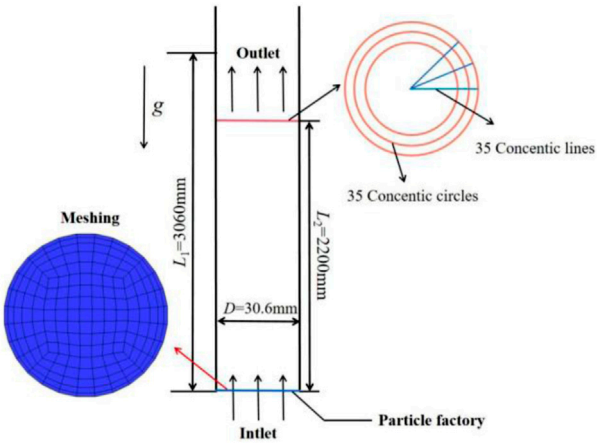

FIGURE 2
The model and structure grid of vertical pipe.

in Table 1, while the vertical pipe model and grid division are shown in Figure 2.

The balance of the particle number in the vertical pipe is attained within 1.8s. The section situated at a height of 2200 mm from the inlet is selected, and simulated data within the interval of 2–3s is collected at intervals of 0.1s. The section is divided into 35 points in both the circumferential and radial directions, thus forming a series of concentric circles consisting of point sets. The data on the corresponding concentric circles are averaged, and time-average processing is performed thereafter. Figure 3 illustrates the relationship between the particle volume fraction, velocity of particles, fluid velocity, fluid root mean square velocity and r/R. It can be observed that the trends of the simulated and experimental results are close and exhibit good agreement, it shows that the CFD-DEM mathematical model adopted in this paper can simulate solid-liquid two-phase flow more accurately.

3.2 Verification of wear model

The wear rate of different positions of the X65 elbow pipe is measured by Zeng et al. (Zeng et al., 2014) using the array electrode technology. In this study, a geometric model consistent with the experiment is established, in which the pipe diameter D is 50mm, the bending diameter ratio R/D is 1.5, and the horizontal section L1 is 20D, while the vertical section L2 is 15D. The RNG k-ε model is selected as the turbulence model, and the turbulence intensity is adjusted to 3.5%. The grid height of the first wall layer is set at 0.3mm, while the calculated y + range is controlled within 30-60, and the particle is generated at the entrance in EDEM, the particle entry time is 0.01s. Additional calibration details of EDEM simulation parameters can be found in Table 2. The elbow model and its grid division are displayed in Figure 4.

Figure 5 displays the experimental and simulation wear rate of the 90° elbow. Here, the azimuth angle that corresponds to the outermost side of the 90° elbow is defined as 180°. It can be observed from the figure that the trend of simulation and experimental results is similar, therefore, the wear of elbows can be more accurately predicted by adopting the E/CRC wear model.

3.3 Analysis of U-shaped elbow model

3.3.1 Geometric model of U-shaped elbow and simulation method

During the process of ore transportation, multiple elbows in series are frequently employed. In this paper, a U-shaped elbow has been established, wherein the two elbows are connected by horizontal and vertical pipelines. The initial value of the pipeline design parameters dictated that the diameter D of the elbow is 30mm, while the bending diameter ratio R/D of the two elbows is fixed at 1.5. Moreover, the distance L_2 between the elbows is set as $7D$, the water inlet vertical section L_1 is designed to be $15D$, and the water outlet vertical section L_3 is specified to be $15D$.

In this study, the turbulent flow model of RNG k-ε model is employed, the turbulent flow intensity is 5%, the calculated range of y + between 40 and 90. The particles are generated at the inlet in EDEM, where the particles started to generate from 0.01s. The wall wear rate is obtained through the E/CRC wear model. In Fluent, velocity inlet and pressure outlet are utilized. Notably, the outlet pressure is fixed at 1atm, and the calculation time step is established to be 1×10^{-4}s. For calibration details of the basic parameters used in EDEM and Fluent, as shown in Table 3. Additionally, Figure 6 presents the U-shaped bend pipe model and the model of grid division.

3.3.2 Independence verification of grid and simulation time

In this study, 81,599, 105,984, and 134,235 three sets of structural girds are established for the U-shaped elbows, by applying the data processing method of the vertical pipe section, the relationship between the fluid velocity of 0° and 90° section of the elbow 1 with the r/R ratio is obtained.

As depicted in Figure 7 (a) and (b), it indicated that the maximum relative error between the coarse grid and the medium grid is 4.21%, whereas the maximum relative error between the fine grid and the medium grid is 1.02% for the 0° section. Meanwhile, the maximum error between the coarse grid and the medium grid is found to be 3.21%, while the maximum error between the fine grid and the medium grid is measured to be 2.35% for the 90° section. Considering the computing resources, the fluid velocity of the medium grid at 0° and 90° sections is closer to the fine grid, it is deemed appropriate to adopt the medium grid for simulation calculations.

In order to evaluate the calculation time error in wear statistics, the simulation time of the U-shaped elbows is verified to be an independent factor. The particle size used for simulation is 1mm, with a corresponding volume fraction of 1%. The wear rate of the elbow 1 and elbow 2 is determined at 1s, 2s, and 3s respectively.

From Figure 8, it can be observed that the trend in wear rate for the outer side of elbow 1 and elbow 2 is similar when the simulation time is set at 1s, 2s, and 3s. Compared with the wear rate corresponding to 1s and 2s, the wear rate at 2s and 3s is found to be closer. Thus, in consideration of achieving high simulation

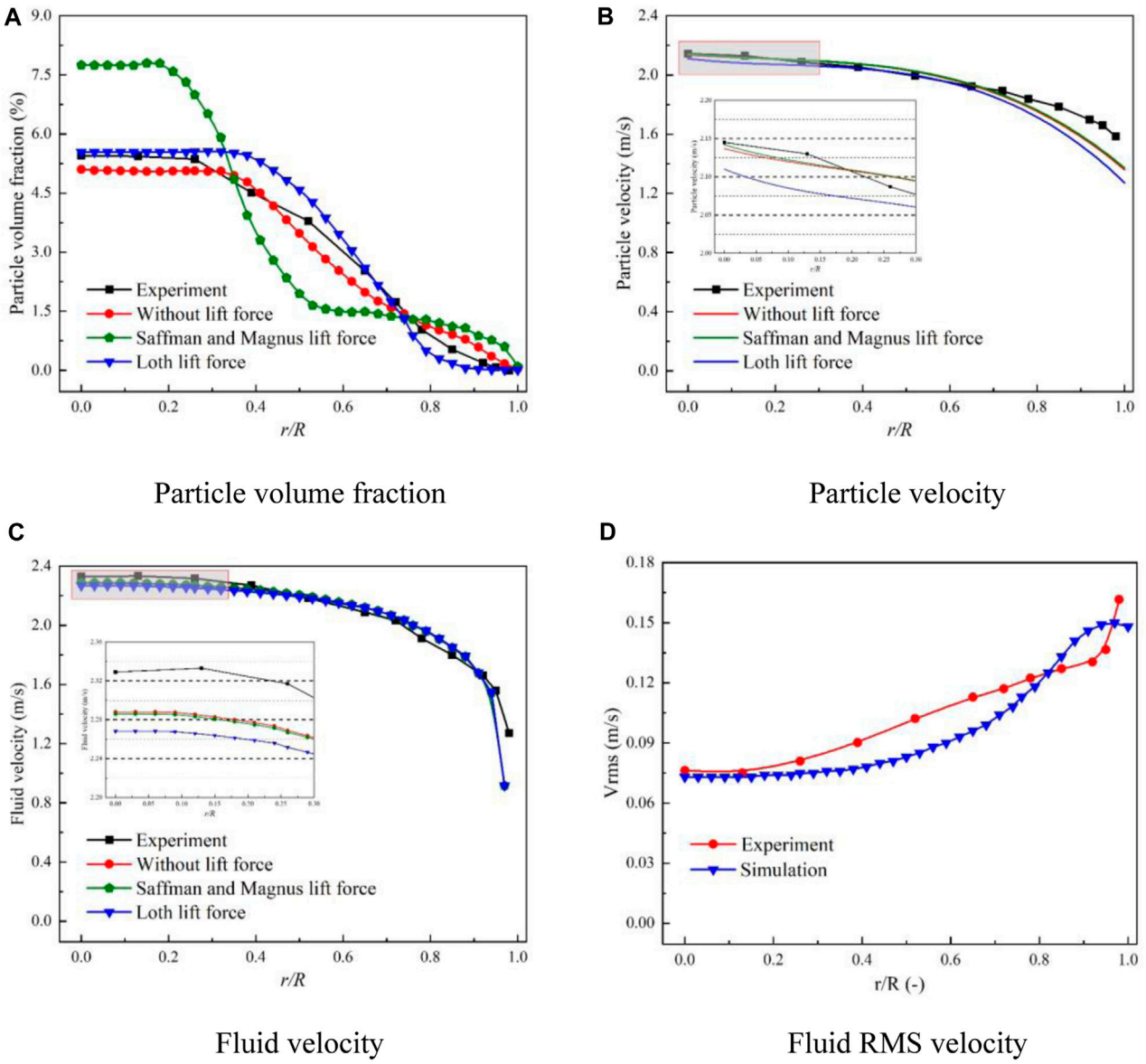

FIGURE 3
The experiment and simulation comparison of solid-liquid two-phase flow. **(A)** Particle volume fraction. **(B)** Particle velocity. **(C)** Fluid velocity. **(D)** Fluid RMS velocity.

accuracy while saving computational time, the simulation time is set as 2s.

4 Results and discussion

4.1 Effect of elbows spacing

Considering the ore transportation process, the distance between the elbows of the series pipelines is often adjusted according to the geographical location. Therefore, the effect of spacing between elbows on wear characteristics is analyzed. As shown in Figure 9A, the spacing model of 2*D*, 7*D*, and 12*D* are established, and the numerical simulations are conducted for transporting particles with a volume concentration of 3%, particle size of 1mm, and speed of 3 m/s through U-shaped elbows.

In Figure 10A, the average impact frequency and wear rate of elbow 1 and elbow 2 different elbows spacing are shown. It can be observed that the average impact frequency (the average number of collisions between a particle and other particles per unit time) and wear rate (the amount of material wear under unit load per unit time) of elbow 1 are generally consistent, while the average impact frequency and wear rate of elbow 2 exhibit a decreasing trend as the elbow spacing increases.

Furthermore, under the elbow spacing of 2*D* and 7*D*, the average impact frequency and wear rate of elbow 2 are much higher than elbow 1. Considering most of the particles concentrate on the outer

TABLE 2 EDEM simulation parameter calibration for 90° elbow.

	Parameter name	Unit	Numerical calibration
Particle properties	Density	kg/m^3	2650
	Particle size	mm	0.5
	Mass flow	kg/s	0.235
	Flow rate	m/s	4
	Poisson's ratio	—	0.23
	Young's modulus	pa	5.9×10^{10}
	Restitution coefficient	—	0.9
Wall properties	Density	kg/m^3	8200
	Poisson's ratio	—	0.3
	Young's modulus	pa	2.07×10^{11}
	Restitution coefficient	—	0.8
	Static friction coefficient	—	0.2

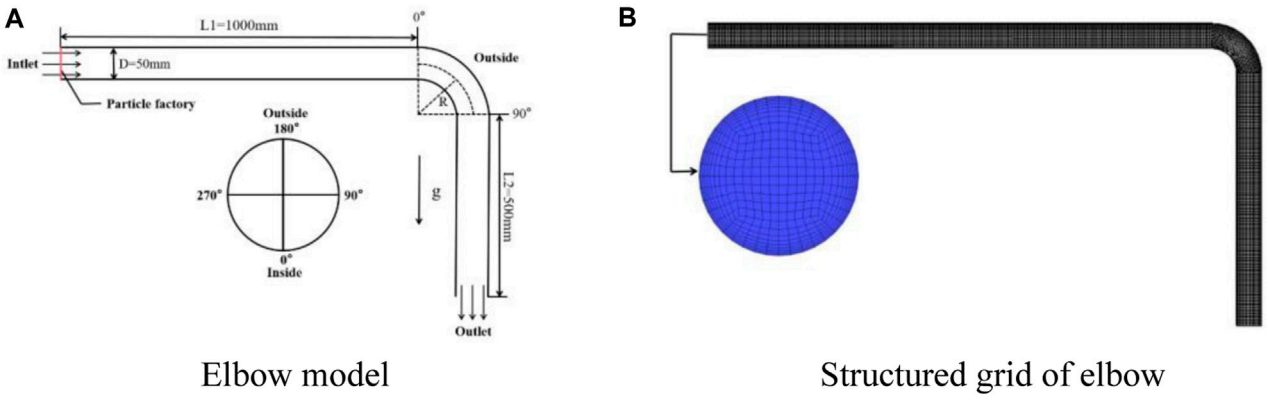

FIGURE 4
Wear model verification. **(A)** Elbow model, **(B)** Structured grid of elbow.

wall after flowing through elbow 1, and insufficient flow is generated due to the short distance between the two elbows, the secondary flow generated by elbow 1 continues to develop with the mainstream, causing the fluid flow outward. What is more, the inertial effects of the particle are dominant compared to the gravity, which causes some particles to be entrained from the elbow inside to the outside, increasing the impact frequency between the particles and elbow 2.

However, when the distance between elbows is 12*D*, the average impact frequency and wear rate of elbow 2 are much lower than elbow 1. Due to the distance between elbows being too long, the flow is relatively sufficient, and the influence of the secondary flow gradually weakens. The gravity of the particles dominates compared to the inertial effect, causing the particles to settle, and the contact between the particles and the wall decreases. Furthermore, with increasing elbows distance, the number of particles flowing through elbow 2 gradually decreases, and the impact frequency reduces significantly. Therefore, the corresponding average impact frequency and wear rate decrease as the distance between the elbows increases.

Figure 10B, (c), and (d) show the relationship between the outer wall impact frequency, wear rate, and collision angle of elbow 2 with bending angle under different elbow spacing. It can be observed that the impact frequency and wear rate increase with improving bending angle, and significantly decrease with increased elbow spacing. Additionally, for elbow spacing of 2*D* and 7*D*, the growth trend of impact frequency and wear rate exhibits a sharp increase at first followed by a slow increase.

When the spacing is 2*D*, the impact frequency after 50° bending angle and the wear rate after 30° bending angle present the slow increasing trend. When the spacing is 7*D*, the starting position of the slow increasing range of the impact frequency and wear rate is relatively backward, and the corresponding bending angle is 75°. However, when the spacing is 12*D*, the impact frequency and wear rate present the slow increasing trend. Additionally, due to the influence of gravity, the particles settle is generated under 7*D* and

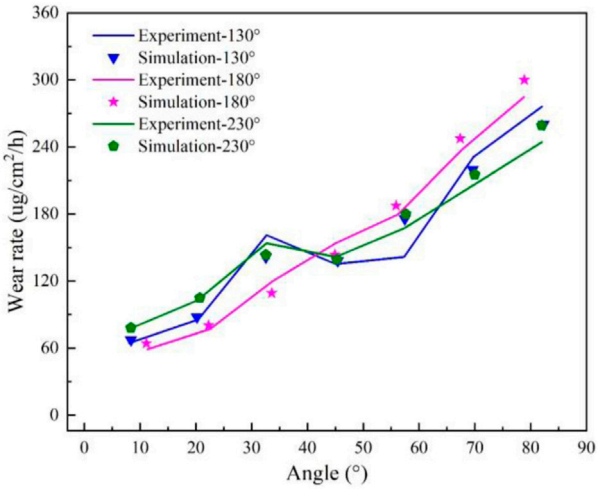

FIGURE 5
Comparison of wear experiment and simulation in 90° elbow.

12*D* elbows spacing, which results in decreasing contact frequency between particles and wall surfaces. Therefore, the impact frequency, wear rate, and impact angle of elbow 2 from 0° to 15° bend angle cannot be found. Starting from 15°, particles impact the pipe wall at a certain angle, increasing the contact frequency between particles and wall surfaces, consequently causing the improvement of impact frequency and wear rate.

However, in contrast to the impact frequency and wear rate, the impact angle initially increases and then decreases as the bending angle improves, and the maximum impact angle and corresponding bending angle are enhanced as the elbows spacing increases. When the spacing is 2*D*, a hump appears near the bending angle of 25°, accompanied by a corresponding impact angle of 3.6°. Similarly, when the spacing is 7*D*, a hump appears near the bending angle of 35°, with a corresponding impact angle of 7.7°. Finally, when the spacing is 12*D*, a hump emerges near the bending angle of 45°, with a corresponding impact angle of 9.3°.

Furthermore, the impact angle becomes more stable closer to the elbow outlet after the hump. Figure 11 shows the particle trajectories, particles settlement is generated under the effect of gravity. With the increasing of elbows spacing, the settlement height is higher, which differs from the contact form of 2*D* spacing. Therefore, as the corresponding bending angle and maximum impact angle increase, the impact angle after the hump also increases, and the falling curve of the impact angle becomes steeper. Moreover, Eq. 36 indicates that when the impact angle is less than 50°, the value of $F(\alpha)$ increases as the impact angle increases, leading to an improvement in the corresponding wear rate. However, due to the influence of impact frequency, the wear rate under different elbow spacing exhibits a downward trend.

4.2 Effec t of bending diameter ratio

The bending diameter ratio represents the bending degree of the elbow and is expressed as R/D, as shown in Figure 12. The fluent flow field of the elbow can be obtained with a larger bending diameter ratio. In this paper, the wear characteristics of the U-shaped elbow with different bending diameter ratios are analyzed, the transport velocity is 3 m/s, particle volume concentration of 3%, and particle diameter of 1 mm are employed, Figure 13 (a) and (b) show the impact frequency and wear rate of elbow 1.

TABLE 3 Basic parameters for EDEM simulation of series elbows.

	Parameter name	Unit	Numerical calibration
Particle properties	Density	kg/m^3	2650
	Particle size	mm	1
	Volume concentration	%	3
	Flow rate	m/s	3
	Poisson's ratio	—	0.17 (Uzi and Levy, 2018)
	Young's modulus	pa	10^7
	Restitution coefficient	—	0.95 (Uzi and Levy, 2018)
	Static friction coefficient	—	0.005 (Uzi and Levy, 2018)
	Coefficient of rolling friction	—	0.4 (Uzi and Levy, 2018)
Wall properties	Density	kg/m^3	7800
	Poisson's ratio	—	0.3 (Uzi and Levy, 2018)
	Young's modulus	pa	2×10^{11} (Uzi and Levy, 2018)
	Restitution coefficient	—	0.737 (Uzi and Levy, 2018)
	Static friction coefficient	—	0.2 (Uzi and Levy, 2018)
	Coefficient of rolling friction	—	0.3 (Uzi and Levy, 2018)

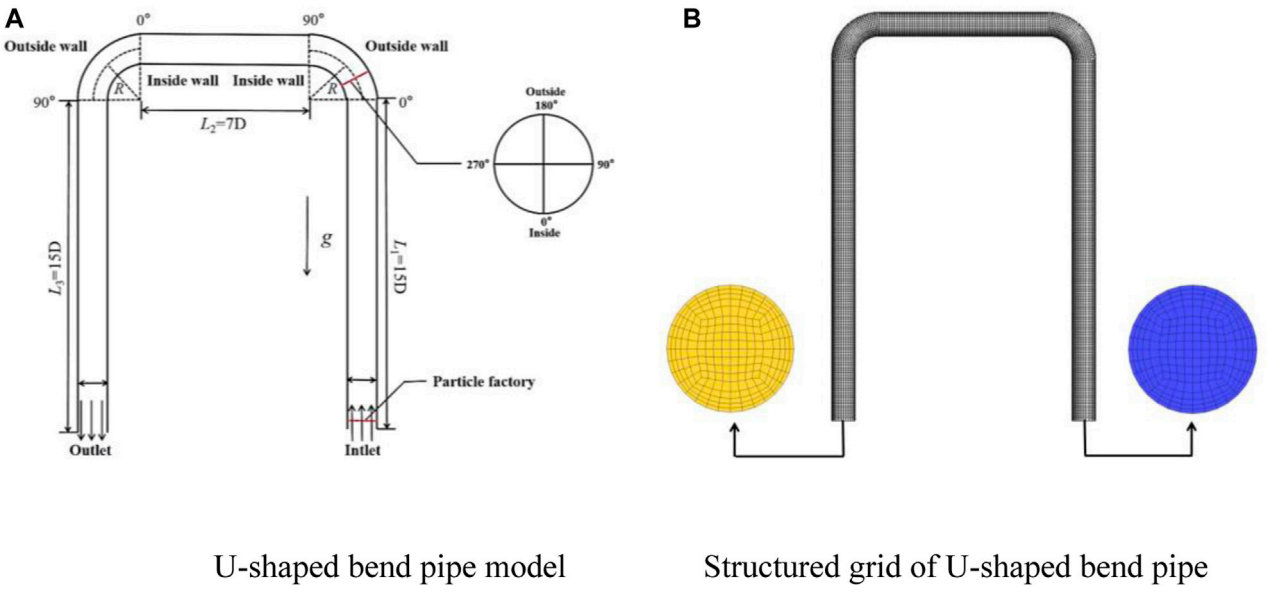

FIGURE 6
U-shaped bend pipe model and structured grid division. **(A)** U-shaped bend pipe model, **(B)** Structured grid of U-shaped bend pipe.

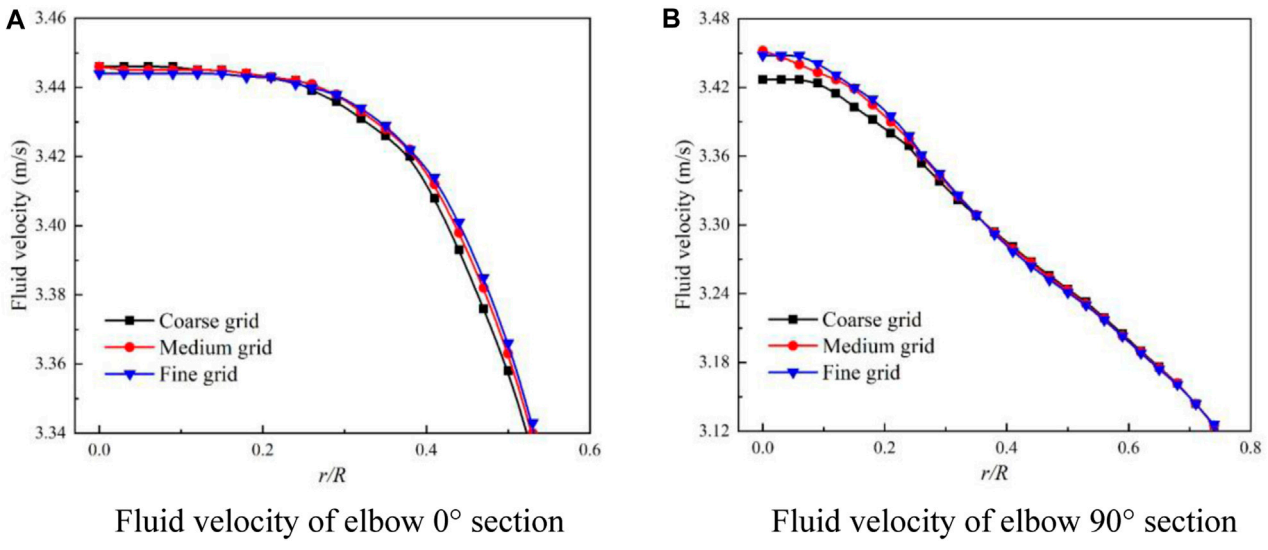

FIGURE 7
Independence verification of U-shaped elbow grid. **(A)** Fluid velocity of elbow 0° section, **(B)** Fluid velocity of elbow 90° section.

As the bending diameter ratio increases from 1.5 to 5, the particle-wall collision area and impact frequency gradually increase, and the curves corresponding to different bending diameter ratios exhibit three growth regulations with the increases of bending angle.

As shown in Figure 13 (a), the slow growth zone is the bend angle from 0° to 35°, where the pipe wall is parallel to the particle motion direction, resulting in less contact between the particles and the wall surface. Therefore, the impact frequency remains close to 0. The medium speed growth zone ranges from 35° to 65°, and the pipe wall and particle movement direction form a certain angle. As particle-wall contact increases, the particles collide with the outer wall surface, which results in the improvement of impact frequency. The rapid growth zone extends from 65° to 83°, where continuous collisions occur between particles and the outer wall, intensifying particle-wall contact and resulting in a sharp increase in impact frequency.

As the bending diameter ratio increases from 1.5 to 3, the impact angle keeps decreasing, but the wear rate still increases. When the bending diameter ratio exceeds 3, the pipeline path becomes longer,

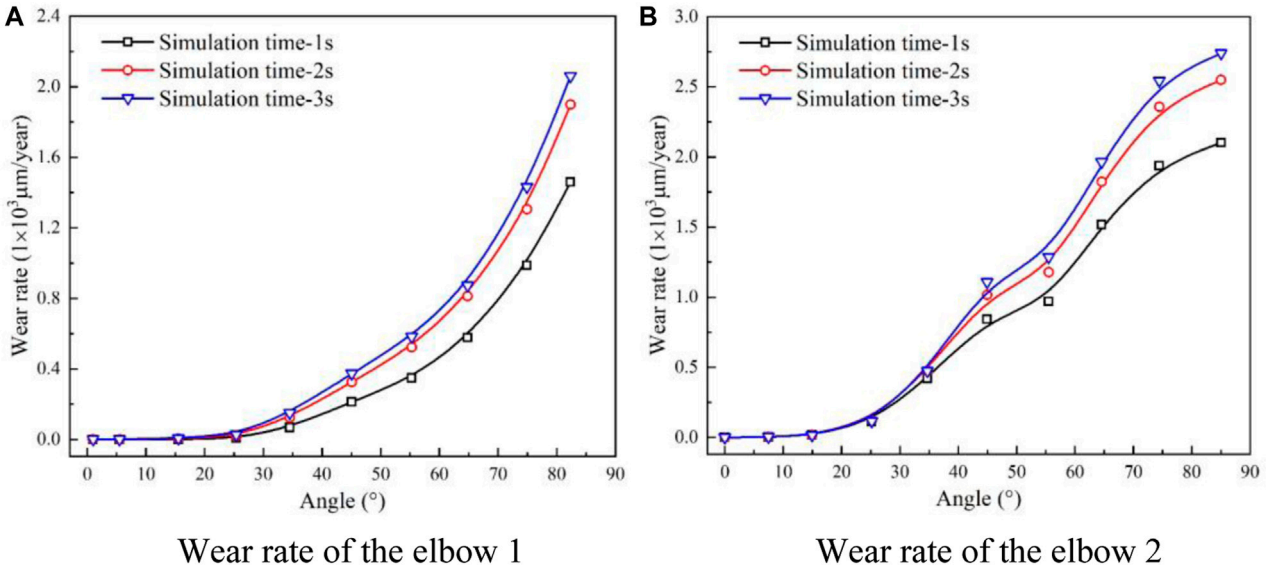

FIGURE 8
Independence verification of simulation time. **(A)** Wear rate of the elbow 1, **(B)** Wear rate of the elbow 2.

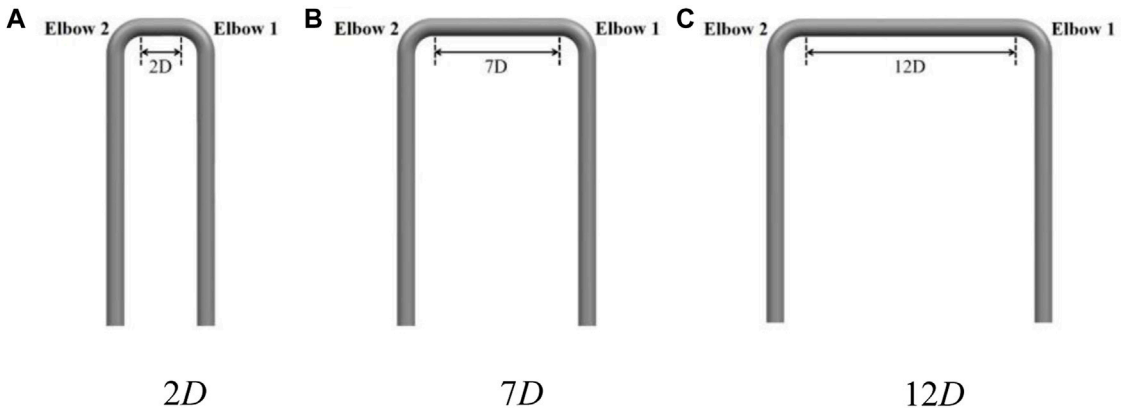

FIGURE 9
U-shaped elbows with different elbow spacing. **(A)** 2D, **(B)** 7D, **(C)** 12D.

allowing particles to pass through the elbow more smoothly, which leads to the decrease of the wall impact and further decreases the impact angle. Additionally, secondary flow is generated and persists for a longer duration with greater particle kinetic energy loss, and the wear rate presents a downward trend, the investigation result is consistent with the experimental findings of Farokhipour (Jia et al., 2021).

Furthermore, Figure 13C reveals the relationship between the impact angle and bending angle under different bending diameter ratios. As the bending diameter ratio increases, the bending degree of the elbow gradually decreases, and solid particles flow more smoothly. Consequently, the impact angle between the particles and wall is small, and the position of the maximum impact angle is closer to the elbow entrance with the increase of the bending diameter ratio.

Figure 14 displays the wear characteristics of elbow 2, the relationship between the impact frequency, wear rate, and impact angle with the bending diameter ratio remains consistent with elbow 1. However, compared to the elbow 1, the impact frequency increasing rate of elbow 2 gradually slows down as the bending diameter ratio increases. The impact angle of elbow 2 exhibits a relatively stable trend within the 65°–85° range, which has a similar variation trend under different elbows spacing.

4.3 Effect of particle volume concentration

In pipeline transportation systems, particle mass loading is a crucial factor that significantly affects pipe wall wear. According to the previous research on the wear of gas-solid two-phase flow in

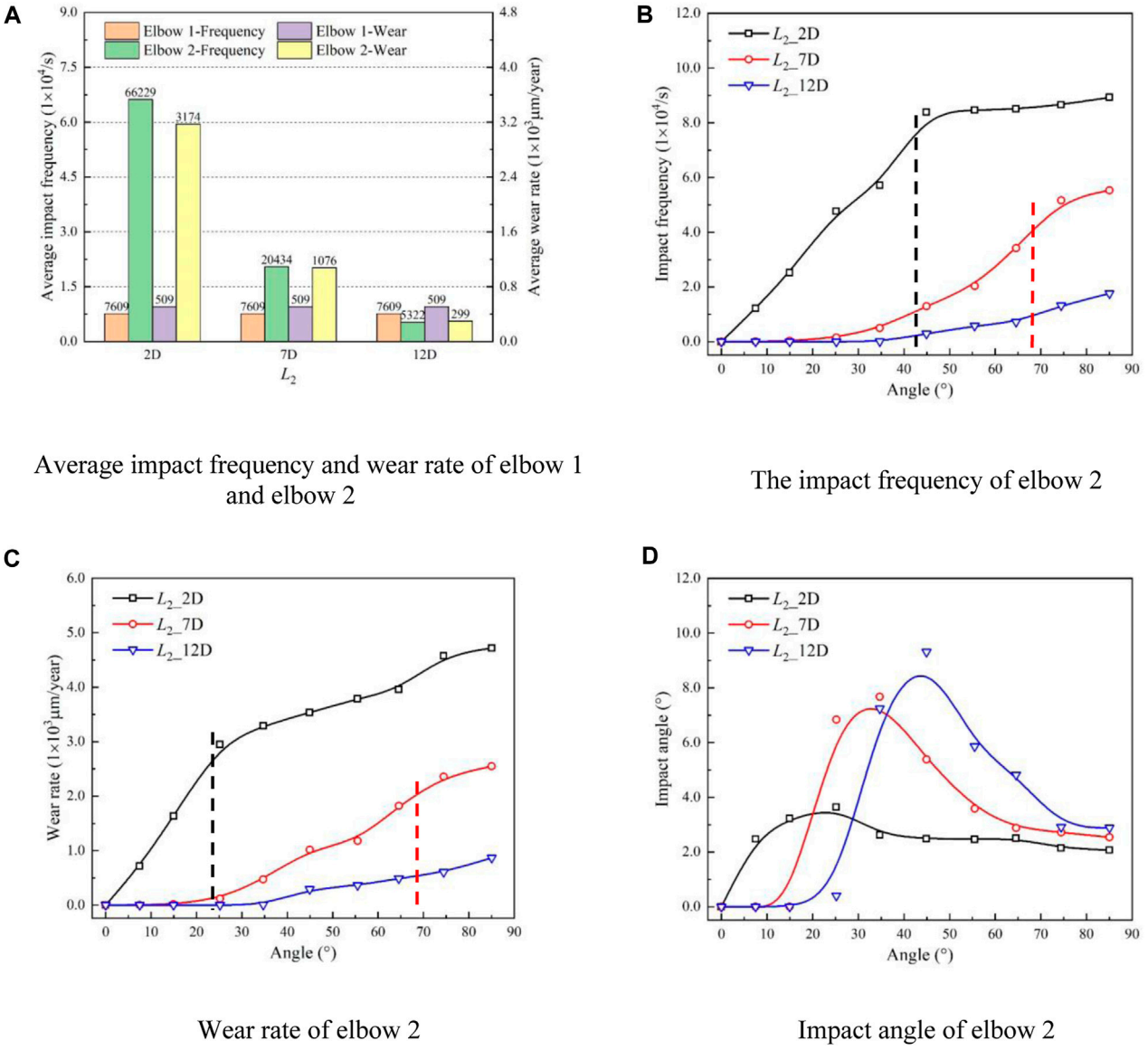

FIGURE 10
The wear characteristics of U-shaped bends under different elbow spacing. **(A)** Average impact frequency and wear rate of elbow 1 and elbow 2, **(B)** The impact frequency of elbow 2, **(C)** Wear rate of elbow 2, **(D)** Impact angle of elbow 2.

pipeline transportation (Jia et al., 2021; Zhao et al., 2023), the shield effect (In particle flow, the shielding effect refers to the phenomenon where smaller particles are constrained by larger particles, preventing them from colliding with the pipeline walls. This reduces the wear on the pipeline walls and provides a certain level of protection) will form with the increases of particle mass loading, which results in the wear saturation. However, few studies have been conducted on this type of flow in solid-liquid two-phase flow. Therefore, the wear characteristics of U-shaped elbows under different particle volume concentrations are simulated in this article using 1 mm particle and 3 m/s flow velocity.

The wear characteristics of elbow 1 under different particle volume concentrations are presented in Figure 15. The corresponding growth rates under operating conditions of 0.5%-1%, 1%–3%, 3%–5%, and 5%–7% are defined as X1, X2, X3, and X4, respectively. It is observed from the results that the growth rate of the maximum impact frequency and wear rate on elbow 1 first increases and then decreases with the increase of particle volume concentration, and the impact frequency and wear rate exhibit a non-linear increase.

When the particle volume concentration is 0.5%, the maximum impact frequency and wear rate are 1,162 times/s and 19.98 nm/year, respectively. As the particle volume concentration rises to 1%, the maximum impact frequency and wear rate increase to 3,110 times/s and 98.32 nm/year, respectively, with growth rates of 170% and 400% for impact frequency and wear rate, respectively. Further increasing the particle volume concentration to 3%, the maximum impact frequency and wear rate improved to 27,681 times/s and 1897.83 nm/year, respectively, with the impact frequency and wear rate showing significant increase and

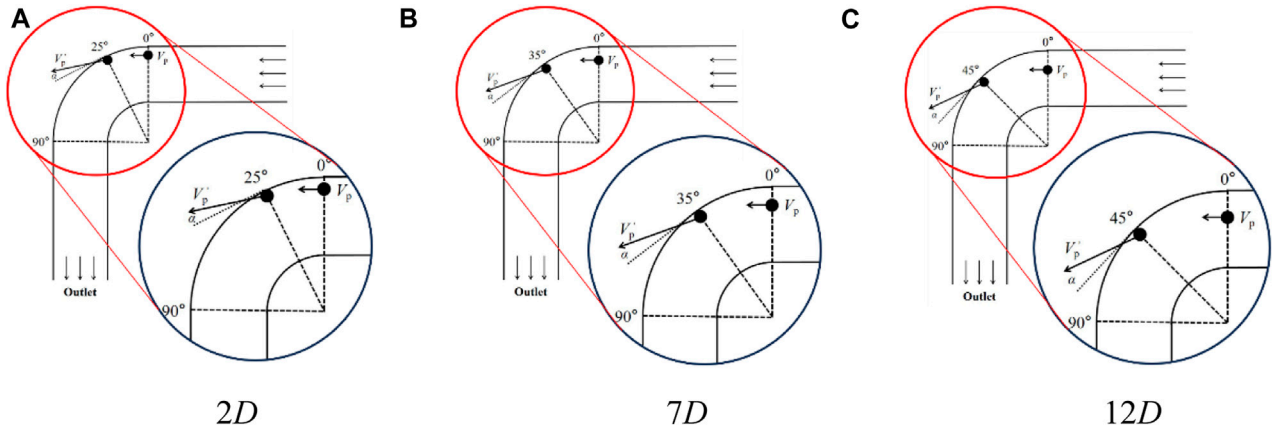

FIGURE 11
Schematic diagram of particle collision under different elbow spacing. **(A)** 2D, **(B)** 7D, **(C)** 12D.

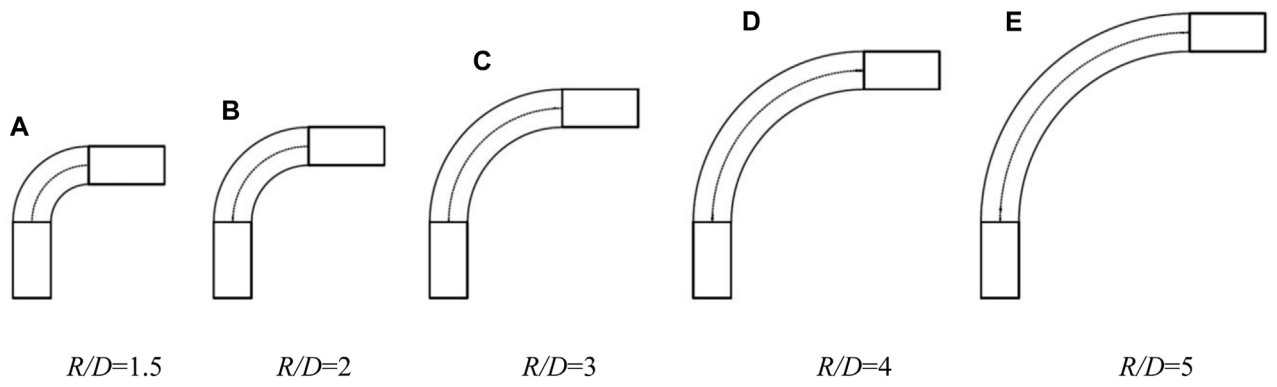

FIGURE 12
Schematic diagram of different bend diameter ratios for the same pipe diameter. **(A)** R/D=1.5, **(B)** R/D=2, **(C)** R/D=3, **(D)** R/D=4, **(E)** R/D=5.

corresponding growth rates of about 790% and 1830%, respectively. With the particle volume concentration increase from 0.5% to 3%, more and more particles impact the wall, which leads to substantial increases in the impact frequency and wear rate, while the corresponding growth rate also reaches a peak.

When the particle volume is 5%, the maximum impact frequency and wear rate are 90,047 times/s and 7556.07 nm/year, respectively. The impact frequency and wear rate are still increasing, but the growth rates decline by about 230% and 300%, respectively. When the particle volume concentration is further increased to 7%, the maximum impact frequency and wear rate reach 139,135 times/s and 11,931.82 nm/year, respectively, with the growth rates of the impact frequency and wear rate further reduced by about 50% and 60%.

This phenomenon is contributed to the improvement of the particle volume concentration, the particle impact at the outer wall, and bounces at a certain angle, which strikes the ensuing particle. So the particles adjacent to the wall form a "virtual barrier" that inhibits the surrounding particles impacting the elbow wall directly, thereby reducing the impact frequency between particles and the elbow wall. This process is further enhanced with an increase in particle volume concentration, which slows down the acceleration of the impact frequency and wear rate.

Figure 15D displays the relationship between the wall impact angle with particle volume concentration and bending angle. When the bending angle increase from 0° to 50°, the impact angle initially increases and then decreases with the improvement of particle volume concentration. Furthermore, when the bending angle is within the range of 50°-90°, particles near the wall exchange momentum with incoming particles, moving toward areas of high particle volume concentration and impacting with the wall again at a lower impact angle. Consequently, the impact angle decreases with an increase in particle volume concentration, thereby further slowing down the increase of wear rate.

Figure 16 displays the wear characteristics of elbow 2, which is the same as that of elbow 1, and the corresponding growth rates under the conditions of 0.5%-1%, 1%–3%, 3%–5%, and 5%–7% are defined as X5, X6, X7, and X8, respectively. As shown in Figure 16 (a), the results indicate that as particle volume concentration increases, the growth trend of the maximum

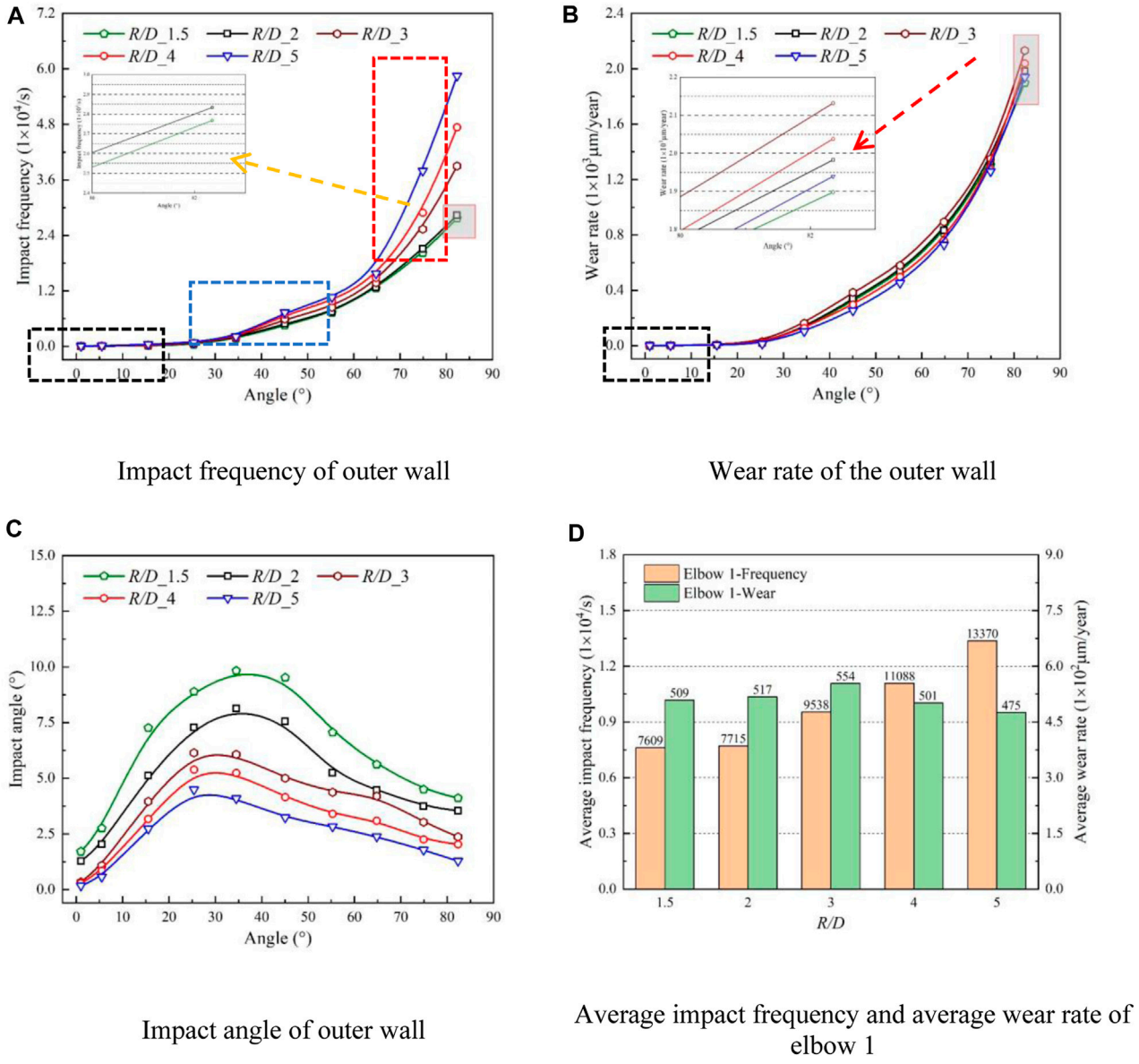

FIGURE 13
Wear characteristics of elbow 1 with different bending diameter ratios. **(A)** Impact frequency of outer wall, **(B)** Wear rate of the outer wall, **(C)** Impact angle of outer wall, **(D)** Average impact frequency and average wear rate of elbow 1.

impact frequency and wear rate on elbow 2 are consistent with elbow 1. Most of the particles are concentrated on the outer wall, which leads to the peak value of impact frequency and wear rate of elbow 2 being higher than in elbow 1 b y 1,520% and 5030%, respectively. The corresponding decline rate of elbow 2 is also greater than elbow 1 b y 40% and 50%, respectively, indicating that the "shield effect" appears earlier in elbow 2 than in elbow 1. Secondly, as revealed in Figure 16. (b) and (c) that impact frequency and wear rate of elbow 1 increase with an improvement of bending angle. However, the growth trend of impact frequency and wear rate of elbow 2 exhibit a trend of sharp increase and then slow increase.

Moreover, the transverse acceleration of particles is continuously influenced by the longitudinal secondary flow that develops alongside the main flow of solid-liquid two-phase flow transported by pipeline, thus hampering the particle acceleration process. Although the impact frequency increases slightly compared to elbow 1, the increase is not sufficient to produce a significantly higher wear rate than that of elbow 1. However, with an increase in particle concentration, the impact frequency between particles and the wall surface obviously increases, leading to a higher wear rate of elbow 2 compared to elbow 1.

4.4 Effect of particle size

In pipeline transportation, particle size is a crucial physical parameter. In this paper, the wear characteristics of U-shaped

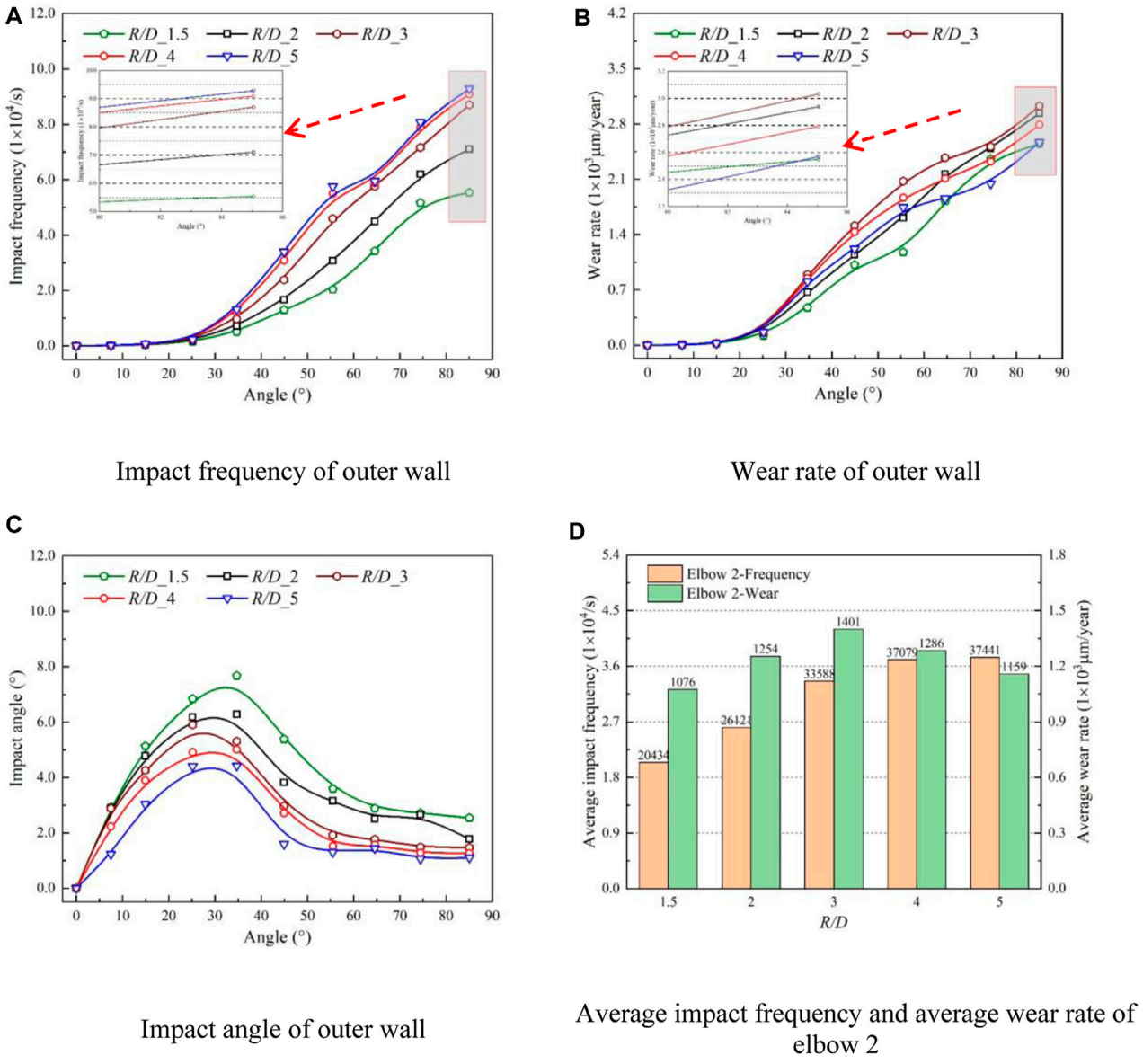

FIGURE 14
Wear characteristics of the elbow 2 with different bending diameter ratios. **(A)** Impact frequency of outer wall, **(B)** Wear rate of the outer wall, **(C)** Impact angle of outer wall, **(D)** Average impact frequency and average wear rate of elbow 2.

elbow with different particle sizes are simulated, the conveying speed is 3 m/s and the particle volume concentration is 3%. Figure 17 illustrates the wear characteristics of elbow 1 with different particle sizes. Considering the particle volume concentration is constant, the number of particles transported in the pipe declines with an increase in particle size. As a result, the contact position of the pipe wall moves relatively backward, and the impact frequency accordingly decreases.

The wear rate exhibits an upward trend with an increase in particle size, this phenomenon is attributed to the increase of particle size, which leads to the decrease of particle number and momentum loss of particle collisions. Furthermore, the influence of inertial force on particle movement is gradually enhanced, but the influence of the secondary flow effect at the elbow on particle movement is weakened, and the particles gradually move away from the streamline. At the same time, under the effect of the inertial force, the particles directly impact the outer wall of the elbow 1, causing serious wear on the outer wall. Nonetheless, as the impact frequency decreases with the improvement of particle size, the growth rate of the wear rate gradually slows down.

Figure 18 presents the impact frequency distribution of the elbow 1 for particle sizes of 1 mm, 1.5 mm, and 2 mm. It is observed that the collision areas are symmetrically distributed about the centerline of the pipeline, beginning from the bending angle of 45° and extending to the elbow outlet. As the particle size

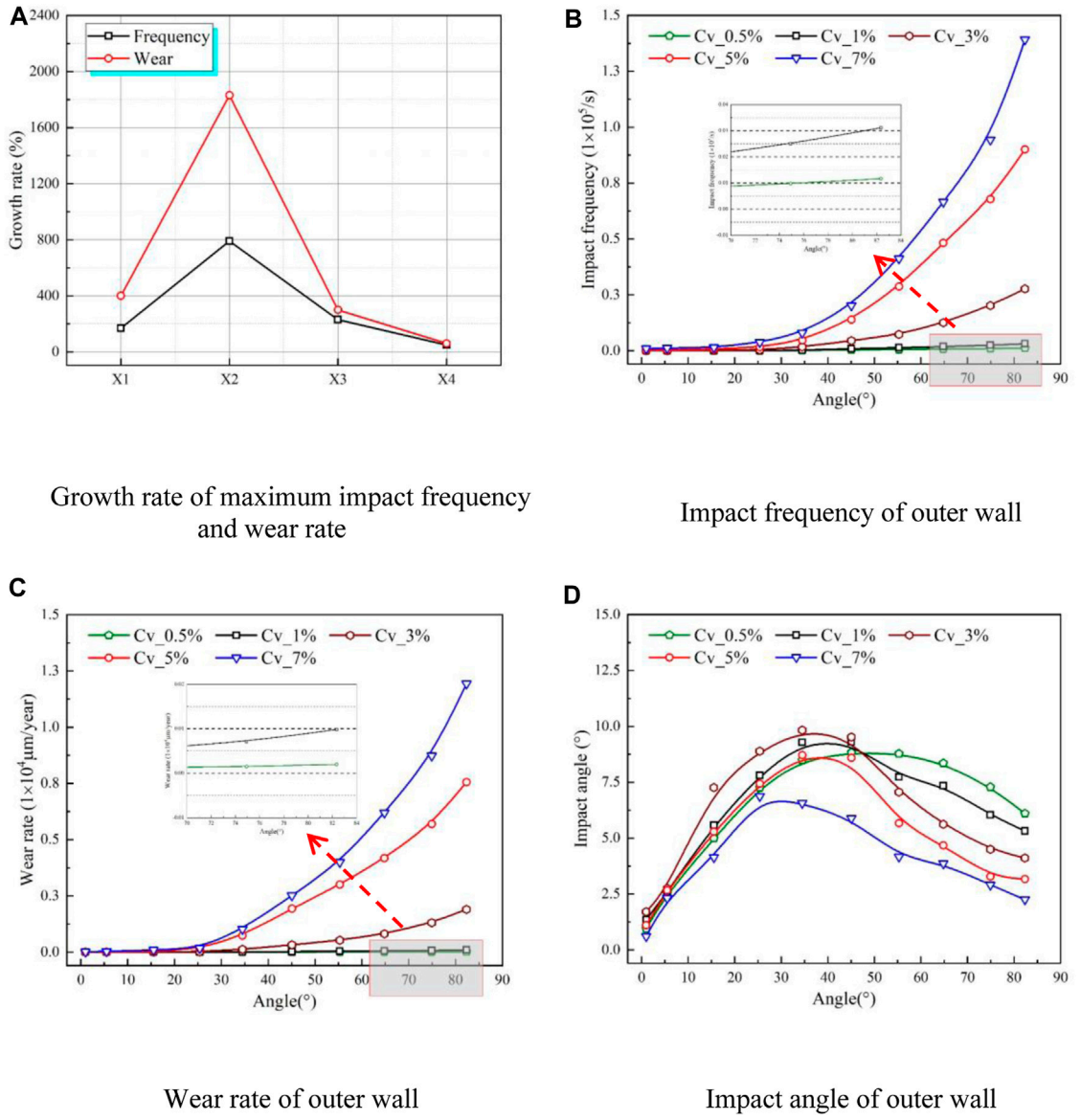

FIGURE 15
Wear characteristics of the elbow 1 under different particle volume concentrations. **(A)** Growth rate of maximum impact frequency and wear rate, **(B)** Impact frequency of outer wall, **(C)** Wear rate of outer wall, **(D)** Impact angle of outer wall.

increases, the number of conveyed particles decreases, and the high-frequency collision area gradually transforms from an original steeple shape to a dot shape while the corresponding maximum impact frequency also gradually decreases. Meanwhile, the low-frequency collision area is gradually narrowed.

Figure 19 shows the wear rate distribution of elbow 1. Consistent with the impact frequency distribution, the wear area is also symmetrically distributed about the centerline. The area of high wear area decreases with the increase in particle size. However, the influence of inertial force gradually dominates, leading particles to directly impact the elbow 1 outer wall, thus promoting the maximum wear rate. Specifically, when the particle size is 1mm, the maximum wear rate is 1897.83 nm/year, and the particle size is 1.5mm, and the maximum wear rate is 2596.77 nm/year. When the particle size is 2mm, the maximum wear rate is 2925.71 nm/year.

In Figure 20, the wear characteristics of elbow 2 are presented. It is observed that the average impact frequency of the two elbows decreases with the improvement of particle size, the average impact frequency and wear rate of elbow 2 is larger than elbow 1. Moreover, the average wear rate of elbow 2 first increases and then declines with the improvement of particle size. In addition, the same as elbow 1, affected by the number of particles transported in the pipe, the impact frequency of elbow 2 also gradually decreases with the increase of particle size, and

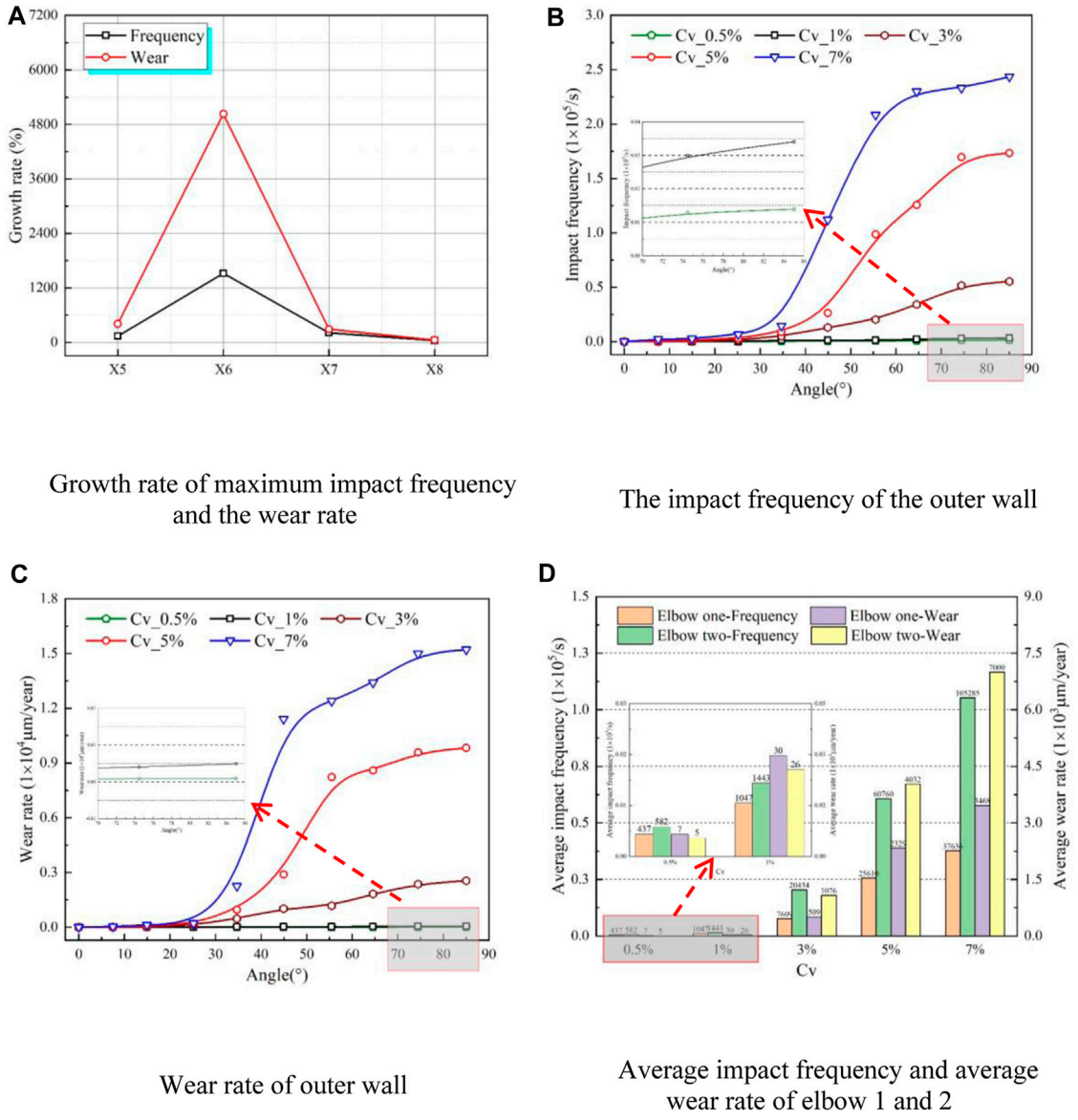

FIGURE 16
Wear characteristics elbow 2 under different particle volume concentrations. **(A)** Growth rate of maximum impact frequency and wear rate, **(B)** The impact frequency of the outer wall, **(C)** Wear rate of outer wall, **(D)** Average impact frequency and average wear rate of elbow 1 and 2.

when the transport particle size is greater than 1mm, the impact frequency does not appear to increase sharply first and then slowly increasing trend, which is consistent with the delivery of low particle volume concentration.

However, the wear rate has the same variation trend as the average wear rate. The critical particle size is 1.5mm, when the particle size is below 1.5mm, the wear rate elevates with an increase in particle size whereas above this particle size, the trend declines. Furthermore, by comparing the wear rate of the pipeline when the particle size of 1 mm and 2mm, it found that the area of bending angle from 0° to 55° and elbow outlet, the wear rate of 2 mm particle is larger than 1 mm. Meanwhile, in the 55°–82° interval, the wear rate for the 2 mm particle size is less than that for the 1 mm particle.

Figure 21 presents the impact frequency distribution of elbow 2, the collision area is symmetrically distributed about the centerline. As the particle size increases, the high-frequency collision area gradually reduces, while the initial position of high-frequency collision shifts toward the elbow outlet. Since the particles are less affected by the secondary flow effect, the inertial force is enhanced, causing the initial collision area position to move toward the elbow inlet.

In Figure 22, the wear rate distribution of elbow 2 is depicted, the wear area is symmetrically distributed about the centerline. The high wear areas are vase-shaped for particle sizes of 1mm and 1.5 mm while becoming spire-shaped for a particle size of 2 mm. Furthermore, the high wear area decreases as particle size increases, and the maximum wear rate shows a trend of initial

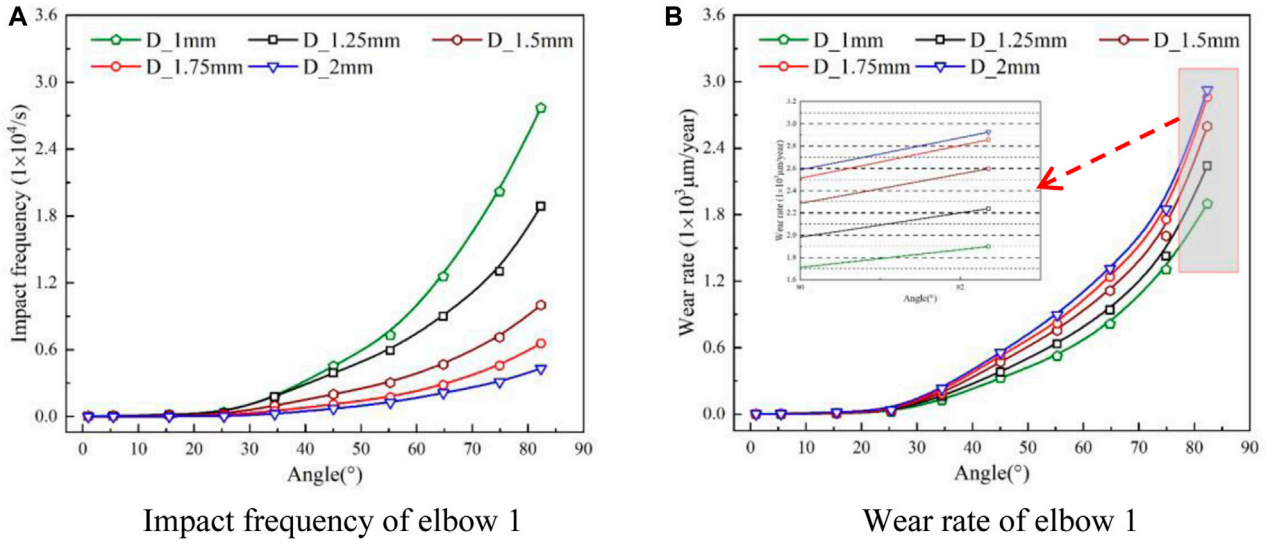

FIGURE 17
Wear characteristics of the elbow 1 under different particle sizes. **(A)** Impact frequency of elbow 1, **(B)** Wear rate of elbow 1.

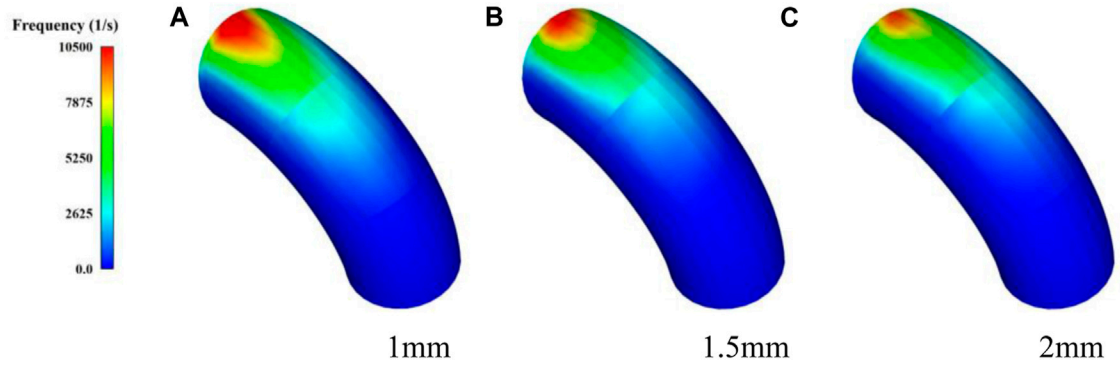

FIGURE 18
Impact frequency distribution of elbow1 under different particle sizes. **(A)** 1 mm, **(B)** 1.5 mm, **(C)** 2 mm.

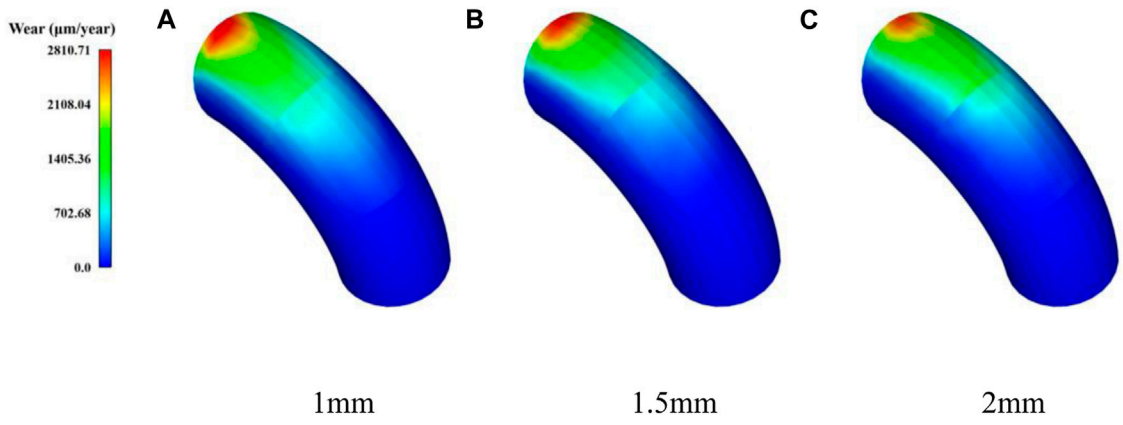

FIGURE 19
The wear rate distribution of elbow 1 under different particle sizes. **(A)** 1 mm, **(B)** 1.5 mm, **(C)** 2 mm.

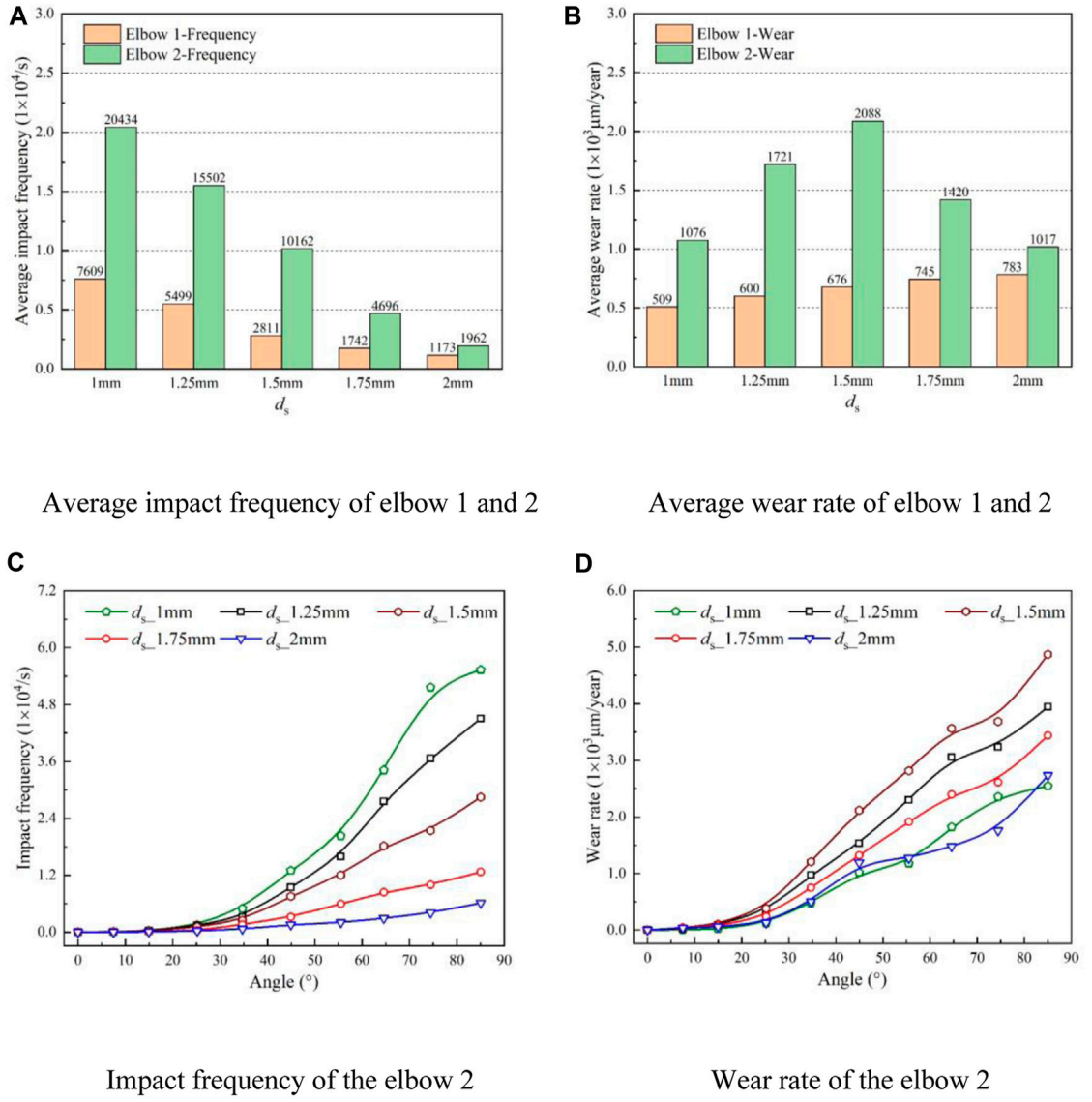

Average impact frequency of elbow 1 and 2

Average wear rate of elbow 1 and 2

Impact frequency of the elbow 2

Wear rate of the elbow 2

FIGURE 20
Wear characteristics of elbow 2 under different particle sizes. **(A)** Average impact frequency of elbow 1 and 2, **(B)** Average wear rate of elbow 1 and 2, **(C)** Impact frequency of the elbow 2, **(D)** Wear rate of the elbow 2.

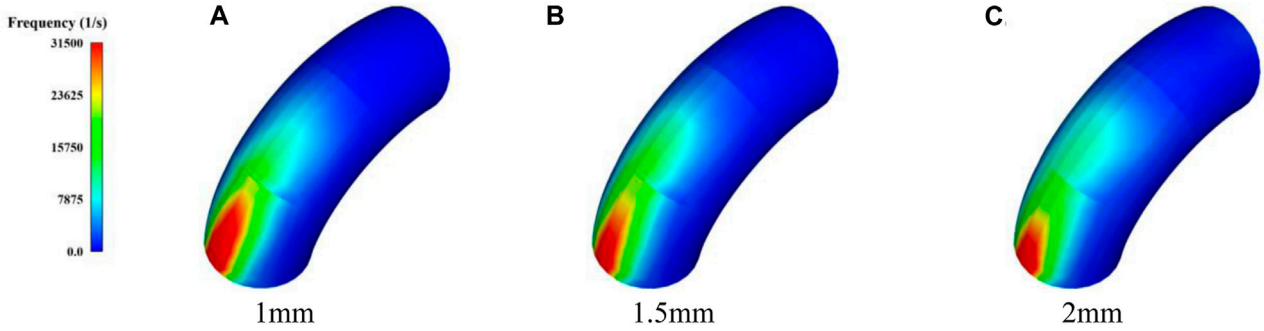

FIGURE 21
Impact frequency distribution of elbow2 under different particle sizes. **(A)** 1 mm, **(B)** 1.5 mm, **(C)** 2 mm.

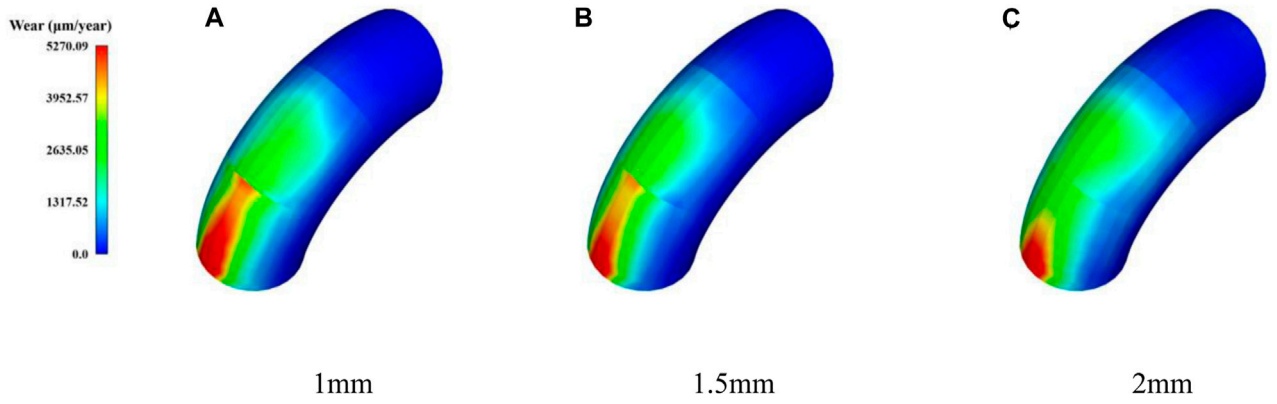

FIGURE 22
The wear rate distribution of elbow 1 under different particle sizes. **(A)** 1 mm, **(B)** 1.5 mm, **(C)** 2 mm.

increase and then decrease. When the particle size is 1mm, the maximum wear rate reaches 2548.47 nm/year, while for particle sizes of 1.5 mm and 2mm, the maximum wear rates are 4873.72 nm/year and 2733.96 nm/year, respectively. Similar to the collision area of elbow 2, the initial position of the wear area shifts towards the elbow inlet as particle size increases.

5 Conclusion

The C++ programming language was utilized to improve the CFD-DEM coupling interface in this paper, and the Loth lift, virtual mass force, and pressure gradient force were introduced for simulating solid-liquid two-phase flows. Meanwhile, the transient fluctuations of flow velocity were employed on the particle motion by using the DRW model. The accuracy of numerical simulation was verified through experiments of the previous research. Subsequently, the improved numerical model of solid-liquid two-phase flow is employed to investigate the wear characteristics of U-shaped elbow under different parameters such as elbow spacing, bending diameter ratio, particle volume concentration, and particle size. The conclusions were obtained as follows:

Increasing the spacing between elbows enhances the effect of gravity on particles, leading to particle settling. The longer the elbow spacing, the higher the settlement, and the lower the position of particle impacts on elbow 2, resulting in increased corresponding bending angles and maximum impact angles. Due to the reduced number of particles inside the pipe, the collision frequency and wear rate decrease significantly, and this improvement in elbow spacing has no impact on Elbow 1. Additionally, under elbow spacing of 2*D* and 7*D*, the average impact frequency and wear rate of elbow 2 are much higher than those of elbow 1. When the elbow distance is 12*D*, the gravity of the particles dominates over the inertial effect, causing the average impact frequency and wear rate of elbow 2 to be much lower than those of elbow 1. Therefore, increasing the elbow spacing is beneficial for reducing wear in elbow pipes.

The improvement of the bending diameter ratio denotes that particles need to traverse a longer pipeline path, thus resulting in larger particle-wall collision areas and gradually increasing impact frequency, the curves corresponding to different bending diameter ratios exhibit three growth regulations of the wear rate. Further, the reduction of the bending degree of the elbow makes the flow of solid particles smoother, and the particles impact the wall at a smaller angle, and the secondary flow will occur earlier and last longer, which will have a greater impact on the kinetic energy loss of the particles, and the wear rate presents the downward trend. Therefore, with the increase of the bending diameter ratio, the wear rate will continue to decrease, and the use of larger-diameter elbows is beneficial to reduce elbow wear.

Considering the influence of inertial force on particle movement is gradually enhanced, the particles move away from the streamline and impact the outer wall of the elbow 1, causing serious wear on the outer wall. Nonetheless, as the impact frequency decreases with the improvement of particle size, the growth rate of the wear rate continually slows down. Additionally, the critical particle size is 1.5 mm, when the particle size is below 1.5mm, the wear rate elevates with an increase in particle size whereas above this particle size, the trend declines. Moreover, with the increase of the particle size, the particles are less affected by the secondary flow effect, and the inertial force is enhanced, causing the initial collision area position to move toward the elbow 2 inlet.

Data availability statement

The original contributions presented in the study are included in the article/supplementary material, further inquiries can be directed to the corresponding authors.

Author contributions

HC: Writing–original draft, Investigation. GJ: Investigation, Writing–review and editing. DY: Data curation, Writing–original draft. GP: Methodology, Writing–original draft. SH: Validation,

Writing–original draft. JD: Methodology, Writing–review and editing.

Funding

The author(s) declare that no financial support was received for the research, authorship, and/or publication of this article.

Acknowledgments

The authors gratefully acknowledge the support from Open Research Subject of Key Laboratory of Fluid Machinery and Engineering (Xihua University) grant number LTJX 2021-003; Open Research Subject of Hubei Key Laboratory of Hydroelectric Machinery Design and Maintenance (China Three Gorges University) grant number 2020KJX07; the 69th batch of general funding from the China Postdoctoral Science Foundation grant number: 2021M691298; Natural Science Research Project of Jiangsu Province Colleges and Universities: 21KJB570004, Priority Academic Program Development of Jiangsu Higher Education Institutions (PAPD).

Conflict of interest

DY was employed by Chongqing Pump Industry Co Ltd.

The remaining authors declare that the conduct of this research does not involve any business or financial relationship that could be interpreted as a potential conflict of interest.

Publisher's note

References

Ahlert, K. R. (1994). *Effects of particle impingement angle and surface wetting on solid particle erosion of AISI 1018 steel*. Tulsa: University of Tulsa.

Alajbegović, A., Assad, A., Bonetto, F., and Lahey, R. (1994). Phase distribution and turbulence structure for solid/fluid upflow in a pipe. *Int. J. Multiph. Flow* 20 (3), 453–479. doi:10.1016/0301-9322(94)90021-3

Archard, J. F. (1953). Contact and rubbing of flat surfaces. *J. Appl. Phys.* 24 (8), 981–988. doi:10.1063/1.1721448

Bai, L., Han, C., Xu, Y. F., Zhou, L., Zhang, L. J., Shi, W. D., et al. (2022). CFD-DEM numerical simulation and experimental study of bubbling fluidized bed based on different drag force models. *J. Drainage Irrigation Mech. Eng.* 40 (01), 49–54.

Bilal, F. S., Sedrez, T. A., and Shirazi, S. A. (2021). Experimental and CFD investigations of 45 and 90 degrees bends and various elbow curvature radii effects on solid particle erosion. *Wear* 476, 203646. doi:10.1016/j.wear.2021.203646

Bitter, J. G. A. (1963a). A study of erosion phenomena part I. *Wear* 6 (1), 5–21. doi:10.1016/0043-1648(63)90003-6

Bitter, J. G. A. (1963b). A study of erosion phenomena: part II. *Wear* 6 (3), 169–190. doi:10.1016/0043-1648(63)90073-5

Di Felice, R. (1994). The voidage function for fluid-particle interaction systems. *Int. J. Multiph. flow* 20 (1), 153–159. doi:10.1016/0301-9322(94)90011-6

Duarte, C. A. R., de Souza, F. J., de Vasconcelos Salvo, R., and dos Santos, V. F. (2017). The role of inter-particle collisions on elbow erosion. *Int. J. Multiph. flow* 89, 1–22. doi:10.1016/j.ijmultiphaseflow.2016.10.001

Farokhipour, A., Mansoori, Z., Rasoulian, M. A., Rasteh, A., Saffar-Avval, M., and Ahmadi, G. (2020). Study of particle mass loading effects on sand erosion in a series of fittings. *Powder Technol.* 373, 118–141. doi:10.1016/j.powtec.2020.06.040

Finnie, I. (1960). Erosion of surfaces by solid particles. *wear* 3 (2), 87–103. doi:10.1016/0043-1648(60)90055-7

Finnie, I. (1979). *The fundamental mechanisms of the erosive wear of ductile metals by solid particles*. West Conshohocken, PA: ASTM Special Technical Publication, 36–58.

Haider, A., and Levenspiel, O. (1989). Drag coefficient and terminal velocity of spherical and nonspherical particles. *Powder Technol.* 58 (1), 63–70. doi:10.1016/0032-5910(89)80008-7

Hu, S., Zhang, X. M., Zheng, L., Zhao, B., Yang, N., Wang, M., et al. (2019). Correction to: morphological characterization and gene expression patterns for melanin pigmentation in rex rabbit. *J. Drainage Irrigation Mach. Eng.* 37 (09), 746–751. doi:10.1007/s10528-019-09934-0

Jia, W., Zhang, Y., Li, C., Luo, P., Song, X., Wang, Y., et al. (2021). Experimental and numerical simulation of erosion-corrosion of 90° steel elbow in shale gas pipeline. *J. Nat. Gas Sci. Eng.* 89, 103871. doi:10.1016/j.jngse.2021.103871

Laín, S., and Sommerfeld, M. (2019). Numerical prediction of particle erosion of pipe bends. *Adv. Powder Technol.* 30 (2), 366–383. doi:10.1016/j.apt.2018.11.014

Li, W., Pan, Y. X., Li, H. M., Qi, H. D., Wu, P., Lu, D. L., et al. (2023). Research progress on flow characteristics and wear issues of solid-liquid two-phase flow centrifugal pumps. *J. Drainage Irrigation Mach. Eng.* 41 (02), 109–117.

Oka, Y. I., Okamura, K., and Yoshida, T. (2005). Practical estimation of erosion damage caused by solid particle impact: part 1: effects of impact parameters on a predictive equation. *Wear* 259 (1-6), 95–101. doi:10.1016/j.wear.2005.01.039

Oka, Y. I., and Yoshida, T. (2005). Practical estimation of erosion damage caused by solid particle impact: part 2: mechanical properties of materials directly associated with erosion damage. *Wear* 259 (1-6), 102–109. doi:10.1016/j.wear.2005.01.040

Peng, W., and Cao, X. (2016). Numerical simulation of solid particle erosion in pipe bends for liquid–solid flow. *Powder Technol.* 294, 266–279. doi:10.1016/j.powtec.2016.02.030

Pouraria, H., Darihaki, F., Park, K. H., Shirazi, S. A., and Seo, Y. (2020). CFD modelling of the influence of particle loading on erosion using dense discrete particle model. *Wear* 460, 203450. doi:10.1016/j.wear.2020.203450

Sun, G. Y., Zhang, Y. J., Zhang, R. Q., Wang, Y. C., and Mao, X. L. (2022b). Numerical prediction and analysis of Francis turbine abrasion in high sediment flow. *J. Drainage Irrigation Mech. Eng.* 40 (12), 1197–1203.

Sun, X. L., Liu, H. L., Tan, M. G., Wu, X. F., and Zhang, K. K. (2022a). Effect of mineral particle size on the wear characteristics of deep sea mining pumps. *J. Drainage Irrigation Mech. Eng.* 40 (11), 1097–1103.

Tarodiya, R., and Gandhi, B. K. (2019). Numerical simulation of a centrifugal slurry pump handling solid-liquid mixture: effect of solids on flow field and performance. *Adv. Powder Technol.* 30 (10), 2225–2239. doi:10.1016/j.apt.2019.07.003

Uzi, A., and Levy, A. (2018). Flow characteristics of coarse particles in horizontal hydraulic conveying. *Powder Technol.* 326, 302–321. doi:10.1016/j.powtec.2017.11.067

Vieira, R. E., Mansouri, A., McLaury, B. S., and Shirazi, S. A. (2016). Experimental and computational study of erosion in elbows due to sand particles in air flow. *Powder Technol.* 288, 339–353. doi:10.1016/j.powtec.2015.11.028

Wang, Q., Huang, Q., Wang, N., Wen, Y., Ba, X., Sun, X., et al. (2021). An experimental and numerical study of slurry erosion behavior in a horizontal elbow and elbows in series. *Eng. Fail. Anal.* 130, 105779. doi:10.1016/j.engfailanal.2021.105779

Wang, Y. Q., Su, X. H., and Zhu, Z. C. (2022). Flow field and coarse particle motion characteristics in deep-sea mining mixed transport pumps. *J. Drainage Irrigation Mech. Eng.* 40 (08), 800–806.

Wang, Y., Wang, X., Shang, P., Xu, Z., and Huang, Q. (2023). A numerical study of the slurry erosion in 90° horizontal elbows. *J. Pipeline Sci. Eng.*, 100149. doi:10.1016/j.jpse.2023.100149

Xu, H., Wu, W. Y., Wang, Z. H., and Wang, Q. L. (2020). Hydraulic characteristics analysis and flow field calculation of inclined tee pipe based on CFD. *J. Drainage Irrigation Mech. Eng.* 38 (11), 1138–1144.

Zeng, D., Zhang, E., Ding, Y., Yi, Y., Xian, Q., Yao, G., et al. (2018). Investigation of erosion behaviors of sulfur-particle-laden gas flow in an elbow via a CFD-DEM coupling method. *Powder Technol.* 329, 115–128. doi:10.1016/j.powtec.2018.01.056

Zeng, L., Zhang, G. A., and Guo, X. P. (2014). Erosion–corrosion at different locations of X65 carbon steel elbow. *Corros. Sci.* 85, 318–330. doi:10.1016/j.corsci.2014.04.045

Zhang, Y., Reuterfors, E. P., McLaury, B. S., Shirazi, S., and Rybicki, E. (2007). Comparison of computed and measured particle velocities and erosion in water and air flows. *Wear* 263 (1-6), 330–338. doi:10.1016/j.wear.2006.12.048

Zhang, Z. C., Li, Y. P., and Chen, D. X. (2023). The influence of two-fluid turbulence model on the calculation of solid-liquid two-phase flow. *J. Drainage Irrigation Mech. Eng.* 41 (04), 376–383.

Zhao, H. B., Cao, Q., Kang, C., Mao, N., Zhen, W. W., Ren, L. B., et al. (2023). The effect of structural form on the wear characteristics of the sealing surface of the front chamber of a slurry pump. *J. Drainage Irrigation Mach. Eng.* 41 (03), 247–252.

Zhao, R., Zhao, Y., Si, Q., and Gao, X. (2022). Effects of different characteristics of the dilute liquid-solid flow on the erosion in a 90° bend. *Powder Technol.* 398, 117043. doi:10.1016/j.powtec.2021.117043

Zhao, R. J., Zhao, Y. L., Zhou, Y., and Zhang, D. S. (2021). Numerical simulation of coarse particle erosion characteristics of solid-liquid two-phase flow in 90° elbow. Journal of Huazhong University of Science and Technology. *Nat. Sci.* 49 (10), 47–52.

Zheng, Y. G., Yu, H., Jiang, S. L., and Yao, Z. (2008). Effect of the sea mud on erosion–corrosion behaviors of carbon steel and low alloy steel in 2.4% NaCl solution. *Wear* 264 (11-12), 1051–1058. doi:10.1016/j.wear.2007.08.008

Zhong, L., Feng, G. H., Zhang, J. C., and Wei, G. (2021). Influence rules of erosion and wear of sewage valves based on CFD numerical simulation. *J. Drainage Irrigation Mech. Eng.* 39 (02), 151–157.

Zolfagharnasab, M. H., Salimi, M., Zolfagharnasab, H., Alimoradi, H., Shams, M., and Aghanajafi, C. (2021). A novel numerical investigation of erosion wear over various 90-degree elbow duct sections. *Powder Technol.* 380, 1–17. doi:10.1016/j.powtec.2020.11.059

Glossary

α_f	the volume fraction occupied by the fluid
α_k	the effective Prandtl reciprocals of k
α_ε	the effective Prandtl reciprocals of ε
BH	the Brinell hardness of the wall material
C_L	the lift coefficient
D	the diameter of the vertical pipe
d_s	particle size
dv_s/dt	particle translational acceleration
ER	the wear rate
f	the resultant force on particle i within a computational unit
f_s	the sliding friction coefficient
F_{bg}	the resultant force of gravity and buoyancy on the particle
F_c	the contact force between particles and between particles and walls
$F_{cn,AB}$	the normal contact force
$F_{ct,AB}$	the tangential contact force
F_{drag}	the drag force on the particle
F_{loth}	the Loth lift force acting on the particle
F_{pg}	the pressure gradient force on the particle
F_s	the shape factor of particles
F_{vm}	the additional mass force on the particle
g	gravitational acceleration
G_b	the turbulent kinetic energy caused by buoyancy
G_k	the turbulent kinetic energy caused by the average velocity gradient
I_s	the moment of inertia of the particle
k	turbulent kinetic energy
$k_{n,AB}$	the normal elastic stiffness of the spring
$k_{t,AB}$	The tangential elastic stiffness of the spring
m	the number of particles in a computational unit
m_s	particle mass
L	the length of the pipe
p	pressure
r	the ratio of the radius of the concentric circle
R	the radius of the vertical pipe
$R_{s,\omega}$	the particle rotation
$Re_{s,\alpha}$	the particle Reynolds number considering the fluid volume fraction
S_k	the source terms of turbulent kinetic energy
S_ε	the source terms of turbulent dissipation rate
T_c	the particle contact torque
T_f	the torque generated by fluid phase
V	the volume of the computational unit
V_k	the volume of particle k in the calculation unit
v_f	fluid mean velocity
$v_{n,AB}$	the normal relative velocity vector of particles A and B during contact
$v_{t,AB}$	the tangential relative velocity vector of particles A and B during contact
$\zeta_{n,AB}$	the normal displacement of particles
$\zeta_{t,AB}$	the tangential displacement of particles
$\zeta_{t,AB}/\lvert\zeta_{t,AB}\rvert$	the tangential unit vector
ω_f	the fluid vorticity
ω_f^*	the relative vorticity of the fluid
ω_s	the particle angular velocity
ω_s^*	the relative angular velocity of the particle
ε	turbulent dissipation rate
$\gamma_{n,AB}$	the normal damping coefficients
$\gamma_{t,AB}$	the tangential damping coefficients
ρ_f	fluid density
ρ_s	the particle density
μ_f	fluid dynamic viscosity
μ_t	turbulent viscosity

frontiers | Frontiers in Energy Research

TYPE Original Research
PUBLISHED 30 November 2023
DOI 10.3389/fenrg.2023.1335227

OPEN ACCESS

EDITED BY
Yang Yang,
Yangzhou University, China

REVIEWED BY
Ye Changliang,
Hohai University, China
Xianghui Su,
Zhejiang Sci-Tech University, China

*CORRESPONDENCE
Desheng Zhang,
zds@ujs.edu.cn

RECEIVED 08 November 2023
ACCEPTED 20 November 2023
PUBLISHED 30 November 2023

CITATION
Lang T, Ni C, Chen K, Xu E, Yin J, Shen X, Wu X and Zhang D (2023), Recognition of cavitation characteristics in non-clogging pumps based on the improved Lévy flight bat algorithm.
Front. Energy Res. 11:1335227.
doi: 10.3389/fenrg.2023.1335227

Recognition of cavitation characteristics in non-clogging pumps based on the improved Lévy flight bat algorithm

Tao Lang, Chen Ni, Keqiang Chen, Enxiang Xu, Jia Yin, Xi Shen, Xing Wu and Desheng Zhang*

Research Center of Fluid Machinery Engineering and Technology, Jiangsu University, Zhenjiang, China

The performance and operational stability of non-clogging pumps can be affected by cavitation. To accurately identify the cavitation state of the non-clogging pump and provide technical references for monitoring its operation, a study was conducted on the optimization of Elman neural networks for cavitation monitoring and identification using the Improved Lévy Flight Bat Algorithm (ILBA) on the basis of the traditional Bat Algorithm (BA). The ILBA employs multiple bats to interact and search for targets and utilizes the local search strategy of Lévy flight, effectively avoiding local minima by taking advantage of the non-uniform random walk characteristics of large jumps. The ILBA algorithm demonstrates superior performance compared to other traditional algorithms through simulation testing and comparative calculations with eight benchmark test functions. On this basis, the optimization of the weights and thresholds of the Elman neural network was carried out by the improved bat algorithm. This leads to an enhancement in the accuracy of the neural network for identifying and classifying cavitation data, and the establishment of the ILBA-Elman cavitation diagnosis model was achieved. Collect pressure pulsation signals at the tongue of the non-clogging pump volute through cavitation tests. Through the cavitation feature extraction method based on Variational Mode Decomposition (VMD) and Multi-scale Dispersion Entropy (MDE), the interference signal can be effectively suppressed and the complexity of the time series can be measured from multiple angles, thereby creating a cavitation feature data set. The improved cavitation diagnosis model (ILBA-Elman) can realize the effective identification of the cavitation characteristics of non-clogging pumps through a variety of algorithm comparison experiments.

KEYWORDS

bat algorithm, Lévy flight, Elman neural network, cavitation recognition, non-clogging pump, VMD, multi-scale dispersion entropy

1 Introduction

The centrifugal non-clogging pumps are essential components for offshore oil platform production and fire protection. Due to the high sediment content in seawater, ocean currents can also stir up sand, gravel, aquatic vegetation, and various suspended solids from the seabed. Single-blade centrifugal non-clogging pumps offer excellent passage capacity, wear resistance, and high efficiency. They provide reliable support for tasks on oil platforms, including seawater cleaning, well maintenance, fire sprinkler systems, and sewage treatment

(Noon et al., 2021; Li et al., 2023; Quan et al., 2021). The non-clogging pump is characterized by strong conveying capacity, wear resistance, and high efficiency. In actual operation, the non-clogging pump may experience cavitation due to improper selection, harsh operating environments, and poor ability to resist cavitation (Kan et al., 2022). When the temperature remains constant in the hydraulic machinery, a significant drop in internal liquid pressure beyond a critical point leads to the formation of numerous vapor bubbles. These bubbles flow along with the liquid and continuously spread within the passage. Upon reaching the high-pressure region, the bubbles rapidly collapse under the high pressure. This collapse creates voids in the original bubble positions, and the surrounding water rushes in, generating a substantial impact force that damages the impeller and the wall (Siano and Panza, 2018; Rauf et al., 2020; Li et al., 2022; Lang et al., 2023). To prevent pump damage from cavitation, timely recognition and warning of cavitation states are crucial. Kumar et al. (2017) employed various analysis methods to extract feature values and used automated algorithms to adjust the support vector machine penalty factor, enhancing the accuracy of centrifugal pump cavitation recognition. Neill et al. (1997) used acoustic emission sensors to collect data signals from cavitation and normal pump operation, concluding that bubble collapse leads to higher amplitude and frequency in sound signals. Lu et al. (2022) defined a dimensionless parameter of power ratio *r*, which divides the vibration power in 1,200–1,400 Hz by the vibration power in 0–200 Hz, to judge the cavitation occurrence. Pressure pulsation and electrical measurements are methods that can detect the cavitation state, but each has advantages and disadvantages. Currently, researches are mainly focused on acoustic and pressure pulsation methods, which allow relatively convenient and intuitive state recognition using test instruments (Lang et al., 2022). The original test signal collected contains a lot of effective information that cannot be used directly. It is necessary to extract the features of the original signal through signal processing methods. The primary feature extraction methods include time-domain, frequency-domain, and time-frequency-domain methods. Azizi et al. (2017) used a hybrid feature selection technique involving empirical mode decomposition and generalized regression neural network to enhance cavitation recognition accuracy.

The Bat Algorithm (BA) was a metaheuristic algorithm created by Yang in 2010 based on swarm intelligence theory. This algorithm imitates bats in nature to search for prey through echolocation. It has the advantages of simple structure, few parameters, and strong stability. Therefore, it has been widely used in fields such as function optimization and pattern recognition (Yang and He, 2013). Eskandari and Seifaddini (2023) proposed a hybrid binary bat particle swarm optimization algorithm to improve the ability to converge to global optimal solutions. Cui et al. (2019) designed two new variants based on Principal Component Analysis, using the golden section method to determine correlation and generation thresholds, enhancing the effectiveness of a new strategy for bat population to find optimal solutions. Elman neural network, as a typical local regression network, is based on the basic structure of BP network. It adds a continuation layer to the hidden layer as a one-step delay operator to achieve the purpose of memory, thereby enabling the system to adapt to time-varying characteristics and enhancing the global stability of the network. It is commonly used to solve fast optimization problems and is widely used in the field of pattern classification and prediction (Alamgir et al., 2022).

This paper optimizes and improves the traditional bat algorithm to enhance its optimization capability and avoid premature entrapment in local optima. The improved bat algorithm is combined with the Elman neural network to form a cavitation recognition program (ILBA-Elman). Through the optimization of weights and thresholds in the Elman neural network using the improved bat algorithm, the accuracy of the neural network in identifying cavitation data features is improved. The research focuses on a single-blade centrifugal non-clogging pump, conducting cavitation experiments on the test pump and collecting pressure pulsation signals at the volute tongue. The paper analyzes the cavitation characteristics of the test pump, summarizes cavitation patterns, and uses Variational Mode Decomposition (VMD) and Multiscale Dispersion Entropy (MDE) to extract cavitation feature data samples. Finally, ILBA-Elman is applied to diagnose and classify the cavitation state of the test pump, providing a basis for cavitation identification and fault diagnosis during the operation of non-clogging pumps on offshore oil platforms.

2 Bat algorithm and its improvement method

2.1 Basic bat algorithm mechanism

Bats utilize echolocation techniques to communicate with each other, navigate in dark environments, avoid obstacles, and detect the location of prey. A bat colony emits loud sound waves and determines the position of prey by listening to the signals reflected back from surrounding objects (Bajaj et al., 2022). In the process of searching for prey, bats search for the optimal solution by changing the frequency, loudness, and emissivity of sound waves (Yang and Hossein, 2012). The bat sound wave frequency, velocity, and position updating process are represented by Eqs 1–3.

$$f_i = f_{min} + (f_{max} - f_{min}) * rand \tag{1}$$

$$v_i^{t+1} = v_i^t + (x_i^t - x_{best}) * f_i \tag{2}$$

$$x_i^{t+1} = x_i^t + v_i^{t+1} \tag{3}$$

Where f_i represents the bat sound wave frequency, *rand* is a random number in the range of [−1, 1] following a uniform distribution, v_i^t and x_i^t denote the bat individual flight velocity and position, respectively. x_{best} represents the global optimal position of the bat population.

After the global search phase, the algorithm proceeds to the local search phase where bat positions are updated according to Eq. 4.

$$x_i^t = x_{best} + \varepsilon A_{ave} \tag{4}$$

$$r_i^{t+1} = r_i^0 * [1 - exp(-\gamma t)] \tag{5}$$

$$A_i^{t+1} = \alpha A_i^t \tag{6}$$

Where γ and α represent the sound wave emission coefficient and sound wave loudness attenuation coefficient, respectively. Subsequently, the global best solution is updated, and the termination condition is checked. If the specified optimization

accuracy or maximum number of iterations is reached, the optimal solution is outputted.

2.2 Improvement methods for the bat algorithm

The Bat Algorithm is highly effective in solving complex problems. However, like other metaheuristic algorithms, it has some limitations that hinder its success rate in optimization problem-solving. While the initial search mechanism of the Bat Algorithm allows the bat population to quickly and thoroughly search for prey, if the current best solution is not in the vicinity of the global optimum, the algorithm may prematurely converge to a local optimum (Bezdan et al., 2022). Additionally, the local search phase can result in a large number of bats congregating near the current best bat, reducing individual diversity and causing the algorithm to converge prematurely around a local extremum (Deotti et al., 2020).

To overcome these limitations, the Bat Algorithm (BA) is optimized and designed primarily in two aspects. Firstly, the improvement lies in the formulation of the new bat position, which is determined by Eq. 7.

$$\boldsymbol{x_i^{t+1} = x_i^t + (x_{b1}^t - x_{b2}^t)rand + (x_{b3}^t - x_{b4}^t)rand + (x_{b5}^t - x_{b6}^t)rand} \tag{7}$$

Where $x_{b1}{}^t$, $x_{b2}{}^t$, $x_{b3}{}^t$, $x_{b4}{}^t$, $x_{b5}{}^t$, $x_{b6}{}^t$ represent six randomly selected bats from the bat population, i.e., $x_{b1}{}^t \neq x_{b2}{}^t \neq x_{b3}{}^t \neq x_{b4}{}^t \neq x_{b5}{}^t \neq x_{b6}{}^t$. This represents a diversification strategy, and if the newly generated position is better than the current position, the bat position is updated.

Secondly, a series of modifications have been made along the basic logic of the Bat Algorithm. Simplify the update procedure of the bat position, improve the efficiency of the bat approaching the prey effectively by not considering the velocity v in the original bat algorithm, the efficiency of bats effectively approaching prey is enhanced. The new position update is represented by Eq. 8.

$$\boldsymbol{x_i^{t+1} = x_i^t + (x^* - x_i^t)f_i} \tag{8}$$

Where x^* represents the bat current best position, which is the position closest to the prey discovered by the bat population at the moment. This equation, as it disregards the influence of velocity on prey search, may lead to a decrease in diversity and insufficient local search capability in the later stages of the search.

Therefore, to address this limitation, a new mathematical formula based on Lévy flights is introduced. Lévy flight is a type of random walk where the step length is drawn from the Lévy distribution. Due to its variance characteristics, significant displacements can occur in this random walk, and the resulting trajectory often exhibits self-similarity, with long jumps interspersed with shorter jumps at all scales. Many metaheuristic algorithms adopt Lévy flights to escape local optima (Vashishtha and Kumar, 2021). It is a more effective randomization strategy than traditional uniform distribution, and some typical features of Lévy flights have been observed in the flight behaviors of various animals and insects in nature (Campeau et al., 2022). To prevent excessive random step lengths that may reduce search accuracy during the Lévy flight process, the Mantegna method is used to generate random step lengths that follow the Lévy distribution. The position update of Lévy flight is shown in Eq. 9.

$$\boldsymbol{x_i^{t+1} = x_i^t + \partial(x^* - x_i^t) \oplus Lévy(\beta)} \tag{9}$$

Where represents the tensor product, β is the Lévy flight exponent, and it is set to $1 < \beta \leq 3$. ∂ represents the step size control amount. Where $(x^*\text{-}x_i^t)$ approximates the current bat position to the location where the bat population has discovered the best solution and scales the Lévy flight accordingly to an appropriate magnitude for each position dimension. After generating the new position, the bat compares it with its current position rather than the current best position, effectively avoiding the neglect of high-quality solutions.

In practical application, in order to prevent the search accuracy from being too large, the Mantegna method is used to generate a random step that obeys the Lévy distribution. The step size s is realized by Eq. 10.

$$\boldsymbol{s = \frac{u}{|v|^{1/\beta}}} \tag{10}$$

Where u and v are drawn from a normal distribution, i.e., $u \sim N(0, \sigma_u{}^2)$ and $v \sim N(0, \sigma_v{}^2)$. $\sigma_u{}^2$ is generated using Eq. 11.

$$\boldsymbol{\sigma_u = \left\{ \frac{\Gamma(1+\beta)\sin(\pi\beta/2)}{\beta\Gamma\left[(1+\beta)/2^{(\beta-1)/2}\right]} \right\}^{1/\beta}} \tag{11}$$

Where Γ is the gamma function, and $\sigma_u{}^2 = 1$.

The algorithm resulting from all the modifications described above is referred to as the Improved Lévy Flight Bat Algorithm (ILBA), or simply ILBA. ILBA overcomes some of the limitations of the traditional BA. It promotes effective exploration of the search space during the global search phase using Eq. 7 and conducts a local search using Eqs 8, 11, enabling the algorithm to find the optimal solution and allowing the bat population to approach the prey as accurately as possible during the iteration process. As in the final stages of the iteration, bats in the population tend to converge towards each other, both equations ensure sufficient exploration of the search space around the best solution, greatly facilitating the ability of ILBA to escape local optima across different iterations. ILBA retains all the premises adopted by BA and further assumes: 1) Initially, each bat interacts with six other bats in the population to acquire crucial signals as feedback, aiming to approach the prey as quickly as possible. 2) After completing this operation, the current bat continues to approach the bat identified as closest to the prey, eventually being able to perform a Lévy flight around it to be the first to reach the prey.

The basic steps of the ILBA algorithm are as follows:

Step 1: Initialize algorithm parameters and define the evaluation function, define the auxiliary parameter for Lévy flight using Eq. 10.

Step 2: Bat population initialization, calculate the initial fitness value for each individual.

Step 3: Select six bats to interact with the current bat. Generate new solutions using Eq. 7, calculate the fitness of each bat, and identify the best individual.

Step 4: Determine the ultrasonic frequency f_i of each bat based on Eq. 1. Update the flight positions of the bats using Eq. 8. Calculate the fitness of each bat using the evaluation function and identify the best individual.

TABLE 1 Test function information.

Function name	Function number	Function expression	Range	Minimum value
Schwefel's2.2	F1	$f(x) = \sum_{i=1}^{n}\lvert x_i\rvert + \prod_{i=1}^{n}\lvert x_i\rvert$	[−10, 10]	0
Schwefel's1.2	F2	$f(x) = \sum_{i=1}^{n}(\sum_{j-1}^{n} x_j)^2$	[−100, 100]	0
Schwefel's2.21	F3	$f(x) = max_i\{\lvert x\rvert, 1 \le i \le n\}$	[−100, 100]	0
Rosenbrock	F4	$f(x) = \sum_{i=1}^{n-1}[100(x_{i+1} - x_i^2)^2 + (x_i - 1)^2]$	[−30, 30]	0
Noise	F5	$f(x) = \sum_{i=1}^{n} ix_i^4 + random[0, 1)$	[−1.28, 1.28]	0
Rastrigin	F6	$f(x) = \sum_{i=1}^{n}[x_i^2 - 10\cos(2\pi x_i) + 10]$	[−5.12, 5.12]	0
Ackley	F7	$f(x) = -20\exp(-0.2\sqrt{\frac{1}{n}\sum_{i=1}^{n}x_i^2})^2 - \exp(\frac{1}{n}\sum_{i=1}^{n}\cos(2\pi x_i)) + 20 + e$	[−32, 32]	0
Shekel's Foxholes	F8	$f(x) = (\frac{1}{500} + \sum_{j=1}^{25}\frac{1}{j+\sum_{i=1}^{2}(x_i - a_{ij})^6})^{-1}$	[−65, 65]	1

Step 5: Perform local search. If $rand > r_i$, generate a local solution using Lévy flight. Utilize Eqs 9, 11 to search for the best solution, update the flight positions of the bats, calculate the fitness of each bat using the evaluation function, and identify the best individual.

Step 6: Update the local new solution: Generate a random number $rand\_ A^t_i$ for each bat individual *i*. If $rand\_ A_i < A^t_i$ and $f(x_i^t) < f(x_{best})$, accept the new solution.

Step 7: Adjust the pulse emission rate r_i^t and loudness A^t_i of each bat according to Eqs 5, 6.

Step 8: Update the global best solution and check the termination condition.

3 Simulation experiments

3.1 Test functions

To validate the efficiency of the ILBA algorithm, multiple sets of test functions are selected in this study. The information of the test functions is presented in Table 1.

The test functions include single-peak (F1, F2, F3, F4 and F5), multi-modal (F6 and F7), and fixed-dimension multi-modal (F8) benchmark functions, which effectively evaluate the performance of the algorithm. The range in the function information represents the boundaries of the search space, with the minimum value being the optimal solution for the function. The dimension space of the first seven functions is set to 30 dimensions, and the last fixed-dimensional multi-modal benchmark function is set to 2 dimensions, which puts forward higher requirements on the optimization calculation ability of the test algorithm.

Experimental comparisons are conducted between the proposed Improved Lévy Flight Bat Algorithm (ILBA), Bat Algorithm (BA), and Particle Swarm Optimization (PSO). All three algorithms belong to meta-heuristics, among which PSO is a search algorithm that simulates the foraging behavior of birds in groups. During the calculation, the particle swarm algorithm is initialized as a random group of particles, and in each iteration the particles update themselves by tracking two extreme values: one is the optimal solution found by the particle itself, and the other is the optimal solution found by the entire population. PSO, like other evolutionary algorithms, realizes the search for the optimal solution of complex space through cooperation and competition between individuals in the concepts of "population" and "evolution." The software MATLAB R2021b is used for operation programming, and the basic parameters of each algorithm are shown in Table 2.

3.2 Analysis of experimental results

Set the initial population of bats to 30, with 500 iterations. Repeat the experiments 30 times and record the average, maximum, minimum, and standard deviation values, synchronize the three algorithms for testing. The results are presented in Table 3.

From the observations in Table 3, it can be seen that the ILBA algorithm shows significant improvement in convergence accuracy compared to the traditional BA and PSO algorithms. The traditional algorithms perform poorly in higher-dimensional solutions, making it difficult to reach near-optimal values. However, the ILBA algorithm demonstrates better accuracy and is able to overcome these challenges. The PSO algorithm shows higher convergence accuracy compared to the basic BA algorithm, but there is still a certain gap compared to ILBA. The ILBA algorithm consistently outperforms the other two algorithms and achieves better results in various complex function tests. This is due to the improvements in the global search equation and the introduction of Lévy flight

TABLE 2 Algorithm parameter setting.

Algorithm name	Parameter settings	Parameter description
ILBA	$NP = 30$, $A_0 = 1$, $A_{\infty} = 1$, $r_0 = 0$, $r_{\infty} = 1$, $F_{\max} = 1$, $F_{\min} = 0$, $\beta = 1.7$	Experimental Value
BA	$NP = 30$, $\alpha = 0.9$, $F_{\max} = 1$, $F_{\min} = 0$, $\gamma = 0.9$, $r_0 = 0.7$	Reference Value
PSO	$NP = 30$, $w_{\max} = 0.9$, $w_{\min} = 0.2$, $c_1 = 2$, $c_2 = 2$	Reference Value

TABLE 3 Comparison of benchmark function results.

Function	Value	PSO	BA	ILBA
F1	Average Value	1.54E−01	3.31E+01	6.15E−02
	Maximum Value	5.99E−01	1.69E+02	2.53E−01
	Minimum Value	6.47E-03	7.80E+00	1.13E−03
	Standard Deviation	1.50E−01	3.75E+01	7.01E−02
F2	Average Value	7.94E+01	5.11E+01	5.82E−02
	Maximum Value	1.40E+02	8.16E+01	4.10E−01
	Minimum Value	3.15E+01	2.28E+01	1.27E−06
	Standard Deviation	3.56E+01	1.47E+01	9.90E−02
F3	Average Value	1.15E+00	1.17E+01	1.87E−02
	Maximum Value	1.80E+00	2.32E+01	6.36E−02
	Minimum Value	7.81E−01	2.24E+00	6.22E−05
	Standard Deviation	2.23E−01	5.20E+00	1.76E−02
F4	Average Value	1.05E+02	8.78E+02	2.91E+01
	Maximum Value	4.77E+02	1.49E+03	2.94E+01
	Minimum Value	2.66E+01	2.30E+02	2.90E+01
	Standard Deviation	8.54E+01	3.33E+02	1.03E−01
F5	Average Value	1.97E−01	4.22E+01	3.81E−03
	Maximum Value	4.03E−01	5.57E+01	8.84E−03
	Minimum Value	1.01E−01	2.40E+01	7.79E−04
	Standard Deviation	7.13E−02	8.70E+00	2.08E−03
F6	Average Value	5.53E+01	2.79E+02	8.52E−03
	Maximum Value	8.86E+01	3.29E+02	6.63E−02
	Minimum Value	3.17E+01	2.24E+02	6.72E−07
	Standard Deviation	1.33E+01	2.41E+01	1.59E−02
F7	Average Value	3.63E−01	1.02E+01	2.23E−02
	Maximum Value	1.50E+00	1.92E+01	1.09E−01
	Minimum Value	4.00E−03	3.12E+00	1.78E−04
	Standard Deviation	5.65E−01	7.26E+00	2.12E−02
F8	Average Value	3.33E+00	2.93E+00	1.13E+00
	Maximum Value	1.08E+01	1.08E+01	4.95E+00
	Minimum Value	9.98E−01	9.98E−01	9.98E−01
	Standard Deviation	2.33E+00	2.11E+00	7.09E−01

strategy in the ILBA algorithm, enabling better search for the optimal solution.

3.3 Algorithm iteration process analysis

Figure 1 depicts the iteration process of the Particle Swarm Optimization (PSO) algorithm, Bat Algorithm (BA), and Improved Lévy Flight Bat Algorithm (ILBA) under eight different test functions. The left side of each graph shows a three-dimensional view of the test function, while the right side displays the convergence curves of the three algorithms. The *x*-axis represents the number of iterations, and the *y*-axis represents the minimum value reached by the algorithm during the iteration process.

Overall, in different dimensions, the ILBA algorithm has higher accuracy and faster convergence speed than the BA algorithm and the PSO algorithm, and can quickly find the optimal solution in a shorter iteration step. The overall convergence performance of the BA algorithm is the worst, and the accuracy is low, it is easy to fall into the local optimal solution trap prematurely in the process of solving complex functions, resulting in large errors in calculation results. The BA algorithm can be faster than the PSO algorithm in only a small part of the lower convergence accuracy environment. This may be due to the search strategy based on acoustic emissivity and loudness in the early stage of the bat algorithm, which led to bat swarms gathering near the local optimal solution and unable to reach the global optimal solution. Although the PSO algorithm can achieve high convergence accuracy in most cases, its convergence speed is relatively slow, and it cannot converge to a smooth-running stage in time in a limited number of iteration steps. From a specific point of view, as shown in Figures 1A–E, the ILBA algorithm can converge to a higher accuracy under the high-dimensional single-mode benchmark function test; under the high-latitude multi-modal benchmark function test, as shown in Figure 1G, Although the accuracy of the ILBA algorithm and the PSO algorithm is close when the number of convergence steps is high, ILBA can improve the convergence accuracy again soon; Although the three algorithms all stop converging after a short number of steps, the ILBA algorithm obviously achieves higher convergence accuracy. In actual engineering, the efficiency of global optimization is particularly critical. Achieving higher accuracy within a shorter number of iterations is conducive to shortening the calculation cycle and saving computing resources. The ILBA algorithm benefits from the improved global and local search and step size adjustment strategies of the bat algorithm. The bat can quickly jump out of the trap of the local extremum and continue the optimization process, so that the improved bat algorithm can quickly converge in the early stage of iteration.

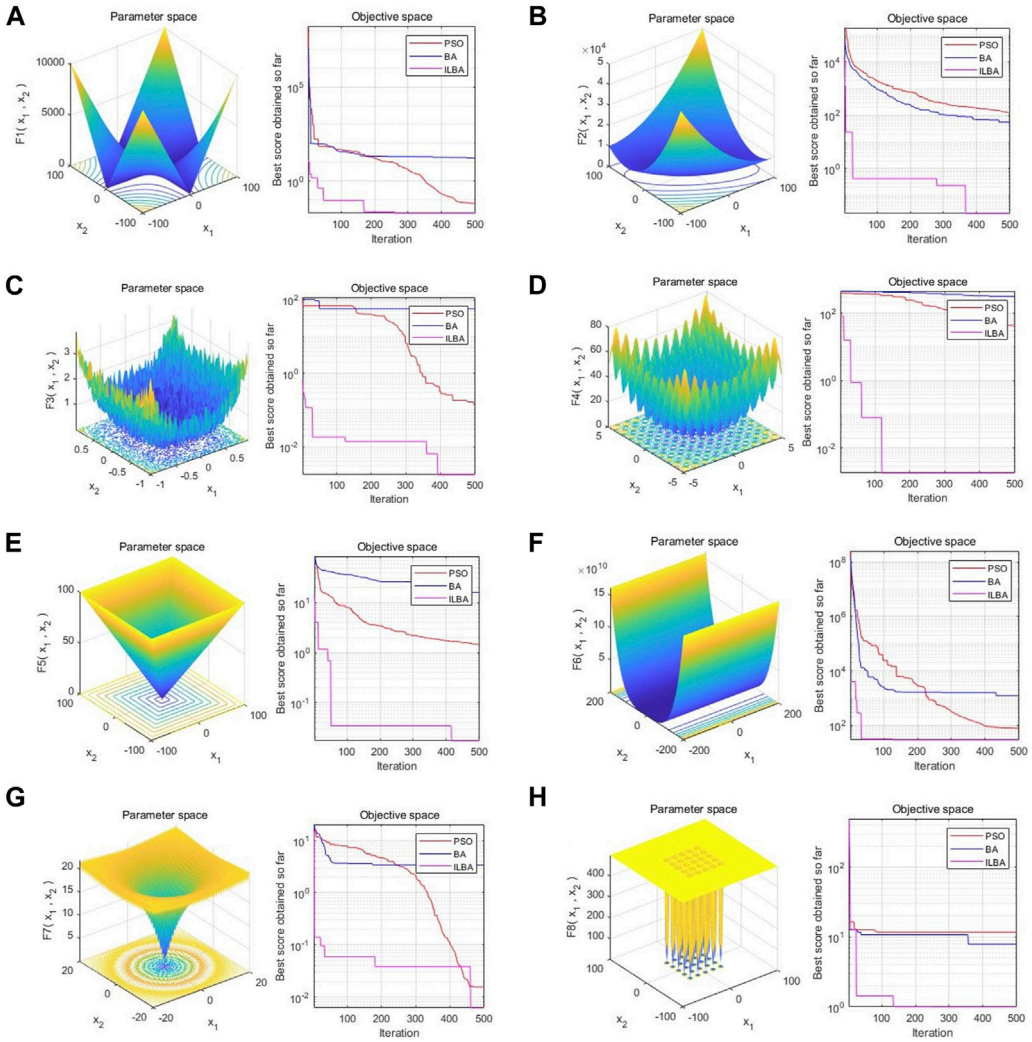

FIGURE 1
Change trend of algorithm iteration. **(A)** F1 Iteration Process. **(B)** F2 Iteration Process. **(C)** F3 Iteration Process. **(D)** F4 Iteration Process. **(E)** F5 Iteration Process. **(F)** F6 Iteration Process. **(G)** F7 Iteration Process. **(H)** F8 Iteration Process.

4 Single-blade non-clogging pump cavitation experiment and data acquisition

4.1 Test equipment and methods

The test pump selected in this paper is a single-blade centrifugal non-clogging pump with a rated power of 2.2 kW. Its main design parameters are: head H_d = 13.8 m, flow Q_d = 20 m^3/h, speed n = 2,940 r/min, specific speed n_s = 132. The non-clogging pump is driven by a three-phase asynchronous motor with a rotation frequency of 49 Hz. The test in this paper was carried out on the closed test bench of the Machinery Industry Drainage and Irrigation Machinery Product Quality Inspection Center (Zhenjiang). The test bench was carried out in accordance with the standard of GB/T 3216-2016 "Hydraulic Performance Acceptance Test of Rotary Power Pump Grade 1, Grade 2 and Grade 3". The precision of the test bench is level 1. The layout diagram of the test bench is shown in Figure 2.

The CYG1102F pressure pulsation sensor is selected for collecting the pressure pulsation signals in the experiment. The sensors V1 and V2 are placed at two different positions in the horizontal direction of the volute casing to collect the pressure pulsation data.

In order to verify the reliability of the test in this paper, three external characteristic tests were carried out on the test pump under different flow conditions. By changing the adjustment mode of the outlet valve, each time at an interval of 0.1 Q_d, record the performance parameters of the experimental pump. Figure 3 shows the external characteristic curve of the test pump under a standard atmospheric pressure. According to the error bar analysis under different working conditions, it can be seen that the minimum error in head and efficiency appears at the rated flow rate (20 m^3/h). The repeatability test results show the stability and reliability of the test equipment and test results.

The sampling frequency in this experiment is set to 24,000 Hz, with a single sampling time of 0.05 s. The experiment is conducted under the rated flow rate of 20 m^3/h

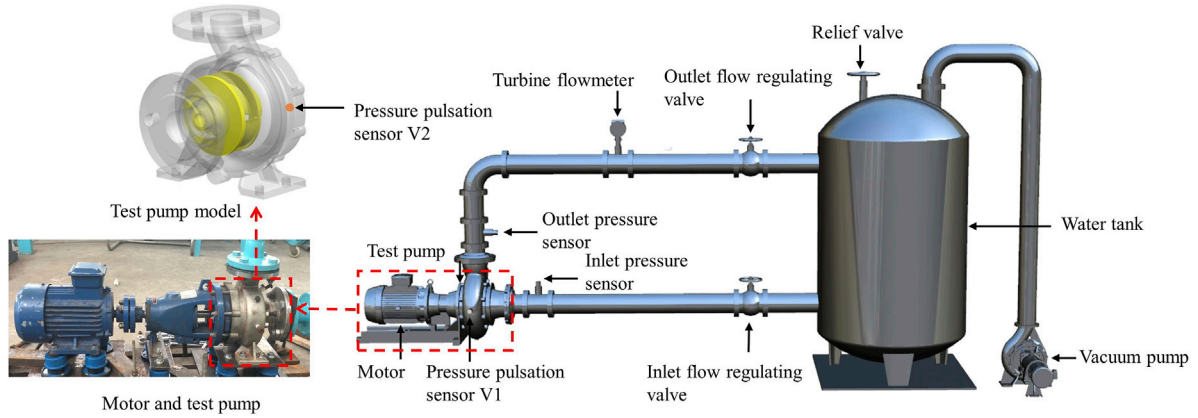

FIGURE 2
Single-blade non-clogging pump closed test stand.

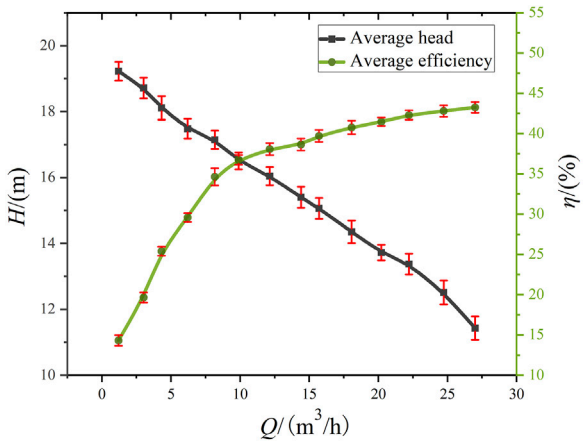

FIGURE 3
Repeatability test.

and the rated rotational speed of 2,940 r/min for the single-blade non-clogging pump. At the beginning of the experiment, the inlet valve is fully open, and the outlet valve is adjusted to stabilize the flow rate at 20 m^3/h. The vacuum pump is then turned on to gradually reduce the inlet pressure and induce cavitation in the pump. To maintain a stable flow rate, the outlet valve is continuously adjusted in real-time until the end of the experiment. Throughout the experiment, the signals of the pump inlet and outlet pressures, flow rate, and volute casing pressure pulsation are synchronously collected.

4.2 Experimental results

The calculation formula for the Net Positive Suction Head Available ($NPSH_a$) in the device is given by:

$$NPSH_a = \frac{p_{in} - p_v}{\rho g} \tag{12}$$

where p_{in} is the pump inlet pressure and p_v is the saturated vapor pressure of water at 25°C, which has a value of 3,469 Pa.

In actual engineering, it is usually considered that the head of the centrifugal pump drops by 3% as the basis for the onset of cavitation (Arendra et al., 2020). In this paper, the cavitation development process is divided into three stages according to the head drop ratio: non-cavitation ($NPSH_a$ = 7.49 m), cavitation inception (head drop 3%, $NPSH_a$ = 1.89 m) and severe cavitation (head drop 6%, $NPSH_a$ = 1.76 m). Carry out cavitation test on the test pump, as the inlet pressure decreases, the head initially remains stable or even shows an increasing trend. However, as the inlet pressure further decreases, the head rapidly drops.

Analyze the collected pressure pulsation signal data. Since the pressure pulsation signal data is huge and the processing is cumbersome, the main variables are dimensionally processed and the pressure pulsation value is converted into the pressure pulsation coefficient C_P. The expression formula is as follows:

$$C_p = \frac{p - \bar{p}}{0.5\rho v^2} \tag{13}$$

Where p is the transient static pressure value, $\bar{p}$ represents the average static pressure value, and v represents the impeller peripheral speed.

Analyze the collected pressure pulsation signal data and use Cmor wavelet transform to compensate for the lack of time axis in conventional Fourier transform, and the time-frequency domain diagram of the pressure fluctuation under different cavitation stages is obtained, as shown in Figure 4, the left and right are the wavelet transform diagrams of the V1 monitoring point and the V2 monitoring point respectively. It can be seen from the figure that when the monitoring point V1 close to the tongue is not in cavitation, since the dynamic and static interference between the blade and the volute tongue is the main cause of the pressure pulsation transformation, the pressure pulsation amplitude signal is mainly concentrated at one times the blade frequency (49 Hz), the amplitude of the secondary main signal is concentrated around double and triple the leaf frequency, and the maximum overall amplitude does not exceed 0.08. With the decrease of the inlet pressure, the periodic cavitation collapse makes the internal flow structure become complicated, and the signal amplitude at high

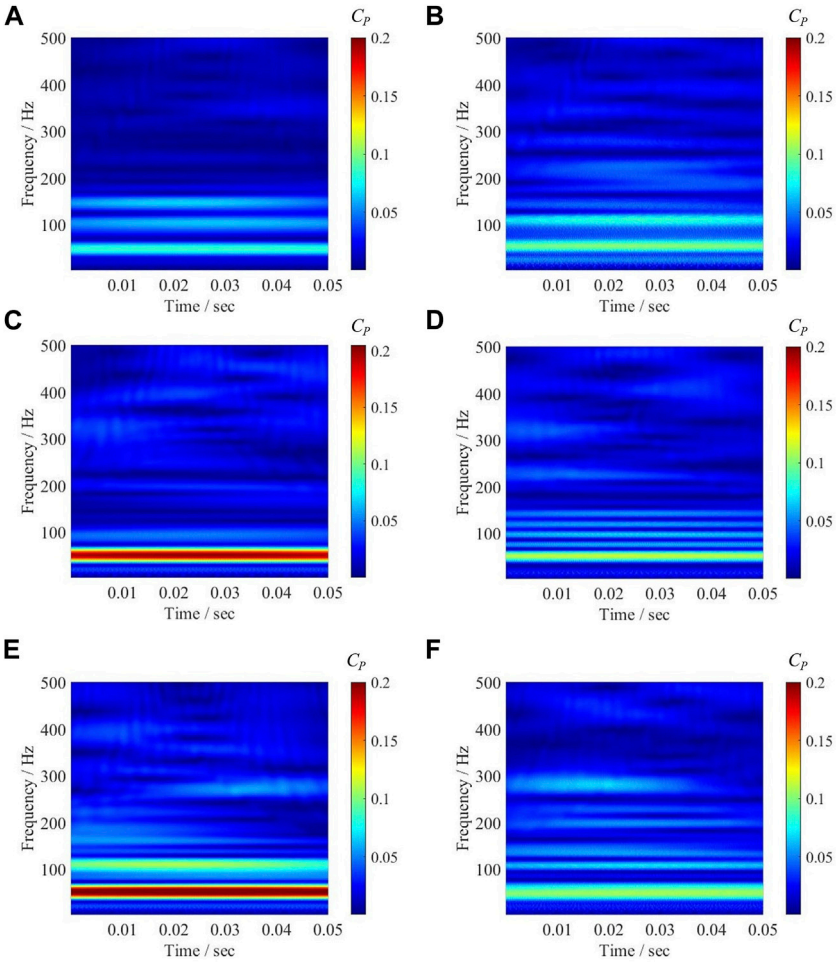

FIGURE 4
Wavelet transform map of pressure pulsation monitoring points. **(A)** V1 Non-cavitation. **(B)** V2 Non-cavitation. **(C)** V1 Cavitation inception. **(D)** V2 Cavitation inception. **(E)** V1 Severe cavitation. **(F)** V2 Severe cavitation.

frequency drops sharply when the cavitation is incipient, and the overall amplitude is concentrated around one times the leaf frequency, and the amplitude ratio is greater than that of the cavitation state has increased significantly, increasing by 0.125. As the cavitation process intensifies, the accumulation of gas in the pump interferes with the continuity of the flow field. In the severe cavitation stage, the overall amplitude is still concentrated at the one-time vane frequency and further increases, and the maximum value is at one-time vane frequency (49 Hz). The amplitude reached 0.2, and at the same time, the amplitude near the second leaf frequency increased compared with the initial stage of cavitation. The amplitude change of the pressure pulsation signal at the monitoring point V2 is not so drastic compared with the monitoring point V1 close to the diaphragm. On the whole, when there is no cavitation, the amplitude of the pressure pulsation signal at V2 is concentrated around the double leaf frequency and double leaf frequency. As the cavitation intensifies, the amplitude of the signal around the double leaf frequency increases. The amplitude and range of the signal amplitude are increasing, and the maximum signal amplitude reaches 0.11 near 49 Hz. The overall transformation law is similar to that of V1, but due to the large flow channel area around the V2 monitoring point, the liquid flow is relatively smooth and the impact is small, and the overall amplitude change is not as obvious as that at V1. The position close to the volute tongue is most strongly affected by the dynamic and static interference between the impeller and the tongue in the test, and it can represent the characteristic signal of the non-clogging pump in the cavitation process, so the monitoring point V1 near the volute tongue is selected. The obtained pressure pulsation signal is further analyzed to extract the representative signal of cavitation characteristics.

5 Numerical simulation of cavitation in a single-blade non-clogging pump

5.1 Meshing and independence verification

The non-clogging pump belongs to the impeller rotating machine, and there are rotating domain and static domain inside. This paper adopts the numerical simulation calculation of the whole flow field, that is, all the liquid flow areas in the pump are calculation domains. UG software is used to model the single-vane test pump in 3D, which is mainly divided into five main parts: impeller, pump

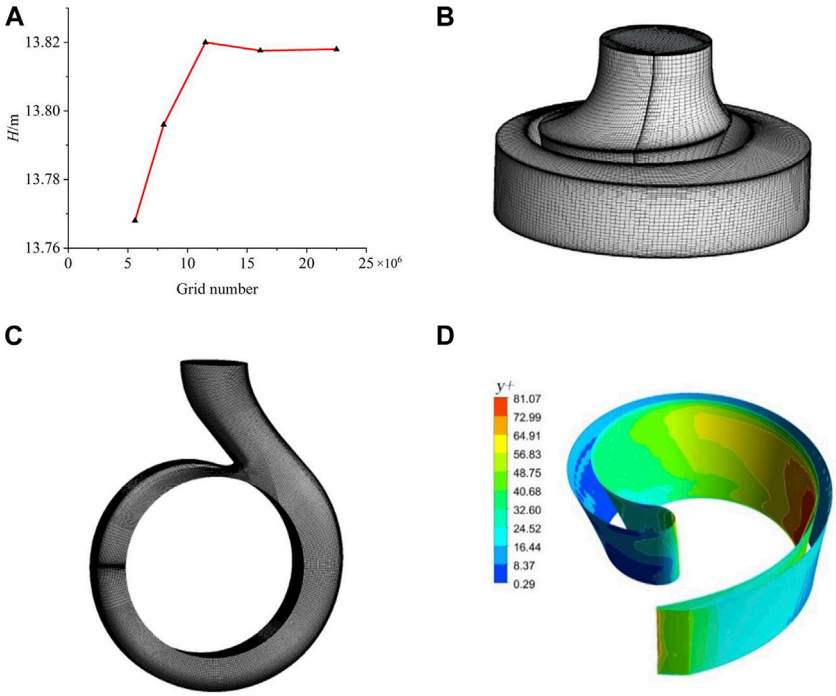

FIGURE 5
Mesh independent verification and water body structure grid. **(A)** Mesh independent verification. **(B)** Impeller. **(C)** Volute. **(D)** Distribution of y^+ on blade surface.

chamber, volute, inlet pipe section and outlet pipe section. The ANSYS ICEM 19.0 software is used to divide the entire numerical calculation model into a hexahedral structured grid. In numerical simulation, the more and denser the grid, the more accurate the calculation structure will be, but this will require too much computing power of the computer and cause a lot of waste of computing resources. Therefore, grid division needs to find a balance between calculation accuracy and efficiency. According to the data in Figure 5A, with the increase of the number of grids, the calculated head of the model pump is stable at about 13.8 m, and the value of the head is getting closer and closer to the head at the rated flow rate. When the number of grids exceeds 11.5×10^6, the head basically tends to be stable. Considering the calculation cost, the number of grids selected for this simulation is 11.5×10^6. The grid numbers of the model pump inlet, outlet, impeller, pump cavity and volute are 2191800, 657900, 2678650, 2938552 and 3043422, respectively. Considering the leakage loss of the mouth ring of the front pump chamber and the disk friction loss of the front and rear pump chambers, all the grids near the wall are encrypted when drawing the grid, so that the global $y+$ is in the range of 0.3~82, which meets the turbulence model calculation requirements. The computational domain grid and blade surface y + are shown in Figures 5B–D.

5.2 Numerical simulation of cavitation

Due to the generation and collapse process of cavitation will affect the turbulent development, resulting in the imbalance between the turbulent kinetic energy generation term and the dispersion term in the cavitation flow during cavitation flow, the SST k-ω turbulent flow model is adopted, which has better accuracy and stability than the standard k-ω model on the near-wall surface (Fu et al., 2020; Mousmoulis et al., 2021). Under the condition of steady state without cavitation, the calculation medium is clear water at 25°C under standard atmospheric pressure, and the solid wall is set as a non-slip wall. Since the impeller and volute are all carbon steel castings, the surface roughness is set as 50 μm. The boundary conditions of the model are set according to the test conditions. The inlet boundary condition is set to the total pressure inlet, the turbulence intensity at the inlet is set to 2%, and the outlet boundary condition is set to the flow outlet. Since the turbulence intensity at the outlet is set to 5%, the reference atmospheric pressure is set to a standard atmospheric pressure of 101.325 kPa. Considering the calculation time and calculation accuracy comprehensively, in the simulation process, the time step is set to 1/ω, equivalent to 0.003248 s, the iteration step is set to 2,000 steps, and the convergence accuracy is 10^{-6}. The solver settings are the same for all the different flow case points.

Figure 6 illustrates a numerical simulation and experimental comparison of the $NPSH_a$ curve, where arrows A and B indicate the points of a 3% and 6% head drop in the pump performance during the cavitation process. The figure also displays three-dimensional schematic representations of the distribution of bubble volumes within the impeller passage at these two distinct cavitation stages in the numerical simulation. The critical $NPSH_a$ obtained by the test and simulation is 1.89 and 1.77 m, respectively, and due to the rougher wall surface of the test and the influence of the leakage of the mouth ring, the head test value corresponding to the critical $NPSH_a$ point is slightly lower than the simulated value. From the point of view of the overall trend of the curve, the variation trend of the

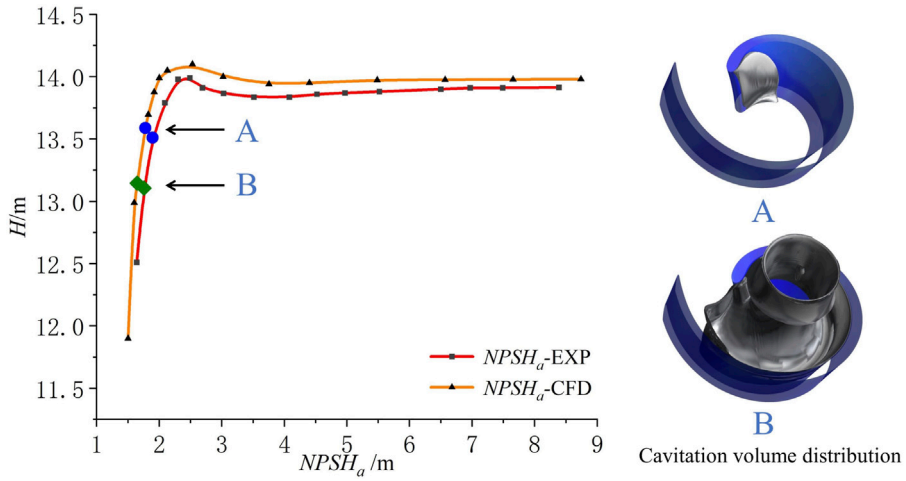

FIGURE 6
$NPSH_a$ curve.

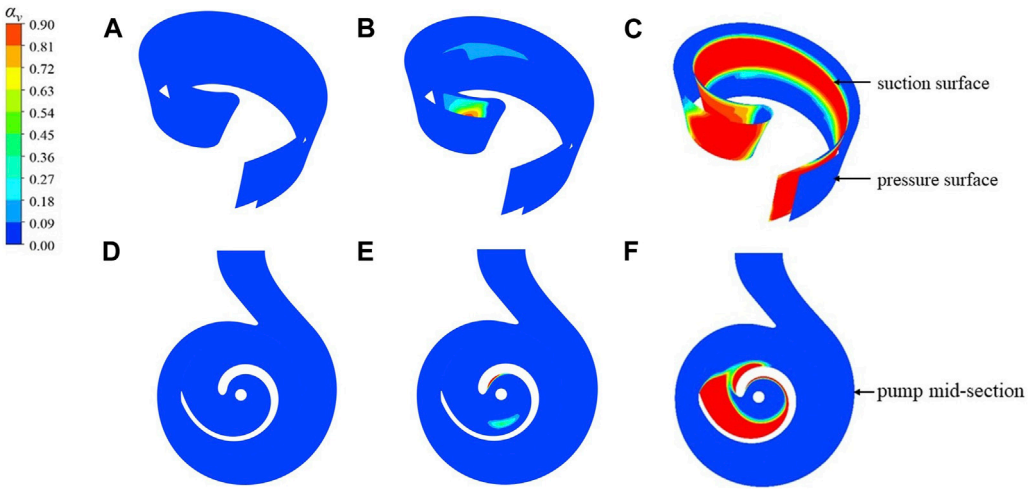

FIGURE 7
Cavitation volume fraction distribution of impeller and pump center section. **(A)** Non-cavitation. **(B)** Cavitation inception. **(C)** Severe cavitation. **(D)** Non-cavitation. **(E)** Cavitation inception. **(F)** Severe cavitation.

simulation and the test is basically consistent, which verifies the accuracy of the numerical calculation. As shown in Figure 7, the cavitation volume fraction distribution of the impeller and the central section of the single-blade non-clogging pump at different stages of cavitation. It can be seen from the figure that in the non-cavitation state, there is no bubble distribution on the central section of the impeller and the pump. When the inlet pressure gradually decreases and the critical cavitation state is reached, bubbles begin to appear near the leading edge of the blade suction surface. Obvious cavitation distribution, the length of the cavitation is continuously extending, and gradually diffuses to the downstream position of the suction surface. When the inlet pressure drops to a certain level and the pump suffers from severe cavitation, the cavitation at the inlet of the vane has been filled with the downstream of the suction surface, and even diffuses along the volute flow path to the pressure surface of the impeller. Due to the particularity of the asymmetry of the single-blade impeller, the cavitation volume distribution gradually develops from the leading edge to the trailing edge along the suction surface, and finally the cavitation blocks the entire impeller flow channel. A large number of cavitation will affect the normal flow of liquid in the pump, hinder the impeller blades from doing work on the fluid in the pump, and cause the pump lift and efficiency to decrease, making it unable to work normally.

6 Validation of cavitation diagnosis model

In this chapter, the cavitation eigenvector is extracted from the pressure pulsation signal near the septum tongue collected in the

TABLE 4 Center frequency under different decomposition levels.

Decomposition layers *k*	Center frequency						
3	0.0035	0.131	0.317				
4	0.0035	0.131	0.2035	0.322			
5	0.0035	0.079	0.133	0.206	0.322		
6	0.0032	0.022	0.131	0.203	0.317	0.35	
7	0.0031	0.021	0.1292	0.147	0.206	0.319	0.362

TABLE 5 Dispersion entropy under different cavitation conditions.

Cavitation state	Dispersion entropy value of each modal component				
	IMF1	IMF2	IMF3	IMF4	IMF5
Non-cavitation	2.040	3.797	4.088	4.232	4.229
Cavitation inception	1.818	2.504	3.180	3.711	4.130
Severe cavitation	1.930	2.469	3.115	3.481	3.989

cavitation test of the single-blade non-clogging pump. Using the feature signal extraction method of Variational Mode Decomposition (VMD) + Multiscale Dispersion Entropy (MDE), the complexity of the time series is measured from multiple angles, and the most representative feature vector in the original signal is extracted as a test ILBA-Elman Dataset for the cavitation recognition program.

6.1 Variational mode decomposition (VMD)

The Variational Mode Decomposition (VMD) is a non-recursive and nearly orthogonal adaptive decomposition method that incorporates the decomposition process of a signal into a variational framework. It aims to find the optimal solution by searching the constrained variational model, thereby achieving the adaptive decomposition of the signal (Kumar et al., 2021). The variational solving constraint model is defined by Eq. 14.

$$\begin{cases} \min\limits_{\{u_k\},\{\omega_k\}} \left\{ \sum\limits_k \left\| \partial_t \left[\left(\delta(t) + \frac{j}{\pi t} \right) * u_k(t) \right] e^{-j\omega_k t} \right\|_2^2 \right\} \\ s.t. \sum\limits_{k=1}^{k} u_k = f(t) \end{cases} \tag{14}$$

Where $\{u_k\} = \{u_1, u_2, \cdots, u_k\}$ represents the k mode components obtained from the decomposition, and $\{\omega_k\} = \{\omega_1, \omega_2, \cdots, \omega_k\}$ represents the central frequencies of each mode component.

When solving constrained variational problems, it is common to introduce the Lagrange function. This is done by utilizing Eq. 15.

$$\begin{aligned} L(\{u_k\},\{\omega_k\},\lambda) = \alpha \sum_{k=1}^{k} \left\| \partial_t \left[\left(\delta(t) + \frac{j}{\pi t} \right) * u_k(t) \right] e^{-j\omega_k t} \right\|_2^2 \\ + \left\| f(t) - \sum_k u_k(t) \right\|_2^2 + \left\langle \lambda(t), f(t) - \sum_k u_k(t) \right\rangle \end{aligned} \tag{15}$$

Where α represents the quadratic penalty operator, $f(t)$ represents the input signal, and $\lambda(t)$ represents the pulse function.

By utilizing the Alternating Direction Method of Multipliers, the saddle point of the Lagrange function can be found. This allows us to obtain the optimal solution to the constrained variational model, resulting in the mode components u_k and central frequencies ω_k, as given by Eqs 16, 17, respectively.

$$\hat{u}_k^{n+1}(\omega) = \frac{\hat{f}(\omega) - \sum_{i \neq k} \hat{u}_i(\omega) + \frac{\hat{\lambda}(\omega)}{2}}{1 + 2\alpha(\omega - \omega_k)^2} \tag{16}$$

$$\omega_k^{n+1} = \frac{\int_0^\infty \omega \left| \hat{u}_k(\omega) \right|^2 d\omega}{\int_0^\infty \left| \hat{u}_k(\omega) \right|^2 d\omega} \tag{17}$$

6.2 Multiscale dispersion entropy (MDE)

Dispersion entropy is an algorithm used to measure the complexity and irregularity of a time series. It calculates the irregularity of a time series based on the sample space dispersion entropy and an adaptive threshold. On the other hand, multiscale dispersion entropy calculates the dispersion entropy at different scales, capturing the dynamic characteristics of the sequence at different time scales. By combining the coarse-grained multiscale dispersion entropy with dispersion entropy, a more comprehensive description of the complexity and regularity of a time series can be achieved. Compared to multiscale sample entropy, multiscale dispersion entropy has advantages in signal feature extraction (Dhandapani et al., 2022). The basic principles of multiscale dispersion entropy are described below.

First, the time series of the initial signal is expressed as: $\{u(i), i = 1, 2, \cdots, L\}$, The sequence is subjected to composite coarse-graining, and the kth coarse-grained sequence under the scale factor τ is

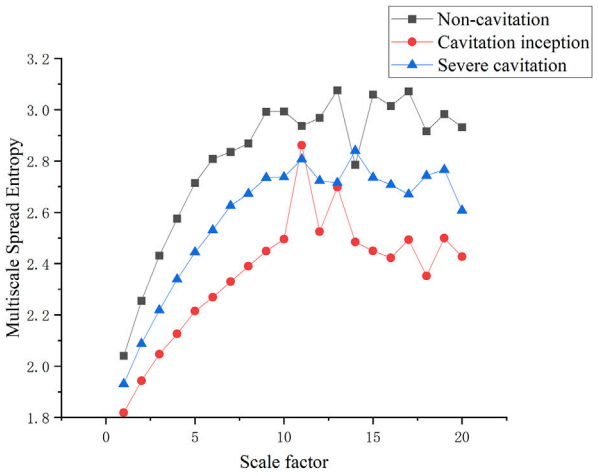

FIGURE 8
MDE feature extraction results.

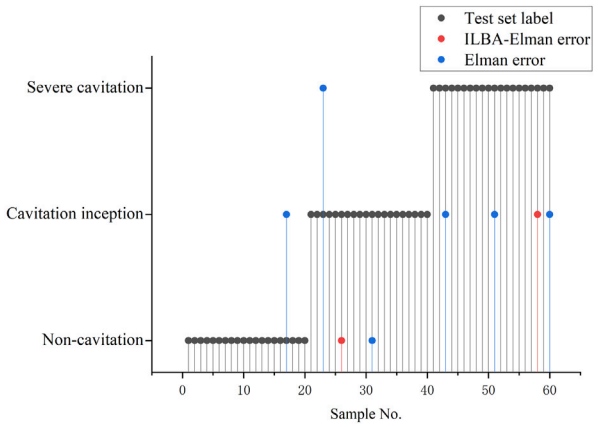

FIGURE 9
Sample test error comparison.

denoted as x_k^t. The calculation formulas for the sequence are given by Eqs 18, 19 as follows.

$$x_{kj}^{(\tau)} = \frac{1}{\tau} \sum_{i=k+(j-1)}^{k+j\tau} u(i), 1 \le j \le L \Big/ \tau, 1 \le k \le \tau \tag{18}$$

$$x_k^{\tau} = \left\{ x_{k,1}^{(\tau)}, x_{k,2}^{(\tau)}, \cdots \right\} \tag{19}$$

Then, for each scale factor τ, the Multiscale Dispersion Entropy (MDE) is defined as shown in Eq. 20.

$$MDE(X, m, c, \tau) = \frac{1}{\tau} \sum_{k=1}^{\tau} DE(x_k^{\tau}, m, c, d) \tag{20}$$

Where X represents the initial time series.

Unlike traditional methods such as multiscale permutation entropy, MDE calculates the coarse-grained sequences for each scale factor τ and computes their dispersion entropy and average. This approach reduces the fluctuations in entropy values caused by increasing values of τ (Minhas et al., 2021).

6.3 Decomposition and feature extraction of pressure pulsation signals

In VMD decomposition, there are two main parameters: the number of modes k and the quadratic penalty factor α. The value of k directly affects the effectiveness of signal decomposition. If k is too large, it will increase computational cost and decrease decomposition efficiency. On the other hand, if k is too small, it may result in mode mixing (González-Cavieres et al., 2021). In this study, α is set to 2000, and the value of k is determined using the center frequency method. Different values of k (3, 4, 5, 6, 7) are chosen, and the central frequencies of each mode component are analyzed, as shown in Table 4. It can be observed that when k is larger than 5, the central frequencies become similar, indicating over-decomposition. Therefore, in this study, $k = 4$ is chosen as the optimal number of mode components. The dispersion entropy of each mode component is computed for $k = 4$, as shown in Table 5. According to the principle of minimum entropy, a smaller entropy value indicates a lower probability of generating new patterns in the decomposed sequences. This implies that the decomposed sequence has fewer frequency components and a lower possibility of mode mixing, resulting in better decomposition performance, it can be seen that IMF1 component is selected as the object for feature extraction.

The Multiscale Dispersion Entropy (MDE) is used to extract features from the optimal mode component IMF1 of the pressure pulsation signals in three different cavitation states. The scale factor is set to 20, and the extraction results are shown in Figure 8.

From Figure 8, it can be observed that as the scale factor increases, the differences in MDE values between different cavitation states become smaller, leading to overlapping and crossing phenomena. If a larger scale factor is chosen to extract feature vectors, it may result in the mixing of feature information, thus affecting the final cavitation diagnosis. On the other hand, when the scale factor is too small, it may not capture sufficient feature information. Therefore, in this study, the MDE values under the first 10 scale factors are selected to construct the feature sample set. Thus, the VMD + MDE method is used to extract cavitation representative features of pressure pulsation signals, decomposing the originally complex and disordered time-domain signals to extract a traceable entropy distribution. By comparing the entropy distribution under different cavitation stages, the recognition and classification of pressure pulsation signals can be achieved, and the entropy distribution can be established as a basic dataset for training the cavitation diagnosis model.

6.4 Model diagnostics

The dataset of 300 samples is randomly divided into a training set and a test set in a 4:1 ratio, with 240 samples used for training and 60 samples used for testing. The three cavitation states in the dataset are labeled as 1, 2, and 3, respectively. The ILBA algorithm is used to optimize the weights and thresholds of the Elman neural network. The ILBA-Elman cavitation diagnostic program is established, and the training set is used to train the model to obtain the best model parameters and optimal network for diagnosing cavitation in the test set. The test results are shown in Figure 9. After training, the neural network achieves a cavitation identification accuracy of 96.67% for the 60 samples in the test set, while the baseline Elman neural network model only achieves a cavitation state identification accuracy of 90% for the test set.

TABLE 6 Comparison of recognition results of three algorithms.

Algorithm model	Average accuracy (%)	Average computing Time/s
ILBA-Elman	96.2	59.8
BA-Elman	90.1	62.4
PSO-Elman	95.8	86.7

To validate the superiority of the proposed ILBA-Elman cavitation diagnosis method, the sample feature data extracted by MDE is inputted into the ILBA-Elman, BA-Elman, and PSO-Elman models for calculation and testing. To ensure the universality of the computational results, the tests are repeated 10 times. The results are shown in Table 6.

From Table 6, it can be observed that all three models demonstrate good performance in terms of classification accuracy. However, the proposed ILBA-Elman model in this paper shows advantages in both computation time and accuracy. Based on this analysis, it can be concluded that the proposed cavitation diagnosis model, which combines VMD with MDE feature extraction and utilizes the improved Lévy flight bat algorithm with Elman neural network, achieves good results in the recognition and classification of cavitation features in non-clogging pumps. It can strike a balance between high classification accuracy and low computation time cost.

7 Conclusion

In order to realize the pattern recognition of the cavitation process of non-clogging pumps, this paper proposes a program for identifying the cavitation characteristics of non-clogging pumps based on the improved Lévy flight bat algorithm. The effectiveness of the proposed method was verified through experiments and the following conclusions were drawn:

1. By making improvements to the conventional bat algorithm, the interaction among initial state bats positions was enhanced, and the Lévy flight was introduced to optimize the bat position update formula. This enhancement has increased the efficiency of bat searching, effectively avoiding local optimal situations.
2. The cavitation tests on a single-blade non-clogging pump are conducted to collect pressure pulsation signals at the volute tongue, and the data is analyzed based on wavelet transform. It was found that the dynamic and static interference between the blades and the spacer tongue is the main cause of pressure pulsations. As cavitation intensifies, the periodic collapse of the bubbles makes the liquid flow in the pump become cluttered. The accumulation of gas interferes with the fluidity of the flow field, leading to an increase in the amplitude of the high-frequency part. The distribution of vapor volume in the impeller channel under cavitation condition was analyzed through numerical simulation, and the accuracy of the experiment was verified by comparing it with experimental data.
3. By employing Variational Mode Decomposition and Multiscale Dispersion Entropy to extract feature vectors, interference signals were effectively suppressed. This approach assessed the complexity of time series from multiple perspectives. The complex and disordered pressure pulsation time domain signal is transformed into a traceable entropy distribution, which improves the accuracy of cavitation recognition.
4. The ILBA-Elman cavitation recognition program was trained and subsequently tested for cavitation data identification and diagnosis in single-blade non-clogging pumps. The BA-Elman and PSO-Elman models were tested for comparison. The results revealed that the ILBA-Elman model outperformed the other models in terms of accuracy and timeliness in identifying the cavitation development stages in non-clogging pumps. The improved Bat Algorithm helps the Elman neural network to identify the cavitation feature information more accurately.

Data availability statement

The data analyzed in this study is subject to the following licenses/restrictions: Due to laboratory policies and confidentiality agreements, raw data cannot be provided. Requests to access these datasets should be directed to CN, 997694655@qq.com.

Author contributions

TL: Writing–original draft, Conceptualization, Methodology. CN: Data curation, Writing–original draft. KC: Investigation, Writing–review and editing. EX: Data curation, Writing–review and editing. JY: Methodology, Writing–review and editing. XS: Validation, Writing–review and editing. XW: Data curation, Writing–review and editing. DZ: Conceptualization, Visualization, Writing–review and editing.

Funding

The authors declare financial support was received for the research, authorship, and/or publication of this article. This research was funded by Key Program of the Joint Fund of the National Natural Science Foundation of China, grant number U2106225; Jiangsu Province Outstanding Youth Fund, grant number BK20211547; 2021 Jiangsu Province Excellent Science and Technology Innovation Team Project, grant number SKJ (2021) -1.

Conflict of interest

The authors declare that the research was conducted in the absence of any commercial or financial relationships that could be construed as a potential conflict of interest.

Publisher's note

References

Alamgir, F. M., and Alam, M. S. (2022). A novel deep learning-based bidirectional elman neural network for facial emotion recognition. *Int. J. Pattern. Recogn.* 36 (10), 2252016. doi:10.1142/S0218001422520164

Arendra, A., Akhmad, S., Winarso, K., and Herianto. (2020). Investigating pump cavitation based on audio sound signature recognition using artificial neural network. *J. Phys. Conf. Ser.* 1569 (3), 032044. doi:10.1088/1742-6596/1569/3/032044

Azizi, R., Attaran, B., Hajnayeb, A., Ghanbarzadeh, A., and Changizian, M. (2017). Improving accuracy of cavitation severity detection in centrifugal pumps using a hybrid feature selection technique. *Measurement* 108, 9–17. doi:10.1016/j.measurement.2017.05.020

Bajaj, A., Sangwan, O. P., and Abraham, A. (2022). Improved novel bat algorithm for test case prioritization and minimization. *Soft Comput.* 26 (22), 12393–12419. doi:10.1007/S00500-022-07121-9

Bezdan, T., Zivkovic, M., Bacanin, N., Strumberger, I., Tuba, E., and Tuba, M. (2022). Multi-objective task scheduling in cloud computing environment by hybridized bat algorithm. *J. Intell. Fuzzy. Syst.* 42 (1), 411–423. doi:10.3233/JIFS-219200

Campeau, W., Simons, A. M., and Stevens, B. (2022). The evolutionary maintenance of Lévy flight foraging. *Plos. Comput. Biol.* 18 (1), e1009490. doi:10.1371/JOURNAL.PCBI.1009490

Cui, Z., Li, F., and Zhang, W. (2019). Bat algorithm with principal component analysis. *Int. J. Mach. Learn. Cyb.* 10, 603–622. doi:10.1007/s13042-018-0888-4

Deotti, L. M. P., Pereira, J. L. R., and da Silva Junior, I. C. (2020). Parameter extraction of photovoltaic models using an enhanced Lévy flight bat algorithm. *Energy Convers. manage.* 221, 113114. doi:10.1016/j.enconman.2020.113114

Dhandapani, R., Mitiche, I., McMeekin, S., and Morison, G. (2022). A novel bearing faults detection method using generalized Gaussian distribution refined composite multiscale dispersion entropy. *Ieee. Trans. Instrum. Meas.* 71, 1–12. doi:10.1109/TIM.2022.3187717

Eskandari, S., and Seifaddini, M. (2023). Online and offline streaming feature selection methods with bat algorithm for redundancy analysis. *Pattern Recogn.* 133, 109007. doi:10.1016/j.patcog.2022.109007

Fu, X., Li, D., Wang, H., Zhang, G., Li, Z., and Wei, X. (2020). Numerical simulation of the transient flow in a pump-turbine during the load rejection process with special emphasis on the cavitation effect. *J. Fluids Eng.* 142 (1), 011103. doi:10.1115/1.4044479

González-Cavieres, L., Perez-Won, M., Tabilo-Munizaga, G., Jara-Quijada, E., Díaz-Álvarez, R., and Lemus-Mondaca, R. (2021). Advances in vacuum microwave drying (VMD) systems for food products. *Trends. Food. Sci. Tech.* 116, 626–638. doi:10.1016/J.TIFS.2021.08.005

Kan, K., Binama, M., Chen, H., Zheng, Y., Zhou, D., Su, W., et al.(2022). Pump as turbine cavitation performance for both conventional and reverse operating modes: a review. *Renew. Sust. Energy Rev.* 168, 112786. doi:10.1016/j.rser.2022.112786

Kumar, A., Gandhi, C. P., Vashishtha, G., Kundu, P., Tang, H., Glowacz, A., et al.(2021). VMD based trigonometric entropy measure: a simple and effective tool for dynamic degradation monitoring of rolling element bearing. *Meas. Sci. Technol.* 33 (1), 014005. doi:10.1088/1361-6501/ac2fe8

Kumar, A., and Kumar, R. (2017). Time-frequency analysis and support vector machine in automatic detection of defect from vibration signal of centrifugal pump. *Measurement* 108, 119–133. doi:10.1016/j.measurement.2017.04.041

Lang, T., Jin, L., Liu, Y., Chen, K., and Xu, E. (2022). Numerical analysis of hydrodynamic noise characteristics of single-blade centrifugal pump. *J. Drain. Irrig. Mach. Eng.* 40 (6), 541–548. doi:10.3969/j.issn.1674-8530.20.0358

Lang, T., Sun, Z., Jin, L., Chen, K., and Xu, X. (2023). Characteristics of cavitation-induced noise in single-blade centrifugal pump. *J. Drain. Irrig. Mach. Eng.* 41 (9), 873–880. doi:10.3969/j.issn.1674-8530.22.0025

Li, G., Ding, X., Wu, Y., Wang, S., Li, D., Yu, W., et al.(2022). Liquid-vapor two-phase flow in centrifugal pump: cavitation, mass transfer, and impeller structure optimization. *Vacuum* 201, 111102. doi:10.1016/j.vacuum.2022.111102

Li, H., Huang, Q., Li, S., Li, Y., Fu, Q., and Zhu, R. (2023). Study on flow characteristics of a single blade breakage fault in a centrifugal pump. *Processes* 11 (9), 2695. doi:10.3390/PR11092695

Lu, Y., Tan, L., Han, Y., and Liu, M. (2022). Cavitation-vibration correlation of a mixed flow pump under steady state and fast start-up conditions by experiment. *Ocean. Eng.* 251, 111158. doi:10.1016/J.OCEANENG.2022.111158

Minhas, A. S., Kankar, P. K., Kumar, N., and Singh, S. (2021). Bearing fault detection and recognition methodology based on weighted multiscale entropy approach. *Mech. Syst. Signal P. R.* 147, 107073. doi:10.1016/j.ymssp.2020.107073

Mousmoulis, G., Kassanos, I., Aggidis, G., and Anagnostopoulos, I. (2021). Numerical simulation of the performance of a centrifugal pump with a semi-open impeller under normal and cavitating conditions. *Appl. Math. Model* 89, 1814–1834. doi:10.1016/j.apm.2020.08.074

Neill, G. D., Reuben, R. L., Sandford, P. M., Brown, E. R., and Steel, J. A. (1997). Detection of incipient cavitation in pumps using acoustic emission. *P. I. Mech. Eng. E-J Pro.* 211 (4), 267–277. doi:10.1243/0954408971529737

Noon, A. A., Jabbar, A. U., Koten, H., Kim, M. H., Ahmed, H. W., Mueed, U., et al.(2021). Strive to reduce slurry erosion and cavitation in pumps through flow modifications, design optimization and some other techniques: long term impact on process industry. *Materials* 14 (3), 521. doi:10.3390/MA14030521

Quan, H., Li, Y., Kang, L., Yu, X., Song, K., and Wu, Y. (2021). Influence of blade type on the flow structure of a vortex pump for solid-liquid two-phase flow. *Machines* 9 (12), 353. doi:10.3390/machines9120353

Rauf, H. T., Malik, S., Shoaib, U., Irfan, M. N., and Lali, M. I. (2020). Adaptive inertia weight Bat algorithm with Sugeno-Function fuzzy search. *J. Comput. Appl. Soft.* 90, 106159. doi:10.1016/j.asoc.2020.106159

Siano, D., and Panza, M. A. (2018). Diagnostic method by using vibration analysis for pump fault detection. *Energy Procedia* 148, 10–17. doi:10.1016/j.egypro.2018.08.013

Vashishtha, G., and Kumar, R. (2021). An effective health indicator for the Pelton wheel using a Levy flight mutated genetic algorithm. *Meas. Sci. Technol.* 32 (9), 094003. doi:10.1088/1361-6501/abeea7

Yang, X. S., and He, X. (2013). Bat algorithm: literature review and applications. *Int. J. Bio-Inspir.* 5 (3), 141–149. doi:10.1504/IJBIC.2013.055093

Yang, X. S., and Hossein Gandomi, A. (2012). Bat algorithm: a novel approach for global engineering optimization. *Eng. Comput.* 29 (5), 464–483. doi:10.1108/02644401211235834

Nomenclature

BA	Bat Algorithm
ILBA	Improved Lévy Flight Bat Algorithm
VMD	Variational Mode Decomposition
MDE	Multi-scale Dispersion Entropy
PSO	Particle Swarm Optimization
SST *k-ω*	Shear stress transport *k-ω* turbulence model
CFD	Computational fluid dynamics
f_i	Bat individual sound frequency
v_i^t	Bat individual flight velocity
x_i^t	Bat individual flight position
x_{best}	Global optimal position of the bat population
ε	A random number in the range of [−1, 1]
r_i^t	Sound wave emission rate
A_i^t	Loudness of the sound waves
γ	Sound wave emission coefficient
α	Loudness of the sound waves
s	Random step size following the Lévy distribution
$\oplus$	The tensor product
β	Lévy flight exponent
∂	Step size control amount
Γ	Gamma function
NP	Number of bat populations
w	Inertia weight
c	Learning factor
H_d	Design head
Q_d	Design flow rate
n	Design speed
n_s	Specific speed
E	Comprehensive uncertainty
E_R	Random uncertainty
E_S	System uncertainty
$NPSH_a$	Net positive suction head available
C_P	Pressure pulsation coefficient
α	Quadratic penalty operator
$f(t)$	Input signal
$\lambda(t)$	Pulse function
ω_k	Central frequencies
τ	Scale factor
k	The number of modes

frontiers | Frontiers in Energy Research

TYPE Original Research
PUBLISHED 29 December 2023
DOI 10.3389/fenrg.2023.1342712

OPEN ACCESS

EDITED BY
Yang Yang,
Yangzhou University, China

REVIEWED BY
Hao Liang,
Beijing Institute of Technology, China
Xun Sun,
Shandong University, China

*CORRESPONDENCE
Fadong Gu,
211911004@stmail.ujs.edu.cn

RECEIVED 22 November 2023
ACCEPTED 11 December 2023
PUBLISHED 29 December 2023

CITATION
Zhang G, Yang X, Li Y, Ge M and Gu F (2023), Numerical investigation of energy loss distribution in the cavitating wake flow around a cylinder using entropy production method.
Front. Energy Res. 11:1342712.
doi: 10.3389/fenrg.2023.1342712

Numerical investigation of energy loss distribution in the cavitating wake flow around a cylinder using entropy production method

Guangjian Zhang[1,2], Xiufei Yang[1], Yan Li[1], Mingming Ge[3] and Fadong Gu[1]*

[1]Research Center of Fluid Machinery Engineering and Technology, Jiangsu University, Zhenjiang, China, [2]Wenling Fluid Machinery Technology Institute of Jiangsu University, Wenling, China, [3]Lab of AI for Fluids, Westlake University, Hangzhou, China

The wake flow of a circular cylinder is numerically investigated by Large Eddy Simulation (LES) combined with the Schnerr–Sauer cavitation model. By comparing entropy production in the presence or absence of cavitation, the energy loss distribution in the wake flow field of a cylinder is explored, shedding light on the interactions between multiscale vortex systems and cavitation. The comparative results reveal that, under non-cavitating conditions, the energy loss region in the near-wake area is more concentrated and relatively larger. Energy dissipation in the wake flow field occurs in regions characterized by very high velocity gradients, primarily near the upper and lower surfaces of the cylinder near the leading edge. The influence of cavitation bubbles on entropy production is predominantly observed in the trailing-edge region (W1) and the near-wake region (W2). The distribution trends of wall entropy production on the cylinder's surface are generally consistent in both conditions, with wall entropy production primarily concentrated in regions exhibiting high velocity gradients.

KEYWORDS

cavitation, energy loss, entropy production, cylinder wake, vortex

1 Introduction

Cavitation is a phase transition process and a phenomenon that manifests in liquids due to fluid dynamic factors, occurring either within the liquid or at the liquid-solid interface (Arndt, 2012; Prosperetti, 2017; Tian et al., 2023). This process induces fluctuations in fluid pressure within the flow field (Lei et al., 2017; Lei et al., 2018), leading to an uneven distribution of surface loads on flow components (Sun et al., 2021) and the generation of hydrodynamic noise (Fry, 1984). In severe instances, cavitation can result in damage to flow components (Hutli et al., 2019; Sun et al., 2023), thereby impacting the operational stability of hydraulic machinery. Therefore, the operation and design of hydraulic machinery are influenced and constrained by cavitation, such as pumps (Li et al., 2018; Al-Obaidi, 2020; Li et al., 2021) and turbines (Khare and Prasad, 2021; Amromin, 2022; Sun et al., 2022). Hence, the research significance lies in the investigation of the distribution of energy loss induced by cavitation in the wake flow around a cylinder.

In the investigation of the wake flow around a cylinder, observations of cavitation bubble occurrences in the wake of a cylindrical body were conducted by Saito and Sato, (2003), utilizing static and high-speed cameras. The mechanisms of cavitation pulsation and

scouring were explored from diverse perspectives, revealing that Karman vortex cavities, detaching downstream of the cylindrical body, can be segmented into distinct components. A pioneering and in-depth analysis of cavitation flow structures in the shear layer and wake of a cylindrical body was carried out by Kumar et al. (2017), employing high-speed photography. The findings concluded that cavities primarily originate in the free shear layer, displaying significant variations in cavitation activity span. Wang et al. (2021) studied the ventilated cavitating flow of a circular cylinder through numerical simulation. The simulation results indicate that the bubble size distribution in the wake is closely related to the turbulence intensity. Observations by Ghahramani et al. (2020), through experiments and numerical simulations, revealed that at high cavitation numbers, vortices detach cyclically, while at very low cavitation numbers, large stationary cavities form in the wake region. A transitional state is evident during the detachment process for moderate cavitation numbers. Cavitation flow on a cylindrical body under laminar (Reynolds number Re = 200) and turbulent (Re = 3,900) conditions within the cavitation number range (σ = 5 to 0.5) was investigated by Brandao et al. (2020). The study observed a transition from non-cavitation to cyclic and transitional cavitation states as the free-stream cavitation number decreased.

In the evolutionary dynamics of multiscale vortex systems within the wake flow field and their interactive processes with cavitation, a consistent manifestation of energy conversion is observed, contributing significantly to the intricacy of the vortex-cavitation flow field. To grasp the characteristics of the vortex-cavitation flow field and unveil the interactions between multiscale vortex systems and cavitation, a comprehensive understanding of energy distribution in the flow field is essential. Traditionally, the evaluation of total pressure loss obtained from Computational Fluid Dynamics (CFD) has been employed by many researchers to associate energy loss. However, this approach does not accurately pinpoint the precise locations of the losses. The reasons behind the reduction in available energy and the resulting entropy production during heat transfer and fluid flow processes were investigated by Bejan, (1996). Unsteady computations of entropy production rates within the laminar boundary layer in the wall region were conducted by Walsh and Hernon, (2006). Denton, (1993) proposed that entropy production serves as an effective means to explain energy losses in hydraulic machinery. This is attributed to the fact that specific entropy in-creases during the most authentic and irreversible adiabatic processes in hydraulic machinery, significantly contributing to energy losses (Zhang et al., 2020). A numerical model for estimating wall roughness based on entropy loss theory was proposed by Herwig et al. (2008), demonstrating the applicability of entropy production methods to both laminar and turbulent flows. Due to the unavailability of transient fluctuation variables in Computational Fluid Dynamics (CFD) computations, an enhanced model based on entropy production theory to assess entropy losses generated directly by dissipation was proposed by Herwig and Kock, (2007). Wang et al. (2020), building upon the previous cavitation entropy production diagnostic model, further considers the influence of mass transfer and slip velocity. Additional terms introduced include interfacial entropy and diffusion entropy in comparison to previous entropy production terms.

Utilizing the Large Eddy Simulation (LES) turbulent model and entropy production theory, numerical simulations and calculations of entropy production are con-ducted on the wake flow of a cylinder in this paper. Through a comparison of entropy production with and without cavitation models, the investigation delves into the energy distribution of cavitation phenomena in the wake flow field of a cylinder. Furthermore, the study explores the characteristics of the cavitation flow field and elucidates the interactions between multiscale vortex systems and cavitation. The objective of this approach is to attain a more profound comprehension of the mechanisms governing cavitation transformation.

2 Methodology

2.1 Governing equations

The cavitating flow involves liquid and vapor phases. In this work, the homogeneous mixture model was adopted, assuming the multiphase fluid components share the same velocity and pressure. The mass and momentum conservation equations for the mixture flow are shown as follows:

$$\frac{\partial \rho_m}{\partial t} + \frac{\partial \left(\rho_m u_j\right)}{\partial x_j} = 0 \tag{1}$$

$$\frac{\partial \left(\rho_m u_i\right)}{\partial t} + \frac{\partial \left(\rho_m u_i u_j\right)}{\partial x_j} = -\frac{\partial p}{\partial x_i} + \frac{\partial}{\partial x_j}\left[\mu_m\left(\frac{\partial u_i}{\partial x_j} + \frac{\partial u_j}{\partial x_i} - \frac{2}{3}\frac{\partial u_k}{\partial x_k}\delta_{ij}\right)\right] \tag{2}$$

$$\rho_m = \rho_v \alpha_v + \rho_l\left(1 - \alpha_v\right) \tag{3}$$

$$\mu_m = \mu_v \alpha_v + \mu_l\left(1 - \alpha_v\right) \tag{4}$$

where u_i represents the velocity in the i direction; p is the pressure; ρ_m and μ_m represent the mixture density and dynamic viscosity respectively; the subscripts l and v denote the water and vapor phases respectively; α_v is the vapor volume fraction.

Solving the above unsteady Navier-Stokes equations directly raises an excessive demand on computing resources, which makes it impossible to be implemented in practical applications. Although Reynolds-Averaged Navier-Stokes (RANS) methods need reasonable computational cost, they fail in the situations dominated by coherent large-scale anisotropic vortical structures. Aiming at better simulating at an affordable cost, the LES approach was used, carrying out filtering in a small-space area, and dividing the turbulent flow into large-scale motion and small-scale motion. The large-scale motion is solved directly while the small-scale motion is modelled using the Smagorinsky-Lilly subgrid-scale model.

2.2 Cavitation model

The mass transfer between the vapor and liquid phases in cavitating flows is depicted using the following governing equation:

$$\frac{\partial}{\partial t}\left(\rho_v \alpha_v\right) + \frac{\partial}{\partial x_j}\left(\rho_v \alpha_v u_j\right) = m_e - m_c \tag{5}$$

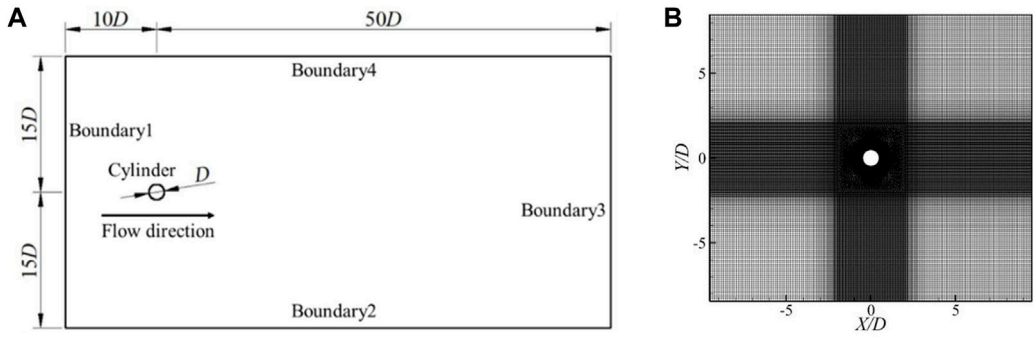

FIGURE 1
Computational model: **(A)** computational domain, **(B)** local grids.

The source terms m_e and m_c represent the evaporation and condensation rates during the phase change. The source terms have different expressions. In the present study, the Schnerr–Sauer cavitation model is used, expressed as,

$$m_e = \frac{3\rho_v\rho_l}{\rho_m}\frac{\alpha_v(1-\alpha_v)}{R_B}\sqrt{\frac{2|p_v-p|}{3\rho_l}},\ (p \le p_v) \tag{6}$$

$$m_c = \frac{3\rho_v\rho_l}{\rho_m}\frac{\alpha_v(1-\alpha_v)}{R_B}\sqrt{\frac{2|P-P_v|}{3\rho_l}},\ (p > p_v) \tag{7}$$

where p_v is the saturated vapor pressure; R_B is the nucleus radius, expressed as $R_B = ((\alpha_v/(1-\alpha_v))(3/4\pi n))^{1/3}$, where n is the given empirical constant and the default value is $n = 1 \times 10^{13}$ (Schnerr et al., 2001).

2.3 Numerical setup

The computational model is shown in Figure 1. The cylinder diameter D is 9.5 mm, and the two-dimensional computational domain is 60D × 30D with an upstream dimension 10D and a downstream dimension 50D. The computational domain is discretized using structured grids, and the grids in the cylinder surface and wake region are locally refined. The total number of elements is about 336,000 and the average wall y + value is less than 4.6.

Boundary 1 of the computational domain is set as a velocity inlet with a value $V_\infty = 1$ m/s, and the corresponding Reynolds number is $Re = 9{,}500$. Boundary 3 is set as a pressure outlet, and the value p_∞ is set according to the cavitation number, defined as $\sigma = (p_\infty - p_v)/(0.5\rho_l V_\infty^2)$. A no-slip boundary condition is imposed on the cylinder surface and the free slip condition on the up and down walls (Boundary 4 and Boundary 2). The solution method adopts pressure base solver and a coupled pressure–velocity coupling algorithm. The pressure dispersion mode is second-order discrete mode, and the momentum equation is discrete by finite central difference scheme. The transient scheme is a second-order backward Euler algorithm. The time step is set to 5×10^{-5} s such that the courant number does not exceed 1.0 in the computations. The convergence standard of all residuals is 10^{-6}. The validation of the present numerical simulation can be found in our previous work (Gu et al., 2021). It should be mentioned that in the following analyses, all parameters shown in the figures are nondimensionalized via the cylinder diameter and the inlet velocity.

2.4 Entropy production method

Entropy production arises from irreversible processes, during which the conversion of mechanical energy into internal energy occurs, resulting in energy dissipation. Entropy, as a state parameter, is governed by an equilibrium equation in a single-phase, incompressible flow, which can be expressed as:

$$\rho\left(\frac{\partial s}{\partial t} + u\frac{\partial s}{\partial t} + v\frac{\partial s}{\partial t} + w\frac{\partial s}{\partial t}\right) = div\left(\frac{q}{T}\right) + \frac{\Phi}{T} + \frac{\Phi_\Theta}{T^2} \tag{8}$$

Kock and Herwig, (2004) proposed that the Reynolds-averaged process can be dissected into two components, namely the averaged and fluctuating components. By extending the traditional Reynolds-averaged process, they formulated the entropy balance equation as follows,

$$\rho\left(\frac{\partial \bar{s}}{\partial t} + \bar{u}\frac{\partial \bar{s}}{\partial t} + \bar{v}\frac{\partial \bar{s}}{\partial t} + \bar{w}\frac{\partial \bar{s}}{\partial t}\right) = \overline{div\left(\frac{\vec{q}}{T}\right)} - \rho\left(\overline{\frac{\partial u's'}{\partial x}} + \overline{\frac{\partial u's'}{\partial y}} + \overline{\frac{\partial u's'}{\partial z}}\right) + \frac{\Phi}{T} + \frac{\Phi_\Theta}{T^2} \tag{9}$$

In the equation, $\frac{\Phi}{T}$ and $\frac{\Phi_\Theta}{T^2}$ represent entropy production. The first term signifies entropy production due to dissipation in the flow process, while the second term accounts for entropy production related to heat transfer during the heat transfer process.

Given the negligible temperature change in the examined cylindrical flow phenomenon, this study excludes the consideration of entropy production during heat transfer. The direct solution method is utilized to compute the entropy production $\frac{\Phi}{T}$ during turbulent flow in this paper, incorporating viscous dissipation $S_{\mathrm{pro},\bar{D}}$ and turbulent dissipation $S_{\mathrm{pro},D'}$ resulting from velocity fluctuations. The formula for the local entropy production rate per unit volume is presented as follows:

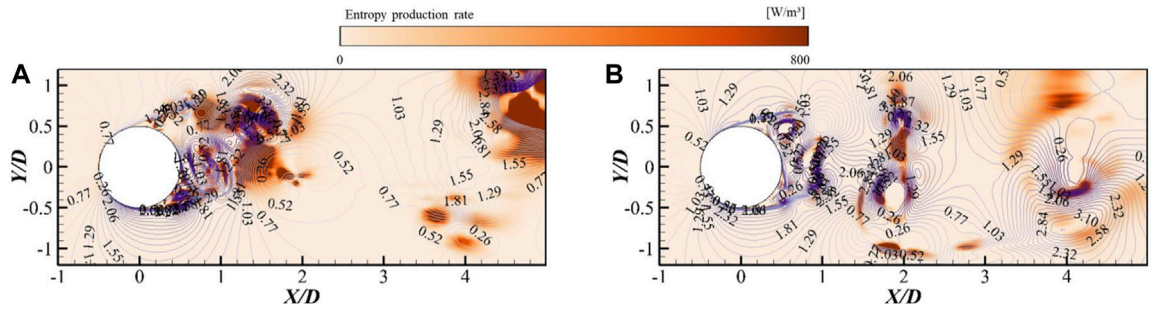

FIGURE 2
Entropy production rate and the distribution of dimensionless isobaric lines in the wake flow field. **(A)** Non-cavitating, **(B)** SS model (σ = 2.92).

$$\frac{\Phi}{T} = S_{\mathrm{pro},\bar{\mathrm{D}}} + S_{\mathrm{pro},\mathrm{D}'} \tag{10}$$

$$S_{\mathrm{pro},\bar{\mathrm{D}}} = \frac{\mu}{\bar{T}}\left\{2\left[\left(\frac{\partial \bar{u}}{\partial x}\right)^2 + \left(\frac{\partial \bar{v}}{\partial y}\right)^2 + \left(\frac{\partial \bar{w}}{\partial z}\right)^2\right] + \left(\frac{\partial \bar{u}}{\partial y} + \frac{\partial \bar{v}}{\partial x}\right)^2 + \left(\frac{\partial \bar{u}}{\partial z} + \frac{\partial \bar{w}}{\partial x}\right)^2 + \left(\frac{\partial \bar{v}}{\partial z} + \frac{\partial \bar{w}}{\partial y}\right)^2\right\} \tag{11}$$

$$S_{\mathrm{pro},\mathrm{D}'} = \frac{\mu}{\bar{T}}\left\{2\left[\overline{\left(\frac{\partial u'}{\partial x}\right)^2} + \overline{\left(\frac{\partial v'}{\partial y}\right)^2} + \overline{\left(\frac{\partial w'}{\partial z}\right)^2}\right] + \overline{\left(\frac{\partial u'}{\partial y} + \frac{\partial v'}{\partial x}\right)^2} + \overline{\left(\frac{\partial u'}{\partial z} + \frac{\partial w'}{\partial x}\right)^2} + \overline{\left(\frac{\partial v'}{\partial z} + \frac{\partial w'}{\partial y}\right)^2}\right\} \tag{12}$$

$S_{\mathrm{pro},\mathrm{D}'}$ cannot be directly calculated due to the inclusion of velocity pulsation terms. Kock assumed that it is related to turbulent dissipation rate ε and temperature T, and its calculation model is as follows:

$$S_{\mathrm{pro},\mathrm{D}'} = \frac{\rho\varepsilon}{\bar{T}}$$

The total entropy generation rate of the wall region is obtained by integrating over the wall region. Calculation formula for wall entropy generation:

$$\Delta S_{\mathrm{pro},W} = \int_S \frac{\vec{\tau_W} \cdot \vec{v_P}}{\bar{T}}\, dS \tag{14}$$

Therefore, the total entropy production rate ψ inside the flow field is defined as follows:

$$\psi = \bar{T} \times S_{\mathrm{pro},\bar{\mathrm{D}}} + \bar{T} \times S_{\mathrm{pro},\mathrm{D}'} \tag{15}$$

The entropy production rate near the cylindrical wall surface is:

$$\psi_W = \vec{\tau_W} \cdot \vec{v_P} \tag{16}$$

3 Results and discussion

3.1 Qualitative analysis of energy loss distribution in the wake flow field

The distribution of the entropy production rate and the dimensionless dynamic pressure in the wake flow field of a cylinder within a swirling flow is depicted in Figure 2. The dimensionless dynamic pressure is defined as follows:

$$h = \frac{0.5\rho_l V^2}{0.5\rho_l U_\infty^2} \tag{17}$$

The magnitude of the dimensionless dynamic pressure is representative of the fluid's dynamic pressure in a specific region. The variation in color along isobars of nondimensional dynamic pressure demonstrates the dimensionless pressure drop in the flow field, with darker hues indicating more significant pressure drops.

In Figure 2A, in the non-cavitating case, energy losses in the vortex separation region near the upper and lower surfaces of the cylinder and in the wake region are revealed. The distribution trend of dimensionless dynamic pressure along the isobars is similar to that of the dimensionless pressure drop. In the region near the stagnation point at the leading edge of the cylinder, the obstructive effect of the cylinder results in lower fluid velocities, leading to a corresponding decrease in dynamic pressure at this location. From the stagnation point to the vicinity of the vortex shedding point on the cylinder surface, the flow separation caused by the acceleration and subsequent deceleration of flow due to the increasing flow velocity in this region results in a variation of dynamic pressure characterized by an initial increase followed by a decrease. In the near-wake region, as multiple-scale vortex structures detach and evolve, the pressure at the center of the vortices is relatively lower than the ambient pressure due to centrifugal forces. The velocity increases gradually from the vortex center to the vortex periphery, and the velocity gradient is significant. Consequently, the dimensionless isobars in the vicinity of the vortex periphery are densely distributed, with relatively higher dynamic pressure values. Upon comparison, it is evident that the regions of energy loss in the wake flow field around the cylinder are typically located in the low-pressure areas and their vicinity where the pressure drop is significant. In these regions, the dimensionless isobars are densely distributed, indicating a high velocity gradient in the flow field. Thus, the energy loss in the wake flow field of the cylinder in the non-cavitating model typically occurs in spatial ranges characterized by significant velocity gradients between the vortex center and its periphery.

Through comparative analysis, it is observed that under the non-cavitation model, energy losses in the wake flow field around the cylinder primarily manifest in low-pressure regions with significant pressure drops and their immediate surroundings. In these regions, a dense distribution of dimensionless dynamic pressure on equipotential lines is noted, indicating a notable velocity gradient in this flow area. Consequently, under the non-cavitation model, energy loss in the wake flow field around the cylinder typically occurs in spatial regions where a substantial velocity gradient exists between the center and the edge of the vortex.

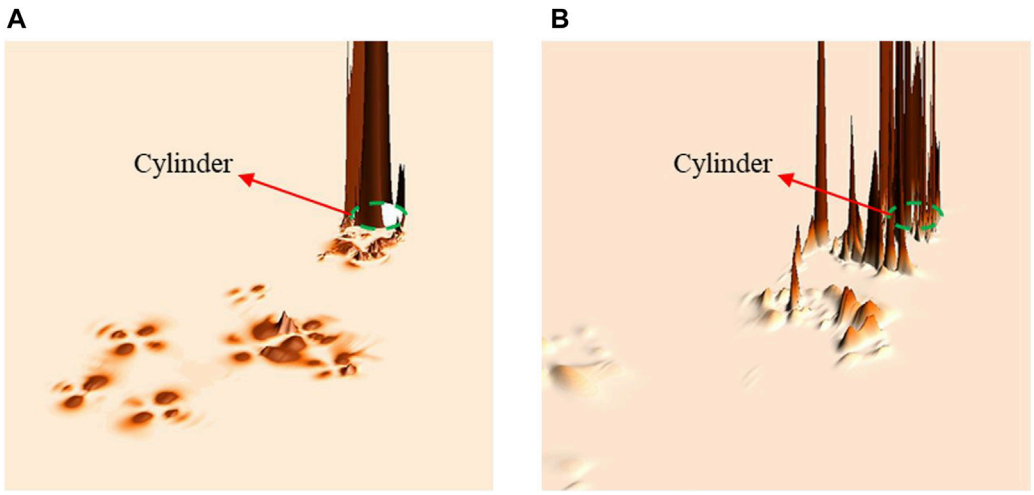

FIGURE 3
Locations of energy loss and the magnitude of entropy production values in the wake flow field. **(A)** Non-cavitating, **(B)** SS model (σ = 2.92).

In Figure 2B, it can be observed that the introduction of the SS cavitation model results in energy loss in the vortex separation region near the upper and lower surfaces of the cylinder, as well as in the wake region. Notably, the areas where energy loss occurs in the wake flow field are relatively dispersed, and the distribution area is comparatively small. The trend in the distribution of dimensionless dynamic pressure on equipotential lines generally aligns with that observed under the non-cavitation model.

Under the SS cavitation model, locations of energy loss in the wake flow field around the cylinder typically coincide with low-pressure regions experiencing substantial pressure drops. In these areas, a dense distribution of dimensionless dynamic pressure on equipotential lines is noted, indicating a significant velocity gradient in this flow region. Consequently, under the influence of the SS cavitation model, energy loss in the wake flow field around the cylinder generally occurs in spatial regions exhibiting a substantial velocity gradient between the center and the edge of the vortex.

When Figures 2A, B are compared, both display energy loss from the vortex separation region on the cylinder surface to the near-wake region. In contrast to the SS cavitation model, under the non-cavitation model, the energy loss region in the near-wake area is more concentrated, and the area is relatively larger. The primary reason for this difference lies in the generation of cavitation bubbles in the wake flow field when employing the SS cavitation model. These bubbles compress the upstream fluid, causing deceleration of the upstream flow and significant deformation of the detached multi-scale vortex system. Consequently, under non-cavitation model, the maximum dimensionless dynamic pressure in the wake flow field is higher than that under combined SS cavitation model conditions. Simultaneously, the compression of the multi-scale vortex system by the cavitation bubbles induces deformation and dispersion of the vortex system, resulting in a more scattered distribution of the regions experiencing energy loss in the wake flow field. However, in both conditions, energy loss in the wake flow field around the cylinder occurs in regions with a significant velocity gradient.

In Figure 3, under non-cavitation model conditions, the areas characterized by higher entropy production values in the wake flow field are larger when compared to those observed under the SS cavitation model. This distinction arises because, under non-cavitation model conditions, the multi-scale vortex system in the flow field remains relatively intact, featuring interactions solely between vortex systems. Consequently, the areas with significant changes in pressure gradient in the wake flow field, and hence higher entropy production values, are relatively larger, and there are nearly no points with exceptionally high entropy production.

Conversely, in the wake flow field under the combined SS cavitation model, the presence of cavitation bubbles results in the compression of the upstream fluid, inducing deceleration in the upstream flow. This leads to a reduction in velocity and velocity gradient within the boundary layer near the cylinder surface. Consequently, in the regions near the cylinder surface, most of the extreme points of entropy production are smaller than those observed under the non-cavitation model. Moreover, the generation of cavitation bubbles in the wake flow field compresses the multi-scale vortex system, causing significant deformation. The initially more concentrated vortices weaken in strength and disperse in the near-wake region due to the compression effect of the cavitation bubbles. This results in the emergence of some regions with significant changes in pressure gradient between interacting vortices, leading to localized extreme points of high entropy production.

3.2 Quantitative analysis of energy loss distribution in the wake flow field

For the facilitation of a quantitative analysis of energy loss in the near-wake flow field around a cylinder, the region is systematically divided into four zones: W0, W1, W2, and W3. These zones correspond to the leading-edge region, trailing-edge region, near-wake region, and far-field region of the wake flow field around the cylinder, as illustrated in Figure 4.

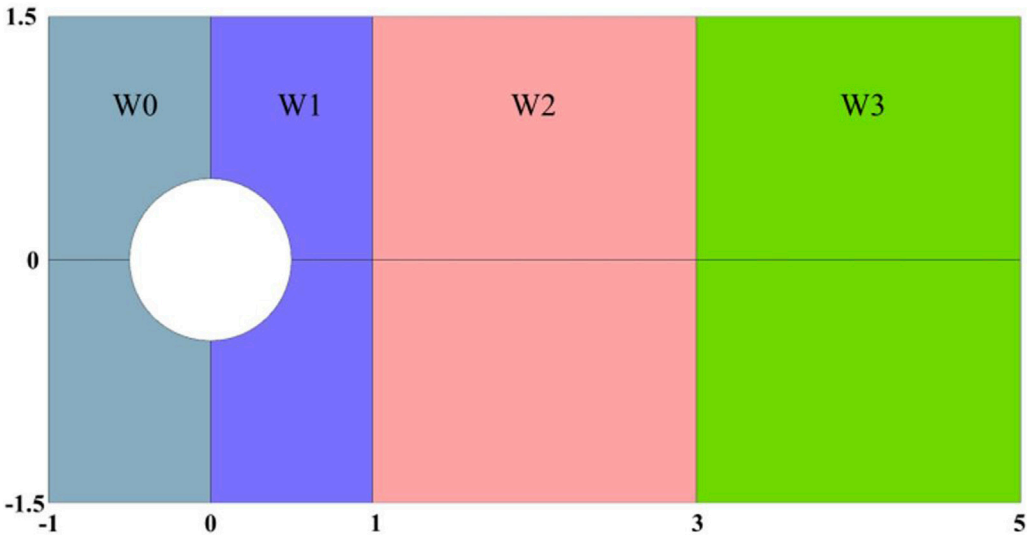

FIGURE 4
Diagram of the partitioned zones in the wake flow field.

TABLE 1 Energy loss in the near wake region of the cylinder.

Flow domain	Non-cavitation model ΔS_{pro} (W/K)	SS cavitation model ΔS_{pro} (W/K) (σ = 2.92)
leading edge (W0)	1.68×10^{-2}	1.55×10^{-2}
trailing-edge region (W1)	5.84×10^{-4}	2.04×10^{-4}
near-wake region (W2)	4.38×10^{-5}	1.33×10^{-5}
far-field region (W3)	8.72×10^{-5}	1.14×10^{-5}

By integrating entropy production rates in each region, the calculation of energy losses is conducted and summarized in Table 1. The results emphasize a significant disparity in total energy loss, with the leading-edge region exhibiting notably greater losses compared to the other three regions, both in the absence of cavitation and when the SS cavitation model is incorporated. Notably, the energy loss in the leading-edge region without cavitation slightly exceeds that with the SS cavitation model. In both operational conditions, energy loss locations in this region concentrate near the upper and lower surfaces of the cylinder's leading edge. In contrast, entropy production in the wake flow region is notably smaller than those in the leading-edge region. Specifically, losses in the trailing-edge region, near-wake region, and far-field region are compared, as illustrated in Figure 5. Observations indicate a gradual decrease in entropy production from the near to the far direction of fluid flow in the wake region. Furthermore, when the SS cavitation model is incorporated, energy losses in each region of the wake flow field are lower compared to the condition without cavitation. This reduction is primarily attributed to the generation of cavitation bubbles in the wake flow field, compressing the upstream fluid and leading to a decrease in flow velocity in the near-wake region. Consequently, the intensity of multiscale vortices diminishes, and the average velocity gradient between vortices decreases, thereby reducing entropy production in the wake flow field.

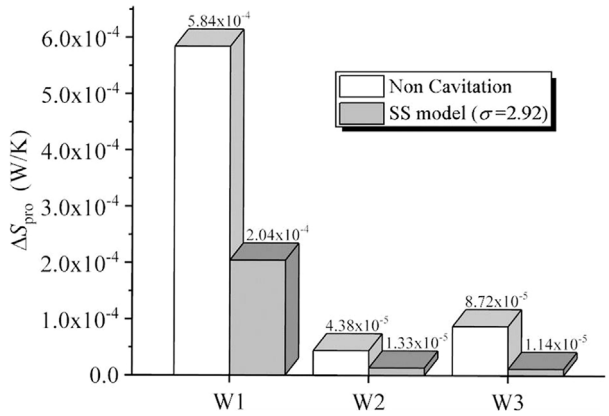

FIGURE 5
Energy loss in each region for different working conditions.

Figure 6 displays the proportions of direct entropy production (left) and fluctuating entropy production (right) in the corresponding regions of the wake flow field. A comparison reveals that in the absence of cavitation, entropy production in the leading-edge region is primarily attributed to direct entropy production. In contrast, in the trailing-edge, near-wake, and far-field

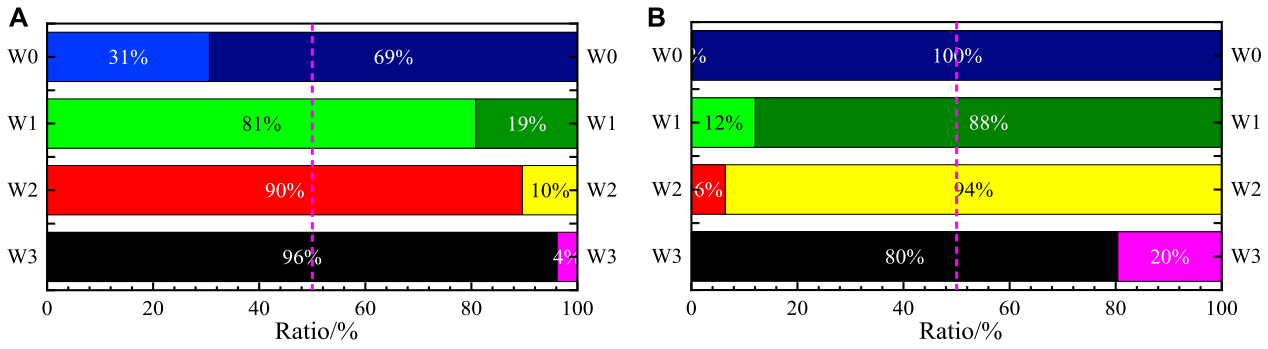

FIGURE 6
Percentage of pulsating entropy production (left) versus direct entropy production (right) in each region. **(A)** Non-cavitating, **(B)** SS model (σ = 2.92).

regions, the proportion of fluctuating entropy production gradually increases, becoming the primary source of entropy production in those areas. However, with the incorporation of the SS cavitation model, entropy production in the leading-edge, trailing-edge, and near-wake regions of the wake flow field are predominantly associated with direct entropy production, while in the far-field region, fluctuating entropy production assumes prominence. Remarkably, in both scenarios, entropy production in the leading-edge region is primarily due to direct entropy production. This is a consequence of significant pressure gradient variation in this region. Simultaneously, the presence of cavitation bubbles in the wake flow field compresses the upstream fluid, causing a decrease in the ratio of fluctuating entropy production to total entropy production in the trailing-edge and near-wake regions. In the far-field region, entropy production is primarily associated with fluctuating entropy production. Due to the influence of cavitation bubbles, the proportion of fluctuating entropy production in this region is slightly lower when the SS cavitation model is applied compared to the condition without cavitation. Combining this information with Figure 5, it is evident that under SS cavitation model conditions, the total entropy production in the trailing-edge, near-wake, and far-field regions of the wake flow field decreases, accompanied by a corresponding reduction in the proportions of fluctuating entropy production in each region.

In summary, under both operational conditions, entropy production in the flow field around the cylinder are predominantly governed by direct entropy production in the leading-edge region (W0) and fluctuating entropy production in the far-field region (W3). The impact of cavitation bubbles on entropy production is primarily manifested in the trailing-edge region (W1) and near-wake region (W2).

3.3 Analysis of wall entropy production

Figure 7 depicts wall entropy production on the surface of the cylinder for both the non-cavitation model and the combined SS cavitation model, with the 180° direction corresponding to the leading-edge stagnation point on the cylinder surface, and the 0° direction corresponding to the trailing-edge stagnation point. The distribution, magnitude, and trends of wall entropy production on

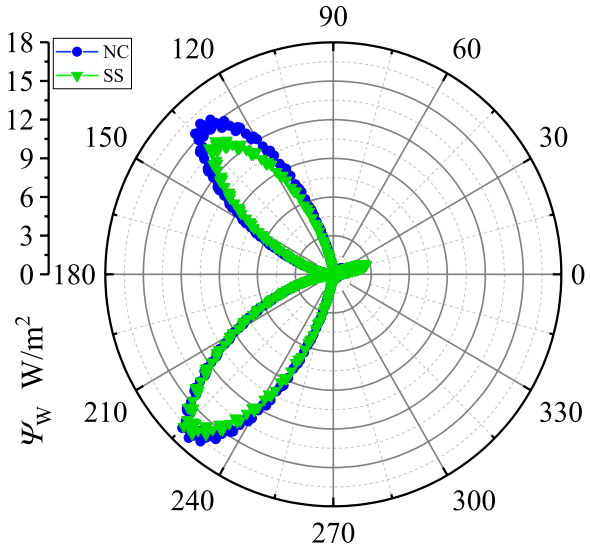

FIGURE 7
Entropy production on the surface of the cylinder with and without cavitation model.

the cylinder surface are generally consistent for both the non-cavitation model and the combined SS cavitation model, as revealed in the graph. In summary, wall entropy production on the cylinder surface primarily concentrates on the upper and lower surfaces near the leading edge. The leading-edge surface exhibits a slightly higher maximum wall entropy production in the non-cavitation model compared to the combined SS cavitation model. However, during minor wall entropy production fluctuations on the trailing-edge surface, the maximum wall entropy production in the combined SS cavitation model surpasses that in the non-cavitation model. According to wall entropy production theory, the magnitude of wall entropy production is primarily related to the velocity of the fluid in the vicinity of the wall and the wall shear stress induced by velocity gradients. Thus, the distribution trend of wall entropy production along the cylinder surface aligns generally with the velocity distribution trend in the nearby region. This suggests

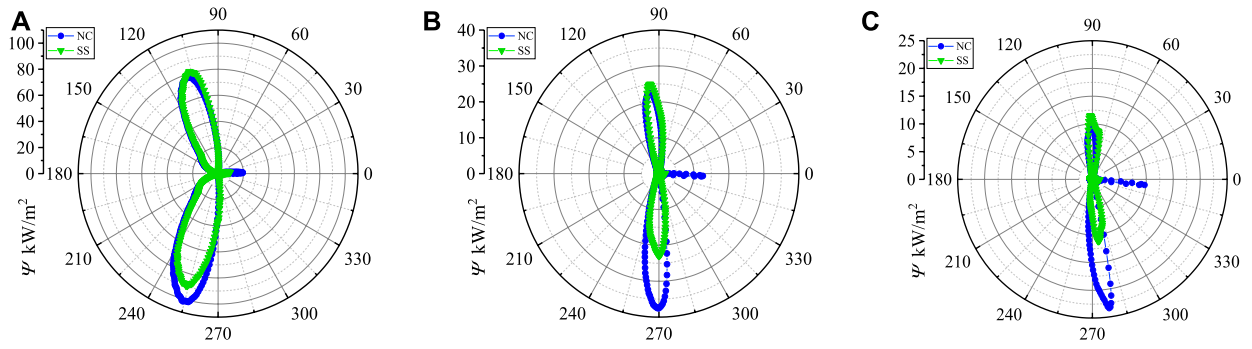

FIGURE 8
Entropy production at different locations and under different conditions in velocity boundary layer. **(A)** C1, **(B)** C2, **(C)** C3.

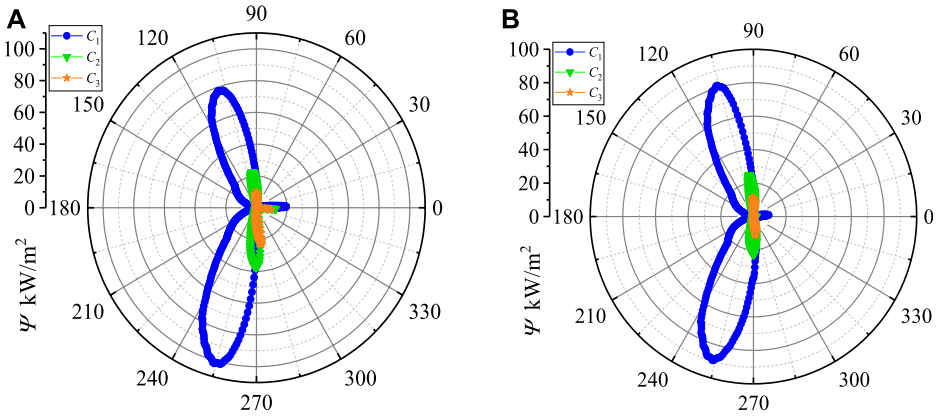

FIGURE 9
Distribution of entropy production in boundary layer under different working conditions. **(A)** Non-cavitating, **(B)** SS model (σ = 2.92).

that wall entropy production is mainly concentrated in regions with higher velocity gradients, and as velocity gradients increase, the values of wall entropy production also increase.

Given the frequent incidence of energy losses in regions characterized by substantial velocity gradients, there arises a necessity for a meticulous investigation into entropy production rates within the velocity boundary layer on the surface of the cylinder. Circles C1, C2, and C3, centered around the cylinder's axis, were deliberately selected within the velocity boundary layer at distances ranging from 0.5D to 0.525D. The visual representation of the distribution of entropy production rates for these circles is presented in Figures 8, 9.

Referring to Figure 8, it becomes evident that the distribution trends of entropy production rates on circles C1, C2, and C3 remain consistently similar for both the non-cavitation model and the combined SS cavitation model. At the leading-edge stagnation point (180°), the entropy production rate is nearly zero for all three circles. Proceeding clockwise from the leading-edge stagnation point to the region near the upper surface flow separation point (ranging from 180° to 90°), in both scenarios, the entropy production rate rapidly increases to a maximum value and then experiences a rapid decrease. On the trailing-edge surface (ranging from 90° to 270°), there is a pronounced fluctuation of entropy production rate only in the vicinity of the trailing-edge stagnation point (0°). Near the lower surface flow separation point and back to the leading-edge stagnation point, the entropy production rate again rapidly increases to a certain maximum value before decreasing rapidly.

Upon comparing C1, C2, and C3, it is apparent that the locations of the maximum entropy production rates on the surface of the cylinder are generally consistent for both the non-cavitation model and the combined SS cavitation model. However, in the region beneath the cylinder, the maximum entropy production rate in the non-cavitation model significantly exceeds that in the combined SS cavitation model. As analyzed earlier, in the trailing-edge region, both operating conditions are significantly influenced by fluctuating entropy production. Consequently, the difference in energy losses mainly depends on the distribution of fluctuating entropy production, which is associated with the dissipation of turbulent kinetic energy in the fluid. Due to the quasi-periodic nature of the wake flow field, the distribution of turbulent kinetic energy dissipation rate on the cylinder surface is also quasi-periodic. At present, the turbulent kinetic energy dissipation on the upper

surface concentrates near the leading edge, which is consistent with the flow separation point on the upper surface. This results in minimal generation of fluctuating entropy production in the velocity boundary layer on the upper surface of the cylinder. Therefore, in the velocity boundary layer on the upper surface of the cylinder, the trends of entropy production rates are similar for both the non-cavitation model and the combined SS cavitation model, with the maximum entropy production rate slightly higher when the SS cavitation model is incorporated.

Concurrently, the turbulent kinetic energy dissipation on the lower surface concentrates near the trailing edge, which is consistent with the flow separation point on the lower surface. Therefore, although the trends of entropy production rate distribution in the region near the lower surface are similar for both cases, the region is closer to the trailing-edge region (W1). Under the influence of cavitation bubble compression, the maximum entropy production rate in the velocity boundary layer on the lower surface of the cylinder is significantly smaller when the SS cavitation model is incorporated compared to the non-cavitation model. Meanwhile, in the region near the trailing-edge stagnation point of the cylinder, the effect of cavitation bubble compression in the wake flow field significantly influences the velocity boundary layer's maximum entropy production rate under non-cavitation model conditions, making it much greater than that under the combined SS cavitation model. This observation indicates that the presence of cavitation bubbles in the wake flow field around the cylinder compresses the upstream fluid, leading to a reduction in the flow velocity and, consequently, a decrease in velocity gradients in the velocity boundary layer on the cylinder surface when the SS cavitation model is incorporated. This further elucidates the sharp decrease in the proportion of fluctuating entropy production in the leading-edge and trailing-edge regions observed in Figure 7 under both non-cavitation and combined SS cavitation model conditions.

According to Figure 9, it is evident that the variation trend of entropy production rate distribution within the velocity boundary layer remains fundamentally consistent under both non-cavitation and combined SS cavitation model conditions. The entropy production rate gradually decreases from the inner to the outer layers, and the location of the maximum entropy production rate also progressively shifts away from the leading-edge stagnation point. This shift is primarily attributed to flow separation occurring on the surface of the cylinder. In summary, the impact of vortex cavitation in the wake flow field around the cylinder on the distribution trend of entropy production rates within the velocity boundary layer on the cylinder surface is relatively minor. However, it significantly affects the magnitude of entropy production rates and the proportion of contributions from different sources to entropy production.

4 Conclusion

1. Energy loss in the wake flow field around a cylinder, from the region of flow separation on the cylinder surface to the near-wake area, is evident irrespective of the presence or absence of cavitation model conditions. However, under non-cavitation conditions, the energy loss region in the near-wake area is more concentrated and relatively larger. Regardless of the conditions, energy loss occurs in regions with very high velocity gradients.
2. The locations of energy loss are concentrated near the upper and lower surfaces of the cylinder, particularly near the leading edge, in both scenarios. In the leading-edge region (W0), energy loss is primarily attributed to direct entropy production, while in the far-field region (W3), fluctuating entropy production dominates. The influence of cavitation bubbles on entropy production is mainly observed in the trailing-edge region (W1) and near-wake region (W2).
3. The distribution trends of wall entropy production on the cylinder surface are generally consistent in both scenarios, with wall entropy production concentrated in regions with high velocity gradients. As velocity gradients increase, the values of wall entropy production also increase. Analysis of entropy production rates at different positions in the velocity boundary layer, on circles C1, C2, and C3, reveals consistent distribution trends under both non-cavitation and combined SS cavitation model conditions, displaying two peaks. However, under non-cavitation model conditions, the maximum entropy production rate in this region's velocity boundary layer is significantly greater than that under the combined SS cavitation model.

Data availability statement

The original contributions presented in the study are included in the article/Supplementary material, further inquiries can be directed to the corresponding author.

Author contributions

GZ: Funding acquisition, Project administration, Resources, Supervision, Writing–original draft. XY: Software, Writing–original draft. YL: Writing–review and editing. MG: Validation, Writing–review and editing. FG: Data curation, Methodology, Writing–review and editing.

Funding

The author(s) declare financial support was received for the research, authorship, and/or publication of this article. This research was funded by the National Natural Science Foundation of China (grant nos 51979125, 52005224, and 52306041) and the senior talents fund of Jiangsu University (No. 21JDG043).

Conflict of interest

The authors declare that the research was conducted in the absence of any commercial or financial relationships that could be construed as a potential conflict of interest.

Publisher's note

References

Al-Obaidi, A. R. (2020). Detection of cavitation phenomenon within a centrifugal pump based on vibration analysis technique in both time and frequency domains. *Exp. Tech.* 44, 329–347. doi:10.1007/s40799-020-00362-z

Amromin, E. (2022). Analysis of scale effects on tide turbine cavitation. *Ocean. Eng.* 264, 112246. doi:10.1016/j.oceaneng.2022.112246

Arndt, R. E. (2012). Some remarks on hydrofoil cavitation. *J. Hydrodynamics, Ser. B* 24, 305–314. doi:10.1016/s1001-6058(11)60249-7

Bejan, A. (1996). Entropy generation minimization: the new thermodynamics of finite-size devices and finite-time processes. *J. Appl. Phys.* 79, 1191–1218. doi:10.1063/1.362674

Brandao, F. L., Bhatt, M., and Mahesh, K. (2020). Numerical study of cavitation regimes in flow over a circular cylinder. *J. Fluid Mech.* 885, A19. doi:10.1017/jfm.2019.971

Denton, J. D. (1993). The 1993 igti scholar lecture: loss mechanisms in turbomachines. *J. Turbomach.* 115 (4), 621–656. doi:10.1115/1.2929299

Fry, S. (1984). Investigating cavity/wake dynamics for a circular cylinder by measuring noise spectra. *J. Fluid Mech.* 142, 187–200. doi:10.1017/S0022112084001051

Ghahramani, E., Jahangir, S., Neuhauser, M., Bourgeois, S., Poelma, C., and Bensow, R. E. (2020). Experimental and numerical study of cavitating flow around a surface mounted semi-circular cylinder. *Int. J. Multiph. Flow.* 124, 103191. doi:10.1016/j.ijmultiphaseflow.2019.103191

Gu, F., Huang, Y., and Zhang, D. (2021). Cavitation of multiscale vortices in circular cylinder wake at Re= 9500. *J. Mar. Sci. Eng.* 9 (12), 1366. doi:10.3390/jmse9121366

Herwig, H., Gloss, D., and Wenterodt, T. (2008). A new approach to understanding and modelling the influence of wall roughness on friction factors for pipe and channel flows. *J. Fluid Mech.* 613, 35–53. doi:10.1017/S0022112008003534

Herwig, H., and Kock, F. (2007). Direct and indirect methods of calculating entropy generation rates in turbulent convective heat transfer problems. *Heat. Mass Transf.* 43, 207–215. doi:10.1007/s00231-006-0086-x

Hutli, E., Fekete, T., and Nedeljkovic, M. (2019). Surface characteristics and cavitation damage progress in ductile materials. *Eng. Fail. Anal.* 106, 104157. doi:10.1016/j.engfailanal.2019.104157

Khare, R., and Prasad, V. (2021). Prediction of cavitation and its mitigation techniques in hydraulic turbines-A review. *Ocean. Eng.* 221, 108512. doi:10.1016/j.oceaneng.2020.108512

Kock, F., and Herwig, H. (2004). Local entropy production in turbulent shear flows: a high-Reynolds number model with wall functions. *Int. J. Heat. Mass Transf.* 47, 2205–2215. doi:10.1016/j.ijheatmasstransfer.2003.11.025

Kumar, P., Chatterjee, D., and Bakshi, S. (2017). Experimental investigation of cavitating structures in the near wake of a cylinder. *Int. J. Multiph. Flow.* 89, 207–217. doi:10.1016/j.ijmultiphaseflow.2016.09.025

Lei, T., Zhifeng, X., Yabin, L., Yue, H., and Yun, X. (2018). Influence of T-shape tip clearance on performance of a mixed-flow pump. *Proc. Inst. Mech. Eng. Part A J. Power Energy* 232, 386–396. doi:10.1177/0957650917733129

Lei, T., Zhiyi, Y., Yun, X., Yabin, L., and Shuliang, C. (2017). Role of blade rotational angle on energy performance and pressure fluctuation of a mixed-flow pump. *Proc. Inst. Mech. Eng. Part A J. Power Energy* 231, 227–238. doi:10.1177/0957650917689948

Li, D., Song, Y., Lin, S., Wang, H., Qin, Y., and Wei, X. (2021). Effect mechanism of cavitation on the hump characteristic of a pump-turbine. *Renew. Energy* 167, 369–383. doi:10.1016/j.renene.2020.11.095

Li, Y., Feng, G., Li, X., Si, Q., and Zhu, Z. (2018). An experimental study on the cavitation vibration characteristics of a centrifugal pump at normal flow rate. *J. Mech. Sci. Technol.* 32, 4711–4720. doi:10.1007/s12206-018-0918-x

Prosperetti, A. (2017). Vapor bubbles. *Annu. Rev. Fluid Mech.* 49, 221–248. doi:10.1146/annurev-fluid-010816-060221

Saito, Y., and Sato, K. (2003). "Cavitation bubble collapse and impact in the wake of a circular cylinder," in *Fifth international symposium on cavitation (CAV2003)* (Osaka, Japan), 1–4.

Schnerr, G. H., and Sauer, J. (2001). "Physical and numerical modeling of unsteady cavitation dynamics," in *Fourth international conference on multiphase flow* (New Orleans, LO, USA: ICMF), 1.

Sun, X., Xia, G., You, W., Jia, X., Manickam, S., Tao, Y., et al. (2023). Effect of the arrangement of cavitation generation unit on the performance of an advanced rotational hydrodynamic cavitation reactor. *Ultrason. Sonochemistry* 99, 106544. doi:10.1016/j.ultsonch.2023.106544

Sun, X., You, W., Xuan, X., Ji, L., Xu, X., Wang, G., et al. (2021). Effect of the cavitation generation unit structure on the performance of an advanced hydrodynamic cavitation reactor for process intensifications. *Chem. Eng. J.* 412, 128600. doi:10.1016/j.cej.2021.128600

Sun, Z., Li, D., Mao, Y., Feng, L., Zhang, Y., and Liu, C. (2022). Anti-cavitation optimal design and experimental research on tidal turbines based on improved inverse BEM. *Energy* 239, 122263. doi:10.1016/j.energy.2021.122263

Tian, B., Huang, B., and Li, L. (2023). Investigation of transient sheet/cloud cavitating flow dynamics from multiscale perspective. *Phys. Fluids* 35 (7). doi:10.1063/5.0159763

Walsh, E. J., and Hernon, D. (2006). Unsteady volumetric entropy generation rate in laminar boundary layers. *Entropy* 8, 25–30. doi:10.3390/e8010025

Wang, C., Zhang, Y., Yuan, Z., and Ji, K. (2020). Development and application of the entropy production diagnostic model to the cavitation flow of a pump-turbine in pump mode. *Renew. Energy* 154, 774–785. doi:10.1016/j.renene.2020.03.065

Wang, Z., Liu, H., Gao, Q., Wang, Z., Wang, Y., Wang, G., et al. (2021). Numerical investigation of ventilated cavitating flow in the wake of a circular cylinder. *Phys. Rev. Fluids* 6, 064303. doi:10.1103/PhysRevFluids.6.064303

Zhang, F., Appiah, D., Hong, F., Zhang, J., Yuan, S., Adu-Poku, K. A., et al. (2020). Energy loss evaluation in a side channel pump under different wrapping angles using entropy production method. *Int. Commun. Heat. Mass Transf.* 113, 104526. doi:10.1016/j.icheatmasstransfer.2020.104526

frontiers | Frontiers in Energy Research

TYPE Original Research
PUBLISHED 29 December 2023
DOI 10.3389/fenrg.2023.1340063

OPEN ACCESS

EDITED BY
Yongfei Yang,
Nantong University, China

REVIEWED BY
Linmin Li,
Zhejiang Sci-Tech University, China
An Yu,
Hohai University, China

*CORRESPONDENCE
Fadong Gu,
211911004@stmail.ujs.edu.cn

RECEIVED 17 November 2023
ACCEPTED 01 December 2023
PUBLISHED 29 December 2023

CITATION
Zhang G, Yang X, Li Y and Gu F (2023), Numerical investigation on the cavitating wake flow around a cylinder based on proper orthogonal decomposition. *Front. Energy Res.* 11:1340063. doi: 10.3389/fenrg.2023.1340063

Numerical investigation on the cavitating wake flow around a cylinder based on proper orthogonal decomposition

Guangjian Zhang[1,2], Xiufei Yang[1], Yan Li[1] and Fadong Gu[1]*

[1]Research Center of Fluid Machinery Engineering and Technology, Jiangsu University, Zhenjiang, China, [2]Wenling Fluid Machinery Technology Institute of Jiangsu University, Wenling, China

The non-cavitating and cavitating wake flow of a circular cylinder, which contains multiscale vortices, is numerically investigated by Large Eddy Simulation combined with the Schnerr–Sauer cavitation model in this paper. In order to investigate the spatiotemporal evolution of cavitation vortex structures, the Proper Orthogonal Decomposition (POD) method is employed to perform spatiotemporal decomposition on the cylinder wake flow field obtained by numerical simulation. The results reveal that the low-order Proper Orthogonal Decomposition modes correspond to large-scale flow structures with relatively high energy and predominantly single frequencies in both non-cavitating and cavitating conditions. The presence of cavitation bubbles in the flow field leads to a more pronounced deformation of the vortex structures in the low-order modes compared to the non-cavitating case. The dissipation of pressure energy in the cylinder non-cavitating wake occurs faster than the kinetic energy. While in the cavitating wake, the kinetic energy dissipates more rapidly than the pressure energy.

KEYWORDS

cylinder wake, cavitation, mode, vortex, proper orthogonal decomposition

1 Introduction

Vortex cavitation is a common physical phenomenon in hydraulic machinery (Arndt, 1981; Lei et al., 2014; Tan et al., 2015), typically occurring at the inlet and outlet edges of hydraulic components (Gu et al., 2024) and at the rear of flow-obstructing bodies (Leonard and Koumoutsakos, 1993; Li et al., 2019; Ghahramani et al., 2020). Cavitation induces fluctuations in fluid pressure within the flow field (Liu et al., 2020; Ji et al., 2020), resulting in uneven surface load distribution on flow components and generating hydrodynamic noise (Sadri and Kadivar, 2023). In severe cases, it can lead to cavitation damage on flow components (Zhang et al., 2016), thereby affecting the operational stability of hydraulic machinery. To mitigate the adverse effects of cavitation on hydraulic machinery, a clear and comprehensive understanding of the evolution mechanism of cavitation vortex structures is imperative. However, direct investigation of cavitation vortex shedding characteristics through hydraulic machinery is extremely challenging. Commonly used hydraulic machinery in engineering exhibits not only com-plex structures but also necessitates substantial computational resources for numerical simulations. Simultaneously, the influence of dynamic and static flow components on each other complicates the accurate capture of intricate vortex systems (Lei et al., 2018). Flow around a circular cylinder is one of

the classical problems in fluid mechanics (Berger and Wille, 1972). At low Reynolds numbers, the flow is steady, and as the Reynolds number gradually in-creases, vortex shedding occurs around the cylinder, eventually forming a pair of wake vortices. At higher Reynolds numbers, the wake vortices become unstable, leading to periodic oscillations and the formation of a von Kármán vortex street (Williamson, 1996). Studies have revealed (Norberg, 2003; Desai et al., 2020) that at high Reynolds numbers, the wake flow field around a cylinder exhibits a rich array of multiscale vortex structures. Starting from the separation points on the upper and lower surfaces of the cylinder, multiscale vortex structures emerge continuously relative to spatial scales. These vortex structures of different scales constitute the unique multiscale vortex system in the wake flow field, making it an ideal model for studying vortex cavitation characteristics (Kumar et al., 2017; Dobroselsky, 2019; Brandao et al., 2020).

For vortex cavitation, accurately describing and understanding the complex variations in flow structures and the mechanisms of instability are crucial. Among the various methods for obtaining main flow structures, Proper Orthogonal Decomposition (POD) has been widely utilized (Berkooz et al., 1993; Holmes et al., 1997; Hu et al., 2023). The POD method is an efficient order reduced technique, grounded in the core principle of identifying an optimal set of standard orthogonal bases (Chatterjee, 2000). These bases are chosen to maximize the successive reduction of the projection of sample data onto them. By selectively retaining the larger projections (containing higher energy), the first few modes are captured. Consequently, this method allows for the representation of the majority of the flow energy with a limited number of low-order POD modes. The classic POD method was first introduced to the fluid-dynamics community by Lumley (Lumley, 1967) as an attempt to reveal the elusive coherent structures that populate turbulent flows. Then Sirovich et al. (Sirovich, 1987a; Sirovich, 1987b) improved the classical POD method by introducing the Snapshot POD approach. In this method, the concept of spatiotemporal transformation is applied, enabling the POD method to handle complex flow fields effectively. The effectiveness of POD has been validated by numerical and experimental studies in analyzing coherent structures. Utturkar et al. (Utturkar et al., 2005) stated that this modal analysis enables to discern the flow structures obtained in numerical simulations considering various turbulence models. Danlos et al. (Danlos et al., 2014) studied the effect of surface roughness on the cavitation shedding behavior using longitudinal grooves, and applied POD on snapshots to classify the cavitation regime of sheet or cloud cavity. Results show that the phase portraits, the Lissajous figure, and the energy content of the first mode are validated to identify different regimes. Miyanawala et al. (Miyanawala and Jaiman, 2019) used the POD method to analyze the dominant coherent structures of wake flow around a square cylinder. Smith et al. (Smith et al., 2020) employed the POD method to identify various cloud cavitation shedding modes by their spatial locations. In this paper, in order to investigate the spatiotemporal evolution mechanism of cavitation vortex structures and reveal the interactions between multiscale vortex systems and cavitation, we employ the POD method to perform spatiotemporal decomposition on the wake flow field around a cylinder and make a comprehensive comparative analysis in the cavitating and non-cavitating conditions.

2 Methodology

2.1 Governing equations and the LES approach

The cavitating flow involves liquid and vapor phases. In this work, the homogeneous mixture model was adopted, assuming the multiphase fluid components share the same velocity and pressure. The mass and momentum conservation equations for the mixture flow are shown as follows:

$$\frac{\partial \rho_m}{\partial t} + \frac{\partial \left(\rho_m u_j\right)}{\partial x_j} = 0 \tag{1}$$

$$\frac{\partial \left(\rho_m u_i\right)}{\partial t} + \frac{\partial \left(\rho_m u_i u_j\right)}{\partial x_j} = -\frac{\partial p}{\partial x_i} + \frac{\partial}{\partial x_j}\left[\mu_m\left(\frac{\partial u_i}{\partial x_j} + \frac{\partial u_j}{\partial x_i} - \frac{2}{3}\frac{\partial u_k}{\partial x_k}\delta_{ij}\right)\right] \tag{2}$$

$$\rho_m = \rho_v \alpha_v + \rho_l \left(1 - \alpha_v\right) \tag{3}$$

$$\mu_m = \mu_v \alpha_v + \mu_l \left(1 - \alpha_v\right) \tag{4}$$

where u_i represents the velocity in the i direction; p is the pressure; ρ_m and μ_m represent the mixture density and dynamic viscosity respectively; the subscripts l and v denote the water and vapor phases respectively; α_v is the vapor volume fraction.

In order to solve the above conservation equations, the LES approach was used, carrying out filtering in a small-space area, and dividing the turbulent flow into large-scale motion and small-scale motion. The large-scale motion is solved directly while the small-scale motion is modelled using the Smagorinsky-Lilly subgrid-scale model.

2.2 Cavitation model

The mass transfer between the vapor and liquid phases in cavitating flows is depicted using the following governing equation:

$$\frac{\partial}{\partial t}\left(\rho_v \alpha_v\right) + \frac{\partial}{\partial x_j}\left(\rho_v \alpha_v u_j\right) = m_e - m_c \tag{5}$$

The source terms m_e and m_c represent the evaporation and condensation rates during the phase change. The source terms have different expressions. In the present study, the Schnerr–Sauer cavitation model is used, expressed as,

$$m_e = \frac{3\rho_v \rho_l}{\rho_m}\frac{\alpha_v\left(1-\alpha_v\right)}{R_B}\sqrt{\frac{2\left|p_v - p\right|}{3\rho_l}}, \left(p \le p_v\right) \tag{6}$$

$$m_c = \frac{3\rho_v \rho_l}{\rho_m}\frac{\alpha_v\left(1-\alpha_v\right)}{R_B}\sqrt{\frac{2\left|P - P_v\right|}{3\rho_l}}, \left(p > p_v\right) \tag{7}$$

where p_v is the saturated vapor pressure; R_B is the nucleus radius, expressed as $R_B = \left(\left(\alpha_v/\left(1-\alpha_v\right)\right)\left(3/4\pi n\right)\right)^{1/3}$, where n is the given empirical constant and the default value is $n = 1\times10^{13}$.

2.3 Numerical setup

The computational model is shown in Figure 1. The cylinder diameter D is 9.5 mm, and the two-dimensional computational domain is 60D × 30D with an upstream dimension 10D and a

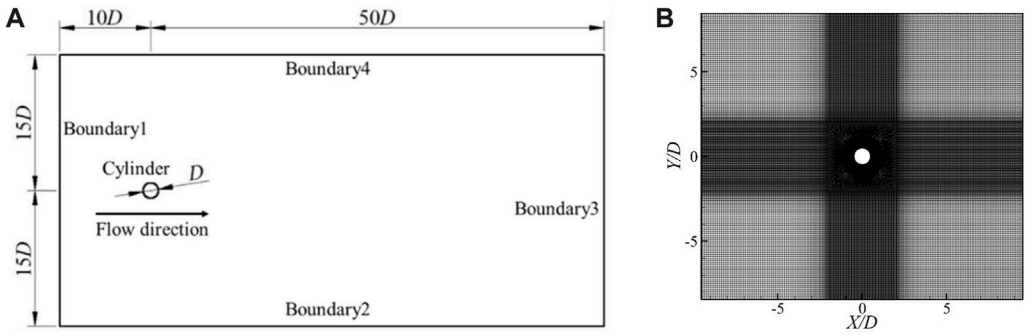

FIGURE 1
Computational model: **(A)** computational domain; **(B)** local grids.

downstream dimension 50D. The computational domain is discretized using structured grids, and the grids in the cylinder surface and wake region are locally refined. The total number of elements is about 336,000 and the average wall y + value is less than 4.6.

In the present study, the commercial software Fluent is employed for numerical simulation. Boundary 1 of the computational domain is set as a velocity inlet with a value V_∞ = 1 m/s, and the corresponding Reynolds number is Re = 9500. Boundary 3 is set as a pressure outlet, and the value p_∞ is set according to the cavitation number, defined as $\sigma = (p_\infty - p_v)/(0.5\rho_l V_\infty^2)$. A no-slip boundary condition is imposed on the cylinder surface and the free slip condition on the up and down walls (Boundary 4 and Boundary 2). The working fluid is water and vapor, in which the density of water is 1,000 kg/m^3, the dynamic viscosity being 0.001 Pa s, and the saturated vapor pressure is 3,540 Pa. The solution method adopts pressure-based solver and a coupled pressure–velocity coupling algorithm. The pressure dispersion mode is second-order discrete mode, and the momentum equation is discrete by finite central difference scheme. The transient scheme is a second-order backward Euler algorithm. The time step is set to 0.05 ms such that the courant number does not exceed 1.0 in the computations. The convergence criterion of all residuals is 10^{-6}. The validation of the present numerical simulation can be found in our previous work (Gu et al., 2021). It should be mentioned that in the following analyses, all parameters shown in the figures are nondimensionalized via the cylinder diameter and the inlet velocity.

2.4 Proper orthogonal decomposition

The core idea of the POD method is to search for the optimal orthogonal basis function space in terms of mean-square sense from a set of spatial data of time series. It uses a smaller number of orthogonal bases to approximate the high-order data description. The flow field information in this study is derived from CFD simulation results, primarily encompassing pressure and velocity fields. The initial step involves selecting a set of sample snapshots. Specifically, N snapshots at different time instants are chosen at equal time intervals from the numerical simulation results. These snapshots constitute a sample information matrix **U**, which combines temporal and spatial dimensions, as described in Eq. (8). Here, M represents the number of grid nodes.

$$\mathbf{U}(x_i,t_j) = \begin{bmatrix} u(x_1,t_1) & u(x_1,t_2) & \cdots & u(x_1,t_N) \\ u(x_2,t_1) & u(x_2,t_2) & \cdots & u(x_2,t_N) \\ \vdots & \vdots & \vdots & \vdots \\ u(x_M,t_1) & u(x_M,t_2) & \cdots & u(x_M,t_N) \end{bmatrix} \tag{8}$$

In general, the spatial length M is much larger than the time length N. Therefore, the covariance matrix constructed from the sample snapshot set **U** is an M×M matrix, making the computation of its eigenvalues and eigenvectors challenging. To address this issue, this paper employs the Snapshot POD method to perform modal decomposition on the matrix **U**, transforming a high-dimensional M-order matrix into a lower-dimensional N-order matrix, significantly simplifying the computation process. The specific calculation procedure is as follows:

Compute the time average of each collected sample,

$$\bar{\boldsymbol{U}}(x_i) = \frac{1}{N}\sum_{j=1}^{N}\boldsymbol{U}(x_i,t_j) \tag{9}$$

The pulsating flow field can be obtained by subtracting the time average from the original sample snapshot,

$$\hat{\boldsymbol{U}}(x_i,t_j) = \boldsymbol{U}(x_i,t_j) - \bar{\boldsymbol{U}}(x_i) \tag{10}$$

The next step is to compute the covariance matrix **C**,

$$\mathbf{C} = \frac{1}{M}\hat{\boldsymbol{U}}^T\hat{\boldsymbol{U}} \tag{11}$$

We then compute the eigenvalues and eigenvectors of **C**,

$$\mathbf{C}\boldsymbol{A} = \lambda\boldsymbol{A} \tag{12}$$

where $\mathbf{A} = (\mathbf{A}_1, \mathbf{A}_2, ..., \mathbf{A}_N)$ represents the eigenvectors of matrix **C**, $\lambda = (\lambda_1, \lambda_2, ..., \lambda_N)^T$ represents the eigenvalues of matrix **C**, and they are arranged in descending order. Utilizing the eigenvalues and eigenvectors, we can calculate the various orders of POD modes $\phi_j(x)$ and their corresponding modal coefficients $a_j(t)$,

$$\phi_j(x) = \frac{1}{\sqrt{\lambda_j}}\hat{\boldsymbol{U}}A_j \tag{13}$$

$$a_j(t) = \frac{\phi_j(x)^T\cdot\hat{\boldsymbol{U}}}{\phi_j(x)^T\cdot\phi_j(x)} \tag{14}$$

The energy of each order of POD mode can be characterized by the eigenvalues λ. Based on the decomposed modes and their

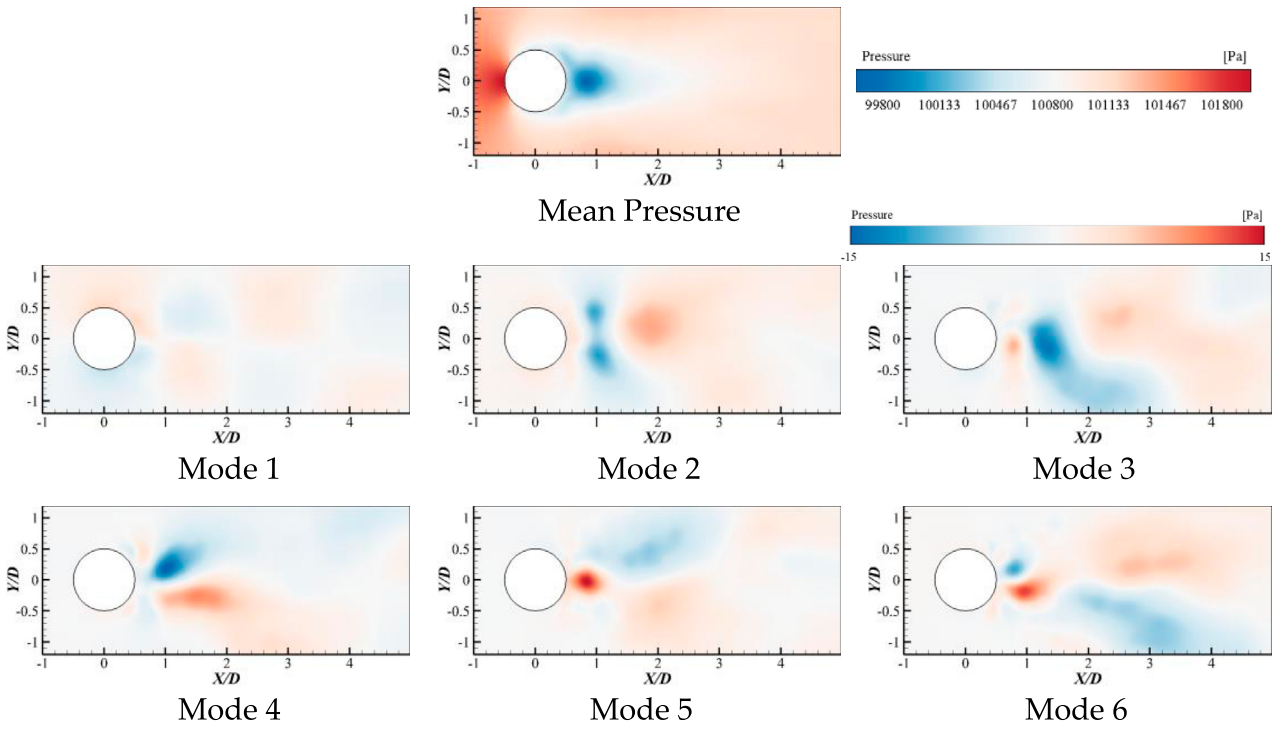

FIGURE 2
Mean pressure field and the first six POD modes based on pressure field (without cavitation).

corresponding modal coefficients, one can select the first modes with a high percentage of energy for flow field reconstruction. For instance, if you choose to use k modes, the reconstructed flow field at any given time can be expressed as:

$$\mathbf{U}\left(x,t_j\right) = \bar{\boldsymbol{U}}\left(x\right) + \sum_{i=1}^{k} a_i\left(t_j\right)^{*}\Phi_i\left(x\right) \tag{15}$$

3 Results and discussion

To provide a comprehensive view of transient flow field information, we extracted 200 transient data files for the wake flow around a cylinder under both non-cavitating and cavitating flow conditions. The total duration covered by these 200 transient files corresponds to 20 quasi-periods of the cylinder's surface lift coefficient for each respective operating condition. For each of these 200 transient files, velocity field snapshots and pressure field snapshots were extracted. Subsequently, the POD on the flow field was performed using MATLAB R2016b.

3.1 Analysis of wake flow field around a cylinder without cavitation

In the non-cavitating case, the first six modes of proper orthogonal decomposition of the wake flow around the cylinder, using the transient pressure field, are shown in Figure 2. The first six POD modes using the transient velocity field are depicted in Figure 3.

From the average pressure field, it can be observed that the non-cavitating wake flow field around the cylinder exhibits basically symmetry about the wake centerline. The region near the leading-edge stagnation point corresponds to the highest average pressure area, while the region near the trailing edge stagnation point represents the lowest average pressure area. When examining the spatial distribution of various order of POD modes of the fluctuating pressure field, it becomes evident that with an increase in mode order, different degrees of localized high-pressure and low-pressure regions appear alternately within the wake flow field around the cylinder. Additionally, the pressure in the wake flow field exhibits an asymmetric distribution along the wake centerline. This asymmetry primarily arises from the interactions and evolution of multi-scale vortices generated within the wake flow field.

From the average velocity field, it is evident that, in the non-cavitating case, the average flow field in the wake region around the cylinder exhibits a symmetric distribution about the wake centerline basically. The areas near the leading-edge stagnation point and trailing-edge stagnation point correspond to the lowest average velocity regions, while the regions near the upper and lower surfaces of the cylinder represent the highest average velocity areas. Examining the spatial distribution of various order of POD modes of the fluctuating velocity field, it becomes apparent that in the lower-order modes, the flow structures corresponding to fluctuating velocity are concentrated in the region near the trailing-edge stagnation point and exhibit basic symmetry about the wake centerline. For instance, in modes 1 and 2, two large, oppositely oriented vortices are present in the region near the trailing-edge stagnation point, and both are distributed along the wake centerline. In mode 2, two smaller shedding vortices are

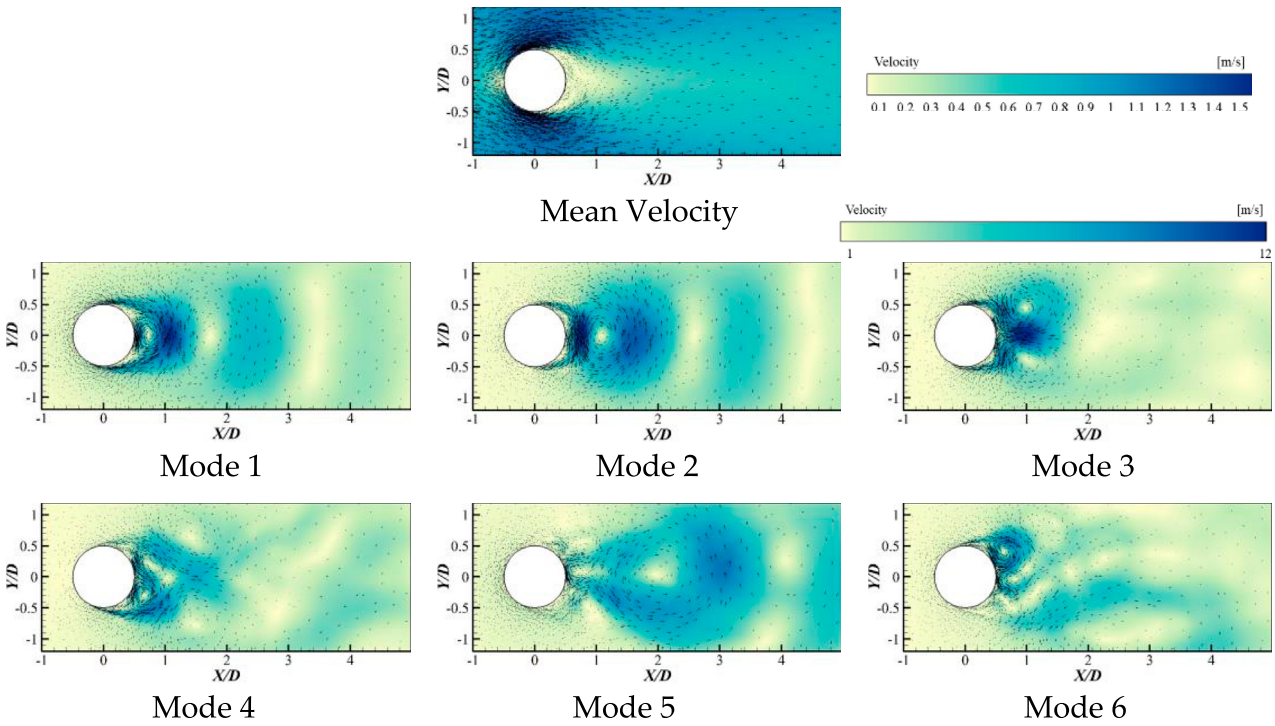

FIGURE 3
Mean velocity field and the first six POD modes based on velocity field (without cavitation).

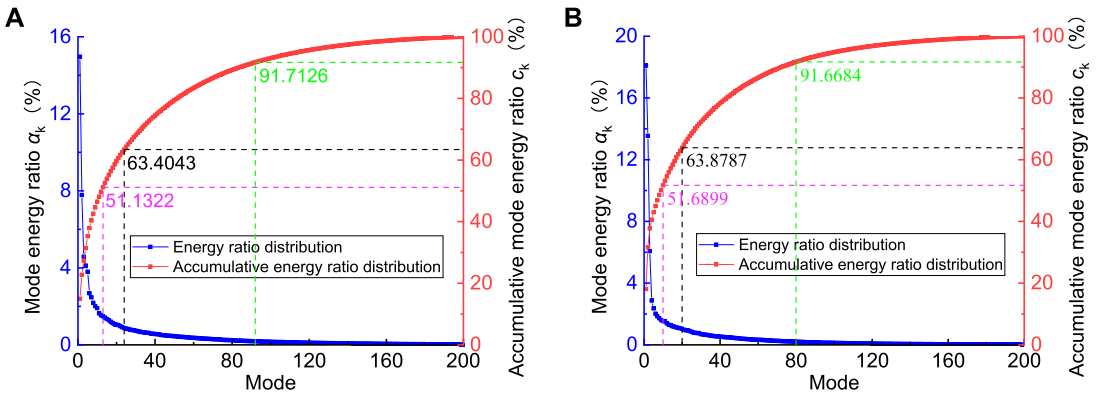

FIGURE 4
Energy distribution of all POD modes based on pulsating pressure field **(A)** and pulsating velocity field **(B)** in the non-cavitating case.

observed near the upper and lower surfaces of the cylinder. In mode 3, two similarly sized and oppositely oriented vortices are present on the cylinder's rear surface and near the wake region, with smaller shedding vortices on the cylinder's surface. Starting from mode 4, the vortex structures in the wake flow field are no longer regular, their spatial distribution lacks strong symmetry, and the flow structures become more fragmented and finer.

Overall, in the non-cavitating wake flow field around the cylinder, the various order of modes obtained through POD of the two types of fluctuating fields tend to exhibit a transition toward finer and more intricate flow scales as the mode order increases.

The eigenvalues obtained through POD represent the energy content of various order mode. The maximum eigenvalue is related to the structure of the flow field with the maximum energy. The energy distribution of various order of POD modes based on fluctuating pressure field and fluctuating velocity field in the non-cavitating wake flow field around the cylinder is depicted in Figure 4.

Research has shown that in the case of flow around a square cylinder at Re = 100, the first four POD modes account for 99.4% of the total energy (Wang et al., 2014). In contrast, for the wake flow field around a cylinder at Re = 9500, the initial modes do not contain

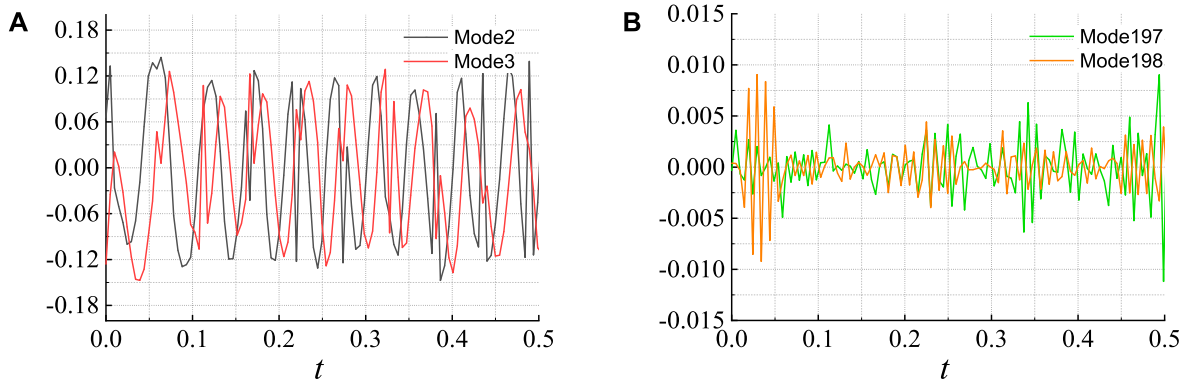

FIGURE 5
Variation of POD modal coefficients of the non-cavitating wake flow around the cylinder based on pulsating pressure field: **(A)** low order modes; **(B)** high order modes.

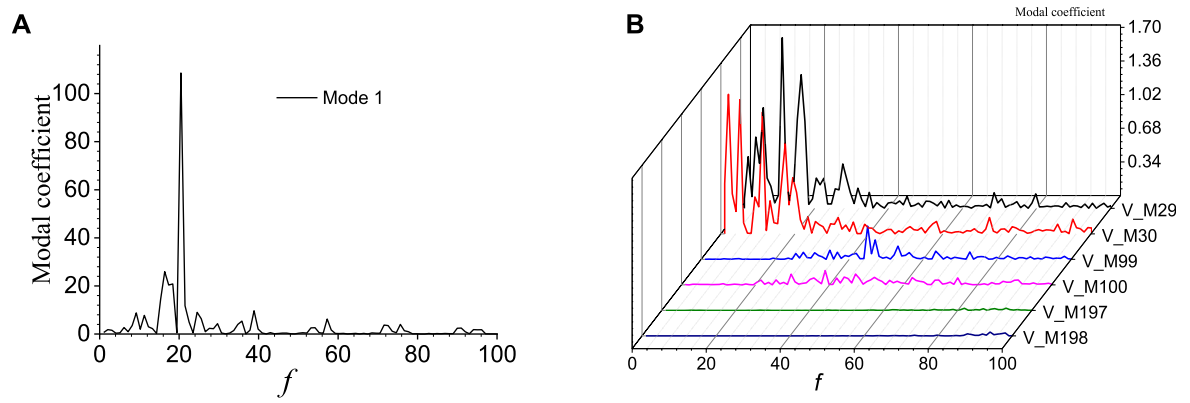

FIGURE 6
Frequency characteristics of POD modal coefficients of the non-cavitating wake flow around the cylinder based on pulsating pressure field: **(A)** mode 1; **(B)** higher order modes.

a significant portion of the energy, and it takes up to the 80th mode to reach 91.67% of the total energy, highlighting the complexity of the flow at Re = 9500. In the non-cavitating wake flow around the circular cylinder, compared to the energy distribution of various POD modes based on the fluctuating velocity field, the energy content in the lower-order modes corresponding to the fluctuating pressure field is lower. In contrast, the higher-order modes correspond to smaller-scale flow structures and have a higher energy contribution, eventually dissipating in the form of heat. These results indicate that in the non-cavitating wake flow around the circular cylinder, the dissipation of pressure energy occurs faster than the dissipation of kinetic energy.

After decomposing the flow field by the POD method, the flow structures corresponding to the low-order modes exhibit "coherent" characteristics. The coherence of the flow structures between modes mainly refer to the similarity in time evolution characteristics of adjacent modes, with a specific phase difference, as shown in Figure 5. The modal coefficients representing the time evolution characteristics of each selected flow field structure are subjected to FFT transformation to obtain the frequency characteristics of the corresponding flow structures for different modes, as shown in Figure 6.

According to Figures 5A, 6A, it can be seen that the frequency composition component of the flow structures in low-order modes is relatively few, and the corresponding main frequency is distributed in the low-frequency band, which is consistent with the main frequency of vortex shedding in the non-cavitating wake flow. When the flow structures are in high-order modes, the frequency composition component is more complex, and both the wavelength and amplitude are significantly reduced compared to those in low-order modes. The fluctuation amplitude is uneven, and the wave composition is more complex, as shown in Figure 5B. Figure 6B shows the frequency distribution of flow structures corresponding to different modes. Modes 29 and 30 represent low-order modes, modes 99 and 100 represent intermediate modes, and modes 197 and 198 represent high-order modes. It can be seen that the frequency corresponding to low-order modes is concentrated in the low-frequency region, while that corresponding to high-order modes is concentrated in the high-frequency region. As the mode increases from low to high, the corresponding frequency also

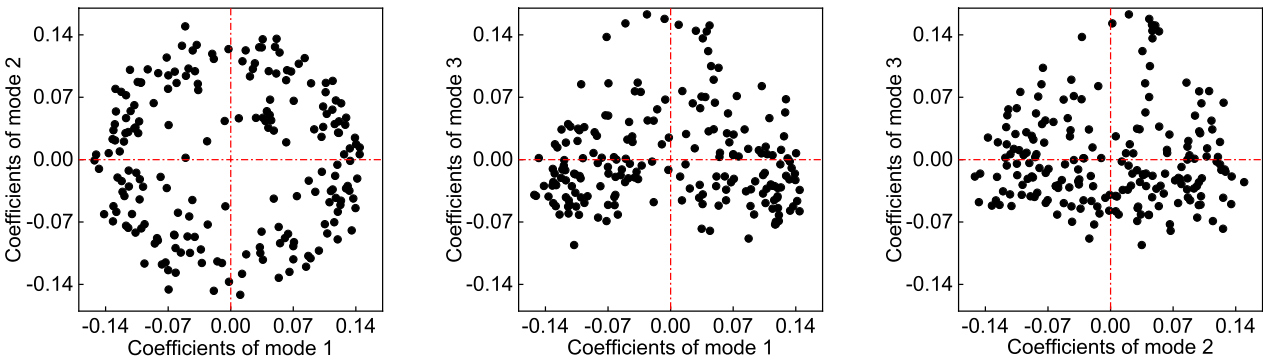

FIGURE 7
Scatter plot of modal coefficients (without cavitation).

changes from low to high, and the frequency concentration area becomes wider, indicating that the flow structures in high-order modes exhibit multi-frequency characteristics.

In summary, as the modal order increases, the frequency of the flow structures in the wake flow around the circular cylinder at Re = 9500 gradually shifts towards high frequency and multi-frequency, indicating that the flow structures corresponding to each mode are not a single flow but are composed of multiple flow scales with different frequency characteristics.

According to the modal energy ratio curve in Figure 4, the first three modes contain relatively high energy ratios in the non-cavitating wake flow around the cylinder. Therefore, scatter plots of two-mode coefficients between each pair are conducted, as shown in Figure 7.

Combined with modes 1 and 2 of the fluctuating velocity field, we can find that there are two opposite-directional vortices near the stagnation point behind the cylinder in mode 1, and the vortex near the stagnation point is stronger. In mode 2, there are also two opposite-directional vortices on the centerline near the stagnation point behind the cylinder, and these two shedding vortices are located at the edge region of two vortices in mode 1. The centers of these two vortices move away from the stagnation point. Meanwhile, there are two small shedding vortices attached symmetrically about the wake centerline on the surface of the cylinder. In mode 3, there are no longer any vortices on the centerline near the wake region. Instead, a pair of vortices with similar sizes and opposite directions are distributed symmetrically on both sides of the centerline near the wake region. The wake centerline region is where two vortex edges are squeezed together and their directions form a 180-degree angle with respect to the mainstream direction, which results in reverse impact on the stagnation point behind the cylinder and flow separation around it on its surface. Therefore, it can be seen from Figure 7 that there is a circular distribution of correlation between the two-mode coefficients being analyzed, indicating that the flow fields corresponding to both modes alternate cyclically.

According to POD modes, complex flows exist in the wake flow around a circular cylinder, including large-scale vortex structures as well as a large number of small-scale vortices. To identify dominant structures in the flow field more clearly, flow field reconstruction can be performed on decomposed flow fields. Figure 8 shows the pressure field reconstruction based using the first 13 modes with an energy content of 51.13% plus mean pressure field. Comparison shows that the POD-reconstructed flow field maintains overall characteristics of the original one. Local high-pressure and low-pressure areas as well as larger-scale vortex distributions in wake flow field are basically consistent with those in original flow field. Meanwhile, reconstructed flow fields remove small-scale flow structures from original ones, making the large-scale coherent structures smoother and more prominent.

3.2 Analysis of cavitating wake flow field around a cylinder

The studied cavitation in the wake flow around a cylinder is induced by reducing the outlet pressure to a certain extent ($\sigma = 2.92$). A Proper Orthogonal Decomposition (POD) analysis is conducted on the cavitating wake flow field around the cylinder aiming to explore the structural features and temporal evolution characteristics of various POD modes. Figure 9 illustrates the first six modes of proper orthogonal decomposition of the cavitating wake flow around the cylinder based on the transient pressure field. Figure 10 presents the first 6 POD modes using the transient velocity field.

From the average pressure field, it is evident that the cavitating wake flow field around the cylinder is also essentially symmetric about the centerline of the wake. The distribution trend is largely consistent with the trend of the average pressure field under non-cavitating conditions. However, under cavitation conditions, the area of the low-pressure region in the wake flow field significantly increases. This is primarily because under non-cavitating conditions, with increasing fluid velocity in the flow field, the local fluid pressure decreases. Thus, under non-cavitating conditions, the pressure in the flow field continues to decrease without restriction. However, after cavitation conditions are reached, when the pressure in the flow field drops below the saturated vapor pressure of the fluid, cavitation occurs. Existing cavitation models use pressure as a criterion to determine cavitation regions. Therefore, it is assumed that the pressure inside the cavitation is equal to the saturated vapor pressure of the liquid. This sets a lower limit on the pressure drop in regions with fast-

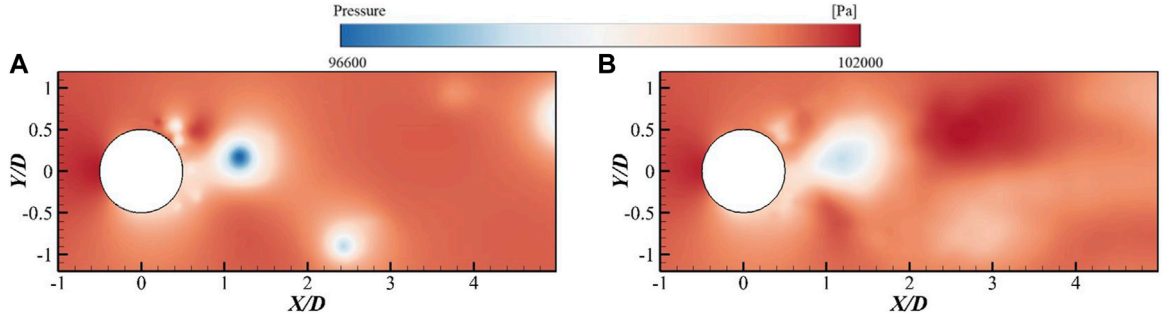

FIGURE 8
Flow field reconstruction [**(A)** original pressure field; **(B)** Reconstructed pressure field].

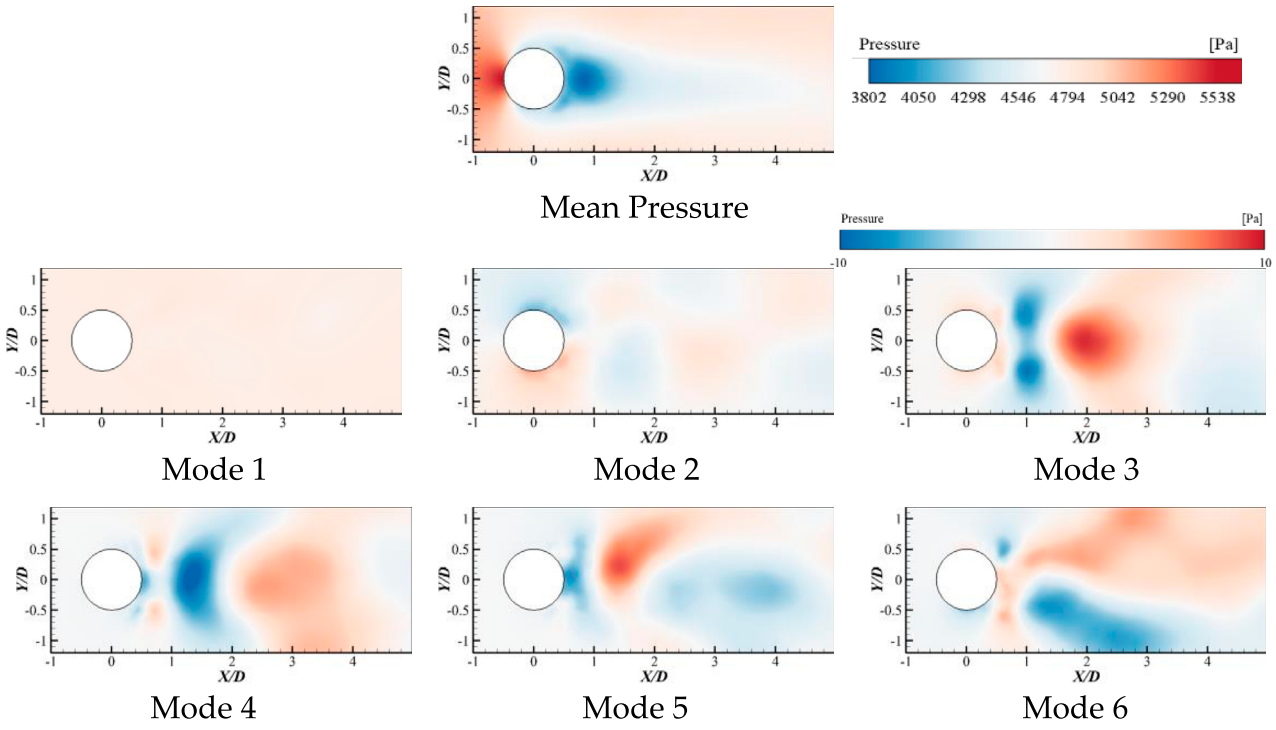

FIGURE 9
Mean pressure field and the first six POD modes based on pressure field (σ = 2.92).

flowing fluid, meaning that once the pressure drops to the saturated vapor pressure, it does not decrease further. Hence, under cavitation conditions, the area of low-pressure regions in the average pressure field is larger than that under non-cavitating conditions. Analyzing the spatial distribution of fluctuating pressure fields at various modes, it is observed that, apart from mode 1, starting from mode 2, the wake flow field exhibits alternating regions of varying degrees of local high and low pressure as the mode order increases. The distribution area is also larger than that under non-cavitating conditions. In mode 1, the pressure field structure in the wake region of the cylinder is predominantly characterized by high-pressure regions, with only occasional locally low-pressure regions near the centerline of the wake in the wake region, but with indistinct boundaries. As the mode order increases, due to the interaction of multiscale vortices in the wake flow field, the pressure exhibits characteristics of an asymmetric distribution along the centerline of the wake.

From the average velocity field, it is apparent that the average wake flow field around the cylinder under cavitation conditions is also essentially symmetric about the centerline of the wake. The specific distribution trend of the flow field is largely consistent with the flow field distribution under non-cavitating conditions. Examining the spatial distribution of various modes of flow in the fluctuating velocity field, it is observed that, compared to non-cavitating conditions, under cavitation conditions, the mode order with large-scale flow structures is increased in the near-wake

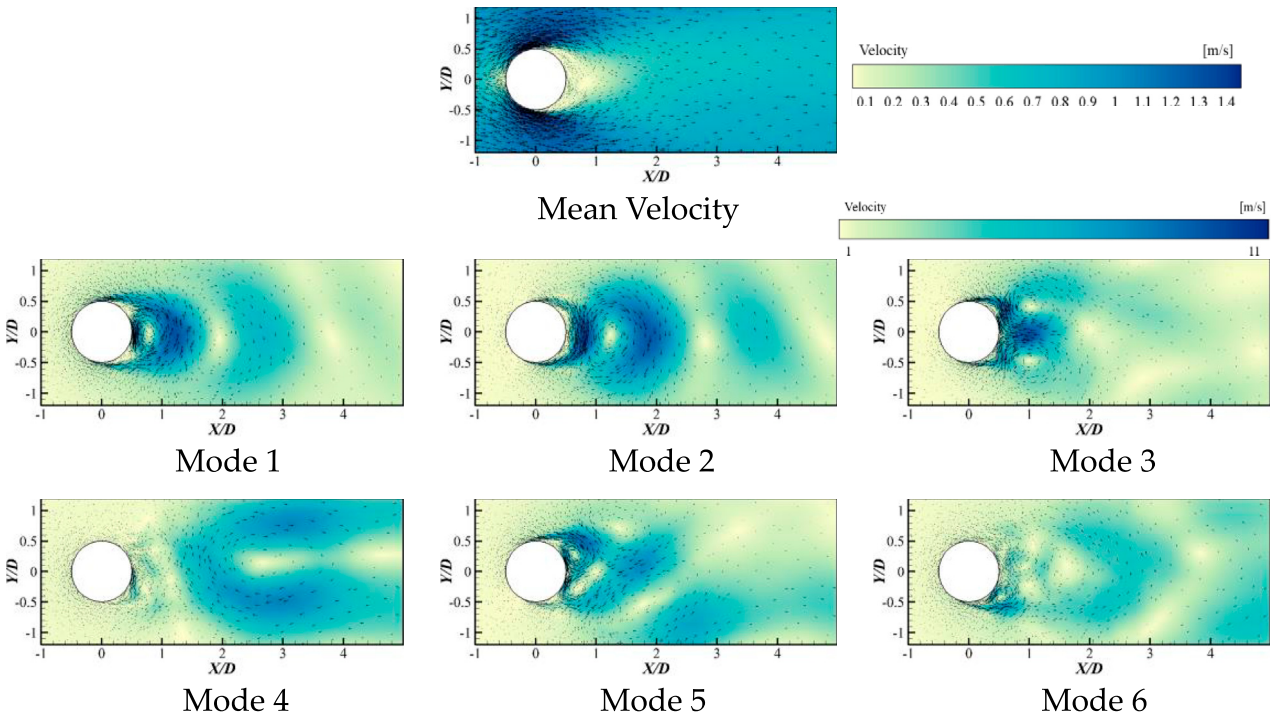

FIGURE 10
Mean velocity field and the first six POD modes based on velocity field (σ = 2.92).

region close to the rear stagnation point. Comparing low-order modes, it is found that the spatial distribution of flow structures in the first three modes under cavitation conditions is generally similar to that under non-cavitating conditions. However, in mode 2 under cavitation conditions, the directions of two larger-scale vortices are opposite to those under non-cavitating conditions. Meanwhile, among the modes under cavitation conditions, the flow structure of mode 5 is similar to that of mode 4 under non-cavitating conditions. This suggests that the generation of cavitation has a certain impact on the evolution of wake flow structures. Overall, the multiscale vortex structures in the fluctuating velocity field corresponding to various modes of flow under non-cavitating conditions are relatively regular, while under cavitation conditions, these structures undergo more severe deformation. Additionally, with the increase in mode order, the flow structures under cavitation conditions gradually exhibit more diverse small-scale flow characteristics.

The energy distribution of various modes obtained through Proper Orthogonal Decomposition based on the fluctuating pressure field and fluctuating velocity field in the cavitating wake flow around the cylinder is presented in Figure 11. The first mode of the fluctuating pressure field contributes to approximately 65.62% of the total energy, with the first five modes accounting for around 79.43%. For the fluctuating velocity field, the first eight modes contribute approximately 52.33% of the total energy, and the first 15 modes contribute about 64.24%. Clearly, the low-order modes of the fluctuating pressure field have a higher energy content than the fluctuating velocity field. Furthermore, in comparison to non-cavitating conditions, where the first 13 modes of the fluctuating pressure field contribute approximately 51.13% of the total energy, and the first 24 modes contribute around 63.40%, as well as the fluctuating velocity field with the first 10 modes contributing approximately 51.69% and the first 20 modes contributing approximately 63.88%, it is evident that under cavitation conditions, the low-order modes of both the fluctuating pressure field and fluctuating velocity field have higher energy content than under non-cavitating conditions. By comparing the modal structures based on the fluctuating pressure field under non-cavitating and cavitation conditions, it is observed that, under cavitation conditions, the pressure field structure becomes similar to that of non-cavitating conditions only from the second mode onward. The first mode under cavitation conditions exhibits a pressure field structure in the wake region characterized predominantly by high-pressure regions, with occasional locally low-pressure regions near the centerline of the wake, but with indistinct boundaries. Therefore, the structure of the first mode based on the fluctuating pressure field under cavitation conditions may be a contributing factor to the overall increase in energy content of the low-order modes.

In the cavitating wake flow field around the cylinder, in comparison to the energy distribution of various flow modes based on the fluctuating pressure field, the energy content in the structures corresponding to low-order modes in the fluctuating velocity field of is relatively low. Conversely, in the structures corresponding to high-order modes, there is a higher proportion of energy associated with small-scale flow structures, ultimately dissipating in the form of thermal energy. These results indicate that in the cavitating wake flow field around the cylinder, the dissipation of kinetic energy is faster than pressure energy, which is opposite to the situation under non-cavitating conditions.

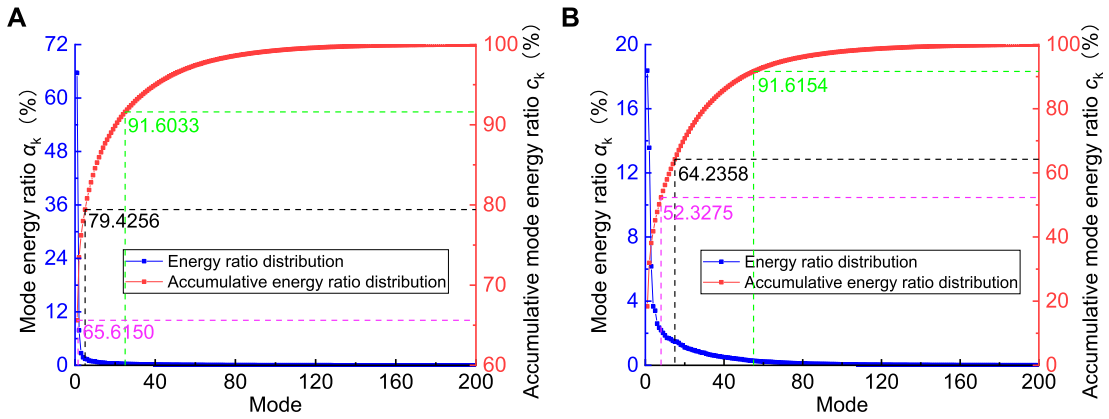

FIGURE 11
Energy distribution of all POD modes based on pulsating pressure field **(A)** and pulsating velocity field **(B)** (σ = 2.92).

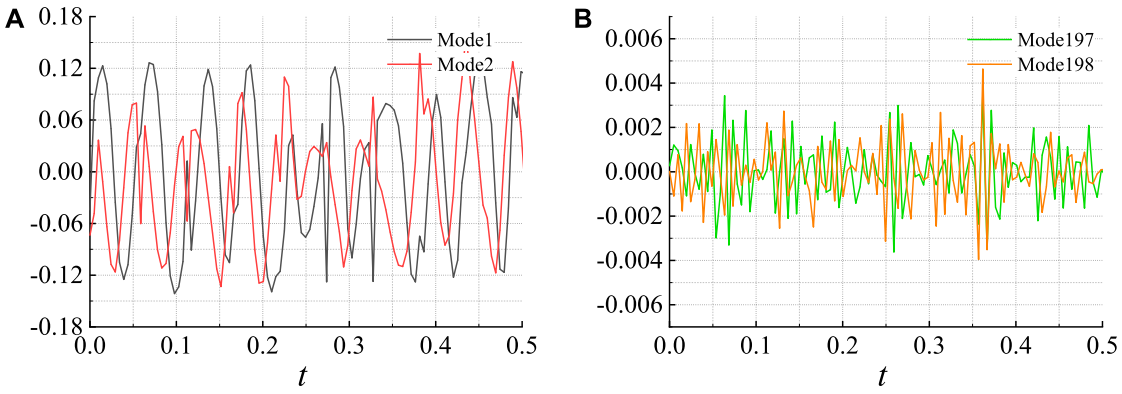

FIGURE 12
Variation of POD modal coefficients of the cavitating wake flow around the cylinder based on pulsating pressure field: **(A)** low order modes; **(B)** high order modes (σ = 2.92).

The temporal and frequency domain distributions of POD modal coefficients for the cavitating wake flow field around the cylinder are illustrated in Figures 12, 13, respectively. In comparison to the non-cavitating conditions, the waveform characteristics of modal coefficients for various flow modes under cavitation conditions are generally similar. The frequencies predominantly exhibit low-frequency, singular characteristics corresponding to the low-order flow structures. Unlike the non-cavitating conditions, under cavitation conditions, the low-order flow structures in the wake flow field correspond to low characteristic frequencies, with relatively smaller amplitudes. As the modal order increases, the wavelength of the modal coefficients shortens, the amplitudes decrease, and the composition of the waves becomes more intricate. Simultaneously, the frequency characteristics of various flow structures tend to evolve towards higher frequency and multifrequency patterns. This suggests that under cavitation conditions, with increasing modal order, the flow structures in the wake flow field become more complex, demonstrating higher-frequency and multifrequency characteristics.

Scatter plots illustrating the pairwise relationship between the modal coefficients for the first three modes of the cavitating flow field are depicted in Figure 14. It can be observed that the correlation between the coefficients of the first and second modes exhibits a circular distribution, indicating that the flow field alternates cyclically between the first and second modes. The correlation between the coefficients of the first and third modes, as well as the second and third modes, displays a weaker circular distribution, suggesting that the flow field for these two modes alternates in a weak cyclic manner. This pattern aligns closely with the observations under non-cavitating conditions.

To facilitate a clearer identification of dominant structures within the flow field, a reconstruction of the wake flow field around the cylinder under cavitation conditions can be performed. Figure 15 presents the reconstructed pressure field with the addition of the first mode, accounting for 65.62% of the energy, and the average pressure field. The left side of the figure displays the original pressure field at the same instant, while the right side shows the reconstructed pressure field. It is evident that the reconstructed flow field eliminates smaller-scale flow structures from the original field, emphasizing the smoother and highlighted larger-scale coherent structures.

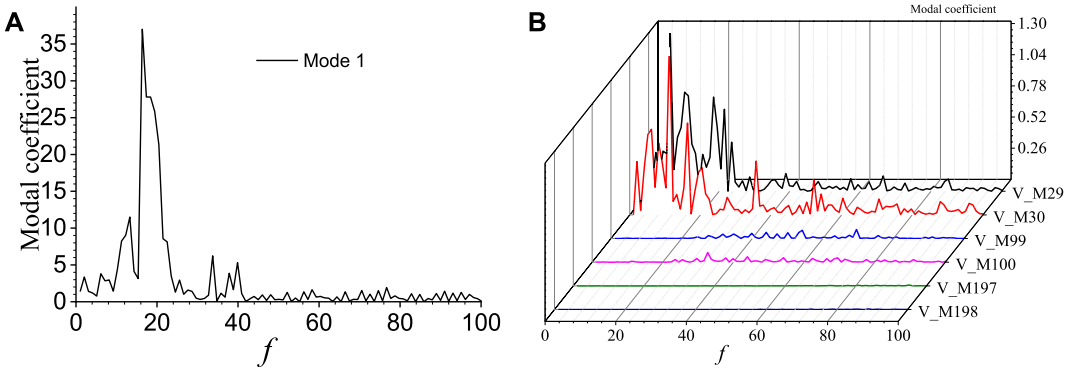

FIGURE 13
Frequency characteristics of POD modal coefficients of the cavitating wake flow around the cylinder based on pulsating pressure field: **(A)** mode 1; **(B)** higher order modes (σ = 2.92).

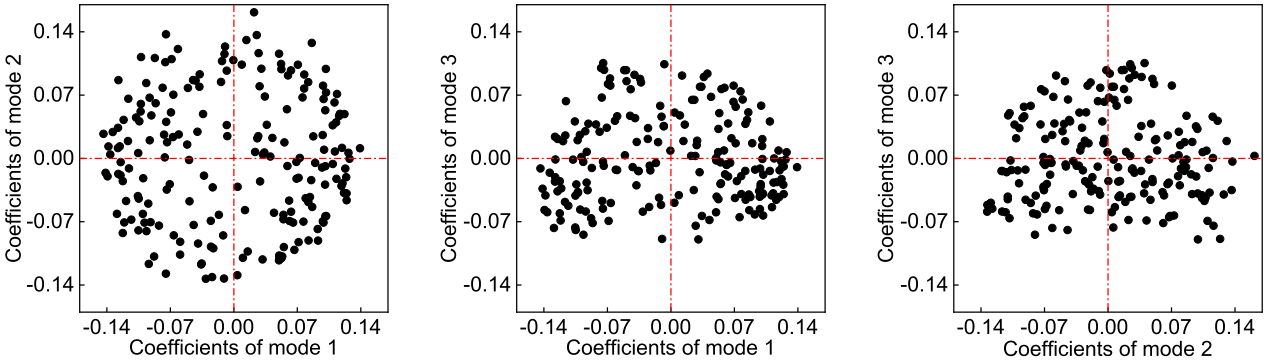

FIGURE 14
Scatter plot of modal coefficients (σ = 2.92).

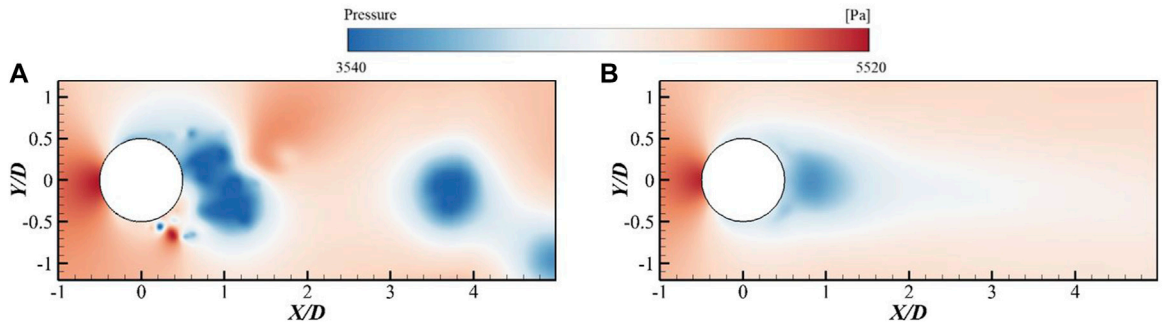

FIGURE 15
Flow field reconstruction at σ = 2.92 [**(A)** original pressure field; **(B)** Reconstructed pressure field).

4 Conclusion

The study based on the Proper Orthogonal Decomposition (POD) method reveals that, under both non-cavitating and cavitating conditions in the wake flow field around a cylinder, low-order modes correspond to large-scale flow structures with relatively high energy and predominantly single frequencies. As the modal order increases, smaller-scale flow structures with higher

frequencies and more complex frequency compositions emerge, accompanied by a decrease in modal coefficients' amplitudes, indicating a relatively minor impact of high-order modes on the flow field. However, under cavitation conditions, the presence of cavitation bubbles in the flow field leads to a more pronounced deformation of the vortex structures in the low-order modes compared to the non-cavitating case. Additionally, modes with similar flow field structures have higher modal orders under cavitation conditions. Moreover, the energy content of low-order modes is significantly greater under cavitation conditions than under non-cavitating conditions. Furthermore, under non-cavitating conditions, the dissipation of pressure energy in the wake flow field around the cylinder occurs faster than the dissipation of kinetic energy. In contrast, under cavitation conditions, the dissipation of kinetic energy occurs more rapidly than the dissipation of pressure energy.

Data availability statement

The raw data supporting the conclusion of this article will be made available by the authors, without undue reservation.

Author contributions

GZ: Funding acquisition, Project administration, Resources, Supervision, Writing–original draft. XY: Software, Writing–original draft. YL: Writing–review and editing. FG: Data curation, Methodology, Validation, Writing–review and editing.

Funding

The authors declare financial support was received for the research, authorship, and/or publication of this article. This research was funded by the National Natural Science Foundation of China (grant no. 52005224, 52306041) and the senior talents fund of Jiangsu University (No. 21JDG043).

Conflict of interest

The authors declare that the research was conducted in the absence of any commercial or financial relationships that could be construed as a potential conflict of interest.

Publisher's note

All claims expressed in this article are solely those of the authors and do not necessarily represent those of their affiliated organizations, or those of the publisher, the editors and the reviewers. Any product that may be evaluated in this article, or claim that may be made by its manufacturer, is not guaranteed or endorsed by the publisher.

References

Arndt, R. E. (1981). Cavitation in fluid machinery and hydraulic structures. *Annu. Rev. Fluid Mech.* 13, 273–326. doi:10.1146/annurev.fl.13.010181.001421

Berger, E., and Wille, R. (1972). Periodic flow phenomena. *Annu. Rev. Fluid Mech.* 4, 313–340. doi:10.1146/annurev.fl.04.010172.001525

Berkooz, G., Holmes, P., and Lumley, J. L. (1993). The proper orthogonal decomposition in the analysis of turbulent flows. *Annu. Rev. Fluid Mech.* 25, 539–575. doi:10.1146/annurev.fl.25.010193.002543

Brandao, F. L., Bhatt, M., and Mahesh, K. (2020). Numerical study of cavitation regimes in flow over a circular cylinder. *J. Fluid Mech.* 885, A19. doi:10.1017/jfm.2019.971

Chatterjee, A. (2000). An introduction to the proper orthogonal decomposition. *Curr. Sci.* 78 (7), 808–817.

Danlos, A., Ravelet, F., Coutier-Delgosha, O., and Bakir, F. (2014). Cavitation regime detection through proper orthogonal decomposition: dynamics analysis of the sheet cavity on a grooved convergent–divergent nozzle. *Int. J. Heat. Fluid Flow.* 47, 9–20. doi:10.1016/j.ijheatfluidflow.2014.02.001

Desai, A., Mittal, S., and Mittal, S. (2020). Experimental investigation of vortex shedding past a circular cylinder in the high subcritical regime. *Phys. Fluids* 32. doi:10.1063/1.5124168

Dobroselsky, K. (2019). "Applying PIV to study a fluid flow in the vicinity of a circular streamlined cylinder," in Journal of Physics: Conference Series, Moscow, Russian (Bristol, England: IOP Publishing), 012015. doi:10.1088/1742-6596/1421/1/012015

Ghahramani, E., Jahangir, S., Neuhauser, M., Bourgeois, S., Poelma, C., and Bensow, R. E. (2020). Experimental and numerical study of cavitating flow around a surface mounted semi-circular cylinder. *Int. J. Multiph. Flow.* 124, 103191. doi:10.1016/j.ijmultiphaseflow.2019.103191

Gu, F., Huang, Y., and Zhang, D. (2021). Cavitation of multiscale vortices in circular cylinder wake at Re= 9500. *J. Mar. Sci. Eng.* 9 (12), 1366. doi:10.3390/jmse9121366

Gu, Y., Sun, H., Wang, C., Lu, R., Liu, B., and Ge, J. (2024). Effect of trimmed rear shroud on performance and axial thrust of multi-stage centrifugal pump with emphasis on visualizing flow losses. *J. Fluids Eng.* 146. doi:10.1115/1.4063438

Holmes, P. J., Lumley, J. L., Berkooz, G., Mattingly, J. C., and Wittenberg, R. W. (1997). Low-dimensional models of coherent structures in turbulence. *Phys. Rep.* 287, 337–384. doi:10.1016/S0370-1573(97)00017-3

Hu, B., Yao, Y., Wang, M., Wang, C., and Liu, Y. (2023). Flow and performance of the disk cavity of a marine gas turbine at varying nozzle pressure and low rotation speeds: a numerical investigation. *Machines* 11, 68. doi:10.3390/machines11010068

Kumar, P., Chatterjee, D., and Bakshi, S. (2017). Experimental investigation of cavitating structures in the near wake of a cylinder. *Int. J. Multiph. Flow.* 89, 207–217. doi:10.1016/j.ijmultiphaseflow.2016.09.025

Lei, T., Shan, Z. B., Liang, C. S., Chuan, W. Y., and Bin, W. B. (2014). Numerical simulation of unsteady cavitation flow in a centrifugal pump at off-design conditions. *Proc. Inst. Mech. Eng. Part C. J. Mech. Eng. Sci.* 228, 1994–2006. doi:10.1177/0954406213514573

Lei, T., Zhifeng, X., Yabin, L., Yue, H., and Yun, X. (2018). Influence of T-shape tip clearance on performance of a mixed-flow pump. *Proc. Inst. Mech. Eng. Part A J. Power Energy* 232, 386–396. doi:10.1177/0957650917733129

Leonard, A., and Koumoutsakos, P. (1993). High resolution vortex simulation of bluff body flows. *J. Wind Eng. Ind. Aerodyn.* 46, 315–325. doi:10.1016/b978-0-444-81688-7.50035-8

Li, Y., Zhou, D., and Yu, A. (2019). Research of swirl cavity flow performance in the draft tube of pump turbine. *Renew. Energy Resour.* 37, 303–309. doi:10.13941/j.cnki.21-1469/tk.2019.02.023

Liu, Y., Han, Y., Tan, L., and Wang, Y. (2020). Blade rotation angle on energy performance and tip leakage vortex in a mixed flow pump as turbine at pump mode. *Energy* 206, 118084. doi:10.1016/j.energy.2020.118084

Lumley, J. L. (1967). The structure of inhomogeneous turbulent flows. *Atmos. Turbul. radio wave Propag.*, 166–178.

Miyanawala, T. P., and Jaiman, R. K. (2019). Decomposition of wake dynamics in fluid–structure interaction via low-dimensional models. *J. Fluid Mech.* 867, 723–764. doi:10.1017/jfm.2019.140

Norberg, C. (2003). Fluctuating lift on a circular cylinder: review and new measurements. *J. Fluids Struct.* 17, 57–96. doi:10.1016/S0889-9746(02)00099-3

Sadri, M., and Kadivar, E. (2023). Numerical investigation of the cavitating flow and the cavitation-induced noise around one and two circular cylinders. *Ocean. Eng.* 277, 114178. doi:10.1016/j.oceaneng.2023.114178

Sirovich, L. (1987a). Turbulence and the dynamics of coherent structures. I. Coherent structures. *Q. Appl. Math.* 45, 561–571. doi:10.1090/qam/910462

Sirovich, L. (1987b). Turbulence and the dynamics of coherent structures. II. Symmetries and transformations. *Q. Appl. Math.* 45, 573–582. doi:10.1090/qam/910463

Smith, S. M., Venning, J. A., Pearce, B. W., Young, Y. L., and Brandner, P. A. (2020). The influence of fluid–structure interaction on cloud cavitation about a flexible hydrofoil. Part 2. *J. Fluid Mech.* 897, A28. doi:10.1017/jfm.2020.323

Tan, L., Zhu, B., Wang, Y., Cao, S., and Gui, S. (2015). Numerical study on characteristics of unsteady flow in a centrifugal pump volute at partial load condition. *Eng. Comput.* 32, 1549–1566. doi:10.1108/ec-05-2014-0109

Utturkar, Y., Wu, J., Wang, G., and Shyy, W. (2005). Recent progress in modeling of cryogenic cavitation for liquid rocket propulsion. *Prog. Aerosp. Sci.* 41, 558–608. doi:10.1016/j.paerosci.2005.10.002

Wang, Y., Chen, J., and Xian, S. (2014). Analysis of square cylinder unsteady flow at low Reynolds number with POD method. *J. Northwest. Polytech. Univ.* 32 (4), 612–617.

Williamson, C. H. (1996). Vortex dynamics in the cylinder wake. *Annu. Rev. Fluid Mech.* 28, 477–539. doi:10.1146/annurev.fl.28.010196.002401

Zhang, Y., Zhang, Y., Qian, Z., Ji, B., and Wu, Y. (2016). A review of microscopic interactions between cavitation bubbles and particles in silt-laden flow. *Renew. Sustain. Energy Rev.* 56, 303–318. doi:10.1016/j.rser.2015.11.052

frontiers | Frontiers in Energy Research

TYPE Original Research
PUBLISHED 04 January 2024
DOI 10.3389/fenrg.2023.1344186

OPEN ACCESS

EDITED BY
Kan Kan,
College of Energy and Electrical Engineering, China

REVIEWED BY
Yonggang Lu,
Tsinghua University, China
Jilai Zeng,
Lanzhou University of Technology, China

*CORRESPONDENCE
Yandong Gu,
guyandong@yzu.edu.cn

RECEIVED 25 November 2023
ACCEPTED 06 December 2023
PUBLISHED 04 January 2024

CITATION
Yang A, Gu Y, Cheng L and Zhao W (2024), Influences of suction pipe structures on hydraulic performance and internal flow of electric coolant pumps.
Front. Energy Res. 11:1344186.
doi: 10.3389/fenrg.2023.1344186

Influences of suction pipe structures on hydraulic performance and internal flow of electric coolant pumps

Anlong Yang, Yandong Gu*, Li Cheng and Wenpeng Zhao

College of Hydraulic Science and Engineering, Yangzhou University, Yangzhou, China

An electric coolant pump (ECP) serves as a critical component in the thermal management of electric vehicles. To fulfill the requirements of pressurizing and circulating coolant for various components, a complex structure with multiple pipes is integrated into the pump inlet. This study focuses on the design and analysis of three suction pipe structures: a straight pipe (Case A), a bend (Case B), and a combination of a bend with manifolds (Case C). The objective of this study is to explore the impacts of suction pipe structures on the hydraulic performance, flow pattern, temperature distribution, and vorticity of ECP. Taking into account the variability of coolant physical parameters with temperature, ECP is numerically simulated using the unsteady Reynolds-averaged Navier–Stokes (RANS) equation and the shear stress transport k–ω turbulence model. The experimental and numerical results exhibit good agreement. Case A demonstrates the highest efficiency, Case B follows as the second most efficient, and Case C displays the lowest efficiency. However, the pressure rise remains essentially consistent in all cases. The average efficiencies of Cases B and C are 1.18% and 2.13% lower than that of Case A. The temperature of ECP increases with an increase in the coolant temperature. The temperature of the printed circuit board (PCB) surpasses that of the motor. Case A exhibits the most favorable flow pattern, while Case C demonstrates the least favorable. The bend introduces secondary flow, further intensified by the manifold, leading to an increase in vorticity. The high-vorticity zones expand as the flow rate increases. This study offers valuable insights into the optimization of the ECP suction pipe structure.

KEYWORDS

electric coolant pump, numerical simulation, experiment, suction pipe, hydraulic performance, vorticity

1 Introduction

During the operation of electric vehicles for various modes of transportation, modules such as batteries, motors, and brakes generate substantial heat, necessitating efficient thermal management to mitigate temperature levels and ensure the safety and optimal functioning of electric vehicles (Zhang et al., 2022). The electric coolant pump (ECP) plays a pivotal role in this thermal management process by pressurizing the coolant for circulation. To address the diverse cooling requirements of various modules, multiple pipes are integrated into the ECP inlet, which are categorized into main pipes and manifolds. The convergence of incoming flows from different pipes induces interactions, resulting in flow irregularities and heightened energy dissipation (Kumar Samal and Moharana, 2021; Minocha and

JyeshtharajJoshi, 2020; Liu et al., 2021), consequently impacting the operational efficacy of ECP. The motor and the printed circuit board (PCB) constitute the heat-generating components of ECP, and variations in incoming flow temperatures from different pipes directly influence the heat dissipation of these components. Additionally, temperature fluctuations affect the physical properties of the coolant, thereby exerting an influence on the hydraulic performance of ECP (Jiang et al., 2019; Li et al., 2021). In this research, due consideration is given to the significant variations in coolant physical property parameters at different temperatures, elucidating the relationship between coolant physical properties and temperature in the simulation model (Johann Friedrich Gülich, 2008).

ECP falls within the category of centrifugal pumps characterized by compact overall dimensions, exhibiting a complexity surpassing that of conventional centrifugal pumps. Primary hydraulic components, including the impeller and volute, stand out as pivotal factors influencing performance. Previous studies by Li et al. (2019) and Yuan et al. (2022) involved the optimization of centrifugal pump blade parameters, resulting in improvements in head, efficiency, and resistance to cavitation. Lu et al. (2021) deduced that augmenting the tongue enhances the hydraulic efficiency of centrifugal pumps, particularly under overload conditions. Lin et al. (2022) proposed an impeller design with a sinusoidal trailing edge, effectively mitigating overall energy losses in centrifugal pumps. Wang et al. (2023) observed that a judicious selection of the number of centrifugal pump blades enhances the flow pattern within the pump. Qi et al. (2023) employed a particle swarm algorithm for impeller optimization, leading to increased efficiency in centrifugal pumps. Gu et al. (2024) highlighted that trimming the rear shroud results in decreased performance of centrifugal pumps. Furthermore, cavitation exacerbates flow instability within the pump (Fecser and Lakatos, 2021) and increases energy losses (Li et al., 2023a). Cui et al. (2019) introduced an injection device to ameliorate the cavitation performance of centrifugal pumps. Jia et al. (2023) emphasized that a reduced incident angle of the sealing ring clearance diminishes flow losses in centrifugal pumps and suppresses cavitation occurrences. Ye et al. (2023) concluded that heightened friction losses on the blade surface constitute the primary factor contributing to the hump in the pump head characteristic curve. Deng et al. (2019) introduced a novel turbulence model that markedly enhances the computational precision of thrust bearings. Li et al. (2023b) proposed a transient head prediction method for mixed-flow pumps, demonstrating good agreement with experimental results. Gu et al. (2023) introduced a novel dynamic mesh simulation method to explore the impact of seal gasket fractures on the hydraulic performance of multistage centrifugal pumps. In summary, numerous factors influence the hydraulic performance of pumps, and the effects of different suction pipe structures on the hydraulic performance of ECP are inherently variable.

Unsteady flow constitutes the primary catalyst for vibration and flow-induced noise (Zeng et al., 2020; Cheng et al., 2021). Li et al. (2020) conducted an examination of the internal flow field within a mixed-flow pump, identifying a pronounced entrainment effect at the impeller inlet. Ji et al. (Leilei et al., 2021) asserted that the internal flow field, as calculated using the Wray–Agarwal turbulence model, exhibits a closer alignment with experimental results. Feng et al. (2021) observed that centrifugal pump internal flow experiences significant separation following sudden power failure, leading to increased vortices within the impeller channel. AhmedAl-Obaidi (2021) ascertained that pressure and velocity within centrifugal pumps increase proportionally with the impeller speed. Guo et al. (2022) scrutinized the flow field within an axial pump, highlighting the conspicuous influence of impeller rotation and end-wall effects. Rao et al. (Zhi et al., 2023) demonstrated that the implementation of a double-tongue volute enhances hydrostatic pressure and velocity gradients in the central region of the centrifugal pump, concurrently mitigating turbulence at the tongue under partial load conditions. In summary, the internal flow field serves as a reflection of the pump flow characteristics, and a thorough analysis of this internal flow field forms the foundational step for investigating the underlying flow mechanisms within the pump.

The generation and shedding of vortices contribute to pronounced pressure fluctuation (Li et al., 2022), exacerbating the unsteady flow within centrifugal pumps. The vortex analysis of centrifugal pumps emerges as a pivotal method for comprehensively investigating the mechanisms underlying unsteady flow phenomena (Yuan et al., 2021; Lv et al., 2022). Yasuyuki et al. (Nishi and Noji, 2020) posited a correlation between impeller-induced losses due to rotation and the distribution of vortices within the volute. Bai et al. (2022) emphasized the substantial impact of volute geometry on the evolution and formation of vortices. Vorticity, serving as a quantifier of vortex strength and fluid flow conditions, plays a crucial role in this analysis (Zhang et al., 2020). Shi et al. (2021) identified conspicuous variations in the internal flow field resulting from differing impeller tip clearances, with larger vorticity resulting from tip leakage. Introducing obstacles within the impeller channel, as demonstrated by Zhao and Guo (2021), led to a significant attenuation of vorticity. Dong et al. (2023) compared the effects of starting schemes on the internal flow field of a centrifugal pump. Ding et al. (2023) reported a substantial reduction in vorticity within the impeller after modifying the trailing edge of the blade, thereby enhancing the stability of centrifugal pumps. In the context of the suction pipe, bends and manifolds induce vortex motion, and the collision between the backflow orifice jet and inflow generates vortices, thereby intensifying flow instability. Consequently, the development of vortex analysis for ECP represents an indispensable prerequisite for the comprehensive study of flow stability.

This study conducts numerical simulations of ECP featuring diverse suction pipe structures. The accuracy of the numerical simulation results is validated through experimental verification. Subsequently, an in-depth analysis is performed to elucidate the impacts of suction pipe structure variations on the hydraulic performance and internal flow field of ECP.

2 Electric coolant pump and numerical simulation

2.1 Pump model

The design specifications for ECP include a design flow rate (Q_d) of 130 L/min, a rotational speed (n) of 5,500 rpm, a design pressure

TABLE 1 Main structural parameters of ECP.

Parameter	Symbol	Value
Impeller inlet diameter	d_1	34 mm
Impeller outlet diameter	d_2	57 mm
Impeller outlet width	b_2	7.5 mm
Number of blades	z_b	7
Volute inlet diameter	d_3	58 mm
Volute inlet width	b_3	11 mm

rise (ΔP) of 110 kPa, and a specific rotational speed ($n_q = nQ^{0.5}/(\Delta P/\rho g)^{0.75}$) of 238 rpm. Here, ρ represents the density of the coolant, considered at 358 K. ECP comprises essential components, namely, a suction pipe, an integrated system consisting of an impeller and motor rotor, a volute, a motor stator, and a PCB. The key parameters of ECP are detailed in Table 1.

This study employs a numerical simulation approach to investigate the impacts of different suction pipe structures on the hydraulic performance and internal flow field of ECP. Three designated suction pipe configurations, denoted as Case A, Case B, and Case C, are devised for examination. Case A features a straight pipe positioned directly opposite the impeller inlet, providing optimal inflow conditions, as illustrated in Figure 1A. In Case B, the suction pipe is inclined at an angle of 30° to the plane of the impeller inlet and connected through a bend, as depicted in Figure 1B. Case C extends the design by incorporating two manifolds in the foundation of Case B, with three pipes intersecting at the bend. This configuration is primarily tailored to address the cooling and heat dissipation requirements of different components simultaneously, as shown in Figure 1C. In this setup, the main pipe has a diameter of 34 mm, while Manifolds A and B have diameters of 14 mm and 12 mm, respectively.

Furthermore, a backflow orifice is strategically positioned at the impeller inlet, establishing a connection between the impeller inlet and the rear chamber through the hollow shaft. This configuration facilitates the dissipation of heat originating from the motor and PCB. The precise location of the backflow orifice is illustrated in Figure 1D.

2.2 Computational mesh

Figure 2 displays the mesh configuration for ECP. Critical hydraulic components, such as the impeller and volute, are discretized using hexahedral meshes with incorporated boundary layers. (Cui et al., 2021; Deng, 2024). Simultaneously, tetrahedral

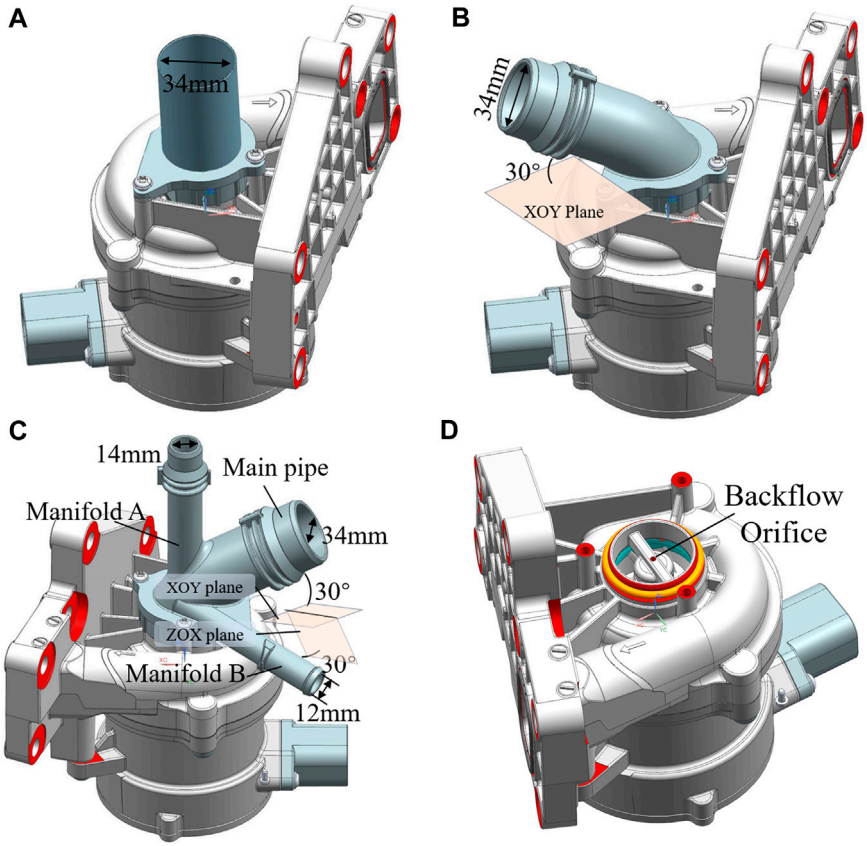

FIGURE 1
Three-dimensional model of ECP. **(A)** Case A; **(B)** Case B; **(C)** Case C; **(D)** The location of backflow orifice.

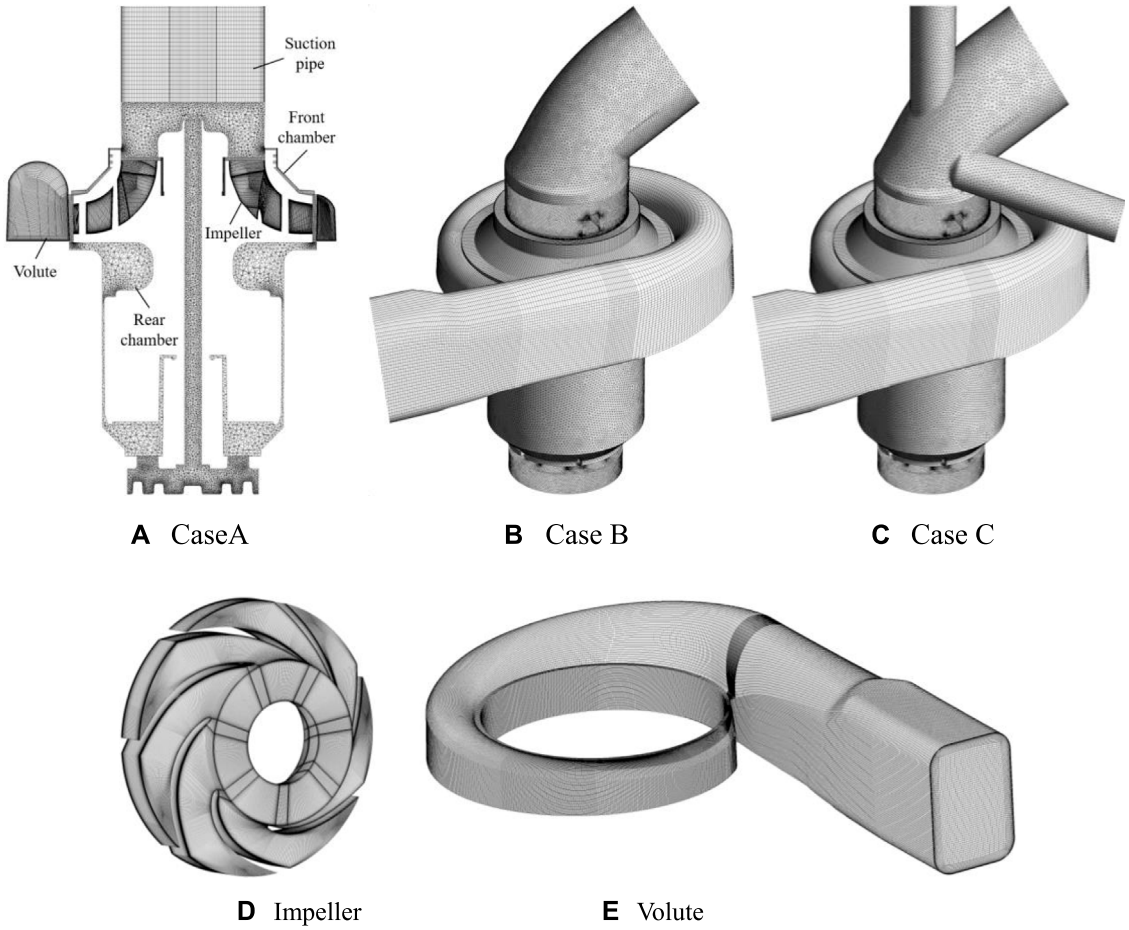

FIGURE 2
Hybrid mesh. **(A)** Case A; **(B)** Case B; **(C)** Case C; **(D)** impeller; **(E)** volute.

meshes are applied to the remaining components. This hybrid meshing approach strikes a balance between computational accuracy and meshing cost (Liu et al., 2015), rendering it well suited for the numerical simulation of intricate fluid machinery.

Figure 3 depicts the correlation between the cell number in Case A and the hydraulic performance of ECP. Six cell numbers, namely, 1.97 million, 3.39 million, 4.91 million, 6.64 million, 8.23 million, and 9.57 million, are employed in the assessment. It is observed that, at the cell number of 4.91 million, the efficiency and pressure rise exhibit a consistent trend. Hence, in light of considerations regarding computational accuracy and efficiency, a cell number of 6.64 million is selected for the numerical calculations.

2.3 Computational setup

The numerical simulations of ECP are conducted utilizing the compressible Reynolds-averaged Navier–Stokes (RANS) equations, coupled with the shear stress transport k–ω turbulence model, and incorporating temperature calculations. These simulations are carried out using Ansys CFX commercial software (Gu et al., 2022). The continuity equation and momentum equation are expressed in Eqs 1, 2:

$$\frac{\partial \rho}{\partial t} + \frac{\partial}{\partial x_i}(\rho u_i) = 0, \tag{1}$$

$$\frac{\partial}{\partial t}(\rho u_i) + \frac{\partial}{\partial x_j}(\rho u_i u_j) = -\frac{\partial p}{\partial x_i} + \frac{\partial}{\partial x_j}\left(\mu_{eff}\left(\frac{\partial u_i}{\partial x_j} + \frac{\partial u_j}{\partial x_i}\right)\right), \tag{2}$$

where t is the time, x stands for the coordinate, u represents the velocity, and p denotes the pressure.

In the energy conservation equation, the effects of pressure, dissipation, and heat source are considered as shown in Eq. 3:

$$\frac{\partial}{\partial t}(\rho C_p T) + \frac{\partial}{\partial x_j}(\rho C_p T u_j) = \frac{\partial}{\partial x_j}\left(\lambda_{eff}\frac{\partial T}{\partial x_j}\right) - \frac{\partial}{\partial x_j}(p u_j) + \Phi + S, \tag{3}$$

where T is the temperature, μ_{eff} denotes the effective viscosity, C_p is the constant pressure specific heat capacity, λ_{eff} represents the effective thermal conductivity, Φ stands for dissipation, and S is the heat source. Subscripts i and j indicate the directions.

In the setup of boundary conditions, all cases are configured with a mass flow rate inlet and a total pressure outlet set at 1.5 bar. Uniform total flow rates are maintained for all cases, with Case C distributing the flow rate based on the pipe cross-sectional area. The mass flow rate inlet coolant temperature for Cases A and B is

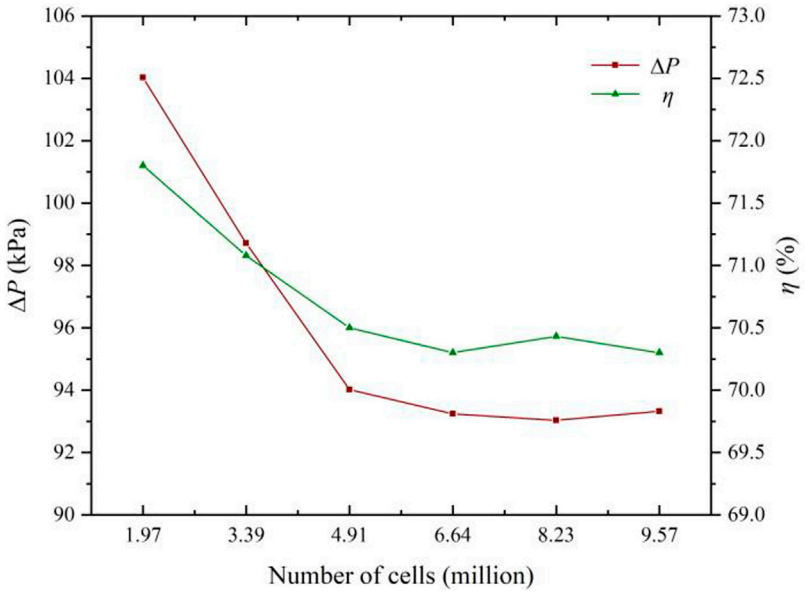

FIGURE 3
Mesh independence.

TABLE 2 Relationship between coolant properties and temperature.

Physical property	Fitting formula
ρ (kg/m^3)	$-3.569 \times 10^{-6}T^4 + 1.56 \times 10^{-3}T^3 - 0.377T^2 + 47.183T - 1256.518$
μ (kg/m/s)	$1.554 \times 10^{-7}T^2 - 1.266 \times 10^{-4}T + 0.026375$
C_p (J/kg/k)	$-7.669 \times 10^{-6}T^4 + 3.929 \times 10^{-3}T^3 - 1.14314\,T^2 + 187.3563\,T - 10743.206$
λ (W/m/k)	$3.259 \times 10^{-9}T^4 - 1.569 \times 10^{-6}T^3 + 4.242 \times 10^{-4}T^2 - 0.06047T + 3.868$

established at 358 K, while the inlet coolant temperature for the main pipe of Case C is also set to 358 K; however, for the manifolds, it is set to 398 K. The thermal flux intensities on the motor and PCB heat dissipation surfaces are specified as 16,211.5 W m^2 and 22,556.4 W m^2, respectively. The remaining walls are configured as adiabatic and non-slip. The relationship between coolant physical properties and temperature is modeled using the CFX Expression Language embedded in Ansys CFX, with the fitting equations detailed in Table 2.

The interface between the rotating and stationary components is configured as a frozen rotor for steady simulations and a transient frozen rotor for unsteady simulations. The accuracy and stability of the numerical calculations are contingent upon the Courant–Friedrichs–Lewy number, which is meticulously maintained at approximately 5 throughout the calculations (Lu et al., 2023). For unsteady calculations, the convergence residual is set at 10^{-4}, and the time step corresponds to the duration required for a 3° rotation of the impeller, totaling 6 cycles of impeller rotation. The final result used for analysis is the average of the outcomes from the last revolution of the calculation.

3 Experimental setup and validation

3.1 Experimental setup

The experimental setup for assessing the efficiency and pressure rise of ECP is illustrated in Figure 4. The experimental bench primarily comprises a test pump, an auxiliary pump, a pressure sensor, a flowmeter, a tank, a tachometer, and a wattmeter. Notably, the tank serves the purpose of heating the coolant and maintaining a constant temperature. The measurement errors for the pressure sensor, flowmeter, tachometer, and wattmeter are specified as 0.1%, 0.3%, 0.1%, and 0.1%, respectively. The pump performance characteristics are computed following the procedures outlined by Johann Friedrich Gülich (2008), and the experiment is conducted in triplicate to mitigate experimental errors and ensure result accuracy. The uncertainties associated with pressure rise and efficiency do not exceed 0.17% and 0.35%, respectively.

In the experiment, the pressure rise is computed based on the differential between inlet and outlet pressures, while the efficiency is determined using Eq. 4:

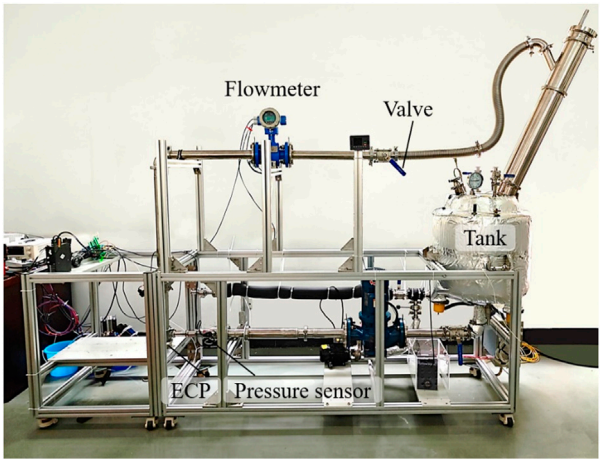

FIGURE 4
ECP test bench.

$$\eta = \frac{\Delta PQ}{P_i}, \tag{4}$$

where P_i represents the input power of the ECP rotor.

3.2 Comparisons of hydraulic performance

The pressure rise and efficiency of Case A are tested in the experiments, and the comparison of the experimental and simulation results is shown in Figure 5. Experimentally, the optimum efficiency reached 64.95%, corresponding to a pressure rise of 87.34 kPa. In numerical simulations, the highest efficiency occurs at Q_d, registering at 70.3%, with a pressure rise of 93.24 kPa. The experimentally obtained optimal efficiency is 5.35% lower than that of the numerical simulation, with the pressure rise being 0.063% lower. These disparities are attributed to external factors such as tube resistance and measurement errors influencing the experiments. However, despite the differences, the performance curve derived from the numerical simulation exhibits a congruent trend with the experimental data, affirming the accuracy of the numerical simulation method.

4 Results and discussion

4.1 Analysis of performance

The pump performance and internal flow field characteristics derived from unsteady simulation exhibit closer alignment with experimental results than those obtained through steady simulation (Kim et al., 2019). The hydraulic performance of ECP under different conditions is determined through unsteady simulation, as illustrated in Figure 6.

For equivalent flow rates, transitioning from Case A to Case C led to a significant decrease in efficiency, while the pressure rise exhibits only a marginal reduction. At $0.769Q_d$, Case A demonstrates a pressure rise of 108.1 kPa with an efficiency of 67.37%, Case B records a pressure rise of 107.94 kPa, achieving 67.1% efficiency, and Case C yields a pressure rise of 107.85 kPa with 66.53% efficiency. At Q_d, Case A exhibits a pressure rise of 93.24 kPa with an efficiency of 70.3%, Case B shows a pressure rise of 93.16 kPa with 69.42% efficiency, and Case C results in a pressure rise of 93.04 kPa with 68.68% efficiency. At $1.231Q_d$, Case A displays a pressure rise of 73.60 kPa with 67.16% efficiency, Case B presents a pressure rise of 73.45 kPa with 65.68% efficiency, and Case C showcases a pressure rise of 73.30 kPa with 63.56% efficiency.

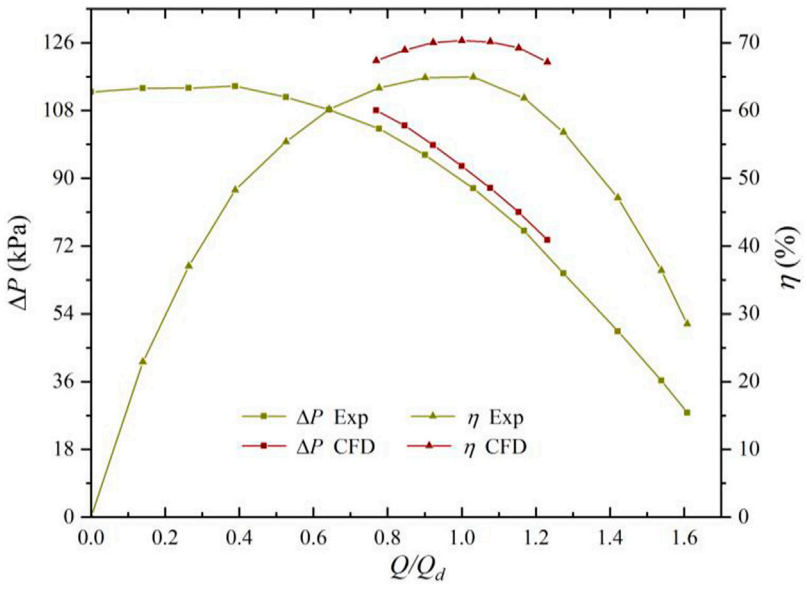

FIGURE 5
Comparison of experimental and simulation results for Case A.

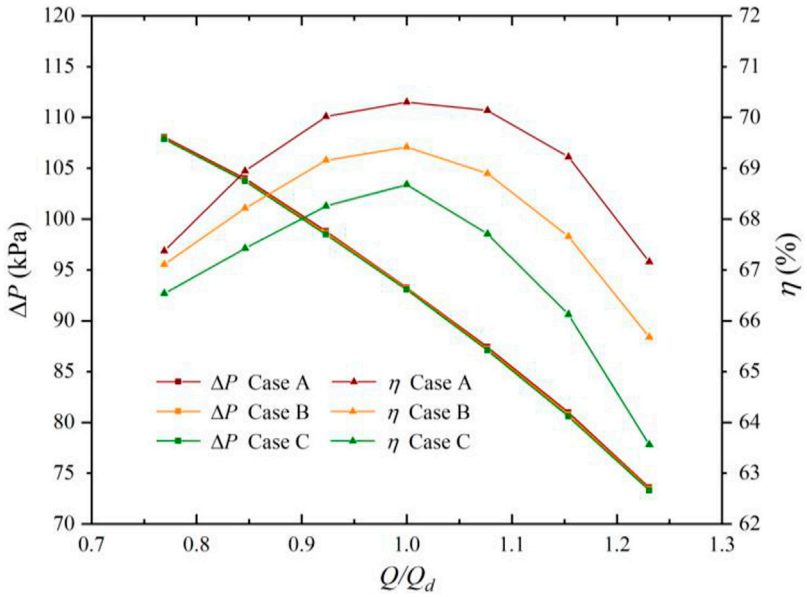

FIGURE 6
Hydraulic performance under different cases.

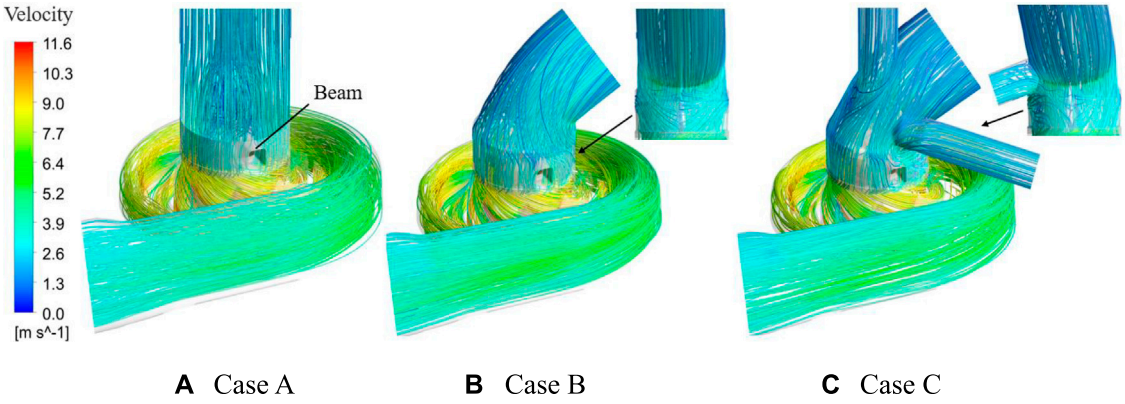

FIGURE 7
Streamlines for different cases at Q_d. **(A)** Case A; **(B)** Case B; **(C)** Case C.

On the other hand, when transitioning from Case A to Case C, efficiency experiences a more pronounced decline at elevated flow rates. Specifically, at $0.769Q_d$, Case A surpasses Cases B and C in efficiency by 0.27% and 0.84%, respectively. At Q_d, Case A exhibits higher efficiency than Cases B and C by 0.88% and 1.62%, respectively. Moreover, at $1.231Q_d$, Case A outperforms Cases B and C with superiority in efficiency of 1.48% and 3.6%, respectively.

In general, the efficiency of Cases B and C exhibits an average reduction of 1.18% and 2.13%, respectively, compared to Case A, while the pressure rise demonstrates marginal decreases of 0.0016% and 0.0032% within the studied flow rate ranges. The suction pipe structure notably impacts ECP efficiency but has almost negligible effects on pressure rise. The underlying reasons for this phenomenon will be analyzed subsequently.

4.2 Analysis of streamline

The ECP suction pipe structure plays a crucial role in influencing the flow pattern at the impeller inlet, with bends and manifolds impacting the inflow pattern and contributing to increased flow losses (Zhang and Li, 2018). The streamlines for all cases at the design flow rate are depicted in Figure 7.

In general, Case A exhibits the most favorable flow pattern, whereas Case C displays the least favorable. The cooling backflow in ECP is characterized by a pressure-driven flow, generating a jet as it exits the backflow orifice and colliding with the inflow from the suction pipe, thereby disrupting the streamlines. In Case A, the influence of the jet from the backflow orifice intertwines the streamlines in the middle of the pipe, causing a disturbance in

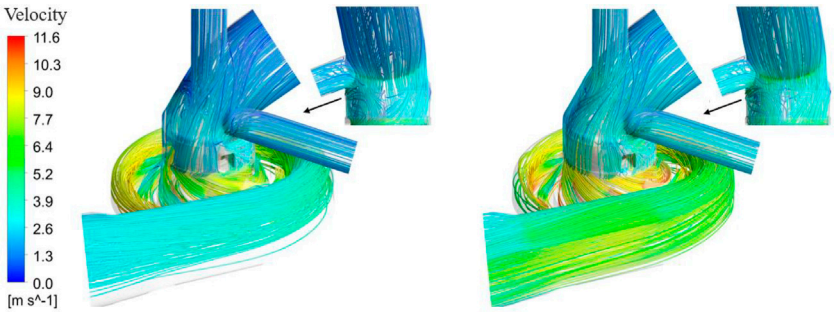

FIGURE 8
Streamlines of Case C at different flow rates. **(A)** 0.769Q_d; **(B)** 1.231Q_d.

the flow pattern. However, other zones maintain smooth and straight streamlines with a favorable flow pattern. The jet has no impact on the impeller inlet flow pattern, resulting in the highest efficiency. When the suction pipe is configured as a bend, the velocity on the outside of the bend surpasses that on the inside, creating a pressure gradient that induces secondary flow generation (Zhang et al., 2022). Simultaneously, the jet collides with the main flow, disrupting the flow pattern and increasing flow losses, leading to a reduction in the efficiency of Case B. In Case C, a circular cylinder flow manifests at the outlet of Manifold A, and the evident occurrence of flow separation is observed. The outflow from Manifold B is influenced by the inflow from the main pipe, inducing heightened disorder in the secondary flow streamlines and markedly impacting the impeller inlet flow pattern. This exerts the most substantial influence on efficiency, culminating in the lowest attainable efficiency.

The corresponding streamlines for Case C at different flow rates are shown in Figure 7C and Figure 8. The pipe streamlines are basically the same for each flow rate, but the disordered flow caused by the jet impact is not the same. The driving pressure of backflow is the pressure difference between the impeller inlet and outlet, and it is largest when the flow rate is 0.769Q_d, corresponding to the highest jet intensity, resulting in the most disordered flow pattern. In addition, as the flow rate increases, the secondary flow on the inside of the bend becomes much more serious. This is because the velocity difference between the inside and outside of the bend increases with the flow rate, and the pressure gradient becomes larger, enhancing the secondary flow.

4.3 Analysis of temperature

In this section, the influences of suction pipe structures on the temperature distribution of ECP is investigated. The temperature distribution corresponding to different suction pipe structures at Q_d is depicted in Figure 9. Due to the integration of electronic components, the PCB surface exhibits unevenness, leading to non-uniform heat dissipation. Consequently, noticeable local high temperatures are observed on PCB in each case, and the overall temperature surpasses that of the motor.

The temperature distribution on the motor heat dissipation surface is generally consistent between Cases A and B. However, in Case B, the local temperature of PCB is marginally higher than that of Case A. For Case C, the temperatures of the manifolds and main pipe differ, and they become more uniform after mixing by the impeller. Nevertheless, it still remains approximately 2.5 K higher than in the other cases, resulting in a weakening of the heat transfer effect. Consequently, the temperatures of the motor and PCB are higher.

Figure 9C and Figure 10 illustrate the temperature distribution of Case C at different flow rates. With an increase in the flow rate, the motor temperature experiences a slight rise, while the local temperature of PCB increases significantly. As the flow rate increases, the impeller inlet temperature mixing diminishes, causing the expansion of the high-temperature zones. Simultaneously, the coolant temperature in the impeller exhibits reduced mixing, leading to noticeable stratification and an overall temperature increase. Consequently, the motor temperature increases as the coolant enters the rear chamber. The reduction in heat transfer efficiency is attributed to the higher thermal flux intensity on the heat dissipating surface of PCB and the prior absorption of heat from the motor by coolant-flowing PCB, yielding a heightened temperature. Subsequently, the temperature rise is notably more pronounced in PCB in contrast to the motor. Hence, PCB is relatively more vulnerable to thermal damage. In the process of optimizing the heat dissipation of ECP, particular attention is given to the thermal management of PCB.

4.4 Analysis of vorticity

Upon analysis of Section 4.2, it is observed that a pressure gradient manifests as the fluid traverses the bend. Notably, two bundles of secondary flow exhibiting relative motion occur on the inner side of the bend, converging in the midpoint of the inner side. This convergence leads to a significant alteration in flow direction, causing a pronounced curling of streamlines and the generation of a vortex (Zuojun et al., 2016). Vorticity is employed to characterize vortex strength and can be visualized in CFD-Post (Zhang et al., 2019). In this section, the vorticity distribution is analyzed for

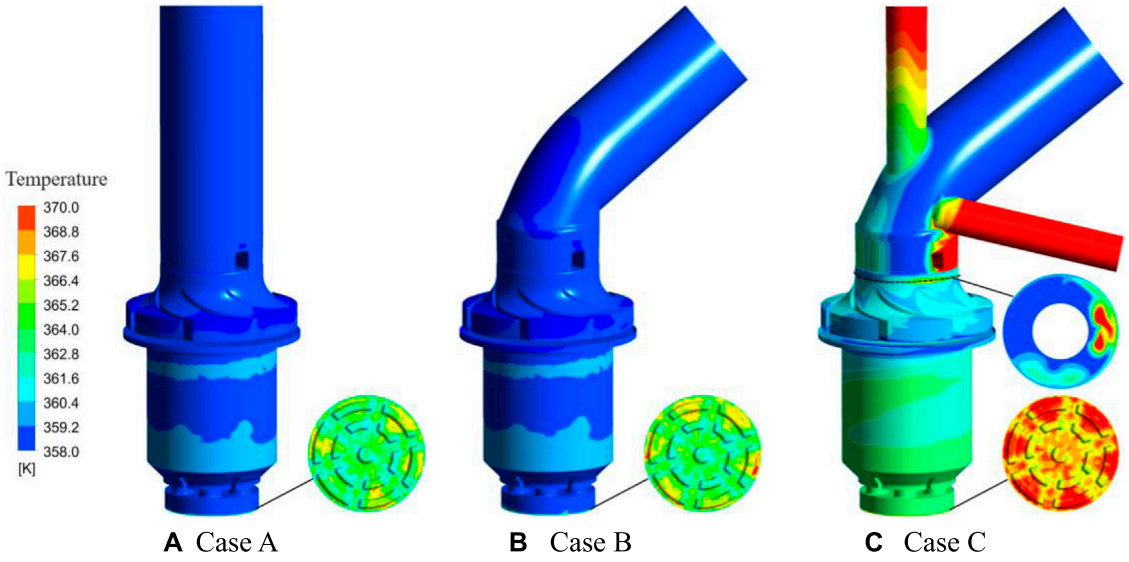

FIGURE 9
Temperature distribution for different cases at Q_d. **(A)** Case A; **(B)** Case B; **(C)** Case C.

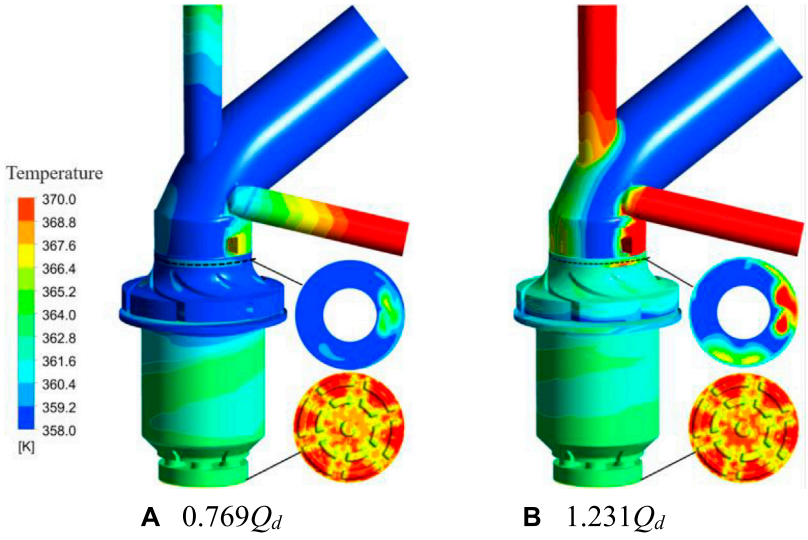

FIGURE 10
Temperature distribution of Case C at different flow rates. **(A)** 0.769Q_d; **(B)** 1.231Q_d.

different suction pipe structures. The vorticity distribution of the cross section of ECP at Q_d is illustrated in Figure 11.

The suction pipe structure significantly influences the vorticity distribution in the pump. At S_1, the backflow orifice jet collides with the main flow, creating a high-intensity vortex (Zong and Kotsonis, 2020). The high-vorticity zone is the smallest in Case A and the largest in Case C. As depicted in Figure 7, the high-vorticity zones emerge at the bend of Case B due to the secondary flow generation. In Case C, the outflow from Manifold B interacts with the inflow from the main pipe, intensifying the secondary flow and increasing the vorticity at the Manifold B outlet.

At S_2, Case A continues to exhibit the lowest vorticity. In Cases B and C, the vorticity distribution caused by the bend and jet is essentially identical. However, the outflow from Manifold B in Case C generates high-vorticity zones. Consequently, when compared, the vorticity in Case C is highest at S_2.

S_3 is situated at the impeller inlet, where the rotation of the impeller induces significant shear stresses and high-vorticity zones close to the wall. In Case A, the high-vorticity zones are uniformly distributed, slightly reduced in Case B, and minimized in Case C. In Case B, the disordered streamlines influence the impeller inlet flow pattern, resulting in an uneven vorticity

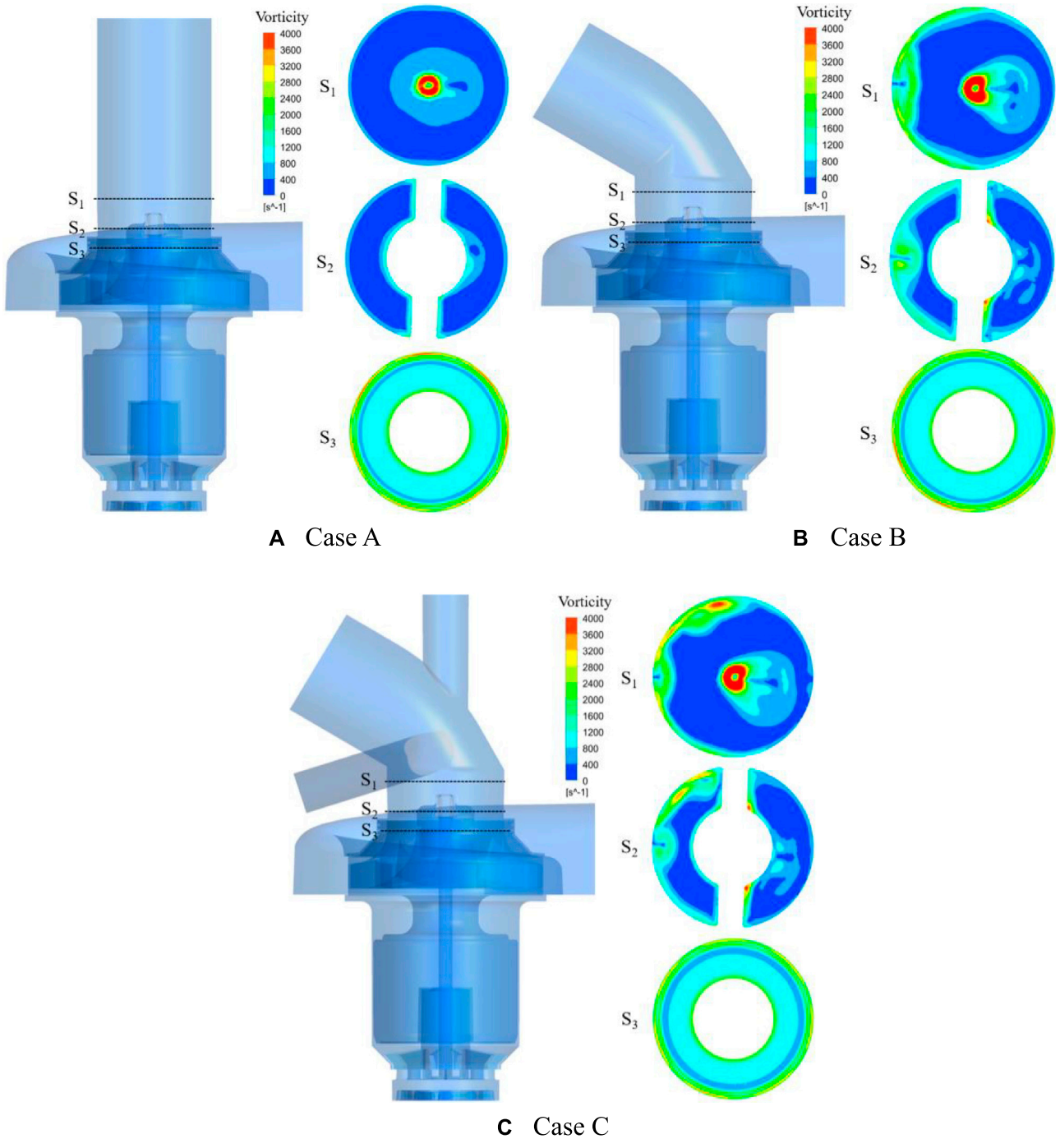

FIGURE 11
Vorticity distribution for different cases at Q_d. **(A)** Case A; **(B)** Case B; **(C)** Case C.

distribution in S_3. When compared to Case A, the coolant temperature is higher in Case C, and the decreased viscosity leads to a weakened wall shear effect, resulting in the smallest high-vorticity zones.

In summary, Case C exhibits the highest vorticity, while Case A has the lowest. The generation of vortices is frequently coupled with turbulence, leading to turbulence losses (Deng et al., 2023; Kan et al., 2023). Furthermore, the vortex introduces additional resistance and increases flow friction, contributing to reduced efficiency. Conversely, pressure rise is primarily associated with the pump geometrical parameters, explaining the significant variations in efficiencies depicted in Figure 6, while the pressure rise remains essentially constant.

Figure 11C and Figure 12 illustrate the vorticity distribution for Case C at different flow rates. With the increase in flow rates, the vorticity intensifies. Despite the diminishing intensity of the backflow

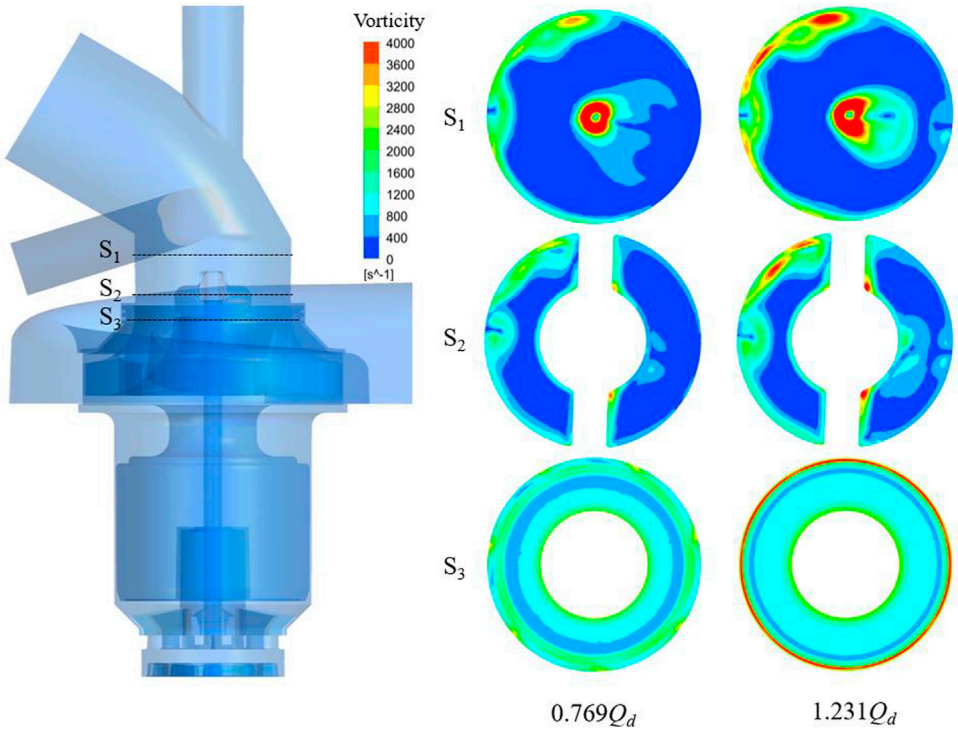

FIGURE 12
Vorticity distribution of Case C at different flow rates.

jet with increased flow rates, the augmented inflow from the pipe extends the reach of the jet influence. Concurrently, the augmentation in flow intensifies the secondary flow, resulting in an elevation of S_1 and S_2 vorticities. Analogously, the domain influenced by the shear stress induced by the rotation of the impeller inlet wall expands following the increase in flow rate, thereby causing an escalation in S_3 wall vorticity.

5 Conclusion

In this study, the effects of three suction pipe structures on the hydraulic performance, temperature distribution, flow pattern, and vorticity of ECP are examined through numerical simulations. The experimental and numerical simulation results are in good agreement. The conclusions are as follows:

(1) The suction pipe structure exerts a notable impact on the efficiency of ECP, with minimal influence on the pressure rise. Compared to Case A, the average efficiency declined by 1.18% for Case B and 2.13% for Case C. Similarly, the average pressure rise experiences a reduction of 0.002% for Case B and 0.003% for Case C.
(2) The suction pipe structure has a small effect on the heat dissipation of ECP. The uneven surface of PCB produces high localized temperatures. Coolant temperature has a significant effect on ECP heat dissipation. The motor and PCB temperatures in Case C are significantly higher than those in other cases. The motor and PCB temperatures increase slightly when the flow rate is increased.
(3) Streamlines illustrate that Case A, with a straight suction pipe, exhibits the optimal flow pattern, while Case C, incorporating manifolds, displays the least favorable flow pattern. Secondary flow is induced on the interior of the bend in Case B and is further intensified by Manifold B in Case C. The flow pattern experiences increased disorder with increasing flow rates. As the flow rate increases, the secondary flow within the bend intensifies, resulting in a more disordered flow pattern.
(4) The vorticity analysis reveals that Case A exhibits the lowest vorticity, while Case C demonstrates the highest vorticity. Higher vorticity is observed on the inside of the bend, and Manifold B further enhances the vorticity in this zone. Vorticity intensifies with an increase in the flow rate.

Data availability statement

The original contributions presented in the study are included in the article/supplementary material; further inquiries can be directed to the corresponding author.

Author contributions

AY: writing–original draft, writing–review and editing, formal analysis, investigation, and software. YG: writing–original draft, writing–review and editing, conceptualization, funding acquisition, methodology, project administration, and

supervision. LC: writing–review and editing. WZ: writing–review and editing.

Funding

The author(s) declare that financial support was received for the research, authorship, and/or publication of this article. This work was supported by the National Natural Science Foundation of China (Grant No. 52206055), Natural Science Fund for Colleges and Universities in Jiangsu Province, China (Grant No. 22KJB570005), Postdoctoral Research Fund of Jiangsu Province, China (Grant No. 2021K569C), Science and Technology Project of Yangzhou City, China (Grant No. YZ2022204), Priority Academic Program Development of Jiangsu Higher Education Institutions (PAPD).

Conflict of interest

The authors declare that the research was conducted in the absence of any commercial or financial relationships that could be construed as a potential conflict of interest.

Publisher's note

References

AhmedAl-Obaidi, R. (2021). Numerical investigation on effect of various pump rotational speeds on performance of centrifugal pump based on CFD analysis technique. *Int. J. Model. Simul. Sci. Comput.* 12 (5), 2150045. doi:10.1142/s1793962321500458

Bai, Y., Appiah, D., and Yi, T. (2022). Computational turbulent flow characteristics in a centrifugal pump. *AIP Adv.* 12 (7), 075025. doi:10.1063/5.0100915

Cheng, X., Wang, P., and Zhang, S. (2021). Correlation Research between turbulent pressure pulsation and internal sound field characteristics of centrifugal pump. *J. Therm. Sci.* 30 (1), 100–110. doi:10.1007/s11630-020-1253-y

Cui, B., Zhu, K., Zhang, Y., and Lin, P. (2019). Experimental and numerical study of the performance and cavitation flow of centrifugal pump with jetting device. *J. Mech. Sci. Technol.* 33 (10), 4843–4853. doi:10.1007/s12206-019-0925-6

Cui, D., Guo, C., Ge, Z., Liu, H., and Dong, L. (2021). Study on drag and noise reduction of bionic blade of centrifugal pump and mechanism. *J. Bionic Eng.* 18 (2), 428–440. doi:10.1007/s42235-021-0021-3

Deng, X. (2024). A mixed zero-equation and one-equation turbulence model in fluid-film thrust bearings. *Journal of Tribology* 146 (3), 034101. doi:10.1115/1.4063945

Deng, X., Harrison, G., Roger, F., and Houston, W. (2019). Methodology of turbulence parameter correction in water-lubricated thrust Bearings. *ASME. Journal Fluids Engineers* 141 (7), 071104. doi:10.1115/1.4042161

Deng, Q., Pei, Ji, Wang, W., and Sun, Ju (2023). Investigation of energy dissipation mechanism and the influence of vortical structures in a high-power double-suction centrifugal pump. *Phys. Fluids* 35 (7), 075147. doi:10.1063/5.0157770

Ding, H., Ge, F., Wang, K., and Lin, F. (2023). Influence of blade trailing-edge filing on the transient characteristics of the centrifugal pump during startup. *Processes* 11 (8), 2420. doi:10.3390/pr11082420

Dong, W., Fan, X., Dong, Y., and Fan, He (2023). Transient Internal Flow Characteristics of centrifugal pump during rapid start-up. *Iran. J. Sci. Technol. Trans. Mech. Eng.* doi:10.1007/s40997-023-00694-2

Fecser, N., and Lakatos, I. (2021). Cavitation measurement in a centrifugal pump. *Acta Polytech. Hung.* 18 (4), 63–77. doi:10.12700/aph.18.4.2021.4.4

Feng, J., Ge, Z., Zhang, Yu, Zhu, G., Wu, G., Lu, J., et al. (2021). Numerical investigation on characteristics of transient process in centrifugal pumps during power failure. *Renew. Energy* 170, 267–276. doi:10.1016/j.renene.2021.01.104

Gu, Y., Bian, J., Wang, C., Sun, H., Wang, M., and Ge, J. (2023). Transient numerical investigation on hydraulic performance and flow field of multi-stage centrifugal pump with floating impellers under sealing gasket damage condition. *Phys. Fluids* 35 (10), 107123. doi:10.1063/5.0168227

Gu, Y., Cheng, J., Wang, P., Cheng, Li, Qiaorui, Si, Wang, C., et al. (2022). A flow model for side chambers of centrifugal pumps considering radial wall shear stress. *Proc. Institution Mech. Eng. Part C J. Mech. Eng. Sci.* 236 (13), 7115–7126. doi:10.1177/09544062211073023

Gu, Y., Sun, H., Wang, C., Lu, R., Liu, B., and Ge, J. (2024). Effect of trimmed rear shroud on performance and axial thrust of multi-stage centrifugal pump with emphasis on visualizing flow losses. *J. Fluids Eng.* 146 (1), 011204. doi:10.1115/1.4063438

Guo, Y., Yang, C., Wang, Y., Lv, T., and Zhao, S. (2022). Study on inlet flow field structure and end-wall effect of axial flow pump impeller under design condition. *Energies (Basel).* 15 (14), 4969. doi:10.3390/en15144969

Jia, X., Yu, Y., Bo, Li, Wang, F., and Zhu, Z. (2023). Effects of incident angle of sealing ring clearance on internal flow and cavitation of centrifugal pump. *Proc. Institution Mech. Eng. Part E J. Process Mech. Eng.*, 095440892311696. doi:10.1177/09544089231169617

Jiang, J., Li, Y., Pei, C., Li, L., Fu, Y., Cheng, H., et al. (2019). Cavitation performance of high-speed centrifugal pump with annular jet and inducer at different temperatures and void fractions. *J. Hydrodynamics* 31, 93–101. doi:10.1007/s42241-019-0011-7

Johann Friedrich Gülich (2008). *Centrifugal pumps*. Berlin: Springer.

Kan, K., Zhao, F., Xu, H., Feng, J., Chen, H., and Liu, W. (2023). Energy performance evaluation of an axial-flow pump as turbine under conventional and reverse operating modes based on an energy loss intensity model. *Phys. Fluids* 35 (1), 015125. doi:10.1063/5.0132667

Kim, J.-H., Cho, B.-M., Kim, S., Lee, Y.-K., and Choi, Y.-S. (2019). Steady and unsteady flow characteristics of a multi-stage centrifugal pump under design and off-design conditions. *Int. J. Fluid Mach. Syst.* 12 (1), 64–70. doi:10.5293/ijfms.2019.12.1.064

Kumar Samal, S., and Moharana, M. K. (2021). Effects of inlet/outlet manifold configuration on the thermo-hydrodynamic performance of recharging microchannel heat sink. *J. Therm. Sci. Eng. Appl.* 13. doi:10.1115/1.4047940

Leilei, Ji, Li, W., Shi, W., and RameshAgarwal, K. (2021). Application of wray-agarwal turbulence model in flow simulation of a centrifugal pump with semispiral suction chamber. *J. Fluids Eng.* 143 (3), 143. doi:10.1115/1.4049050

Li, D., Zhang, N., Jiang, J., Gao, Bo, Zhou, W., Shi, J., et al. (2022). Numerical investigation on the unsteady vortical structure and pressure pulsations of a centrifugal pump with the vaned diffuser. *Int. J. Heat Fluid Flow* 98, 109050. doi:10.1016/j.ijheatfluidflow.2022.109050

Li, W., Huang, Y., Leilei, Ji, Ma, L., RameshAgarwal, K., and Awais, M. (2023b). Prediction model for energy conversion characteristics during transient processes in a mixed-flow pump. *Energy* 271, 127082. doi:10.1016/j.energy.2023.127082

Li, W., Leilei, Ji, Shi, W., Li, E., Ma, L., and Yang, Z. (2020). Particle image velocimetry experiment of the inlet flow field in a mixed-flow pump during the startup period. *Proc. Institution Mech. Eng. Part A J. Power Energy* 234 (3), 300–314. doi:10.1177/0957650919857425

Li, W., Liu, M., Leilei, Ji, Li, shuo, Song, R., Wang, C., et al. (2023a). Study on the trajectory of tip leakage vortex and energy characteristics of mixed-flow pump under cavitation conditions. *Ocean. Eng.* 267, 113225. doi:10.1016/j.oceaneng.2022.113225

Li, W., Wu, Pu, Yang, Y., Shi, W., and Li, W. (2021). Investigation of the cavitation performance in an engine cooling water pump at different temperature. *Proc. Institution Mech. Eng. Part A J. Power Energy* 235, 1094–1102. doi:10.1177/0957650920984646

Li, Z., Ding, H., Xiao, S., and Jiang, Y. (2019). Performance optimization of high specific speed centrifugal pump based on orthogonal experiment design method. *Processes* 7 (10), 728. doi:10.3390/pr7100728

Lin, Y., Li, X., Zhu, Z., Wang, X., Tong, L., and Cao, H. (2022). An energy consumption improvement method for centrifugal pump based on bionic optimization of blade trailing edge. *Energy* 246, 123323. doi:10.1016/j.energy.2022.123323

Liu, H., Liu, M., Bai, Yu, and Dong, L. (2015). Effects of mesh style and grid convergence on numerical simulation accuracy of centrifugal pump. *J. Central South Univ.* 22, 368–376. doi:10.1007/s11771-015-2531-9

Liu, S., Zhuge, W., and Zhang, Y. (2021). Numerical and experimental investigation of exhaust manifold configurations of turbo-charged diesel engines. *Proc. Institution Mech. Eng. Part A J. Power Energy* 235, 1119–1130. doi:10.1177/0957650920970307

Lu, J., Gong, Y., Li, L., Liu, X., Kan, N., Zhang, F., et al. (2023). Investigation of pressure pulsation induced by quasi-steady cavitation in a centrifugal pump. *Phys. Fluids* 35 (4), 045144. doi:10.1063/5.0135095

Lu, R., Yuan, J., Wang, L., Fu, Y., Hong, F., and Wang, W. (2021). Effect of volute tongue angle on the performance and flow unsteadiness of an automotive electronic cooling pump. *Proc. Institution Mech. Eng. Part A J. Power Energy* 235 (2), 227–241. doi:10.1177/0957650920915306

Lv, J., Xu, W., Yin, H., Zhang, Y., and Dou, H. (2022). Numerical simulation of the internal flow stability in a centrifugal pump with high specific speed at partial load. *Iran. J. Sci. Technology-Transactions Mech. Eng.* 46, 1245–1260. doi:10.1007/s40997-021-00468-8

Minocha, N., and JyeshtharajJoshi, B. (2020). 3D CFD simulation of turbulent flow distribution and pressure drop in a dividing manifold system using openfoam. *Int. J. Heat Mass Transf.* 151, 119420. doi:10.1016/j.ijheatmasstransfer.2020.119420

Nishi, Y., and Noji, T. (2020). Flow structure in casing of closed-type centrifugal pump with single blade. *Int. J. Fluid Mach. Syst.* 13 (1), 114–125. doi:10.5293/ijfms.2020.13.1.114

Qi, H., Li, W., Leilei, Ji, Liu, M., Song, R., Pan, Y., et al. (2023). Performance optimization of centrifugal pump based on particle swarm optimization and entropy generation theory. *Front. Energy Res.* 10. doi:10.3389/fenrg.2022.1094717

Shi, G., Liu, Z., Xiao, Y., Li, H., and Liu, X. (2021). Velocity characteristics in a multiphase pump under different tip clearances. *Proc. Institution Mech. Eng. Part A J. Power Energy* 235 (3), 454–475. doi:10.1177/0957650920946533

Wang, C., Chen, X., Ge, J., Cao, weidong, Zhang, qiqi, Zhu, yong, et al. (2023). Internal flow characteristics of high-specific-speed centrifugal pumps with different number of impeller blades under large flow conditions. *Machines* 11 (2), 138. doi:10.3390/machines11020138

Ye, C., Tang, Y., An, D., Wang, F., Zheng, Y., and van Esch, B. P. M. (2023). Investigation on stall characteristics of marine centrifugal pump considering transition effect. *Ocean. Eng.* 280, 114823. doi:10.1016/j.oceaneng.2023.114823

Yuan, Ye, Jin, R., Tang, L., and Lin, Y. (2022). Optimization design for the centrifugal pump under non-uniform elbow inflow based on orthogonal test and GA_PSO. *Processes* 10 (7), 1254. doi:10.3390/pr10071254

Yuan, Z., Zhang, Y., Wang, C., and Lu, B. (2021). Study on characteristics of vortex structures and irreversible losses in the centrifugal pump. *Proc. Institution Mech. Eng. Part A J. Power Energy* 235 (5), 1080–1093. doi:10.1177/0957650920983061

Zeng, G., Li, Q., Wu, P., Qian, Bo, Huang, B., Li, S., et al. (2020). Investigation of the impact of splitter blades on a low specific speed pump for fluid-induced vibration. *J. Mech. Sci. Technol.* 34 (7), 2883–2893. doi:10.1007/s12206-020-0620-7

Zhang, J., Wang, D., Wang, W., and Zhu, Z. (2022b). Numerical investigation and optimization of the flow characteristics of bend pipe with different bending angles. *Processes* 10 (8), 1510. doi:10.3390/pr10081510

Zhang, N., Jiang, J., Gao, Bo, Liu, X., and Ni, D. (2020). Numerical analysis of the vortical structure and its unsteady evolution of a centrifugal pump. *Renew. Energy* 155, 748–760. doi:10.1016/j.renene.2020.03.182

Zhang, N., Liu, X., Gao, Bo, and Xia, B. (2019). DDES analysis of the unsteady wake flow and its evolution of a centrifugal pump. *Renew. Energy* 141, 570–582. doi:10.1016/j.renene.2019.04.023

Zhang, W., and Li, A. (2018). Resistance reduction via guide vane in dividing manifold systems with parallel pipe arrays (DMS-PPA) based on analysis of energy dissipation. *Build. Environ.* 139, 189–198. doi:10.1016/j.buildenv.2018.04.010

Zhang, X., Zhao, Li, Luo, L., Fan, Y., and Du, Z. (2022a). A review on thermal management of lithium-ion batteries for electric vehicles. *Energy* 238, 121652. doi:10.1016/j.energy.2021.121652

Zhao, W., and Guo, B. (2021). Investigations on the effects of obstacles on the surfaces of blades of the centrifugal pump to suppress cavitation development. *Mod. Phys. Lett. B* 35 (20), 2150327. doi:10.1142/s0217984921503279

Zhi, R., Tang, L., and Zhang, hui (2023). Double-tongue worm shell structure on plastic centrifugal pump performance study. *Appl. Sci.* 13 (14), 8507. doi:10.3390/app13148507

Zong, H., and Kotsonis, M. (2020). Three-dimensional vortical structures generated by plasma synthetic jets in crossflow. *Phys. Fluids* 32 (6), 061701. doi:10.1063/5.0009530

Zuojun, W., Qiao, W., Liu, J., and Duan, W. (2016). Reduction of endwall secondary flow losses with leading-edge fillet in a highly loaded low-pressure turbine. *Proc. Institution Mech. Eng. Part A J. Power Energy* 230 (2), 184–195. doi:10.1177/0957650915619560

Nomenclature

Symbols

b_2	Impeller outlet width, mm
b_3	Volute inlet width, mm
C_p	Pressure specific heat capacity, J/kg/K
d_1	Impeller inlet diameter, mm
d_2	Impeller outlet diameter, mm
d_3	Volute inlet diameter, mm
n	Rotating speed of the impeller, r/min
n_q	Specific speed for pumps (p, pressure, Pa)
P_i	Input power for the rotor, W
Q	Flow rate, L/min
S	Heat source, W
T	Temperature, K
t	Time, s
u	Velocity, m/s
x	Coordinate, m
z_b	Number of blades

Greek letters

ΔP	Design pressure rise, Pa
η	Efficiency, -
λ	Thermal conductivity, W/m/K
λ_{eff}	Effective thermal conductivity, W/m/K
μ	Viscosity, Pa·s
μ_{eff}	Effective viscosity, Pa·s
ρ	Density, kg/m^3
Φ	Dissipation, W/m^3

Superscripts

-	Time-averaged component
’	Fluctuating component

Subscripts

d	At design condition
i	Free index
j, k	Dummy index

Abbreviations

ECP	Electric coolant pump
Exp	Experimental
PCB	Printed circuit board
CFD	Computational fluid dynamics

frontiers | Frontiers in Energy Research

TYPE Original Research
PUBLISHED 08 January 2024
DOI 10.3389/fenrg.2023.1346674

OPEN ACCESS

EDITED BY
Leilei Ji,
Jiangsu University, China

REVIEWED BY
Qiang Pan,
Jiangsu University, China
Haoru Zhao,
Tsinghua University, China

*CORRESPONDENCE
Songshan Chen,
yzcss08@163.com

RECEIVED 29 November 2023
ACCEPTED 19 December 2023
PUBLISHED 08 January 2024

CITATION
Zhu Y, Jiao H, Wang S, Lu Z and Chen S (2024), Impact of impeller blade count on inlet flow pattern and energy characteristics in a mixed-flow pump. *Front. Energy Res.* 11:1346674. doi: 10.3389/fenrg.2023.1346674

Impact of impeller blade count on inlet flow pattern and energy characteristics in a mixed-flow pump

Yadong Zhu[1,2], Haifeng Jiao[1], Shihui Wang[3], Zelin Lu[3] and Songshan Chen[1]*

[1]College of Electrical, Energy and Power Engineering, Yangzhou University, Yangzhou, China, [2]Yangzhou Polytechnic College, Yangzhou, China, [3]Suzhou Water Conservancy Design and Research Co., Ltd., Suzhou, China

Mixed-flow pumps, which amalgamate centrifugal and axial-flow attributes, play a pivotal role in various sectors due to their high efficiency and versatility. This paper, utilizing numerical simulation and experimental validation, addresses the critical role of impeller blade count in mixed-flow pump performance. It investigates the effect of the number of impeller blades on the energy dissipation mechanism and inlet flow pattern of a mixed-flow pump. The results reveal that dynamic and static interference effects, along with the separation vortex due to flow separation, are the main sources of energy dissipation in the pump. Under part-load and part-overload conditions, the increase in the number of blades contributes to the improvement of the flow pattern and performance but may induce more intense rotating stall effects under part-load conditions. In overload conditions, the increase in the number of blades significantly amplifies the volume of the inlet vortex structure, consequently deteriorating the inlet conditions of the impeller. This study provides valuable insights for the design and optimization of mixed-flow pumps.

KEYWORDS

mixed-flow pump, number of blades, energy characteristics, flow separation, flow pattern

1 Introduction

Mixed-flow pumps amalgamate the attributes of centrifugal pumps and axial flow pumps, exhibiting high efficiency and versatile applicability, making them extensively employed in various sectors such as water treatment, agricultural irrigation, and industrial production. The effectiveness of the fluid transfer system and energy efficiency directly hinges on the performance and operational stability of these pumps. Consequently, delving into the energy dissipation mechanisms and optimizing the hydraulic performance

Abbreviations: ∇, gradient operator; ∇^2, Laplace operator; C_ω, coefficient related to the production term; F_1, mixing function; k, turbulent kinetic energy; n_{des}, rated speed; P, production term; Q_{des}, rated flow rate; S_t, turbulent dissipation entropy production; v, fluid velocity vector; β_k, modeling constant; ρ, fluid density; σ_k, Prandtl numbers associated with turbulence kinetic energy; σ_ω, Prandtl numbers associated with specific dissipation rate; ω, turbulent vortex viscous frequency; EPR, entropy production rate; LDV, laser Doppler velocimetry; PAT, pumps used as turbines; PS, pressure side; RANS, Reynolds-Averaged Navier-Stokes; SS, suction side; VS, vortex stretching.

of mixed-flow pumps has emerged as a focal point in contemporary research within related domains (Kim et al., 2010).

With the rapid advancement of the social economy, the project's evolving demands continually elevate, placing increased demands on the performance and operational stability of mixed-flow pumps. In the pump design process, a pivotal factor is the number of impeller blades. This quantity directly impacts the cascade solidity, resulting in variations in the pump's performance and operational characteristics. Elyamin et al. (2019), employing numerical simulations, scrutinized the influence of different impeller blade numbers on centrifugal pump performance. The findings revealed that, at seven impeller blades, the pump exhibited the highest head coefficient and efficiency, coinciding with the weakest intensity of secondary flow inside the impeller. Kocaaslan et al. (2017) utilized numerical methods to dissect the correlation between the number of impeller blades and the performance of centrifugal pumps, establishing a positive relationship between head and torque with the impeller blade count. Simultaneously, Ramadhan (2019) delved into the impact of impeller blade number on cavitation characteristics in centrifugal pumps, highlighting a substantial influence on cavitation at the suction of the impeller when the blade count was 5. Yang et al. (2012) conducted a comprehensive evaluation of the number of impeller blades' effects on the performance and pressure pulsation of pumps used as turbines (PAT) through experimental and numerical studies. Their research unveiled that an augmented blade count effectively mitigates pressure pulsation intensity within the device. Al-Obaidi (2020) analyzed unsteady flow behavior in an axial pump, with a particular focus on the coupling effect of the impeller blade count. Their conclusions underscored the sensitivity of pressure, shear stress, axial velocity, radial velocity, tangential velocity, and mean pressure to the impeller blade count. It is evident that the selection of the impeller blade count significantly influences the pump's performance and operational stability. However, existing studies predominantly concentrate on the impact of impeller blade number on low specific speed pumps, with glaring gaps in research concerning mixed-flow pumps.

During operation, the pump is usually operated at off-rated conditions. Particularly at low flow rates, backflow (Alpan and Peng, 1991) may occur at the impeller inlet. The mixing of backflow with the main stream will lead to changes in the flow angle and significantly deteriorate the flow conditions of the impeller, resulting in energy dissipation, which seriously affects the performance of the device and operational stability (Bing and Cao, 2014). At the same time, existing research shows that the leading edge of the blade on the incoming medium there is a significant crowding effect, which in turn affects the impeller inlet flow and unsteady flow characteristics of the flow channel. The difference in the number of blades will inevitably change the crowding effect to a certain extent. As early as in the 1990s, Abramian et al. (1988) visualized the flow field near the leading edge of impeller blades by laser Doppler velocimetry (LDV), and effectively suppressed the backflow by setting the front perforated disk. Miyabe et al. (2009) based on experiments and numerical simulations found that the fluctuation of the performance of the device under the part-load condition was caused by the reflux of the impeller blades inlet. Based on the Reynolds time-averaged method, Kang et al. (2021) discussed the mechanism of the backflow phenomenon on the cavitation behavior and cavitation stability of a typical centrifugal pump, and concluded that the backflow is an important influence factor on the cavitation performance of the device. Immediately after that, Kang et al. (2019) investigated the effect of backflow on cavity volume and found that the generation and collapse of cavities induced by backflow is the main reason for the oscillation of cavity volume. Si et al. (2013) investigated the flow noise of centrifugal pumps under inlet backflow conditions. The flow field analysis shows that the impeller inlet under 0.7 times the design flow rate condition shows backflow, the blade passing frequency and shaft frequency dominate the spectrum of flow-induced noise. Therefore, there is a close relationship between the impeller inlet flow pattern and the performance and operational stability of the device. It is not difficult to find that the existing research mainly focuses on the inlet reflux on the device of cavitation, noise and hydraulic performance of the impact of the inlet from a variety of perspectives to analyze the inlet bad flow generation mechanism, clear with the main flow of the two-way coupling law. However, it must be recognized that, as a key parameter in pump design, the study of different impeller blade numbers on the inlet bad flow state is not yet sufficient. The induction mechanism of the number of blades on the inlet bad flow structure is not clear, and the influence law of the inlet bad flow state on the operation of the pump device under different impeller blade conditions has not been fully grasped.

This paper, based on numerical simulation and experimental validation, centers around a typical mixed-flow pump as the subject of investigation, delving into the variations in internal flow characteristics and energy performance of the device under distinct impeller blade conditions. The primary focus lies on scrutinizing unsteady flow and vortex characteristics within the impeller inlet and inlet pipe across different blade counts. The study illuminates the impact of varying blade numbers on device performance and inlet flow. This not only contributes to the theoretical understanding of internal flow in rotating machinery but also holds significant guidance for the design and optimization of mixed-flow pumps.

2 Geometric model

The focus of this paper is a representative small mixed-flow pump designed for agricultural sprinkler irrigation systems. It operates at a rated flow rate (Q_{des}) of 30 m^3/h and a rated speed (n_{des}) of 6,000 rpm. The key components of the mixed-flow pump include a closed impeller, a space diffuser, and a chamber. Figure 1 illustrates the meridional shapes of its primary overflow components. Specifically, the impeller features an outer diameter at the inlet (D_h) of 21.6 mm, an inner diameter at the inlet (D_s) of 50 mm, and an outlet width (W_o) of 13 mm. The diffuser includes an outer diameter at the outlet (D_{sd}) of 50 mm and an inner diameter at the outlet (D_{hd}) of 21.6 mm.

3 Numerical model

3.1 3D modeling

A 3D numerical model of the mixed-flow pump is established based on UG NX 12.0, as shown in Figure 2. During the model building process, parametric design is used to introduce adjustable

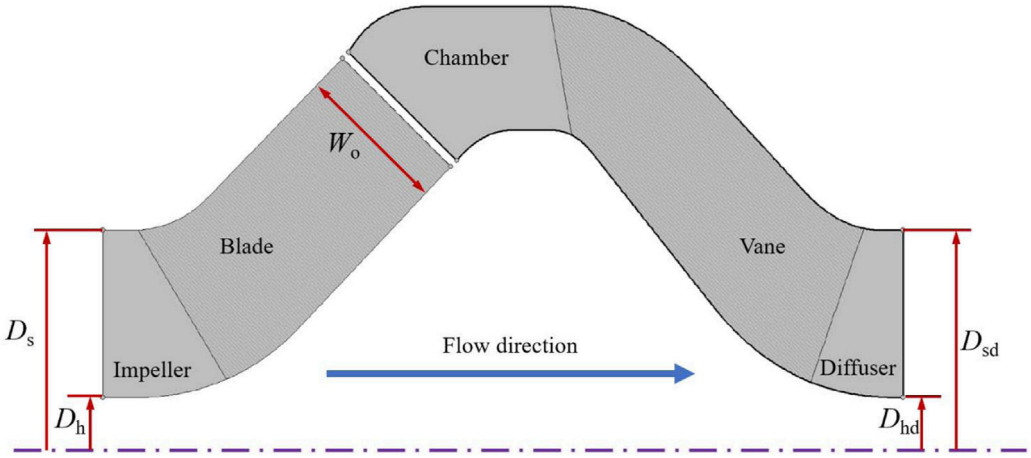

FIGURE 1
Meridian surfaces of overflow components.

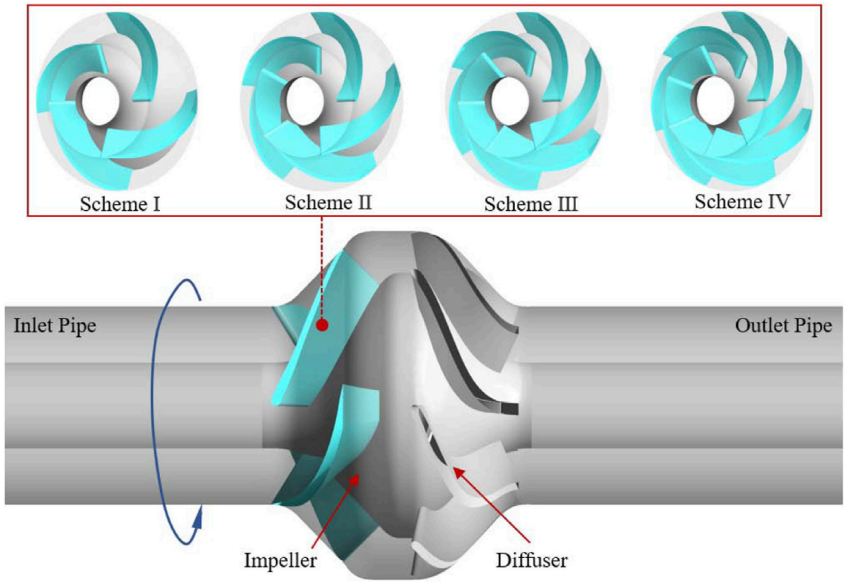

FIGURE 2
3D modeling of the mixed-flow pump.

parameters for key geometric components such as blades. This approach significantly simplifies the adjustment and modification of the 3D model, thus ensuring a high degree of consistency between the numerical model and the geometric features of the actual pump. In this study, in order to investigate the effect of different impeller blade numbers on the pump, four independent impeller schemes are set up, with impeller blade numbers of 4, 5, 6, and 7. Meanwhile, the spatial diffuser adopts the determined 7-vane scheme. It is worth mentioning that, in order to ensure the full development of turbulence and thus enhance the accuracy of the prediction results, the inlet and outlet of the model are equipped with extension pipes, the length of which is set to be 10 times the outer diameter of the impeller inlet.

3.2 Mesh and irrelevance validation

The quantity and quality of the mesh play a crucial role in numerical calculations, with good mesh quality contributing significantly to the accuracy of numerical computations. Structured meshes, characterized by regularity in geometry and topology, offer a more organized arrangement of nodes and cells. This regularity enhances the solver's access to data, making it more intuitive and efficient, thereby significantly improving the efficiency and accuracy of numerical computation. In this paper, ANSYS TurboGrid is selected for the automatic generation of structured meshes to complete the discretization of the computational domain.

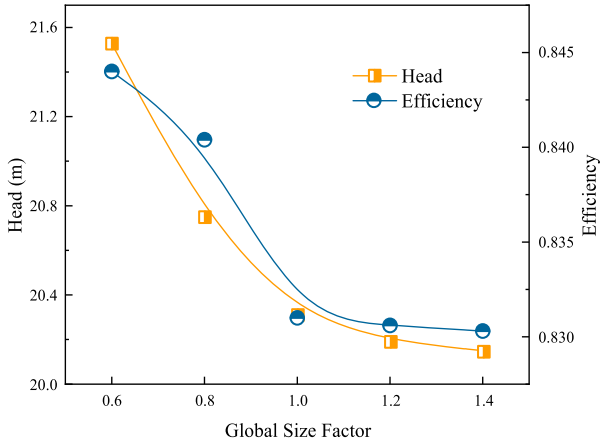

FIGURE 3
Mesh-independent analysis.

Simultaneously, to strike a balance between computational cost and accuracy, Scheme II is selected for the mesh independence analysis. In ANSYS TurboGrid, the number of meshes is globally regulated by the Global Size Factor. A larger Size Factor results in a smaller height for the first mesh layer near the wall, yielding a denser mesh. The key indices for the irrelevance test are chosen as the head and efficiency of the device, and a total of five groups of mesh schemes with varying numbers are configured. The numerical prediction results of each group of mesh schemes are given in Figure 3. From the figure, it can be seen that with the encryption of the mesh, the head and efficiency of the mixed-flow pump are gradually reduced. When Size Factor is not less than 1.2, the predicted values of head and efficiency gradually converge, and the relative fluctuation is only 0.22% and 0.04%, which can be considered that the prediction results at this time have been relatively independent of the number of meshes. Therefore, the Size Factor of the mesh used for subsequent numerical calculations in this study is 1.2, and the total number of meshes at this time is 2.36 million, and the total number of nodes is 2.18 million (excluding the extension pipe).

In addition, the velocity gradient and pressure gradient of the medium near the wall are high. In order to accurately simulate the boundary layer effect of the flow, the boundary layer mesh is encrypted accordingly. As shown in Figure 4, the mean value of y^+ on the blade surface is controlled to be around 30 to meet the requirements of numerical calculations. The final structured mesh scheme used in this numerical simulation study is shown in Figure 5.

3.3 Numerical scheme and boundary condition

Turbulence is a complex flow phenomenon characterized by kinematic structures at various scales. The direct resolution of turbulence is computationally expensive. Consequently, a turbulence model based on the Reynolds-Averaged Navier-Stokes (RANS) equations is incorporated into numerical simulations to approximate turbulence behavior at a relatively lower computational cost. With the mixing pump's rated speed reaching 6,000 rpm, the internal flow is expected to exhibit strong unsteady characteristics (Wang et al., 2023). The SST k-ω turbulence model, accounting for turbulent shear stress transport, is selected for its ability to accurately predict fluid separation under negative pressure gradient conditions. Hence, the SST k-ω turbulence model is employed to close the governing equations.

The equations for the turbulent kinetic energy k and the specific dissipation rate ω are as follows (Menter, 1994):

$$\frac{\partial(\rho k)}{\partial t}+\frac{\partial(\rho u_i k)}{\partial x_i}=P-\frac{\rho k^{1.5}}{k^{0.5}\beta_k\omega}+\frac{\partial}{\partial x_i}\left[(\mu+\sigma_k\mu_t)\frac{\partial k}{\partial x_i}\right] \quad (1)$$

$$\frac{\partial(\rho\omega)}{\partial t}+\frac{\partial(\rho u_i\omega)}{\partial x_i}=C_\omega P-\beta\rho\omega^2+\frac{\partial}{\partial x_i}\left[(\mu_l+\sigma_\omega\mu_t)\frac{\partial\omega}{\partial x_i}\right]+2(1-F_1)\frac{\rho\sigma_{\omega2}}{\omega}\frac{\partial k}{\partial x_i}\frac{\partial\omega}{\partial x_i} \quad (2)$$

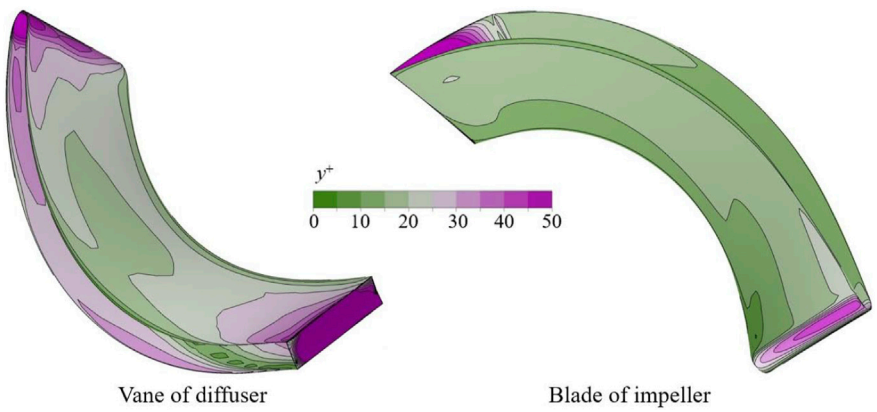

FIGURE 4
Distribution of y^+ values on the blade surface.

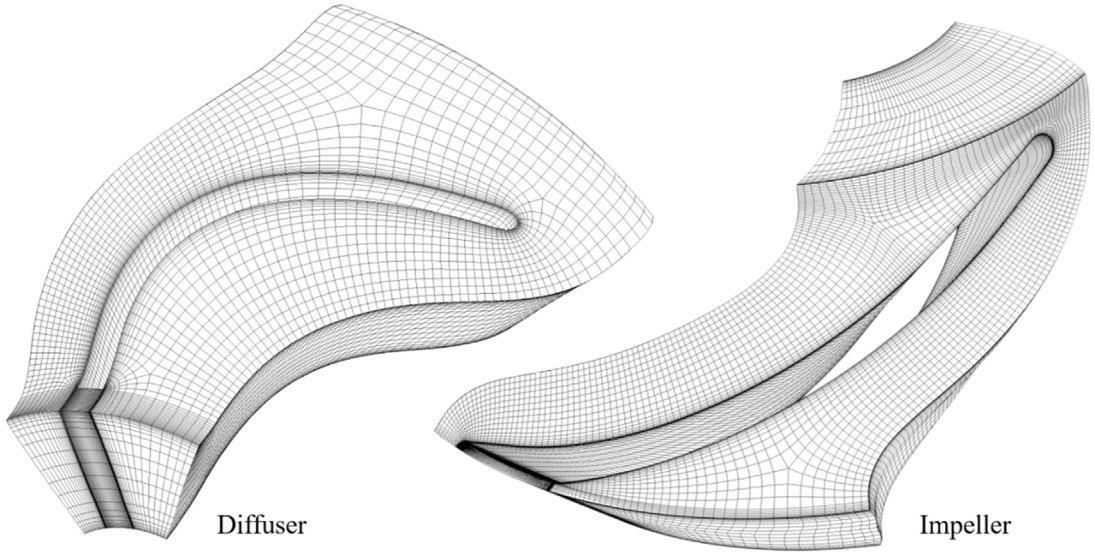

FIGURE 5
Structured meshes for the diffuser and impeller.

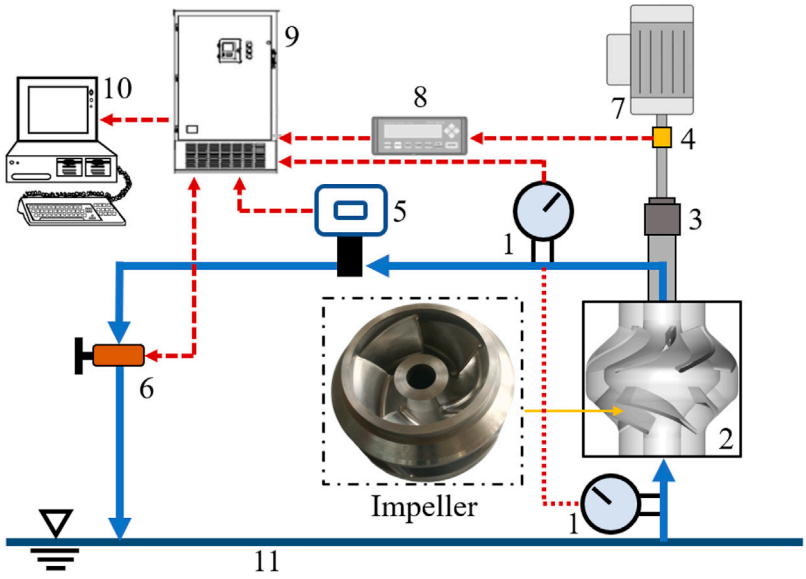

FIGURE 6
Schematic diagram of test bench. 1. Pressure transmitter 2. Pump 3. Coupling 4. Torque meter 5. Electromagnetic flowmeter 6. Solenoid valve 7. Motor 8. RPM and torque collector 9. Control and data terminal 10. Computer 11. Sink.

where ρ represents fluid density, μ_t is turbulent viscosity, P stands for the production term, C_ω is the coefficient related to the production term, F_1 denotes the mixing function, σ_k and σ_ω are the Prandtl numbers associated with turbulence kinetic energy k and specific dissipation rate ω, respectively. The modeling constant β_k is set to 0.09.

The current investigation employs ANSYS CFX for constant calculation with a reference pressure of 1 atm and a constant temperature of 25°C. To enhance numerical convergence, Total Pressure is employed as the inlet condition, with a relative pressure set to 0 Pa, and Mass Flow Rate specified for the outlet. Computational domains are interconnected through the intersection interface, wherein the interface between the rotor and stator necessitates the use of the Frozen Rotor option, with a rotation angle set to 360°. The wall surfaces are designated as no-slip, and the roughness is configured at 10 μm. The solver is set to second-order upwind, with 1,500 iteration steps and a convergence accuracy of 10^{-5}.

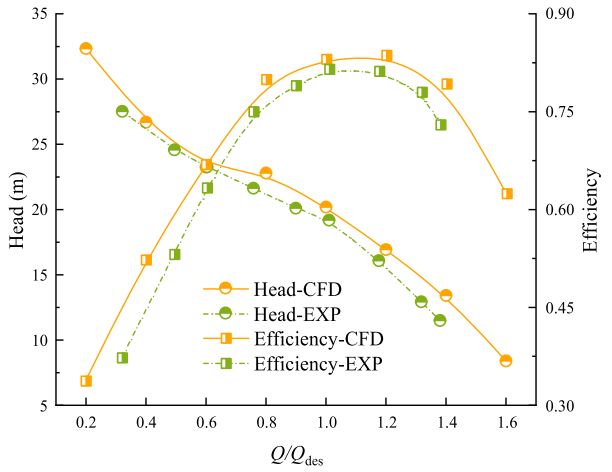

FIGURE 7
Comparison of predicted and experimental values.

4 Experimental verification

To validate the accuracy of the numerical method employed in this study, Scheme II is selected for conducting experiments on the external characteristics of the mixed-flow pump. Figure 6 illustrates the open test bench utilized in this experimental investigation. Two sets of pressure transmitters monitor the inlet and outlet pressures of the mixed-flow pump in real time, with data uploaded for head conversion. The torque meter provides real-time output of the motor's output torque and speed, uploaded to the RPM and torque collector for pump shaft power monitoring. The electromagnetic flowmeter and solenoid valve work in tandem to adjust and monitor the flow rate in real time. Data from each experimental instrument are uploaded to a computer through a control and data terminal. Except for the electromagnetic flowmeter with a precision level of 0.3, the precision level of each data sampling instrument is 0.2, ensuring the systematic error of the experiment stays within 0.5%. It is noteworthy that the impeller is fabricated from stainless steel precision casting to meet geometric and installation accuracy requirements.

Figure 7 illustrates the predicted and experimental values of the external characteristics of the mixed flow pump with Scheme II impeller. As evident from the figure, the experimental and predicted values of head and efficiency exhibit a high level of consistency with the flow rate. In general, the predicted values of head and efficiency surpass the corresponding experimental values. This phenomenon can be ascribed to the numerical simulation's limitation in accurately capturing the volumetric and mechanical losses within the pump. Additionally, the numerical calculations represent highly ideal scenarios, while practical factors such as installation precision and operational stability of the pump unit during experiments may influence the experimental results. However, the relative errors between the experimental and predicted values are 4.9% (head) and 1.5% (efficiency) under the rated flow condition, and the numerical prediction results can be considered to have high accuracy. The above numerical model and method can be used in this research work.

5 Results and analysis

5.1 Effect of blade count on performance

Figure 8 compares the hydraulic performance of mixed-flow pumps using impellers with different number of blades. From the figure, it can be seen that there is a significant effect of the number of impeller blades on the performance of the device. The head curves of Scheme III and Scheme IV closely resemble each other at part-load and rated operating conditions. However, as the flow rate continues to rise, the head of Scheme IV gradually becomes smaller than that of Scheme III, with the difference between the two increasing. Concurrently, the efficiency of Scheme IV at this

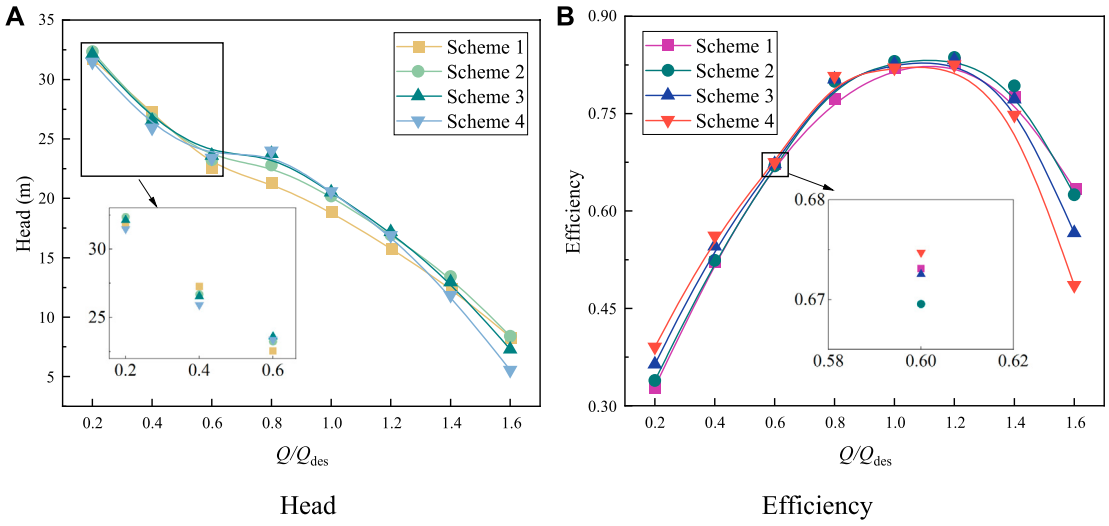

FIGURE 8
Performance of mixed-flow pumps using various sets of impeller. **(A)** Head **(B)** Efficiency.

10.3389/fenrg.2023.1346674

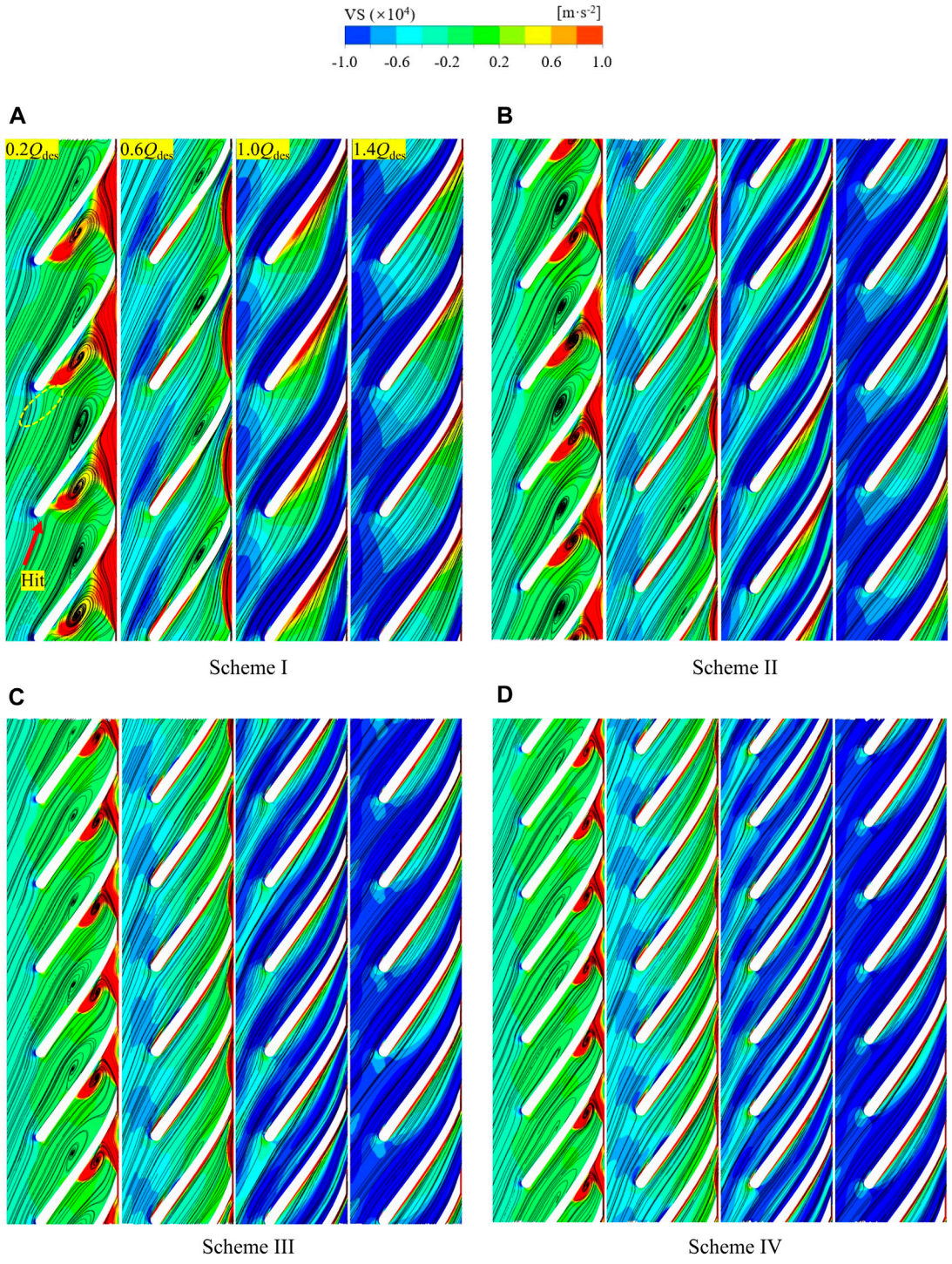

FIGURE 9
VS distribution on impeller blade-to-blade cross section (Span = 0.5). **(A)** Scheme I **(B)** Scheme II **(C)** Scheme III **(D)** Scheme IV.

juncture is notably lower than that of Scheme III. This observation indicates that under high-flow conditions, a greater number of blades may elevate resistance and friction loss in the flow path, thereby influencing the pump's performance. Nevertheless, in general, an increased number of blades has a positive impact on the hydraulic performance of the pump device during part-load and part-overload conditions. With an augmented number of blades, the cascade solidity increases, leading to a reduction in the velocity slip of the medium. The smaller velocity slip can effectively improve the flow pattern in the impeller channel and inhibit the generation of unsteady flow structures such as flow separation and secondary flow. However, observation of the flow-head curve can be found. Compared to the mixed-flow pump with fewer impeller blades,

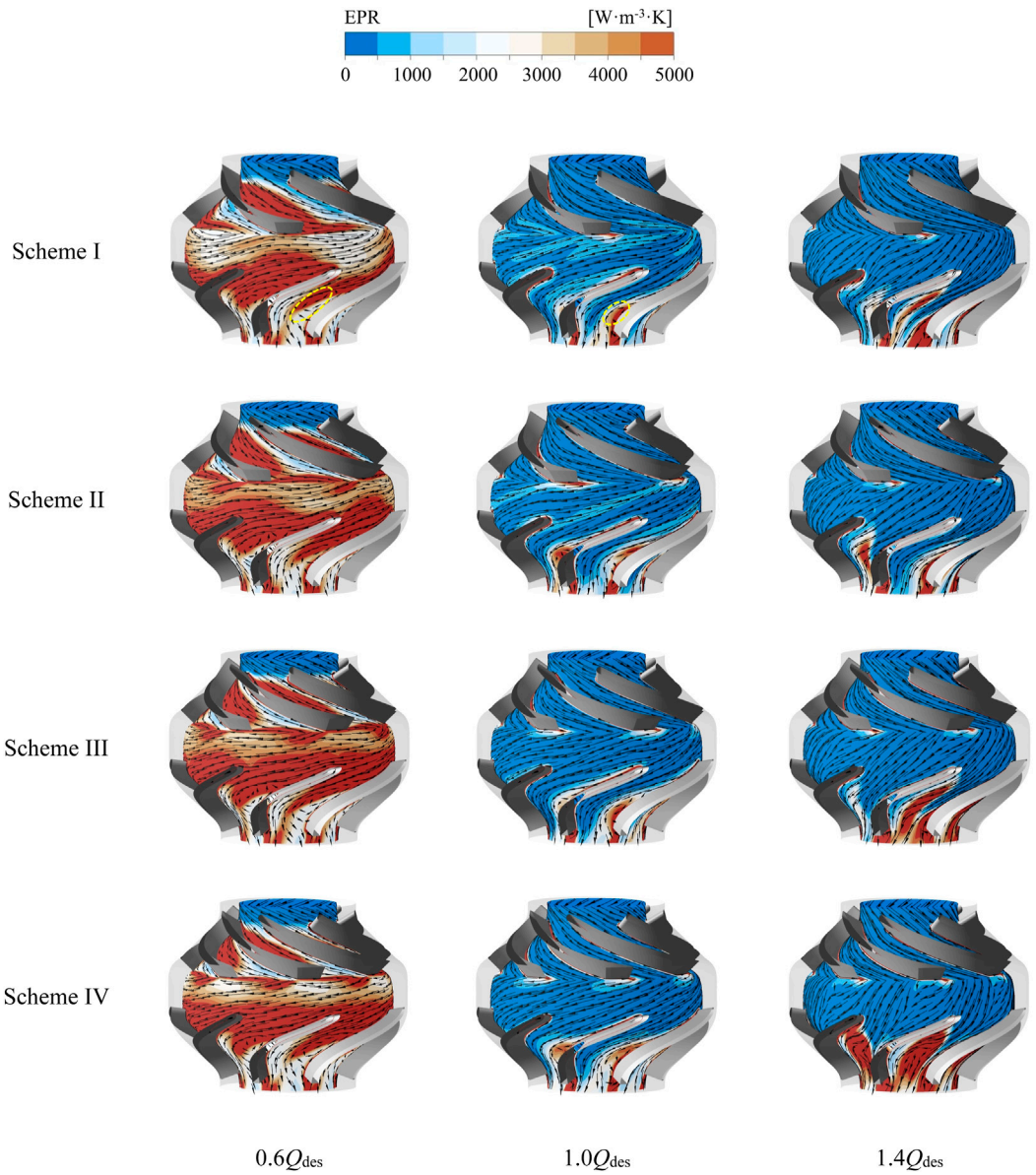

FIGURE 10
EPR distribution in mixed-flow pumps (Span = 0.5).

the rotating stall effect of the pump in the flow interval of $0.6Q_{des}$-$0.8Q_{des}$ is more significant when there are more impeller blades. This is due to the fact that a smaller number of blades will significantly enhance the impeller passability. This results in the stalled vortex clusters not being able to be retained in the flow channel, but instead propagating downstream as they are wrapped by the main flow.

5.2 Effect of blade count on flow characteristics

The vortex transport equation describes the evolution and transport of vortices in a fluid and is expressed as follows (Brown and Line, 2005):

$$\frac{d\omega}{dt} = (\omega \cdot \nabla)v - \omega(\nabla \cdot v) - 2\nabla \times (\omega \times v) + \frac{\nabla\rho_m \times \nabla p}{\rho_m^2} + v\nabla^2\omega \quad (3)$$

where $\frac{d\omega}{dt}$ represents the rate of change of vortex volume over time, while v denotes the fluid velocity vector. The symbols ∇ and ∇^2 correspond to the gradient operator and the Laplace operator, respectively. Additionally, the term $(\omega \cdot \nabla)v$ represents vortex stretching (VS), which characterizes the localized stretching or squeezing occurring within the vortex. This formulation is crucial for understanding the dynamics of vortex structures and their evolution in the fluid flow.

In order to further investigate the influence law of the number of blades on the internal flow characteristics of the mixed-flow pump, the VS distributions of the impeller with different numbers of blades in the blade-to-blade cross-section are given in Figure 9 for the filling of the surface streamlines at each flow condition. From the figure, it can be seen that at

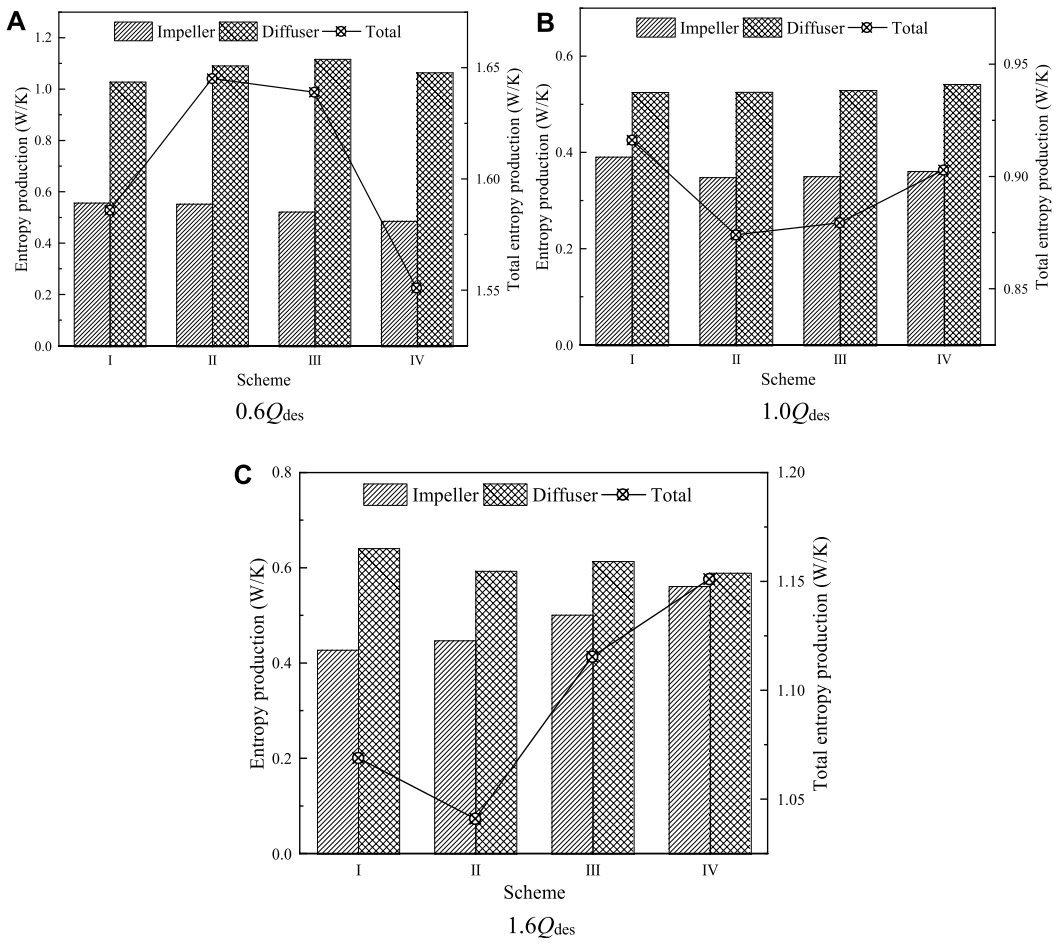

FIGURE 11
Entropy production of mixed-flow pumps at different flow conditions. **(A)** 0.6Q_{des} **(B)** 1.0Q_{des} **(C)** 1.6Q_{des}.

low flow conditions (0.2 Q_{des}), a large number of vortex structures appear in the impeller channel of Scheme I and are regularly distributed in the suction side (SS) and pressure side (PS) of the blades. As the flow rate decreases, the flow angle at the impeller inlet also decreases. Consequently, the medium directly impacts the PS of the impeller, leading to the random generation of flow separation and the promotion of separation vortices near the PS of the blade. This vortex structure gives rise to a localized high-pressure region within the flow channel, thereby increasing the pressure gradient between the PS and SS. The pressure gradient is directed from the SS to the PS, which significantly enhances the intensity of the secondary flow in the flow channel. This is the main reason for the flow separation near the SS. It can be observed that at this point, a large area of high VS appears at the impeller outlet, which is the result of the dynamic and static interference of the outflow medium in the pump chamber. With the increase of the number of blades, the impeller cascade solidity rises, which effectively suppresses the flow separation on the PS side. The separation vortex caused by the secondary flow on the SS side still exists, but the intensity is significantly weakened and shifted to the outlet.

As the flow rate increases, the inlet condition of the impeller improves, effectively suppressing all separation vortices within the flow channel. At 0.6 Q_{des}, small-scale vortex structures can still be observed on the SS of both Scheme I and Scheme II, elongated by the main flow in the direction of the blade bone line. When the number of blades is increased to Scheme III, the flow pattern inside the impeller is good in both part-load and overload condition, and no obvious vortex structure is found. In addition, the intensity of VS near the impeller outlet decays rapidly with the increase of flow rate. However, at this time, a low VS region with regular arrangement appeared on the leading-edge side of each blade of the impeller. This is related to the crowding effect of the blades on the incoming medium.

5.3 Effect of blade count on energy characteristics

The entropy production theory, derived from the second law of thermodynamics, holds significance in thermodynamics, offering a reliable method to quantify and visualize energy dissipation within rotating machines (Hou et al., 2016; Yang et al., 2023). In an independent adiabatic flow system, entropy production includes direct dissipation entropy production, turbulent dissipation entropy production, and wall entropy production, excluding thermal entropy (Ji et al., 2020). It is worth mentioning that since the RANS-based turbulence model is not able to capture the pulsating velocity information within the flow field, the turbulent dissipation entropy production S_t is computed utilizing the method proposed by Kock and Herwig (2004):

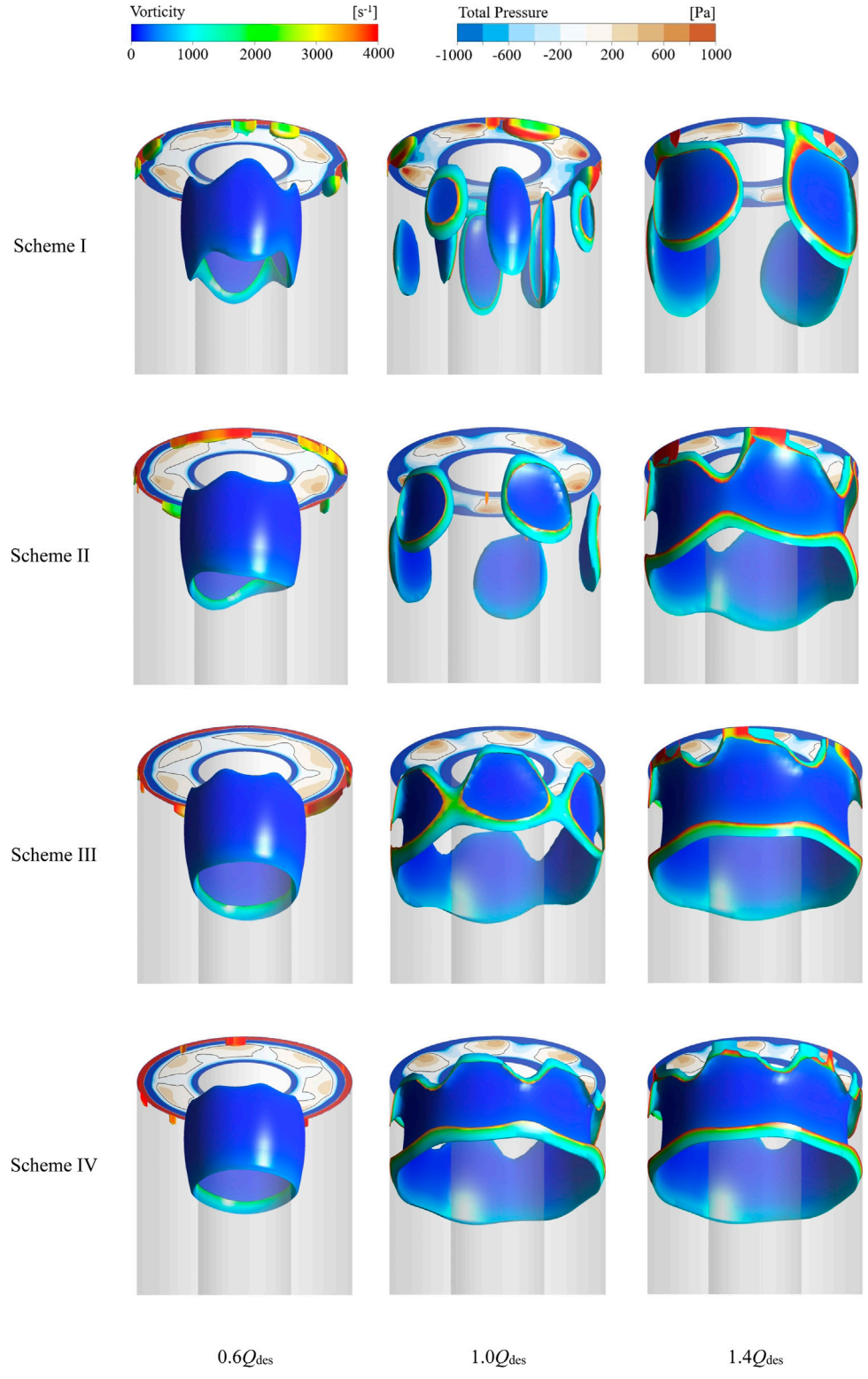

FIGURE 12
Pressure distribution with vortex structure in the inlet pipe.

$$S_t = 0.09\frac{\rho\omega k}{T} \quad (4)$$

where ρ is the fluid medium density; ω is the turbulent vortex viscous frequency; k represents the turbulent kinetic energy.

Figure 10 illustrates the distribution of entropy production rate (EPR) within the inner flow channel of the mixed-flow pump under different operating conditions. The energy dissipation characteristics are closely linked to flow conditions, with higher EPR observed in

part-load conditions for schemes with varying blade numbers. Notably, high EPR regions appear on the SS side of the impeller channel, extending from the inlet to the outlet, indicating energy dissipation due to the "jet-wake" phenomenon. Moreover, the periodic distribution of high EPR areas in the pump chamber aligns with the number of blades. It is noteworthy that a smaller number of blades is associated with a decrease in EPR at the diffuser inlet, indicating potential advantages for optimizing the match between the diffuser and the impeller discharge medium. Additionally, separation vortices near the diffuser outlet are observed during part-load conditions, and with an increase in flow rate under design conditions, the EPR inside the pump experiences a significant decrease. During this phase, the high EPR region is concentrated near the trailing edge of the blade, radiating to the pump chamber. Although the scale of the separation vortex near the diffuser outlet decreases, it remains associated with a higher EPR, affirming the applicability of the entropy production theory in visualizing energy dissipation within the pump.

With a further increase in flow, the separating vortex near the diffuser outlet disappears when the mixed-flow pump is in overload. This is related to the increase in the strength of the main flow. The higher main flow strength can inhibit the generation of flow separation to some extent. However, compared with the rated condition, although the EPR at the impeller outlet decreases in all schemes, the EPR at the diffuser outlet increases significantly. Especially in Scheme IV, the match between the medium flow angle and the inlet placement angle of the vane becomes significantly worse, and the high EPR region near the outlet of the diffuser occupies almost the whole flow channel.

It is noteworthy to mention that to obtain the comprehensive entropy production of the hydraulic system, one must conduct the relevant volume integrals within the hydraulic system for direct dissipation entropy production rate and turbulent dissipation entropy production rate, along with the corresponding area integrals for the wall entropy production rate. The integrated results are summed to obtain the total entropy production of the hydraulic system. Figure 11 provides a quantification of the entropy production for the mixed-flow pump under various flow conditions. The figure reveals that, at small flow conditions, the entropy production of the impeller decreases with an increase in the number of impeller blades. Conversely, the entropy production in the diffuser exhibits a trend of increasing and then decreasing with the number of blades, reaching its maximum value at Scheme III. During this scenario, the total entropy production of the pump is maximized at Scheme II and minimized at Scheme IV. Under design conditions, the distribution of entropy production in the primary overflow components is more uniform, and the total entropy production is minimized at Scheme II. In overload conditions, the energy dissipation of the impeller increases with the number of blades, and the total entropy production is also minimized at Scheme II.

5.4 Effect of blade count on inlet flow pattern

To explore the impact of the number of impeller blades on the inlet flow pattern of the mixed-flow pump, Figure 12 presents the pressure distribution at the impeller inlet with the vortex structure in the inlet pipe for each scheme at different flow conditions. The vortex structure is identified using the Q criterion with the level set to 0.0002 and visualized using vorticity. The figure reveals a strong correlation between the number of relative high-pressure regions in the impeller inlet and the number of impeller blades, indicating a significant crowding effect of the impeller blades on the incoming flow.

During part-load conditions, the inlet vortex primarily distributes on the inner surface of the pipe. With an increase in flow rate, the vortex structures progressively shift towards the outer pipe wall. Their volume steadily increases, and they merge, ultimately distributing on the outer surface of the pipe under overload conditions. Furthermore, the number of vortex cores corresponds to the number of blades in the separated state of the vortex structure. The substantial increase in the number of blades during design and overload conditions significantly amplifies the volume of vortex structures in the inlet pipe, adversely affecting the inlet conditions of the impeller and impacting the device's performance. This phenomenon explains the higher entropy production of the mixed-flow pump in design and overload conditions, contrasting with lower entropy production in the part-load condition, as depicted in Figure 11.

6 Conclusion

In this comprehensive study, the impact of varying the number of impeller blades on the internal flow characteristics and energy performance of a mixed-flow pump is thoroughly examined through numerical simulation and experimental validation. The key findings are summarized as follows:

1) The employed numerical method, validated through performance experiments, demonstrates high accuracy with slight overestimation (4.9% for rated head, 1.5% for efficiency) compared to experimental values. The adopted numerical scheme and SST k-ω turbulence model prove to be accurate and applicable for simulating mixed-flow pumps.
2) The study reveals that an increased number of blades under part-load and part-overload conditions enhances flow patterns and pump performance. However, a higher blade count may elevate flow resistance, particularly in the $0.6Q_{des}$-$0.8Q_{des}$ flow range, leading to a more pronounced rotating stall effect.
3) Augmenting the number of blades significantly increases cascade solidity, improving undesirable flow structures. The primary source of energy dissipation, identified as the separation vortex, decreases within the impeller under low-flow conditions with an increased number of vanes. Conversely, impeller entropy production rises with an increased number of blades under overload conditions.

In summary, this study validates the numerical method's accuracy in simulating mixed-flow pumps and highlights the impact of blade count on flow patterns, performance, and energy dissipation. While an increased number of blades enhances flow patterns and mitigates undesirable structures, careful consideration is needed to manage elevated flow resistance and potential rotating stall effects. These findings provide valuable insights for the industrial application, design, and optimization of mixed-flow pumps, emphasizing the importance of balancing blade count for optimal performance across varying operating conditions.

Data availability statement

The original contributions presented in the study are included in the article/supplementary material, further inquiries can be directed to the corresponding author.

Author contributions

YZ: Conceptualization, Methodology, Writing–original draft. HJ: Methodology, Writing–original draft. SW: Formal Analysis, Software, Writing–review and editing. ZL: Writing–review and editing. SC: Writing–review and editing.

Funding

The author(s) declare financial support was received for the research, authorship, and/or publication of this article. This research was funded by the Funding for high-end training projects for teachers' professional leaders in vocational colleges in Jiangsu Province (Grant No. 2023GRFX084).

Conflict of interest

Authors SW and ZL were employed by Ltd.

The remaining authors declare that the research was conducted in the absence of any commercial or financial relationships that could be construed as a potential conflict of interest.

Publisher's note

All claims expressed in this article are solely those of the authors and do not necessarily represent those of their affiliated organizations, or those of the publisher, the editors and the reviewers. Any product that may be evaluated in this article, or claim that may be made by its manufacturer, is not guaranteed or endorsed by the publisher.

References

Abramian, M., Howard, J. H. G., and Hermann, P. (1988). An investigation of axial pump backflow and a method for its control. *Turbo Expo Power Land, Sea, Air* 79184, V001T01A006. doi:10.1115/88-GT-31

Al-Obaidi, A. R. (2020). Investigation of the influence of various numbers of impeller blades on internal flow field analysis and the pressure pulsation of an axial pump based on transient flow behavior. *Heat. Transf.* 49 (4), 2000–2024. doi:10.1002/htj.21704

Alpan, K., and Peng, W. W. (1991). *Suction reverse flow in an axial-flow pump*. doi:10.1115/1.2926503

Bing, H., and Cao, S. (2014). Parametrization of blade leading and trailing edge positions and its influence on mixed-flow pump performance. *Proc. Institution Mech. Eng. Part C J. Mech. Eng. Sci.* 228 (4), 703–714. doi:10.1177/0954406213490104

Brown, R. E., and Line, A. J. (2005). Efficient high-resolution wake modeling using the vorticity transport equation. *AIAA J.* 43 (7), 1434–1443. doi:10.2514/1.13679

Elyamin, G. R. A., Bassily, M. A., Khalil, K. Y., and Gomaa, M. S. (2019). Effect of impeller blades number on the performance of a centrifugal pump. *Alexandria Eng. J.* 58 (1), 39–48. doi:10.1016/j.aej.2019.02.004

Hou, H., Zhang, Y., Li, Z., Jiang, T., Zhang, J., and Xu, C. (2016). Numerical analysis of entropy production on a LNG cryogenic submerged pump. *J. Nat. Gas Sci. Eng.* 36, 87–96. doi:10.1016/j.jngse.2016.10.017

Ji, L., Li, W., Shi, W., Tian, F., and Agarwal, R. (2020). Diagnosis of internal energy characteristics of mixed-flow pump within stall region based on entropy production analysis model. *Int. Commun. Heat Mass Transf.* 117, 104784. doi:10.1016/j.icheatmasstransfer.2020.104784

Kang, W., Zhou, L., Liu, D., and Wang, Z. (2021). Backflow effects on mass flow gain factor in a centrifugal pump. *Sci. Prog.* 104 (2), 003685042199886. doi:10.1177/0036850421998865

Kang, W. Z., Zhou, L. J., Wang, Z. W., and Wang, W. (2019). Analysis of backflow effect in a centrifugal pump. In IOP conference series: earth and environmental science. *IOP Publ.* 240 (3), 032007. doi:10.1088/1755-1315/240/3/032007

Kim, J. H., Ahn, H. J., and Kim, K. Y. (2010). High-efficiency design of a mixed-flow pump. *Sci. China Ser. E Technol. Sci.* 53 (1), 24–27. doi:10.1007/s11431-009-0424-6

Kocaaslan, O., Ozgoren, M., Babayigit, O., and Aksoy, M. H. (2017). Numerical investigation of the effect of number of blades on centrifugal pump performance. *AIP Publ.* 1863 (1). doi:10.1063/1.4992181

Kock, F., and Herwig, H. (2004). Local entropy production in turbulent shear flows: a high-Reynolds number model with wall functions. *Int. J. heat mass Transf.* 47 (10-11), 2205–2215. doi:10.1016/j.ijheatmasstransfer.2003.11.025

Menter, F. R. (1994). Two-equation eddy-viscosity turbulence models for engineering applications. *AIAA J.* 32 (8), 1598–1605. doi:10.2514/3.12149

Miyabe, M., Furukawa, A., Maeda, H., and Umeki, I. (2009). Investigation of internal flow and characteristic instability of a mixed flow pump. *Fluids Eng. Div. Summer Meet.* 43727, 315–321. doi:10.1115/FEDSM2009-78277

Ramadhan Al-Obaidi, A. (2019). Monitoring the performance of centrifugal pump under single-phase and cavitation condition: a CFD analysis of the number of impeller blades. *J. Appl. Fluid Mech.* 12 (2), 445–459. doi:10.29252/jafm.12.02.29303

Si, Q., Yuan, S., Yuan, J., and Liang, Y. (2013). Investigation on flow-induced noise due to backflow in low specific speed centrifugal pumps. *Adv. Mech. Eng.* 5, 109048. doi:10.1155/2013/109048

Wang, H., Yang, Y., Xi, B., Shi, W. D., Wang, C., Ji, L. L., et al. (2023). Inter-stage performance and energy characteristics analysis of electric submersible pump based on entropy production theory. *Petroleum Sci.* doi:10.1016/j.petsci.2023.10.032

Yang, S. S., Kong, F. Y., Qu, X. Y., and Jiang, W. M. (2012). Influence of blade number on the performance and pressure pulsations in a pump used as a turbine. doi:10.1115/1.4007810

Yang, Y., Wang, H., Wang, C., Zhou, L., Ji, L., Yang, Y., et al. (2023). An entropy efficiency model and its application to energy performance analysis of a multi-stage electric submersible pump. *Energy* 288, 129741. doi:10.1016/j.energy.2023.129741

frontiers | Frontiers in Energy Research

TYPE Original Research
PUBLISHED 08 January 2024
DOI 10.3389/fenrg.2023.1341289

OPEN ACCESS

EDITED BY
Mostafa S. Shadloo,
Institut National des Sciences Appliquées de Rouen, France

REVIEWED BY
Qixiang Hu,
Changzhou Institute of Technology, China
Ce An,
Lanzhou University of Technology, China
Linwei Tan,
Nantong University, China

*CORRESPONDENCE
Xiaogang Ma,
hhdxmxg@126.com

RECEIVED 20 November 2023
ACCEPTED 14 December 2023
PUBLISHED 08 January 2024

CITATION
Ma X, Yang J, Dai T, Wang J, Tang L and Yang Y (2024), Influence of the vertically arranged front injector system on the performance and operational stability of the short jet pump.
Front. Energy Res. 11:1341289.
doi: 10.3389/fenrg.2023.1341289

Influence of the vertically arranged front injector system on the performance and operational stability of the short jet pump

Xiaogang Ma[1]*, Jun Yang[1], Tingting Dai[2], Jun Wang[3], Lei Tang[4,5] and Yang Yang[3]

[1]School of Civil Engineering, North Minzu University, Yinchuan, Ningxia, China, [2]Ningxia Water Resources & Hydropower Survey Design & Research Institute Co., Ltd., Yinchuan, Ningxia, China, [3]College of Animal Science and Technology, Yangzhou University, Yangzhou, Jiangsu, China, [4]Henan Key Laboratory of Water Resources Conservation and Intensive Utilization in Yellow River Basin, North China University of Water Resources and Electric Power, Zhengzhou, Henan, China, [5]College of Water Resources, North China University of Water Resources and Electric Power, Zhengzhou, Henan, China

As the core component of a water conservancy sprinkler irrigation system, the self-priming jet pump is required not only to meet performance criteria for self-priming but also to align with the growing trend toward compactness in sprinkler irrigation systems. This paper takes the short compact self-priming jet pump as the research object whose injector is perpendicular to the main flow direction of the impeller inlet in order to reduce the volume of the jet pump and adopts the method of numerical simulation combined with experimental validation to study the effect of vertical arrangement of the injector on the hydraulic characteristics and operational instability of the self-priming jet pump. The results show that compared with the traditional hydraulic structure, the front injector leads to a significant reduction in the applicable flow range of the short jet pump. The hydraulic efficiency of the jet pump is notably inferior to that of traditional pumps across various flow conditions. This discrepancy arises from the eccentric rotation induced by the front-mounted injector, leading to pronounced circumferential asymmetry in the media flow within the individual impeller channels. Consequently, this asymmetry contributes to increased hydraulic losses in the flow channel. At the same time, the smaller overflow area within the injector enhances the turbulent flow characteristics of the medium, leading to increased instability of the subsequent flow field. This induces the generation of unwieldy low-frequency pressure pulsation signals within the flow channel, which are more readily propagated throughout the sprinkler system. In the practical application of short jet pumps, the circumferentially asymmetric distribution of the media flow in the impeller channel may result in the eccentric rotation of the rotor, thereby diminishing the service life of the pump. Furthermore, the complicated low-frequency signals will induce low-frequency vibration of the hydraulic sprinkler system, reducing the operational stability of the sprinkler system.

KEYWORDS

short-type jet pump, hydraulic performance, instream flow structure, pressure pulsation, unsteady flow

1 Introduction

A jet pump has the characteristics of a simple structure and safe and reliable operation, and it is widely used in the field of water conservancy effuser system and other fields (Xu et al., 2021; Zhang et al., 2022; Winoto et al., 2000). In order to better adapt to the diversity and complexity of the sprinkler irrigation system environment, related scholars have performed many experiments with jet pumps as research objects, with a view to revealing the hydraulic performance and internal flow structure of jet pumps and to provide data support for the application of the pumps in engineering practice (Lu et al., 2015a; Lyu et al., 2016; Aissa et al., 2021). Xu et al. (2022) observed the cavitation phenomenon in jet pumps by means of an experimental system, thus revealing two cavitation mechanisms and properties in jet pumps. Banasiak et al. (2012) conducted performance experiments on the R744 jet pumps which contain different shapes of ejectors and found that the coefficient of performance (COP) is highly dependent on the diffuser length and diameter in the ejector. Furthermore, the structure of the ejector was optimized. Xu et al. (2012) conducted performance experiments on the adjustable ejector with transcriptive CO_2 and analyzed the effect of the pressure at the high-pressure side on the pump system. The results showed that increasing the pressure on the high-pressure side was beneficial in improving the hydraulic characteristics of the pump. Pounds et al. (2013) conducted performance experiments on an injector refrigeration system under different temperature conditions in order to determine the optimum size and installation position of the nozzle. They found that although the ejector refrigeration system can achieve 1.7 times the COP, there will be a problem of critical back pressure. Long et al. (2016) performed performance experiments on a jet pump cavitation reactor at different pressure states. During the limit operation stage, a very violent cavitation phenomenon occurs in the pump, which indicates that the ejector pump has a potential application as a cavitation reactor. Lu et al. (2015b) also conducted performance experiments on a jet pump cavitation reactor at limit state; jet pump operation was also experimentally investigated, and it was found that low flow ratios produce high critical pressure ratios, giving the jet pump a greater ability to cope with the unsteady downstream flow. This provides a reference for jet pumps in realizing automatic dosing control of suction.

With the rapid development of computer technology, numerical simulation has also become one of the important means of academic research (Zhu et al., 2013; Wang et al., 2012a; Zhao et al., 2021). A comparative analysis of shear stress assessment models and Reynolds stress models was conducted by Morrall et al. (2020) The results show that the shear stress transfer analysis has higher accuracy than the Reynolds stress model at high eddy current levels. This improves the theoretical reference for subsequent numerical simulations. Haidl et al. (2021) numerically simulated the hydraulic performance of an ejector in an unstable configuration and safely predicted the minimum gas entrainment for different geometries, orientations, and operating conditions, which provided a theoretical reference for the operation of a conventional liquid–air ejector pump. Shah et al. (2011) numerically simulated a steam jet pump using the direct-contact condensation model in FLUENT to investigate its performance when pumping water using saturated steam. The results show that the mass ratio increases with an increase in steam pressure at constant suction pressure. This provides a theoretical basis for the practical application of jet pumps. Wang et al. (2012b) also used numerical simulation to investigate the internal flow law of steam jet pumps and proposed a wet steam model for transonic flow and found that there is spontaneous condensation when the supersonic flow passes through the nozzle. Kwon et al. (2002) discussed the effect of the mixing chamber shape on the hydraulic characteristics of jet pumps at different jet velocities based on a two-dimensional numerical simulation. The effect of the hydraulic characteristics of the jet pump is discussed, and the optimal mixing chamber structural parameters are derived. Deng et al. (2017) investigated the modified jet pump by numerical simulation and found that self-introduced oscillations cause successive rupture and the formation of liquid–gas interfaces, and the phenomenon is characterized by periodicity. The results of this study help understand the flow pattern within the liquid–air jet pump and, thus, improve the unsteady operation of the pump.

Based on the above study, it was found that although the flow direction of the medium within the traditional jet pump system is the same as that of the impeller inlet medium, there are still problems with its hydraulic performance and operational stability (Saker and Hassan, 2013; Sharifi, 2020; Wang et al., 2019). In order to meet the requirements of limited installation space in engineering practice, a more compact structure, a smaller size of the short section, of the jet pump was proposed (Yang et al., 2023; Yu et al., 2023). The jet pump positions the ejector structure perpendicular to the impeller, significantly reducing the overall footprint of the jet pump. This design is particularly advantageous for adapting to the intricate and variable conditions present in water conservancy sprinkler irrigation environments. However, in cases where the direction of media flow within the jet pump system diverges from that within the impeller, there is a heightened risk of inducing unstable flow within the pump. Therefore, this paper concentrates on a typical short-type jet pump, examining the impact of the vertically oriented injector

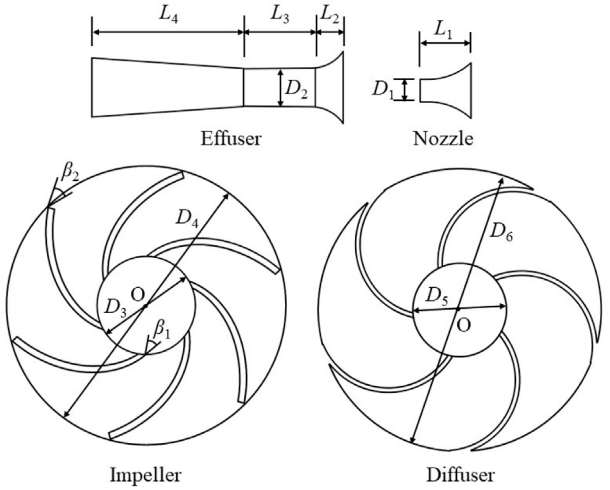

FIGURE 1
Schematic diagram of the main dimensions of a short jet pump.

TABLE 1 Geometric specifications of the impeller and the diffuser.

Nozzle		Impeller	
		Number of blades	$Z = 6$
Nozzle length	L_1 = 22 mm	Inlet diameter	D_3 = 47.5 mm
Outlet diameter	D_1 = 9.2 mm	Outlet diameter	D_4 = 129.5 mm
Effuser		Blade inlet angle	$\beta_1 = 36^\circ$
		Blade outlet angle	$B_2 = 37.5^\circ$
Throat diameter	D_2 = 15 mm	Diffuser	
Inlet area length	L_2 = 12.5 mm	Number of vanes	$Z = 5$
Throat length	L_3 = 25 mm	Inlet diameter	D_5 = 53 mm
Diffuser tube length	L_4 = 62 mm	Outlet diameter	D_6 = 160 mm

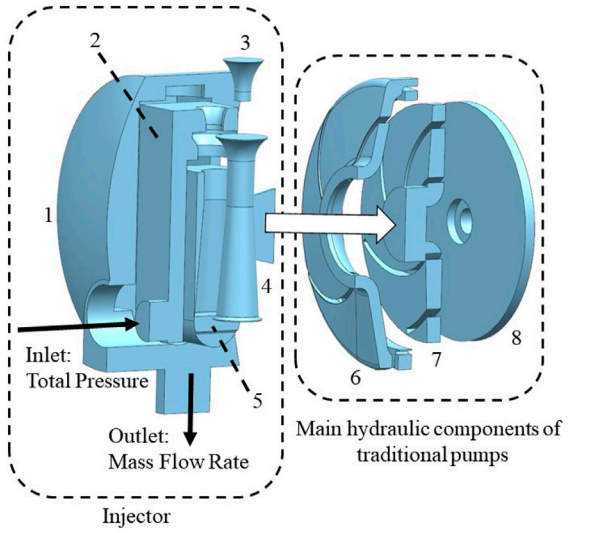

1: Front chamber; 2: Injector front chamber; 3: Nozzle; 4: Effuser; 5: Injector rear chamber; 6: Diffuser; 7: Impeller; 8: Rear chamber

FIGURE 2
3D model of the short-type jet pump.

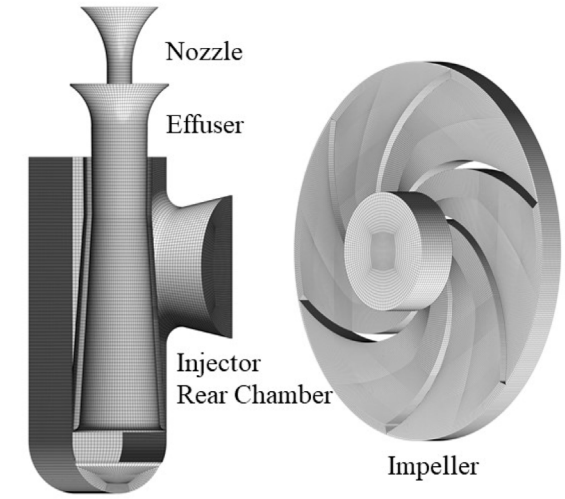

FIGURE 3
Partial computational domain grid of the jet pump.

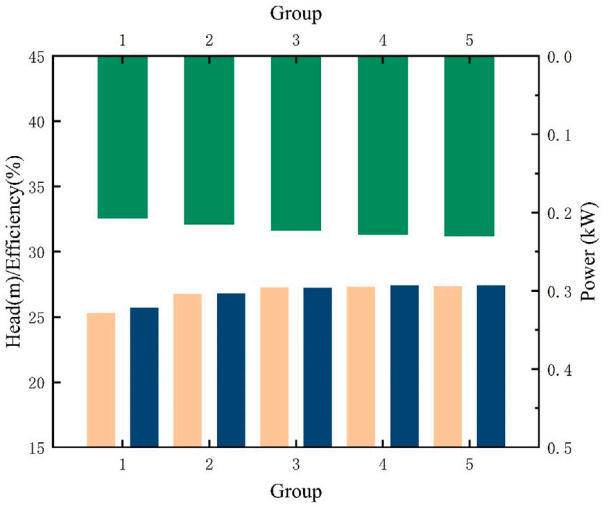

FIGURE 4
Grid irrelevance analysis.

structure on the hydraulic characteristics and internal flow state of the jet pump.

2 Geometry and parameters

This paper adopts a JET1100 short-type jet pump as the research object, which utilizes an effuser to eject the high-pressure medium to form the negative pressure of the jet, so as to suck the air into the nozzle, thus realizing the self-priming function of the pump. The short jet pump mainly includes an effuser, nozzle, impeller, and diffuser and other structures shown in Figure 1, and its main structural parameters are shown in Table 1. Under the rated flow condition, its hydraulic parameters are as follows: a flow rate of 3 m^3/h, head of 28 m, and speed of 2,850 r/min.

3 Numerical simulation

3.1 3D model

This paper employs the "point-line-surface" method for the 3D modeling of the short jet pump, as illustrated in Figure 2. Diverging from the conventional jet pump design, the independent injector structure is vertically fixed at the impeller inlet. This configuration

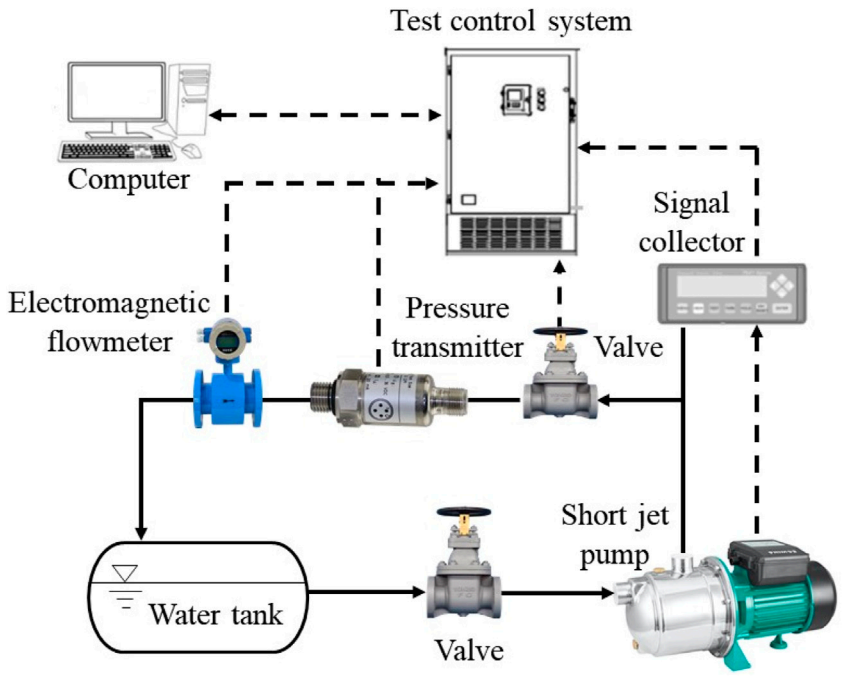

FIGURE 5
Schematic diagram of the test bench.

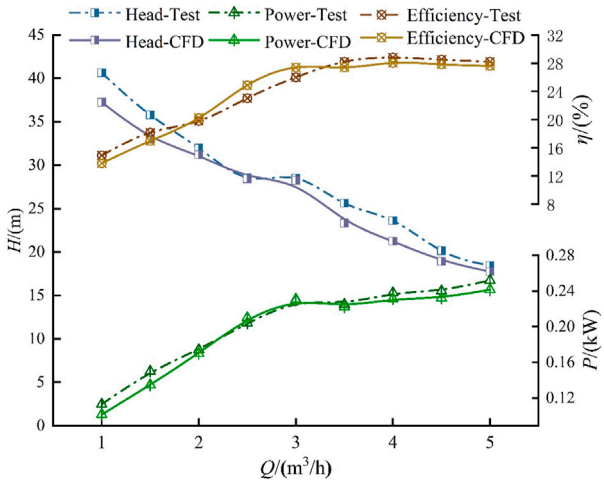

FIGURE 6
Comparison between numerical simulation results and test results.

contributes to the compactness of the jet pump, minimizing its overall size.

3.2 Grid division and irrelevance analysis

In order to improve the efficiency of numerical computation, this paper adopts ICEM software to carry out structured grid delineation of the main overflow components and irrelevance analysis of the mesh number of the impeller and effuser. Part of the computational domain grid is shown in Figure 3. In this paper, five groups of grids are mainly selected for the irrelevance discussion, and the grid numbers are 43,000, 150,000, 442,000, 1,019,000, and 1,473,000. As depicted in Figure 4, an increase in the number of grids results in a gradual reduction in the magnitude of changes observed in head, efficiency, and power. Specifically, when the number of grids reaches 1.019 million in group 4, the growth rate in head, efficiency, and power is less than 0.1%. This suggests that the number of grids in group 4 is economically viable. Consequently, all subsequent numerical simulations in this paper will employ the grid size of group 4.

3.3 Boundary condition setting

In this paper, ANSYS CFX software is used to numerically simulate the computational domain. Pressure inlet with a mass flow outlet is used. The impeller is set as the rotating domain, and other parts are set as the stationary domain. All the intersection interfaces are connected by GGI. Among them, the cross-interface related to the impeller is set as the frozen rotor, and the other cross-interfaces are set as general connection. The residual of the control equation is set as 10^{-4}. For the non-stationary calculation, it is chosen to calculate one step for every 3° rotation of the impeller and 20 iterations for each step. Therefore, the set time step is 1.75×10^{-4}, and the total time is 0.168 s. The standard k-ε turbulence model is used for both stationary and non-stationary calculations in this paper.

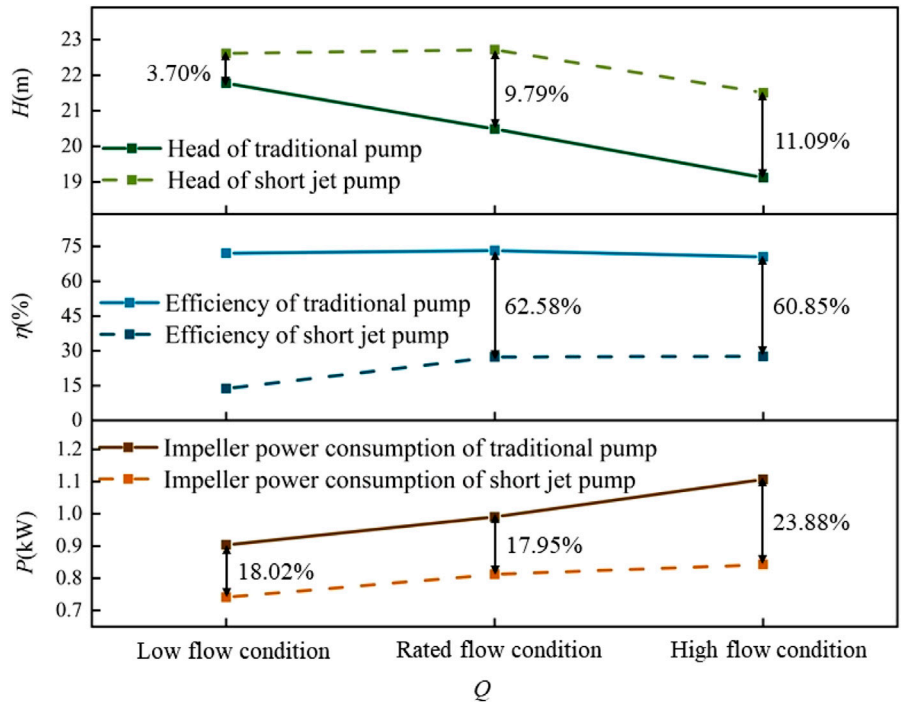

FIGURE 7
Comparison of the hydraulic performance of the two pump types under different flow conditions.

The turbulent kinetic energy k and dissipation rate equations are shown as follows:

$$\frac{\partial(\rho k)}{\partial t} + \nabla \cdot (\rho U k) = \nabla \cdot \left[\left(\mu + \frac{\mu_t}{\sigma_k}\right)\nabla k\right] + P_k + P_b - \rho\varepsilon + S_k, \quad (1)$$

$$\frac{\partial(\rho\varepsilon)}{\partial t} + \nabla \cdot (\rho U \varepsilon) = \nabla \cdot \left[\left(\mu + \frac{\mu_t}{\sigma_\varepsilon}\right)\nabla \varepsilon\right] + C_1\frac{\varepsilon}{K}(P_k + C_3 G_b) - C_2\rho\frac{\varepsilon^2}{k} + S_\varepsilon, \quad (2)$$

where P_k is the turbulent kinetic energy generated by the mean velocity gradient (J); P_b indicates the turbulence kinetic energy generated by buoyancy (J); σ_k and σ_ε are the Prandtl numbers of k and ε, respectively; S_k and S_ε are user-defined; C_1, C_2, C_3, and C_μ are constants; and μ_t is the turbulent viscosity (mPa-s).

Unlike other turbulence models, the damping function is used in the ANSYS CFD solver, which enables more accurate prediction of the turbulent motion near the wall. Furthermore, the standard k–ε turbulence model is economical and robust (Launder and Sharma, 1974; Launder and Spalding, 1983).

4 Test verification

In order to verify the accuracy of the numerical simulation results in this paper, a performance test was conducted on the short-type jet pump, and the test process is shown in Figure 5. As shown in the figure, when the short-type jet self-priming pump is running, the pressure transmitter and electromagnetic flow meter are used to monitor and record the pressure and flow data of the test process, respectively. The sensors transmit the collected data to the test control system, and the computer connected to the control system processes the data and provides real-time feedback.

The comparison between the numerical simulation results and the test results for different flow conditions is shown in Figure 6. As shown in the figure, the experimental and numerical simulation values of efficiency and power increase with the increase in the flow rate, while the experimental and numerical simulation values of head decrease with the increase in the flow rate. At full flow conditions, both results have the same trend. In the off-rated flow conditions, the head and power test results and numerical simulation results deviate more. This is due to the fact that the jet pump contains an independent injector structure, which enhances the transient characteristics of the pump, and the steady-state numerical simulation results cannot better capture the transient changes in pump performance. Nevertheless, at the rated flow condition, the numerical simulation results for head, efficiency, and power exhibit a marginal variance of only 0.9%, 1.2%, and 0.3%, respectively, when compared to their corresponding experimental results. This indicates that the numerical simulation method used in this study demonstrates a high level of accuracy.

5 Analysis of results

Figure 7 shows a comparison of the hydraulic performance of the short jet pump and the traditional pump (without a built-in ejector) under different flow conditions. As shown in the figure, with the increase in the flow rate, the head of both the traditional pump and the short jet pump gradually decreased, and the impeller power

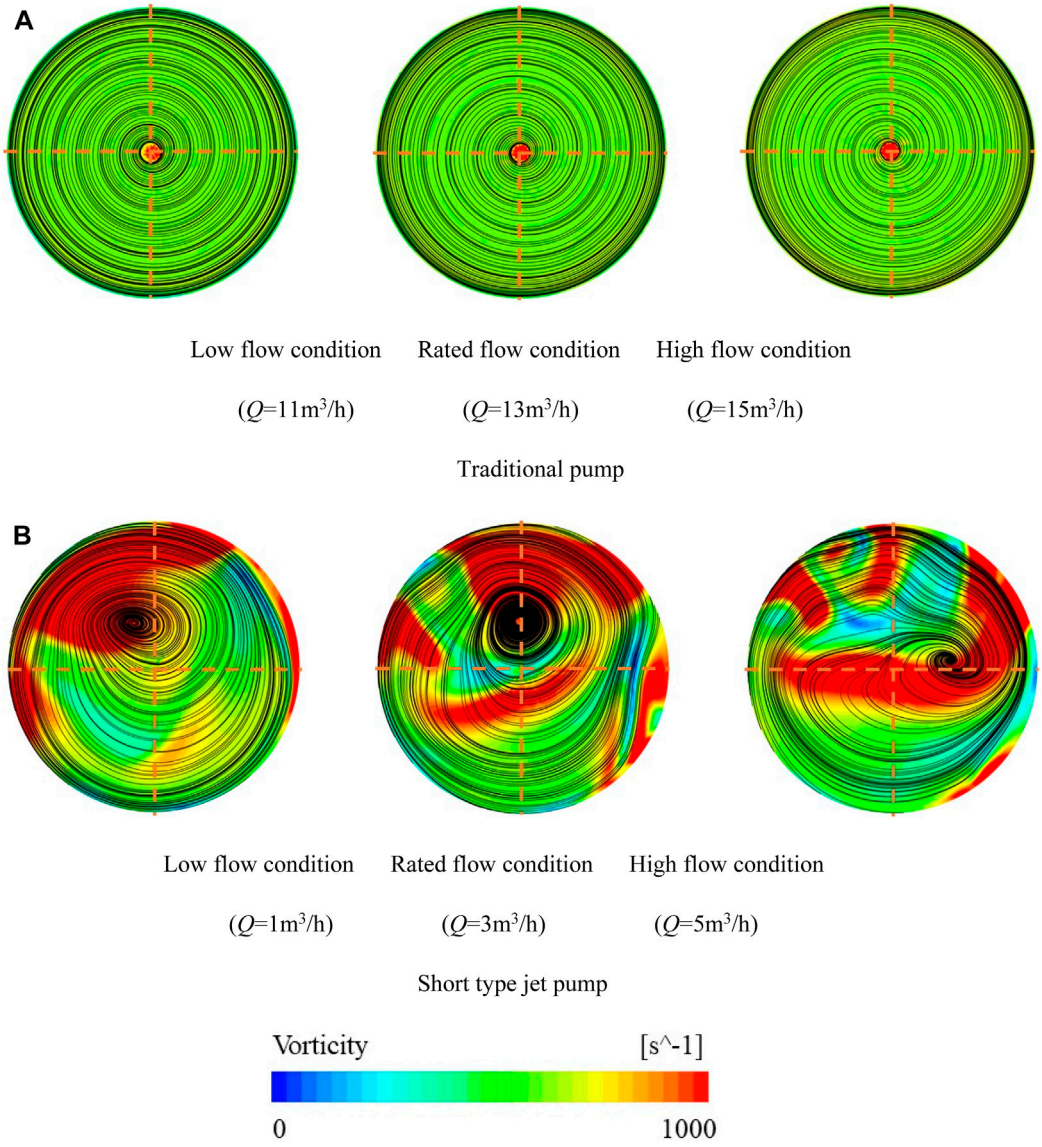

FIGURE 8
Comparison of the vorticity distribution at the inlet of the two pump impellers under different flow conditions.

consumption of the two increased. However, in the same flow conditions, the hydraulic performance of the two shows a noticeable gap. Specifically, in low-flow conditions, the impeller power consumption and efficiency of the short jet pump are lower than those of the traditional pump. Notably, the pump efficiency exhibits a substantial difference, reaching 80.84%. Conversely, the head of the short jet pump under low-flow conditions is significantly higher than that of the traditional pump, with a difference of 3.70%. In the high-flow conditions, the efficiency of the short jet pump and impeller power consumption are also lower than those of the traditional pump, but the difference between the two is relatively small. At this time, the difference in the efficiency and impeller power consumption is 60.85% and 23.88%, respectively, but the jet pump head is still greater than the traditional pump head, and the difference between the two is 11.09%. Under rated flow conditions, while the head of the short jet pump surpasses that of the traditional pump by 3.3%, there persists a noticeable gap in efficiency and impeller power consumption between the two. This observation suggests that despite the short jet pump's ability to suction media to a certain height, the presence of the front injector induces varying flow directions within the pump, potentially leading to unstable flow. Consequently, this may significantly decrease the energy conversion rate of the jet pump.

A comparison of the vorticity distribution of the impeller inlet of the short jet pump and the conventional pump for different flow conditions is shown in Figure 8. As shown in the figure, the addition of jets in the pump leads to a great reduction in the value of the rated flow rate. In this paper, the rated flow rate of the traditional pump is $Q = 13\ m^3/h$, while the rated flow rate of the jet pump is $Q = 3\ m^3/h$. For the traditional pump, there is only high vortex at the center of the impeller inlet in the three flow conditions, and the vortex distribution around the pump is

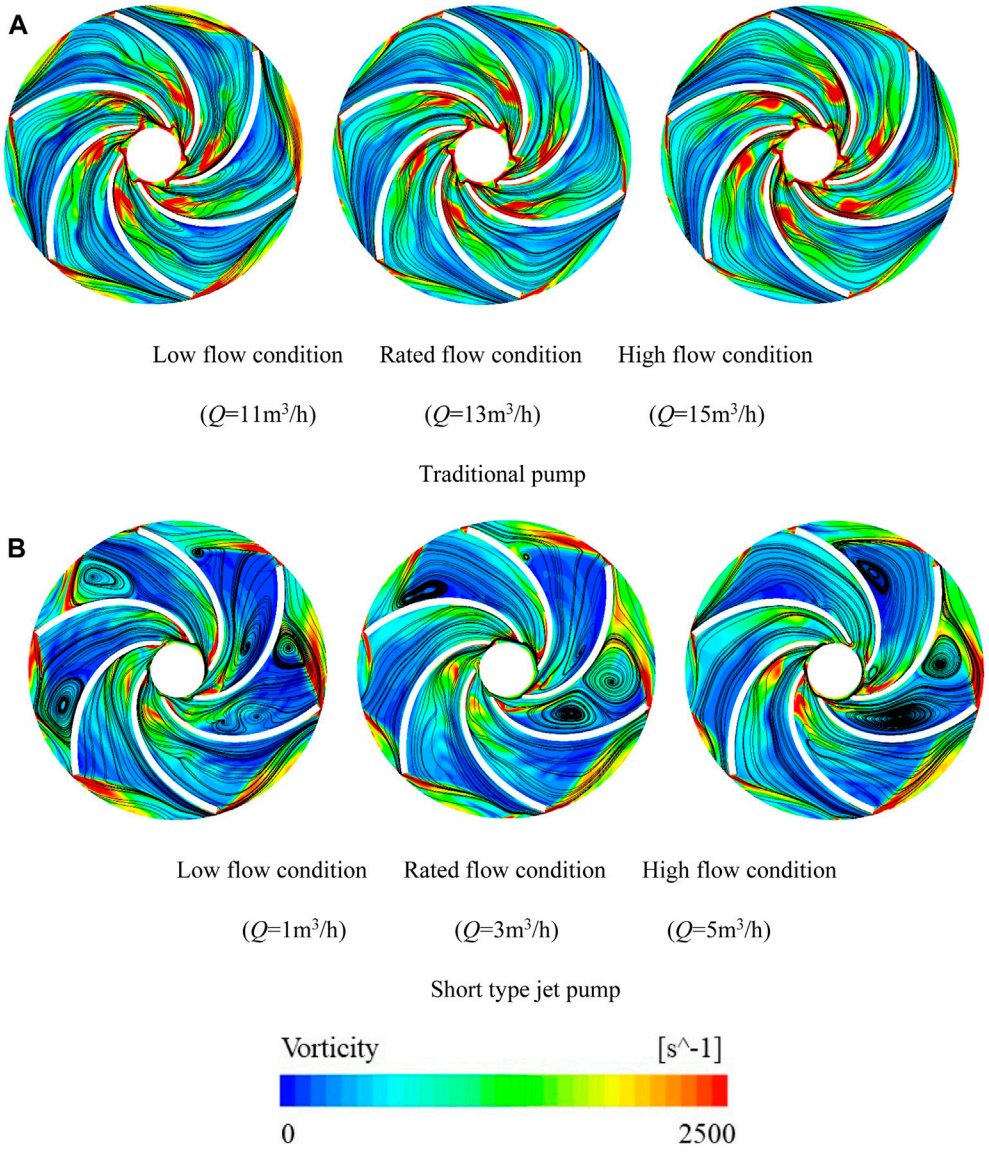

FIGURE 9
Comparison of the impeller mid-span vortex distribution for the two pump types under different flow conditions.

relatively uniform. As the flow rate increases, the traditional pump impeller inlet high-vortex area has to expand outward performance, but the change is not noticeable. However, in different flow conditions, there is a wide range of high-vortex phenomena within the short type of the jet pump. This suggests that, during this period, the energy loss in the pump is more pronounced, resulting in lower pump efficiency, aligning with the previously discussed results. Simultaneously, a comparison of the speed distribution in the two pump types reveals that the traditional pump's impeller inlet vortex exhibits a generally centrosymmetric distribution. In contrast, the vortex inside the short jet pump displays varying degrees of eccentricity. As the flow rate increases, the center of the vortex inside the jet pump gradually moves from the left to the right. This indicates that the front-end transverse jet will lead to the mainstream direction, and the impeller inlet surface normal direction is not consistent, resulting in an uneven distribution of the media at the impeller inlet, thus generating an asymmetric vortex phenomenon.

A comparison of the vorticity distribution at the impeller mid-span of the conventional pump and the short jet pump for three flow conditions is shown in Figure 9. As shown in the figure, the phenomenon of high vorticity occurs at this position in the conventional pump under different flow conditions. The high vortex region is mainly distributed in the blade root and blade tip. At this time, the distribution position of the high-vortex phenomenon at the impeller mid-span in the jet pump is the same as that of the traditional pump, but its distribution range is noticeably larger. In addition, by observing the velocity streamline distribution, it can be found that the streamline shapes in the six impeller channels of the short jet pump are different. Some of the streamlines are uniformly distributed within the flow channels, but single or even multiple vortices appear in some of the flow channels. The range of vortices within the impeller channels is relatively

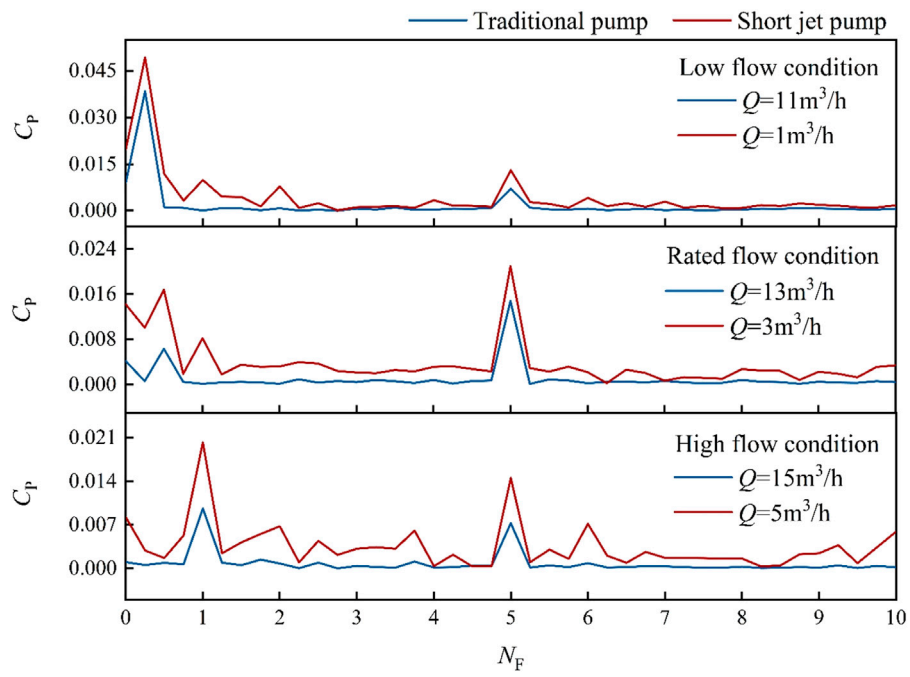

FIGURE 10
Comparison of the pressure pulsation characteristics of the two pump types under different flow conditions.

small under rated flow conditions. This is most likely influenced by the asymmetric distribution of the impeller inlet vortex. Eccentric rotation of the impeller inlet medium induces subsequent flow inconsistencies in each flow channel, which may lead to the presence of large radial forces in the impeller, causing the impeller to rotate eccentrically. The long-term eccentric rotation will cause serious wear and tear of the pump shaft, shortening the service life of the pump.

In order to facilitate the comparison of the pressure pulsation characteristics between traditional pumps and short-type jet pumps, the frequency of the two is converted into a multiple of the impeller rotation frequency, and the rotation frequency multiple N_F is defined as follows:

$$N_F = \frac{60f}{n}, \tag{3}$$

where n represents the rotational speed of the impeller, r/min; f represents the frequency obtained after the fast Fourier transform, Hz.

Figure 10 shows a comparison of the pressure pulsation characteristics at the impeller channel in the two pumps under three flow conditions. Under small flow conditions, the primary frequency in the impeller channel of traditional pumps and short-type jet pumps is distributed in the vicinity of 0.5 times the frequency of rotation, and the secondary frequency is distributed in the vicinity of 5 times the frequency of rotation (diffuser frequency). However, the jet pump also exhibits numerous multi-frequency signals, indicating that the media pressure within the short-type jet pump impeller channel is not only influenced by the impeller and diffuser but also significantly affected by the injector. Under rated flow conditions, the primary frequency of both pumps is concentrated at the diffuser lobe frequency. Additionally, as the frequency increases, the amplitude of pressure pulsations decreases. This phenomenon can be attributed to media fluctuations during the flow process, consequently impacting the pressure distribution in the impeller channel. Moreover, under high-flow conditions, the primary frequency of both pumps is distributed around one times rpm and five times rpm. Compared with the pressure pulsation intensity of conventional pumps, the pressure pulsation amplitude of the jet pump is intense and more frequent. This indicates that the small overflow area at the nozzle and effuser throat will significantly strengthen the turbulent flow characteristics of the medium here, which induces the instability of the subsequent flow field, and the pressure pulsation signal caused by the unstable flow in the flow field will be propagated to the impeller and the diffuser in the flow channel. This characteristic is further amplified under high-flow conditions, thus showing a noticeable pressure fluctuation phenomenon.

6 Conclusion

In this paper, a combination of numerical simulation and experimental verification is used to compare the hydraulic characteristics, internal flow structure, and pressure pulsation characteristics of the JET1100 short-type jet pump with the corresponding conventional pump. The main conclusions are as follows:

(1) Compared with the conventional pump, the rated flow value of the short-type jet pump is significantly lower. Through the comparison of the three different flow conditions of the hydraulic performance of the short-type jet pump and the traditional pump, it was found that the difference between the two heads is small, and the head value of the jet pump is higher than that of the traditional pump. However, the

efficiency of the jet pump is much smaller than the efficiency of the traditional pump. This shows that in the same flow conditions, the short-type jet pump will lose more energy.

(2) Based on the comparison of the flow structure of the two pumps, the front injector will lead to the direction of the medium in the pump, different from the impeller inlet normal direction, which leads to the eccentric rotation of the impeller inlet medium, leading to the phenomenon of unstable flow in the pump. At the same time, the eccentric rotation of the impeller inlet will also induce the subsequent flow inconsistency of each flow channel of the impeller, which will lead to the eccentric rotation of the impeller and reduce the service life of the pump.

(3) By comparing the pressure pulsation characteristics of the two pumps, the narrow overflow area in the injector enhances the turbulent flow characteristics of the medium and induces the instability of the subsequent flow field, which leads to a wide range of low-frequency signals in the pump. This suggests that short-type jet pumps may have low-frequency vibration problems in engineering applications, thus affecting the operational stability of hydraulic sprinkler irrigation systems.

Data availability statement

The original contributions presented in the study are included in the article/Supplementary Material; further inquiries can be directed to the corresponding author.

Author contributions

XM: conceptualization, formal analysis, and writing–review and editing. JY: methodology and writing–original draft. TD: conceptualization and writing–original draft. JW: methodology and writing–review and editing. LT: software and writing–review and editing. YY: supervision and writing–review and editing.

Funding

The authors declare financial support was received for the research, authorship, and/or publication of this article. This work was supported by the Natural Science Foundation of Ningxia Province of China (No. 2021AAC03188), the Ningxia Hui Autonomous Region Key R&D Projects (No. 2021BEG02012), and the General Scientific Research Project of North Minzu University (No. 2021XYZTM06).

Conflict of interest

Author TD was employed by Ningxia Water Resources and Hydropower Survey Design and Research Institute Co., Ltd.

The remaining authors declare that the research was conducted in the absence of any commercial or financial relationships that could be construed as a potential conflict of interest.

Publisher's note

References

Aissa, W. A., Eissa, M. S., and Mohamed, A. H. H. (2021). Experimental and theoretical investigation of water jet pump performance. *Int. J. Appl. Energy Syst.* 3 (1), 1–14. doi:10.21608/ijaes.2021.169900

Banasiak, K., Hafner, A., and Andresen, T. (2012). Experimental and numerical investigation of the influence of the two-phase ejector geometry on the performance of the R744 heat pump. *Int. J. Refrig.* 35 (6), 1617–1625. doi:10.1016/j.ijrefrig.2012.04.012

Deng, X., Dong, J., Wang, Z., and Tu, J. (2017). Numerical analysis of an annular water–air jet pump with self-induced oscillation mixing chamber. *J. Comput. Multiph. Flows* 9 (1), 47–53. doi:10.1177/1757482X16688476

Haidl, J., Mařík, K., Moucha, T., Rejl, F. J., Valenz, L., and Zednikova, M. (2021). Hydraulic characteristics of liquid–gas ejector pump with a coherent liquid jet. *Chem. Eng. Res. Des.* 168, 435–442. doi:10.1016/j.cherd.2021.02.022

Kwon, O. B., Kim, M. K., Kwon, H. C., and Bae, D. S. (2002). Two-dimensional numerical simulations on the performance of an annular jet pump. *J. Vis.* 5, 21–28. doi:10.1007/bf03182599

Launder, B. E., and Sharma, B. I. (1974). Application of the energy-dissipation model of turbulence to the calculation of flow near a spinning disc. *Lett. heat mass Transf.* 1 (2), 131–137. doi:10.1016/0094-4548(74)90150-7

Launder, B. E., and Spalding, D. B. (1983). The numerical computation of turbulent flows. *Comput. Methods Appl. Mech. Eng.* 3, 269–289. doi:10.1016/0045-7825(74)90029-2

Long, X., Zhang, J., Wang, Q., Xiao, L., Xu, M., Lyu, Q., et al. (2016). Experimental investigation on the performance of jet pump cavitation reactor at different area ratios. *Exp. Therm. Fluid Sci.* 78, 309–321. doi:10.1016/j.expthermflusci.2016.06.018

Lu, X., Wang, D., Shen, W., and Zhu, C. (2015a). Experimental investigation of the propagation characteristics of an interface wave in a jet pump under cavitation condition. *Exp. Therm. Fluid Sci.* 63, 74–83. doi:10.1016/j.expthermflusci.2015.01.008

Lu, X., Wang, D., Shen, W., Zhu, C., and Qi, G. (2015b). Experimental investigation on liquid absorption of jet pump under operating limits. *Vacuum* 114, 33–40. doi:10.1016/j.vacuum.2015.01.004

Lyu, Q., Xiao, Z., Zeng, Q., Xiao, L., and Long, X. (2016). Implementation of design of experiment for structural optimization of annular jet pumps. *J. Mech. Sci. Technol.* 30, 585–592. doi:10.1007/s12206-016-0112-y

Morrall, A., Quayle, S., and Campobasso, M. S. (2020). Turbulence modelling for RANS CFD analyses of multi-nozzle annular jet pump swirling flows. *Int. J. Heat Fluid Flow* 85, 108652. doi:10.1016/j.ijheatfluidflow.2020.108652

Pounds, D. A., Dong, J. M., Cheng, P., and Ma, H. B. (2013). Experimental investigation and theoretical analysis of an ejector refrigeration system. *Int. J. Therm. Sci.* 67, 200–209. doi:10.1016/j.ijthermalsci.2012.11.001

Saker, A. A., and Hassan, H. Z. (2013). Study of the different factors that influence jet pump performance. *Open J. Fluid Dyn.* 3 (2), 44–49. doi:10.4236/ojfd.2013.32006

Shah, A., Chughtai, I. R., and Inayat, M. H. (2011). Experimental and numerical analysis of steam jet pump. *Int. J. Multiph. flow* 37 (10), 1305–1314. doi:10.1016/j.ijmultiphaseflow.2011.07.008

Sharifi, N. (2020). Numerical study of non-equilibrium condensing supersonic steam flow in a jet-pump based on supersaturation theory. *Int. J. Mech. Sci.* 165, 105221. doi:10.1016/j.ijmecsci.2019.105221

Wang, J., Cheng, H., Xu, S., Ji, B., and Long, X. (2019). Performance of cavitation flow and its induced noise of different jet pump cavitation reactors. *Ultrason. Sonochemistry* 55, 322–331. doi:10.1016/j.ultsonch.2019.01.011

Wang, X. D., Dong, J. L., Wang, T., and Tu, J. Y. (2012a). Numerical analysis of spontaneously condensing phenomena in nozzle of steam-jet vacuum pump. *Vacuum* 86 (7), 861–866. doi:10.1016/j.vacuum.2011.02.016

Wang, X. D., Lei, H. J., Dong, J. L., and Tu, J. Y. (2012b). The spontaneously condensing phenomena in a steam-jet pump and its influence on the numerical simulation accuracy. *Int. J. heat mass Transf.* 55 (17-18), 4682–4687. doi:10.1016/j.ijheatmasstransfer.2012.04.028

Winoto, S. H., Li, H., and Shah, D. A. (2000). Efficiency of jet pumps. *J. Hydraulic Eng.* 126 (2), 150–156. doi:10.1061/(ASCE)0733-9429(2000126:2(150)

Xu, K., Wang, G., Zhang, L., Wang, L., Yun, F., Sun, W., et al. (2021). Multi-objective optimization of jet pump based on RBF neural network model. *J. Mar. Sci. Eng.* 9 (2), 236. doi:10.3390/jmse9020236

Xu, S., Wang, J., Cai, B., Cheng, H., Ji, B., Zhang, Z., et al. (2022). Investigation on cavitation initiation in jet pump cavitation reactors with special emphasis on two mechanisms of cavitation initiation. *Phys. Fluids* 34 (1). doi:10.1063/5.0075099

Xu, X. X., Chen, G. M., Tang, L. M., and Zhu, Z. J. (2012). Experimental investigation on performance of transcritical CO2 heat pump system with ejector under optimum high-side pressure. *Energy* 44 (1), 870–877. doi:10.1016/j.energy.2012.04.062

Yang, Y., Wu, S., Wang, C., Jiao, W., Ji, L., An, C., et al. (2023). Effect of effuser throat diameter on the internal flow structure and energy characteristics of the jet pump. *Energy Rep.* 9, 2075–2086. doi:10.1016/j.egyr.2023.01.025

Yu, H., Wang, C., Li, G., Wang, H., Yang, Y., Wu, S., et al. (2023). Steady and unsteady flow characteristics inside short jet self-priming pump. *Sustainability* 15 (18), 13643. doi:10.3390/su151813643

Zhang, H., Zou, D., Yang, X., Mou, J., Zhou, Q., and Xu, M. (2022). Liquid–gas jet pump: a review. *Energies* 15 (19), 6978. doi:10.3390/en15196978

Zhao, G., Liang, N., Zhang, Y., Cao, L., and Wu, D. (2021). Dynamic behaviors of blade cavitation in a water jet pump with inlet guide vanes: effects of inflow non-uniformity and unsteadiness. *Appl. Ocean Res.* 117, 102889. doi:10.1016/j.apor.2021.102889

Zhu, F. N., Liu, D., Yang, X. Y., and Wang, C. L. (2013). Numerical simulation of the three-dimensional turbulent flow in roto-jet pump. *Appl. Mech. Mater.* 341, 375–378. doi:10.4028/www.scientific.net/AMM.341-342.375

frontiers | Frontiers in Energy Research

TYPE Original Research
PUBLISHED 09 January 2024
DOI 10.3389/fenrg.2023.1259729

OPEN ACCESS

EDITED BY
Kan Kan,
College of Energy and Electrical Engineering, China

REVIEWED BY
Guangjie Peng,
Jiangsu University, China
Yandong Gu,
Yangzhou University, China

*CORRESPONDENCE
Yong-Lei Qu,
quyonglei@hrbeu.edu.cn

RECEIVED 16 July 2023
ACCEPTED 21 December 2023
PUBLISHED 09 January 2024

CITATION
Wang Z-Y, He C, Wu Y and Qu Y-L (2024), Equivalent simulation method for total pressure distortion of ship inlet.
Front. Energy Res. 11:1259729.
doi: 10.3389/fenrg.2023.1259729

Equivalent simulation method for total pressure distortion of ship inlet

Zhong-Yi Wang[1], Chenxin He[1], Yue Wu[2] and Yong-Lei Qu[1]*

[1]College of Power and Energy Engineering, Harbin Engineering University, Harbin, Heilongjiang, China, [2]Unit 92942 of the People's Liberation Army of China, Beijing, China

According to the use of marine gas turbines, inlet distortion is caused by the bending of the compressor inlet port. The total pressure distortion is the external stability reduction factor that has the greatest impact on the engine's aerodynamic stability. This research designs a pressure distortion simulation device, which achieves the goal of providing the target distortion flow field for marine compressors by inserting plugboards of different heights and shapes into the inlet duct. The variation pattern of the entire flow field after inserting different parameter plugboards is obtained through distortion experiments and numerical simulations. Summarizes a prediction formula for total pressure distortion under different working conditions, with a verified error of less than 1.5%. In addition, the straight plugboard is changed to arc plugboard or concave and convex plugboard, the total pressure distortion distribution pattern can be changed while the range of the circumferential low-pressure zone remains unchanged. The distortion index of the distortion simulator designed by this research institute can be adjusted within the range of 0.5%–5%, while providing various distortion pattern. The distortion simulator meets the requirements of the comprehensive distortion index needed for the relevant distortion test of the marine engine and provides assistance for ship engine design and optimization.

KEYWORDS

ship engine, inlet distortion, distortion generator, plugboard method, equivalent simulation

1 Introduction

The engine may experience decreased performance due to an uneven intake flow field during operation, resulting from changes in the external environment and its own operating conditions. The study of inlet distortion is essential in engine development processes. If the influence of flow field distortion factors is not considered, excessive flow field distortion at the inlet may result in compressor instability and have serious consequences. With the increasing attention on the inlet flow field distortion, various simulation technologies for inlet distortion have emerged as the need arises. Through these simulation technologies, a flow field with the same effect as the inlet distortion can be generated, allowing for efficient and rapid experimentation related to engine distortion, thus providing assistance in anti-distortion design and optimization. Common simulation technologies for total pressure distortion include simulation network technology, turbulence generator, air jet distortion simulator, simulation board technology, plugboard simulation technology, etc.

Regarding the simulation of total pressure distortion, scholars have conducted extensive research in the field of testing and simulation. Since the 1960s, organizations such as AEDC and NASA in the United States have developed devices such as distortion screens (Bobula,

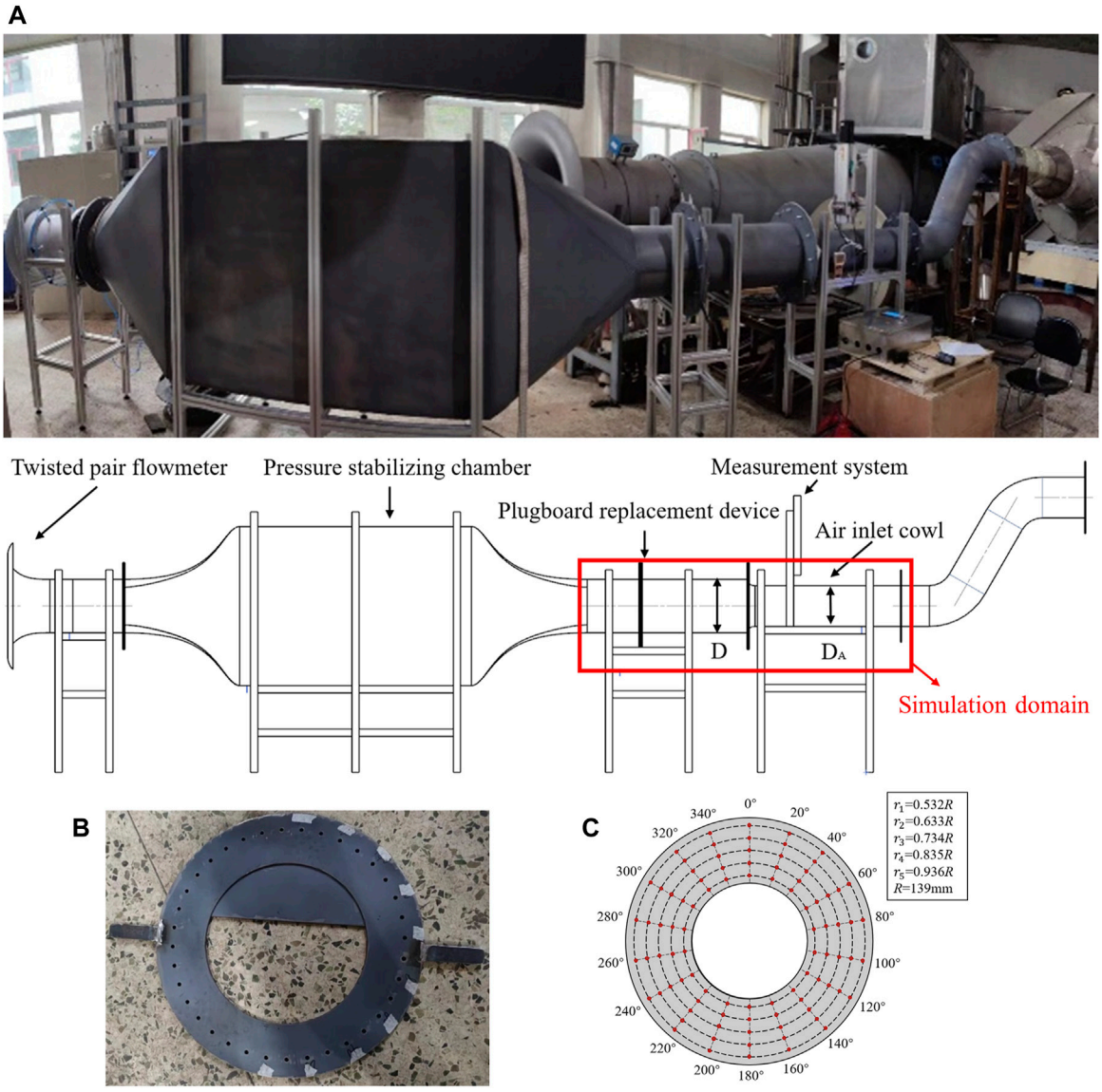

FIGURE 1
The distortion equivalent simulation test rig.

1979), plane wave method (Kutschenreuter et al., 1973), random frequency distortion generators, and air jet distortion simulation generators to achieve distortion simulation (Braithwaite et al., 1970; Meyer et al., 1970; Overall and Harper, 1974; Hubble and Smith, 1979; Mcllveen, 1979; Beale et al., 2002; Beale et al., 2006; Beale et al., 2007) and others have introduced research on transient total pressure distortion simulation technology and proposed concepts such as total temperature distortion simulation devices and eddy current distortion simulation devices based on the characteristics of various simulation devices. Zhang et al. (2017) designed a crescent-shaped pressure distortion simulator with a continuously adjustable distortion index achieved by increasing the curvature of the plugboard. Naseri et al. (2012) used a jet injector to simulate steady-state circumferential intake distortion on a micro jet engine test rig. With the development of distortion simulation, scholars have proposed new methods such as the delta wing method, blade method, square cylinder method, strip distortion generator, complex total pressure distortion screen, curved edge plate, and swirl chamber method (Mankbadi and Georgiadis, 2015; Yusoof and Deshpande, 2015; Sivapragasam, 2019; Cheng et al., 2020; Song et al., 2021). Wu et al. (2022) used the BP ANN method to predict the dynamic distortion flow field of a crescent shaped distortion generator. Through numerous experiments, the United States has developed definition criteria and relevant industry standards for aerospace inlet distortion (SAE S-16 Committee ARP 1420, Revision B, 2002; SAE Aerospace Information Report AIR-1419, 1999). However, China and Russia typically use the plugboard method for total pressure equivalent simulation. Conduct compressor distortion experiments using distortion generators such as straight plates, controllable moving plates, and double plate (Xia et al., 2018; Tu et al., 2021; Chen et al., 2023), the influence of different types of plugboard devices on

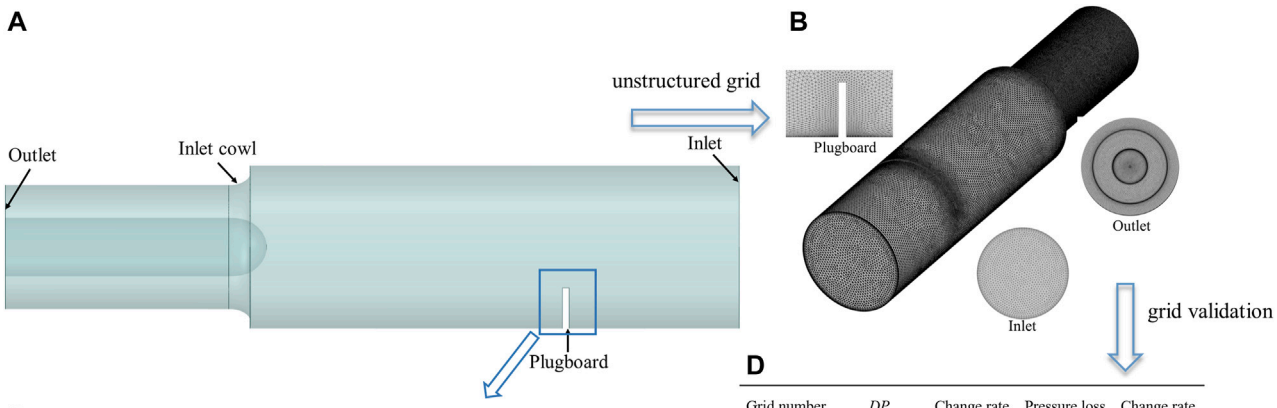

Grid number	*DP*	Change rate	Pressure loss	Change rate
0.25 million	2.58	/	1987 Pa	/
0.52 million	3.02	14.69%	1936 Pa	2.57%
1.1 million	3.12	3.21%	1921 Pa	0.78%
2.01 million	3.13	0.32%	1919.8 Pa	0.06%
2.7 million	3.13	0%	1919 Pa	0.04%

FIGURE 2
Grid independence verification.

compressor inlet flow field parameters is analyzed, and the reasons for compressor early stall caused by distortion are summarized (Jiang et al., 2007; Jiang et al., 2009; Zhang et al., 2019; Liu et al., 2022; Liu et al., 2022).

In order to analyze the impact of distortion on the compressor, scholars combined numerical simulation methods to further study the flow field of the compressor under distortion conditions. Many scholars' research (Jinghua and Baofeng, 2015; Zhang et al., 2017; Maghsoudi et al., 2020; Chen et al., 2023) has shown that under different operating conditions, the plugboard has a significant impact on the different pressure distortion indices *DC* (90°), *DC* (60°), and *PC/P* of the measuring cross-section section, leading to circumferential flow in the rotor inlet section, disturbance of corner vortices on rotor tip leakage vortices, and changes in shock waves and positions. These factors affect the stable boundaries of low-speed, subsonic, and transonic compressors, leading to early stall of the compressor. By combining novel simulation models such as three-dimensional torsional force model, time-stepping simulation, and RANS/LES hybrid method, enhancements in both computational efficiency and simulation accuracy have been achieved. Through more comprehensive capture of flow field details, conducted thorough analysis of the impact of parameters, such as inlet conditions and plugboard types, on the internal flow of pipelines and compressors (Yin et al., 2015; Zhou et al., 2017; Zhou et al., 2018; Liu et al., 2021; Liu et al., 2021).

While numerous scholars have extensively researched the equivalent simulation of inlet distortion, there exists a notable gap in relevant studies concerning inlet distortion in marine gas turbines. Consequently, this study focuses on the equivalent simulation of inlet distortion in marine compressors and analyzes the impact of insertion plate parameters on distortion through approach combining experiments and simulations. Describe the simulation method and experimental verification results in Section 2; In Section 3, the impact of changes in parameters such as plugboard height and shape on the flow field is discussed. Finally, Section 4 provides a summary of the research findings.

2 Methods

2.1 Distortion equivalent simulation test rig

The distortion equivalent simulation test rig is shown in Figure 1A). The inlet of the test rig consists of a twisted pair flowmeter DLN-DN365, followed by a connecting segment and a pressure stabilizing chamber. The twisted pair flowmeter is a throttling flow meter, with its inlet surface consisting of a twisted pair wire rotating 360°, which then smoothly transitions to the cylindrical segment. This design ensures minimal pressure loss of air entering the flow meter, allowing for the neglect of throttling loss impact on the flow rate. Calculate the experimental flow rate using Eq. 1. During the experiment, the pressure difference at the measuring point is obtained using the differential pressure sensor MG 2000. The atmospheric temperature and pressure are acquired through the temperature sensor PT100 and absolute pressure sensor 3351AP. Real-time display of the flow rate is facilitated by the flow integrator F2000X, with the error of this flow measurement system being less than 1%.

$$Q_m = \frac{\pi}{4} \cdot D^2 \cdot \alpha \cdot \varepsilon \cdot \sqrt{\frac{2\Delta P}{\rho_1}} \tag{1}$$

α is the flow coefficient, ε is the expandable coefficient, D is the pipeline diameter, ρ_1 is the fluid density.

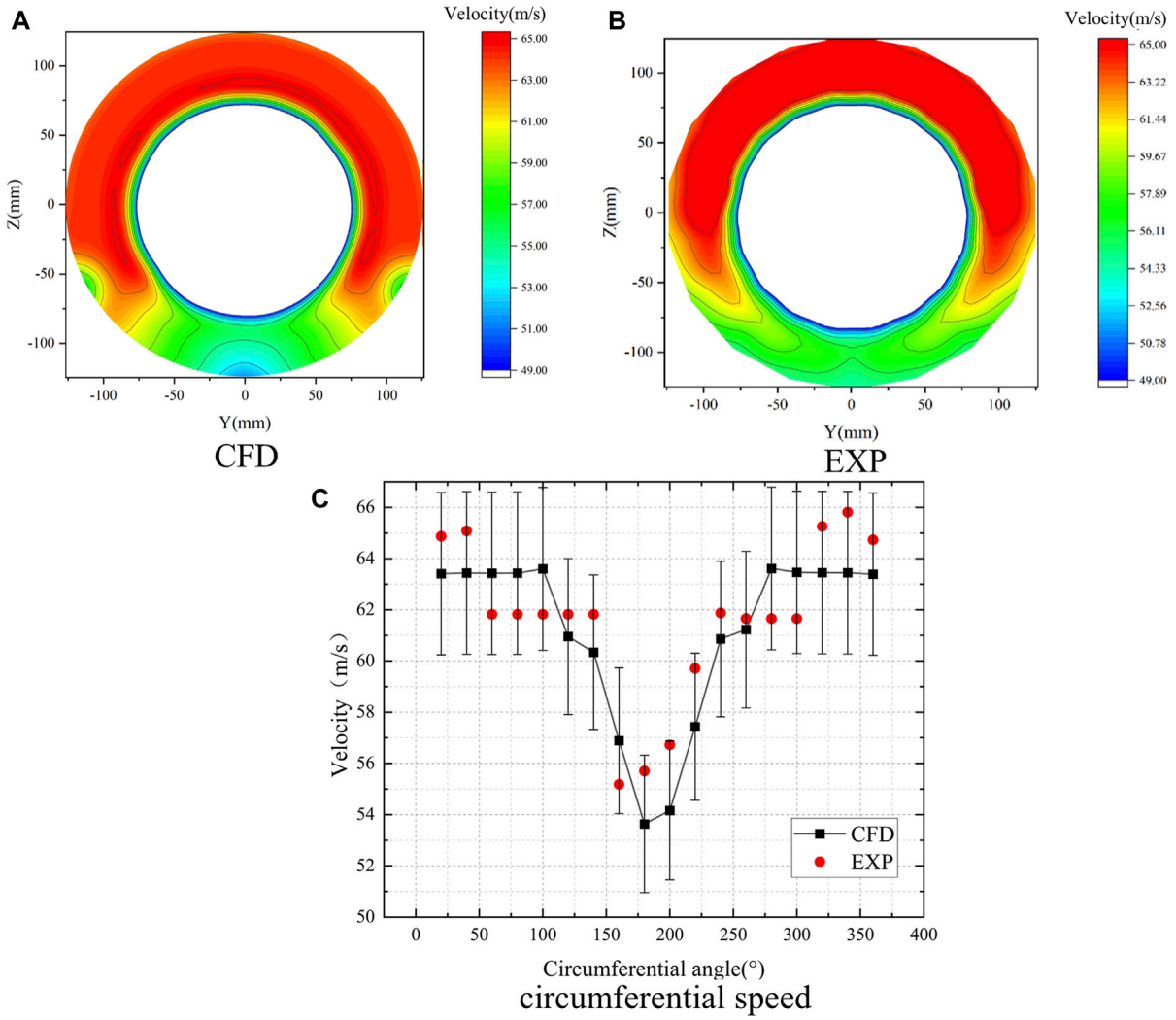

FIGURE 3
Verification of simulation results.

The inlet and outlet curves of the pressure stabilization chamber are Vickers curves, with a contraction ratio of 1:3. A convergent transition pipe is used to reduce the inner diameter to D = 365 mm. Different plugboard replacement devices (show in Fingure(b)) with various plugboard modes can be assembled between the transition pipe section and the air inlet cowl.

To assess the steady-state total pressure distortion on the compressor inlet surface AIP (Aerodynamic Interface Plane), located 250 mm away from the inlet fairing, a flow field parameter measurement system is installed at this specific location. The system consists of a probe, a probe displacement mechanism, and a flow field parameter acquisition and processing system RET-400. The displacement mechanism has a stroke of 200 mm and an accuracy of 0.01 mm. The flow field parameter acquisition and processing system offer a range of ±20 KPa and an accuracy of 1%. The measured AIP section is circular ring cross-section, with an outer diameter Dout and an inner diameter Din of 278 mm and 131mm, respectively. Multiple groups of data are collected at each measurement point and calculated by the flow field parameter acquisition and processing system to obtain an average value. After completing the radial five-point measurement, the plugboard replacement device's circumferential rotation function is utilized to collect data from ninety measurement points on the AIP section. Finally, the AIP sectional flow field parameters are obtained, and the non-uniformity of the AIP section flow field is analyzed.

2.2 Plugboard parameters

In order to obtain various distortion pattern to meet the relevant distortion test requirements, select the height of the plugboard as the main research parameter, and the study is carried out in combination with the shape of the plugboard, as shown in Figure 2C. The shortest distance H from the plugboard to the center is defined as the plugboard height, and the effect of changing the plugboard height on the flow field is studied. Change the shape of the plugboard based on the plugboard with H = 100 mm and define the distances C and Z from the arc plate and the concave and convex plate to the center. Conduct dimensionless processing on each parameter $h = H/D$, $c = C/D$ and $z = Z/D$, analyze

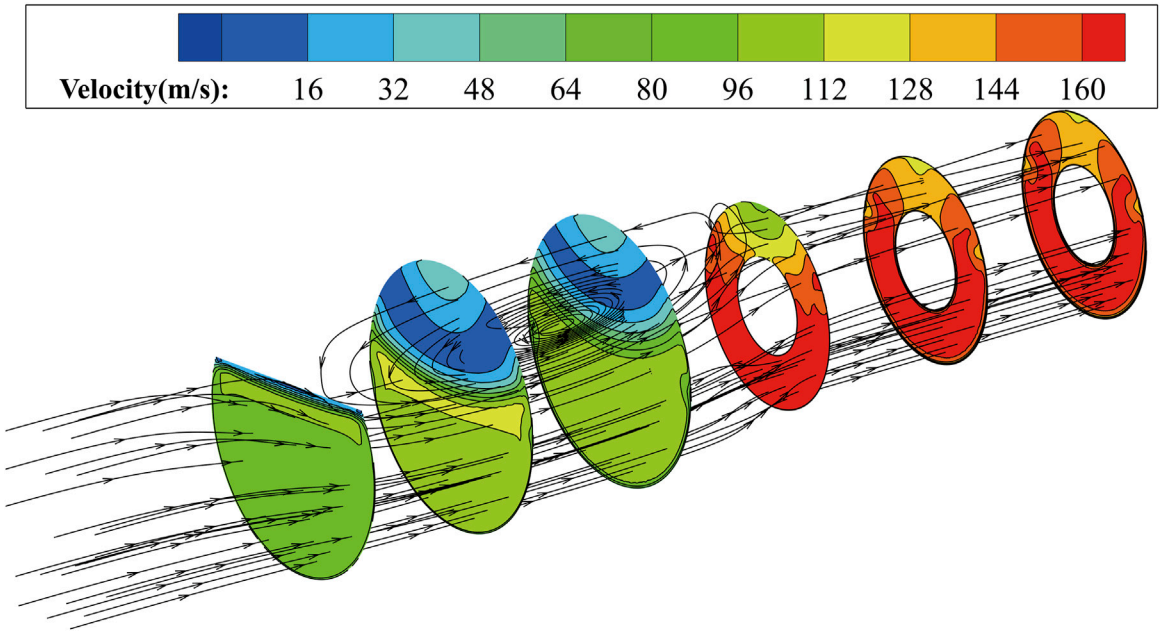

FIGURE 4
Velocity nephogram and streamline of each section.

the impact of various parameter changes on the total pressure distribution on the AIP surface, and summarize the influence of plugboard parameters on total pressure distortion.

2.3 Distortion assessment method

To quantify the non-uniformity of the inlet flow field of the compressor, the experimental and simulation results are analyzed using the non-dimensional parameter distortion index. Based on the characteristics of ship distortion, velocity distortion δ and total pressure distortion DP are defined. Divide the analysis section into 5% area sectors, process the data to obtain the maximum velocity $V_{i(5\%)_{max}}$, average velocity $\bar{V}_{i(5\%)}$, and the ratio of the difference between the maximum velocity and the average velocity to the average velocity within the sector. Compare all ratios to find the sector region with the most significant velocity change within the cross-section, where the ratio represents velocity distortion δ. The calculation method is shown in Eq. 2.

$$\delta = \max\left[\frac{V_{i(5\%)_{max}} - \bar{V}_{i(5\%)}}{\bar{V}_{i(5\%)}}\right] \tag{2}$$

The definition method of total pressure distortion DP degree is to divide the solution area, taking 1/6 of the ring area, which is divided into every 60 sector angle, firstly obtain the average total pressure $\bar{P}$, and then further according to the needs in each individual sector interval Divide, solve the average total pressure value in each independent unit separately and then perform global sorting to obtain $P_{i(60)}$. Use Eq. 3 to find the total pressure distortion.

$$DP = \frac{\bar{P} - P_{i(60)min}}{\bar{P}} \tag{3}$$

2.4 Ω criterion

In 2016, Liu et al. proposed the Ω criterion vortex identification method based on the second-generation vortex identification method (Q criterion, etc.). This method decomposes vorticity using the concepts of rotating and non-rotating parts for the first time. Choosing a reasonable threshold Ω within the range of 0–1 can effectively identify the vortex structure in the flow field. In the calculation process, the velocity gradient tensor is decomposed into a symmetric tensor A representing fluid deformation and an antisymmetric tensor B representing fluid rotation. Determine the vortex structure based on the proportion of rotation effect in the entire velocity gradient tensor. The calculation formula is as follows:

$$\Omega = \frac{\|B\|_F^2}{\|A\|_F^2 + \|B\|_F^2 + \varepsilon} \tag{4}$$

During the calculation process of Eq. 4, there may be situations where the values of A and B are small, leading to calculation errors. Therefore, a small positive number ε is added to the denominator.

$$\varepsilon = 0.02Q_{max} = 0.01\left(\|B\|_F^2 - \|A\|_F^2\right)_{max} \tag{5}$$

A large number of related experiments have shown that when Ω is greater than 0.52, the main vortex structures in the flow can be clearly identified.

$$\Omega > 0.52 \tag{6}$$

2.5 Modeling and simulation validation

The simulation domain is shown in Figure 2A, which corresponds to the labeled area in Figure 1. The calculation

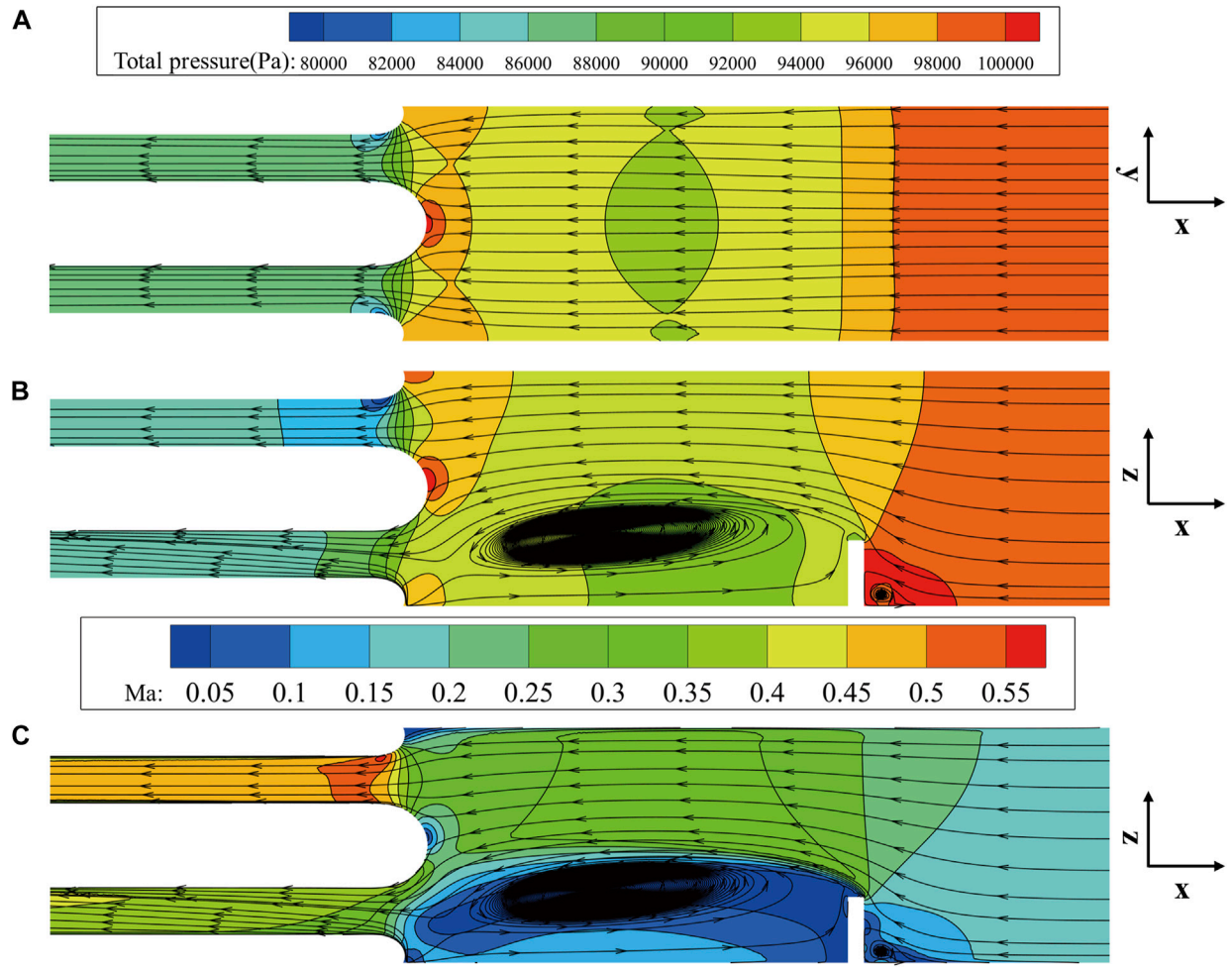

FIGURE 5
Total pressure Ma and streamline diagram.

domain includes the test section, plugboard replacement device, air inlet cowl, and measurement section. Figure 2B is a schematic diagram of unstructured grid partitioning of the computational domain using the Fluent Meshing tool module. Due to the complexity of the model's structure, the grid is densified in the key survey section and the smaller parts of the structure. To ensure computational accuracy, the boundary layer was refined to ensure that is y^+ less than 100, meeting the requirements of the turbulence model. The mainstream within the computational domain is characterized by subsonic, compressible, and ordinary temperature, with a Reynolds number exceeding 10,000, thereby indicating fully developed turbulence. Choose Fluent software for numerical solution based on the research object. The gradient discretization scheme utilized the Least Squares Cell-Based approach, while the pressure discretization employed the Second Order scheme. Discretization for density, momentum, energy, and other parameters followed the Second Order Upwind method, and calculations are conducted using the k-ε turbulence model. The inlet of the computational domain is configured as pressure boundary, specifying total pressure of 101,325 Pa and temperature of 288.15 K. The outlet of the computational domain is set as pressure outlet, with a target mass flow rate specified as 7.5 kg/s. Grid independence verification is performed for five different mesh distribution schemes to ensure the effectiveness of the grid generation method (Kan et al., 2021a; Kan et al., 2021b). As observed in Figure 2D, it can be noted that the total pressure loss and the relative variation in pressure parameters remain essentially constant when the grid count exceeds 1.1 million. Consequently, considering the achievable maximum accuracy and the available computational resources, a grid scheme consisting of 1.1 million cells is selected to simulate the flow characteristics downstream of the plugboard.

2.6 Test verification

Use Eq. 7 to process the data of 90 measuring points of the AIP section, calculate the measured total pressure and static pressure according to the local temperature, atmospheric pressure and other data, and convert them into the velocity value of the measured section.

$$\frac{1}{2}v^2 = \frac{kRT}{k-1}\left[1-\left(\frac{P_s}{P_T}\right)^{\frac{k-1}{k}}\right] \tag{7}$$

In the above formula, v represents the velocity value at this point, P_s represents the static pressure value, and P_T represents the total

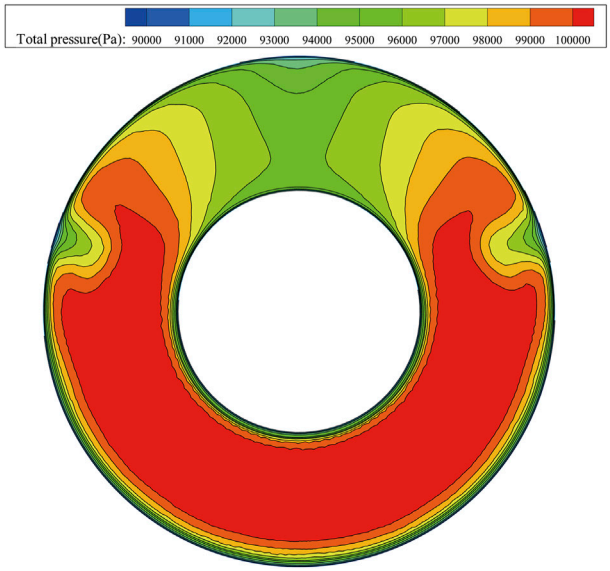

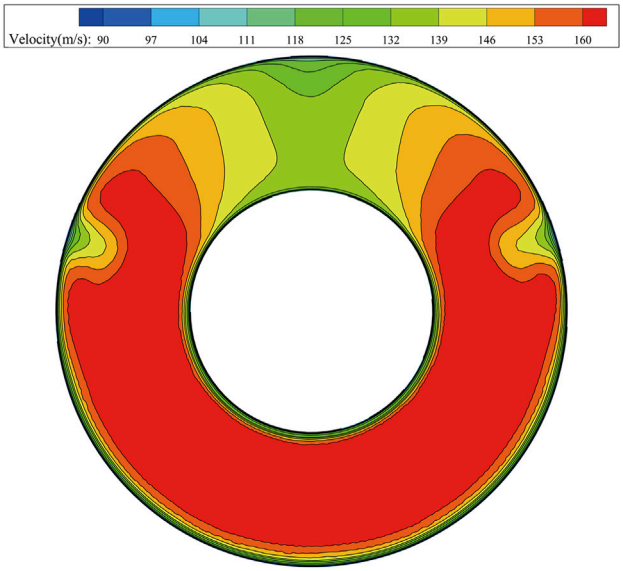

FIGURE 6
Total pressure and Ma contour of AIP section.

pressure value. After performing calculations, the velocity nephogram of the AIP cross-section experiment and simulation comparison is shown in Figure 3. After processing the simulation results obtain the average velocity of the AIP surface $\bar{V}_{AIP}$ = 60.83 m/s, δ = 10.38%; the experimental result is $\bar{V}_{AIP}$ = 61.73 m/s, δ = 10.10%. The comparison between the simulated and experimental values indicates that the error between the two falls less than 3% within an acceptable range. In Figure 3C, an error bar, representing a 5% margin of error, is incorporated based on the velocity values at measurement points in the circumferential direction of the measurement section. It is evident that the simulation results for all comparison points errors of less than 5% when compared to the experimental values, and the distribution pattern of total pressure aligns. The accuracy of the numerical simulation has been substantiated through the aforementioned comparative analysis.

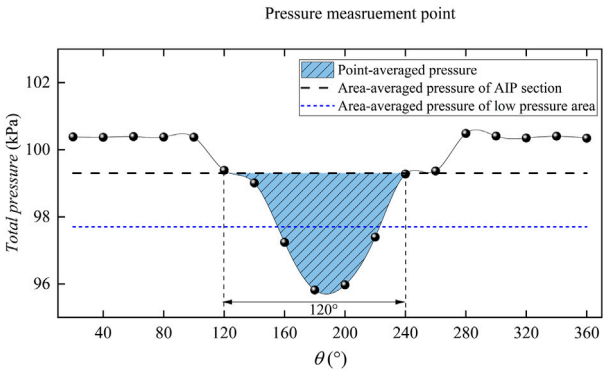

FIGURE 7
Identification of the low pressure area in AIP section.

3 Results and discussion

Using the rated operating state of a ship compressor with 7.5 kg/s (n_{1r} = 100%) as an example, the flow structure variation of the flow field after the plugboard is analyzed. Figure 4 shows the velocity distribution and three-dimensional streamline of five cross sections with an interval of 250 mm along the flow direction after the plugboard. It can be observed that the blocking effect of the plugboard on the mainstream causes it to be divided into two strands. The airflow that is not affected by the plugboard increased in speed due to a decrease in the flow area. And some of the airflow bypasses the plugboard, forming a large range of strong eddies due to the blockage of the plugboard, forming a low-pressure and low-speed zone. Under the influence of the plugboard, there is a significant non-uniformity in the flow. Although the continuous mixing of the airflow and the rectification effect of the inlet cowl effectively weaken the non-uniformity of the flow, there is still a clear low-pressure and low-speed zone at the inlet section of the compressor.

In order to study the flow structure of the plugboard in detail, the total pressure, Mach number, and velocity vector of the Y and Z direction cross-section are analyzed (as shown in Figure 5). The analysis revealed that the large area reflux zone after plugboard has a relatively high flow velocity in the external and whereas the flow velocity inside the reflux zone remains at only 0.05 Ma. This process leads to substantial flow losses, resulting in a significant decrease in total pressure compared to the inlet pressure. Meanwhile, when the airflow bypasses the plugboard, the flow area decreases, and radial velocity is generated due to shear force, creating a high-speed flow area behind the board. The high-speed region experiences a decrease followed by an increase in the flow area under the influence of shear forces. Downstream of the plugboard, the airflow accelerates to the max 0.35 Ma. A transition zone forms between the low-speed

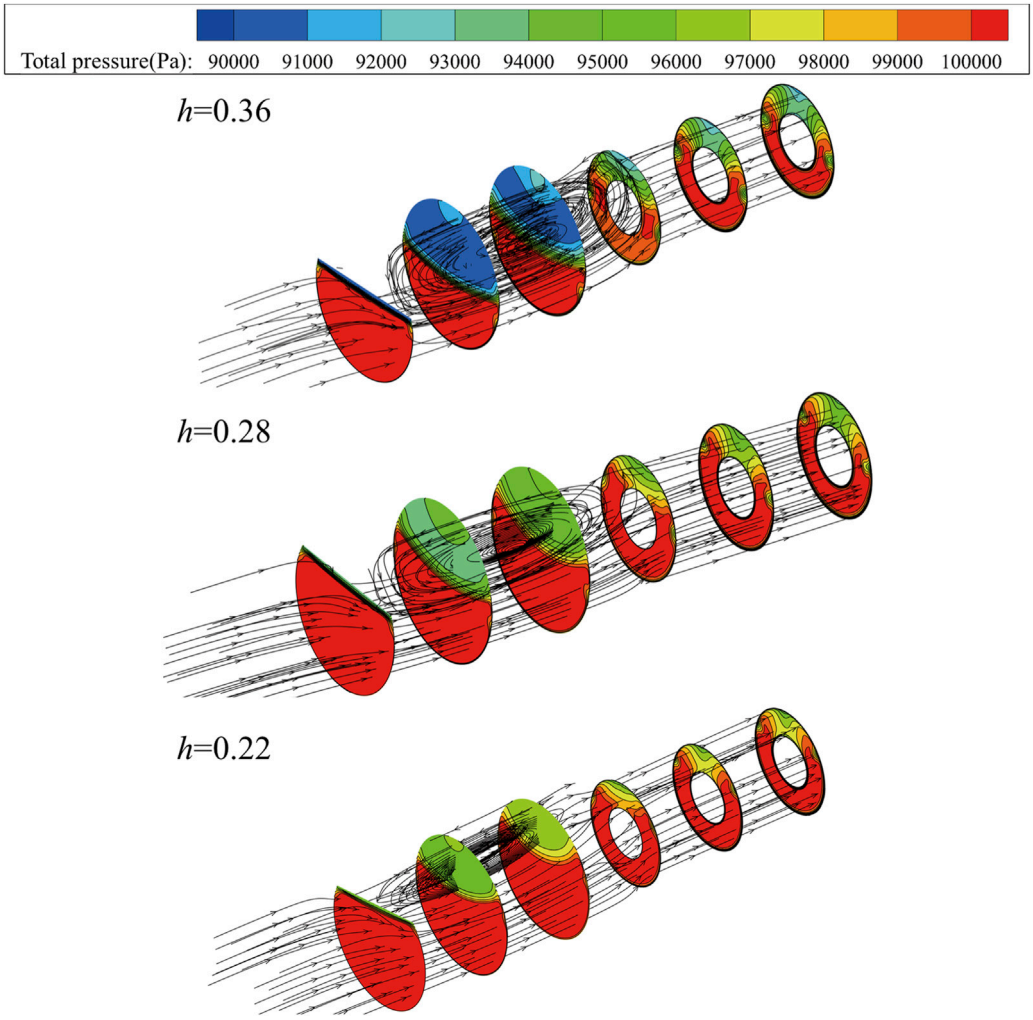

FIGURE 8
The flow fields behind the baffle under different baffle depths.

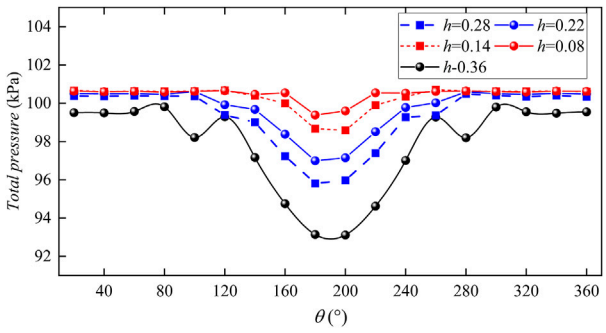

FIGURE 9
AIP section (n_{1r} = 100%) under different plugboard depths.

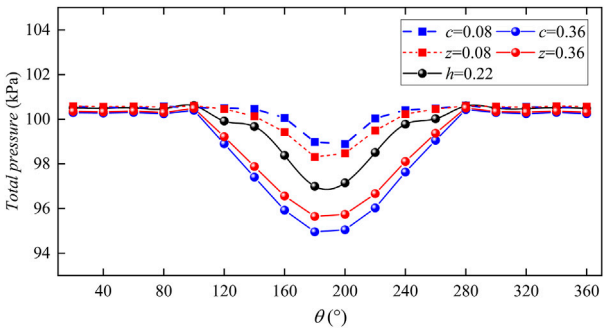

FIGURE 10
Total pressure of AIP section (n_{1r} = 100%) under different plugboard parameters.

reflux area and the high-speed area behind the board. The momentum transfer and continuous mixing of the airflow behind the plate, along with the wall viscous effect, blur the boundary between the high and low-pressure zones. This leads to a reduction in flow non-uniformity. The shape of the inlet cowl has a rectifying effect on the airflow, which can further reduce the non-uniformity of the flow, but cannot completely eliminate the distortion of total pressure and velocity.

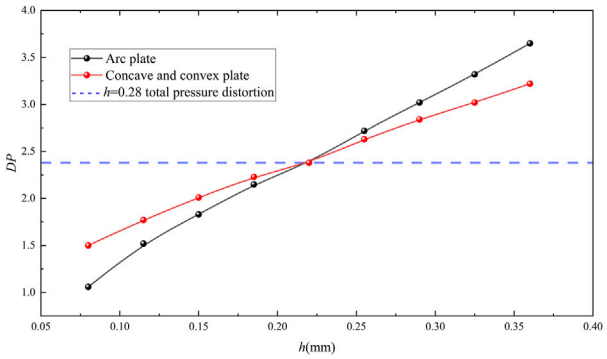

FIGURE 11
DP of AIP section (n_{1r} = 100%) under different plugboard parameters.

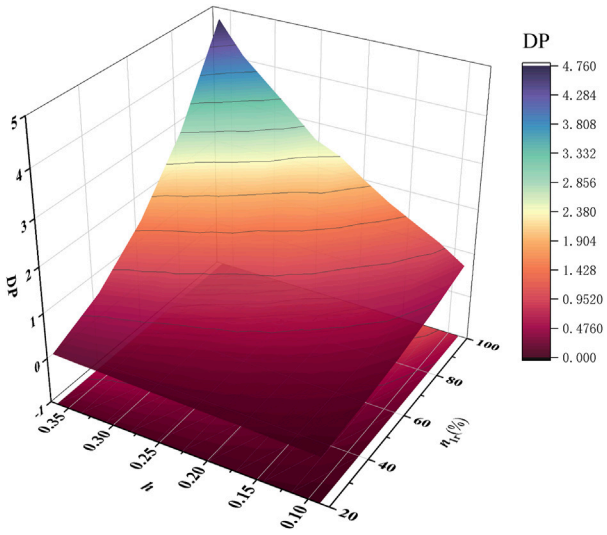

FIGURE 12
AIP section under different plugboard depths and n_{1r}.

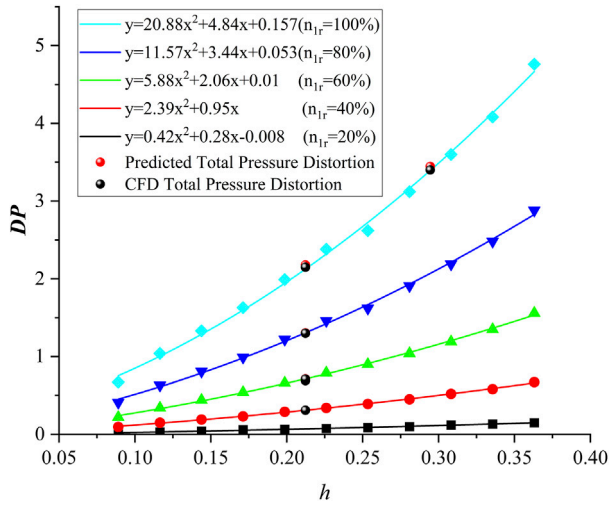

FIGURE 13
AIP section under different plugboard depths and n_{1r}.

Figure 6 and Figure 7 show the distribution of AIP cross-sectional flow field parameters. The section pressure of AIP is 99.3 kPa. The area where the pressure is lower than this value constitutes the low-pressure area, with an average pressure of 97.7 kPa. From the figure, it can be observed that the low-pressure area occupies a significant portion of the entire AIP section. By using linear difference analysis, it has been determined that the low-pressure area spans from 120° to 240°, amounting to a range of 120° which accounts for 33% of the compressor inlet plane.

In order to investigate the impact of plugboard depth on the flow field, the plugboard is operated at the rated flow rate. Figure 8 shows the changes in the flow field behind the plugboard as the depth of the plugboard changes. To assess the influence of *h*, record the total pressure of the cross section every 250 mm after the plugboard and display the streamline in the entire flow area. With an increase in the depth of the plugboard, the area of backflow behind the board also increases. During the analysis of the plugboard's flow field, it is concluded that a high and low pressure zone will form behind the plate. As the relative depth *h* of the plugboard increases, the area ratio of the plugboard to the inlet section increases, and its blocking effect on the airflow increases, leading to a further decrease in the total pressure value in the low-pressure zone. Additionally, an increase in *h* will result in more flow blockage. When *h* = 0.22, the reflux area accounts for 30% of the flow area, and when *h* = 0.36, the counter current area accounts for 80% of the flow area, resulting in increased flow loss, a wider range of low-pressure areas, and greater flow non-uniformity.

Figure 9 illustrates the changes in the total pressure nephogram of the AIP section under the condition of n_{1r} = 100%. The total pressure distribution of the AIP section changes as the depth of the plugboard increases. The low-pressure area continuously expands, causing throttling of the airflow and consequently an increase in total pressure for the parts not covered by the plugboard. This leads to an enhancement in the overall total pressure non-uniformity of the AIP section. The average total pressure of the AIP section at five different insertion depths is as follows: 98.3kPa, 99.3kPa, 99.8kPa, 100.3kPa, and 100.5 kPa. Additionally, the average total pressure of the low-pressure area is 95.0, 96.7, 97.5, 98.2, and 98.1 kPa, respectively. The increase in plugboard depth results in a wider range of the low-pressure zone and a continuous increase in the total pressure loss of the AIP section.

Figures 10, 11 depict the variation in total pressure and *DP* counter of the AIP section under the condition of n_{1r} = 100%. The starting and ending positions of the plugboards with different parameters in the circumferential direction of the flow path are identical, resulting in a nearly identical area of the low-pressure region in the AIP cross-section. However, when the straight plate is substituted with a circular arc plate or a concave-convex plate, the area of blockage by the plugboard alters. Consequently, the larger the blockage area, the greater the total pressure loss, leading to lower average total pressure across the AIP section and increased total pressure distortion.

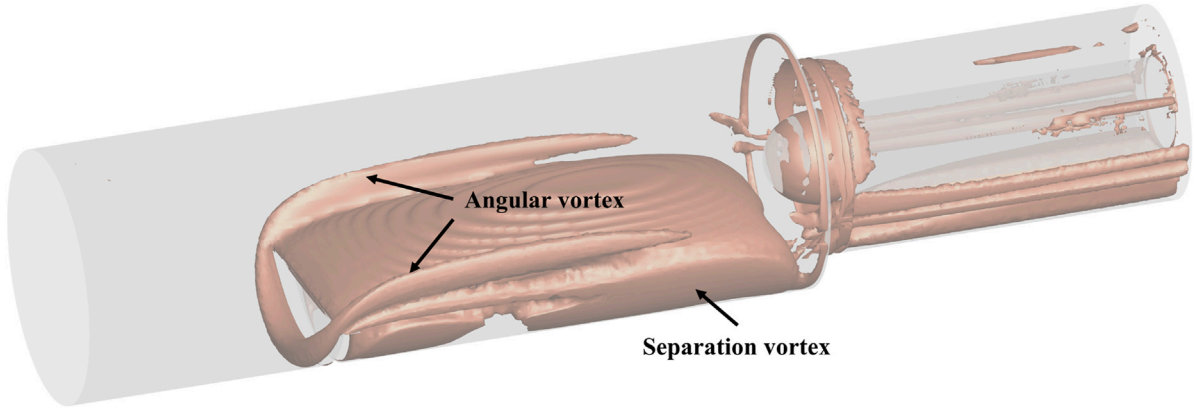

FIGURE 14
Ω-criterion vortex analysis.

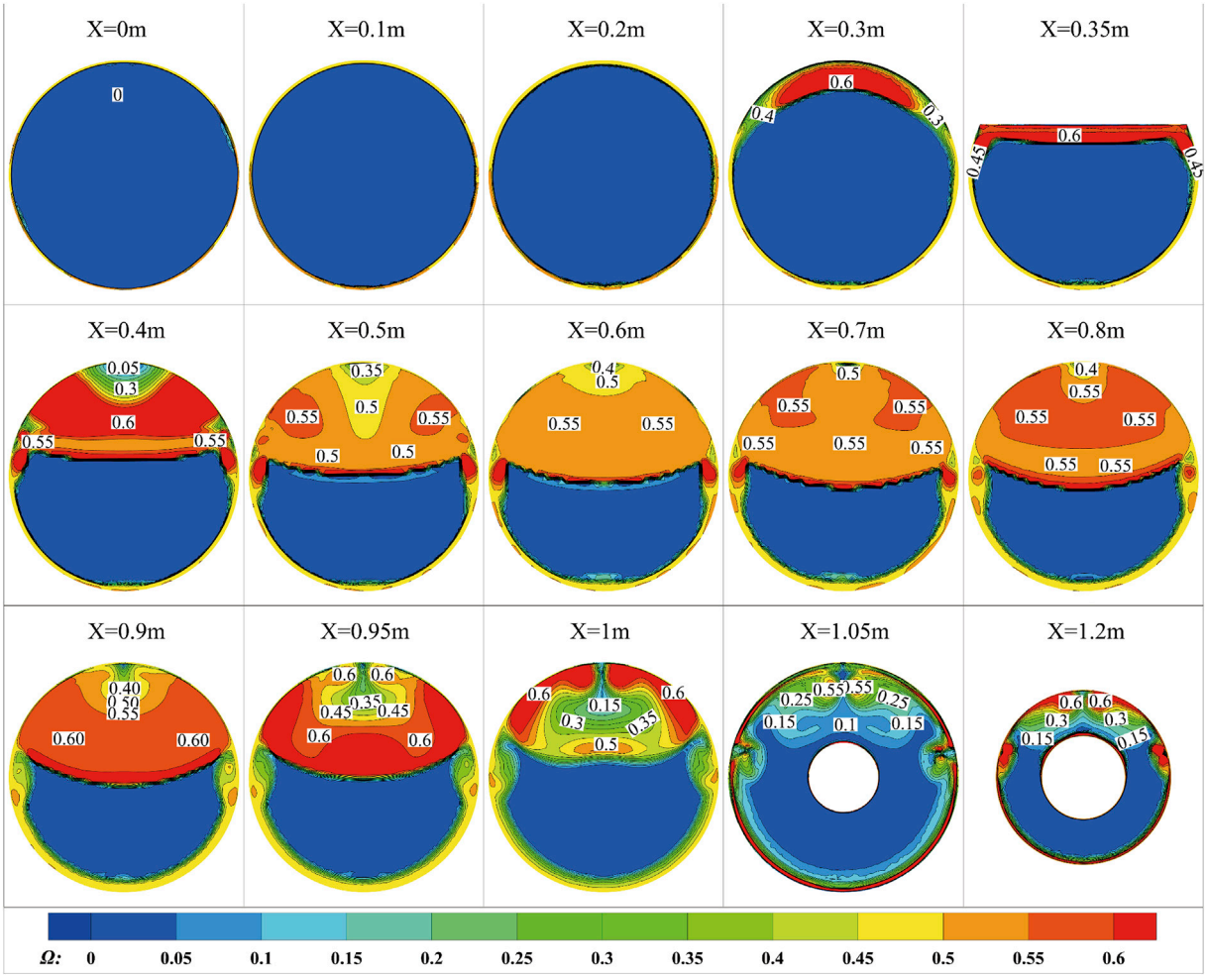

FIGURE 15
AIP section (n_{1r} = 100%) Ω vortex distribution.

When compared with the straight plate, the arc plate affects the flow blockage to a greater extent than the concave-convex plate under the same h condition. Upon comparing the data in Figure 11, it becomes apparent that when the plugboard possesses a concave shape, the total pressure non-uniformity of the AIP section using the circular plate is less than that of the concave-convex plate. Conversely, when the plugboard has a convex shape, the total pressure non-uniformity of the AIP section using the circular plate is greater than that of the concave-convex plate. Through analysis, it is evident that changing the shape parameters of the plugboard can modify the total pressure distortion and yield expected distortion equivalent simulation results without altering the circumferential area of the low-pressure region in the AIP section.

The total pressure distortion DP of the AIP section under five working conditions of n_{1r} = 20%–100% (inlet mass flow of 1.5–7.5 kg/s) and different plugboard heights is summarized in Figure 12. Increasing the working flow at the same plugboard height leads to higher flow velocity in the flow channel, greater difference between the low pressure and low-speed zone formed after the airflow is blocked by the plugboard and the main flow, increased flow non-uniformity after the plugboard, and greater distortion in the AIP section. Similarly, increasing the height of the plugboard at the same working flow rate also results in higher flow non-uniformity and distortion. The influence of plugboard height on total pressure distortion becomes stronger with increasing working flow. The working flow and plugboard height are positively correlated with the total pressure distortion of the AIP section. The relationship between h and DP under various working conditions is summarized in Figure 13, which also analyzes the relationship between h, DP, and n_{1r}. Flow simulation is conducted under the conditions of n_{1r} = 100%, h = 0.29, and under all operating conditions h = 0.21. The comparison error between the results and the relationship is less than 1.5%, confirming the accuracy of the relationship for predicting the total pressure distortion DP of the AIP section. Using this formula, the necessary plugboard parameters for the required distortion test conditions can be quickly obtained before conducting the compressor distortion test.

Figure 14 displays the results obtained from the implementation of the Ω criterion vortex identification method to examine the flow characteristics after the plugboard. The visualization indicates the formation of a stagnant vortex in the upstream region of the plugboard. As the airflow proceeds past the plugboard, a portion deviates towards the flow channel wall, leading to the creation of an angled vortex at the intersection between the plugboard and the wall. This corner vortex maintains relative independence and gradually dissipates along the flow direction, exhibiting a positive correlation with the plugboard's height. Simultaneously, the bypassing airflow generates a separation vortex due to shear forces. A comparative analysis reveals similarities in the position and extent of the low-speed reflux zone and the separation vortex. Upon entering the inlet cowl, contributing to a more uniform flow field through airflow mixing and momentum transfer, consequently diminishing its spatial extent.

Figure 15 shows the distribution of Ω at different positions in the X direction. As can be seen from the figure, the upstream vortices of the plugboard are mainly concentrated near the wall in front of the plugboard, with a small influence range of vortices, but a large value of central vortex Ω.

The intensity of vortices in the 0.35–0.4 and 0.8–0.9 m regions behind the plugboard is larger, while the intensity and velocity of vortices in the middle region are smaller. The range and intensity of the rectification vortex caused by the intake rectifying cap during the process of air flow passing through X = 1–1.1 m are significantly smaller. However, it cannot completely eliminate the non-uniformity of the airflow. The area with a large Ω value at X = 1.1 m is essentially the same as the low-pressure area. By comparing the Ω criterion values with the changes in fluid along the flow, it can be observed that regions with large Ω values are basically the same as the low-speed regions of the flow. The Ω value may be suitable for correlating eddy currents with flow parameters. It is important to note that due to the complexity of geometric characteristics, the Ω value cannot be directly equated to the flow velocity. Non-etheless, the Ω criterion still can be used as an auxiliary method for analyzing the flow field non-uniformity caused by the plugboard.

4 Conclusion

This article selects the distortion of ship inlet as the research object and conducts distortion equivalent tests and simulation calculations on plugboard devices of different heights and shapes. By analyzing the changes in the flow field structure of the computational domain and compressor inlet, the relationship between the insertion plate parameters and total pressure distortion is summarized. The following conclusions are summarized:

1. On the premise that the height of the plugboard h is constant, change the shape of the plugboard to arc plugboard or concave and convex plugboard, the total pressure distortion DP can be adjusted while the area of the circumferential low-pressure zone remains unchanged. The distortion DP of Total pressure is positively correlated with the blocking area of the plug plate.
2. The increase in work flow and plugboard height leads to an increase in flow non-uniformity, resulting in an increase in total pressure distortion of the AIP section. Based on the summary of the research results, the relationship between the plugboard height h and the total pressure distortion DP is obtained. This relationship can realize the rapid prediction of the total pressure distortion DP of the AIP section under different working conditions.
3. The analysis of the equivalent simulated flow field through the Ω criterion can reflect the change of the range and intensity of vortices in the flow process. The augmentation of vortex range and intensity within the flow field leads to an increase in flow losses, and further decreases in total pressure and velocity, resulting in an enhancement of flow non-uniformity. This indicates that the Ω criterion may serve as an auxiliary method for analyzing flow distortion caused by the plugboard.

Data availability statement

The original contributions presented in the study are included in the article/Supplementary material, further inquiries can be directed to the corresponding author.

Author contributions

Z-YW: Methodology, Supervision, Writing–original draft, Writing–review and editing. CH: Software, Validation, Writing–original draft, Writing–review and editing. YW: Funding acquisition, Resources, Writing–review and editing. Y-LQ: Project administration, Validation, Writing–review and editing.

Funding

The author(s) declare financial support was received for the research, authorship, and/or publication of this article. The work of this paper was completed with the support of National Natural Science Foundation of China (NO. 52101348) and the National Science and Technology Major Project (2017-V-0002-0051), and I would like to express my sincere gratitude.

Conflict of interest

The authors declare that the research was conducted in the absence of any commercial or financial relationships that could be construed as a potential conflict of interest.

Publisher's note

All claims expressed in this article are solely those of the authors and do not necessarily represent those of their affiliated organizations, or those of the publisher, the editors and the reviewers. Any product that may be evaluated in this article, or claim that may be made by its manufacturer, is not guaranteed or endorsed by the publisher.

References

Beale, D., Cramer, K., and King, P. (2002). "Development of improved methods for simulating aircraft inlet distortion in turbine engine ground tests," in *Aiaa aerodynamic measurement technology and ground testing conference*. St. Louis, Missouri: (ASME). doi:10.2514/6.2002-3045

Beale, D., Davis, M., and Sirbaugh, J. (2006). "Requirements and advances in simulating aircraft inlet total-pressure distortion in turbine engine ground tests," in *ASME turbo expo 2006:power for land, sea and air*. Barcelona, Spain: (ASME). doi:10.1115/GT2006-90038

Beale, D., Wieland, S., Reed, J., and Wilhite, L. (2007). "Demonstration of a transient total-pressure distortion generator for simulating aircraft inlet distortion in turbine engine ground test," in *ASME turbo expo 2007: power for land, sea and air*. Montreal, Canada: (ASME). doi:10.1115/GT2007-27222

Bobula, G. A. (1979). Effects of steady-state pressure distortion on the stall margin of a J85-21 turbojet engine. NASA Thechnical Reports.

Braithwaite, W. M., Dicus, J. H., and Moss, J. E. (1970). Evaluation with a turbofan engine of air jets as a steady-state inlet flow distortion device technical memorandum. NASA Thechnical Reports.

Chen, F., Ren, X., Li, Y., and Gu, C. (2023). Experimental and numerical study on aerodynamic stability of compressor L-inlet duct. *Aerosp. Sci. Technol.* 139, 108368. doi:10.1016/j.ast.2023.108368

Cheng, B., Wang, J., Feng, L., Wei, Y., Wang, Z., and Li, J. (2020). Review of aero-engine inlet swirl distortion research. *J. Aerosp. Power* 35 (12), 2465–2481. doi:10.13224/j.cnki.jasp.2020.12.001

Hubble, J. D., and Smith, R. E. (1979). *Evaluation of an airjet distortion generator used to produce steady-state, total pressure distortion at the inlet of a general electric F101-GE-I00 turbofan engine*. AEDC.

Jiang, Y., Zhang, B., Chen, S., Chen, G., and Mei, F. (2009). Test-based syntonic analysis of the aero-engine inserted-board inlet dynamic distortion pressure. *J. Aerosp. Power* 9, 2057–2062.

Jiang, Y., Zhang, F., Zhang, B., Kong, W., Tang, Y. B., Huang, M. C., et al. (2007). Caveolin-1 sensitizes rat pituitary adenoma GH3 cells to bromocriptine induced apoptosis. *J. Air Force Eng. Univ. Sci. Ed.* 7 (02), 1–3. doi:10.1186/1475-2867-7-1

Jinghua, C., and Baofeng, T. (2015). Full annulus numerical simulation of aerodynamic stability of compressor with total pressure distortion. *J. Propuls. Technol.* 36 (5), 729–736. doi:10.13675/j.cnki.tjjs.2015.05.012

Kan, K., Chen, H., Zheng, Y., Zhou, D., Binama, M., and Dai, J. (2021b). Transient characteristics during power-off process in a shaft extension tubular pump by using a suitable numerical model. *Renew. Energy* 164, 109–121. doi:10.1016/j.renene.2020.09.001

Kan, K., Yang, Z., Lyu, P., Zheng, Y., and Shen, L. (2021a). Numerical study of turbulent flow past a rotating axial-flow pump based on a level-set immersed boundary method. *Renew. Energy* 168, 960–971. doi:10.1016/j.renene.2020.12.103

Kutschenreuter, J. P., Collins, T., and Vier, W. I. (1973). P 3G-A new dynamic distortion generator. *J. Aircr.* 11 (6), 344–348. doi:10.2514/3.59256

Liu, Y., Chen, J., and Huang, G. (2022b). Study on stability and dynamic flow law of baffle in pipe. *Mach. Build. Automation* 51 (03), 125–129. doi:10.13477/j.cnki.aeroengine.2022.03.016

Liu, Z., Cai, C., He, Z., Xu, G., Gao, L., and Yang, L. (2022a). Inlet pressure distortion test of aeroengine under different plug. *Aeroengine* 48 (03), 101–105.

Liu, Z., Zhang, S., Yin, Y., Wang, Z., Luan, Y., and Zhou, S. (2021). Research on thrust calibration technology of aeroengine indoor test bench. *J. Appl. Fluid Mech.* 15 (1), 109–116.

Maghsoudi, I., Vaziry, A. M., and Mahmoodi, M. (2020). Experimental investigation of flow and distortion mitigation by mechanical vortex generators in a coupled serpentine inlet-turbofan engine system. *Chin. J. Aeronautics* 33 (05), 1375–1391. doi:10.1016/j.cja.2019.12.002

Mankbadi, M. R., and Georgiadis, N. J. (2015). Examination of parameters affecting large-eddy simulations of flow past a square cylinder. *AIAA J.* 53 (6), 1706–1712. doi:10.2514/1.j053684

Mcllveen, M. W. (1979). *Further test results with the airjet distortion generator system*. Las Vegas,NV,U.S.A.: AIAA, 79–1185. doi:10.2514/6.1979-1185

Meyer, C. L., Mc Aulay, J. E., and Biesiadny, T. J. (1970). Technique for inducing controlled steady-state and dynamic inlet pressure disturbances for jet engine tests. NASA Thechnical Reports.

Naseri, A., Boroomand, M., and Tousi, A. M. (2012). "The effect of inlet flow distortion on performance of a micro-jet engine," in *ASME 2012 international mechanical engineering congress and exposition*. Houston, Texas, USA: ASME. doi:10.1115/IMECE2012-86865

Overall, B., and Harper, R. (1974). "The airjet distortion generator system: a new tool for aircraft turbine engine testing," in *13th propulsion conference* (Orlando,FL,U.S.A: AIAA), 77–993. doi:10.2514/6.1977-993

SAE Aerospace Information Report AIR-1419 (1999). *Inlet total-pressure distortion considerations for gas turbine engines*. Society of Automotive Engineers.

SAE S-16 Committee ARP 1420, Revision B (2002). *Gas turbine inlet flow distortion guidelines*. Society of Automotive Engineers.

Sivapragasam, M. (2019). Flow field behind a complex total pressure distortion screen. *Proc. Institution Mech. Eng. Part G J. Aerosp. Eng.* 233 (14), 5075–5092. doi:10.1177/0954410019837862

Song, G., Li, J., Tang, M., Wu, Y., and Luo, Y. (2021). Experimental simulation methodology and spatial transition of complex distortion fields in a S-shaped inlet. *Aerosp. Sci. Technol.* 2021, 116.

Tu, B., Xuan, B., Li, C., Zhang, X., and Hu, J. (2021). Experimental and numerical investigation on total pressure distortion generated by a rectangular movable flat baffle. *Adv. Mech. Eng.* 13 (2), 168781402199439. doi:10.1177/1687814021994397

Wu, Z., Cai, W., Zhang, T., Chen, X., and Li, W. (2022). An improved model for predicting dynamic total pressure distortion. *Aerosp. Sci. Technol.* 130, 107932. doi:10.1016/j.ast.2022.107932

Xia, A., Huang, X., Wei, T., and Zhou, M. (2018). Experimental study of a controlled variable double-baffle distortion generator engine test rig. *Chin. J. Aeronautics* 31 (9), 1880–1893. doi:10.1016/j.cja.2018.06.015

Yin, C., Hu, J., Guo, J., Yan, W., and Zhang, C. (2015). Three-dimensional body-force model for effect on compressor performance of inlet distortion. *J. Aerosp. Power* 30 (9), 2241–2250. doi:10.13224/j.cnki.jasp.2015.09.025

Yusoof, M. S., and Deshpande, M. D. (2015). Strip distortion generator for simulating inlet flow distortion in gas turbine engine ground test facilities. *Propuls. Power Res.* 5 (4), 287–301. doi:10.1016/j.jppr.2016.11.004

Zhang, T., Zhao, Y., Zhao, W., and Chen, B. (2017). Design and research of movable total pressure distortion generator. *J. Propuls. Technol.* 38 (12), 2706–2715. doi:10.13675/j.cnki.tjjs.2017.12.009

Zhang, X., Li, J., Song, G., Zhou, Y., and Xie, H. (2019). Numerical simulation on flat baffle inlet of axial compressor. *J. Aerosp. Power* 34 (5), 1153–1165.

Zhou, Y., Li, J., Peng, S., Song, G., Jiang, A., and Zhang, Y. (2017). Numerical simulation of flat baffle inlet distortion coupled with compressor. *J. Aerosp. Power* 32 (3), 568–576. doi:10.13224/j.cnki.jasp.2017.03.007

Zhou, Y., Li, J., Song, G., and Nie, Y. (2018). Experimental study of the flat battle inlet distortion with compressor. *J. Eng. Thermophys.* 3 (39), 489–496.

frontiers | Frontiers in Energy Research

TYPE Original Research
PUBLISHED 05 February 2024
DOI 10.3389/fenrg.2024.1344676

OPEN ACCESS

EDITED BY
Maria Grazia De Giorgi,
University of Salento, Italy

REVIEWED BY
Guangjie Peng,
Jiangsu University, China
Hamid Reza Rahbari,
Aalborg University, Denmark

*CORRESPONDENCE
Ruofu Xiao,
xrf@cau.edu.cn

RECEIVED 26 November 2023
ACCEPTED 22 January 2024
PUBLISHED 05 February 2024

CITATION
Xiao W, Gui Z, Lu Z, Xiao R and Tao R (2024), Pressure pulsation of pump turbine at runaway condition based on Hilbert Huang transform. *Front. Energy Res.* 12:1344676.
doi: 10.3389/fenrg.2024.1344676

Pressure pulsation of pump turbine at runaway condition based on Hilbert Huang transform

Wei Xiao[1], Zhonghua Gui[1], Zhaoheng Lu[2,3], Ruofu Xiao[2,3]* and Ran Tao[2,3]

[1]Pumped Storage Technology and Economy Research Institute of State Grid Xinyuan Company Ltd., Beijing, China, [2]College of Water Resources and Civil Engineering, China Agricultural University, Beijing, China, [3]Beijing Engineering Research Center of Safety and Energy Saving Technology for Water Supply Network System, China Agricultural University, Beijing, China

Pumped storage is an important component of electrified wire netting. The safe and stable operation of pump turbines is extremely important. Among them, pressure pulsation is one of the main causes of pump turbine vibration. The characteristics of pressure pulsation are relatively complex, and it is difficult to directly observe their temporal changes using commonly used FFT methods. The division of frequency characteristics is often vague. Meanwhile, it is difficult to explain some phenomena such as frequency doubling. This article focuses on a certain model of pump turbine and uses SST model to numerically simulate the runaway condition of the pump turbine. And the Hilbert Huang transform method is used to analyze the pressure pulsation in the vaneless region and draft tube. The results show that the main characteristic frequencies of the vaneless region are blade passing frequency 112.5 Hz and rotational frequency 12.5 Hz. The main characteristic frequencies of the draft tube are vortex rope frequency near 3 Hz which energy ratio is up to 50%, rotational frequency, and blade passing frequency. The pressure pulsation characteristics in the vaneless region have changed from a complex composition of double blade passing frequency and rotational frequency to a distribution dominated by blade passing frequency. In the passage of the guide vane, the pressure pulsation is almost only characterized by blade passing frequency. The frequency characteristics of the vaneless region between the runner and the guide vane become complex again. Meanwhile, the results show that the characteristic frequencies of the vaneless region and the draft tube propagate upstream and downstream.

KEYWORDS

pump turbine, pressure pulsation, hilbert huang transform, runaway, rotor stator interaction

1 Introduction

Due to environmental damage, traditional energy is gradually transitioning towards new energy. New energy sources such as solar energy, wind energy, and nuclear energy have been vigorously developed (Carlson and Davidson, 2021; Ji et al., 2022; Kong et al., 2022). However, it poses a huge burden on the safe and stable operation of the electrified wire netting (Quaranta et al., 2021). Therefore, pumped storage units, as a typical energy storage system, have been widely used in electrified systems (Li et al., 2019; Bahzad et al., 2022). The vibration problem of pumped storage power plants has always been an inevitable important problem. Unit vibration can reduce the operating efficiency of the unit, causing vibrations in

the volute, inflow pipeline, and plant structure (Pei et al., 2014). The causes of typical hydraulic machinery vibration are divided into mechanical vibration, hydraulic vibration, and electromechanical vibration. During the operation of the "Anapo" pumped storage power plant in Sicily, Italy, there was significant vibration in the guide vanes, and the vibration mainly came from the vaneless region (Mauro et al., 2019). Egusquiza et al. (2012). Reported an investigation into a malfunction of a large pump turbine runner caused by rotor stator interaction. Further research has shown that the pressure pulsation in the vaneless region is the main cause of failure. The powerhouse structure of pumped storage power stations is mainly located underground. With the advancement of technology, pump turbines are required to develop towards the direction of high efficiency, high flow rate, and high operating range. The diverse operating conditions have made it easier for the unit to operate at deviations from the design point, resulting in increasingly severe harm caused by hydraulic vibration. Therefore, for the safety and economic considerations of personnel and equipment, vibration urgently need to be reduced.

At the turbine conditions of pump turbines, the stability problem of the transition process is mainly caused by the S characteristic (Trivedi et al., 2017; Suh et al., 2021). Due to the fact that reversible water pump turbines often have lower specific speeds, larger runner diameters, and stronger centrifugal effects. The inflow of the runner will quickly decrease due to inertia when passing through the runaway condition. Because of the obstruction of liquid, the runner rotation speed will decrease. When at the reverse pump condition, the runner rotation speed will increase again. The characteristic forming a curve shaped like "S", named as "S" characteristic. "S" characteristic may cause pump turbines into different condition, leading to significant instability. For example, Zeng et al. (2017) found that the water hammer pressure during load rejection of a pump turbine is highly correlated with the S characteristic. Zhang et al. (2020) found that the strong radial force on the runner may cause the shaft oscillation of the generator set at runaway condition.

In order to clarify the pressure pulsation and vibration characteristics, a large number of scholars have conducted relevant experimental and numerical simulation studies. The pressure pulsation in the vaneless region is mainly caused by the interaction between the runner blades and guide vanes, which is also known as rotor stator interaction. The phenomenon of rotor stator interaction is mainly caused by two factors. One is that the blades of the runner rotate periodically and interfere with the inviscid flow field in the vaneless region, resulting in periodic changes in the flow field. Secondly, the viscous effect of the fluid leads to unstable flow phenomena (Agnalt et al., 2019). Therefore, rotor stator interaction can be considered as inviscid interaction and viscous interaction (Zuo et al., 2015). Trivedi et al. (2013) found that the rotor stator interaction leads to unstable pressure pulsations, which are high-frequency pressure pulsations through experiments and numerical simulations. KC et al. (2014) and Goyal et al. (2016), Goyal et al. (2018) found that the pressure pulsation in the vaneless region is mainly caused by rotor stator interaction with a frequency several times number of the guide vanesSome scholars at home and abroad have studied the influence conditions of rotor stator interaction to control its amplitude. Trivedi (Chirag et al., 2014; Trivedi et al., 2014; Trivedi et al., 2016; Trivedi et al., 2018a; Trivedi et al., 2018b) has conducted long-term research on the transient process of mixed flow hydraulic turbines. During the research process, it was found that during the transient process, the amplitude of pressure pulsation in the vaneless region showed a significant increase, and there was a certain functional relationship between the amplitude of pressure pulsation and the opening of the guide vanes. When the transient process ends, the amplitude of pressure pulsation will sharply increase by 30 times. Laouari and Ghenaiet, (2019) demonstrated that the amplitude of pressure pulsation caused by rotor stator interaction increases with the increase of guide vane opening. And the pressure pulsation generated varies with the angle of rotation. Wallimann and Neubauer (2015) found comparison that found that the radial distance of the vaneless region affects its amplitude through three-dimensional unsteady calculations and experimental results.

As one of the typical characteristics of pressure pulsation, the vortex rope mainly appears in the draft tube at partial load conditions. Due to its generally low frequency, resonance is prone to occur. Baya et al. (2010) found that the frequency of the vortex rope in the draft tube is 0.2–0.4 times the rotational frequency at partial load conditions caused vibration. Yexiang et al. (2010) indicated that as the load increases from small to large, the pressure pulsation in the draft tube first increases, then decreases, and then increases again. Nicolet et al. (2010), Nicolet et al. (2011) and Kuznetsov et al. (2014) found that the vortex rope in the draft tube is the excitation source of resonance phenomenon, and due to the comprehensive excitation of rotation, cavitation, and fluid structure coupling effects of the vortex rope in the draft tube, a typical pressure pulsation characteristic of 1–3 times the rotational frequency was generated. Favrel et al. (2014) found that the resonance phenomenon is mainly caused by the precession frequency of the vortex rope in the draft tube. Duparchy et al. (2015) found that the synchronous component signal of vortex rope was amplified, causing severe vibration of the unit. Pasche et al. (2019) found that the synchronous component signal is the coupling between the draft tube vortex rope and the draft tube wall, which propagates upstream and downstream. Its source may be located at the impact of the draft tube wall and vortex rope. Favrel et al. (2016) also observed three forms of vortex rope in the draft tube through PIV technology and found that there is a sudden change in the vortex rope during the flow state change process, exacerbating instability.

This article focuses on the model machine of a certain model of water pump turbine. By using the Hilbert Huang transform method, analyze the pressure pulsation in the vaneless region and draft tube under runaway conditions. To explain and analyze the pressure pulsations in the vaneless region and draft tube under runaway conditions and the reasons for their formation. The innovation of this article is to use the HHT method to analyze the pressure pulsation characteristics under runaway conditions, clarify the main sources of pressure pulsation in each region, and prove its propagation characteristics towards upstream and downstream as the flow direction changes.

2 Research objective

2.1 Reversible pump-turbine model

In this study, the research objective is a reversible pump-turbine in model scale. The model is 1:9 times that of the prototype. As shown in Figure 1, the reversible pump-turbine has five components

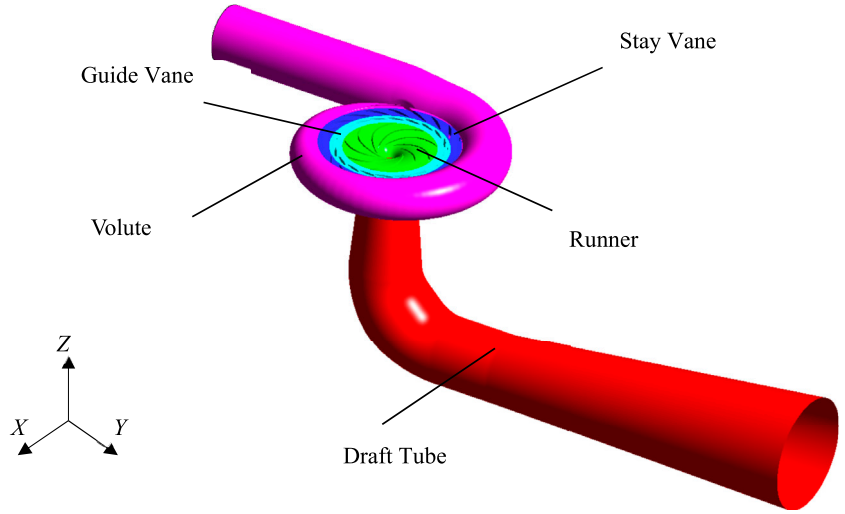

FIGURE 1
Components of the reversible pump-turbine model.

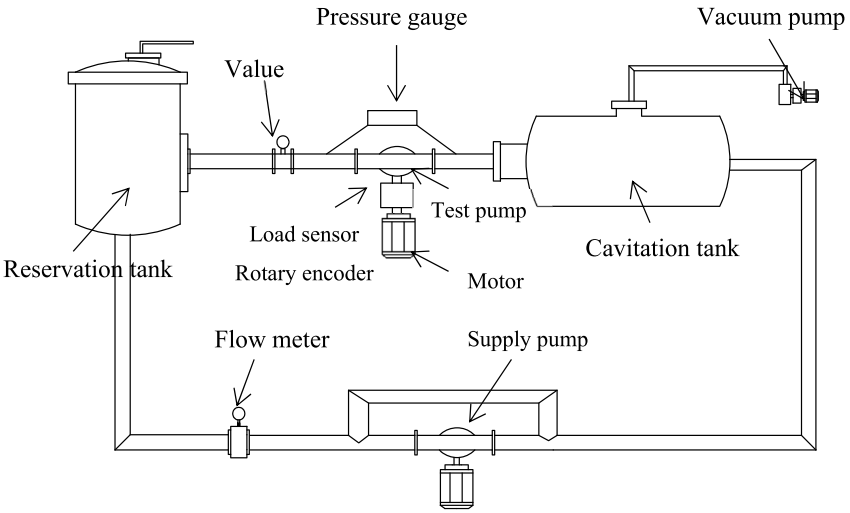

FIGURE 2
Schematic of the test rig.

as follows: volute, stay vane, guide vane, runner and draft tube. The runner rotates around Z-axis. In turbine mode, the flow is from volute to draft tube and the runner rotates counterclockwise. In pump mode, the flow is from draft tube to volute and the runner rotates clockwise. The high-pressure side and low-pressure side diameters of runner are 560 mm and 300 mm, respectively. The width of runner high pressure side is 57.2 mm. The numbers of runner blade, guide vane blade and stay vane blade are 9, 20 and 20, respectively. The maximum angle of guide vane opening is 38°.

Unit speed n_{11} and unit discharge Q_{11} are defined as:

$$Q_{11} = \frac{Q}{D^2 \times H^{0.5}} \quad (1)$$

TABLE 1 Test apparatus and uncertainty.

Quantity	Apparatus	Uncertainty
Flow Rate	Electromagnetic Flow Meter	±0.18%
Rotation Speed	Rotary Encoder	±0.02%
Head	Differential Pressure Sensor	±0.05%
Torque	Load Sensor	±0.05%
Torque	Excitation Amplifier	±0.02%
Tailwater Pressure	Static Pressure Sensor	±0.10%
Guide Vane Opening Angle	Angular Displacement Sensor	±0.10°

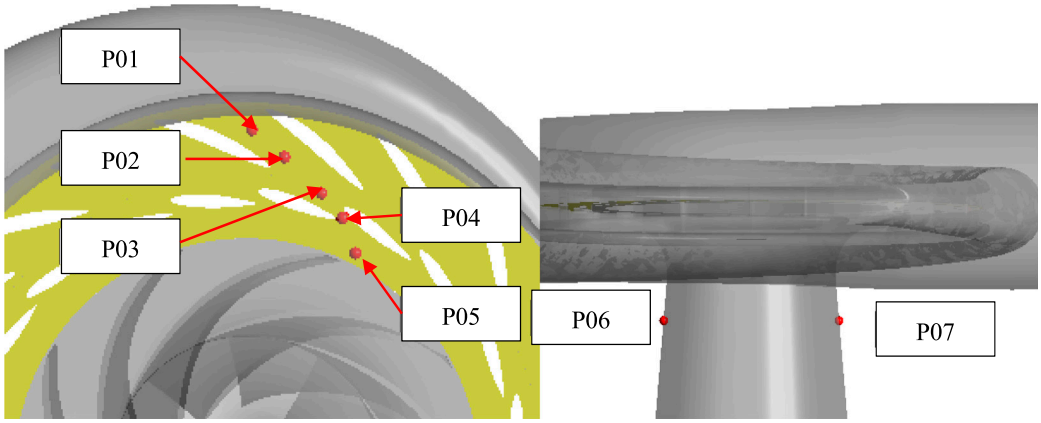

FIGURE 3
Schematic of monitoring points.

TABLE 2 Evaluation results of discretization error.

	P01	P02	P03	P04	P05
ϕ_1	162563.8	209644.2	212537.3	212911.1	212967.5
ϕ_2	162547.9	206980	210109.5	210595.7	210683.3
ϕ_3	161477.6	200084.8	203303.1	203577.3	203746.7
p	16.17965	3.585788	3.896462	4.199812	4.206775
ϕ_{ext}^{21}	162564	211454.4	213988.1	214138.6	214175.2
e_{ext}^{21}	1.68E-06	0.00856	0.00678	0.005732	0.005639
GCI_{fine}^{21}	0.0002%	1.0793%	0.8532%	0.7207%	0.7089%

$$n_{11} = \frac{n \times D}{H^{0.5}} \tag{2}$$

where Q is the flow rate (m^3/s), H is the head (m), D is the high pressure side diameter of the runner (m).

2.2 Model test rig and apparatus

The experimental study was conducted on the test rig shown in Figure 2. The components of test rig are as follows: test pump-turbine model, reservation tank, motor, cavitation tank, flow stabilization tank, flow meter, supply pump, pipe and valve. The test rig is designed for the experiment of pump-turbine. Based on the IEC-60193–1999, 'S' shape characteristics were measured. The maximum test head of test rig is 120 m. The maximum flow rate of test rig is 1.2 m^3/s. The dynamometer output of test rig is 600 kw. The dynamometer maximum rotating speed of test rig is 1900rpm. The tailwater pressure of test rig is -85-250kpa.

Data acquisition is based on PXI (Peripheral Component Interconnection extensions for Instrumentation) system. The test parameters are measured by corresponding sensors. The apparatuses used for pump-turbine testing and the corresponding uncertainties are shown in Table 1. The flow rate is measured by using electromagnetic flowmeter with the uncertainty of ± 0.18%. The rotation speed is measured by using rotary encoder with the uncertainty of ± 0.02%. The head is measured by using differential pressure sensor with the uncertainty of ±0.05%. The Torque is measured by using load sensor with the uncertainty of ±0.05% and excitation amplifier with the uncertainty of ± 0.02%. The tailwater pressure is measured by using static pressure sensor with the uncertainty of ± 0.10%. The guide vane opening angle is measured by using angular displacement sensor with the uncertainty of ± 0.10°. The shaft power is calculated by torque and rotational speed. The efficient is calculated by the flow rate, head and shaft power, with uncertainty within ± 0.25%.

3 Numerical method and setup

3.1 Numerical method for turbulent flow and energy dissipation

In this study, the numerical simulation is based on the CFD. The three-dimensional incompressible flow is simulated based on the Reynolds average Navier-Stokes (RANS) method. Because of the turbulent pulsation term, the equations are not closed. Therefore, it is necessary to construct a turbulence model to close the equations. In this paper, the SST k-ω model (Menter, 1994) is chosen to close by establishing the relationship between Reynold's stress and eddy viscosity. This model has good simulation results for large curvature flow and separated flow. A large number of researches show that this model can be used in CFD simulation of engineering problems. The kinetic energy k equation and specific dissipation rate ω equation are as follows:

$$\frac{\partial(\rho k)}{\partial t} + \frac{\partial(\rho u_i k)}{\partial x_i} = \tilde{P}_k - \beta^* \rho \omega k + \frac{\partial}{\partial x_i}\left[(\mu + \sigma_k \mu_t)\frac{\partial k}{\partial x_i}\right] \tag{3}$$

$$\frac{\partial(\rho \omega)}{\partial t} + \frac{\partial(\rho u_i \omega)}{\partial x_i} = \alpha \rho S^2 - \beta \rho \omega^2 + \frac{\partial}{\partial x_i}\left[(\mu + \sigma_\omega \mu_t)\frac{\partial \omega}{\partial x_i}\right] + 2(1 - F_1)\rho \sigma_{\omega 2}\frac{1}{\omega}\frac{\partial k}{\partial x_i}\frac{\partial \omega}{\partial x_i} \tag{4}$$

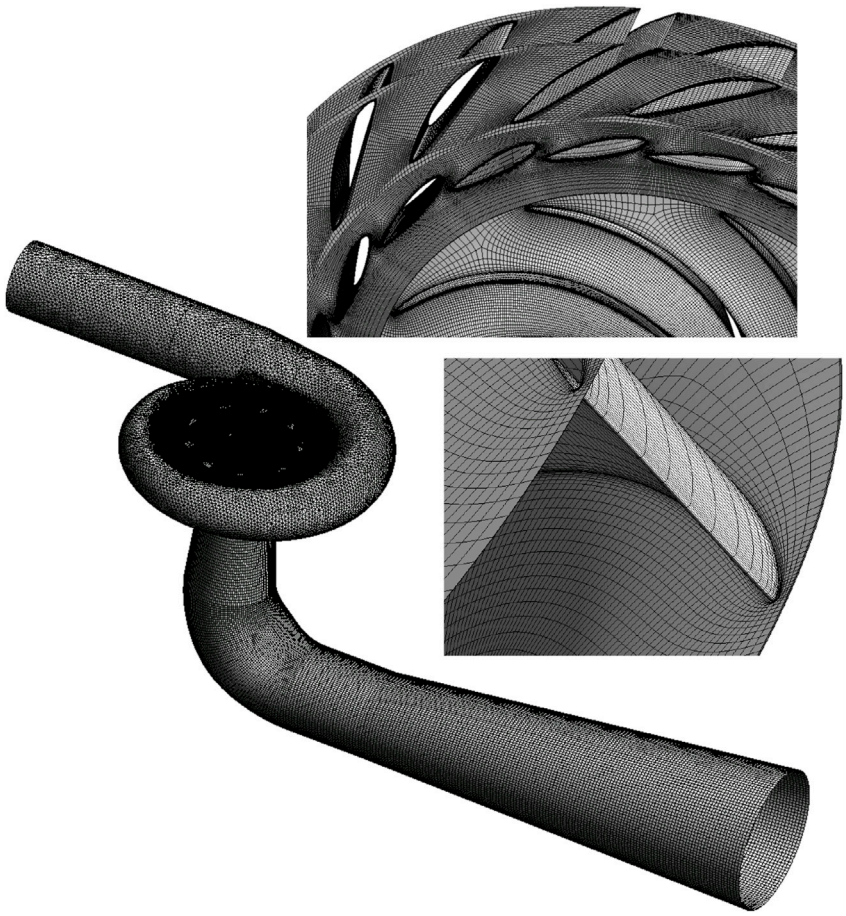

FIGURE 4
Schematic map of grid using in CFD simulation.

TABLE 3 Mesh number details of the computational domain.

Part	Element type	Elements
Draft Tube	Hexahedral	661010
Runner	Hexahedral	1417500
Guide Vane	Hexahedral	1272960
Stay Vane	Hexahedral	1157856
Volute	Tetrahedral	676265
Total	—	5185591

where P_k is the production term of turbulent kinetic energy, S is the invariant measure of the strain rate, Parameters β, β^*, σ_k, and σ_ω are constants of the turbulence model, μ is the dynamic viscosity, and F_1 is the blending function, μ_t is turbulent eddy viscosity.

The analysis method of Fourier transform is mainly based on the assumption of linearity and stationarity, but in most systems, the data is closer to including both nonlinearity and non-stationary. The signal of pressure pulsation is often complex and non-sinusoidal. Therefore, FFT often presents many fallacies or incorrect information. Meanwhile, non-periodic, time-varying or impulsive features are often hidden. HHT has effectively solved the above problems. Therefore, new methods are needed to address this type of data analysis. Hilbert Huang Transform (HHT) is an empirical data analysis method with adaptive expansion basis, which can obtain physically meaningful representations of nonlinear non-stationary data (Huang et al., 1998). HHT is divided into two parts: empirical mode decomposition (EMD) and Hilbert transform (HT). This method was proposed by Huang in 1998. Huang believes that any complex signal can be decomposed into a finite number of intrinsic mode functions (IMF), and then HT is performed on each IMF component to obtain physically meaningful instantaneous frequencies, Hilbert spectra, and energy distributions, in order to intuitively represent the time-frequency characteristics of each component of the original signal.

The IMF has two conditions:

1) In the entire data, the number of extreme points and zero crossing points is either equal or at most 1 difference.
2) The mean of the envelope defined by the local maximum and the envelope defined by the local minimum at any point is equal to 0.

Each IMF represents a simple oscillation mode, corresponding to a simple harmonic function, but it is more general: it replaces the constant amplitude and frequency in a simple harmonic function, and the IMF

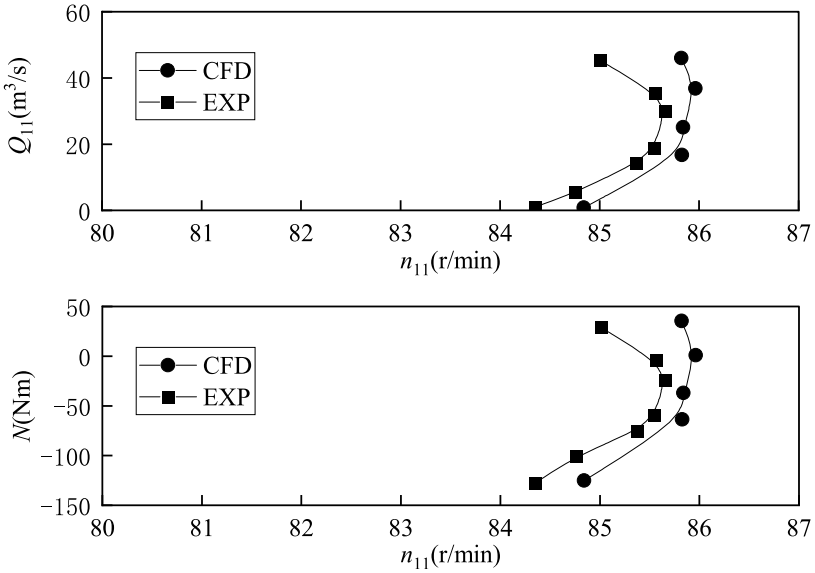

FIGURE 5
Comparison between CFD and experimental of 'S' shape characteristic.

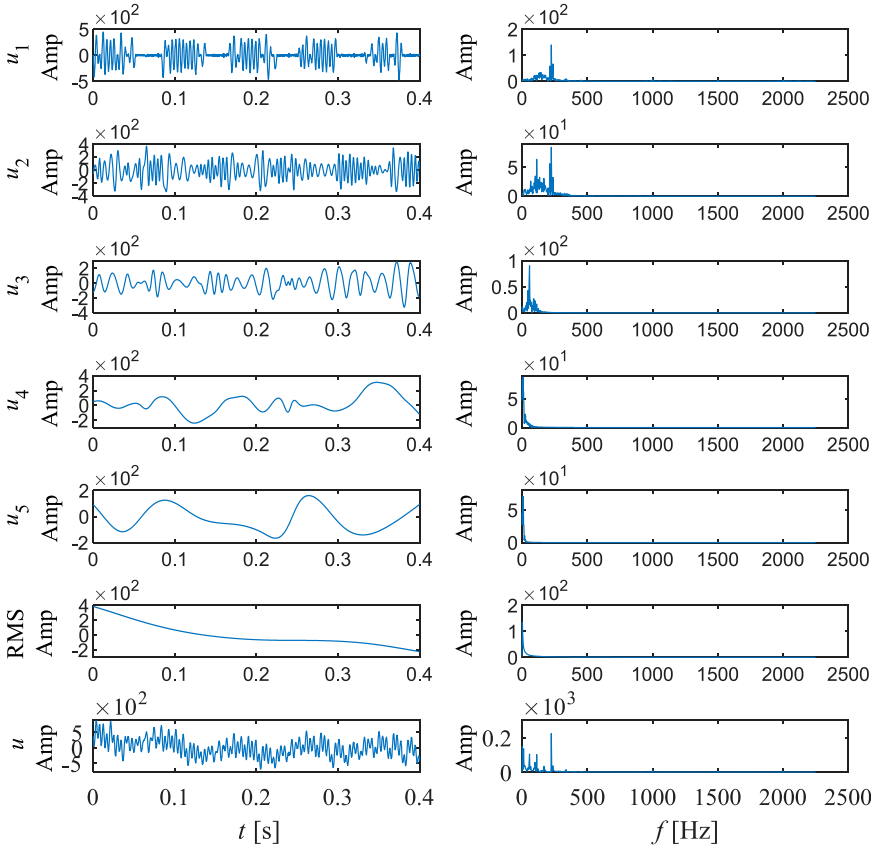

FIGURE 6
Empirical mode decomposition of pressure pulsation signal at P01.

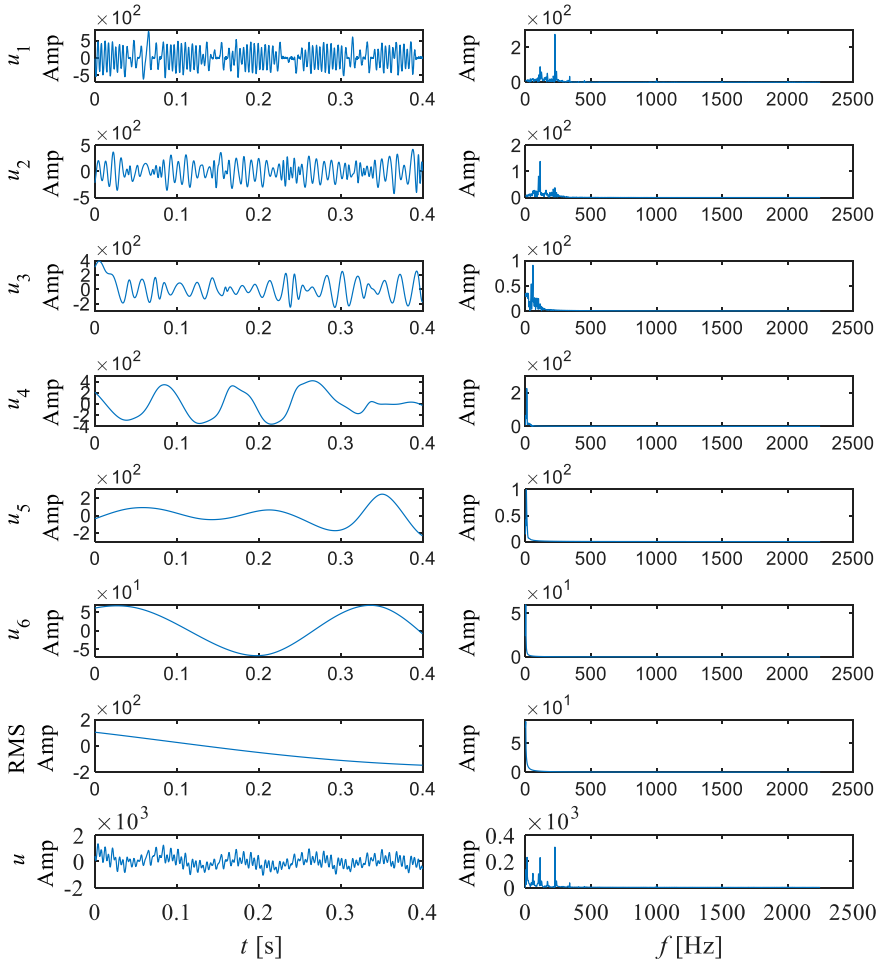

FIGURE 7
Empirical mode decomposition of pressure pulsation signal at P02.

can have varying amplitude and frequency as a function of time. Usually, the original signal cannot meet the conditions of IMF, so Huang obtained IMF through empirical mode decomposition. According to the definition of the IMF, decomposition is carried out by identifying all local extremum values, obtaining the upper and lower envelopes using a cubic spline function. The upper and lower envelopes should cover all data, and then taking the mean of the envelopes to obtain the IMF. Subtract the obtained IMF from the original signal to obtain the intermediate signal, and then repeat the above steps. Stop decomposition until the requirements are met. In this way, the raw data can be decomposed into several IMF and one residual term Rn.

For a given IMF, the Cauchy principal value of the convolutional integral can be obtained through Hilbert transform to obtain the HT result:

$$\mathcal{H}f(t) = \frac{1}{\pi} p.v \int_{-\infty}^{+\infty} \frac{f(\tau)}{t-\tau} d\tau \tag{5}$$

Where t is the integral variable of HT, and p. v is the Cauchy principal value integral. By using the Hilbert transform, the analytical signal can be obtained as follows:

$$f_A(t) = f(t) + i\mathcal{H}f(t) = A(t)e^{i\phi(t)} \tag{6}$$

In the formula, ÅÅ t Å is the instantaneous phase, A (t) is the instantaneous amplitude, and their functional relationship with the original signal is as follows:

$$A(t) = \sqrt{f(t)^2 + \mathcal{H}f(t)^2} \tag{7}$$

$$\phi(t) = \arctan\left(\frac{\mathcal{H}f(t)}{f(t)}\right) \tag{8}$$

The instantaneous frequency $\omega(t)$ is the derivative of the instantaneous phase:

$$\omega(t) = \phi'(t) \tag{9}$$

After obtaining the IMF and its HT results and corresponding analytical signals, correlation analysis of the Hilbert spectrum can be performed on them. After using the Hilbert transform, the obtained Hilbert amplitude spectrum $H(\omega,t)$ can be represented in the real part of the analytical signal:

$$H(\omega,t) = \Re\left\{\sum_{k=1}^{K} A_k(t) e^{i\phi_k(t)}\right\} \tag{10}$$

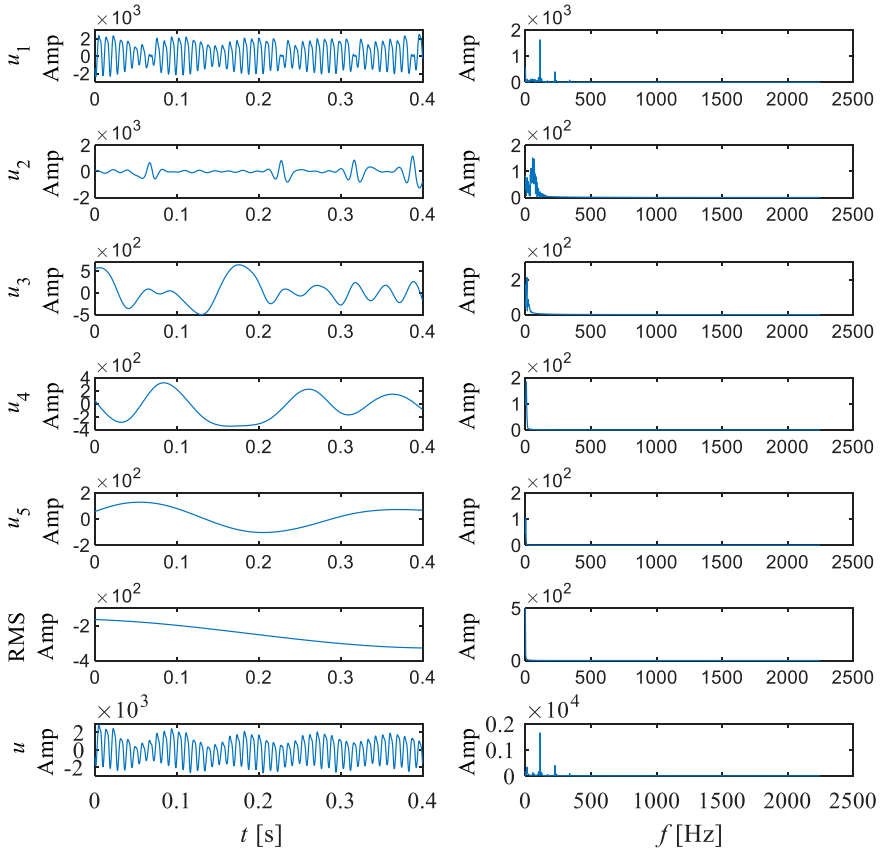

FIGURE 8
Empirical mode decomposition of pressure pulsation signal at P03.

Where K is the number of IMF. In order to further clarify the importance and proportion of each IMF in the signal, the energy ratio E_p is defined as follows

$$E_p = \frac{\sum A_k^2(t)}{\sum_{k=1}^{K}\sum A_k^2(t)} \tag{11}$$

3.2 Setup of CFD

The CFD simulation was based on ANSYS CFX. In this study, the analyzed working condition is the runaway condition of the pump turbine. The multiple reference frame is adopted to analyze the rotating model. The impeller was defined as a rotating domain by 750 r/min and others were defined as stationary. General grid interface (GGI) is used for the data transfer between the two adjacent domains. In this case, environment variables are set as follows. The reference pressure is set as 101.325 kPa. The fluid medium is water under the reference temperature of 20°C, which is continuous fluid. The simulation con-siders the heat transfer. The turbulence model is chosen SST k-ω model. The steady simulation finishes in 1000 iterations.

The boundary conditions of steady RANS simulation are as follows. In pump mode, the draft tube inflow is set as mass flow rate inlet boundary. The value depends on the flow rate. Turbulence intensity on the inlet boundary is 5%. The draft tube outflow is set as the average static pressure outlet boundary, which relative pressure is 0 Pa. All the wall boundaries are set as no-slip wall where velocity on the wall is zero. The volute inflow is set as flow rate inlet boundary which values are based on the experiment. All the wall boundaries are set as no-slip wall where velocity on the wall is zero.

Because of the need of pressure pulsation analysis, the unsteady RANS simulation is conducted. The steady CFD result is set as the initial condition. The unsteady simulation conducts totally 10 runner revolutions which 1 revolution is divided for 360 steps. The one steps need 20 iterations. The convergence criterion was the root mean square residual (RMS) of the momentum equation and the continuity equation less than 5×10^{-5}. Considering the stability of unsteady calculations, the last five cycles were selected as the results for analysis.

In this study, the arrangement of discrete monitoring points was used to study pressure pulsation as shown in the Figure 3. Due to the pressure pulsation of the pump turbine, the main sources are the vaneless region and the draft tube, seven monitoring points were selected in the draft tube and vaneless region. Five monitoring points are located in the middle of the flow streamline in the middle of the crown and ring of guide vane and stay vane. And two monitoring points are located 0.1 m away from the runner low pressure side in the draft tube.

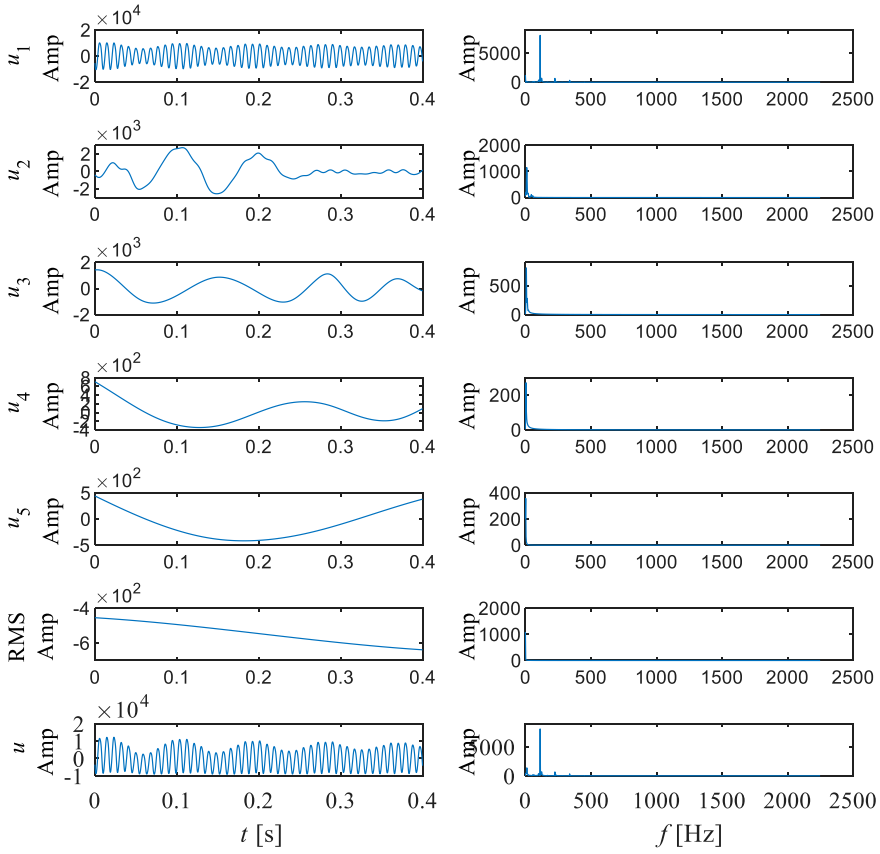

FIGURE 9
Empirical mode decomposition of pressure pulsation signal at P04.

3.3 Grid preparation for CFD

To carry out CFD simulation, it is necessary to discretizes the convective domain, which is based on finite volume method. The number of grid elements has an obvious influence on the result. The type of grid has an obvious influence on the convergence and efficiency of calculation. Hence, the Hexahedral grid is selected to improve computational efficiency. The grid convergence index (GCI) (Celik and Karatekin, 1997)is used to check the three different grid schemes.

The fine, medium and coarse grids have 11056456, 5185591 and 2376580 elements based on refinement ratio of 1.3. The index is the pressure of the monitoring points in the vaneless, guide vane and stay vane. As shown in Table 2, ϕ_1 to ϕ_3 are evaluated variables. P is observation accuracy order. ϕ_{ext}^{21} are extrapolated values. e_{ext}^{21} are the relative error of extrapolated value. $\mathrm{GCI}_{\mathrm{fine}}^{21}$ are the convergence index of the grid. For the different key parameters between M1 and M2, the relative errors of extrapolated values are under 1%. The grid convergence index is between 0.0002% and 1.0793%. Obviously, the mesh scheme meets the requirement of convergence criteria and the accuracy of simulation can be well guaranteed. However, there is a high computational cost for the fine grid scheme, which should be considered. Hence, the medium scheme is selected used to simulate finally.

The detailed information of mesh nodes and elements of medium scheme is shown in Figure 4 and Table 3. In this study, the values of y^+ are about 10–100 for most of the areas on the surface of the flow domain. The maximum values of y^+ on the surface of draft tube, runner, guide vane, stay vane and volute are approximately 75, 120, 150, 200 and 75.

4 Results and analyses

4.1 Experimental-numerical accuracy

For the accuracy of the numerical simulation results, a validation is necessary to compare CFD and experimental data. The 'S' shape characteristic curve of the pump turbine is shown in Figure 5. The figure shows the relationship between torque N and unit speed n_{11}, as well as the relationship between unit discharge Q_{11} and unit speed n_{11}. It can be observed that at the runaway point position ($N = 0$), the experimental and CFD results are in good agreement, with a unit speed error of approximately 0.4%. The overall curve trend is relatively matched, with a clear 'S' shape. Explain that the numerical simulation results are relatively accurate.

4.2 Pressure pulsation analysis in the vaneless region

In this study, the direction of flow is from the volute to the draft tube. Figure 6, Figure 7, Figure 8, Figure 9, Figure 10 show the

10.3389/fenrg.2024.1344676

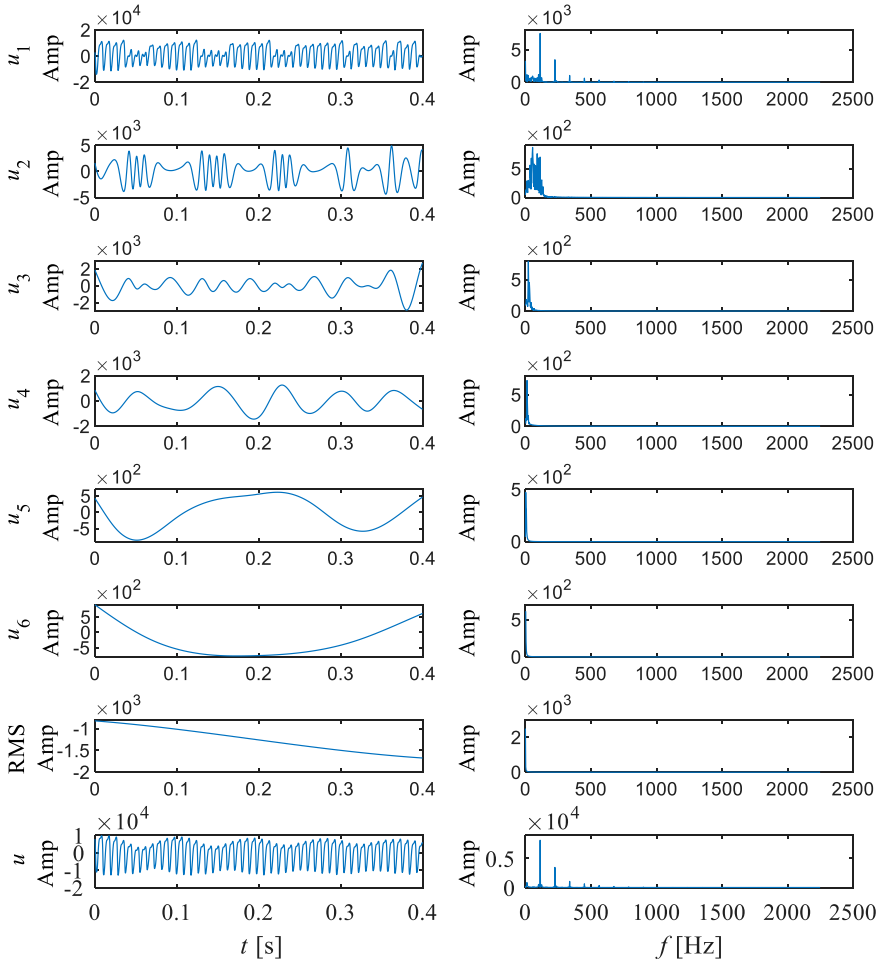

FIGURE 10
Empirical mode decomposition of pressure pulsation signal at P05.

TABLE 4 Energy ratio of each IMF.

Type	IMF1 (%)	IMF2 (%)	IMF3 (%)	IMF4 (%)	IMF5 (%)	IMF6
P01	31.36	22.93	15.27	19.51	10.93	—
P02	38.33	15.85	9.63	29.04	5.77	1.38%
P03	88.04	5.39	4.07	2.17	0.33	—
P04	94.29	3.88	1.47	0.16	0.20	—
P05	88.78	7.76	1.52	0.97	0.44	0.53%

TABLE 5 Center frequency of each IMF.

Type	IMF1	IMF2	IMF3	IMF4	IMF5	IMF6
P01	261.22	166.54	68.56	13.79	6.62	—
P02	194.23	135.28	62.37	10.56	6.84	3.02
P03	115.39	49.04	18.38	7.61	2.77	—
P04	112.55	20.05	8.08	4.56	2.24	—
P05	115.36	50.37	30.70	13.06	4.06	2.05

empirical mode decomposition results of monitoring points in the vaneless region. Table 4 shows the energy ratios of each IMF at this point. Table 5 shows the center frequencies of each IMF after monitoring point decomposition. Point P01 is located near the volute in the stay vane flow channel. There are five main modes of pressure pulsation at this point, among which the energy proportion of IMF1 is the highest, accounting for 31.36%. And IMF2 is the second highest, accounting for 22.93%. It can be observed that overall, the energy share of the five IMF's is relatively close. According to Figure 6 and Table 4, it can be

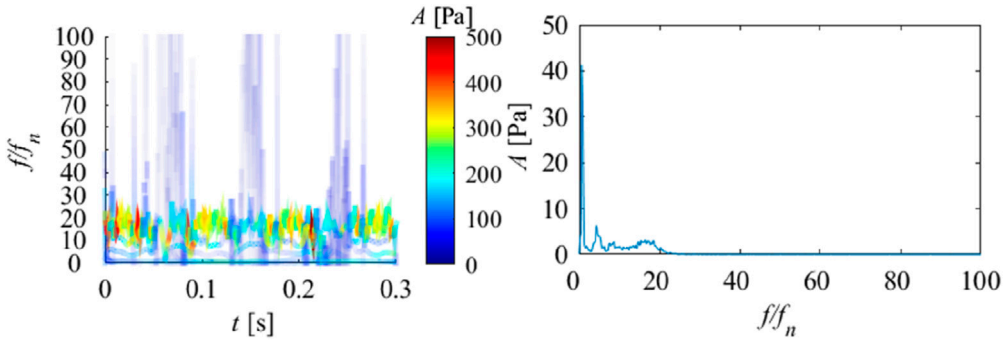

FIGURE 11
Hilbert spectrum (right) and marginal spectrum (left) of pressure pulsation signal at P01.

observed that the center frequency of IMF1 is 261.22, and the overall time signal of IMF1 shows a discontinuous pattern. After Fourier transform, the double blade passing frequency is the main high amplitude frequency. The center frequency of IMF2 is 166.54. The time signal of IMF2 is relatively continuous, and after Fourier transform, it contains blade passing frequency components and double blade passing frequency components. The center frequency of IMF3 is 68.56, and after Fourier transform, the main frequency of the components is similar to the center frequency. The center frequency of IMF4 is 13.79, and after Fourier transform, its main component is rotational frequency. The center frequency of IMF5 is 6.62, which is a typical low frequency. It can be observed that at point P01, except for IMF5, all other components account for a considerable proportion, indicating that the frequency component at this point is relatively complex. According to Figure 11, it can be observed that there is a significant periodic signal present at the double blade passing frequency position, and the components at this position also occupy the main position. But the corresponding instantaneous frequency changes quickly. In contrast, the instantaneous frequency of low-frequency components is relatively stable. From the marginal spectrum, it can also be seen that compared to high-frequency components, low-frequency components have a strong influence. This indicates that in this region, the influence of blade passing frequency is relatively discontinuous and varies greatly, while the influence of rotational frequency components is more stable and sustained.

Point P02 should be located in the middle of the stay vane flow channel. It can be observed that the energy proportion of IMF1 at this position is the highest, accounting for 38.33%, while IMF4 is the second highest, accounting for 29.04%. According to Figure 7 and Table 4, it can be observed that the center frequency of IMF1 is 194.23, and after Fourier transform, the double blade passing frequency is the main high amplitude frequency. Compared to point P01, the discontinuity of IMF1 significantly weakens. The center frequency of IMF2 is 135.28, and after Fourier transform, the blade passing frequency is the main frequency component. The center frequency of IMF3 is 62.37, and after Fourier transform, the main frequency of the components is similar to the center frequency. The center frequency of IMF4 is 10.56, and after Fourier transform, its main component is rotational frequency. The center frequencies of IMF5 and IMF6 are 6.84 and 3.02, which are low-frequency components. It can be observed that the frequency components of this point are still relatively complex, but compared to point P01, the amplitudes of IMF2 and IMF4 are significantly enhanced. This indicates a significant increase in the intensity of blade passing frequency and rotation frequency. According to Figure 12, it can be observed that the Hilbert spectrum and marginal spectrum of P02 are similar to those of P01, but it is evident that at the double blade passing frequency position, the instantaneous frequency is more stable, while the originally occurring high-frequency instantaneous frequency is significantly reduced. This indicates that in this region, the double blade passing frequency and blade passing frequency gradually tend to be stable and continuous, but the rotational frequency is still the most stable and has the longest impact duration.

Point P03 is located in the vaneless region between the stay vane and the guide vane. It can be observed that the energy ratio of IMF1 at this position dominates, accounting for 88.04%. The proportion of other IMF components is extremely low. According to Figure 8 and Table 4, it can be observed that the center frequency of IMF1 is 115.39, and the time signal waveform of IMF1 is relatively continuous. After Fourier transform, the blade passing frequency is the main high amplitude frequency. The center frequency of IMF2 is 49.04. After Fourier transform, it can be found that the frequency component of IMF2 is similar to the IMF3 component of P01 and P02. The center frequencies of IMF4 and IMF5 are 7.61 and 2.77, which are obvious low-frequency components. It can be observed that at point P03, the frequency component becomes clearly defined, and the blade passing frequency becomes the dominant signal. Compared to P01 and P02, the component of blade passing frequency is greatly enhanced, and through Fourier transform, it can be observed that the amplitude of other components has not changed significantly. Double the blade passing frequency becomes the harmonic of the blade passing frequency and is divided into IMF1. According to Figure 13, it can be observed that the instantaneous frequency of high frequency almost disappears, and the instantaneous frequency of blade passing frequency becomes dominant, and is more stable compared to P01 and P02. However, overall, the low-frequency components are the most stable and have the most sustained impact.

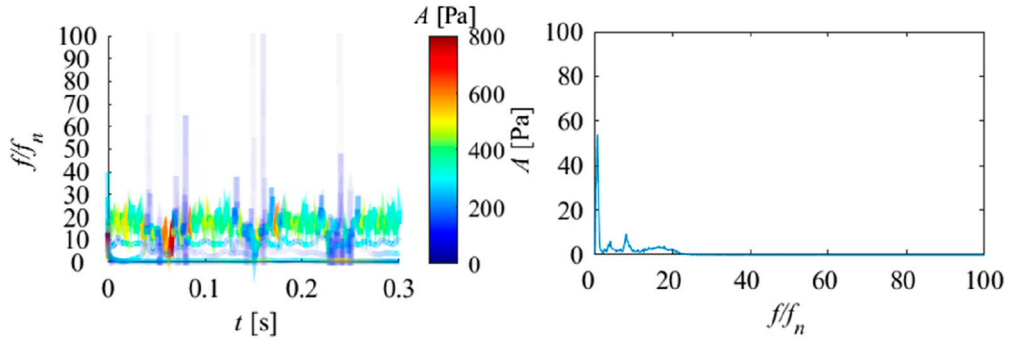

FIGURE 12
Hilbert spectrum (right) and marginal spectrum (left) of pressure pulsation signal at P02.

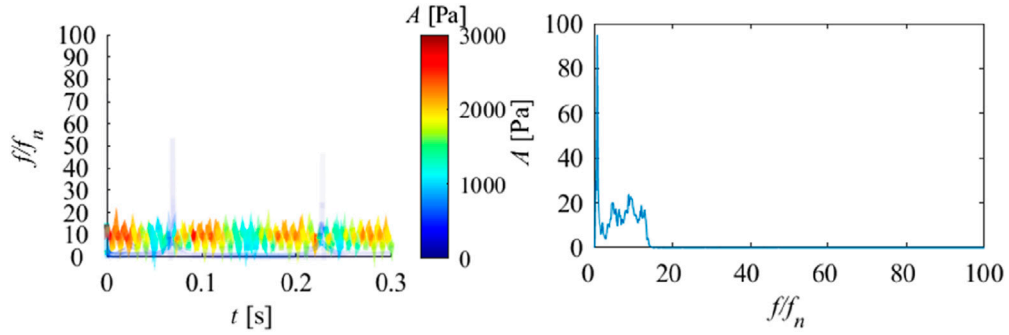

FIGURE 13
Hilbert spectrum (right) and marginal spectrum (left) of pressure pulsation signal at P03.

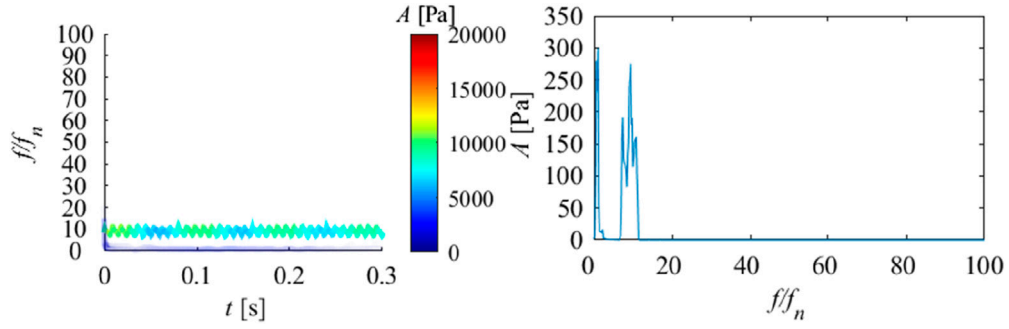

FIGURE 14
Hilbert spectrum (right) and marginal spectrum (left) of pressure pulsation signal at P04.

Point P04 is located in the middle of the guide vane channel, and it can be observed that the energy proportion of IMF1 at this position is the highest, accounting for 38.33%, while IMF4 is the second highest, accounting for 94.29%. According to Figure 9 and Table 4, it can be observed that the signal characteristics of P04 and P03 are very similar. But compared to P03, the original features of IMF2 have disappeared, and IMF1 is almost entirely composed of blade passing frequency components. At the same time, rotational frequency is further enhanced. This indicates that at this location, the characteristics of the signal are relatively pure, mainly composed of blade passing frequency and rotation frequency. According to Figure 14, it can be observed that there are only two frequency features, one near the rotation frequency and the other near the blade passing frequency. Both marginal spectrum and Hilbert spectrum prove that these two frequency features are relatively stable and have the greatest impact.

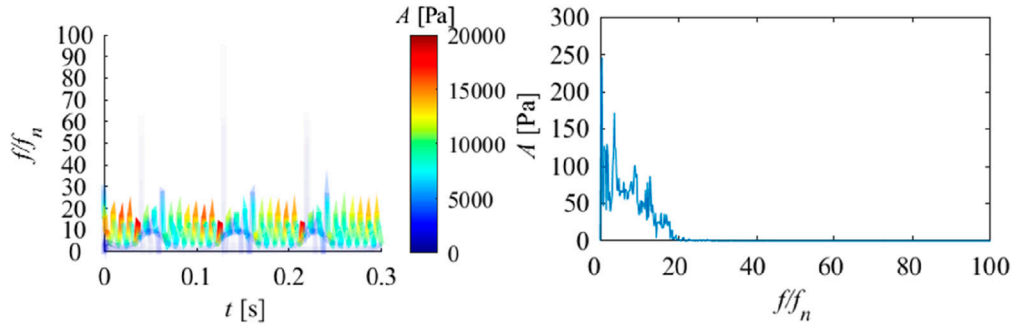

FIGURE 15
Hilbert spectrum (right) and marginal spectrum (left) of pressure pulsation signal at P05.

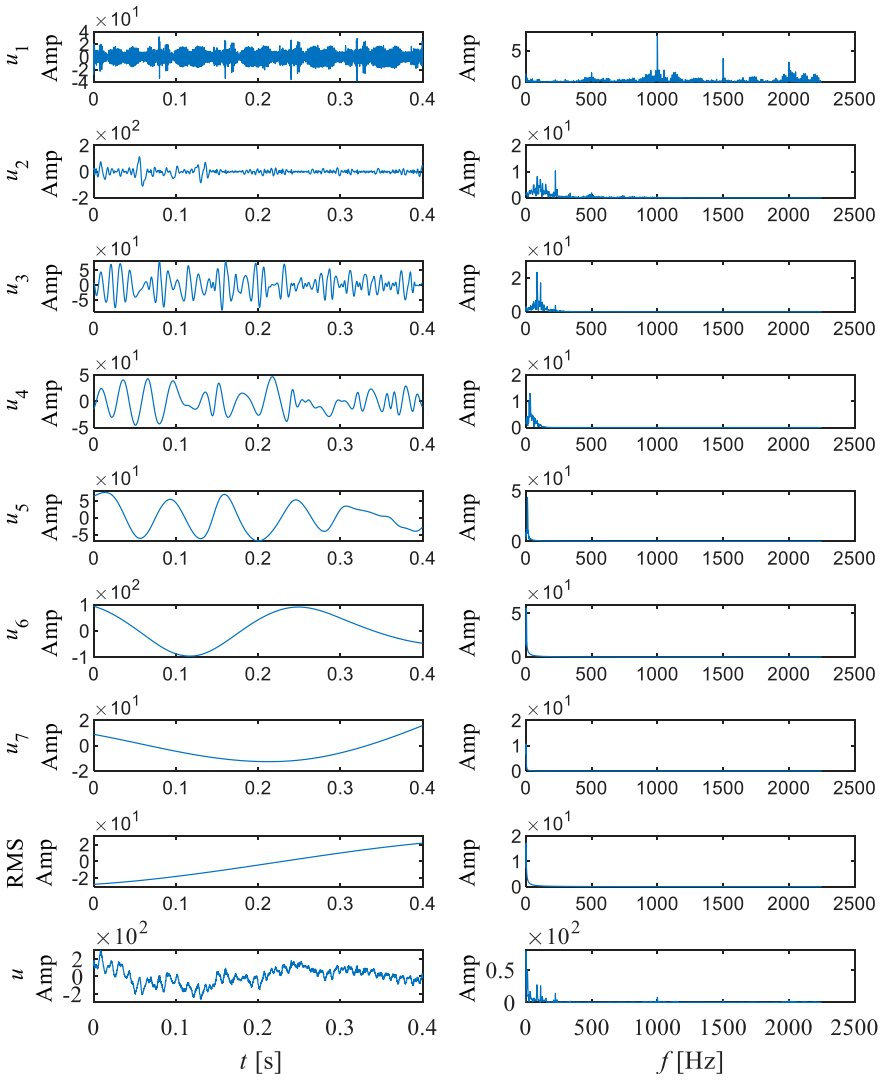

FIGURE 16
Empirical mode decomposition of pressure pulsation signal at P06.

Point P05 should be located in the vaneless region between the guide vanes and the runner. It can be observed that the energy proportion of IMF1 at this position is the highest, accounting for 88.78%. According to Figure 10 and Table 4, it can be observed that the center frequency of IMF1 is 115.36, and the overall time signal of IMF1 is continuous. After Fourier transform, it is found that it is

10.3389/fenrg.2024.1344676

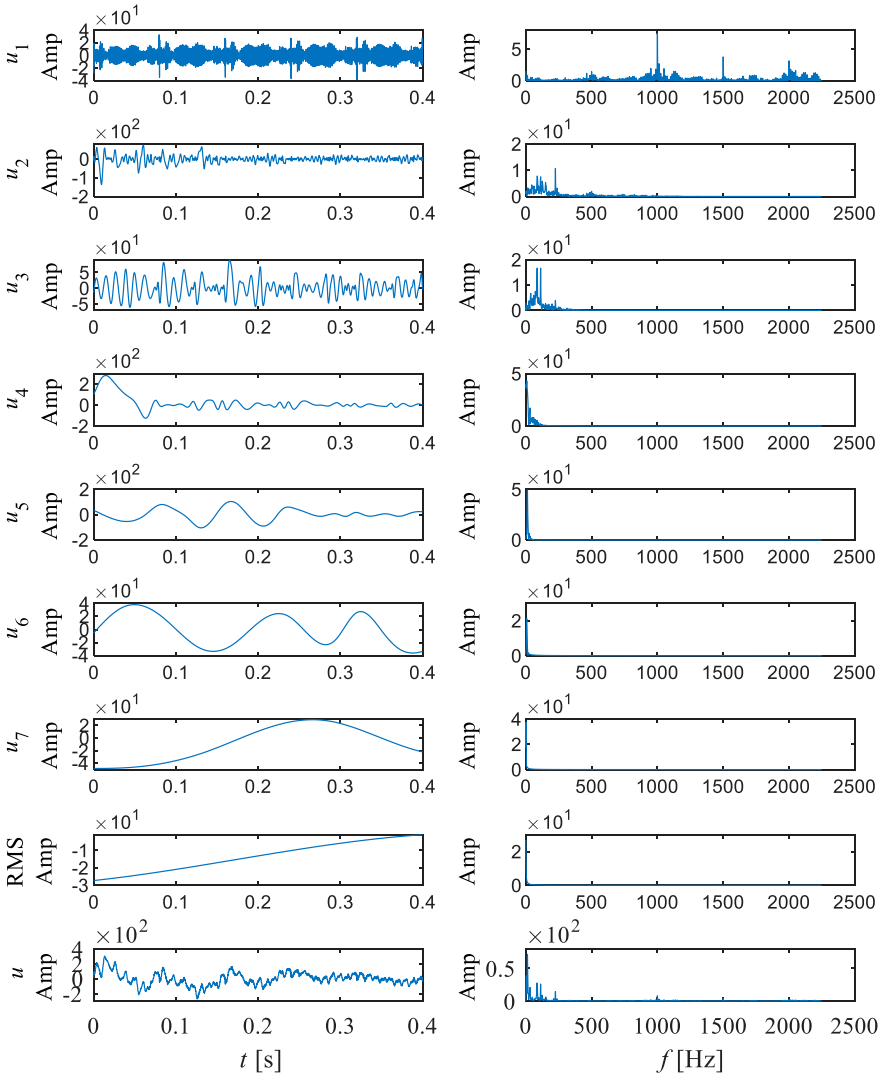

FIGURE 17
Empirical mode decomposition of pressure pulsation signal at P07.

TABLE 6 Energy ratio of each IMF in draft tube.

Type	IMF1 (%)	IMF2 (%)	IMF3 (%)	IMF4 (%)	IMF5 (%)	IMF6 (%)	IMF7 (%)
P06	1.19	6.50	13.21	5.69	23.05	49.44	0.92
P07	0.92	4.29	7.97	5.45	22.04	51.51	7.83

TABLE 7 Center frequency of each IMF in draft tube.

Type	IMF1	IMF2	IMF3	IMF4	IMF5	IMF6	IMF7
P06	1006.26	290.62	113.29	37.64	12.43	3.83	2.19
P07	975.17	275.24	118.84	35.82	17.81	7.44	2.42

composed of blade passing frequency and its harmonics. This indicates that in this region, the frequency caused by the rotation of the runner blades is more pronounced, and due to other factors interfering, harmonics occur. The center frequency of IMF2 is 50.37. After Fourier transform, the frequency component of IMF2 is similar to that of IMF2 in P03. It can be observed that at point P05, the IMF components representing blade passing frequency become more complex, while the rotational frequency still has a certain impact. At the same time, specific frequency components between blade passing frequency and rotational frequency have reappeared. According to Figure 15, it can be observed that although the instantaneous frequency near the blade passing frequency still occupies the highest instantaneous amplitude, it becomes unstable again. The low-frequency components have also become relatively unstable. The marginal

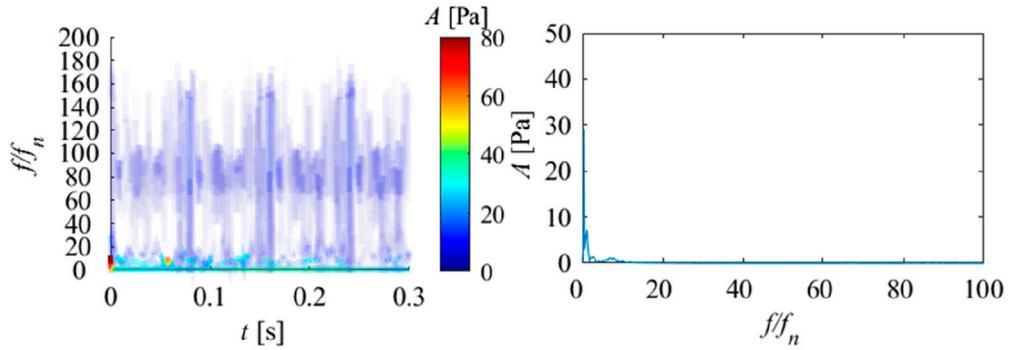

FIGURE 18
Hilbert spectrum (right) and marginal spectrum (left) of pressure pulsation signal at P06.

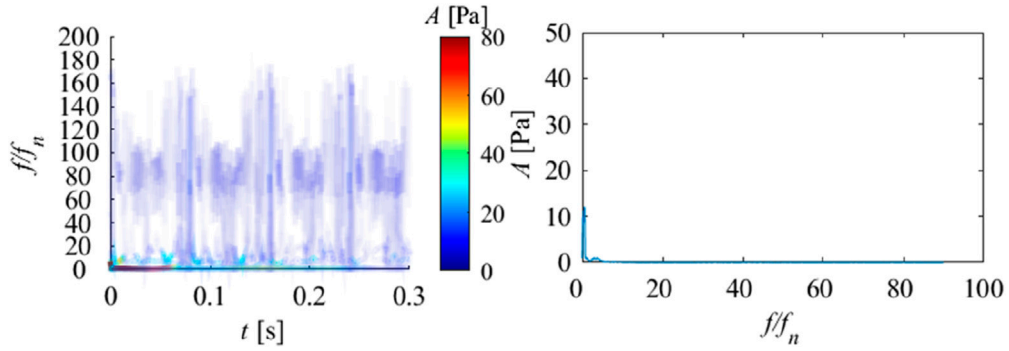

FIGURE 19
Hilbert spectrum (right) and marginal spectrum (left) of pressure pulsation signal at P07.

spectrum also fully proves this point. The effect of rotor stator interaction in the vaneless region between the runner and the guide vane leads to the complexity of pressure pulsation. Overall, in the vaneless and guide vane regions, the blade passing frequency and rotor frequency components are the main sources of pressure pulsations in this region. As water flows from the volute to the runner, the intensity of pressure pulsation gradually increases. The pressure pulsation initially consists of blade passing frequency, double blade passing frequency, rotational frequency, and specific frequency. This specific frequency may be caused by flow separation. Subsequently, as the flow towards the runner increases, the intensity of blade passing frequency and double blade passing frequency significantly increases, and the stability of each IMF under pressure pulsation significantly improves. As the flow reaches the vaneless region of the fixed and guide vanes, the blade passing frequency suddenly increases sharply and becomes more stable. The characteristics of the specific frequency also change, which may be caused by the chaotic flow pattern inside the vaneless region. As the flow reaches the middle of the guide vane, due to the small opening, the flow is constrained, which also leads to the most stable frequency change of the flow in this region, consisting only of blade passing frequency and rotor frequency, and the intensity of blade passing frequency and rotor frequency is improved. Afterwards, in the vaneless region between the runner and the guide vane, due to the effect of rotor stator interaction, harmonics appeared in the blade passing frequency, making the frequency related to the blade passing frequency unstable and greatly enhancing its strength. The frequency also slightly increased, while a specific frequency appeared in the vaneless region between the stay vanes and the guide vanes, further indicating that this frequency may be caused by the chaotic flow pattern inside the vaneless region. At this location, the composition of the pressure pulsation signal becomes extremely complex.

4.3 Pressure pulsation analysis in the draft tube

Figure 16, Figure 17 show the empirical mode decomposition results of monitoring points in the draft tube. Table 6 shows the energy ratios of each IMF at this point. Table 7 shows the center frequencies of each IMF. P06 and P07 are located symmetrically on the straight cone section of the draft tube. From Table 7, it can be observed that the energy proportion of IMF6 in P06 and P07 is the highest, at 49.44% and 51.51%, with center frequencies of 3.83 and

7.44. It can be seen that in the draft tube, low-frequency components occupy the main energy of pressure pulsation. This indicates that the pressure pulsation caused by the vortex rope in the draft tube has a significant impact on it. Among other IMF, IMF5 accounts for the second largest amount of energy. From the center frequency and Fourier transform of IMF5, it can be seen that this corresponds to rotational frequency. Meanwhile, it can be observed that the third highest energy ratio is IMF3, which corresponds to the blade passing frequency component. As shown in Figures 18, 19, in the Hilbert spectrum and marginal spectrum, it can be found that low-frequency plays an absolute dominant role and is also the main source of pressure pulsation, while other IMF components play a very low role in the entire pressure pulsation. At the same time, there are extremely unstable frequency characteristics at high frequencies, which are speculated to be influenced by fine vortex ropes. Through analysis, it can be found that the pressure pulsations in the vaneless region and the draft tube interact and influence each other. The obvious low-frequency components, rotation frequency, and blade passing frequency can be observed at different monitoring points. At the same time, it indicates that the low-frequency frequency in the vaneless region comes from the action and propagation of the vortex rope in the draft tube. This indicates the characteristic of pressure pulsation propagating upstream and downstream. Overall, under the runaway condition, the pressure pulsation of the draft tube is significantly weaker than that in the vaneless region.

5 Conclusion

This article adopts the Hilbert Huang transform method to study the pressure pulsation in the vaneless region and draft tube of the runaway condition of the pump turbine. Through research, the following conclusions were obtained:

1) The main components of pressure pulsation in the vaneless region are blade passing frequency, rotational frequency, double blade passing frequency, vortex rope frequency, and specific frequency. The overall composition is relatively complex. The main components of pressure pulsation in the draft tube are vortex rope frequency and rotational frequency. The pressure pulsations in the vaneless region and the draft tube interact and interact with each other. The obvious low-frequency vortex rope characteristics, rotation frequency, and blade passing frequency can be observed at different monitoring points.
2) Through the Hilbert Huang transform, the characteristics of each IMF can be clearly observed, making the signal composition more clear. In stay vanes, the energy of double blade passing frequency and rotational frequency plays a dominant role in pressure pulsation. In the vaneless region of fixed and guide vanes, the blade passing frequency and its harmonics occupy the highest energy. In the guide vane channel, the blade passing frequency occupies almost all of the energy. In the vaneless region of the guide vanes and runners, blade passing frequency and its harmonics play a dominant role, but the overall composition is very complex. At the same time, special frequency characteristics caused by channel separation in stay vanes and chaotic flow patterns in vaneless region were discovered. They have different frequency characteristics.
3) In the vaneless region, as water flows from the volute to the runner, the intensity of pressure pulsation gradually increases. The initial frequency composition of pressure pulsation is caused by blade passing frequency, double blade passing frequency, rotation frequency, and flow separation. Subsequently, as the flow towards the runner increases, the intensity of blade passing frequency and double blade passing frequency significantly increases, and the stability of each IMF under pressure pulsation significantly improves. As the flow reaches the vaneless region of the fixed and guide vanes, the blade passing frequency suddenly increases sharply and becomes more stable. The characteristic frequency caused by the chaotic flow pattern inside the vaneless region has occurred. As the flow reaches the middle of the guide vane, due to the small opening, the flow is constrained, resulting in the most stable frequency variation of the flow in this region, consisting only of blade passing frequency and rotor frequency. Afterwards, in the vaneless region between the runner and the guide vane, due to the effect of rotor stator interaction, harmonics appeared in the blade passing frequency, making the frequency related to the blade passing frequency unstable and greatly enhancing its strength.

Through the research in this article, it has been proven that the Hilbert Huang transform can be effectively applied to the analysis of pressure pulsations in pump turbines. The composition and specificity of pressure pulsation can be observed more effectively and intuitively. It provides a more powerful tool and intuitive display for pressure pulsation analysis. This study provides a reference for the pressure pulsation characteristics generated during the actual operation of pump turbines. Subsequently, based on this research, further research can be conducted on the variation law of pressure pulsation over time under the S-characteristic, and corresponding time-varying analysis can be carried out.

Data availability statement

The original contributions presented in the study are included in the article/Supplementary material, further inquiries can be directed to the corresponding author.

Author contributions

WX: Conceptualization, Data curation, Investigation, Methodology, Software, Supervision, Writing–review and editing. ZG: Data curation, Formal Analysis, Methodology, Project administration, Supervision, Writing–review and editing. ZL: Conceptualization, Formal Analysis, Methodology, Validation, Writing–original draft. RX: Funding acquisition, Resources, Visualization, Writing–review and editing. RT:

Formal Analysis, Project administration, Writing–review and editing.

Funding

The author(s) declare financial support was received for the research, authorship, and/or publication of this article. This research was funded by State Grid Xinyuan Group Co., Ltd. Technology Project, grant number SGXYKJ-2023-049.

Acknowledgments

The authors would like to acknowledge the financial support of State Grid Xinyuan Group Co., Ltd. Technology Project, grant number SGXYKJ-2023-049.

Conflict of interest

Authors WX and ZG were employed by Pumped Storage Technology and Economy Research Institute of State Grid Xinyuan Company Ltd.

The remaining authors declare that the research was conducted in the absence of any commercial or financial relationships that could be construed as a potential conflict of interest.

Publisher's note

References

Agnalt, E., Iliev, I., Solemslie, B. W., and Dahlhaug, O. G. (2019). On the rotor stator interaction effects of low specific speed francis turbines. *Int. J. Rotating Mach.* 2019, 1–11. doi:10.1155/2019/5375149

Bahzad, H., Fennell, P., Shah, N., Hallett, J., and Ali, N. (2022). Techno-economic assessment for a pumped thermal energy storage integrated with open cycle gas turbine and chemical looping technology. *Energy Convers. Manag.* 255, 115332. doi:10.1016/j.enconman.2022.115332

Baya, A., Muntean, S., Câmpian, V. C., Cuzmoș, A., Diaconescu, M., and Bălan, G. (2010). Experimental investigations of the unsteady flow in a francis turbine draft tube cone. *IOP Conf. Ser. Earth Environ. Sci.* 12, 012007. doi:10.1088/1755-1315/12/1/012007

Carlson, F., and Davidson, J. H. (2021). Parametric study of thermodynamic and cost performance of thermal energy storage coupled with nuclear power. *Energy Convers. Manag.* 236, 114054. doi:10.1016/j.enconman.2021.114054

Celik, I., and Karatekin, O. (1997). Numerical experiments on application of richardson extrapolation with nonuniform grids. *J. Fluids Eng.* 119, 584–590. doi:10.1115/1.2819284

Chirag, T., Cervantes, M. J., Bhupendrakumar, G., and Dahlhaug, O. G. (2014). Pressure measurements on a high-head francis turbine during load acceptance and rejection. *J. Hydraulic Res.* 52, 283–297. doi:10.1080/00221686.2013.854846

Duparchy, F., Favrel, A., Lowys, P.-Y., Landry, C., Müller, A., Yamamoto, K., et al. (2015). Analysis of the Part Load helical vortex rope of a francis turbine using on-board sensors. *J. Phys. Conf. Ser.* 656, 012061. doi:10.1088/1742-6596/656/1/012061

Egusquiza, E., Valero, C., Huang, X., Jou, E., Guardo, A., and Rodriguez, C. (2012). Failure investigation of a large pump-turbine runner. *Eng. Fail Anal.* 23, 27–34. doi:10.1016/j.engfailanal.2012.01.012

Favrel, A., Landry, C., Müller, A., Yamamoto, K., and Avellan, F. (2014). Hydro-acoustic resonance behavior in presence of a precessing vortex rope: observation of a lock-in phenomenon at Part Load francis turbine operation. *IOP Conf. Ser. Earth Environ. Sci.* 22, 032035. doi:10.1088/1755-1315/22/3/032035

Favrel, A., Müller, A., Landry, C., Yamamoto, K., and Avellan, F. (2016). Space and time reconstruction of the precessing vortex core in francis turbine draft tube by 2D-PIV. *IOP Conf. Ser. Earth Environ. Sci.* 49, 082011. doi:10.1088/1755-1315/49/8/082011

Goyal, R., Trivedi, C., Gandhi, B. K., Cervantes, M. J., and Dahlhaug, O. G. (2016). Transient pressure measurements at Part Load operating condition of a high head model francis turbine. *Sādhanā* 41, 1311–1320. doi:10.1007/s12046-016-0556-x

Goyal, R., Trivedi, C., Kumar Gandhi, B., and Cervantes, M. J. (2018). Numerical simulation and validation of a high head model francis turbine at Part Load operating condition. *J. Institution Eng. (India) Ser. C* 99, 557–570. doi:10.1007/s40032-017-0380-z

Huang, N. E., Shen, Z., Long, S. R., Wu, M. C., Shih, H. H., Zheng, Q., et al. (1998). The empirical mode decomposition and the Hilbert spectrum for nonlinear and non-stationary time series analysis. *Proc. R. Soc. Lond. Ser. A Math. Phys. Eng. Sci.* 454, 903–995. doi:10.1098/rspa.1998.0193

Ji, T., Wang, J., Li, M., and Wu, Q. (2022). Short-term wind power forecast based on chaotic analysis and multivariate phase space reconstruction. *Energy Convers. Manag.* 254, 115196. doi:10.1016/j.enconman.2021.115196

Kc, A., Thapa, B., and Lee, Y.-H. (2014). Transient numerical analysis of rotor–stator interaction in a francis turbine. *Renew. Energy* 65, 227–235. doi:10.1016/j.renene.2013.09.013

Kong, L., Chen, X., Gong, J., Fan, D., Wang, B., and Li, S. (2022). Optimization of the hybrid solar power plants comprising photovoltaic and concentrating solar power using the butterfly algorithm. *Energy Convers. Manag.* 257, 115310. doi:10.1016/j.enconman.2022.115310

Kuznetsov, I., Zakharov, A., Arm, V., and Akulaev, R. (2014). Model and prototype investigations of upper partial load unsteady phenomena on the francis turbine designed for head up to 120 m. *IOP Conf. Ser. Earth Environ. Sci.* 22, 032032. doi:10.1088/1755-1315/22/3/032032

Laouari, A., and Ghenaiet, A. (2019). Predicting unsteady behavior of a small francis turbine at several operating points. *Renew. Energy* 133, 712–724. doi:10.1016/j.renene.2018.08.111

Li, H., Xu, B., Mahmud, Md.A., Chen, D., and Zhang, J. (2019). Pumping phase modulation analysis for operational quality of a pumped-storage generating system. *Energy Convers. Manag.* 199, 111989. doi:10.1016/j.enconman.2019.111989

Mauro, S., Lanzafame, R., Brusca, S., and Messina, M. (2019). Unsteady computational fluid dynamics analysis of the hydrodynamic instabilities in a reversible francis turbine used in a storage plant. *Heliyon* 5, e02441. doi:10.1016/j.heliyon.2019.e02441

Menter, F. R. (1994). Two-equation eddy-viscosity turbulence models for engineering applications. *AIAA J.* 32, 1598–1605. doi:10.2514/3.12149

Nicolet, C., Zobeiri, A., Maruzewski, P., and Avellan, F. (2010). On the upper Part Load vortex rope in francis turbine: experimental investigation. *IOP Conf. Ser. Earth Environ. Sci.* 12, 012053. doi:10.1088/1755-1315/12/1/012053

Nicolet, C., Zobeiri, A., Maruzewski, P., and Avellan, F. (2011). Experimental investigations on upper Part Load vortex rope pressure fluctuations in francis turbine draft tube. *Int. J. Fluid Mach. Syst.* 4, 179–190. doi:10.5293/IJFMS.2011.4.1.179

Pasche, S., Gallaire, F., and Avellan, F. (2019). Origin of the synchronous pressure fluctuations in the draft tube of francis turbines operating at Part Load conditions. *J. Fluids Struct.* 86, 13–33. doi:10.1016/j.jfluidstructs.2019.01.013

Pei, J., Yuan, S. Q., Li, X. J., and Yuan, J. P. (2014). Numerical prediction of 3-D periodic flow unsteadiness in a centrifugal pump under part-load condition. *J. Hydrodynamics* 26, 257–263. doi:10.1016/S1001-6058(14)60029-9

Quaranta, E., Aggidis, G., Boes, R. M., Comoglio, C., De Michele, C., Ritesh Patro, E., et al. (2021). Assessing the energy potential of modernizing the European hydropower fleet. *Energy Convers. Manag.* 246, 114655. doi:10.1016/j.enconman.2021.114655

Suh, J.-W., Yang, H.-M., Kim, J.-H., Joo, W.-G., Park, J., and Choi, Y.-S. (2021). Unstable S-shaped characteristics of a pump-turbine unit in a lab-scale model. *Renew. Energy* 171, 1395–1417. doi:10.1016/j.renene.2021.03.013

Trivedi, C., Agnalt, E., and Dahlhaug, O. G. (2017). Investigations of unsteady pressure loading in a francis turbine during variable-speed operation. *Renew. Energy* 113, 397–410. doi:10.1016/j.renene.2017.06.005

Trivedi, C., Agnalt, E., and Dahlhaug, O. G. (2018a). Experimental investigation of a francis turbine during exigent ramping and transition into total load rejection. *J. Hydraulic Eng.* 144. doi:10.1061/(ASCE)HY.1943-7900.0001471

Trivedi, C., Agnalt, E., and Dahlhaug, O. G. (2018b). Experimental study of a francis turbine under variable-speed and discharge conditions. *Renew. Energy* 119, 447–458. doi:10.1016/j.renene.2017.12.040

Trivedi, C., Cervantes, M., and Gandhi, B. (2016). Investigation of a high head francis turbine at runaway operating conditions. *Energies (Basel)* 9, 149. doi:10.3390/en9030149

Trivedi, C., Cervantes, M. J., Gandhi, B. K., and Dahlhaug, O. G. (2013). Experimental and numerical studies for a high head francis turbine at several operating points. *J. Fluids Eng.* 135. doi:10.1115/1.4024805

Trivedi, C., Cervantes, M. J., Gandhi, B. K., and Ole, D. G. (2014). Experimental investigations of transient pressure variations in a high head model francis turbine during start-up and shutdown. *J. Hydrodynamics* 26, 277–290. doi:10.1016/S1001-6058(14)60031-7

Wallimann, H., and Neubauer, R. (2015). Numerical study of a high head francis turbine with measurements from the francis-99 Project. *J. Phys. Conf. Ser.* 579, 012003. doi:10.1088/1742-6596/579/1/012003

Yexiang, X., Zhengwei, W., Zongguo, Y., Mingan, L., Ming, X., and Dingyou, L. (2010). Numerical analysis of unsteady flow under high-head operating conditions in francis turbine. *Eng. Comput. Swans.* 27, 365–386. doi:10.1108/02644401011029934

Zeng, W., Yang, J., and Hu, J. (2017). Pumped storage system model and experimental investigations on S-induced issues during transients. *Mech. Syst. Signal Process* 90, 350–364. doi:10.1016/j.ymssp.2016.12.031

Zhang, X., Cheng, Y., Yang, Z., Chen, Q., and Liu, D. (2020). Influence of rotational inertia on the runner radial forces of a model pump-turbine running away through the S-shaped characteristic region. *IET Renew. Power Gener.* 14, 1883–1893. doi:10.1049/iet-rpg.2019.1476

Zuo, Z., Liu, S., Sun, Y., and Wu, Y. (2015). Pressure fluctuations in the vaneless space of high-head pump-turbines—a review. *Renew. Sustain. Energy Rev.* 41, 965–974. doi:10.1016/j.rser.2014.09.011

frontiers | Frontiers in Energy Research

TYPE Original Research
PUBLISHED 20 March 2024
DOI 10.3389/fenrg.2024.1358911

OPEN ACCESS

EDITED BY
Xiaohu Yang,
Xi'an Jiaotong University, China

REVIEWED BY
Benqing Liu,
Yangzhou University, China
Guilin Hu,
Zhejiang University of Science and Technology, China
Zhengkai Tu,
Huazhong University of Science and Technology, China

*CORRESPONDENCE
Huanle Zhai,
jszhaihl@163.com

RECEIVED 20 December 2023
ACCEPTED 08 March 2024
PUBLISHED 20 March 2024

CITATION
Zhai H, Li W, Li J, Shen C, Ji L and Xu Y (2024), Multifactor and multi-objective coupling design of hydrogen circulation pump.
Front. Energy Res. 12:1358911.
doi: 10.3389/fenrg.2024.1358911

Multifactor and multi-objective coupling design of hydrogen circulation pump

Huanle Zhai[1]*, Wei Li[2], Jiwei Li[1], Chaoping Shen[1], Leilei Ji[2] and Yuanfeng Xu[3]

[1]Aviation Engineering Institute, Jiangsu Aviation Technical College, Jiangsu, China, [2]China National Research Center of Pumps, Jiangsu University, Zhenjiang, China, [3]The Third Pipeline Branch Office, Beijing Drainage Group, Beijing, China

The hydrogen circulation pump (HCP) is an important power component of the hydrogen fuel system, used to recover the unconsumed hydrogen from the anode and transport it back to the inlet of the battery stack to improve the hydrogen utilization efficiency. In this paper, to determine the optimal parameter configuration of the HCP, a multifactor and multi-objective optimization design method is proposed, and the influences of various design parameters on the performance of the HCP are analyzed based on the verified overset grid simulation method. The research results show that the proposed coupling design method can effectively achieve the optimal parameter configuration of the HCP, with diameter-to-pitch ratio κ = 1.47, rotor blade number Z = 3, and helix angle φ = 60°, which is validated using another model with significant performance advantages. In the process of studying the influence of design parameters, it is found that the average flow rate of the HCP is directly proportional to the diameter-to-pitch ratio and the blade number, gradually decreases in the range of helix angle from 0° to 22.5°, and increases in the range of helix angle from 22.5° to 60°. The flow pulsation value and pressure pulsation value of the HCP are less affected by the diameter-to-pitch ratio, decrease with the increase of the blade number, and show a trend of first increasing and then decreasing with the increase of the helix angle.

KEYWORDS

hydrogen circulation pump (HCP), optimal parameter configuration, flow pulsation, pressure pulsation, overset mesh

1 Introduction

The hydrogen fuel cell system can meet the demand of society for clean energy and renewable energy. It has the advantages of high efficiency, zero emissions, quiet operation, quick start-up, low operating temperature, and high energy density, and has become one of the best choices for automotive power sources in the 21st century (Liu et al., 2018). When the fuel cell system is in operating mode, the high content of water generated by the combination of hydrogen ions and oxygen ions will hinder the gas diffusion, resulting in performance deterioration of fuel cells during long-term operation (Liu et al., 2021a). Using exhaust gas recirculation devices (ejector/pump) in the fuel cell stack can help in effectively mitigating water flooding and chemical degradation of the membrane electrode assembly (Liu et al., 2023a). The ejector-based exhaust gas recirculation can greatly improve the water balance of fuel cells, but the performance of the ejector is seriously affected by the flow characteristics of water vapor in the secondary flow (Liu et al., 2021b). The hydrogen

circulation pump (HCP) is an important power component of the hydrogen fuel system (Zhou et al., 2022). Its role is to recover the unconsumed hydrogen from the anode and transport it back to the inlet of the battery stack to improve the hydrogen utilization efficiency and optimize the life and performance of the fuel cell stack (Wiebe et al., 2020). Research has shown that when the rotating speed of recirculation pump reaches 5,000 revolutions per minute, it can increase the gas flow rate inside the stack channel to 0.44 ms^{-1}, which facilitates the removal of liquid water inside the stack (Liu et al., 2023b). The HCP includes three structural forms: claw type, Roots type, and vortex type (Zhang et al., 2019). Among them, Roots-type HCP has the advantages of simple structure, high reliability, and low cost, which is suitable for high-flow application environments and has become the current mainstream research direction (Wang et al., 2019). The performance of Roots type HCP is affected not only by the shape of the profile (Zhou et al., 2021), but also by design parameters such as working clearance diameter-to-pitch ratio, blade number, and helix angle (Singh et al., 2019; Li et al., 2021; Rao and Zhong, 2021).

Analyze the impact of the diameter-to-pitch ratio on the performance of the HCP. Yang (2022); Yang et al. (2022) studied the influence of diameter-to-pitch ratio on the performance of a Roots-type HCP. Six HCP models with different diameter-to-pitch ratios (from 1.34 to 1.45) were established for numerical calculation and comparative analysis. It was found that the average flow rate and instantaneous flow pulsation amplitude at the pump outlet showed an upward trend with the increase of diameter-to-pitch ratio, and were more obvious in the range of 1.38–1.40. When the rotor diameter-to-pitch ratio is 1.40, the vortex distribution in the pump cavity is small, indicating that the gas return flow rate is the smallest at this time. Zhang (2018). and Li et al. (2020) established six models with different diameter-to-pitch ratios for a Roots-type rotor. The results showed that the average flow rate at the cam pump outlet showed a trend of first increasing and then decreasing as the diameter-to-pitch ratio increased, while the instantaneous flow pulsation amplitude showed a continuous downward trend. Summarizing the above research, it can be concluded that changes in the diameter-to-pitch ratio have a significant impact on the flow characteristics of HCPs, but the relationship between the two may vary due to different models.

Analyze the impact of helical angle on the performance of the HCP. Xing et al. (2023) calculated and compared the flow characteristics of gear pumps with helical angles of 23.74°, 28.11°, 32.14°, and 39.24°, respectively. The results showed that as the helical angle increased, the outlet flow of the gear pump showed a trend of first increasing and then decreasing, and the pulsation coefficient showed a continuous downward trend. The pressure distribution between adjacent cavities of the gears gradually became uniform. Li et al. (2018) conducted simulation calculations on three-blade pendulum pumps with nine different helical angles (0°–60° range). As the helical angle gradually increased from 0° to 60°, the average flow rate at the pump outlet first decreased and then increased, reaching a minimum value at a helical angle of 20°, reaching a peak point at a helical angle of 60°, and the average flow peak was 97% of the straight blade rotor. The instantaneous flow pulsation amplitude showed a decreasing trend with the increase of the helical angle. Zhang (2018) conducted a study on the three-blade pendulum rotor pumps with a larger helix angle range (0°–120°) and found that as the helix angle increased, the average flow rate at the pump outlet experienced a decreasing-increasing-decreasing trend. It also reached its maximum value at a helix angle of 60° and showed a continuous downward trend of the flow pulsation amplitude. To summarize the above research, the flow rate of the HCP showed a phenomenon of first increasing and then decreasing with the increase of the helix angle, rather than a linear relationship.

Analyze the impact of blade number on the performance of the HCP. Chen and Zou (2019) established three models of two-blade, three-blade, and four-blade for the circular arc rotor and carried out numerical calculations and comparisons. In the low-speed operation state, the increase of the blade number can increase the volumetric efficiency, reduce the speed fluctuation at the outlet, and improve the stability of the flow field inside the pump body. In the high-speed operation state, the increase of the blade number can increase the number of pulsations at the outlet in unit time, which leads to a decrease in the volumetric efficiency. Zhang (2018) conducted research on multi-blade pendulum rotors and believed that as the number of rotor blades increased, the pump outlet flow showed a downward trend, but the flow inside the pump cavity was more stable. Li et al. (2022) found that when the number of rotor blades increased from 2 to 4, the average flow rate at the pump outlet decreased, and the diversity of pressure changes in the cavity increased. Li et al. (2021b) conducted simulation calculations on four HCP models with different blade numbers (3-6 blades). As the number of rotor blades increased, the average flow rate and total outlet pressure at the pump outlet decreased, and the intensity of outlet flow and pressure pulsation was effectively weakened. The main reason was that the increase in the number of rotor blades led to an increase in the transition chamber, resulting in an increase in the number of pressurization stages and a more stable pressurization effect. Summarizing the above research, some results indicated that the number of rotor blades was directly proportional to the flow rate of the hydrogen circulation pump, while others indicated an inverse relationship between the two, without forming a unified conclusion.

Analyze the influence law under the coupling effect of multiple design parameters. Li (2021) studied the coupling effect of design parameters such as rotor blade number, helix angle, and diameter-to-pitch ratio using the three-dimensional unsteady numerical calculation method. It was found that as the blade number increased, the average flow rate at the pump outlet showed a downward trend, and the intensity of flow and pressure pulsation also decreased. As the helix angle gradually increased from 0° to 120°, the average flow rate and volumetric efficiency showed a declining trend, and the more rotor blades, the greater the decline. However, the pressure fluctuation coefficient gradually decreased with the increase of the helix angle. When the diameter-to-pitch ratio of the rotor decreased from 1.29 to 1.20, the outlet volumetric efficiency decreased by 14.61%, and the pressure fluctuation coefficient decreased by 44.37%. Gu et al. (2021) used the Taguchi method to study the influence of six factors on the performance of claw-shaped HCP, including speed, pressure ratio, inlet pressure, radial clearance between rotor and shell, radial clearance between rotors, and axial clearance. The quantitative contribution of these six factors to volumetric efficiency and shaft power was obtained by the ANOVA method, and it was found that the pressure ratio (36.2%), axial clearance (29.4%), and rotating speed (21.5%) have

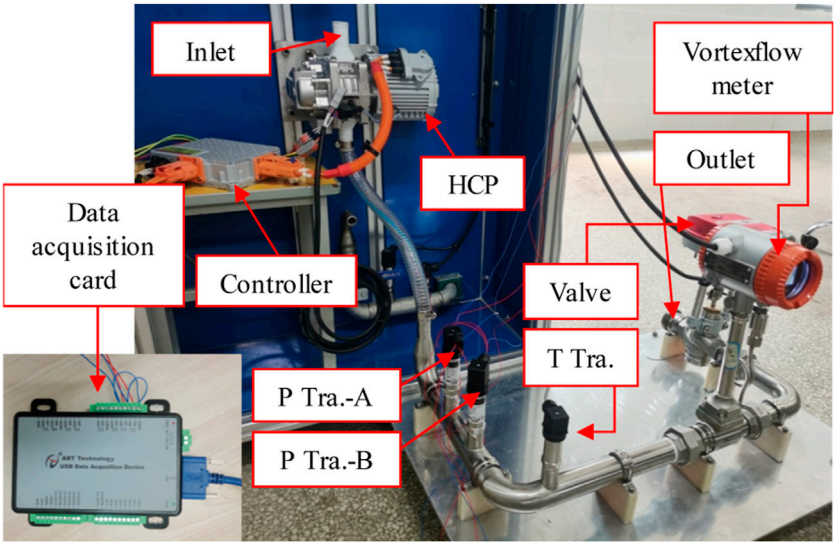

FIGURE 1
Test system physical picture.

a greater impact on volumetric efficiency, while pressure ratio (64.6%), rotating speed (23.0%) and inlet pressure (5.2%) have a greater impact on shaft power. Gao (2022) used the quadratic regression orthogonal combination experimental method to study the influence of main structural parameters such as rotor length, rotor radial clearance, rotor blade number, and pipe diameter on the performance of HCP. Taking the structural parameters as the influencing factors, and taking the volumetric efficiency and flow non-uniformity coefficient as the evaluation factors, the optimal combination of the structural parameters of the HCP was determined through orthogonal tests and variance analysis. The research results showed that the influence on the volumetric efficiency was in descending order of rotor clearance, rotor length, rotor blade number, and pipe diameter, while the influence on the non-uniform coefficient of flow rate was in descending order of rotor blade number, rotor length, and radial clearance.

It can be found that there is relatively little research on the parameter optimization of HCP currently, and more research is focused on rotor pumps with similar structures in other industries. In different application environments, there are also certain differences in the research conclusions on the influence of design parameters such as diameter-to-pitch ratio, blade number, and helix angle, which cannot be directly referenced. At the same time, although some scholars have analyzed the coupling effect of multiple parameters, the research conclusion is discretization and the optimal parameter configuration of the HCP cannot be determined because a unified objective function has not been established for multiple optimization objectives. Therefore, this article will establish a multi-objective optimization method that covers performance parameters such as average flow rate, flow pulsation, and pressure pulsation, using diameter-to-pitch ratio, blade number, and helix angle as design variables, and ultimately achieve the optimal parameter configuration of the HCP.

2 Simulation method and experimental verification

The overset mesh method for simulation calculation using STAR-CCM software is adopted in this paper, which can well analyze the model with a motion clearance of only 0.1 mm. Using the pump cavity grid model as the background region and the rotor grid model as the overlapping region, the overset mesh method couples the two regions by exchanging data between the acceptor grid cells in the background region and the donor grid cells in the overlapping region. Compared with conventional dynamic grids, this method reduces the difficulty of generating computational grids by dividing the computational model into blocks, avoiding problems such as mesh entanglement, distortion, and negative volume, thus ensuring the accuracy of the calculation results. The model is divided into hexahedral grids, with the grid edge length dimensions of the background area and overlapping area at the clearance position both 0.025 mm to meet the accuracy of the data exchange.

Establish the HCP testing system to verify the reliability of the simulation method, as shown in Figure 1. The HCP testing system uses high-frequency pressure sensors to test the real-time pressure pulsation curve and uses the indirect flow measurement method (Zhai et al., 2023) to test the real-time flow pulsation curve. Figure 2 shows the comparison of the simulation and testing results of the HCP prototype under air medium. The results show that the pressure waveforms of the two have a high degree of agreement, with an average pressure error of 2.1%, and the measured flow waveform is lower than the simulated flow waveform, with an average flow rate error of 6.2%. The reason for the large flow rate error is that the simulation calculation did not consider the axial clearance. Overall, the simulation results are relatively close to the experimental results, indicating that using the overset mesh method to optimize the design of HCP is feasible.

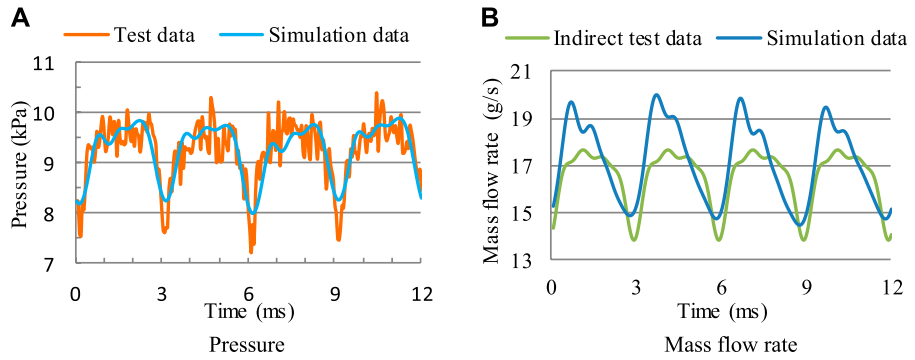

FIGURE 2
Comparison of test data and simulation data. **(A)** Pressure **(B)** Mass flow rate.

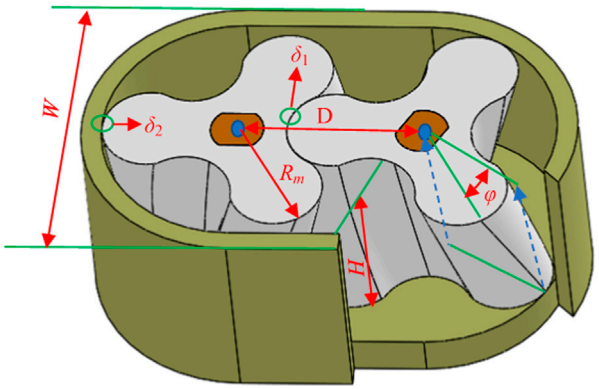

FIGURE 3
Marking of design parameters for the HCP.

3 Multifactor and multi-objective coupling design method

3.1 Multifactor design condition

The design parameters of the HCP labeled in Figure 3 are divided into two categories: invariant parameters and variable parameters, as shown in Table 1. The invariant parameters include the width W and the height H of the pump cavity, the radial clearance δ_1 between the rotor and the pump casing, and the radial clearance δ_2 between rotors. The variable parameters include the diameter-to-pitch ratio κ, the blade number Z, and the helix angle φ. Design the elliptical profile of the HCP based on the design formula proposed in the reference (Zhai et al., 2022). It can be found that there is a certain correlation between the diameter-to-pitch ratio κ and the blade number Z. The smaller the κ value, the higher the maximum number of rotor blades Z that can be designed. When the value of κ is large, the rotor profile will experience the self-crossing phenomenon. For example, when κ = 1.47, only 2-blade and 3-blade rotors can be designed, and the conjugate curve will undergo a self-crossing phenomenon while designing 4-blade rotors. Similarly, the maximum number of rotor blades that can be designed is 4 when κ = 1.39, and 5 when κ = 1.32. After the blade number Z is determined, the rotor helix angle φ can be changed to obtain different HCP models. Considering the symmetry of the left and right rotors, the maximum helix angle is taken as 180°/Z. Therefore, the three variable parameters of the diameter-to-pitch ratio κ, the blade number Z, and the helix angle φ are used as design factors for the hydrogen circulation pump, with each design factor containing a series of numerical values. Therefore, three variable parameters are considered multiple factors in the design of the HCP, with each design factor containing a series of numerical values.

3.2 Definition of the multi-objective optimization function

The average flow rate is the main indicator to measure the delivery capacity of the HCP, which directly affects the efficiency of the fuel cell system. As a positive displacement pump, the output flow rate and pressure of the HCP have periodically fluctuated. The flow and pressure pulsation characteristics will have a certain impact on the stability of the fuel cell system and are also important indicators to measure the performance of HCP. Therefore, optimizing the design of multi-objective parameters such as average flow rate, flow pulsation, and pressure pulsation can develop HCP products with the best comprehensive performance.

Take the average flow rate actually output as the target parameter to measure the flow rate. Record the ratio of the real-time flow fluctuation amplitude to the average flow rate as the flow fluctuation factor K_Q, which is the target parameter to measure the amplitude of flow fluctuation. Record the ratio of the real-time pressure fluctuation amplitude to the average outlet relative pressure as the pressure fluctuation factor K_P, as the target parameter to measure the pressure fluctuation amplitude.

Define the multi-objective optimization function, see Eq. 1:

$$f(\kappa, Z, \varphi) = Q_{avg} + \frac{k_1}{K_Q} + \frac{k_2}{K_P} \tag{1}$$

In the equation, K_Q is the flow pulsation value, $K_Q = \frac{Q_{max} - Q_{min}}{Q_{avg}}$; k_1 is the weight factor of flow pulsation value, with a value of 1; K_P is

TABLE 1 Invariant and variable parameters of the HCP.

Design factor		Value		
invariant parameters	the width of the pump cavity W (mm)		66	
	the height of the pump cavity H (mm)		60	
	the radial clearance between the rotor and the pump casing δ_1 (mm)		0.1	
	the radial clearance between the rotors δ_2 (mm)		0.1	
variant parameters	diameter-to-pitch ratio $\kappa = 2R_m/D$	1.47	1.39	1.32
	blade number Z	2/3	2/3/4	2/3/4/5
	helix angle φ		0°–180°/Z	

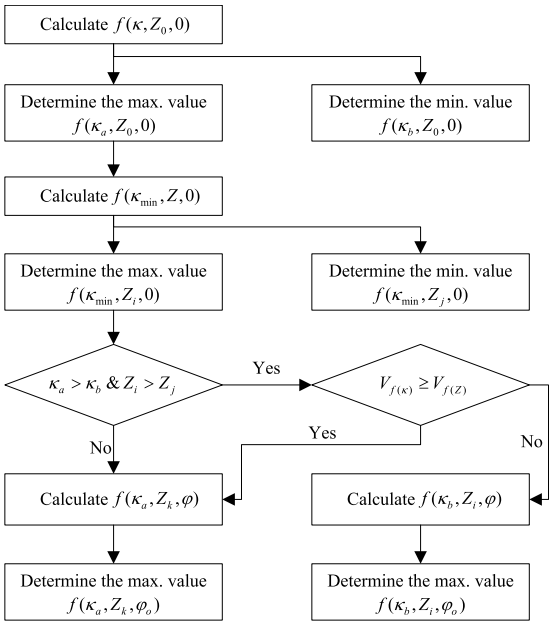

FIGURE 4
Flow chart of multi-objective optimization method.

the pressure pulsation value, $K_P = \frac{P_{\max} - P_{\min}}{P_{avg}}$; k_2 is the weight factor of pressure pulsation value, with a value of 0.001, since the pressure value is of a larger order of magnitude compared to the flow rate value. The values of the three weight factors can be adjusted based on the importance attached to each parameter in the actual application environment.

3.3 Multifactor and multi-objective coupling design process

Considering that there are a series of values available for selection in terms of the diameter-to-pitch ratio κ, the blade number Z, and the helix angle φ. Any combination of parameters will correspond to different multi-objective optimization function values. If all combinations are calculated to obtain the maximum value of the multi-objective optimization function, the computational workload is very large, and a reasonable multi-objective optimization process needs to be designed to quickly achieve the optimal assignment of parameters.

Figure 4 shows the multifactor and multi-objective coupling design process. Firstly, under the condition of a certain number of blades Z_0, design straight blade rotor models with different diameter-to-pitch ratios κ and conduct simulation, calculate the value of the multi-objective optimization function $f(\kappa, Z_0, 0)$, and determine the maximum value $f(\kappa_a, Z_0, 0)$ and corresponding diameter-to-pitch ratio κ_a, the minimum value $f(\kappa_b, Z_0, 0)$ and corresponding diameter-to-pitch ratio κ_b. Secondly, under the condition of the minimum diameter-to-pitch ratio $\kappa_{\min}$, design straight blade rotor models with different blade numbers Z and conduct simulation, calculate the value of the multi-objective optimization function $f(\kappa_{\min}, Z, 0)$ and determine the maximum value $f(\kappa_{\min}, Z_i, 0)$ and corresponding blade number Z_i, the minimum value $f(\kappa_{\min}, Z_j, 0)$ and corresponding blade number Z_j. Afterward, a series of comparisons will be conducted, where $V_{f(\kappa)}$ represents the influence factor of the diameter-to-pitch ratio on the objective function, and $V_{f(Z)}$ represents the influence factor of the blade number on the objective function, expressed using Eqs 2, 3 respectively.

$$V_{f(\kappa)} = \sum \frac{f(\kappa_a, Z_0, 0) - f(\kappa_b, Z_0, 0)}{(N_\kappa - 1) f(\kappa_a, Z_0, 0)} \tag{2}$$

$$V_{f(Z)} = \sum \frac{f(\kappa_a, Z_i, 0) - f\left(\kappa_a, Z_j, 0\right)}{(N_Z - 1) f(\kappa_a, Z_i, 0)} \tag{3}$$

In the two equations, N_κ represents the number of different diameter-to-pitch ratios κ, N_Z represents the number of different blade numbers Z.

Based on the comparison results, choose to design the rotor profile with the maximum number of blades Z_i under the condition of $\kappa = \kappa_b$, or with the maximum number of blades Z_k under the condition of $\kappa = \kappa_a$, and simulate and calculate rotor models with different helix angles φ, and ultimately obtain the maximum value of the multi-objective optimization function and the corresponding helix angle.

4 Analysis of the influence of design factors

Define the expression of the HCP to reflect its parameter configuration, such as expressing the HCP with diameter-to-pitch

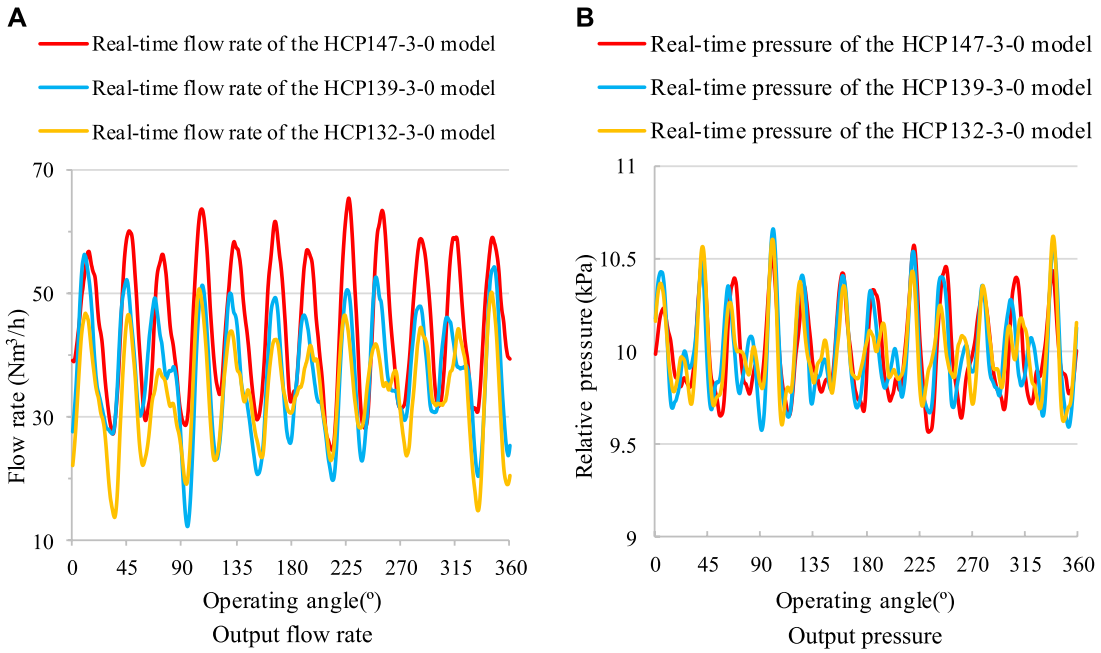

FIGURE 5
Performance of HCP models with different diameter-to-pitch ratios. **(A)** Output flow rate **(B)** Output pressure.

ratio $\kappa = 1.47$, rotor blade number $Z = 3$, and helix angle $\varphi = 30°$ as HCP147-3-30. Determine the optimal parameter configuration of the HCP based on the multifactor and multi-objective coupling design process. The pressure ratio for the working condition is 1.1.

4.1 The influence of diameter-to-pitch ratio on the performance of HCP

The influence analysis of the diameter-to-pitch ratio is conducted under the condition of 3 rotor blades. Figure 5 shows the comparison of the flow rate and the pressure of HCP under different diameter-to-pitch ratios. Firstly, analyze the impact of diameter-to-pitch ratio on the average flow rate of HCP: the average flow rate of the HCP147-3-0 model is 45.0 Nm^3/h, the HCP139-3-0 model is 37.0 Nm^3/h, the HCP132-3-0 model is 33.6 Nm^3/h, indicating a directly proportional relationship between the diameter-to-pitch ratio and the average flow rate. Secondly, analyze the impact of diameter-to-pitch ratio on the real-time flow pulsation characteristics of HCP: on the one hand, when the diameter-to-pitch ratio changes, the pulsation frequency of the flow rate waveform, the positions of the peaks and valleys do not change, and the similarity of the waveform is high; on the other hand, the flow pulsation value of the HCP147-3-0 model is $K_Q = 0.914$, the HCP139-3-0 model $K_Q = 1.194$, the HCP132-3-0 model $K_Q = 1.098$. The difference in flow pulsation among the three models is small and there is no obvious change pattern, indicating that the diameter-to-pitch ratio has a small impact on the flow pulsation characteristics. Thirdly, analyze the impact of diameter-to-pitch ratio on the real-time pressure pulsation characteristics of HCP: the pressure pulsation value of the HCP147-3-0 model is $K_P = 1.01 \times 10^{-3}$, the HCP139-3-0 model $K_P = 1.08 \times 10^{-3}$, the HCP132-3-0 model $K_P = 1.02 \times 10^{-3}$, and their values are close, indicating that the influence of the diameter-to-pitch ratio on the pressure fluctuation characteristics is relatively small.

Figure 6 shows the back-flow at the radial clearance of different diameter-to-pitch ratio models. The back-flow velocity at the clearance of the HCP147-3-0 model is 728 m/s, the HCP139-3-0 model is 720 m/s, and the HCP132-3-0 model is 641 m/s. From this, it can be concluded that the back-flow rates at the clearance of the HCP147-3-0 model and the HCP139-3-0 model are similar, and the HCP132-3-0 model is relatively low. Analyzing the absolute decrease of the average output flow rate of the three models relative to the theoretical flow rate, the theoretical flow rate of the HCP147-3-0 model is 75.1 Nm^3/h, which decreases by 30.1 Nm^3/h under the 1.1 pressure ratio condition, the HCP139-3-0 model is 67.2 Nm^3/h, which decreased by 30.2 Nm^3/h under the 1.1 pressure ratio condition, and the HCP132-3-0 model is 59.4 Nm^3/h, which decreased by 25.8 Nm^3/h under the 1.1 pressure ratio condition. The absolute decrease value results are consistent with the analysis results of the back-flow rate at the clearance, indicating that the decrease in leakage caused by a decrease in the diameter-to-pitch ratio of the HCP is weaker than the decrease in delivery capacity caused by a decrease in the area utilization coefficient, resulting in a decrease in the final output flow rate.

Figure 7 shows the comparison of the internal pressure distribution of HCP models under different diameter-to-pitch ratios. It can be found that in the first two states, the maximum pressure of the HCP132-3-0 model is basically the same as that of the HCP147-3-0 model, but in the third state, the maximum pressure of the HCP132-3-0 model is significantly lower than that of the HCP147-3-0 model, which is consistent with the trend of the pressure fluctuation factor of each model in Figure 5B.

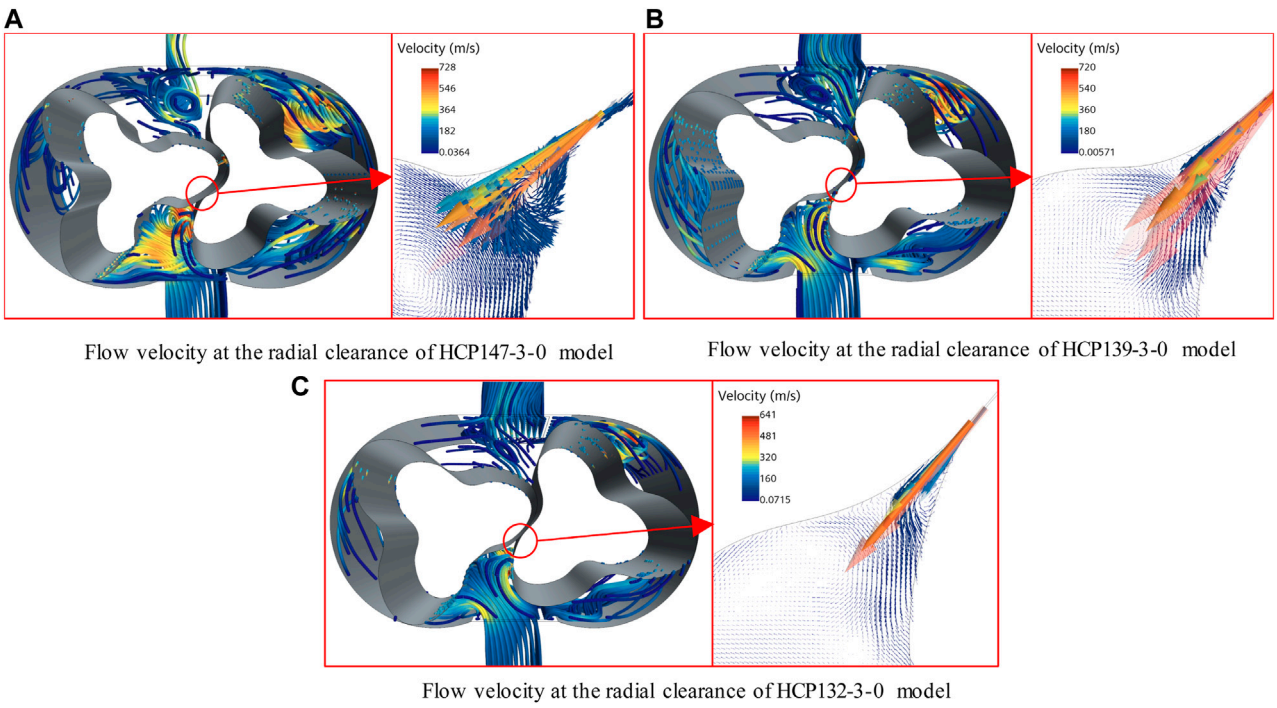

FIGURE 6
Radial clearance flow velocity comparison of HCPs with different diameter-to-pitch ratios. **(A)** Flow velocity at the radial clearance of HCP147-3-0 model **(B)** Flow velocity at the radial clearance of HCP139-3-0 model **(C)** Flow velocity at the radial clearance of HCP132-3-0 model.

4.2 The influence of blade number on the performance of HCP

Design HCP models with different blade numbers at the lowest diameter-to-pitch ratio for simulation calculations. Figure 8 shows the comparison of the flow rate and the pressure of HCP under different blade numbers. Firstly, analyze the impact of blade number on the average flow rate of HCP: the average flow rate of the HCP132-2-0 model is 32.4 Nm^3/h, the HCP132-3-0 model 33.6 Nm^3/h, the HCP132-4-0 model 36.1 Nm^3/h, and the HCP132-5-0 model 38.0 Nm^3/h, indicating a directly proportional relationship between the blade number and the average flow rate. Secondly, analyze the impact of blade number on the real-time flow pulsation characteristics of HCP: on the one hand, when the rotor operates for one cycle (360°), the number of periodic flow pulsation waveforms output by the HCP132-2-0 model is 4, the HCP132-3-0 model is 6, the HCP132-4-0 model is 8, and the HCP132-5-0 model is 10, indicating that the number of pulsation waveforms output by the HCP during one operating cycle is twice the number of rotor blades; on the other hand, the flow pulsation value of the HCP132-2-0 model is $K_Q = 2.412$, the HCP132-3-0 model $K_Q = 1.097$, the HCP132-4-0 model $K_Q = 0.909$, and the HCP132-5-0 model $K_Q = 0.656$, indicating an inverse relationship between the blade number and the flow pulsation value. Thirdly, analyze the impact of blade number on the real-time pressure pulsation characteristics of HCP: the output pressure of all four models shows pulsating changes, but their periodic pulsation pattern is not as obvious as the real-time flow rate curve; the pressure pulsation value of the HCP132-2-0 model is $K_P = 1.65 \times 10^{-3}$, the HCP132-3-0 model $K_P = 1.01 \times 10^{-3}$, the HCP132-4-0 model $K_P = 0.74 \times 10^{-3}$, and the HCP132-5-0 model $K_P = 0.63 \times 10^{-3}$, indicating an inverse relationship between the blade number and the pressure pulsation value.

Figure 9 shows the back-flow at the radial clearance of different blade number models. The back-flow velocity at the clearance of the HCP132-2-0 model is 677 m/s, the HCP132-3-0 model is 561 m/s, the HCP132-4-0 model is 453 m/s, and the HCP132-5-0 model is 441 m/s, indicating that the back-flow rate at the clearance of the HCP model decreases as the number of rotor blades increases. Analyze the absolute decrease of the average output flow rate relative to the theoretical flow rate, while the theoretical flow rates of the four models are not significantly different. The HCP132-2-0 model decreased by 26.6 Nm^3/h under 1.1 pressure ratio conditions, the HCP132-3-0 model decreased by 25.8 Nm^3/h, the HCP132-4-0 model decreased by 24.0 Nm^3/h, and the HCP132-5-0 model decreased by 23.0 Nm^3/h. This result is consistent with the analysis results of the back-flow rate at the clearance.

Figure 10 shows the comparison of the internal pressure distribution of HCP models under different blade numbers. It can be found that in any state, the maximum pressure of the HCP132-2.0 model is the highest, followed by the HCP132-4-0 model, and the HCP132-5-0 model is the lowest. The maximum pressure fluctuation amplitude of the HCP132-2.0 model is 1.2 kPa, the HCP132-4-0 model is 0.6 kPa, and the HCP132-5-0 model is 0.4 kPa. The results show that the more blades the rotor has, the smaller the pressure fluctuation inside the pump chamber, and the lower the amplitude of the output pressure fluctuation, which is consistent with the trend of the pressure fluctuation factor of each model in Figure 8B.

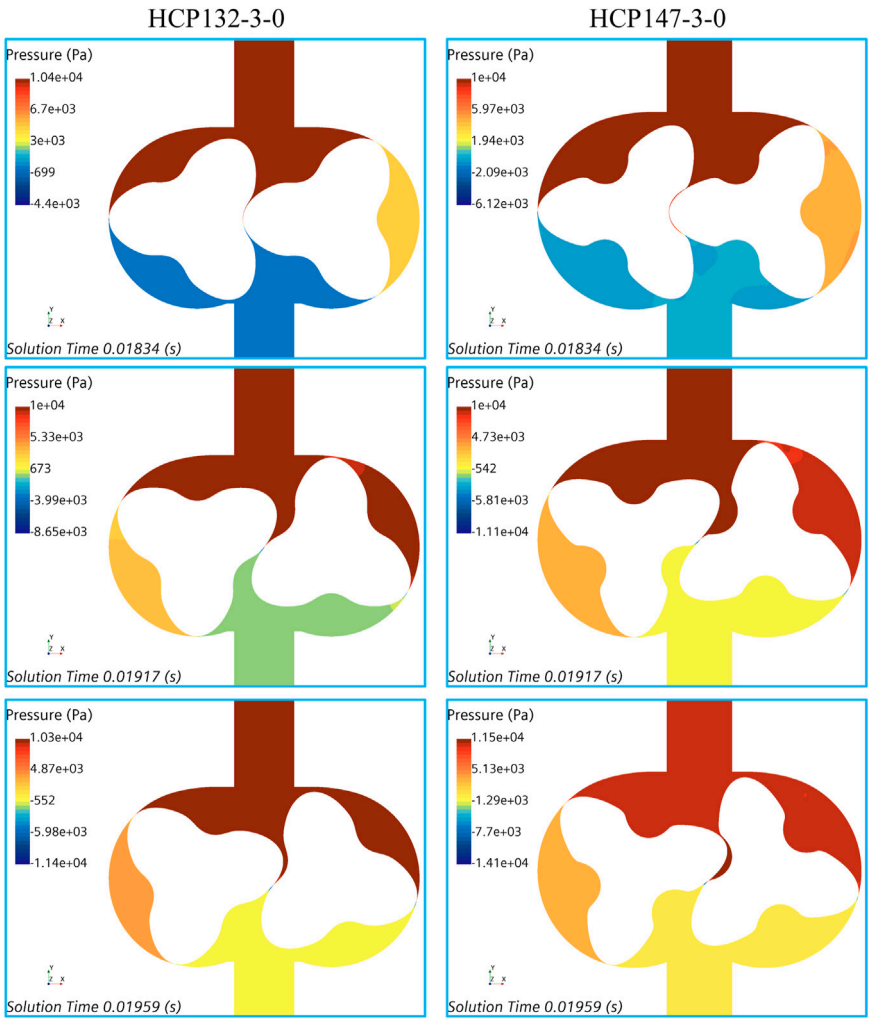

FIGURE 7
Pressure distribution comparison of HCP models with different diameter-to-pitch ratios.

4.3 Phase comparison of the models

According to the multifactor and multi-objective coupling design method, the optimal stage selection of the HCP model is carried out in the following stages.

(1) Based on the simulation calculation results, calculate the objective functions $f(\kappa, Z, \varphi)$ of the different diameter-to-pitch ratio models and the different rotor blade number models, the influence factor of diameter-to-pitch ratio on the objective functions $V_{f(\kappa)}$, and the influence factor of the blade number on the objective functions $V_{f(Z)}$, as shown in Tables 2, 3.

(2) Based on the calculation results, $\kappa_a = 1.47$, $\kappa_b = 1.32$, $Z_i = 5$, and $Z_j = 2$ are determined. Due to $\kappa_a > \kappa_b$ and $Z_i > Z_j$, the comparison process between influencing factors $V_{f(\kappa)}$ and $V_{f(Z)}$ is activated

(3) As $V_{f(\kappa)} = 12.3\%$ and $V_{f(n)} = 6.2\%$, it can be found that $V_{f(\kappa)} > V_{f(n)}$. It is necessary to design the rotor profile with the maximum number of blades $Z = Z_k$ under the condition $\kappa = \kappa_a$, that is, $\kappa = 1.47$, $Z = 3$. Based on this profile, analyze the influence of the helix angle on the flow characteristics of the HCP.

4.4 The influence of helix angle on the performance of HCP

Figure 11 shows the average flow rate, flow pulsation value, and pressure pulsation value changes of different helix angle models, used to summarize the influence of helix angle on the flow characteristics of the HCP. Firstly, analyze the impact of the helix angle on the average flow rate of HCP: as the helix angle increases, the average flow rate of the HCP gradually decreases within the range of 0°–22.5°, and increases within the range of 22.5°–60°; the HCP147-3-22.5 model with a helix angle of 22.5° has the smallest average flow rate of 33.6 Nm^3/h, and the HCP147-3-60 model with a helix angle of 60° has the highest average flow rate of 45.1 Nm^3/h, which is equivalent to the flow rate of the straight blade rotor model. Secondly, analyze the impact of the helix angle on the

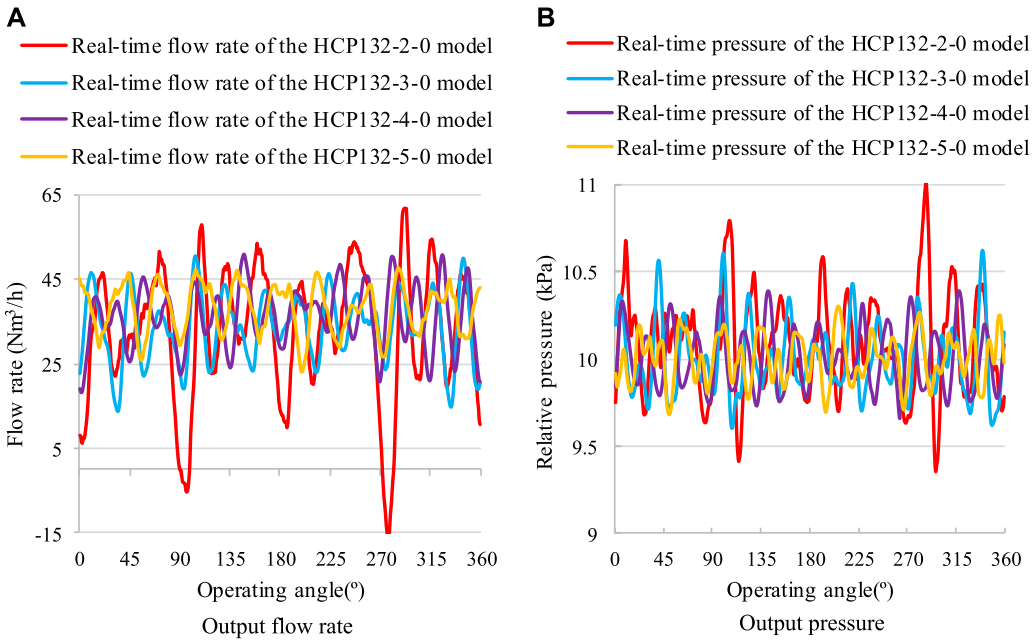

FIGURE 8
Performance of HCP models with different blade numbers. **(A)** Output flow rate **(B)** Output pressure.

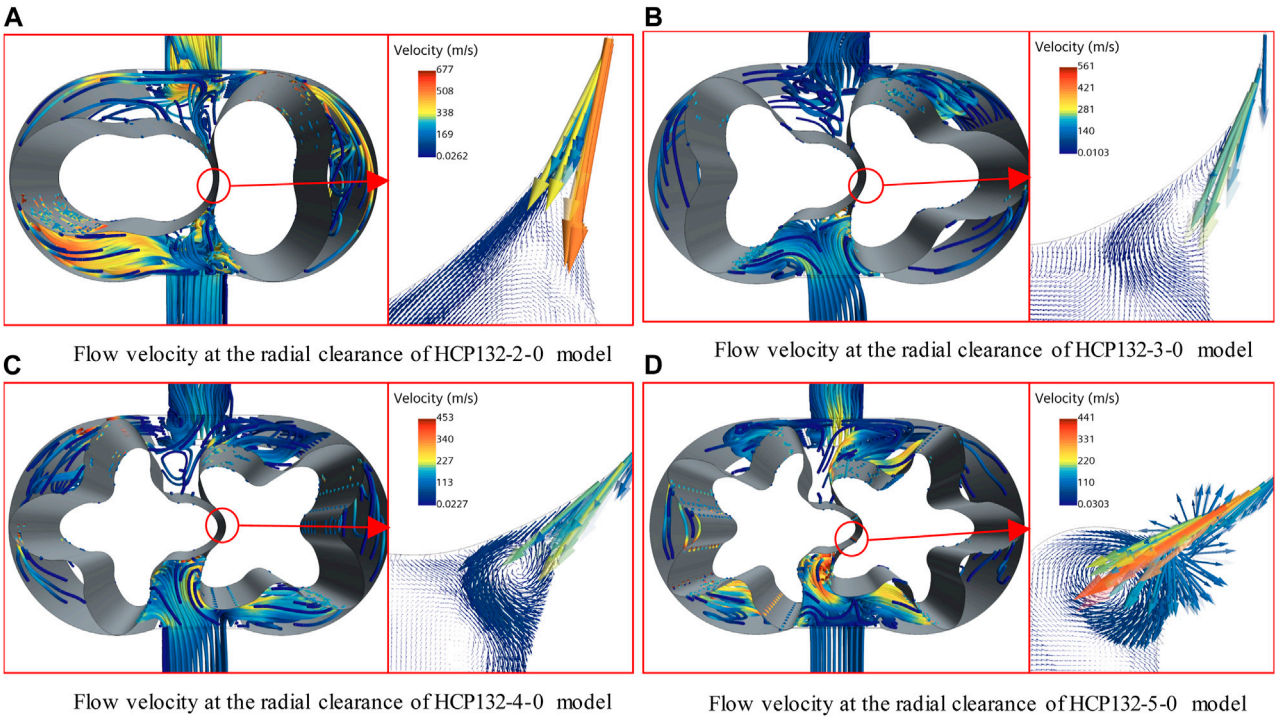

FIGURE 9
Variation of flow velocity at the radial clearance in HCP models with different blade numbers. **(A)** Flow velocity at the radial clearance of HCP132-2-0 model **(B)** Flow velocity at the radial clearance of HCP132-3-0 model **(C)** Flow velocity at the radial clearance of HCP132-4-0 model **(D)** Flow velocity at the radial clearance of HCP132-5-0 model.

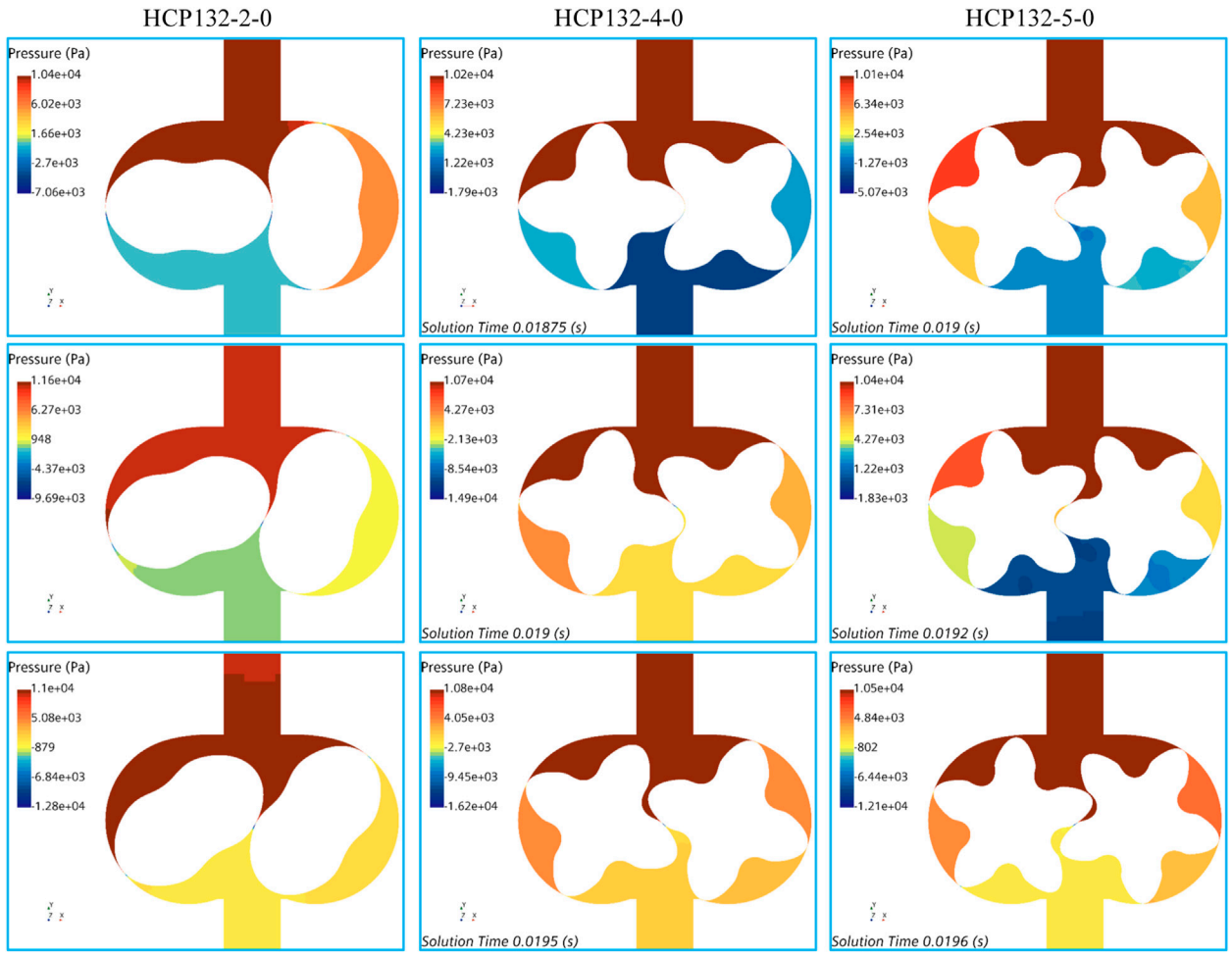

FIGURE 10
Pressure distribution comparison of HCP models with different blade numbers.

TABLE 2 Calculation of HCP models under different diameter-to-pitch ratios.

Models	Q_{avg}	K_Q	K_P	f (κ, Z, φ)	V_f (k) (%)
HCP147-3-0	45.0	0.914	1.01e-3	47.1	12.3
HCP139-3-0	37.0	1.194	1.08e-3	38.8	
HCP132-3-0	33.6	1.098	1.02e-3	35.5	

TABLE 3 Calculation of HCP models with different blade numbers.

Models	Q_{avg}	K_Q	K_P	f (κ, Z, φ)	V_f (Z) (%)
HCP132-2-0	32.4	2.412	1.65e-3	33.4	6.2
HCP132-3-0	33.6	1.097	1.01e-3	35.5	
HCP132-4-0	36.1	0.909	0.74e-3	38.6	
HCP132-5-0	38.0	0.656	0.63e-3	41.1	

real-time flow pulsation characteristics of HCP: as the helix angle increases, the average flow rate of the HCP gradually increases within the range of 0°–15°, and decreases within the range of 15°–60°; the model with a helix angle of 15° has the maximum flow pulsation value of K_Q = 1.28, and the model with a helix angle of 60° has the minimum flow pulsation value of K_Q = 0.41. Thirdly, analyze the impact of helix angle on the real-time pressure pulsation characteristics of HCP: the pressure pulsation value of the HCP shows a decreasing trend as the helix angle increases, with a small declining rate within the range of 0°–30°, and even an increase at the helix angle of 7.5°; the declining rate is significant within the range of 30°–60°, and the pressure pulsation reaches its minimum value of $K_P = 0.27 \times 10^{-3}$ when the helix angle is 60°.

The change in helix angle does not change the theoretical flow rate of the HCP model but causes a change in the actual output flow rate, which is because the change in helix angle can cause a change in the back-flow rate at the clearance. Figure 12 shows the flow velocity vectors of the horizontal and vertical sections at the middle position of the HCP models under different helix angles, used for in-depth

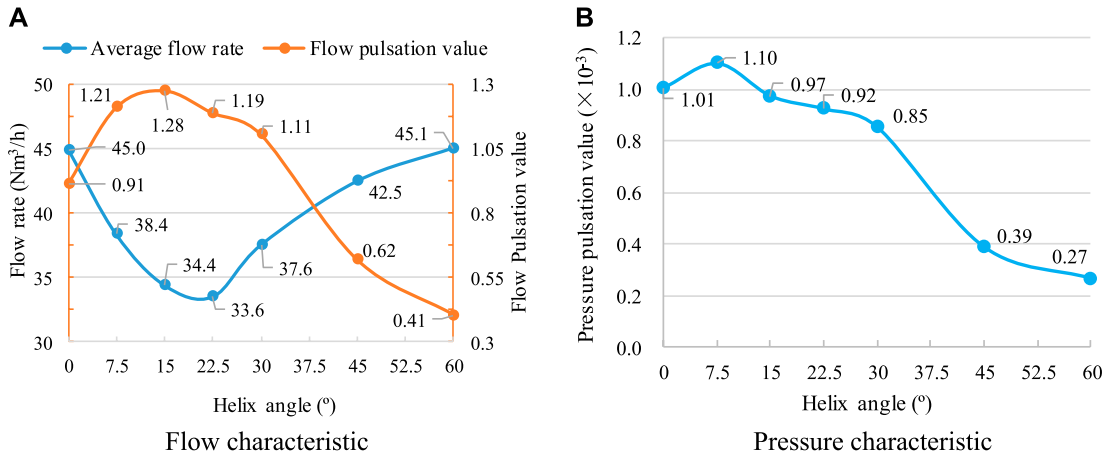

FIGURE 11
Changes in fluid characteristics of HCP models with different helix angles. **(A)** Flow characteristic **(B)** Pressure characteristic.

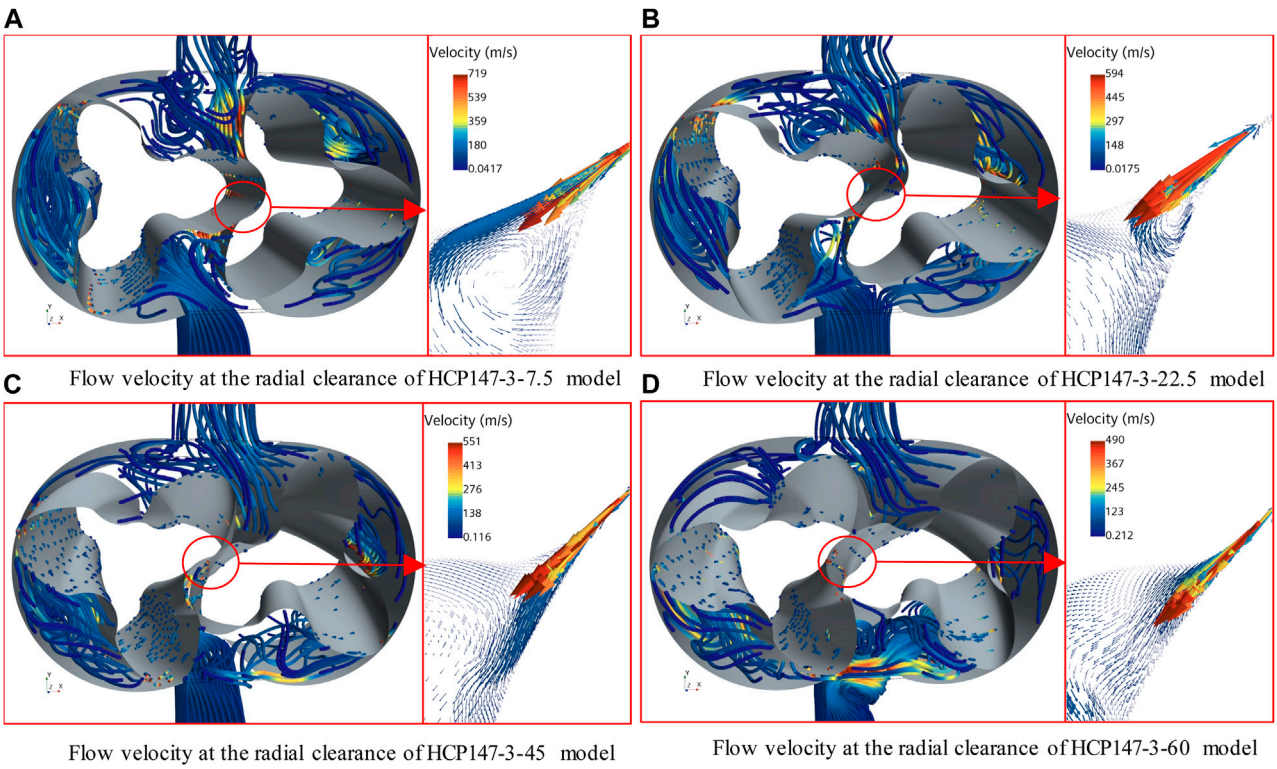

FIGURE 12
Variation of flow velocity at the radial clearance in HCP models with different helix angles. **(A)** Flow velocity at the radial clearance of HCP147-3-7.5 model **(B)** Flow velocity at the radial clearance of HCP147-3-22.5 model **(C)** Flow velocity at the radial clearance of HCP147-3-45 model **(D)** Flow velocity at the radial clearance of HCP147-3-60 model.

analysis of the influence of helix angles on the back-flow at the clearance. Analyzing the flow velocity at the clearance, it is found that the maximum flow velocity decreases with the increase of the helix angle. However, an increase in helix angle will result in an extension of the length of the meshing clearance, which in turn leads to an increase in the cross-sectional area of the back-flow. Under the combined effect of reduced back-flow velocity and increased clearance cross-sectional area, the average flow rate at a 22.5° helix angle is minimized.

Figure 13 shows the comparison of the internal pressure distribution of HCP models under different helix angles. It can be found that the average pressure difference between the

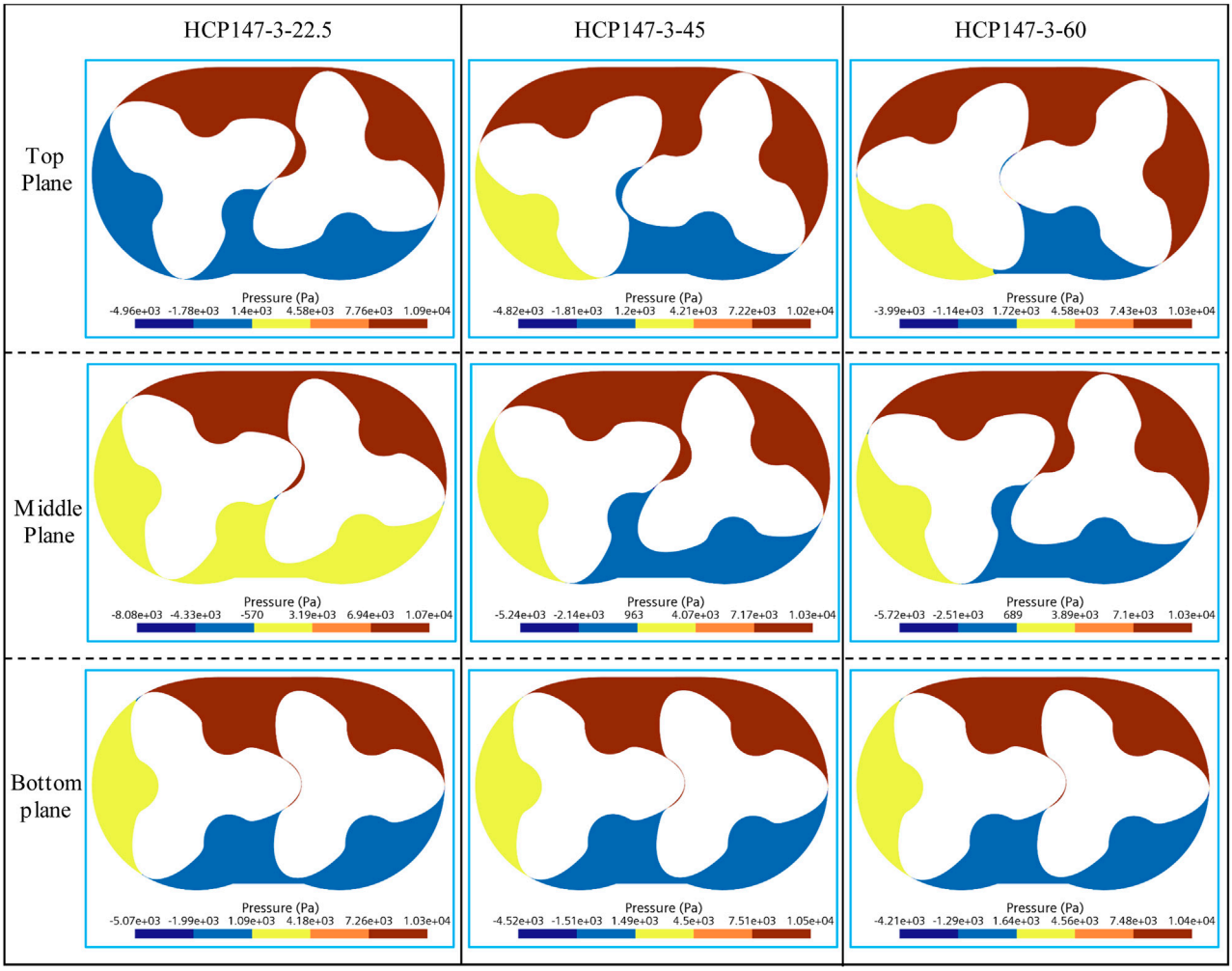

FIGURE 13
Pressure distribution comparison of HCP models with different helix angles.

high-pressure and low-pressure areas inside the HCP147-3-22.5 model is 16.7 kPa, while the HCP147-3-45 model is 15.2 kPa and the HCP147-3-60 model is 15.0 kPa. This indicates that the larger the helix angle, the smaller the internal pressure difference, which is consistent with the trend of the pressure fluctuation factor of each model in Figure 11B. Analyzing its internal mechanism, as the helix angle increases and the volume of the high-pressure zone also increases, the longer the high pressure can be maintained, the smoother the output pressure curve.

5 Determination and verification of the optimal parameter configuration

5.1 Determination of the optimal parameter configuration

According to the multi-objective optimization design method, the effects of two parameters, namely, the diameter-to-pitch ratio and the blade number, on the flow characteristics of the HCP are first analyzed, and the optimal stage model HCP147-3-0 is obtained through comparison. Afterward, rotor models with different helix angles are designed based on the stage optimal model, and the relationship between helix angles and flow characteristics is analyzed.

TABLE 4 Calculation of multi-objective optimization functions under different helix angles.

Models	Q_{avg}	K_Q	K_P	$f(\kappa, Z, \varphi)$
HCP147-3-0	45.0	0.914	1.01e-3	47.0
HCP147-3-7.5	38.4	1.212	1.1e-3	40.1
HCP147-3-15	34.4	1.277	0.97e-3	36.2
HCP147-3-22.5	33.6	1.190	0.92e-3	35.5
HCP147-3-30	37.6	1.106	0.85e-3	39.6
HCP147-3-45	42.5	0.619	0.39e-3	46.7
HCP147-3-60	45.1	0.405	0.27e-3	51.3

Table 4 shows the multi-objective optimization function values for different helix angle models. It can be found that the HCP147-3-

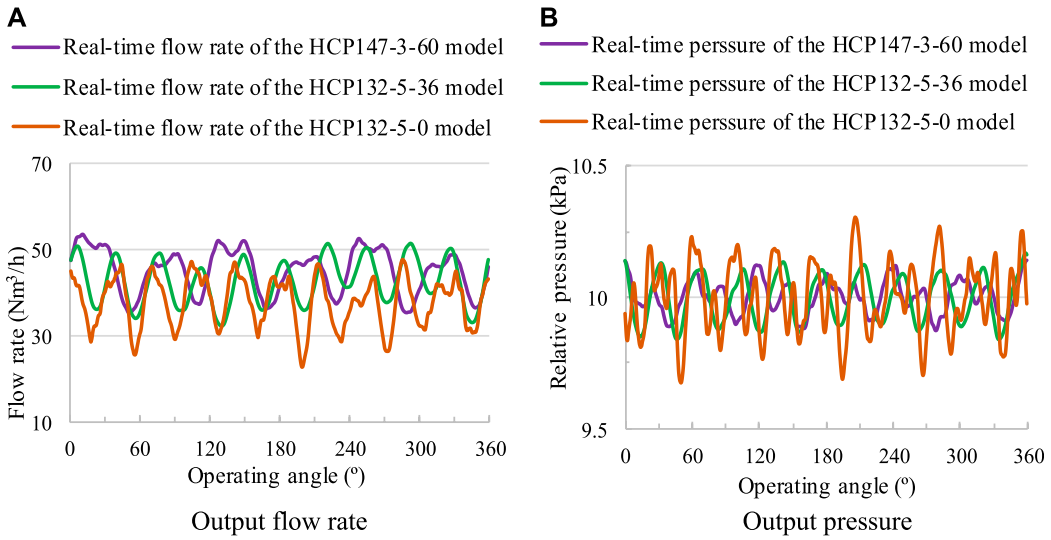

FIGURE 14
Performance comparison between the optimal configuration model and the example model. **(A)** Output flow rate **(B)** Output pressure.

60 model has the highest value of the multi-objective optimization function $f(\kappa, Z, \varphi) = 51.3$, which determines the optimal parameter configuration of the HCP: diameter-to-pitch ratio $\kappa = 1.47$, rotor blade number $Z = 3$, and helix angle $\varphi = 60°$.

5.2 Verification of the optimal parameter configuration

Select some examples with relatively obvious performance advantages to compare with the optimal model HCP147-3-60. Figure 14 shows the performance comparison between the HCP132-5-36 model, the HCP132-5-0 model, and the optimal configuration model. Comparing the flow curves of the HCP132-5-36 model with the HCP132-5-0 model, the average flow rate increased from 37.9 Nm^3/h to 42.5 Nm^3/h after the straight blade rotor became a spiral rotor, the flow fluctuation value decreased from 0.657 to 0.454, and the pressure fluctuation value decreased from 0.63×10^{-3} to 0.33×10^{-3}, indicating that the overall performance of the HCP132-5-36 model is better than that of the HCP132-5-0 model. However, compared with the HCP147-3-60 model, the average flow rate of the HCP132-5-36 model is relatively low, and the flow fluctuation value and pressure fluctuation value are relatively high, resulting in relatively poor overall performance. After calculation, the multi-objective optimization function value of the HCP132-5-36 model is slightly smaller than that of the HCP147-3-60 model, verifying that the HCP147-3-60 model is the optimal configuration model.

6 Conclusion

This article proposes a multifactor and multi-objective coupling design method based on the elliptical profile. By calculating and analyzing the effects of factors such as diameter-to-pitch ratio, blade number, and helix angle on the performance of HCPs based on the verified overset grid simulation method, the optimal configuration of the HCP model is determined, and the optimal results are verified through examples. The main conclusions formed are as follows:

(1) A multifactor and multi-objective coupling design method is proposed. A multi-objective optimization function has been defined, which can adapt to different needs by adjusting the weight factor of the flow pulsation value and the pressure pulsation value. A multifactor and multi-objective coupling design process has been established, and the optimal stage model is determined by comparing the influence factors of the diameter-to-pitch ratio and the blade number on the objective function. Based on this, the influence of the helix angle is considered to determine the optimal model. The proposed coupling design method can effectively achieve the optimal parameter configuration of the HCP, which is beneficial for improving the overall performance.

(2) The effects of design parameters such as diameter-to-pitch ratio, blade number, and helix angle on the flow characteristics of HCP are studied. It is found that the average flow rate of the HCP is directly proportional to the diameter-to-pitch ratio and the blade number, gradually decreases in the range of helix angle from 0° to 22.5°, and increases in the range of helix angle from 22.5° to 60°. The flow pulsation value and pressure pulsation value of the HCP are less affected by the diameter-to-pitch ratio, decrease with the increase of the blade number, and show a trend of first increasing and then decreasing with the increase of the helix angle, and both reach their minimum values when the helix angle is 60°.

(3) The optimal parameter configuration of the HCP model has been completed, and the optimal model is determined as HCP147-3-60, with a diameter-to-pitch ratio $\kappa = 1.47$, rotor blade number $Z = 3$, helix angle $\varphi = 60°$. The average flow rate of the optimal model is 45.1 Nm^3/h, the flow pulsation value $K_Q = 0.405$, the pressure pulsation value $K_P = 0.27 \times 10^{-3}$, and the multi-objective optimization function value is 51.3. The

design result is validated using another model HCP132-5-36 with significant performance advantages, the multi-objective optimization function value of which is slightly lower than the optimal model HCP147-3-60. The comparison results verified the feasibility of the multifactor and multi-objective coupling design method.

7 Recent developments and future directions

HCP has gradually become a hot spot in the development of the fuel cell industry, which is significant to the advancement of fuel cell industrialization in the future. In recent years, numerous researches have been conducted on the internal flow characteristics of the HCP. However, there are still some knowledge gaps, especially, the HCP generates significant noise during operation due to the high-speed rotation of the rotor and gas compression, which reduces user comfort and is of great research significance and difficulty. It has become an important research direction in the future.

Data availability statement

The original contributions presented in the study are included in the article/supplementary material, further inquiries can be directed to the corresponding author.

Author contributions

HZ: Writing–original draft, Writing–review and editing. WL: Writing–review and editing. JL: Writing–review and editing, Data curation. CS: Writing–review and editing, Software. LJ: Writing–review and editing, Methodology. YX: Writing–review and editing, Methodology.

Funding

The author(s) declare that financial support was received for the research, authorship, and/or publication of this article. The work was sponsored by the sixth phase of the “169 Project” scientific research project in Zhenjiang, the National Natural Science Foundation of China (No. 52179085), the National Key R&D Program Project (No. 2020YFC1512405), the Sixth “333 High Level Talented Person Cultivating Project” of Jiangsu Province, Funded projects of “Blue Project” in Jiangsu Colleges and Universities.

Conflict of interest

YX was employed by the Beijing Drainage Group.

The remaining authors declare that the research was conducted in the absence of any commercial or financial relationships that could be construed as a potential conflict of interest.

Publisher’s note

References

Chen, Z. B., and Zou, Y. Z. (2019). The effect of rotor blade number on performance of rotor pump. *Mach. Des. Manuf.* 03, 196–199. doi:10.19356/j.cnki.1001-3997.2019.03.048

Gao, P. T. (2022). Flow field calculation and internal transient flow characteristics of hydrogen circulating pump. *Jiangsu Univ.* doi:10.27170/d.cnki.gjsuu.2022.002661

Gu, P. T., Xing, L. F., Wang, Y. F., Feng, J. M., and Peng, X. Y. (2021). A multi-objective parametric study of the claw hydrogen pump for fuel cell vehicles using Taguchi method and ANN. *Int. J. Hydrogen Energy* 46 (9), 6680–6692. doi:10.1016/j.ijhydene.2020.11.186

Li, D. T., He, Z. L., Sun, S. H., Wang, C., Chen, W. Q., and Xing, Z. W. (2021a). Development and analysis of novel six-lobe helical rotors for hydrogen fuel cell vehicle roots blowers. *Int. J. Hydrogen Energy* 46 (59), 30479–30493. doi:10.1016/j.ijhydene.2021.06.199

Li, L. (2021). Design of rotor geometric parameters and aerodynamic performance of cam gas circulating pump for fuel cell. *Lanzhou Univ. Technol.* doi:10.27206/d.cnki.ggsgu.2021.000632

Li, Q., Wang, H., and Huang, Z. Q. (2022). Research on influence of meshing clearance and number of rotor blades on pump performance. *Chin. J. Process Eng.* 22 (12), 1666–1675. doi:10.12034/j.issn.1009-606X.221438

Li, Y. B., Guo, D. S., and Tang, Y. L. (2020). Effect of the rotor diameter-length ratio on the rotary lobe pump performance based on numerical simulations and experimental tests. *J. Vib. shock* 39 (09), 194–200+220. doi:10.13465/j.cnki.jvs.2020.09.027

Li, Y. B., Li, L., and Liu, J. F. (2021b). Numerical study on the aerodynamic performance of multi-blade rotor cavity in the gas circulating pump of fuel cell. *J. XiAn Jiaot. Univ.* 55 (03), 46–56. doi:10.7652/xjtuxb202103006

Li, Y. B., Zhang, X. Z., Guo, D. S., and Wang, X. F. (2018). Numerical analysis and verification of flow characteristics of rotor cavity of spiral rotary lobe pump. *Trans. CSAE* 34 (10), 62–67. doi:10.11975/j.issn.1002-6819.2018.10.007

Liu, Y., Tu, Z. K., and Siew, H. C. (2021b). Applications of ejectors in proton exchange membrane fuel cells: a review. *Fuel Process. Technol.* 214, 106683. doi:10.1016/j.fuproc.2020.106683

Liu, Y., Tu, Z. K., and Siew, H. C. (2023a). Performance evaluation and degradation mechanism for proton exchange membrane fuel cell with dual exhaust gas recirculation. *Adv. Energy Sustain. Res.* 4, 22200180. doi:10.1002/aesr.202200180

Liu, Y., Tu, Z. K., and Siew, H. C. (2023b). Performance analysis and dynamic characteristics of a proton exchange membrane fuel cell with dual recirculation pumps for air-free applications. *J. Power Sources* 566, 232923. doi:10.1016/j.jpowsour.2023.232926

Liu, Y., Xiao, B., Zhao, J. J., Fan, L. X., Luo, X. B., Tu, Z. K., et al. (2021a). Performance degradation of a proton exchange membrane fuel cell with dual ejector-based recirculation. *Energy Convers. Manag. X.* 12, 100114. doi:10.1016/j.ecmx.2021.100114

Liu, Y. F., Fan, L., Pei, P. C., Yao, S. Z., and Wang, F. (2018). Asymptotic analysis for the inlet relative humidity effects on the performance of proton exchange membrane fuel cell. *Apply Energy* 213, 573–584. doi:10.1016/j.apenergy.2017.11.008

Rao, L., and Zhong, Y. C. (2021). Axial clearance effects on performance of gerotor pump using numerical simulation. *Mach. Build. Automation* 50 (05), 110–112. doi:10.19344/j.cnki.issn1671-5276.2021.05.029

Singh, G., Sun, S. H., Ahmed, K., Li, Q. H., and Bruecker, B. (2019). Transient flow analysis in a Roots blower: experimental and numerical investigations. *Mech. Syst. Signal Process.* 134, 106305. doi:10.1016/j.ymssp.2019.106305

Wang, Y. P., Ma, Q. Y., and Zhao, H. H. (2019). Fuel cell engine technology overview. *Automot. Dig.* 01, 42–47.

Wiebe, W., Thomas, U., and Sven, S. (2020). Hydrogen pump for hydrogen recirculation in fuel cell vehicles. *E3S Web Conf.* 155, 01001. doi:10.1051/e3sconf/202015501001

Xing, Y. Z., Li, Y. B., and Zhang, S. F. (2023). Effects of helical angle on performance and flow pulsation characteristics of aviation fuel gear pump. *J. Propuls. Technol.* 44 (03), 142–153. doi:10.13675/j.cnki.tjjs.2205089

Yang, Y. M. (2022). Fuel cell gas circulating pump rotor chamber internal transient research on the flow and pneumatic properties. *Lanzhou Univ. Technol.* doi:10.27206/d.cnki.ggsgu.2022.001413

Yang, Y. M., Zhang, Z. Y., and Li, L. (2022). Influence of rotor diameter-distance ratio on performance of fuel cell gas circulating pump. *J. Aerosp. Power* 37 (09), 1970–1978. doi:10.13224/j.cnki.jasp.20210348

Zhai, H. L., Li, W., Ji, L. L., Li, J. W., Li, S., et al. (2022). Profile design and performance research of hydrogen circulation pump in fuel cell system. *Mechanika* 28 (4), 283–293. doi:10.5755/j02.mech.31528

Zhai, H. L., Li, W., Ji, L. L., Li, S., Cao, Y. H., and Li, Y. K. (2023). Research on measurement method for high-frequency pulsation flow of hydrogen circulating pump. *Int. J. Hydrogen Energy* 48 (39), 14853–14865. doi:10.1016/J.IJHYDENE.2022.12.358

Zhang, Q. Q., Feng, J. M., Zhang, Q. Q., and Peng, X. Y. (2019). Performance prediction and evaluation of the scroll-type hydrogen pump for FCVs based on CFD-Taguchi method. *Int. J. Hydrogen Energy* 44 (29), 15333–15343. doi:10.1016/j.ijhydene.2019.04.019

Zhang, X. Z. (2018). Influence of rotor geometric parameters on flow characteristics of rotary lobe pump. *Lanzhou Univ. Technol.*

Zhou, S., Fan, L., Zhang, G., Gao, J. H., Lu, Y., Zhao, P., et al. (2022). A review on proton exchange membrane multi-stack fuel cell systems: architecture, performance, and power management. *Appl. Energy* 310, 118555. doi:10.1016/j.apenergy.2022.118555

Zhou, S. M., Jia, X. H., Yan, H. M., and Peng, X. Y. (2021). A novel profile with high efficiency for hydrogen-circulating Roots pumps used in FCVs. *Int. J. Hydrogen Energy* 46 (42), 22122–22133. doi:10.1016/j.ijhydene.2021.04.038

10.3389/fenrg.2024.1358911

Nomenclature

κ	Diameter-to-pitch ratio
Z	Rotor blade number
φ	Helix angle
Q_{avg}	The Fourier pressure curve fitted according to
K_Q	The flow pulsation value
K_P	The pressure pulsation value
$V_{f(\kappa)}$	The influence factor of the diameter-to-pitch ratio on the objective function
$V_{f(Z)}$	The influence factor of the blade number on the objective function.

Frontiers in
Energy Research

Advances and innovation in sustainable, reliable and affordable energy

Explores sustainable and environmental developments in energy. It focuses on technological advances supporting Sustainable Development Goal 7: access to affordable, reliable, sustainable and modern energy for all.

Discover the latest Research Topics

See more →

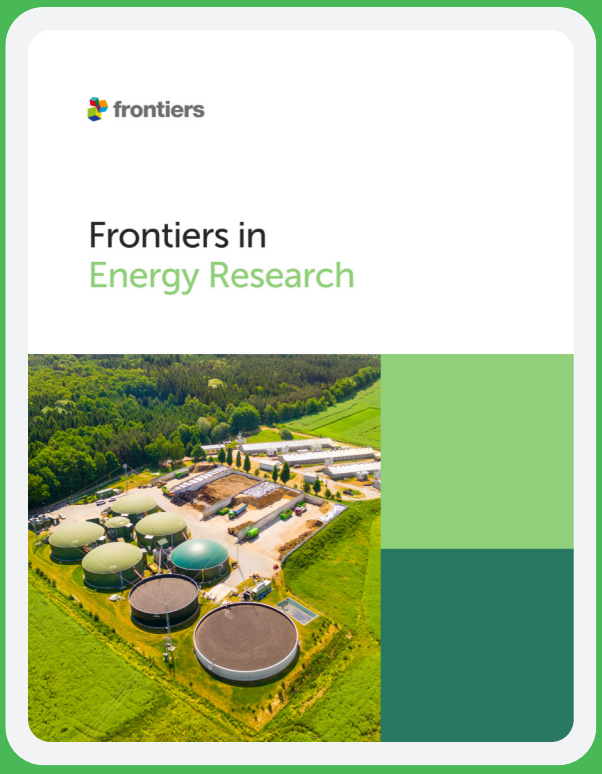

Frontiers

Avenue du Tribunal-Fédéral 34
1005 Lausanne, Switzerland
frontiersin.org

Contact us

+41 (0)21 510 17 00
frontiersin.org/about/contact